



UNIVERSIDAD NACIONAL DEL LITORAL
DOCTORADO EN INGENIERÍA

**Vulnerabilidad y riesgo a amenazas
múltiples por eventos
hidrometeorológicos extremos en el
centro-noreste de Argentina**

Ing. María Josefina Pierrestegui

FICH

FACULTAD DE INGENIERÍA Y CIENCIAS HÍDRICAS

INTEC

INSTITUTO DE DESARROLLO TECNOLÓGICO PARA LA INDUSTRIA QUÍMICA

CIMEC

CENTRO DE INVESTIGACIÓN DE MÉTODOS COMPUTACIONALES

sinc(i)

INSTITUTO DE INVESTIGACIÓN EN SEÑALES, SISTEMAS E INTELIGENCIA
COMPUTACIONAL

Tesis de Doctorado **2025**



Doctorado en Ingeniería mención Recursos Hídricos

Título de la obra:

Vulnerabilidad y riesgo a amenazas múltiples por eventos hidrometeorológicos extremos en el centro-noreste de Argentina

Autora: Ing. María Josefina Pierrestegui

Lugar: Santa Fe, Argentina

Palabras Claves:

eventos hidrometeorológicos extremos, amenazas múltiples, riesgo, vulnerabilidad



UNIVERSIDAD NACIONAL DEL LITORAL
Facultad de Ingeniería y Ciencias Hídricas
Instituto de Desarrollo Tecnológico para la Industria Química
Centro de Investigación de Métodos Computacionales
Instituto de Investigación en Señales, Sistemas e Inteligencia Computacional

**VULNERABILIDAD Y RIESGO A AMENAZAS
MÚLTIPLES POR EVENTOS
HIDROMETEOROLÓGICOS EXTREMOS EN EL
CENTRO-NORESTE DE ARGENTINA**

Ing. María Josefina Pierrestegui

Tesis remitida al Comité Académico del Doctorado
como parte de los requisitos para la obtención
del grado de
DOCTOR EN INGENIERÍA
Mención Recursos Hídricos
de la
UNIVERSIDAD NACIONAL DEL LITORAL

2025

Secretaría de Posgrado, Facultad de Ingeniería y Ciencias Hídricas, Ciudad Universitaria, Paraje “El Pozo”, S3000, Santa Fe, Argentina



ACTA DE EVALUACIÓN DE TESIS DE DOCTORADO

En la sede de la Facultad de Ingeniería y Ciencias Hídricas de la Universidad Nacional del Litoral, a los dieciocho días del mes de junio del año dos mil veinticinco, se reúnen en forma online sincrónica los miembros del Jurado designado para la evaluación de la Tesis de Doctorado en Ingeniería, Mención Recursos Hídricos, titulada "*Vulnerabilidad y riesgo a amenazas múltiples por eventos hidrometeorológicos extremos en el centro-noreste de Argentina.*", desarrollada por la Ing. María Josefina PIERRESTEGUI, DNI N° 31.022.132, bajo la dirección de la Dra. Gabriela Müller y la codirección del Dr. Miguel Lovino. Ellos son: Dra. Olga Penalba, el Dr. Marcelo Barreiro y el Dr. René Garreauad.

La Presentación oral y defensa de la Tesis se efectúan bajo la modalidad online sincrónica según lo establecido por Resolución CS N° 382/21.

Luego de escuchar la Defensa Pública y de evaluar la Tesis, el Jurado considera:

Que el estudio consistió en el análisis de amenazas múltiples asociadas a eventos hidrometeorológicos extremos en el centro-norte de Argentina cuyo objetivo final es evaluar los niveles de vulnerabilidad y riesgo.

Se destaca la integralidad del análisis que considera desde la escala regional al detalle departamental. Sus resultados son novedosos y constituyen un aporte al desarrollo de políticas públicas de mitigación del riesgo.

El manuscrito está bien estructurado y redactado con mucha claridad, siguiendo un orden lógico con el apoyo de figuras de buena calidad.

La tesis resultó en dos publicaciones en revistas de alto impacto siendo la tesista la primera autora, y además participó en otros artículos.

La presentación ha sido muy clara, fluida y didáctica, y ha respondido con solvencia las preguntas y observaciones formuladas por el jurado.

Por lo tanto, el jurado aprueba la tesis con calificación 10 (Diez) Sobresaliente.

Sin más, se da por finalizado el Acto Académico con la firma de los miembros del Jurado al pie de la presente.

Dra. Olga Penalba

Dr. Marcelo Barreiro

Dr. René Garreauad

Dr. JOSE LUIS MACOR
SECRETARIO DE POSGRADO
Facultad de Ingeniería y Cs. Hídricas

Universidad Nacional del Litoral

Facultad de Ingeniería y
Ciencias Hídricas

Secretaría de Posgrado

Ciudad Universitaria

C.C. 217

Ruta Nacional N° 168 – Km. 472,4
(3000) Santa Fe

Tel: (54) (0342) 4575 229

Fax: (54) (0342) 4575 224

E-mail: posgrado@fich.unl.edu.ar

DECLARACIÓN DEL AUTOR

Esta disertación ha sido remitida como parte de los requisitos para la obtención del grado académico de Doctora en Ingeniería ante la Universidad Nacional del Litoral y ha sido depositada en Repositorio Institucional de Acceso Abierto -RIAA- de la Facultad de Ingeniería y Ciencias Hídricas para que esté disponible a sus lectores bajo las condiciones estipuladas.

Citaciones breves de esta disertación son permitidas sin la necesidad de un permiso especial, en la suposición de que la fuente sea correctamente citada. Solicitudes de permiso para una citación extendida o para la reproducción parcial o total de este manuscrito serán concedidos por el portador legal del derecho de propiedad intelectual de la obra.

M. Josefina Pierrestegui

DEDICATORIA

A Milo, por su fuerza desde antes de nacer y por inspirarme a dejarle un mundo más habitable

A Esteban, por creer en mí y ser un pilar constante que me impulsa a seguir adelante

A mis padres, Marina y Juan Carlos, por su apoyo incondicional y guía en cada paso del camino

A mis cuatro abuelos, por inculcarme el amor por la naturaleza y el interés por comprenderla

Ustedes son mi mayor inspiración para soñar y construir un futuro mejor

AGRADECIMIENTOS

Al Estado Argentino, por financiar mi formación de grado y posgrado de calidad a través de la Universidad Pública y una Beca Interna Doctoral del Consejo Nacional de Investigaciones Científicas y Técnicas (CONICET), que hicieron posible mi desarrollo académico y este trabajo.

Al CEVARCAM de la Facultad de Ingeniería y Ciencias Hídricas (UNL), donde desarrollé esta tesis, y a la UNL, el CONICET y la Agencia I+D+i, por el financiamiento de proyectos que apoyaron este trabajo.

A Miguel Lovino y Gabriela Müller, por su invaluable guía, generosidad y motivación para alcanzar mis objetivos. Su apoyo profesional y humano fue esencial para la culminación de este trabajo.

A mis compañeros del CEVARCAM, por su confianza y apoyo para contribuir a mi desarrollo; a los docentes de las Facultades de Ingeniería y Ciencias Hídricas y Químicas (UNL), Ciencias Exactas y Naturales (UBA), y de la Escuela de Ciencia y Tecnología (UNSAM), por su excelencia formativa.

A la comunidad científica, que brinda herramientas de libre acceso que me permitieron trabajar con mayor eficiencia y calidad, y a los colegas de quienes tuve el privilegio de aprender. A Fabio Cramerí por sus mapas de color científicos inclusivos utilizados en este trabajo para garantizar la accesibilidad y precisión en la visualización de los datos.

A mis amigos del doctorado, Edna, Flor, Gabi y Fer, por compartir conocimientos y charlas esenciales en este camino.

A mis amigos de la vida, Ceci, Vico, Belu, Cari y Migue, por su aliento y apoyo constante.

Y a Milo, Esteban, mi familia y la familia de Esteban, por su amor y por ser mi pilar en cada paso de este camino.

ÍNDICE GENERAL

| | |
|---|----|
| ÍNDICE GENERAL | I |
| ÍNDICE DE FIGURAS..... | IV |
| ÍNDICE DE TABLAS..... | IV |
| RESUMEN | V |
| ABSTRACT..... | VI |
| Capítulo 1: Introducción | 1 |
| 1.1. Introducción general..... | 1 |
| 1.2. Región de estudio | 3 |
| 1.3. Hipótesis..... | 5 |
| 1.4. Objetivos | 5 |
| 1.4.1. Objetivo general | 5 |
| 1.4.2. Objetivos específicos..... | 5 |
| 1.5. Estructura de la tesis doctoral..... | 5 |
| Capítulo 2: Evaluación de amenazas múltiples por eventos hidrometeorológicos extremos | 7 |
| 2.1. Introducción | 7 |
| 2.2. Datos | 8 |
| 2.3. Metodología | 9 |
| 2.3.1. Detección de eventos hidrometeorológicos extremos de largo plazo | 9 |
| 2.3.2. Detección de eventos hidrometeorológicos extremos de corto plazo | 10 |
| 2.3.3. Cuantificación de las amenazas..... | 11 |
| 2.4. Resultados | 13 |
| 2.4.1. Amenazas por eventos hidrometeorológicos extremos de largo plazo | 13 |
| 2.4.1.1. Eventos extremos de exceso de precipitación | 13 |
| 2.4.1.2. Eventos extremos de déficit de precipitación | 16 |
| 2.4.2. Amenazas por eventos hidrometeorológicos extremos de corto plazo | 19 |
| 2.4.2.1. Olas de calor..... | 19 |
| 2.4.2.2. Eventos de precipitación intensa | 20 |
| 2.4.2.3. Sequías repentinas | 22 |
| 2.4.3. Amenazas hidrometeorológicas múltiples de largo y corto plazo | 23 |

| | | |
|----------|--|----|
| 2.4.3.1. | Amenazas múltiples de largo plazo | 23 |
| 2.4.3.2. | Amenazas múltiples de corto plazo | 25 |
| 2.4.3.3. | Composición total de amenazas múltiples..... | 27 |
| 2.5. | Síntesis | 28 |
| | Capítulo 3: Vulnerabilidad y riesgo a amenazas hidrometeorológicas múltiples | 31 |
| 3.1. | Introducción | 31 |
| 3.2. | Datos | 32 |
| 3.3. | Metodología | 35 |
| 3.3.1. | Marco utilizado para evaluar vulnerabilidad y riesgo | 35 |
| 3.3.2. | Amenazas hidrometeorológicas individuales y múltiples | 36 |
| 3.3.3. | Componentes de vulnerabilidad | 38 |
| 3.3.4. | Cuantificación de la vulnerabilidad..... | 39 |
| 3.3.5. | Cuantificación del riesgo..... | 41 |
| 3.4. | Resultados | 41 |
| 3.4.1. | Componentes de vulnerabilidad | 41 |
| 3.4.1.1. | Exposición..... | 41 |
| 3.4.1.2. | Sensibilidad | 43 |
| 3.4.1.3. | Capacidad adaptativa..... | 45 |
| 3.4.2. | Índice de vulnerabilidad | 47 |
| 3.4.3. | Evaluación del riesgo | 48 |
| 3.4.3.1. | Riesgo por amenazas hidrometeorológicas individuales | 48 |
| 3.4.3.2. | Riesgo debido a amenazas hidrometeorológicas múltiples | 52 |
| 3.5. | Síntesis | 54 |
| | Capítulo 4: Discusión y conclusiones | 56 |
| 4.1. | Síntesis del marco metodológico..... | 56 |
| 4.2. | Evaluación de amenazas hidrometeorológicas múltiples | 57 |
| 4.3. | Vulnerabilidad y riesgo a amenazas hidrometeorológicas múltiples | 59 |
| 4.4. | Conclusiones y recomendaciones finales | 61 |
| | Listado de siglas y abreviaturas | 64 |
| | Referencias..... | 65 |

| | |
|--|-----|
| Anexo I: Material Suplementario..... | 77 |
| Material Suplementario 1 (MS1): Respuesta de la humedad del suelo y la profundidad del nivel freático ante eventos extremos de precipitación en la región núcleo de cultivos de Argentina (Bernal-Mujica et al. 2023)..... | 78 |
| Material Suplementario 2 (MS2): Metodología y análisis del ciclo de vida de sequías agrícolas repentinas (Lovino et al. 2024; 2025) | 81 |
| Material Suplementario 3 (MS3): Eventos extremos de precipitación en la región del Chaco Austral (Lovino et al. 2022) | 88 |
| Material Suplementario 4 (MS4): Análisis adicional de los componentes de la vulnerabilidad | 93 |
| Anexo II: Artículos científicos compilados en la tesis | 99 |
| Contribuciones de la autora y relevancia de los artículos científicos en el marco de la tesis..... | 99 |
| Publicaciones de los artículos científicos..... | 104 |

ÍNDICE DE FIGURAS

| | |
|--|----|
| Figura 1.1. Región de estudio. | 4 |
| Figura 2.1. Diagrama metodológico del análisis de amenazas múltiples. | 13 |
| Figura 2.2. Amenaza por eventos extremos de exceso de precipitación. | 15 |
| Figura 2.3. Amenaza por eventos extremos de déficit de precipitación. | 17 |
| Figura 2.4. Amenaza por eventos de olas de calor. | 20 |
| Figura 2.5. Amenaza por eventos de precipitación intensa. | 21 |
| Figura 2.6. Amenaza por eventos de sequías repentinas. | 22 |
| Figura 2.7. Amenazas hidrometeorológicas múltiples de largo plazo. | 24 |
| Figura 2.8. Amenazas hidrometeorológicas múltiples de corto plazo. | 26 |
| Figura 2.9. Amenazas hidrometeorológicas múltiples totales. | 28 |
| Figura 3.1. Diagrama metodológico para evaluar la vulnerabilidad y el riesgo. | 37 |
| Figura 3.2. Composición del índice de exposición. | 42 |
| Figura 3.3. Composición del índice de sensibilidad. | 44 |
| Figura 3.4. Composición del índice de capacidad adaptativa. | 47 |
| Figura 3.5. Composición del índice de vulnerabilidad. | 48 |
| Figura 3.6. Composición de los riesgos por amenazas hidrometeorológicas individuales. | 50 |
| Figura 3.7. Composición de los riesgos por amenazas hidrometeorológicas múltiples. | 53 |

ÍNDICE DE TABLAS

| | |
|---|----|
| Tabla 3.1. Componentes de amenaza y vulnerabilidad. | 34 |
| Tabla 3.2. Pesos relativos obtenidos mediante análisis de componentes principales. | 43 |

RESUMEN

La tesis presenta un análisis de las amenazas múltiples asociadas a eventos hidrometeorológicos extremos (EHEs), así como la vulnerabilidad y el riesgo correspondiente, en el centro-noreste de Argentina. Se examina la frecuencia, duración e intensidad de los EHEs en los períodos 1961-1990 y 1991-2020 con datos de ERA5. Esto permite identificar amenazas de largo plazo—excesos y déficits hídricos—, y de corto plazo—olas de calor, precipitaciones intensas y sequías repentinas. Se estudian los cambios históricos y la distribución espacial de las amenazas tanto individuales como múltiples, derivadas por combinación de amenazas individuales. El riesgo se evalúa a escala subnacional para el período 1991-2020, producto de la interacción entre las amenazas por EHEs y la vulnerabilidad específica de la región. La evaluación de la vulnerabilidad se realiza integrando datos físicos y socioeconómicos provenientes de múltiples fuentes, analizando sus componentes claves: exposición, sensibilidad y capacidad adaptativa. Las amenazas múltiples de largo plazo predominan en el suroeste y centro-oeste de la región, afectando la región núcleo de cultivos. En el sur los excesos hídricos son frecuentes, mientras que en el norte y oeste prevalecen las sequías. Las amenazas de corto plazo impactan más en el noreste de la región, con olas de calor (aumentaron un 30% en décadas recientes), sequías repentinas y precipitaciones intensas. Las amenazas totales son más elevadas y espacialmente más extendidas que en 1960-1990. La vulnerabilidad promedio en la región tiene un nivel medio, con diferencias regionales marcadas. En el centro-sur (sur de Santa Fe, este de Córdoba y norte de Buenos Aires), la alta exposición se compensa con baja sensibilidad y alta capacidad adaptativa, resultando en vulnerabilidad media. En el noroeste y centro-oeste (Formosa, Chaco, Santiago del Estero, este de Salta) la vulnerabilidad es alta por su elevada sensibilidad y baja capacidad adaptativa, a pesar de una baja exposición. El riesgo más elevado corresponde a olas de calor, especialmente en el norte. Los excesos y déficits hídricos tienen patrones diferenciados: alto riesgo por déficit en el noroeste y riesgo medio-alto por excesos en el este. Mientras tanto, el riesgo por precipitaciones intensas es alto localmente en el noreste. Pese a las limitaciones derivadas de los datos y los indicadores socioeconómicos, se enfatiza en la necesidad de estrategias de gestión del riesgo específicas. En el sur, se requiere adaptar los sistemas expuestos a las amenazas mediante infraestructura adecuada y prácticas agrícolas inteligentes. En el norte, urge fomentar un desarrollo resiliente para mejorar la capacidad adaptativa y disminuir la sensibilidad.

ABSTRACT

The thesis provides a comprehensive multi-hazard analysis of extreme hydrometeorological events (EHEs) and evaluates vulnerability and risk in central-northeastern Argentina. It investigates the frequency, duration, and intensity of EHEs during 1961-1990 and 1991-2020 using ERA5 data, enabling the identification of long-term hazards—such as water excesses and deficits—and short-term hazards—including heatwaves, intense precipitation, and flash droughts. Historical changes and spatial distributions of individual and multi-hazards (resulting from the interaction of individual hazards) are analyzed. Risk is assessed sub-nationally for 1991-2020 as an interplay between EHE hazards and regional vulnerability. Vulnerability is evaluated through physical and socioeconomic data from multiple sources, focusing on exposure, sensitivity, and adaptive capacity. Long-term hazards dominate the southwest and center-west, impacting the core crop region. Water excesses are prevalent in the south, while droughts affect the north and west. In the northeast, short-term hazards are more severe, with frequent heatwaves (increasing by 30% in recent decades), flash droughts, and intense precipitation. The multi-hazard index is currently higher and more expansive than in 1960-1990, with short-term hazards often coinciding in time, while long-term hazards alternate. Regional vulnerability shows a medium average, with notable variations. In the center-south (southern Santa Fe, eastern Córdoba, and northern Buenos Aires), medium vulnerability results from high exposure balanced by low sensitivity and high adaptive capacity. Conversely, the northwest and center-west (Formosa, Chaco, Santiago del Estero, and eastern Salta) display high vulnerability due to elevated sensitivity and low adaptive capacity, despite low exposure. Heatwaves pose the greatest risk, particularly in the north. The water deficits risk is higher in the northwest, while excess precipitation risks are higher in the east. Locally, intense precipitation risk is significant in the northeast. Despite data and socioeconomic limitations, the findings underline the urgency for region-specific risk management strategies. Infrastructure upgrades and smart agricultural practices are vital in the central region, while fostering resilient development to improve adaptive capacity and reduce sensitivity is imperative in the north.

Keywords: extreme hydrometeorological events; multiple hazards; risk; vulnerability

Capítulo 1: Introducción

1.1. Introducción general

Los eventos hidrometeorológicos extremos (EHEs) producen impactos negativos en los ecosistemas, asentamientos humanos, la producción de alimentos, los recursos hídricos y la salud pública (AghaKouchak et al. 2020; Hagen et al. 2022; Pörtner et al. 2022; Stalhandske et al. 2024). Las sequías y las olas de calor amenazan los recursos de los agricultores y la seguridad alimentaria de las comunidades (Dasgupta y Robinson 2022; Lesk et al. 2022), y pueden desencadenar incendios forestales que devastan los hábitats naturales y la biodiversidad (Sutanto et al. 2020; Vogel et al. 2019). Del mismo modo, las tormentas e inundaciones afectan la actividad agrícola, deterioran la infraestructura urbana, contaminan fuentes de agua e interrumpen las actividades económicas (Kreibich et al. 2022; Müller et al. 2024; Rahmstorf y Coumou 2011).

En los últimos años, la frecuencia e intensidad de los EHEs se ha incrementado en la mayor parte del mundo, con principal atribución al cambio climático de origen antrópico (Clarke et al. 2022; Stott 2016). La magnitud y frecuencia de las olas de calor extremo han aumentado a nivel mundial como consecuencia del calentamiento global, mientras que ciertos eventos extremos de precipitación se han intensificado en regiones específicas (Perkins et al. 2012; Seneviratne et al. 2021; Thackeray et al. 2022). El continuo incremento de las temperaturas a nivel mundial favorece la aparición de extremos sin precedentes, exacerbados por la ocurrencia en simultáneo de múltiples eventos extremos, lo que puede generar impactos inéditos en la sociedad y los ecosistemas (Fischer et al. 2021; Seneviratne et al. 2021; Sun et al. 2019).

Los riesgos y vulnerabilidades asociados al cambio climático y los eventos extremos no solo dependen de la ocurrencia de amenazas de origen climático—como olas de calor, tormentas, inundaciones o sequías—sino también de factores socioeconómicos que influyen en la capacidad de las comunidades para prepararse y responder (Birkmann et al. 2013, 2022; IPCC 2022a; UNDRR 2019). Comprender la interacción entre las amenazas climáticas y la población e infraestructura en áreas específicas es fundamental para planificar estrategias efectivas de mitigación y adaptación (Jurgilevich et al. 2017; O'Neill et al. 2022). Las evaluaciones de vulnerabilidad y riesgo, que combinan datos físicos y socioeconómicos, han surgido como herramientas esenciales para identificar y

abordar estos riesgos en una región o sector determinado (Birkmann et al. 2022; Füssel 2007; Stalhandske et al. 2024).

Si bien los eventos climáticos individuales representan riesgos significativos, muchas localidades están expuestas a múltiples eventos extremos (Garschagen et al. 2021; Tabari y Willems 2023). Dado que el riesgo aumenta cuando las amenazas coinciden en tiempo o espacio, adoptar un marco de amenazas múltiples proporciona un análisis más completo para comprender el riesgo climático (Binita et al. 2021). Además, determinados sectores de la sociedad enfrentan riesgos climáticos magnificados. Las áreas urbanas son particularmente vulnerables debido a sus densa población e infraestructura (Wamsler et al. 2013). Grupos sociodemográficos específicos, como los menores, los mayores, las comunidades dependientes de recursos naturales y las poblaciones de bajos ingresos, se ven desproporcionadamente afectados por las amenazas climáticas (Binita et al. 2021).

En el sudeste de Sudamérica (SESA), consistentemente con la tendencia global, la frecuencia y severidad de eventos extremos han aumentado significativamente en las últimas décadas (Almazroui et al. 2021a; Avila-Diaz et al. 2020; Lovino et al. 2018a; Olmo et al. 2022). En concordancia con los patrones globales, los extremos cálidos de temperatura son significativamente más frecuentes y severos desde 1960 (Almazroui et al. 2021a; Dereczynski et al. 2020; Reboita et al. 2022), presentando evidencia robusta de una contribución humana a este cambio (Seong et al. 2021; Wang et al. 2017). Además, se proyecta que la intensidad y frecuencia de eventos cálidos aumenten con el calentamiento global de 1.5 °C, 2 °C y 4 °C (Gulizia et al. 2022; Li et al. 2021). Los extremos de precipitación, incluidos eventos como excesos de precipitación y sequías, no muestran tendencias significativas, y existe poca confianza sobre la contribución humana a las tendencias observadas (Avila-Diaz et al. 2023; Lovino et al. 2018a; Regoto et al. 2021). Sin embargo, los eventos de precipitación intensa, definidos como episodios de lluvia intensa de corta duración, han aumentado significativamente (Avila-Diaz et al. 2020; Dunn et al. 2020; Olmo et al. 2020) y se proyecta que aumenten a lo largo del siglo XXI (Almazroui et al. 2021b; Li et al. 2021). Las sequías meteorológicas, agrícolas y ecológicas exhiben señales mixtas de tendencias observadas y proyectadas (Seneviratne et al. 2021). Las sequías hidrológicas constituyen la única categoría que muestra una reducción en su ocurrencia en SESA, con un nivel de confianza medio (Dai y Zhao 2017; Rivera y Penalba 2018).

La región de SESA enfrenta una elevada vulnerabilidad a las amenazas hidrometeorológicas debido a su alta densidad poblacional y fuerte dependencia de la

agricultura (Castellanos et al. 2022; Lovino et al. 2018b). El crecimiento demográfico, la expansión urbana y las actividades agrícolas desarrolladas en áreas propensas a este tipo de amenazas, contribuyen a potenciar las condiciones de riesgo, agravadas por patrones climáticos cambiantes (Blaikie et al. 2014; Ward et al. 2020). La región del centro y noreste de Argentina es particularmente vulnerable a estos EHEs recurrentes debido a su gran población, su papel como principal región productora agrícola y sus altos índices de pobreza (Lovino et al. 2018b; Lovino 2020; Naumann et al. 2019).

La falta de investigación integral y evaluaciones de riesgo específicas para abordar las vulnerabilidades de esta región agrava aún más la situación. Avanzar hacia un desarrollo resiliente al clima es un objetivo clave para el centro-noreste de Argentina. En este contexto, es necesario comprender en profundidad los riesgos que representan los EHEs para desarrollar estrategias efectivas de gestión del riesgo climático, incluyendo el desarrollo de planes de adaptación acordes a la realidad de la región. Para ello, es también indispensable estudiar las amenazas hidrometeorológicas múltiples en diversas escalas espaciales y temporales.

En este sentido, la presente tesis busca abordar las siguientes preguntas científicas:

- ¿Cómo se caracterizan las amenazas por EHEs en el centro noreste de Argentina? ¿Han presentado cambios? ¿Cuáles son las principales zonas críticas?
- ¿Cómo se distribuye espacialmente la vulnerabilidad en el centro-noreste de Argentina? ¿Qué factores determinan la vulnerabilidad?
- ¿Cómo varía el riesgo frente a los EHEs en el centro-noreste de Argentina?

1.2. Región de estudio

La región de estudio incluye el centro-noreste de Argentina que se localiza en el SESA, abarcando una extensa zona mayormente plana delimitada por 63°W–53°W y 35°S–22°S (Figura 1.1). Esta zona presenta un clima relativamente uniforme, clasificado como templado sin estación seca y con verano cálido, según la clasificación de Köppen-Geiger (Beck et al. 2018). La precipitación anual sigue un gradiente de noreste a centro-oeste y suroeste de la región. Los valores máximos anuales se registran en el noreste de Argentina y el sureste de Brasil, mientras que la precipitación anual mínima se observa en el borde oeste de la región, incluyendo el centro de Argentina y el oeste de Paraguay (Berbery y Barros 2002). La temperatura sigue un gradiente latitudinal, disminuyendo de norte a sur (Caffera y Berbery 2006).

La región del centro-noreste de Argentina es clave para el desarrollo socioeconómico del continente, cuenta con un complejo sistema de recursos hídricos, y contribuye con un alto porcentaje a la producción agrícola a nivel continental (Houspanossian et al. 2023; Lovino et al. 2018b). A su vez, el centro-noreste de Argentina hospeda gran parte de la población del país (excluyendo el área metropolitana de Buenos Aires) y funciona como centro neurálgico de actividades económicas. Además, la zona de estudio experimenta una variabilidad hidroclimática en escalas temporales desde interanual hasta decadal y es propensa a eventos extremos, los cuales podrían aumentar en frecuencia y severidad en los próximos años (Garreaud et al. 2009; Hagen et al. 2022; Olmo et al. 2020; Zhang et al. 2016). Estos factores climáticos, combinados con la alta concentración de actividades económicas, hacen que la región sea particularmente vulnerable a la variabilidad y a los extremos hidroclimáticos.

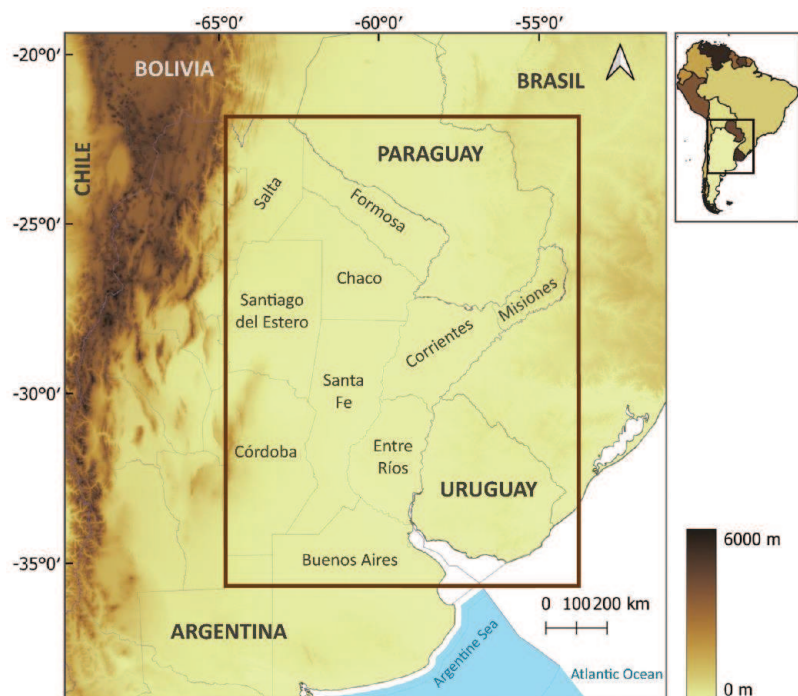


Figura 1.1. Región de estudio.

Mapa topográfico del sudeste de Sudamérica, en el que se destaca el área de estudio dentro del rectángulo marrón oscuro. El mapa nombra las provincias del centro-noreste de Argentina incluidas en el estudio de vulnerabilidad y riesgo. Fuente: Pierrestegui et al. 2025.

1.3. Hipótesis

El riesgo a eventos hidrometeorológicos extremos en el centro-noreste de Argentina varía espacialmente debido a la distribución diferenciada de amenazas múltiples y condiciones socioeconómicas que determinan un nivel de vulnerabilidad con diferencias importantes entre subregiones.

1.4. Objetivos

1.4.1. Objetivo general

Determinar y evaluar las amenazas múltiples, la vulnerabilidad, y el riesgo asociados a eventos hidrometeorológicos extremos en el centro-noreste de Argentina.

1.4.2. Objetivos específicos

1. Estudiar espacial y temporalmente las principales características (frecuencia, duración e intensidad) de los EHEs en el centro-noreste de Argentina.
2. Identificar y evaluar las principales amenazas múltiples asociadas a los EHEs, mediante un enfoque multi-amenaza.
3. Desarrollar y evaluar métricas para los componentes de la vulnerabilidad frente a los EHEs (exposición, sensibilidad y capacidad adaptativa).
4. Determinar y evaluar los niveles de vulnerabilidad y riesgo frente a los EHEs.

1.5. Estructura de la tesis doctoral

La tesis doctoral se presenta en el formato de memoria por compilación, estructurada de forma tal de abordar los objetivos específicos a través de la organización por capítulos. El Capítulo 2 aborda los objetivos específicos 1 y 2, desarrollando un análisis multi-amenaza de eventos hidrometeorológicos extremos y sus variaciones temporales en el centro-noreste de Argentina, identificándose áreas críticas de amenazas por EHEs y su evolución temporal. Estos resultados (incluyendo texto y figuras) se corresponden con la publicación científica Pierrestegui et al. (2024), publicado por primera vez en Earth Systems and Environment (2024) por Springer Nature (reproducido con permiso de Springer Nature). Se incluyen de manera complementaria métodos y hallazgos publicados en Lovino et al. (2024) y Lovino et al. (2025), así como resultados analizados y discutidos en Lovino et al. (2022) y Bernal-Mujica et al. (2023), trabajos en coautoría de la tesis.

Capítulo 1: Introducción

El Capítulo 3 responde a los objetivos específicos 3 y 4, desarrollando un estudio de la vulnerabilidad y el riesgo del centro-este de Argentina frente a EHEs tanto para amenazas individuales como para amenazas múltiples, elaborándose métricas de las componentes de la vulnerabilidad. Estos resultados (incluyendo texto, tablas y figuras) se corresponden con la publicación científica Pierrestegui et al. (2025), publicado por primera vez en *Earth Systems and Environment* (2025) por Springer Nature (reproducido con permiso de Springer Nature). El Capítulo 4 presenta una discusión y reflexión sobre los resultados encontrados en este trabajo de tesis en el contexto de la literatura existente y señalando las principales conclusiones de estos análisis.

Los anexos contienen información complementaria a esta memoria de compilación. El Anexo I incluye el material suplementario (MS), dividido en tres secciones (MS1, 2, 3) que aportan información adicional derivada de los trabajos de coautoría de la autora, y una sección (MS4) que incluye un análisis adicional de los componentes de la vulnerabilidad, aportando mayor contexto al estudio de riesgos. En el Anexo II se adjuntan los artículos científicos que forman parte de la tesis. En el mismo anexo, se detallan las contribuciones propias y de otros autores en dichos artículos, así como su relevancia para la tesis.

Capítulo 2: Evaluación de amenazas múltiples por eventos hidrometeorológicos extremos

2.1. Introducción

Las estrategias de gestión del riesgo climático y los planes de adaptación suelen centrarse en amenazas individuales que afectan a los sistemas expuestos. Sin embargo, múltiples amenazas pueden ocurrir simultáneamente o de forma independiente, teniendo un impacto sustancial en estos sistemas (AghaKouchak et al. 2020; Stalhandske et al. 2024). Dado que el riesgo aumenta cuando las amenazas coinciden en tiempo o espacio, adoptar un marco de amenazas múltiples proporciona un análisis más completo para comprender el riesgo climático (Binita et al. 2021). Un enfoque de amenazas múltiples considera las principales amenazas que enfrenta una región, ya sea de forma concurrente o independiente (UNDRR 2020). La combinación de múltiples amenazas individuales asumiendo su independencia, conocida como análisis de amenazas individuales en múltiples capas, representa un primer paso hacia una evaluación de riesgos más integral (Stalhandske et al. 2024). Este estudio utiliza un análisis de amenazas múltiples para identificar amenazas que son espacialmente relevantes o "zonas críticas" donde la ocurrencia de amenazas es particularmente alta (De Angeli et al. 2022; Gill y Malamud 2014).

En diversas regiones del mundo se han realizado estudios de amenazas múltiples (AghaKouchak et al. 2020; Bathrellos et al. 2017; Pourghasemi et al. 2020; Ridder et al. 2020; Sfetsos et al. 2023; Skilodimou et al. 2019). En Europa, se proyecta que las amenazas múltiples por eventos extremos aumenten en el sur y suroeste debido a la ocurrencia de olas de calor, sequías e incendios forestales más frecuentes, con zonas críticas proyectadas a lo largo de costas marítimas y llanuras de inundación donde predomina la ocurrencia de inundaciones y tormentas de viento (Forzieri et al. 2016). En Estados Unidos también se prevé un aumento de las amenazas múltiples, especialmente en zonas críticas como Florida y los condados de la Costa del Golfo, debido a la frecuencia de olas de calor y precipitaciones extremas; el centro-oeste del país, debido a una intensificación en las olas de calor y sequías; y el noroeste del Pacífico, debido a la ocurrencia de olas de frío y precipitaciones extremas (Binita et al. 2021). También se han realizado estudios de amenazas múltiples a escala local, como en Hong Kong, donde se identifica un alto riesgo de amenazas múltiples por inundaciones, aluviones y

deslizamientos de tierra en más del 15% de las áreas (Lyu y Yin 2023). Sin embargo, en el SESA los estudios de amenazas múltiples son escasos, aun siendo una región frecuentemente impactada por EHEs.

Este capítulo presenta un análisis de amenazas múltiples por eventos hidrometeorológicos extremos y sus variaciones temporales en el centro-noreste de Argentina. Se estima la frecuencia, duración e intensidad de los EHEs tanto de corto como de largo plazo para los períodos 1961-1990 y 1991-2020. Mediante un análisis de amenazas individuales en múltiples capas (multi-capas), se identifican zonas críticas de amenazas por EHE y se analiza su evolución temporal.

2.2. Datos

Los EHEs a escala regional se estudian utilizando datos de precipitación, humedad del suelo y temperatura provenientes de la quinta versión del reanálisis del European Centre for Medium-Range Weather Forecasts (ECMWF), conocido como ERA5 (Hersbach et al. 2020; 2023a, b). Los datos de ERA5 presentan una resolución espacial de $0.25^\circ \times 0.25^\circ$ en una grilla de latitud-longitud y cubren el período 1961–2020. Aunque ERA5 presenta algunas incertidumbres conocidas (Hersbach et al. 2020; Soci et al. 2024), los datos de precipitación y temperatura han demostrado un buen desempeño al compararse con observaciones *in situ* en el SESA, particularmente en la representación de eventos extremos (Balmaceda-Huarte et al. 2021; Lavers et al. 2022; Olmo et al. 2022). Asimismo, los datos de humedad del suelo de ERA5 han demostrado una precisión superior en comparación con otros productos de reanálisis, cuando se validan frente a observaciones *in situ* en diversas ubicaciones a nivel mundial (e.g., Li et al. 2020; Yang et al. 2022). Además, las simulaciones de humedad del suelo de ERA5 han demostrado estabilidad temporal desde 1960 en América del Sur (Soci et al. 2024), y muestran una precisión confiable en el SESA (Xu et al. 2021). Por otro lado, la utilización de ERA5 para todas las variables permite asegurar una simulación físicamente consistente de los procesos debido a su representación completa del sistema acoplado tierra-atmósfera.

En este capítulo, se utilizan datos mensuales de precipitación para estudiar los EHEs de largo plazo. Además, se emplean datos diarios de temperatura máxima y precipitación (calculados a partir de datos horarios) para estudiar los EHEs de corto plazo. Se utiliza la media de cinco días no superpuestos (pentadas) de humedad del suelo en la zona radicular (primer metro del suelo), calculadas a partir de datos horarios, para el estudio de sequías agrícolas repentinas.

2.3. Metodología

2.3.1. Detección de eventos hidrometeorológicos extremos de largo plazo

Los EHEs de largo plazo incluyen fenómenos que se desarrollan y generan impactos significativos en escalas temporales prolongadas, que abarcan desde varias semanas hasta meses (Seneviratne et al. 2021). En esta tesis se estudian los eventos extremos de largo plazo constituidos por excesos y déficits de precipitación, que se analizan utilizando el Índice Estandarizado de Precipitación (SPI, por sus siglas en inglés; Farahmand y AghaKouchak 2015; Hao y AghaKouchak 2014). El SPI es una métrica estandarizada para evaluar anomalías de precipitación, diseñada específicamente para cuantificar tanto déficits como excesos de precipitación en diversas escalas temporales. Se utiliza el SPI no paramétrico, estimado a partir de datos mensuales de precipitación; por lo tanto, las escalas temporales de los eventos detectados son mensuales. El método no paramétrico permite obtener índices estandarizados sin asumir distribuciones teóricas. Este método, basado en la función empírica de Gringorten (1963), ha demostrado representar mejor la severidad de las sequías (Mallenahalli 2020; Soláková et al. 2014) y evita limitaciones asociadas a valores extremos o nulos.

El SPI se calcula utilizando una función de probabilidad empírica de no excedencia para eventos extremos (Gringorten 1963) (Ecuación 2.1):

$$p(x_i) = (i - 0.44)/(n + 0.12) \quad (2.1)$$

Donde $p(x_i)$ representa la probabilidad de no excedencia asociada al i -ésimo elemento de la serie, x corresponde a la precipitación mensual, i es el rango de los valores distintos de cero de la muestra, y n es el tamaño de la muestra. Esta probabilidad se transforma luego en el SPI, aplicando la inversa de la función de distribución normal estándar a los resultados de $p(x_i)$ (Farahmand y AghaKouchak 2015) como muestra la Ecuación 2.2:

$$SPI = \phi^{-1}(p(x_i)) \quad (2.2)$$

Se identifican eventos extremos de exceso y déficit de precipitación, denominados WEP (exceso de precipitación, por sus siglas en inglés) y DEP (déficit de precipitación, por sus siglas en inglés), respectivamente. Un evento WEP se identifica cuando $SPI > 1$ durante una secuencia de meses, con al menos un mes donde $SPI > 1.5$. Por el contrario, un evento DEP se identifica cuando $SPI < -1$, con al menos un mes donde $SPI < -1.5$. Cabe destacar que el umbral de ± 1.5 indica la ocurrencia de un evento extremo al alcanzar esta

intensidad en al menos un mes, mientras que el umbral de ± 1 se utiliza para determinar la duración del evento. Por lo tanto, siguiendo la clasificación propuesta por Lloyd-Hughes y Saunders (2002), se distinguen períodos —sin imponer una duración mínima o máxima— caracterizados por condiciones moderadamente húmedas o secas ($SPI > 1$ o $SPI < -1$), siempre que al menos un mes experimente condiciones húmedas o secas severas ($SPI > 1.5$ o $SPI < -1.5$).

Se calcularon los eventos WEP y DEP basados en el SPI en escalas temporales de 3 meses (SPI3) y 18 meses (SPI18). De este modo, los eventos extremos en la escala de 3 meses se denominan WEP3 y DEP3, mientras que los de la escala de 18 meses se denominan WEP18 y DEP18. Los WEP3 y DEP3 reflejan períodos de condiciones húmedas o secas que afectan la humedad del suelo, pudiendo tener impactos en etapas críticas de crecimiento de cultivos, por lo que proporcionan información climática valiosa para aplicaciones agrícolas (Sgroi et al. 2021). Por su parte, los WEP18 y DEP18 identifican anomalías más extendidas en la precipitación, que se ven reflejadas en el caudal de ríos, almacenamiento de embalses y niveles freáticos, proporcionando información que permite el análisis de sequías hidrológicas y excesos hídricos de largo plazo (Lovino et al. 2014; Sirdas y Sen 2003). Bernal-Mujica et al. (2023) presenta un análisis más detallado sobre la respuesta de la humedad del suelo y la profundidad del nivel freático ante eventos extremos de precipitación, así como sobre su variabilidad espacio-temporal y sus cambios en la región núcleo agrícola de Argentina (ver Anexo I, MS1).

2.3.2. Detección de eventos hidrometeorológicos extremos de corto plazo

Los EHEs de corto plazo incluyen fenómenos que se desarrollan rápidamente y generan impactos significativos en escalas temporales breves, generalmente de días (Seneviratne et al. 2021). Los EHEs de corto plazo estudiados en esta tesis son olas de calor (HW, por sus siglas en inglés), precipitación intensa (HP, por sus siglas en inglés) y sequías repentinas (FD, por sus siglas en inglés). Estos eventos pueden afectar de manera inmediata la agricultura y las áreas urbanas, impactando negativamente la producción de alimentos, la salud pública y la infraestructura (Hagen et al. 2022) y requiriendo respuestas rápidas para mitigar sus impactos.

Una HW se identifica como un período de al menos 3 días consecutivos con una temperatura máxima diaria que excede el percentil 90 del período de referencia (De Luca y Donat 2023; Perkins y Alexander 2013). Un evento HP se identifica como una secuencia de días consecutivos en los cuales la precipitación diaria supera el percentil 95 de los días

húmedos (≥ 1 mm) durante el período de referencia (Weber et al. 2020). Cabe destacar que el percentil 90 de la temperatura máxima diaria y el percentil 95 de la precipitación diaria en días húmedos se calculan para el período de referencia 1991-2020.

Las FD agrícolas se identifican siguiendo la metodología descrita por Lovino et al. (2024) (ver Anexo I – Figura MS2.1), que integra la humedad del suelo en la zona radicular y las propiedades hidráulicas del suelo para captar el rápido decaimiento de la humedad junto con el estrés de la vegetación. Este enfoque se basa en el Índice de Déficit de Humedad del Suelo (SWDI, por sus siglas en inglés; Martínez-Fernández et al. 2015) para evaluar la disponibilidad de agua en el suelo. Una FD se detecta mediante un rápido descenso de la humedad del suelo, cuantificado por una disminución del SWDI desde valores superiores a -3 hasta valores inferiores a -5 en un período de 20 días (o 4 pentadas). El umbral superior del SWDI marca el inicio del déficit de humedad en el suelo, mientras que el umbral inferior indica condiciones de estrés hídrico para los cultivos. El método también incorpora un período de intensificación de duración suficiente para filtrar eventos sinópticos de corto plazo que puedan agotar rápidamente la humedad del suelo pero que luego se recuperen abruptamente. Además, requiere que la humedad del suelo antes del inicio de la FD no presente niveles significativos de estrés para las plantas. Más detalles sobre el método de identificación de FD pueden encontrarse en Lovino et al. (2024) y en el Anexo I, MS2.

2.3.3. Cuantificación de las amenazas

En primer lugar, se estima la frecuencia decadal, la duración promedio y la intensidad máxima media de cada EHE durante dos períodos distintos: 1961-1990 (pasado) y 1991-2020 (presente). La frecuencia decadal se calcula como el número total de eventos dividido por el número de décadas en cada período. La duración se refiere a la longitud de cada evento, expresada en días o meses. La duración promedio se calcula dividiendo la suma de todas las duraciones de los eventos por el número total de eventos en el período de estudio. La intensidad máxima media se obtiene promediando las intensidades máximas de todos los eventos en el período especificado, siendo la intensidad máxima el máximo valor alcanzado por la variable durante el evento.

En segundo lugar, acorde a Tabari et al. (2021), se calcula el componente de amenaza individual (h) para cada EHE multiplicando la frecuencia decadal (DF , por su sigla en inglés), la duración promedio (AD , por su sigla en inglés) y la intensidad máxima media (MMI , por su sigla en inglés) de los eventos identificados (Ecuación 2.3):

$$h = DF * AD * MMI \quad (2.3)$$

Se asigna igual peso a los tres componentes de amenaza, considerando su importancia equivalente en la generación de impactos adversos, como lo sugieren Tabari et al. (2021). Para el caso de eventos en condiciones secas, en que las intensidades (valores de MMI) tienen valores negativos de SPI o SWDI, se convierten a valores positivos para evitar que los valores de amenaza sean negativos. Cabe destacar que se mantiene la magnitud del MMI durante esta conversión, asegurando que el valor final del componente de amenaza individual no se vea afectado. Luego, siguiendo a Binita et al. (2021), los componentes de amenaza resultantes se reescalan en un rango de 0-1 obteniéndose la amenaza individual normalizada (Ecuación 2.4):

$$H(0,1) = (h - \min(h)) / (\max(h) - \min(h)) \quad (2.4)$$

Donde $H(0,1)$ es la amenaza individual normalizada para cada EHE, y $\min(h)$ y $\max(h)$ son los valores mínimo y máximo del componente de amenaza individual, respectivamente. El reescalamiento se realiza utilizando los valores mínimo y máximo globales para todo el período de estudio —incluidos ambos períodos, 1961-1990 y 1991-2020—, lo que permite comparar las amenazas individuales normalizadas entre los dos períodos.

Finalmente, también siguiendo a Binita et al. (2021), los componentes de amenaza individual normalizados se suman y dividen por el número total de componentes para obtener el índice de amenaza múltiple (Ecuación 2.5):

$$mH(0,1) = \sum H_i(0,1) / n \quad (2.5)$$

Donde $mH(0,1)$ es el índice de amenaza múltiple que varía entre 0 y 1, $H_i(0,1)$ es la amenaza individual normalizada, con $i = 1, \dots, n$, y n es el número de componentes de amenaza. De esta forma se calculan índices de amenaza múltiple de largo plazo (LT-mH), corto plazo (ST-mH) y total (T-mH). Tanto los componentes individuales de amenaza como los índices de amenaza múltiple se comparan entre los períodos 1961-1990 y 1991-2020 para determinar los cambios observados.

La Figura 2.1 presenta un esquema del proceso utilizado para estimar los índices de amenaza múltiple. Primero, se obtienen los componentes individuales de amenaza normalizados de largo plazo que incluyen eventos WEP y eventos DEP, derivados de una combinación de sus variables en escalas temporales de 3 y 18 meses (WEP3, WEP18,

DEP3 y DEP18, como se detalla en la sección 2.3.1). Luego, el LT-mH integra las amenazas por EHEs de largo plazo incluyendo tanto los componentes de amenaza normalizados de los eventos WEP como de los eventos DEP. De manera similar, el ST-mH combina las amenazas por EHEs de corto plazo que incluyen HW, HP, y FD, con sus componentes de amenaza normalizados. Finalmente, el LT-mH y el ST-mH se combinan para estimar el T-mH, que representa la amenaza múltiple total por EHEs.

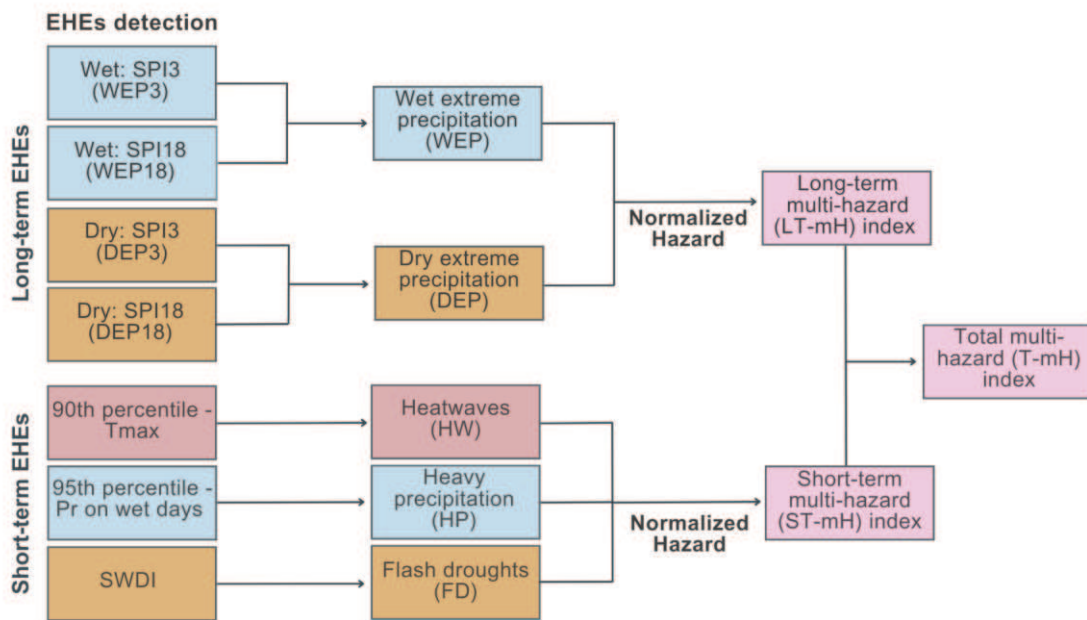


Figura 2.1. Diagrama metodológico del análisis de amenazas múltiples.

Diagrama esquemático que resume la metodología empleada para evaluar los índices de amenaza múltiple. SPI denota el índice estandarizado de precipitación, mientras que SWDI representa el índice de déficit de humedad del suelo (ver más detalles en el texto). A su vez, Tmax representa temperatura máxima, y Pr indica precipitación.

Fuente: Pierrestegui et al. 2024.

2.4. Resultados

2.4.1. Amenazas por eventos hidrometeorológicos extremos de largo plazo

2.4.1.1. Eventos extremos de exceso de precipitación

La Figura 2.2 muestra la frecuencia decadal, la duración promedio, la intensidad máxima media y la amenaza normalizada de los eventos WEP3 y WEP18 para los períodos 1991-2020 y 1961-1990, junto con los cambios en la amenaza entre los períodos presente y pasado. La frecuencia decadal actual de los WEP3 presenta un gradiente de suroeste a noreste en el área de estudio, disminuyendo de 5-6 eventos por década en el sur a 1-2 eventos por década en el norte (Figura 2.2a). La duración promedio varía entre 2.5 y 4.4 meses (Figura 2.2b). Las frecuencias más altas hacia el centro y el sur corresponden a

duraciones más cortas (1.5-2.5 meses), mientras que las frecuencias más bajas hacia el norte y el este se relacionan con duraciones más largas (4.4-5.7 meses). La intensidad máxima media presenta un patrón espacial heterogéneo, con un SPI3 promedio regional alcanzando 1.9 (Figura 2.2c). La amenaza normalizada de los WEP3 muestra valores máximos hacia el centro-sur y noreste del área de estudio, abarcando la provincia de Entre Ríos y gran parte de la región núcleo de cultivos de Argentina (CCR, según lo definido por Sgroi et al. 2021) que abarca el centro-sur de Santa Fe, suroeste de Córdoba y norte de Buenos Aires, y extendiéndose a zonas aledañas como Uruguay (Figura 2.2d). La máxima amenaza de WEP3 se localiza en Entre Ríos y norte de Buenos Aires, seguidos por el sur de Santa Fe y el este de Misiones, influida en gran medida por la mayor frecuencia de eventos WEP3 en esas zonas. Estos resultados sugieren que el sur de la región está expuesto a eventos extremos de exceso de precipitación frecuentes e intensos en escalas de tiempo de 3 meses, lo que representa un riesgo sustancial de anegamientos e inundaciones. Esto podría afectar la agricultura, particularmente en tierras altamente productivas de la Pampa argentina.

La amenaza actual por WEP3 muestra un cambio en comparación con los resultados del período 1961-1990 (Figura 2.2e-h). La Figura 2.2i indica que la amenaza por WEP3 aumentó notablemente en el sur (centro-sur de Santa Fe, Entre Ríos y norte de Buenos Aires) y noreste (norte de Misiones) de la región, mientras que disminuyó en una franja que se extiende en el centro y este (norte de Corrientes y sur de Misiones). Estos cambios están principalmente impulsados por alteraciones en la frecuencia y duración de los WEP3. Las Figura 2.2a-b y 2.2e-f indican que la frecuencia decadal de los WEP3 aumentó hacia el sur y disminuyó en el centro de la región de estudio, mientras que la duración de los WEP3 aumentó en el centro-este y disminuyó principalmente en el noreste. La amenaza promedio regional por WEP3 aumentó en un 9% en la región de estudio, aunque con un patrón espacial de cambio no homogéneo.

Los eventos WEP18 son menos frecuentes, pero tienen mayor duración que los WEP3 en el período actual (Figura 2.2j-k). La frecuencia decadal de los WEP18 varía desde 0 eventos por década en el norte hasta más de 2 eventos por década en el sur (Figura 2.2j). La duración promedio abarca de 0 a 23 meses, con las mayores duraciones hacia el noreste, alcanzando entre 23 y 34 meses (Figura 2.2k). La intensidad máxima media alcanza un valor de 2.4 (Figura 2.2l). Las áreas con las frecuencias más bajas de WEP18 en el noreste exhiben las mayores duraciones e intensidades. Similar a los WEP3, la mayor amenaza por WEP18 se encuentra en el centro y sur de la región de estudio (centro-

sur de Santa Fe, Entre Ríos, oeste de Córdoba, centro sur de Corrientes, y norte de Buenos Aires) (Figura 2.2m), aunque la amenaza por WEP18 es ligeramente inferior a la de WEP3. Los resultados sugieren que la porción sur de la región de estudio está más expuesta a excesos de precipitación que afectan variables hidrológicas en comparación con las áreas del norte. Por lo tanto, se espera inundaciones más frecuentes en suelos productivos del sur de la región, aunque eventos severos (de larga duración y alta intensidad, pero menos frecuentes) también pueden ocurrir principalmente en Misiones y zonas aledañas como el sureste de Paraguay.

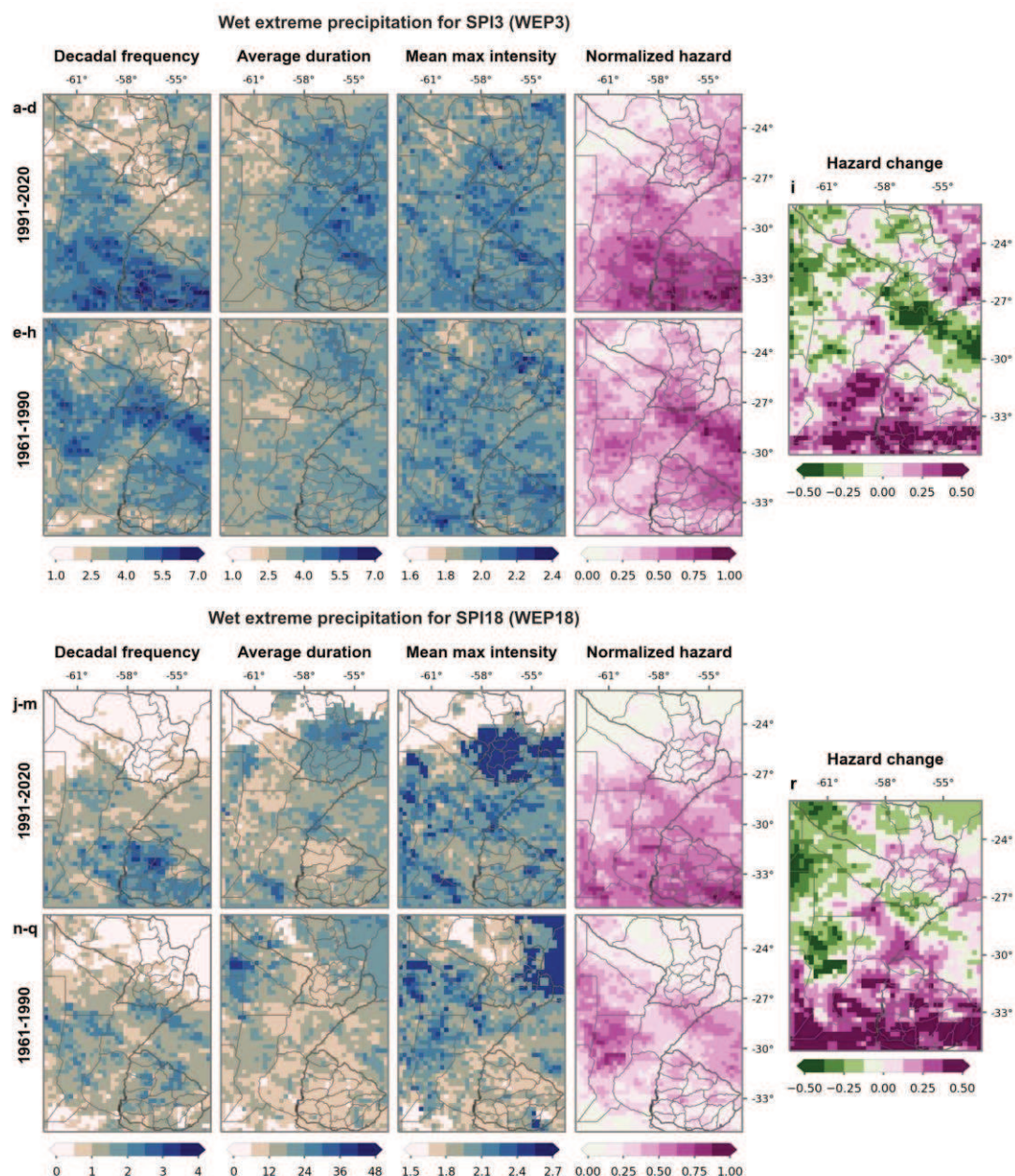


Figura 2.2. Amenaza por eventos extremos de exceso de precipitación.

Análisis de amenazas por eventos extremos de exceso de precipitación calculados utilizando SPI3 (WEP3, paneles a-i) y SPI18 (WEP18, paneles j-r). El análisis abarca

dos períodos de tiempo: 1991-2020 (paneles a-d, j-m) y 1961-1990 (paneles e-h, n-q). Cada fila de paneles presenta la frecuencia decadal (número de eventos por década, primera columna), la duración promedio (meses, segunda columna), la intensidad máxima media (valor de SPI, tercera columna) y la amenaza normalizada (adimensional, cuarta columna). Los paneles (i) y (r) ilustran los cambios en la amenaza entre los dos períodos. Fuente: Pierrestegui et al. 2024.

La amenaza de WEP18 muestra un cambio al comparar los períodos 1991-2020 y 1961-1990 (Figura 2.2m,q). La amenaza de WEP18 aumentó notablemente hacia el sur y disminuyó hacia las regiones central y noroeste (Figura 2.2r). La distribución espacial de la amenaza tanto por WEP3 como por WEP18 muestra un cambio de norte a sur en ambas escalas de tiempo, indicando un aumento de las amenazas de largo plazo asociadas a eventos extremos de exceso de precipitación en el sur y una disminución de las amenazas en el norte. La amenaza promedio regional por WEP18 aumentó un 21%, más del doble del aumento observado para los WEP3. Este incremento se debe principalmente a un aumento en la duración de los eventos WEP18, mientras que la frecuencia e intensidad se mantuvieron estables en promedio.

2.4.1.2. Eventos extremos de déficit de precipitación

La Figura 2.3 presenta la frecuencia decadal, la duración promedio, la intensidad máxima media y la amenaza normalizada de los eventos DEP3 y DEP18 para los períodos 1991-2020 y 1961-1990, junto con los cambios en la amenaza entre los períodos presente y pasado. En el presente, las mayores frecuencias y duraciones de los DEP3 se encuentran en el norte y oeste de la región de estudio (Figura 2.3a-b). La frecuencia decadal de los DEP3 varía entre 2 y 4.3 eventos por década (Figura 2.3a), mientras que la duración promedio oscila entre 2.3 y 3.7 meses (Figura 2.3b). La intensidad máxima media tiene un valor promedio de 1.9, con una distribución relativamente uniforme en la región (Figura 2.3c). Es particularmente notable que en las regiones norte y oeste las frecuencias superen los 4.3 eventos por década y las duraciones excedan los 4 meses. Así, la distribución espacial de la amenaza por DEP3 muestra un gradiente decreciente de noroeste a sureste (Figura 2.3d), exhibiendo una mayor amenaza en las áreas norte y oeste (Formosa, oeste de Chaco, este de Salta, este de Santiago del Estero, este de Córdoba y oeste de Santa Fe) debido a frecuencias más altas y duraciones más largas. Los resultados sugieren que el oeste y norte de la región de estudio están más expuestos a los DEP3, favoreciendo el desarrollo de sequías estacionales que afectan la agricultura en la porción occidental de la CCR (oeste de Córdoba y este de Santa Fe), y el norte del país.

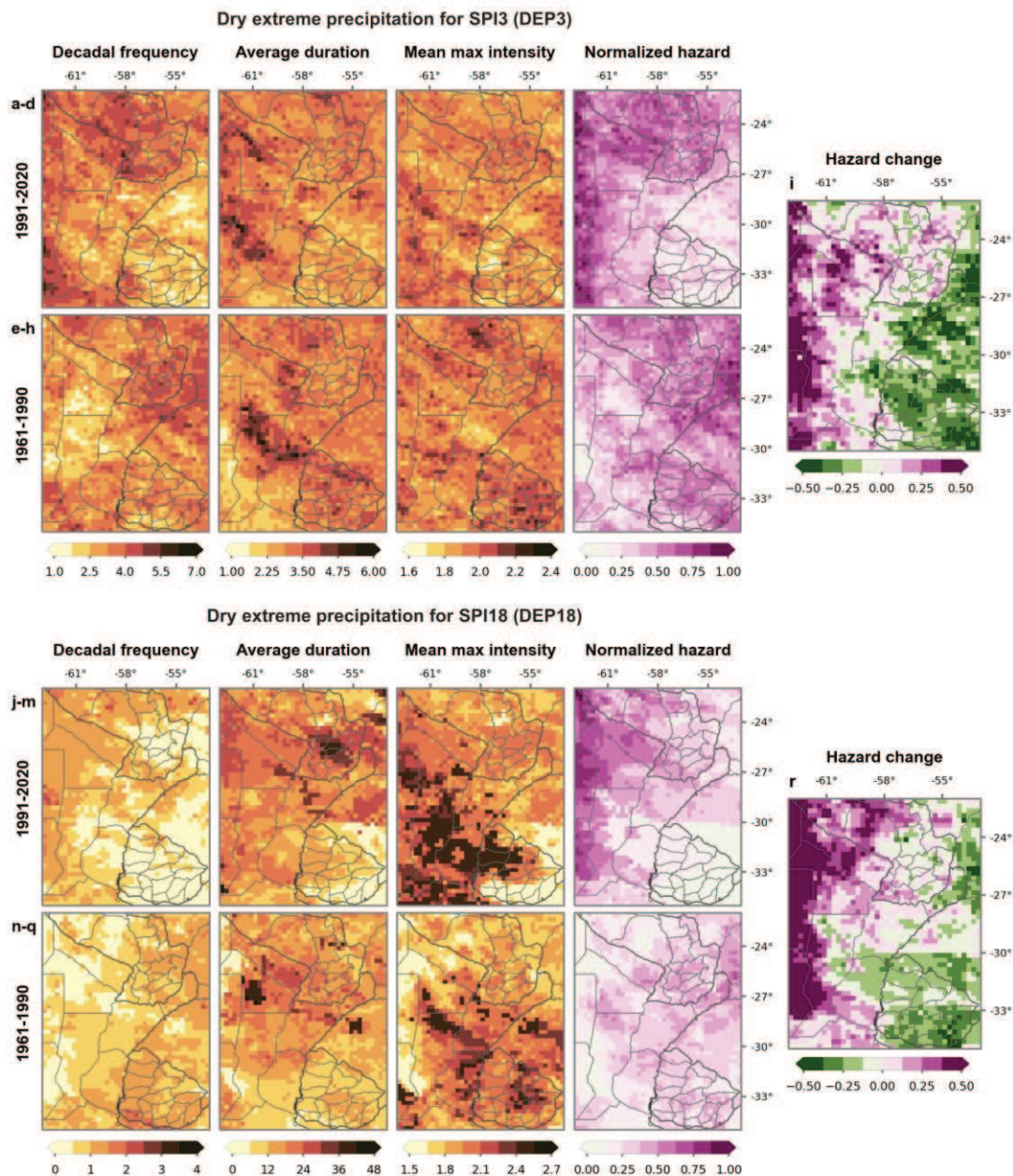


Figura 2.3. Amenaza por eventos extremos de déficit de precipitación.

Análisis de amenazas por eventos extremos de déficit de precipitación calculados utilizando SPI3 (DEP3, paneles a-i) y SPI18 (DEP18, paneles j-r). El análisis abarca dos períodos de tiempo: 1991-2020 (paneles a-d, j-m) y 1961-1990 (paneles e-h, n-q). Cada fila de paneles presenta la frecuencia decadal (número de eventos por década, primera columna), la duración promedio (meses, segunda columna), la intensidad máxima media (valor de SPI convertido a su equivalente positivo, tercera columna) y la amenaza normalizada (adimensional, cuarta columna). Los paneles (i) y (r) ilustran los cambios en la amenaza entre los dos períodos. Fuente: Pierrestegui et al. 2024.

La amenaza por DEP3 muestra un cambio marcado al comparar los períodos 1991-2020 y 1961-1990 (Figura 2.3i). En el período 1961-1990, el patrón espacial de la amenaza por DEP3 presenta valores más altos en el este, disminuyendo gradualmente hacia el oeste (Figura 2.3h). Sin embargo, en el período 1991-2020, la amenaza por DEP3 aumenta

considerablemente en el oeste y disminuye en el este de la región de estudio (Figura 2.3i). Estos resultados indican un aumento notorio en las últimas décadas en la amenaza de sequías estacionales en el centro de Formosa y Chaco, en el oeste de Santiago del Estero y Córdoba, y en el este de Santa Fe, mientras que se observa una disminución en Misiones, y en el norte de Corrientes y Entre Ríos.

La frecuencia actual de los DEP18 es menor que la de los DEP3, mientras que su duración es mayor (Figura 2.3j-k), lo cual es consistente con su escala temporal más larga. La distribución espacial de la frecuencia decadal de los DEP18 es relativamente uniforme, oscilando entre 0.3 y 1 evento por década, con valores más altos observados en las regiones norte y oeste (1 a 1.5 eventos por década). Las duraciones promedio varían entre 7 y 27 meses en toda la región, con las mayores duraciones (excediendo los 27 meses) concentradas en el este de Paraguay, y en el caso de Argentina las máximas duraciones superan los 24 meses y se encuentran en las provincias del centro-norte. Por el contrario, las duraciones más cortas de los DEP18 (menos de 7 meses) se presentan en las áreas del sur. Es notable que la duración máxima de los eventos extremos de déficit de precipitación (27 a 48 meses, localizada en el este de Paraguay) supera la de los eventos extremos de exceso de precipitación (hasta 34 meses). La intensidad máxima media mantiene un valor promedio de 2. Los eventos más intensos (excediendo SPI18 = -2,4) se registran en el centro-este de Argentina (Figura 2.3l), en las provincias de Santa Fe, Entre Ríos y norte de Buenos Aires, si bien a su vez presentan menor frecuencia de ocurrencia. La amenaza por DEP18 es mayor en la zona norte y oeste (Figura 2.3m), mostrando un gradiente similar al de la amenaza por DEP3. Por lo tanto, la amenaza de sequías hidrológicas es alta en estas regiones (Formosa, Chaco, este de Santiago del Estero, y este de Córdoba), aunque eventos DEP18 intensos y menos frecuentes también ocurren en zonas productivas de la región núcleo de cultivos en Argentina.

El cambio en la amenaza por DEP18 (Figura 2.3r) presenta una distribución espacial similar al de la amenaza por DEP3 (Figura 2.3i), con una disminución observada en el este y un aumento en el oeste. El cambio promedio regional en la amenaza por DEP18 aumentó un 22.5 %. Este notorio aumento, particularmente evidente en las áreas occidentales, resulta principalmente de un incremento en la duración y la intensidad, mientras que la frecuencia se ha mantenido estable en promedio. En consecuencia, de manera similar a la amenaza de sequías estacionales, la amenaza de sequías hidrológicas aumentó considerablemente hacia la porción occidental de la región de estudio.

2.4.2. Amenazas por eventos hidrometeorológicos extremos de corto plazo

2.4.2.1. Olas de calor

La Figura 2.4 ilustra la frecuencia decadal, la duración promedio, la intensidad máxima media y la amenaza normalizada de las olas de calor (HW) para los períodos 1991-2020 y 1961-1990, junto con los cambios en la amenaza entre estos períodos. La frecuencia decadal actual de las HW varía entre 35 y 42 eventos por década, alcanzando ocasionalmente hasta 51 ocurrencias (Figura 2.4a). Las duraciones promedio oscilan entre 3.8 y 4.3 días, con valores máximos de 4.8 días observados en el norte y noreste, mientras que las duraciones mínimas de 3.4 días ocurren hacia el suroeste en Entre Ríos y norte de Buenos Aires y principalmente en el país vecino Uruguay (Figura 2.4b). La intensidad máxima media muestra un gradiente marcado de noroeste a sureste (Figura 2.4c), con valores que disminuyen de 39 a 29 °C, siguiendo en cierta medida el gradiente climatológico de temperatura máxima. La amenaza por olas de calor es alta en toda la región (Figura 2.4d), mostrando un gradiente espacial decreciente de norte a sur. Las mayores intensidades y duraciones contribuyen a una elevada amenaza por HW en el norte, principalmente en las provincias de Misiones, Formosa, Chaco y Santiago del Estero.

En comparación con el período pasado (1961-1990), la amenaza por HW muestra una expansión desde el noroeste hacia todas las áreas del norte y centro (Figura 2.4d, h). La Figura 2.4i muestra un aumento notable en la amenaza por HW en el noreste (Misiones, Corrientes y este de Formosa) siendo más importante en regiones cercanas como el país vecino de Paraguay. Este aumento se debe principalmente a un incremento significativo en la frecuencia de HW, que pasó de 15-25 eventos por década a 40-45 eventos en esta zona (Figura 2.4a, e). Por el contrario, la amenaza por HW disminuyó en las áreas occidentales (principalmente en el oeste de Formosa y Chaco), relacionado principalmente con una reducción en la frecuencia de HW, que pasó de 45-50 eventos por década a 35-40 eventos en esta zona. El cambio promedio regional de la amenaza por HW es positivo, con un aumento del 31.5 %. El componente de frecuencia decadal promedio areal muestra el mayor incremento, pasando de 31.3 eventos por década a 38.8 eventos por década en promedio, seguido por la intensidad en menor proporción, mientras que la duración se mantiene estable en promedio.

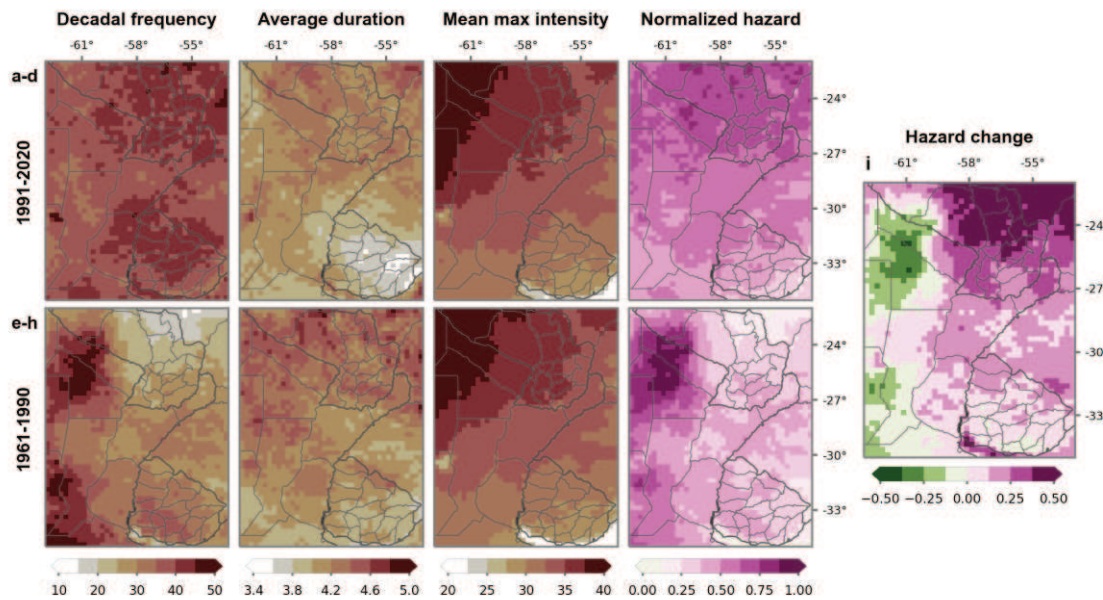


Figura 2.4. Amenaza por eventos de olas de calor.

Análisis de amenazas por eventos de olas de calor (HW). El análisis abarca dos períodos de tiempo: 1991-2020 (paneles a-d) y 1961-1990 (paneles e-h). Cada fila de paneles presenta la frecuencia decadal (número de eventos por década, primera columna), la duración promedio (días, segunda columna), la intensidad máxima media (temperatura en °C, tercera columna) y la amenaza normalizada (adimensional, cuarta columna). El panel (i) ilustra el cambio en la amenaza por HW entre los dos períodos. Fuente: Pierrestegui et al. 2024.

2.4.2.2. Eventos de precipitación intensa

La Figura 2.5 presenta la frecuencia decadal, la duración promedio, la intensidad máxima media y la amenaza normalizada de los eventos de precipitación intensa (HP) para los períodos 1991-2020 y 1961-1990, junto con los cambios en la amenaza entre estos períodos. En el período actual, las HP son frecuentes en la región de estudio, con frecuencias decadales que oscilan entre 43 y 67 eventos por década, alcanzando frecuencias máximas cercanas a 80 eventos por década (Figura 2.5a). La distribución espacial de la frecuencia decadal exhibe un gradiente de noreste a suroeste, con las frecuencias más altas en el noreste (alrededor de 67-77 eventos por década en Misiones) y las más bajas en el suroeste (alrededor de 39-43 eventos por década en el sur de Santa Fe), reflejando la climatología de precipitación de la región. Sin embargo, la intensidad y duración de los eventos HP no siguen el mismo patrón espacial. La intensidad máxima de las HP se concentra en el centro de la región de estudio (Figura 2.5c), abarcando Corrientes, Entre Ríos, y el este de Santa Fe (con intensidades máximas promedio que superan los 61 mm/día). Aunque la duración promedio no presenta un patrón espacial definido, las mayores duraciones se observan en el noreste sobre Misiones (Figura 2.5b).

En promedio, los eventos HP duran 1 día, pero pueden extenderse hasta 5 días. La mayor amenaza por HP se observa en Misiones y Corrientes (Figura 2.5d), con un gradiente decreciente de noreste a suroeste. Por lo tanto, la amenaza por HP es mayor en las regiones más húmedas y menor en las regiones más secas de la región de estudio.

Al comparar el período actual con el pasado, la amenaza por HP muestra cambios bajos y heterogéneos en toda la región de estudio (Figura 2.5i). La amenaza por HP aumentó hacia las áreas sur y noreste principalmente en el este de Misiones, pero disminuyó en una franja que se extiende por el centro y este de la región sobre el sur de Misiones y norte de Corrientes, reflejando un patrón de cambio similar al de WEP3 y WEP18 (ver Figura 2.2i, r). Aunque los componentes de la amenaza por HP no presentan cambios importantes en promedio en comparación con el período 1961-1990 (Figura 2.5e-g), hay un ligero aumento en la frecuencia y la intensidad, acompañado de una disminución en la duración. A pesar de estos cambios menores, la amenaza promedio por HP ha aumentado un 6 % en toda la región de estudio.

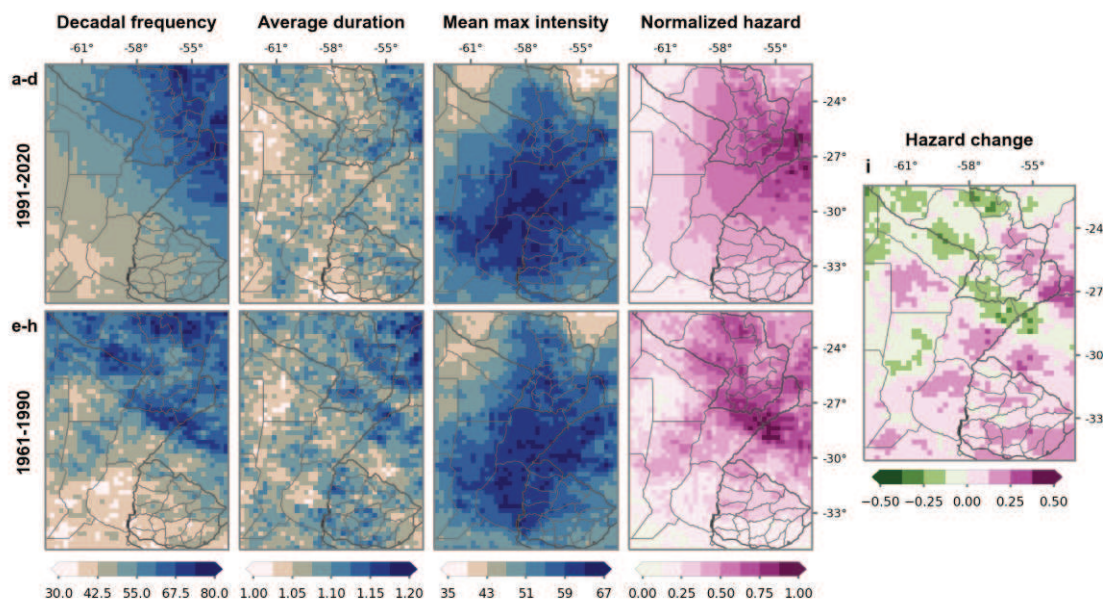


Figura 2.5. Amenaza por eventos de precipitación intensa.

Ánálisis de amenazas por eventos de precipitación intensa (HP). El análisis abarca dos períodos de tiempo: 1991-2020 (paneles a-d) y 1961-1990 (paneles e-h). Cada fila de paneles presenta la frecuencia decadal (número de eventos por década, primera columna), la duración promedio (días, segunda columna), la intensidad máxima media (mm/día, tercera columna) y la amenaza normalizada (adimensional, cuarta columna).

El panel (i) ilustra el cambio en la amenaza por HP entre los dos períodos. Fuente: Pierrestegui et al. 2024.

2.4.2.3. Sequías repentinas

La Figura 2.6 muestra la frecuencia decadal, la duración promedio, la intensidad máxima media y la amenaza normalizada de las sequías repentinas (FD) para los períodos 1991-2020 y 1961-1990, junto con los cambios en la amenaza entre estos períodos. Las frecuencias decadales actuales de FD oscilan entre 0.3 y 6.3 eventos por década (Figura 2.6a), con las mayores frecuencias (6.3 a 11 eventos por década) ubicadas en el centro este de la región. La duración de las condiciones de sequía que le siguen al período de intensificación de las FD, referida aquí como duración de FD, varía entre 5 y 22 pentadas en promedio (Figura 2.6b). La duración más prologada de FD (que exceden las 22 pentadas) se observan en el sureste y en el extremo occidental de la región. La intensidad máxima media presenta valores típicos de SWDI entre -5.6 y -8.1 (Figura 2.6c). Si bien la amenaza es baja en la región, se observa una mayor amenaza en la zona de Corrientes y Entre Ríos y zonas aledañas como Uruguay y sur de Brasil (Figura 2.6d). En Uruguay y el sur de Brasil, las FD combinan altas frecuencias con largas duraciones e intensidades altas, resultando en valores de amenaza más elevados. A pesar de las altas duraciones e intensidades observadas en el extremo occidental de la región la amenaza por FD se mantiene baja, posiblemente debido a las bajas frecuencias de FD.

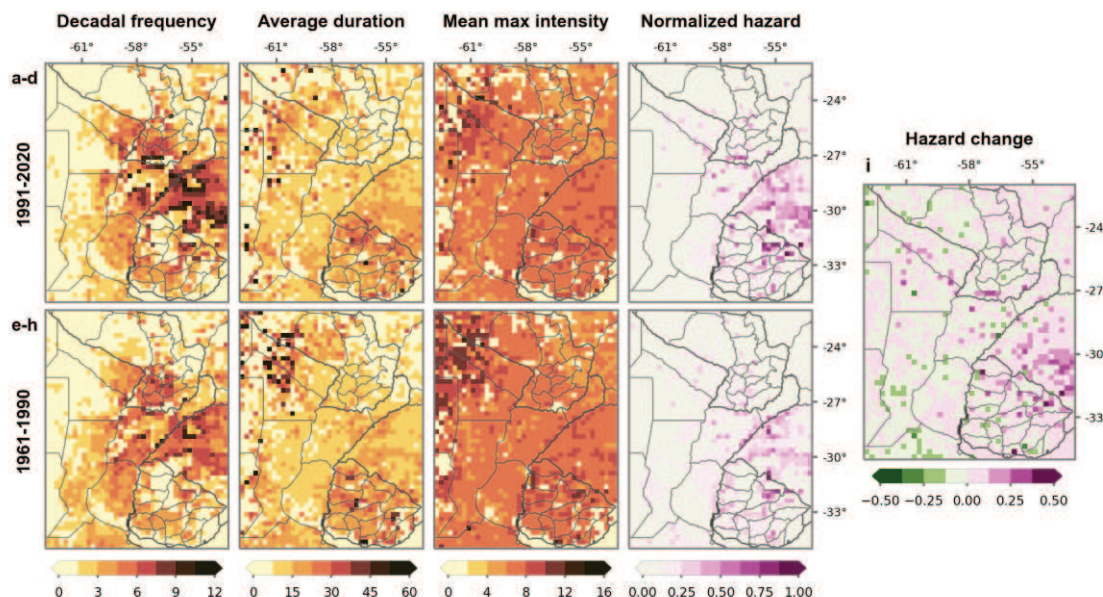


Figura 2.6. Amenaza por eventos de sequías repentinas.

Análisis de amenazas por eventos de sequías repentinas (FD). El análisis abarca dos períodos de tiempo: 1991-2020 (paneles a-d) y 1961-1990 (paneles e-h). Cada fila de paneles presenta la frecuencia decadal (número de eventos por década, primera columna), la duración promedio (pentadas, segunda columna), la intensidad máxima media (valor de SWDI convertido a su equivalente positivo, tercera columna) y la

amenaza normalizada (adimensional, cuarta columna). El panel (i) ilustra el cambio en la amenaza por FD entre los dos períodos. Fuente: Pierrestegui et al. 2024.

El cambio en la amenaza por FD muestra variaciones mínimas y una distribución espacial heterogénea (Figura 2.6i). En promedio, la amenaza por FD experimentó un leve cambio positivo, con un aumento del 1.9% en la amenaza promedio regional. Sin embargo, el aumento es más marcado en regiones cercanas como el norte de Uruguay y el sur de Brasil, y en menor medida en las provincias de Corrientes, Chaco y Formosa. Este cambio se atribuye a un incremento en la frecuencia de FD en estas áreas (Figura 2.6a y e).

2.4.3. Amenazas hidrometeorológicas múltiples de largo y corto plazo

2.4.3.1. Amenazas múltiples de largo plazo

La Figura 2.7 muestra las amenazas hidrometeorológicas múltiples de largo plazo (LT-mH) para los períodos 1991-2020 (Figura 2.7a) y 1961-1990 (Figura 2.7b), junto con el cambio en la amenaza entre estos períodos (Figura 2.7c). Tal como se discutió en la Sección 2.3.3, el índice LT-mH integra los componentes de amenaza de WEP3, WEP18, DEP3 y DEP18. La distribución espacial del LT-mH presenta un gradiente de suroeste a noreste, con valores más altos en el dominio suroeste. La zona crítica de máxima LT-mH (marcada con un rectángulo violeta en la Figura 2.7a) exhibe una alta amenaza tanto de eventos WEP como DEP, con una mayor amenaza de WEP hacia la porción sur de la región de estudio (ver Figura 2.2d, m) y una mayor amenaza de DEP en las áreas occidentales (ver Figura 2.3d, m). Estos resultados subrayan la importancia de las LT-mH para la CCR del centro de Argentina, donde la coexistencia de extremos húmedos y secos puede tener impactos importantes en la agricultura, principalmente en el sur de Santa Fe y Entre Ríos, norte de Buenos Aires y este de Córdoba.

La amenaza múltiple de largo plazo ha aumentado considerablemente hacia el suroeste, impulsada por el incremento simultáneo en ambos componentes de amenaza por WEP y DEP en esta área (Figura 2.2i, r; Figura 2.3i, r). Por otro lado, el índice LT-mH disminuyó en una franja que se extiende en el centro y este de la región sobre el sur de Misiones y norte de Corrientes, principalmente debido a una reducción en el componente de amenaza WEP. Además, la amenaza DEP también disminuyó en la parte oriental de la región de estudio. El promedio regional del índice LT-mH aumentó en un 10.4 % en toda la región de estudio.

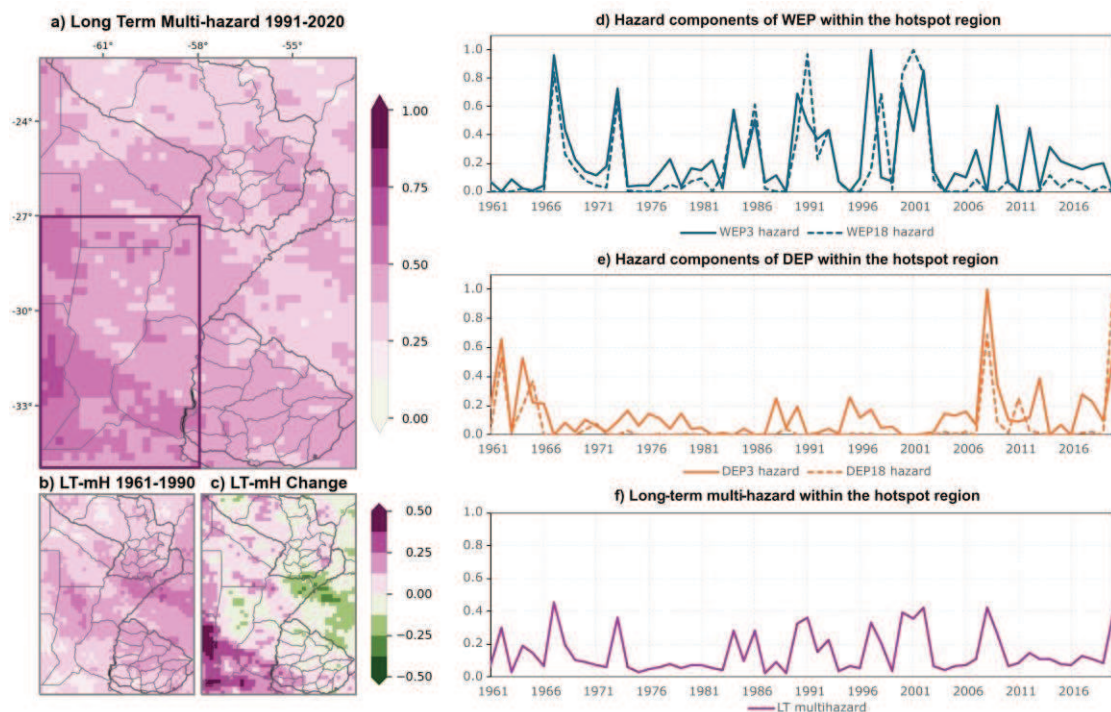


Figura 2.7. Amenazas hidrometeorológicas múltiples de largo plazo.

Análisis de amenazas hidrometeorológicas múltiples de largo plazo (LT-mH). La columna izquierda muestra la distribución espacial del índice LT-mH (adimensional) para los períodos 1991-2020 (panel a) y 1961-1990 (panel b), y el panel (c) ilustra los cambios entre estos períodos. La zona crítica de LT-mH en el período actual está marcada con un rectángulo violeta. La columna derecha muestra las series temporales de los componentes de amenaza por WEP (panel d) y DEP (panel e), así como del índice LT-mH (panel f), todos calculados como promedios areales realizados en la zona crítica.

Fuente: Pierrestegui et al. 2024.

Las Figura 2.7d y 2.7e muestran las series temporales para cada componente de amenaza WEP y DEP promediados en la zona crítica (rectángulo violeta). Entre 1966 y 2004 se observa un período dominado por amenazas debidas a WEP, presentando varios picos que superaron 0.6 tanto en amenazas por WEP3 como por WEP18, incluso algunos picos alcanzaron el valor máximo de amenaza (1.0) en los años 1967, 1991, 1997 y 2001 (Figura 2.7d). En contraste, antes de 1966 predominaron las amenazas por DEP, con valores de DEP3 y DEP18 cercanos a 0.6 (Figura 2.7e). A su vez, desde 2005 las amenazas por WEP3 y DEP3 se han mantenido altas, lo que sugiere que en las últimas dos décadas tanto las amenazas por eventos extremos estacionales húmedos como secos han ocurrido simultáneamente. La amenaza por DEP18 también muestra valores altos (0.7 en 2008 y 1.0 en 2020), lo que sugiere que tanto las amenazas de sequía agrícola como de sequía hidrológica se han intensificado en las últimas dos décadas. Por el contrario, la amenaza por WEP18 se ha mantenido baja desde 2006, indicando que los eventos extremos húmedos han preponderado en la escala estacional en las últimas

décadas. Estos resultados son consistentes con los períodos húmedos y secos de eventos extremos de precipitación de largo plazo identificados por Lovino et al. (2022) para la región del Chaco Austral (ver discusión en el Anexo I, Figura MS3.2). Esto sugiere que dichos períodos podrían influir en una región más amplia del centro-noreste de Argentina, afectando la ocurrencia de amenazas hidrometeorológicas de largo plazo.

La Figura 2.7f muestra que el índice LT-mH exhibe valores máximos que coinciden con picos de eventos húmedos y secos. La variabilidad temporal del LT-mH está influenciada por la coexistencia de eventos húmedos y secos en escalas temporales de 3 meses y 18 meses, observándose picos de amenaza por LT-mH durante todo el periodo. Luego de 2005, el índice LT-mH muestra valores más bajos a pesar de las altas amenazas por WEP3 y DEP3, debido a que en este período se mantiene baja la amenaza por WEP18, y en ciertos años también la amenaza por DEP18.

2.4.3.2. Amenazas múltiples de corto plazo

La Figura 2.8 muestra las amenazas hidrometeorológicas múltiples de corto plazo (ST-mH) para los períodos presente (1991-2020, Figura 2.8a) y pasado (1961-1990, Figura 2.8b), junto con los cambios en la amenaza entre estos períodos (Figura 2.8c). Como se señala en la Sección 2.3.3, el índice ST-mH combina los componentes de amenaza por HW, HP y FD. Las amenazas múltiples de corto plazo exhiben un patrón de distribución espacial inverso en comparación con las de largo plazo, con un gradiente de noreste a suroeste que muestra valores más altos en las porciones noreste y centro-este de la región de estudio. Esta zona crítica de máxima ST-mH (marcada con un rectángulo violeta en la Figura 2.8a) se caracteriza por una coexistencia de amenazas altas por eventos HW, HP y FD. Dentro de esta zona crítica, la amenaza por HW es mayor hacia el norte (ver Figura 2.4d), la amenaza por HP hacia el este (ver Figura 2.5d) y la amenaza por FD hacia el sur (ver Figura 2.6d).

La amenaza múltiple de corto plazo ha mostrado un incremento hacia las provincias del litoral principalmente en Misiones, seguido por Corrientes y Entre Ríos, así como el este de Formosa, Chaco y Santa Fe (Figura 2.8c). Este cambio ha sido impulsado principalmente por un aumento simultáneo en los componentes de la amenaza por HW y HP en esta área (ver Figura 2.4i y 2.5i). El componente de amenaza por FD contribuye principalmente al incremento del índice ST-mH en zonas aledañas como el sur de Brasil. Por el contrario, el índice ST-mH muestra una ligera disminución en la zona occidental de Formosa, Chaco, y Santa Fe, así como el este de Santiago del Estero y Córdoba. Este

cambio se debe principalmente a una disminución conjunta en esta área en los componentes de amenaza por HW, HP y FD. En términos generales, el índice ST-mH ha aumentado en promedio un 17.3 % en la región de estudio. Este aumento en el promedio regional del índice ST-mH es superior al incremento en el índice LT-mH (10.7 %), aunque el índice LT-mH muestra valores locales de cambio más elevados.

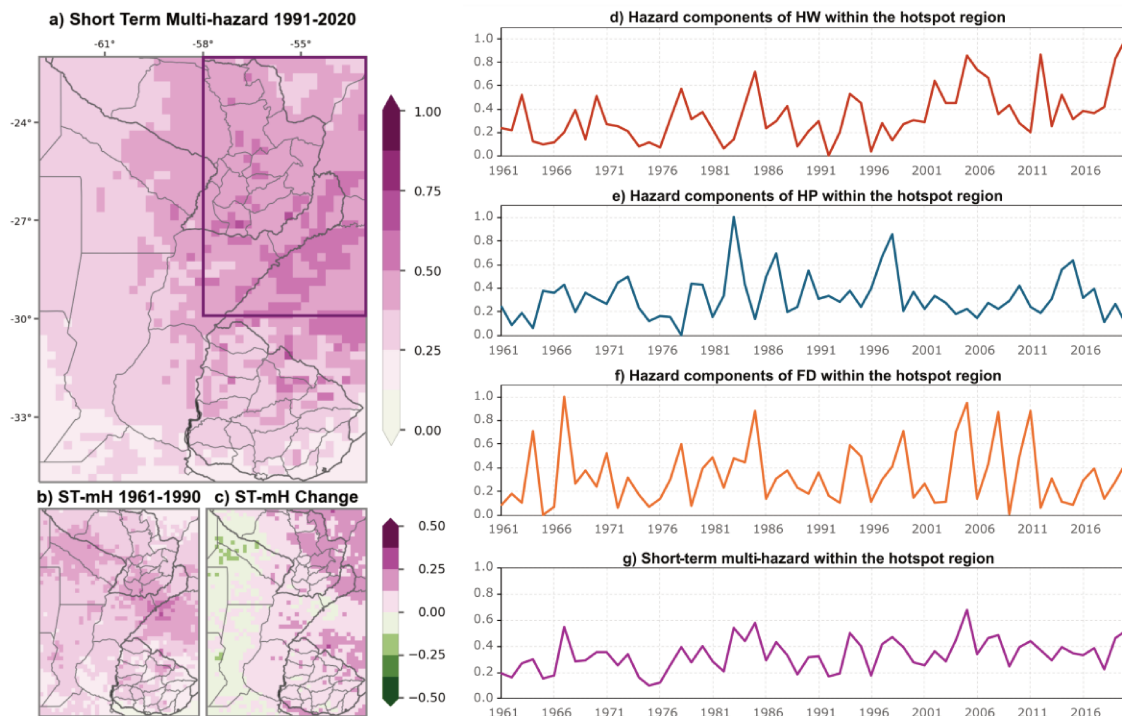


Figura 2.8. Amenazas hidrometeorológicas múltiples de corto plazo.

Análisis de amenazas hidrometeorológicas múltiples de corto plazo (ST-mH). La columna izquierda muestra la distribución espacial del índice ST-mH (adimensional) para los períodos 1991-2020 (panel a) y 1961-1990 (panel b), y el panel (c) ilustra los cambios entre estos períodos. La zona crítica de ST-mH en el período actual está marcada con un rectángulo violeta. La columna derecha muestra las series temporales de los componentes de amenaza por HW (panel d), HP (panel e) y FD (panel f), así como del índice ST-mH (panel g), todos calculados como promedios areales realizados en la zona crítica. Fuente: Pierrestegui et al. 2024.

Las Figura 2.8d a 2.8f presentan las series temporales de los componentes de amenaza por HW, HP y FD promediados en la zona crítica (rectángulo violeta en la Figura 2.8a). La amenaza por HW muestra un aumento importante desde la década de 1990 hasta el presente, mostrando valores más elevados después de 2004 que superan 0.8 (2005 y 2012) y alcanzando el máximo de 1.0 en 2020 (Figura 2.8d). De forma similar a lo que ocurre con las amenazas por WEP, la amenaza por HP muestra magnitudes más altas entre 1966 y 2004, con picos que van de 0.6 a 1.0 (Figura 2.8e). Por el contrario, la amenaza por FD exhibe mayores valores antes de 1966 y después de 2005 (Figura 2.8f), similar a lo que

ocurre con las amenazas por DEP. Resulta de interés destacar que el mayor valor de amenaza por FD ocurre después de 2004, coincidiendo con un período de alta amenaza por HW. A su vez, se observa que entre 1966 y 2004 persistió una amenaza por FD de relevancia (con un valor medio de 0.3 normalizado). Este resultado se alinea con las características inherentes al fenómeno de sequías repentinas, que implica un agotamiento rápido de la humedad del suelo que puede ocurrir junto con anomalías de alta temperatura y un aumento de la evapotranspiración cuando los niveles de humedad del suelo son inicialmente altos (ver Lovino et al. 2025; Pendergrass et al. 2020; mayor detalle en Anexo I – Figura MS2.2). Finalmente, el índice ST-mH alcanzó mayores valores entre 1966 y 2006, con picos de amenaza de hasta 0,6 (Figura 2.8g). En este período se da la mayor superposición en la ocurrencia de los tres componentes de amenaza de corto plazo (HW, HP y FD).

2.4.3.3. Composición total de amenazas múltiples

La Figura 2.9 presenta la composición total de amenazas hidrometeorológicas múltiples (T-mH), combinando los índices de amenaza múltiple de largo plazo y corto plazo. El índice T-mH actual en la región (Figura 2.9a) exhibe una distribución espacial más uniforme en comparación con el período histórico (Figura 2.9b). Actualmente, la amenaza múltiple por eventos hidrometeorológicos extremos es alta en casi toda la región. Los valores más altos de T-mH predominan en las provincias del litoral como Misiones, Corrientes y Entre Ríos, así como el este de Formosa y Chaco, y en la CCR como sur de Santa Fe, este de Córdoba y norte de Buenos Aires. Esta región es una de las áreas agrícolas más productivas del continente y del mundo, por lo que una alta ocurrencia de amenazas hidrometeorológicas diversas pueden impactar los rendimientos de los cultivos y afectar la seguridad alimentaria de la región.

La amenaza múltiple por EHEs ha aumentado en la mayor parte de la región de estudio en las últimas décadas (Figura 2.9c). Durante el período 1961-1990, los valores más altos de amenaza se concentraban en una franja que abarcaba las partes central y oriental de la región, particularmente sobre el sur de Misiones y norte de Corrientes. Al comparar los dos períodos (Figura 2.9c), se observa que el índice T-mH se redujo dentro de esta franja y se distribuyó más uniformemente. A pesar de esta disminución localizada, el promedio regional del índice T-mH muestra un aumento de 13.6 %, lo que indica un incremento generalizado tanto en las amenazas de largo plazo como en las de corto plazo.

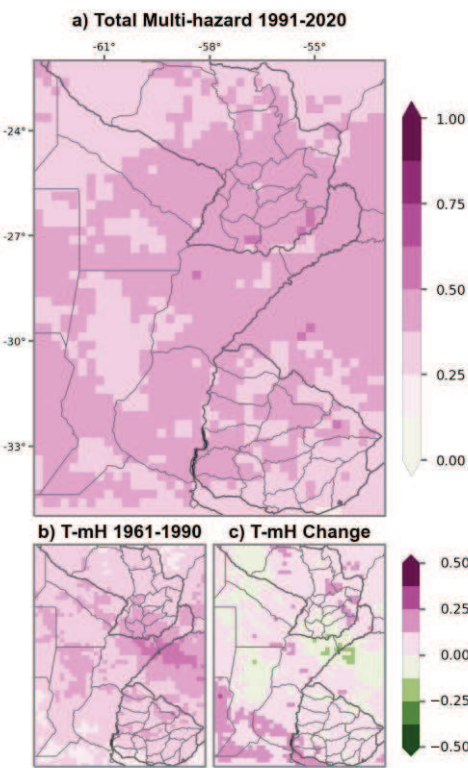


Figura 2.9. Amenazas hidrometeorológicas múltiples totales.

Análisis de amenazas hidrometeorológicas múltiples totales (T-mH). El análisis abarca dos períodos de tiempo: 1991-2020 (panel a) y 1961-1990 (panel b). El panel (c) ilustra el cambio en el índice T-mH entre los dos períodos. Fuente: Pierrestegui et al. 2024.

2.5. Síntesis

Este capítulo presenta un análisis de las amenazas múltiples por eventos hidrometeorológicos extremos de largo y corto plazo, así como sus cambios, en el centro-noreste de Argentina durante los periodos 1961-1990 y 1991-2020, utilizando datos diarios a mensuales de ERA5. Los EHEs de largo plazo se analizan mediante el índice de precipitación estandarizado en escalas temporales de 3 y 18 meses. Los EHEs de corto plazo se caracterizan por olas de calor, precipitaciones intensas y sequías repentinas. Los componentes individuales de amenaza se obtienen multiplicando la frecuencia, duración e intensidad de los EHEs identificados. Los índices de amenazas múltiples por EHEs de largo y corto plazo se obtienen mediante la agregación de los componentes individuales de amenaza.

La amenaza de largo plazo por eventos extremos de exceso de precipitación, que combina los eventos de escala temporal de 3 y de 18 meses, es mayor en la provincia de Entre Ríos, sur de Santa Fe, y norte de Buenos Aires, así como en el norte de Misiones. A su vez, en estas mismas áreas esta amenaza aumentó notoriamente entre los dos períodos.

En cuanto a los eventos extremos de déficit de precipitación en ambas escalas temporales (3 y de 18 meses), existe un mayor nivel de amenaza en la provincia de Formosa, el oeste de Chaco y Santa Fe, así como en el este de Salta, Santiago del Estero y Córdoba. Además, en esta misma área, la amenaza por déficits de precipitación aumentó considerablemente, mientras que en el este de la región experimentó una disminución. En promedio, la amenaza por eventos a escala hidrológica (18 meses) es ligeramente inferior a la de eventos estacionales (3 meses) a nivel regional, sin embargo, su incremento fue notoriamente superior al de los eventos estacionales.

Entre las amenazas de corto plazo, las olas de calor constituyen la amenaza más extendida en la región, con un mayor nivel de amenaza en el norte, principalmente en las provincias de Corrientes, Misiones y Formosa. A su vez, la amenaza por olas de calor ha aumentado de forma generalizada en el este, con un aumento promedio para la región del 31.5% que responde a un marcado aumento en la frecuencia. Los eventos de precipitación intensa también son muy frecuentes en la región de estudio. La mayor amenaza por precipitaciones intensas se observa en Misiones y Corrientes, con un gradiente decreciente de noreste a suroeste, siendo mayor en las regiones más húmedas y menor en las regiones más secas. Si bien la mayor frecuencia de eventos de precipitaciones intensas se da en Misiones, los eventos más intensos se registran en las provincias de Corrientes, Entre Ríos y el este de Santa Fe. Finalmente, la amenaza por sequías repentinas es baja en la región, registrándose el mayor nivel en el centro-este de la región, y en países vecinos como Uruguay y el sur de Brasil. Esta amenaza también registró un aumento en las últimas décadas, aunque de menor magnitud.

Los hallazgos de este capítulo indican que la región del centro-noreste de Argentina enfrenta una amenaza múltiple por EHEs con patrones temporales y espaciales distintos para amenazas de corto y largo plazo. Temporalmente, las amenazas múltiples por EHEs de corto plazo son más propensas a coexistir, mientras que las amenazas de largo plazo tendieron a alternarse en el tiempo hasta 2006, observándose mayor coexistencia de eventos de escala estacional luego de ese año. Espacialmente, las amenazas múltiples de largo plazo son más elevadas hacia el suroeste, donde también han aumentado considerablemente debido al aumento simultáneo de déficits y excesos de precipitación. Por otro lado, las amenazas múltiples de corto plazo muestran un patrón espacial opuesto, con niveles más altos en el noreste y centro-este de la región de estudio, donde también se registra un aumento entre períodos. Aunque ambos tipos de amenazas han experimentado un aumento, el promedio regional de las amenazas de corto plazo aumentó

Capítulo 2: Evaluación de amenazas múltiples

1.7 veces más que el de largo plazo, si bien este último presenta un incremento mayor a escala local. Las amenazas múltiples totales en el periodo actual exhiben una distribución espacial más uniforme en comparación con el período histórico, extendiéndose a gran parte de la región.

Capítulo 3: Vulnerabilidad y riesgo a amenazas hidrometeorológicas múltiples

3.1. Introducción

Los riesgos asociados al clima resultan de la interacción entre las amenazas climáticas y la vulnerabilidad de los sistemas sociales y naturales afectados (Birkmann et al. 2013; Oppenheimer et al. 2014). Las amenazas climáticas están determinadas por las características físicas de los eventos climáticos, mientras que la vulnerabilidad se refiere a la predisposición de los sistemas a sufrir impactos negativos, y está asociada a factores sociales y ecológicos que influyen en la capacidad de los sistemas para anticiparse y responder a los efectos de estos eventos (Ara Begum et al. 2022; Sharma y Ravindranath 2019). La vulnerabilidad es dinámica y está moldeada por elementos como la sensibilidad y la capacidad adaptativa, que determinan la severidad que tendrán los daños sufridos por diferentes comunidades ante un mismo evento climático (Ford et al. 2018; McDowell et al. 2016; Naylor et al. 2020; Viner et al. 2020). En consecuencia, el riesgo climático—definido como el potencial de sufrir consecuencias adversas para los sistemas humanos o ecológicos—varía entre comunidades, influido por desigualdades y condiciones específicas de cada contexto (IPCC 2022a; Rising et al. 2022).

A pesar de su importancia, se ha prestado poca atención a ampliar nuestro entendimiento sobre los riesgos y vulnerabilidades asociados a eventos extremos en el SESA. Los principales impactos asociados a factores climáticos identificados para la región incluyen: (1) inseguridad alimentaria por sequías recurrentes y severas, (2) amenazas a la vida e infraestructura por inundaciones y deslizamientos de tierra, (3) escasez de agua, y (4) riesgos para la salud pública debido al incremento de epidemias de enfermedades transmitidas por vectores (Castellanos et al. 2022 y sus referencias; Hagen et al. 2022; Magrin et al. 2014). La vulnerabilidad a sequías e inundaciones tiende a ser inversamente proporcional al nivel de desarrollo económico y social. Factores como el crecimiento poblacional, la urbanización rápida de asentamientos informales, la existencia de infraestructuras inadecuadas, altos niveles de desigualdad social y pobreza, economías dependientes de la agricultura, y prácticas ambientales insostenibles exacerbان la vulnerabilidad, intensificando los impactos negativos que pueden tener los déficits y excesos hídricos (Alvala et al. 2024; Barros et al. 2015; Camilloni et al. 2020; Liu et al. 2025; Pizzorni et al. 2024). En Argentina, las sequías y las inundaciones, agravadas por

vulnerabilidades locales como escasez de recursos y falta de infraestructura, pueden desencadenar desastres generalizados que afectan la economía nacional (Agosta et al. 2021; Bert et al. 2021; Bohn y Piccolo 2019; Bortz y Toftum 2023; Borzi et al. 2021; González et al. 2021; Houspanossian et al. 2023; Naumann et al. 2019; Tomasz et al. 2024). Dado el papel crítico que desempeñan estas vulnerabilidades al magnificar los impactos de eventos extremos, abordar las brechas persistentes en la comprensión de los riesgos y vulnerabilidades regionales es esencial para generar políticas públicas hacia un desarrollo resiliente al clima y estrategias efectivas de prevención y adaptación ante desastres relacionados con el clima.

En este capítulo se evalúan la vulnerabilidad y el riesgo frente a los eventos hidrometeorológicos extremos en el centro-noreste de Argentina. Se desarrollan y analizan métricas para estudiar los componentes de la vulnerabilidad, incluyendo exposición, sensibilidad y capacidad adaptativa. Además, se estudian los niveles de riesgo tanto para amenazas individuales como para amenazas múltiples asociadas con los EHEs. Las amenazas individuales abarcan eventos extremos de déficit y exceso de precipitación de largo plazo, y eventos extremos de corto plazo como olas de calor, precipitación intensa, y sequías repentinas. Las amenazas múltiples a su vez combinan EHEs de largo plazo, corto plazo, y totales.

3.2. Datos

Las amenazas individuales por EHEs y las amenazas múltiples se derivan del capítulo anterior. En dicho capítulo se utilizó datos de precipitación, humedad del suelo y temperatura de la quinta versión del reanálisis del Centro Europeo de Predicción Meteorológica a Medio Plazo (ECMWF, ERA5, Hersbach et al. 2020; 2023a, b) con una resolución espacial de $0.25^\circ \times 0.25^\circ$, cubriendo el período de 1991 a 2020 (ver más detalles en el capítulo 2). Este período se eligió porque representa el período climático más reciente de 30 años, según lo definido por la Organización Meteorológica Mundial (WMO, 2017).

Los riesgos por EHEs se analizan utilizando diferentes conjuntos de datos, como se detalla en la Tabla 3.1. Los componentes de vulnerabilidad se cuantifican utilizando datos de instituciones nacionales argentinas, a nivel de unidades geográficas departamentales (divisiones administrativas por debajo de las provincias). Los indicadores sociales —que incluyen población total, poblaciones vulnerables, dependencia potencial, acceso a la tecnología, nivel educativo y cobertura de salud— se derivan del último Censo Nacional

Capítulo 3: Vulnerabilidad y riesgo

de Población, Hogares y Viviendas realizado en 2022 por el Instituto Nacional de Estadística y Censos (INDEC 2022). Los datos de rendimiento de cultivos de maíz y soja, que cubren el período 2000–2020, se obtienen de registros históricos proporcionados por el Ministerio Agricultura, Ganadería y Pesca de la Nación (MAGyP 2021a, b). Los datos sobre infraestructura crítica e ingresos se derivan de la información proporcionada por el Instituto Geográfico Nacional (IGN 2021), con información geoespacial actualizada al año 2021. Finalmente, los datos sobre cambio en el uso del suelo se obtienen de Bracalenti et al. (2024), quienes estimaron la cobertura de suelo dominante y su evolución entre 2001 y 2015 utilizando mapas de uso de suelo derivados del producto MODIS Land Cover Climate Modeling Grid (MCD12C1) con una grilla de 0.05° , y siguiendo la clasificación del Programa Internacional Geosfera-Biósfera. Cabe destacar que los indicadores socioeconómicos representan los datos más actualizados disponibles, los rendimientos de cultivos se estiman sobre un período de 20 años para garantizar una calidad de datos robusta, y los datos de uso del suelo provienen de Bracalenti et al. (2024). Todos estos conjuntos de datos se consideran representativos del período utilizado para estudiar las amenazas (1991–2020).

Tabla 3.1. Componentes de amenaza y vulnerabilidad.

Tabla resumen de las variables utilizadas, junto con sus fuentes de datos.

| Componente | Variable | Descripción | Relevancia | Fuente |
|----------------------|----------------------------------|--|--|----------------------------|
| Amenazas | WEP | Eventos extremos de exceso de precipitación basados en SPI3 y SPI18. | Excesos hídricos a escala agrícola e hidrológica. | Pierrestegui et al. (2024) |
| | DEP | Eventos extremos de déficit de precipitación basados en SPI3 y SPI18. | Sequías agrícolas e hidrológicas. | |
| | HW | Olas de calor según De Luca y Donat (2023). | | |
| | HP | Eventos de precipitación intensa según Weber et al. (2020). | Impactos inmediatos en producción de alimentos, salud pública, e infraestructura. | |
| | FD | Sequías repentinas según Lovino et al. (2024). | | |
| Amenazas múltiples | LT-mH | Amenazas múltiples de largo plazo compuestas por WEP y DEP. | Eventos extremos húmedos y secos con impactos a escala estacional e hidrológica. | Pierrestegui et al. (2024) |
| | ST-mH | Amenazas múltiples de corto plazo compuestas por HW, HP y FD. | Eventos extremos húmedos, secos y cálidos con impactos a escala diaria. | |
| | T-mH | Amenazas múltiples totales compuestas por LT-mH y ST-mH. | Eventos extremos húmedos, secos y cálidos con impactos a escala diaria, estacional e hidrológica. | |
| Exposición | Población total | Número total de habitantes. | Impactos directos en la población: salud, seguridad, vivienda, medios de vida | INDEC (2022) |
| | Rendimiento de cultivos | Rendimiento promedio de maíz y soja desde 2000 hasta 2020. | Impactos en los medios de vida, la producción de alimentos, la seguridad alimentaria. | MAGyP (2021a, b) |
| | Infraestructura crítica | Cantidad de sistemas e instalaciones esenciales para el funcionamiento de la sociedad. | Interrupción en servicios y sistemas esenciales, con efectos en cascada. | IGN (2021) |
| Sensibilidad | Población sensible | Porcentaje de la población menor de 14 años y mayor de 65 años. | Sensibilidad sanitaria y socioeconómica. | INDEC (2022) |
| | Dependencia potencial | Relación entre población potencialmente inactiva y activa por edad. | Condiciones materiales que predisponen a sufrir efectos adversos. | |
| | Sensibilidad asociada a ingresos | Inverso de la relación entre el ingreso laboral promedio del sector privado registrado y el ingreso total. | Condiciones materiales que predisponen a sufrir efectos adversos. | IGN (2021) |
| Capacidad adaptativa | Cambio en el uso del suelo | Cambios en el uso del suelo que incluyen deforestación entre 2001 y 2015. | Condiciones ambientales que favorecen o intensifican los efectos negativos. | Bracalenti et al. (2024) |
| | Acceso a la tecnología | Porcentaje de hogares con acceso a la tecnología. | Capacidad para prepararse ante amenazas, aprovechar oportunidades y responder a las consecuencias. | INDEC (2022) |
| | Nivel educativo | Porcentaje de la población mayor de 25 años con secundario completo. | Capacidad para prepararse ante amenazas, aprovechar oportunidades. | |
| | Cobertura de salud | Porcentaje de la población con acceso a servicios de salud privados o públicos. | Capacidad para prepararse ante amenazas y responder a las consecuencias. | |

3.3. Metodología

3.3.1. Marco utilizado para evaluar vulnerabilidad y riesgo

La Figura 3.1a presenta un diagrama esquemático que resume el enfoque utilizado para evaluar los índices de vulnerabilidad y riesgo. El riesgo climático surge de la interacción entre las amenazas climáticas y la vulnerabilidad de una sociedad determinada, y puede generar impactos significativos a nivel económico, social y ambiental. (Birkmann et al. 2013; O'Neill et al. 2022; Stalhandske et al. 2024). Las amenazas se refieren a eventos físicos relacionados con el clima, ya sean naturales o inducidos por el ser humano, que tienen el potencial de causar pérdidas de vidas, afectaciones u otros impactos en la salud, así como daños o pérdidas en bienes, infraestructura, medios de vida, provisión de servicios, ecosistemas y recursos ambientales (IPCC 2022b). En este estudio, las amenazas climáticas incluyen amenazas hidrometeorológicas individuales y amenazas múltiples.

La vulnerabilidad indica la predisposición o propensión de un sistema a ser afectado adversamente por un evento climático peligroso (IPCC 2022b). Por lo tanto, la vulnerabilidad define cómo la interacción entre las amenazas y las sociedades configura el riesgo y se analiza a través de sus tres componentes: exposición, sensibilidad y capacidad adaptativa (por ejemplo, Weis et al. 2016; Yu et al. 2021). Aunque la vulnerabilidad es un componente del riesgo, también es un factor independiente importante que mejora la comprensión de los impactos diferenciados de las amenazas climáticas en diversos contextos socioeconómicos.

Este marco metodológico adaptado de Birkmann et al. (2013) (Figura 3.1a), ofrece una perspectiva holística para la evaluación de la vulnerabilidad, integrando factores físicos, sociales y ambientales. A diferencia de enfoques que delimitan la exposición como componente separado de la vulnerabilidad, este marco incluye explícitamente la exposición como parte constitutiva de la vulnerabilidad. Esta decisión responde a la necesidad de capturar no solo la sensibilidad o susceptibilidad al daño, sino también las condiciones contextuales que influyen en la vulnerabilidad social, tales como la ubicación geográfica, la infraestructura disponible y el acceso desigual a recursos. Al integrar la exposición dentro del concepto de vulnerabilidad, se reconoce que la presencia en zonas de riesgo es en sí misma una condición de fragilidad que interactúa con factores sociales y estructurales, fortaleciendo así el análisis de riesgos en entornos complejos y cambiantes. Esta perspectiva es especialmente relevante en estudios de amenazas

hidrometeorológicas, donde la intensidad de la exposición y la capacidad de respuesta local definen el impacto final sobre las comunidades. Como resultado de este enfoque, se obtiene un solo mapa de vulnerabilidad regional para conjugar con las distintas amenazas, que será el resultado de la combinación de diferentes condiciones contextuales.

3.3.2. Amenazas hidrometeorológicas individuales y múltiples

Este capítulo evalúa los riesgos climáticos asociados con las amenazas por EHEs derivadas del Capítulo 2. El análisis incorpora amenazas individuales, caracterizadas por su frecuencia, duración e intensidad, y amenazas múltiples, evaluadas a través de un análisis multi-capas de las amenazas individuales. Las amenazas individuales y múltiples se analizan en escalas de tiempo de largo y corto plazo (Tabla 3.1). Las amenazas individuales incluidas en el análisis son los eventos extremos de exceso de precipitación (WEP) y déficit de precipitación (DEP), olas de calor (HW), precipitación intensa (HP) y sequías repentinas (FD) (ver Tabla 3.1).

Las series temporales de los componentes individuales de amenazas para cada EHE se construyen multiplicando la frecuencia decadal, la duración promedio y la intensidad máxima media de los eventos en el período 1991-2020. Cada serie temporal se normaliza en una escala de 0-1 (ver Capítulo 2 para detalles metodológicos). Los componentes individuales de amenaza normalizados se combinan posteriormente para generar tres índices de amenaza múltiple: el índice de amenaza múltiple de largo plazo (LT-mH), que combina WEP y DEP; el índice de amenaza múltiple de corto plazo (ST-mH), que integra HW, HP y FD; y el índice de amenaza múltiple total (T-mH), que agrega LT-mH y ST-mH (ver Tabla 3.1). El índice LT-mH caracteriza las amenazas por eventos húmedos y secos en escalas estacionales e hidrológicas. El índice ST-mH representa amenazas por eventos húmedos, secos y cálidos en escalas temporales diarias a semanales. El T-mH combina amenazas por EHEs en todas las escalas de tiempo.

Espacialmente, los valores de amenaza individuales y múltiples se interpolan de una resolución de $0.25^\circ \times 0.25^\circ$ (derivada del Capítulo 2) a $0.125^\circ \times 0.125^\circ$. Esta interpolación se realiza para ajustar la resolución espacial del grillado a la mayoría de los departamentos provinciales de Argentina. Posteriormente, se promedian para los puntos de grilla dentro de los límites departamentales, proporcionando un único valor de amenaza por departamento para el análisis de riesgo.

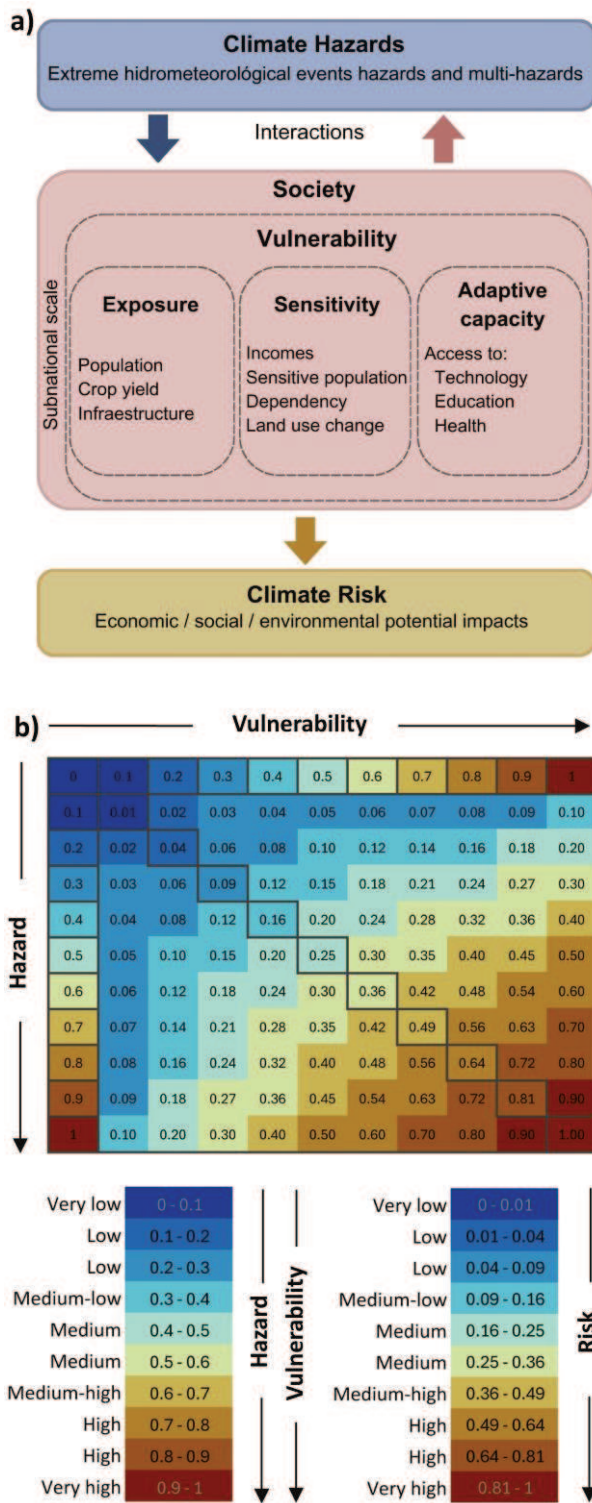


Figura 3.1. Diagrama metodológico para evaluar la vulnerabilidad y el riesgo.
Diagrama esquemático que detalla la metodología para evaluar la vulnerabilidad y el riesgo. (a) Esquema del marco metodológico, adaptado de Birkmann et al. (2013). (b)

Matriz del nivel de riesgo que muestra la relación entre los niveles de amenaza y vulnerabilidad. Las escalas muestran las categorías o niveles de amenaza, vulnerabilidad y riesgo, que van desde muy bajo (azul oscuro) hasta muy alto (marrón oscuro). Fuente: Pierrestegui et al. 2025.

3.3.3. Componentes de vulnerabilidad

La vulnerabilidad se analiza a través de sus tres componentes fundamentales: exposición, sensibilidad y capacidad adaptativa, siguiendo las definiciones proporcionadas por el IPCC (2022b). La exposición se refiere a la presencia de personas, medios de vida e infraestructura en áreas propensas a posibles amenazas. La sensibilidad refleja el grado en que un sistema o sociedad puede ser afectado por dicha exposición, ya sea positiva o negativamente. La capacidad adaptativa representa la habilidad de un sistema para modificar sus características o comportamiento para adaptarse y afrontar los cambios, incluyendo la capacidad de anticiparse a las amenazas, aprovechar las oportunidades y responder eficazmente a sus consecuencias. Para evaluar estos componentes en la región de estudio, se seleccionan variables representativas, considerando su relevancia y confiabilidad.

La exposición se cuantifica mediante tres variables: población total, rendimiento de cultivos e infraestructura crítica (Tabla 3.1). La población total, definida como el número de habitantes por departamento, representa la exposición social directa a las amenazas. El rendimiento de cultivos, calculado como el rendimiento promedio de maíz y soja entre 2000 y 2020, captura la exposición agrícola a las amenazas climáticas, dado que estos son los cultivos predominantes en la región (Sgroi et al. 2021). La infraestructura crítica abarca los sistemas, instalaciones y activos esenciales para el funcionamiento de la sociedad, cuya interrupción puede desencadenar impactos en cascada, afectando múltiples sectores de manera significativa. Incluye sistemas de energía (centrales eléctricas y estaciones transformadoras), instalaciones de gestión de agua y residuos (plantas de tratamiento de agua, plantas de tratamiento de aguas residuales, plantas de tratamiento de residuos sólidos, y rellenos sanitarios) y redes de transporte (aeropuertos, puentes, túneles, estaciones ferroviarias, rutas, y autopistas).

La sensibilidad se evalúa mediante cuatro variables: población sensible, dependencia potencial, sensibilidad asociada a los ingresos y cambio en el uso del suelo (Tabla 3.1). La población sensible se refiere a grupos con resiliencia limitada debido a factores físicos, sociales y/o económicos, calculada en función del porcentaje de personas menores de 14 años y mayores de 65 años en relación con la población total. La dependencia potencial mide la proporción de personas en edades potencialmente inactivas en relación con aquellas en edades potencialmente activas, expresándose como el número de personas inactivas por cada 100 personas activas. La sensibilidad asociada a los ingresos evidencia

la vulnerabilidad generada por recursos financieros limitados, y es definida como la inversa del ingreso laboral promedio de hombres y mujeres en el sector privado registrado, en relación con el ingreso total de su grupo. El cambio en el uso del suelo refleja sensibilidad ambiental y pone de manifiesto la degradación del ecosistema, lo cual intensifica los impactos de las amenazas. Está basado en datos de deforestación que reflejan transiciones desde categorías de vegetación con mayor cobertura arbórea hacia otras con menor cobertura entre 2001 y 2015 (Bracalenti et al. 2024).

La capacidad adaptativa abarca la habilidad para reducir los impactos negativos, mitigar los daños o aprovechar las oportunidades positivas que surgen de los eventos climáticos extremos y del cambio climático a largo plazo. Se incluye en este estudio tres indicadores clave de capacidad adaptativa (basados en USAID 2016): acceso a la tecnología, nivel educativo y cobertura de salud (Tabla 3.1). El acceso a la tecnología, medido como el porcentaje de hogares con internet, teléfonos móviles y dispositivos informáticos, refleja la capacidad de anticiparse y responder a las amenazas. El nivel educativo, definido como el porcentaje de personas mayores de 25 años que han completado la educación secundaria o superior, refleja la capacidad de la población para adaptarse a los desafíos cambiantes y capitalizar las oportunidades que se presentan ante estas amenazas. La cobertura de salud, medida como el porcentaje de la población que cuenta con acceso a programas de salud prepagos o financiados por el estado, representa la capacidad para responder y recuperarse de los impactos negativos de los EHE.

3.3.4. Cuantificación de la vulnerabilidad

En primer lugar, las variables seleccionadas (Tabla 3.1) se normalizan para generar índices comparables y combinables entre sí. Siguiendo la metodología de Tabari y Willems (2023), la normalización se realiza mediante un reescalado lineal basado en los valores mínimo y máximo, ajustados entre los percentiles 0.05 (mínimo) y 0.95 (máximo) (Ecuación 3.1):

$$Nv(0,1) = (vc - \min(vc)) / (\max(vc) - \min(vc)) \quad (3.1)$$

donde $Nv(0,1)$ son los índices normalizados de los componentes de la vulnerabilidad, vc son las variables individuales de los componentes de la vulnerabilidad, y $\min(vc)$ y $\max(vc)$ son los valores mínimos (percentil 0.05) y máximos (percentil 0.95) de las variables correspondientes. Los valores que exceden $\max(vc)$ se establecen como 1, mientras que los valores por debajo de $\min(vc)$ se establecen en 0.

En segundo lugar, siguiendo la metodología de Naumann et al. (2014), los índices normalizados se combinan para obtener los tres componentes de vulnerabilidad: exposición (C_e), sensibilidad (C_s) y capacidad adaptativa (C_{ac}). Todos los índices normalizados $Nv_i(0,1)$ tienen valores entre 0 y 1. De esta forma, para cada unidad geográfica (departamento), el componente de vulnerabilidad $C_k(0,1)$ tendrá valores entre 0 y 1 y se calcula como la media ponderada de los n índices normalizados $Nv_i(0,1)$ que definen cada componente (Ecuación 3.2):

$$C_k(0,1) = \sum_{i=1}^n w_i Nv_i(0,1) \quad (3.2)$$

donde $C_k(0,1)$ representa cada componente de la vulnerabilidad (C_e , C_s , C_{ac}) con valores entre 0 y 1, y w_i son los pesos de los índices normalizados de cada componente $Nv_i(0,1)$, siendo n el número total de índices normalizados por componente. Los pesos del promedio ponderado se determinan a través del Análisis por Componentes Principales (PCA) (Abdi y Williams 2010; Jolliffe y Cadima 2016). El PCA es un método robusto de reducción de dimensionalidad que identifica patrones en datos multivariados al capturar la máxima varianza a lo largo de ejes ortogonales. En este estudio, los pesos se determinan a partir de las cargas del primer componente principal (PC1), el cual explica la mayor proporción de la varianza de las variables en cada componente. Las cargas asociadas al PC1, que representan la contribución relativa de cada variable al componente, se convierten en valores absolutos y se normalizan para que su suma sea igual a uno. Este proceso asegura que los pesos representen con precisión la contribución relativa de cada variable a la variabilidad total del conjunto de datos. Este enfoque basado en datos elimina sesgos subjetivos, aborda de manera eficiente las correlaciones entre las variables y garantiza una ponderación objetiva dentro de cada componente.

En tercer lugar, los tres componentes de vulnerabilidad se combinan en un índice general de vulnerabilidad, obtenido como la media ponderada de los tres componentes (Ecuación 3.3):

$$V(0,1) = (w_e C_e + w_s C_s + w_{ac} (1 - C_{ac})) \quad (3.3)$$

donde $V(0,1)$ representa el índice de vulnerabilidad, C_e el componente de exposición, C_s el componente de sensibilidad, y C_{ac} el componente de capacidad adaptativa. Para determinar los pesos de los componentes (w_e, w_s, w_{ac}), se realiza un PCA adicional sobre los tres componentes ($C_e, C_s, 1 - C_{ac}$). Este enfoque garantiza que se capture la máxima variabilidad entre los componentes, manteniendo la consistencia en las contribuciones de

las variables dentro de cada componente y su influencia en el índice general (Abdi y Williams 2010). Dado que existe una relación inversa entre la capacidad adaptativa y la vulnerabilidad (es decir, una menor capacidad adaptativa corresponde a una mayor vulnerabilidad), se utiliza $1 - C_{ac}$ para la cuantificación de la vulnerabilidad (Tabari y Willems 2023). Este enfoque garantiza que todos los componentes de la vulnerabilidad se encuentren en un rango que va desde el valor menos vulnerable (0) hasta el más vulnerable (1), proporcionando una escala uniforme y coherente para su interpretación.

3.3.5. Cuantificación del riesgo

Finalmente, el riesgo se cuantifica como el producto entre la amenaza y la vulnerabilidad (Peduzzi et al. 2009; Ward et al. 2020; Zhou et al. 2015), asignando pesos iguales a cada componente (Binita et al. 2021) (Ec. 3.4):

$$R(0,1) = H(0,1) \times V(0,1) \quad (3.4)$$

donde $R(0,1)$ es el índice de riesgo, $H(0,1)$ es el índice de amenaza, y $V(0,1)$ es el índice de vulnerabilidad. Tanto $H(0,1)$ como $V(0,1)$ están normalizados en una escala lineal de 0 a 1. A medida que cualquiera de los componentes se aproxima a cero, el valor del riesgo también se acerca a cero. Por el contrario, cuando tanto la amenaza como la vulnerabilidad alcanzan sus valores máximos, el riesgo se aproxima a su valor máximo de 1. En consecuencia, $R(0,1)$ varía entre 0 y 1, aunque no sigue una escala lineal. En la Figura 3.1b se ilustran las categorías de riesgo correspondientes a los distintos rangos de $R(0,1)$, derivadas de la combinación de los valores de amenaza y vulnerabilidad.

3.4. Resultados

3.4.1. Componentes de vulnerabilidad

3.4.1.1. Exposición

La Figura 3.2 presenta el índice de exposición derivado de la agregación de tres índices normalizados: población total, rendimiento de cultivos e infraestructura crítica. El índice de población total (Figura 3.2a) indica que la población es generalmente baja en toda la región, con un índice promedio de 0.23. Las mayores concentraciones de población se encuentran en departamentos que albergan importantes áreas metropolitanas, incluyendo Corrientes, Santa Fe, Paraná, Rosario y el área metropolitana de Buenos Aires. Se destacan La Matanza (Buenos Aires) y Rosario (Santa Fe), cuyas poblaciones son 2.4 y 1.8 veces mayores que el tercer departamento más poblado, La Plata (Buenos Aires).

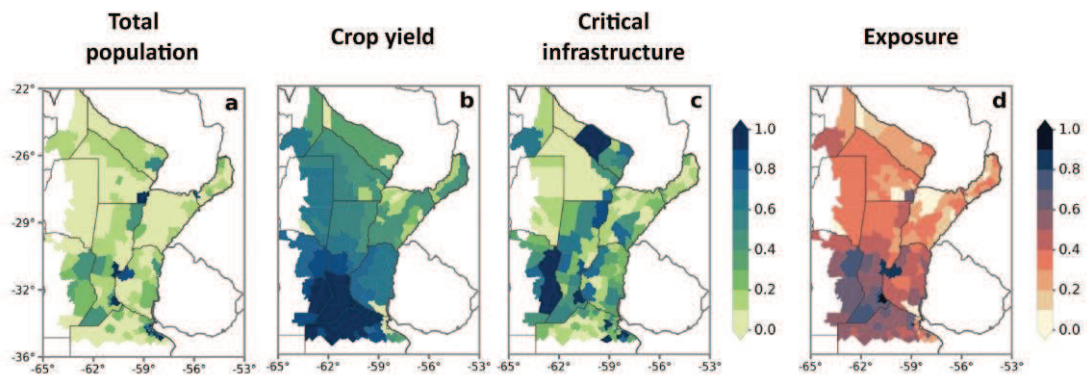


Figura 3.2. Composición del índice de exposición.

Distribución espacial del índice de exposición (panel d), derivada de la combinación de tres índices normalizados: (a) población total, (b) rendimiento de cultivos y (c) infraestructura crítica. Los mapas se presentan a nivel de unidades geográficas departamentales. Fuente: Pierrestegui et al. 2025.

El índice de rendimiento de cultivos tiene un promedio de 0.49 para toda la región y sigue un marcado gradiente de sur a norte. Los valores más altos se concentran en la región núcleo de cultivos de Argentina (Figura 3.2b), donde se encuentran los rendimientos más altos de maíz y soja (ver Anexo I, Figura MS4.1). En contraste, los valores más bajos se observan en las provincias del norte como Formosa, Corrientes y Misiones. No obstante, el índice de rendimiento de cultivos se mantiene alto en la mayor parte del área de estudio, con más de la mitad de la región obteniendo valores superiores a 0.6.

El índice de infraestructura crítica (Figura 3.2c) exhibe valores elevados en las provincias centrales y del sur, como Santa Fe, Buenos Aires y Córdoba, donde la actividad económica, la población y la infraestructura están altamente concentradas. El índice también resalta los principales corredores viales que conectan Argentina con Paraguay, Uruguay y Brasil (ver Anexo I, Figura MS4.2, para más detalles sobre la composición del índice). La Figura MS4.2 muestra que la infraestructura más numerosa incluye redes de transporte terrestre (rutas nacionales y provinciales, puentes y ferrocarriles), instalaciones de energía (centrales eléctricas y estaciones transformadoras), y plantas de tratamiento de agua y aguas residuales.

Los índices normalizados de las variables contribuyen al índice de exposición con pesos de 0.534 para el rendimiento de cultivos, 0.392 para la población total y 0.074 para la infraestructura crítica (determinados en el PCA, Tabla 3.2). El índice de rendimiento de cultivos presenta la mayor influencia, impulsado por su alta variabilidad espacial y su dominancia en la región, particularmente en las áreas del sur con alta productividad agrícola. La población total también desempeña un papel importante, reflejando las altas

concentraciones urbanas. El menor peso relativo obtenido por el índice de infraestructura crítica, a pesar de su variabilidad espacial, puede atribuirse a su correlación con los patrones de población. Dado que la infraestructura a menudo se concentra en áreas con mayor densidad poblacional, se reduce su contribución única a la varianza capturada por el PCA.

El índice general de exposición varía ampliamente, con valores entre 0 y 0.96 (Figura 3.2d), y un promedio regional de 0.37. Los niveles más altos de exposición se concentran en el centro y sur de Santa Fe, este de Córdoba y norte de Buenos Aires. Esto se debe a la convergencia de altos rendimientos de cultivos en la CCR, junto con alta densidad poblacional e infraestructura crítica. Por el contrario, los valores más bajos de exposición se encuentran en las provincias del noreste, como Corrientes, Chaco, Formosa, y Misiones, debido a bajos valores de población e infraestructura crítica.

Tabla 3.2. Pesos relativos obtenidos mediante análisis de componentes principales.

Distribución de los pesos relativos asociados a los índices normalizados y a los componentes de la vulnerabilidad, calculados mediante la técnica de análisis de componentes principales (PCA).

| | Realización del PCA | Índices y componentes | Pesos |
|-------------------------------|---------------------|----------------------------------|-------|
| Índices normalizados | 1 | Población total | 0.392 |
| | | Rendimiento de cultivos | 0.534 |
| | | Infraestructura crítica | 0.074 |
| | 2 | Población sensible | 0.043 |
| | | Dependencia potencial | 0.272 |
| | | Sensibilidad asociada a ingresos | 0.306 |
| | | Cambio en el uso del suelo | 0.379 |
| | 3 | Acceso a la tecnología | 0.361 |
| | | Nivel educativo | 0.289 |
| | | Cobertura de salud | 0.351 |
| Componentes de vulnerabilidad | 4 | Exposición | 0.208 |
| | | Sensibilidad | 0.306 |
| | | Capacidad adaptativa | 0.485 |

3.4.1.2. Sensibilidad

La Figura 3.3 presenta el componente de sensibilidad, derivado de la agregación de cuatro índices normalizados: población sensible, dependencia potencial, sensibilidad asociada a ingresos y cambio en el uso del suelo. El índice de población sensible (Figura 3.3a) presenta un promedio de 0.46 en toda la región, con máximos concentrados en el sur

(hasta 0.7), donde una mayor proporción de la población tiene más de 65 años (ver Anexo I, Figura MS4.3). En contraste, el índice de dependencia potencial (Figura 3.3b) tiene un promedio regional de 0.54, con valores notablemente más elevados en las zonas norte y sur de la región. Este comportamiento refleja la distribución etaria, caracterizada por una mayor proporción de personas menores de 14 años en el norte y mayores de 65 años en el sur (ver Anexo I, Figura MS4.3).

El índice de sensibilidad asociada a los ingresos (Figura 3.3c, ver también Anexo I, Figura MS4.4) muestra un claro gradiente norte-sur, con un valor regional promedio relativamente alto de 0.67. Los valores más bajos se concentran en el centro y sur de la región, específicamente en el centro y sur de Santa Fe, noreste de Buenos Aires y centro-oeste de Córdoba. Esta menor sensibilidad asociada a los ingresos puede atribuirse a la dominancia de actividades agrícolas en la CCR y a los niveles más altos de actividades industriales y del sector de servicios, como lo indica el índice de infraestructura crítica (Figura 3.2c). Por el contrario, el norte de la región presenta una mayor sensibilidad asociada a los ingresos, principalmente debido a su menor desarrollo agroindustrial.

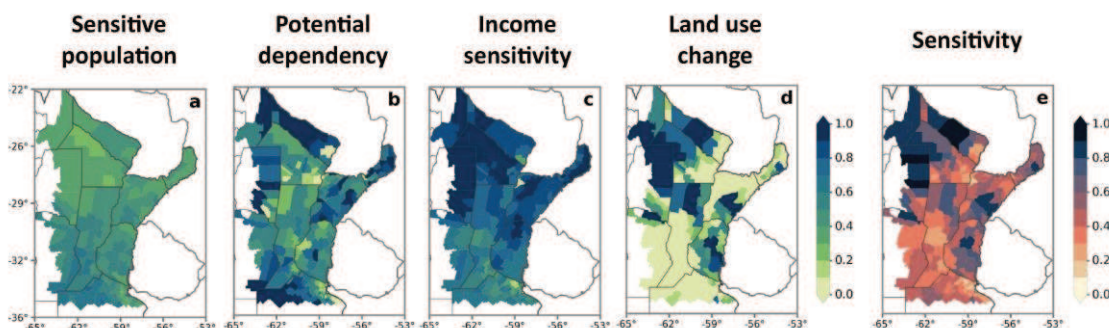


Figura 3.3. Composición del índice de sensibilidad.

Distribución espacial del índice de sensibilidad (panel e), derivada de la combinación de cuatro índices normalizados: (a) población sensible, (b) dependencia potencial, (c) sensibilidad asociada a los ingresos y (d) cambio en el uso del suelo. Los mapas se presentan a nivel de unidades geográficas departamentales. Fuente: Pierrestegui et al. 2025.

El índice de cambio en el uso del suelo (Figura 3.3d) muestra una alta variabilidad espacial. Se observan valores altos en el noroeste y centro-este de la región, mientras que valores muy bajos se encuentran en el suroeste y noreste. Comparando este patrón de distribución con el índice de rendimiento de cultivos (Figura 3.2b), se observa que las regiones con rendimientos muy altos, como la CCR en el suroeste, y las áreas con rendimientos muy bajos, como el noreste dominado por sabanas y bosques (ver Bracalenti et al. 2024), coinciden con los mínimos valores del índice de cambio en el uso del suelo.

En áreas de altos rendimientos como la CCR, esto puede deberse al uso extensivo del suelo para el cultivo. En contraste, las regiones con rendimientos agrícolas intermedios presentan los valores más altos del índice de cambio en el uso del suelo, probablemente atribuibles a la expansión de la frontera agrícola en las últimas décadas (Stanimirova et al. 2022; Volante et al. 2016).

Los índices normalizados de las variables contribuyen al índice de sensibilidad con pesos de 0.379 para el cambio en el uso del suelo, 0.306 para la sensibilidad asociada a los ingresos, 0.272 para la dependencia potencial y 0.043 para la población sensible (pesos determinados en el PCA, Tabla 3.2). El índice de cambio en el uso del suelo tiene el peso más alto debido a su significativa variabilidad espacial y su impacto en la sensibilidad, especialmente en regiones que experimentan una rápida expansión agrícola como en el noroeste. La sensibilidad asociada a ingresos y la dependencia potencial se encuentran en segundo lugar, con valores cercanos entre sí, mostrando una variabilidad y contribución similar, y reflejando la vulnerabilidad económica frente a eventos extremos. El índice de población sensible presenta el peso más bajo, probablemente debido a su menor variabilidad relativa y al rango de datos más limitado, lo que reduce su contribución a la varianza general capturada por el PCA.

Los valores de sensibilidad varían entre 0.02 y 0.97 en la región de estudio (Figura 3.3e), con un promedio regional de 0.44, superior al promedio regional mostrado por la exposición. Los máximos valores de sensibilidad están asociados a una alta sensibilidad asociada a ingresos, cambio en el uso del suelo y dependencia potencial, principalmente en el noroeste (oeste de Formosa, oeste de Chaco, norte de Santiago del Estero y este de Salta). Por el contrario, los mínimos valores de sensibilidad se encuentran en las áreas centrales y del sur (centro y sur de Santa Fe, noreste de Buenos Aires y centro-oeste de Córdoba), donde la menor sensibilidad asociada a ingresos refleja la concentración de las principales actividades económicas del país.

3.4.1.3. Capacidad adaptativa

La Figura 3.4 ilustra el componente de capacidad adaptativa derivado de la agregación de tres índices normalizados: acceso a la tecnología, cobertura de salud y nivel educativo. Los índices de acceso a la tecnología y cobertura de salud (Figura 3.4a-b) presentan un marcado gradiente sur-norte, con promedios regionales de 0.57 y 0.56, respectivamente. Comparando con el índice de sensibilidad asociada a los ingresos (Figura 3.3c), las regiones con mayor acceso a la tecnología y a los servicios de salud muestran una menor

sensibilidad asociada a los ingresos, lo que sugiere un posible vínculo con una mayor disponibilidad de recursos. Estas regiones también coinciden con zonas de elevada actividad productiva, caracterizadas por mayores rendimientos de cultivos y una infraestructura crítica más desarrollada (Figura 3.2b-c).

El acceso a la tecnología en la región se logra principalmente a través de teléfonos celulares con conectividad a internet, alcanzando a más del 70% de la población en toda la región, y superando el 90% en las áreas del sur (ver Anexo I, Figura MS4.6). En cuanto a la cobertura de salud, se observa un mayor acceso en el sur para todos los grupos etarios, destacándose los adultos mayores de 65 años, de los cuales más del 95% cuentan con cobertura social (ver Anexo I, Figura MS4.7). Por su parte, el índice de nivel educativo (Figura 3.4c) muestra un gradiente sur-norte similar, aunque con una transición más gradual y un promedio regional más bajo de 0.40.

Los índices normalizados de las variables contribuyen al índice de capacidad adaptativa con pesos de 0.361 para el acceso a la tecnología, 0.351 para la cobertura de salud y 0.289 para el nivel educativo (pesos determinados en el PCA, Tabla 3.2). Los índices de acceso a la tecnología y cobertura de salud presentan los pesos más altos, reflejando su mayor variabilidad espacial y su papel significativo en el fortalecimiento de la capacidad adaptativa, especialmente en las regiones del sur. Aunque el índice de nivel educativo también muestra relevancia, su peso es ligeramente menor debido a su rango más limitado y su menor variabilidad relativa en toda la región. A pesar de que todas estas variables comparten patrones espaciales similares—con valores más altos en el sur y más bajos en el norte—sus contribuciones comparables, ya que su variabilidad e impacto en la capacidad adaptativa están estrechamente vinculados.

El índice de capacidad adaptativa muestra una marcada variabilidad espacial, siguiendo un gradiente sur-norte (Figura 3.4d). Debido a su relación inversa con la vulnerabilidad, los valores más altos reflejan una mayor capacidad para adaptarse y enfrentar los impactos. El centro y sur de la región concentran los valores más elevados de capacidad adaptativa, que oscilan entre 0.6 y 1, gracias a un acceso más amplio a tecnología, salud y educación. En contraste, la capacidad adaptativa disminuye notablemente en el norte, con valores que oscilan entre 0 y 0.4. Esta disparidad pone de manifiesto la desigual capacidad de la región para afrontar eventos extremos: mientras el acceso a la educación y tecnología en el sur favorece la aplicación de medidas preventivas, la cobertura de salud refuerza las estrategias de recuperación y respuesta ante desastres.

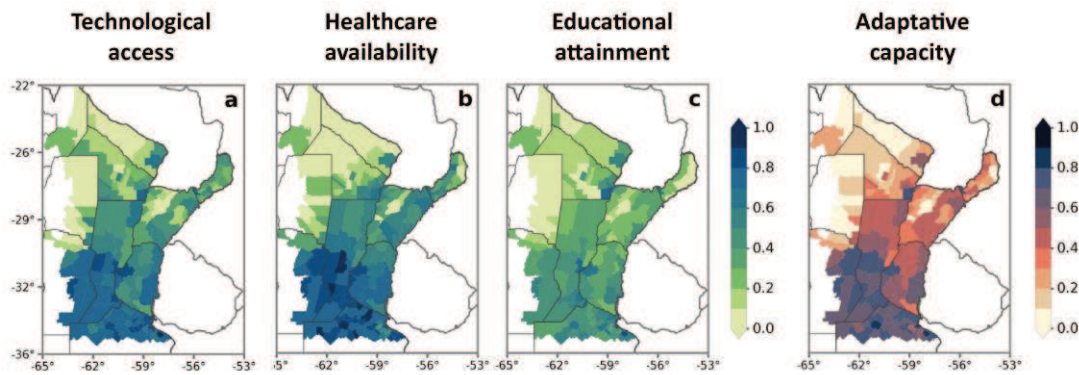


Figura 3.4. Composición del índice de capacidad adaptativa.

Distribución espacial del índice de capacidad adaptativa (panel d), derivada de la combinación de tres índices normalizados: (a) acceso a la tecnología, (b) cobertura de salud y (c) nivel educativo. Los mapas se presentan a nivel de unidades geográficas departamentales. Fuente: Pierrestegui et al. 2025.

3.4.2. Índice de vulnerabilidad

La Figura 3.5 ilustra el índice de vulnerabilidad junto con sus componentes constituyentes. El índice de vulnerabilidad se construye utilizando pesos relativos de 0.208 para la exposición, 0.306 para la sensibilidad y 0.485 para la capacidad adaptativa (pesos determinados en el PCA, Tabla 3.2). La capacidad adaptativa tiene el mayor peso, reflejando su importante rol en la reducción de la vulnerabilidad, particularmente en las áreas con mejor acceso a recursos e infraestructura. Le sigue la sensibilidad con un peso intermedio, destacando la importancia de los factores socioeconómicos y ambientales en la configuración de la vulnerabilidad en esta región. La exposición presenta el menor peso, debido a su menor variabilidad relativa en comparación con los otros componentes y a su distribución más homogénea a nivel regional.

La vulnerabilidad en la región de estudio varía de baja a alta, con un rango entre 0.1 y 0.84 y un promedio regional de 0.45. La mayor parte de la región exhibe niveles medios de vulnerabilidad ante EHEs (entre 0.3 y 0.7). Las áreas con mayor vulnerabilidad (0.7 – 0.84) se localizan en el noroeste y centro-oeste, donde se combinan una alta sensibilidad con una baja capacidad adaptativa, a pesar de presentar una menor exposición. En contraste, los valores más bajos de vulnerabilidad (de 0.1 a 0.4) se encuentran en la zona central y sur, donde una menor sensibilidad y una mayor capacidad adaptativa contrarrestan los niveles más altos de exposición.

En las áreas centro y centro-oeste de la región (centro y sur de Santa Fe, centro-este de Córdoba), la vulnerabilidad es media-baja a media (de 0.3 a 0.5), y resulta de una mayor exposición, pero contrarrestada por una baja sensibilidad y alta capacidad adaptativa. La

región noreste de la provincia de Buenos Aires muestra una baja vulnerabilidad (entre 0.2 y 0.3) debido a una sensibilidad y exposición medias combinadas con una alta capacidad adaptativa. En el noreste (provincias de Misiones y Corrientes), los valores de vulnerabilidad media a media-alta (de 0.5 a 0.7) se deben a una combinación de baja exposición, sensibilidad media y baja capacidad adaptativa.

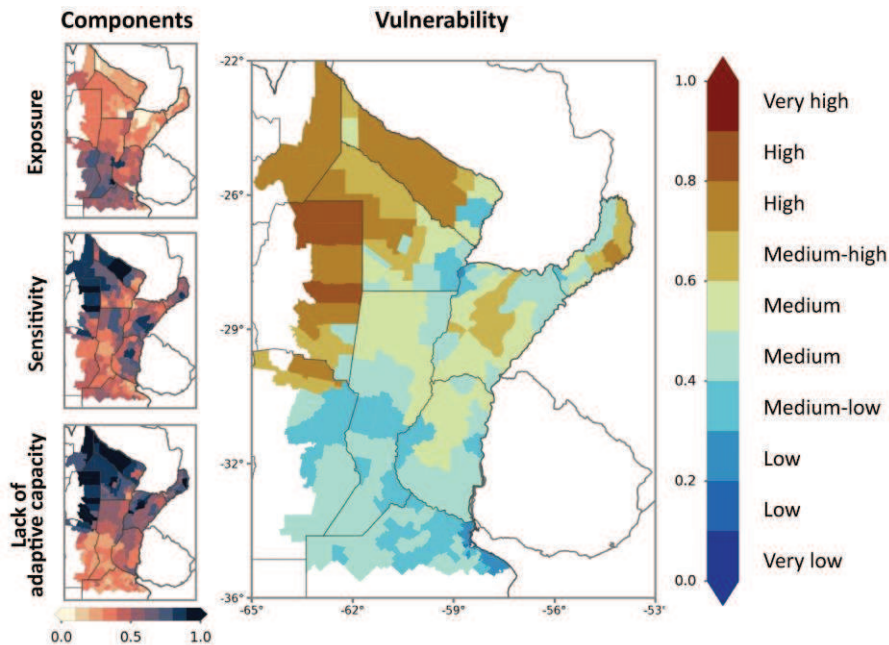


Figura 3.5. Composición del índice de vulnerabilidad.

Distribución espacial del índice de vulnerabilidad (panel principal), derivada de la combinación de los tres componentes de la vulnerabilidad mostrados en los paneles de la izquierda: exposición, sensibilidad y el inverso de la capacidad adaptativa (falta de capacidad adaptativa o dificultad de adaptación). Los componentes de la vulnerabilidad se desagregan en la Figura 3.2, Figura 3.3 y Figura 3.4, respectivamente. La capacidad adaptativa se presenta en una escala invertida en comparación con la Figura 3.4: una menor capacidad adaptativa (aumentando la vulnerabilidad) se acerca a 1, mientras que una mayor capacidad (reduciendo la vulnerabilidad) se aproxima a 0. Los niveles de vulnerabilidad se muestran junto a la escala de colores, que varían desde muy bajo (azul oscuro) hasta muy alto (marrón oscuro). Fuente: Pierrestegui et al. 2025.

3.4.3. Evaluación del riesgo

3.4.3.1. Riesgo por amenazas hidrometeorológicas individuales

La Figura 3.6 ilustra la evaluación del riesgo para las amenazas hidrometeorológicas individuales, derivada del producto de cada amenaza y el índice de vulnerabilidad. Para las amenazas por EHEs de largo plazo, se examinan los eventos WEP y DEP. La amenaza por WEP presenta un promedio regional de 0.51, con valores que varían desde muy bajos en el noroeste hasta altos en el sureste (Figura 3.6b). El mapa de riesgo correspondiente

(Figura 3.6c) presenta una distribución espacial similar al de amenaza, aunque con valores más bajos y homogéneos. Esto se debe a los patrones espaciales opuestos entre amenaza y vulnerabilidad, lo que atenúa la magnitud de la amenaza y reduce el nivel de riesgo resultante (Figura 3.6b y a). En el sureste (Entre Ríos, norte de Buenos Aires y sur de Santa Fe), la alta amenaza por WEP se modera con una vulnerabilidad más baja, resultando en un riesgo medio. En el noroeste (este de Salta, oeste de Formosa y Chaco, norte de Santiago del Estero), a pesar de la baja amenaza por WEP, la alta vulnerabilidad eleva el riesgo a niveles medio-bajos. En términos generales, el riesgo debido a WEP varía desde bajo en el noroeste hasta medio-alto en el sureste, con un promedio regional de 0.21 y una alta frecuencia dentro del rango medio [0.17-0.21] (ver histograma). Los niveles de riesgo debido a WEP más elevados, clasificados como de nivel medio, están concentrados en Entre Ríos, Corrientes y Misiones.

El mapa de amenaza por DEP (Figura 3.6d) muestra un patrón espacial claro, con amenazas por DEP que varían de bajas en el este a altas en el oeste y norte de la región. En las provincias del norte y oeste (Formosa, Chaco, Salta y Santiago del Estero), las altas amenazas por DEP combinadas con altos niveles de vulnerabilidad (Figura 3.6a) resultan en niveles de riesgo de medio a medio-alto (Figura 3.6e). Estos niveles de riesgo están potenciados principalmente por una alta sensibilidad y una capacidad adaptativa limitada. En la región oriental (Misiones, Corrientes y Entre Ríos), donde la amenaza por DEP es baja, la existencia de una vulnerabilidad media eleva la amenaza a niveles de riesgo medio-bajo y medio. A nivel regional, el riesgo debido a DEP es de 0.2, clasificándose como riesgo medio, con la mayor frecuencia de valores dentro del rango medio-bajo [0.10-0.16]. Los niveles de riesgo debido a DEP más elevados, clasificados como de nivel medio a medio-alto, están localizados en el este de Salta, oeste de Formosa y Chaco, y norte de Santiago del Estero.

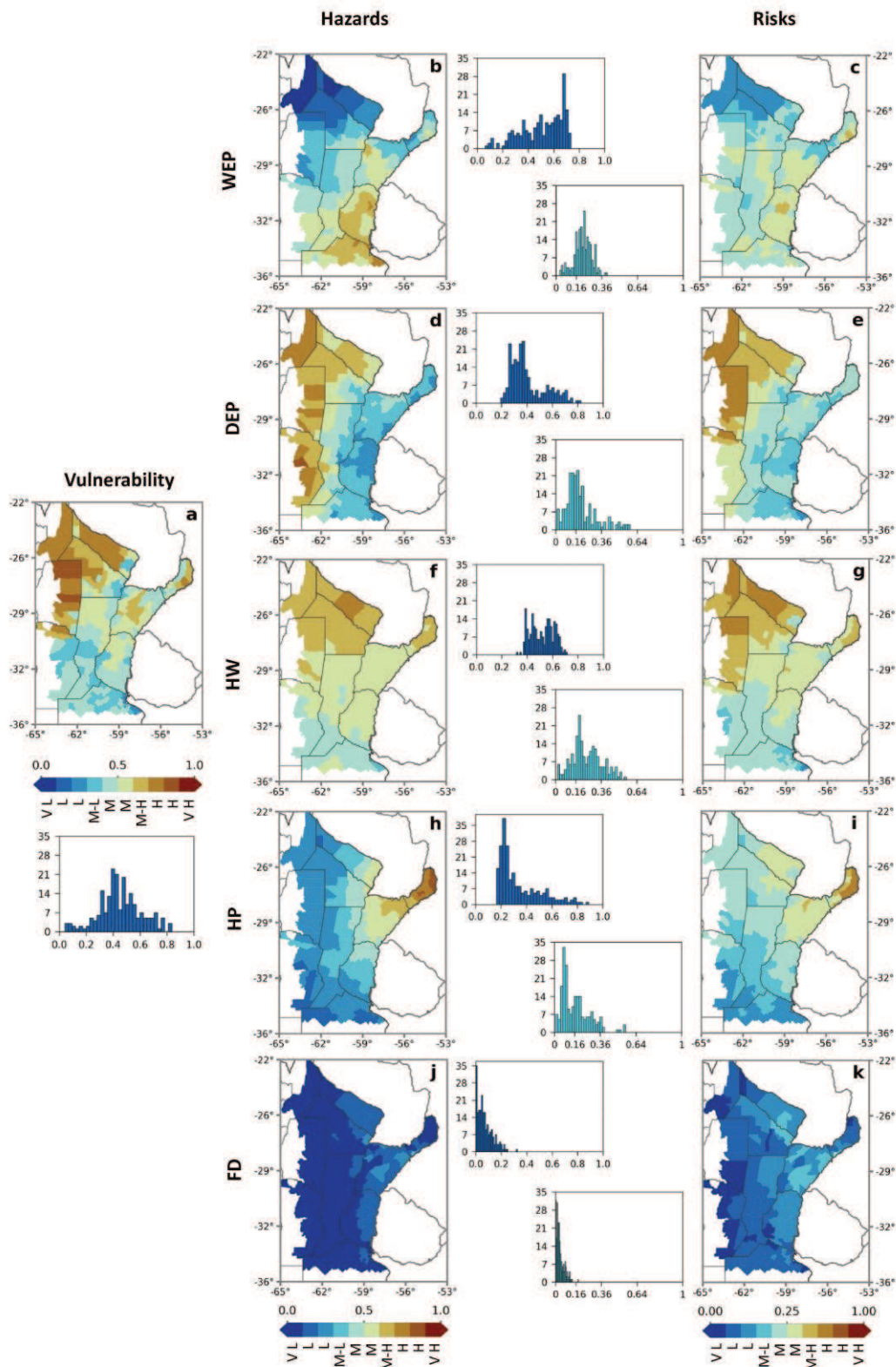


Figura 3.6. Composición de los riesgos por amenazas hidrometeorológicas individuales.

Análisis espacial de los riesgos debido a amenazas hidrometeorológicas individuales. El panel (a) muestra el índice de vulnerabilidad (previamente detallado en la Figura 3.5) como apoyo visual para el análisis de los componentes del riesgo. La figura muestra las diferentes amenazas (columna izquierda) y sus riesgos asociados (columna derecha) para cinco tipos de amenazas individuales por EHEs: exceso de precipitación (WEP,

paneles b y c), déficit de precipitación (DEP, paneles d y e), olas de calor (HW, paneles f y g), precipitación intensa (HP, paneles h e i) y sequías repentinas (FD, paneles j y k).

Cada mapa está acompañado por un histograma que representa la distribución de frecuencias de los valores. Fuente: Pierrestegui et al. 2025.

Para las amenazas por EHEs de corto plazo, se analizan las olas de calor, los eventos de precipitación intensa y las sequías repentinas. La amenaza por HW (Figura 3.6f) exhibe un marcado gradiente norte-sur, caracterizado por altos niveles de amenaza en el norte que disminuyen a niveles medios en el sur. En las provincias del norte (Formosa, Chaco, Salta, Santiago del Estero), los niveles de amenazas por HW medio-altos combinados con una alta vulnerabilidad (Figura 3.6a) generan riesgos debido a HW con niveles medio-alto a altos (Figura 3.6g). Estas provincias, que comúnmente enfrentan calor extremo, presentan alta sensibilidad y limitada capacidad adaptativa, lo que explica el riesgo elevado debido a HW. En las provincias del sur de la región, una amenaza por HW de nivel medio combinada con vulnerabilidad de media a medio-baja da lugar a riesgos debido a HW que oscilan entre medio y medio-bajo, es decir que en este caso los niveles bajos de vulnerabilidad contribuyen a atenuar la amenaza. En términos generales, el riesgo debido a HW disminuye siguiendo un gradiente descendente de alto en el norte a medio en el sur, con un promedio regional de 0.25 y las frecuencias más altas observadas en el rango medio [0.16-0.20].

El mapa de amenaza por HP (Figura 3.6h) muestra un máximo en el noreste de la región, disminuyendo gradualmente hacia el sur y el oeste. En Misiones, al combinarse un nivel alto de amenaza por HP con una vulnerabilidad medio-alta (Figura 3.6a) genera un riesgo por HP que va de medio-alto a alto (Figura 3.6i), es decir que la amenaza es atenuada en cierta medida. En Corrientes y el este de Formosa, una vulnerabilidad más baja contribuye a reducir el riesgo general. El resto de la región presenta un riesgo debido a HP clasificado entre medio y bajo, impulsado principalmente por una baja amenaza por HP. Los valores de riesgo más frecuentes en la región se observan en un rango de nivel bajo [0.05-0.08]. La amenaza por FD (Figura 3.6j) presenta un nivel predominante muy bajo en toda la región. Sin embargo, dado que la vulnerabilidad adquiere niveles medios y altos en ciertas áreas, el riesgo resultante debido a FD se eleva a bajo (Figura 3.6k). El riesgo debido a FD muestra un gradiente suave este-oeste, que varía de medio-bajo a bajo en el este, y de muy bajo a bajo en el oeste.

3.4.3.2. Riesgo debido a amenazas hidrometeorológicas múltiples

La Figura 3.7 presenta la evaluación del riesgo debido a amenazas hidrometeorológicas múltiples, derivada del producto de cada amenaza múltiple y el índice de vulnerabilidad. Se evalúan las amenazas múltiples de largo plazo (LT-mH) y de corto plazo (ST-mH), así como la amenaza total (T-mH) que combina los índices LT-mH y ST-mH.

El índice LT-mH (Figura 3.7b) muestra un valor promedio regional de 0.46, con niveles de medio a medio-altos en el oeste y suroeste, y medio-bajos en el norte y noreste. En la región suroeste, que abarca el suroeste de Córdoba, el sur de Santa Fe y el norte de Buenos Aires, los valores de medio a medio-altos en el índice LT-mH están asociados con la coexistencia de amenazas altas por WEP y DEP. A nivel regional, el riesgo por LT-mH (Figura 3.7c) se clasifica mayoritariamente como medio, con las mayores frecuencias dentro del rango [0.17-0.21]. Cabe destacar que el riesgo debido a LT-mH tiene el promedio regional más elevado entre todos los riesgos evaluados para amenazas múltiples (Figura 3.7c, e, y g). Aunque el riesgo debido a LT-mH se mantiene en niveles medios en la mayor parte de la región, sus factores determinantes varían: en las provincias del norte, los valores medio-bajos en la amenaza LT-mH combinados con vulnerabilidades de nivel medio-alto a alto, elevan el riesgo a niveles medios; mientras que en el sur, los valores de medio a medio-altos en la amenaza LT-mH, junto con vulnerabilidades de nivel medio a medio-bajo, moderan el riesgo a niveles medios.

El índice ST-mH (Figura 3.7d) muestra valores predominantemente bajos a medio-bajos, con un promedio regional de 0.31, siguiendo un gradiente noreste-suroeste. Los valores máximos de amenaza múltiple de corto plazo (cerca de 0.5) se presentan en el noreste de la región debido a una combinación de altas amenazas por HW y HP (ver Figura 3.6f y h). El riesgo asociado a ST-mH varía de bajo a medio en la región, clasificándose como el más bajo entre las amenazas múltiples evaluadas. En muchas áreas, los niveles de riesgo superan los niveles de amenaza debido a la combinación de valores de amenaza bajos a medio-bajos con niveles de vulnerabilidad de medio-alto a altos. Es decir que las condiciones socioeconómicas potencian la amenaza por ST-mH en la mayor parte del área de estudio.

El índice T-mH (Figura 3.7f) presenta valores predominantes que varían de medio-bajo a medio, distribuidos de manera heterogénea en toda la región de estudio. En el oeste, los valores medios están asociados con una preponderancia de amenazas múltiples de largo plazo, mientras que en el noreste están determinados por amenazas múltiples de corto

plazo más elevadas. Al combinarse con la vulnerabilidad, la amenaza T-mH genera un riesgo en general más alto, donde muchas áreas experimentan una magnificación de amenaza, pasando de niveles de amenaza medio-bajos a niveles de riesgo medio (Figura 3.7g). El promedio regional del riesgo debido a T-mH es de 0.18, lo que indica un nivel de riesgo medio en la región.

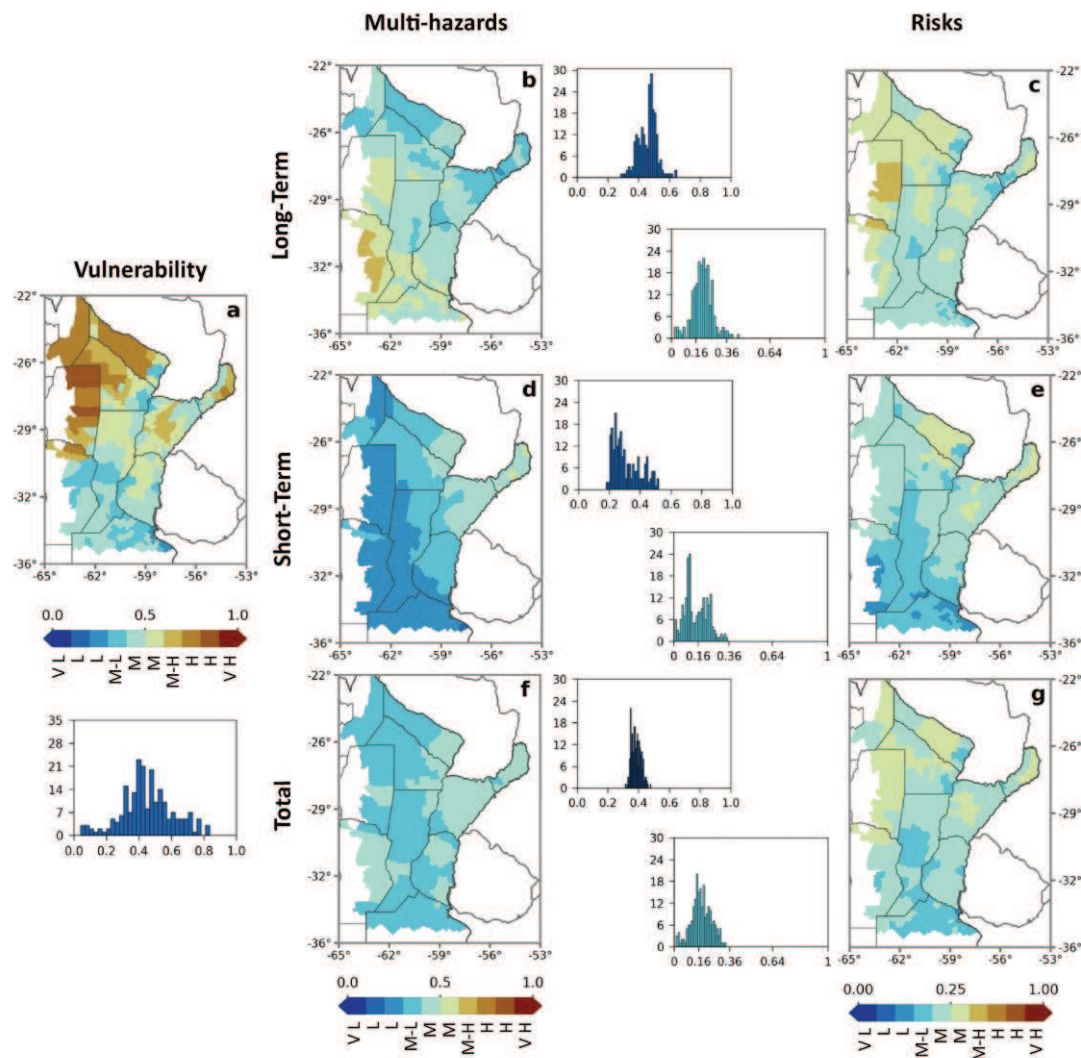


Figura 3.7. Composición de los riesgos por amenazas hidrometeorológicas múltiples.

Análisis espacial de los riesgos por amenazas hidrometeorológicas múltiples. El panel (a) muestra el índice de vulnerabilidad (previamente detallado en la Figura 3.5) como apoyo visual para el análisis de los componentes del riesgo. La figura muestra las diferentes amenazas (columna izquierda) y sus riesgos asociados (columna derecha) para los tres tipos de amenazas múltiples: de largo plazo (paneles b y c), de corto plazo (paneles d y e), y totales (paneles f y g). Cada mapa está acompañado por un histograma que representa la distribución de frecuencias de los valores. Fuente: Pierrestegui et al. 2025.

3.5. Síntesis

Este capítulo integra datos físicos y socioeconómicos para evaluar los riesgos asociados a amenazas hidrometeorológicas individuales y múltiples en escalas temporales de largo y corto plazo. El riesgo se evalúa como la interacción entre las amenazas por EHEs y la vulnerabilidad. La vulnerabilidad se analiza a través de la exposición, la sensibilidad y la capacidad adaptativa.

La vulnerabilidad promedio en la región de estudio se estima en un nivel medio, aunque con marcadas diferencias espaciales. La región central, comprendiendo el sur de Santa Fe, este de Córdoba y norte de Buenos Aires, presenta una vulnerabilidad de media-baja a media debido a una alta exposición contrarrestada por una baja sensibilidad y una alta capacidad adaptativa. Esta región combina la mayor exposición debido a la convergencia de alta población, infraestructura crítica y rendimientos de cultivos significativos, con baja sensibilidad y alta capacidad adaptativa debido a los avances agroindustriales y tecnológicos. Las regiones noroeste y centro-oeste, incluyendo Formosa, Chaco, y este de Salta y de Santiago del Estero, así como el este de Misiones, exhiben la mayor vulnerabilidad (niveles de medio-alto a alto) debido principalmente a una alta sensibilidad y una muy baja capacidad adaptativa, a pesar de los menores niveles de exposición. El limitado desarrollo agroindustrial y tecnológico de estas regiones—representado por un menor rendimiento de cultivos y una menor existencia de infraestructura crítica, el bajo nivel de ingresos, así como el limitado acceso a la tecnología—contrasta fuertemente con las zonas centrales. El resto de la región experimenta una vulnerabilidad media, caracterizada por una exposición de baja a moderada, una sensibilidad de media-alta y una capacidad adaptativa de media-baja.

El riesgo debido a olas de calor es el más alto y extendido en todo el centro-noreste de Argentina, alcanzando niveles de medio-alto a alto en el norte y de bajo a medio en el sur. Los eventos extremos de excesos y déficit de precipitación a largo plazo exhiben niveles de riesgo medios, con distribuciones espaciales distintas. En el noroeste, el riesgo de eventos extremos por déficit de precipitación es alto y el riesgo de eventos extremos por excesos de precipitación es bajo. Por el contrario, en el sureste, el riesgo de eventos extremos por déficit de precipitación es de bajo a medio-bajo, mientras que el riesgo de eventos extremos por excesos de precipitación es de medio a medio-alto. El riesgo de precipitación intensa es alto en las provincias del noreste, donde se producen precipitaciones convectivas frecuentes y severas. El riesgo de sequía repentina es más

bajo en la región de estudio debido a la relativamente baja frecuencia de estos eventos en comparación con otras amenazas.

El riesgo multi-amenaza a largo plazo es el de mayor extensión espacial y severidad en toda la región, lo que indica el potencial de que los eventos extremos de excesos y déficit de precipitación impacten grandes áreas. Este riesgo es particularmente medio-alto en el oeste, donde las sequías agrícolas e hidrológicas y los períodos prolongados de excesos hídricos son frecuentes e intensos. El riesgo multi-amenaza a corto plazo es menos generalizado, principalmente debido a la amenaza concentrada de fuertes precipitaciones en el noreste y una baja amenaza de sequías repentinas en toda la región, a pesar de existir una amenaza de gran extensión espacial y severidad para las olas de calor. Finalmente, los riesgos de olas de calor y los eventos extremos de déficit de precipitación a largo plazo, que exhiben el mayor riesgo local y regional, coinciden con los niveles de amenaza más altos en el norte y noroeste, donde la vulnerabilidad también es mayor.

Comprender cómo los diferentes contextos socioeconómicos influyen en los riesgos por EHEs es esencial para integrar las estrategias de adaptación climática con los esfuerzos de reducción del riesgo de desastres. Las condiciones socioambientales que determinan la vulnerabilidad actúan como atenuantes o amplificadores de la amenaza, configurando el riesgo resultante. Por ejemplo, en el noroeste la alta vulnerabilidad potencia las amenazas existentes de eventos extremos de déficit de precipitación y olas de calor, mientras que en sur y el este de la región, la menor vulnerabilidad actúa como atenuante para disminuir la amenaza existente de eventos extremos de exceso de precipitación, olas de calor, y precipitación intensa. El capítulo destaca la importancia de considerar la vulnerabilidad y el riesgo por EHEs a escala subnacional en el centro-noreste de Argentina, y subraya la necesidad de estrategias de adaptación específicas, que se centren en preparar los sistemas expuestos en el sur y fortalecer la capacidad adaptativa en el norte.

Capítulo 4: Discusión y conclusiones

4.1. Síntesis del marco metodológico

Esta tesis presenta un análisis de las amenazas múltiples asociadas a eventos hidrometeorológicos extremos, así como la vulnerabilidad y el riesgo correspondiente, en el centro-noreste de Argentina. En primer lugar, se presenta un análisis de las amenazas hidrometeorológicas múltiples asociadas a EHEs y sus cambios utilizando datos de reanálisis ERA5. Se realiza a través de un análisis de amenazas individuales en múltiples capas para identificar zonas críticas de amenazas por EHEs de corto y largo plazo, examinando sus cambios entre los períodos 1961-1990 y 1991-2020. Mediante la utilización de índices de amenazas múltiples, desarrollados en función de la frecuencia, duración e intensidad de los EHEs individuales, se logra una comprensión más profunda tanto de cada tipo de amenaza por separado como de las amenazas múltiples que afectan a la región. Además, el análisis de las series temporales de las amenazas individuales asociadas a los EHEs, junto con los índices compuestos de amenazas múltiples, permite identificar las dinámicas temporales y la co-ocurrencia de estas amenazas a lo largo del tiempo.

En segundo lugar, se realiza un estudio de la vulnerabilidad y el riesgo de la región ante estas amenazas múltiples por EHEs a escala subnacional. El enfoque utilizado combina datos físicos y socioeconómicos de múltiples fuentes para evaluar la vulnerabilidad y considera tanto las amenazas por EHEs individuales como las amenazas múltiples para el corto y largo plazo. Al examinar los riesgos individuales y los riesgos por amenazas múltiples por separado, el estudio ofrece una comprensión más profunda de cómo se compone el riesgo general de la región frente a los EHEs. El riesgo asociado a los EHEs resulta de la interacción entre las amenazas generadas por estos eventos y la vulnerabilidad de las áreas afectadas. La vulnerabilidad se analiza a través de sus tres componentes fundamentales: exposición, sensibilidad y capacidad adaptativa. De esta manera, se aborda la vulnerabilidad como un componente clave del riesgo y como un factor independiente, permitiendo mejorar la comprensión de cómo contextos socioeconómicos específicos pueden moldear los riesgos vinculados a los EHEs. Esta comprensión es fundamental para conectar las estrategias de adaptación al cambio climático con los esfuerzos orientados a la reducción del riesgo de desastres (IPCC 2022a).

4.2. Evaluación de amenazas hidrometeorológicas múltiples

El estudio realizado revela una amenaza significativa de largo plazo por excesos hídricos tanto a escalas estacionales (3 meses) como hidrológicas (18 meses) en la parte sur de la región de estudio—abarcando el sur de Santa Fe y Entre Ríos, y el norte de Buenos Aires. Esta amenaza ha aumentado en el período 1991-2020 en comparación con el período 1961-1990. En consecuencia, las regiones agrícolas y ganaderas más productivas, incluyendo gran parte de la zona núcleo de cultivos de Argentina, así como las zonas más densamente pobladas, se encuentran expuestas a excesos hídricos recurrentes de escalas tanto estacionales como hidrológicas. Estos extremos húmedos de largo plazo aumentan los caudales de los ríos, afectando tierras agrícolas y áreas densamente pobladas (Camilloni et al. 2020; Ridder et al. 2020). Además, estudios previos proyectan que las precipitaciones durante la temporada húmeda y los eventos de precipitación intensa aumenten en esta región durante el siglo XXI (Almazroui et al. 2021a, b; Olmo et al. 2022; Ortega et al. 2021). También se espera que el caudal del río Uruguay aumente un 15% para 2050 (Müller et al. 2024). De este modo, es probable que las amenazas por excesos hídricos se agraven aún más en las próximas décadas.

En contraste, las áreas del norte y oeste de la región de estudio—abarcando Formosa, Chaco, el oeste de Salta, y el este de Santiago del Estero y Córdoba—enfrentan la mayor amenaza de largo plazo por déficits de precipitación. Las sequías de escala estacional pueden impactar la agricultura en la porción occidental de la región núcleo de cultivos y el norte de Argentina, mientras que las sequías hidrológicas pueden generar escasez de agua para uso urbano, reducción del potencial hidroeléctrico, e interrupciones en el suministro de agua potable (Lovino et al. 2018b; Naumann et al. 2019). Adicionalmente, la ocurrencia de sequías en la región del SESA suele coincidir con otras amenazas de corto plazo como olas de calor e incendios forestales (Lovino et al. 2025; Ridder et al. 2020). Esta combinación de amenazas, junto con vulnerabilidades socioeconómicas locales como infraestructura inadecuada y pobreza, puede agravar los impactos de la sequía, afectando no solo la productividad agrícola sino también la integridad de los ecosistemas y las ciudades (Castellanos et al. 2022; Coppola et al. 2021).

Los eventos hidrometeorológicos extremos de corto plazo presentan los niveles más altos de amenaza en la porción noreste de la región de estudio—incluyendo las provincias de Misiones y Corrientes, y el este de Chaco y Formosa en Argentina, y extendiéndose a zonas aledañas como el sur de Brasil y el sureste de Paraguay. Esta alta amenaza por

EHEs de corto plazo se debe a la ocurrencia de frecuentes olas de calor, sequías repentinas y eventos de precipitación intensa en esa zona. La amenaza por olas de calor muestra un aumento de un 30% entre 1961-1990 y 1991-2020, lo cual se encuentra en línea con las tendencias globales (Perkins-Kirkpatrick y Lewis 2020). Este aumento en la amenaza de olas de calor puede impactar negativamente en la salud humana, las ciudades, los ecosistemas, la agricultura y la producción de energía (Coppola et al. 2021). La amenaza de precipitación intensa, que es mayor en el noreste de la región de estudio—coincidente con las áreas más húmedas—, puede generar extensos anegamientos e inundaciones que pueden afectar la infraestructura urbana y las actividades agrícolas (Cerón et al. 2021). La amenaza por sequías repentinas, atribuida principalmente al aumento de su frecuencia en las últimas décadas, puede afectar la agricultura en el sur de Brasil, noreste de Argentina y Uruguay. Estas sequías repentinas pueden reducir los rendimientos agrícolas ya que frecuentemente ocurren durante períodos críticos para los cultivos (Lovino et al. 2024; 2025). Además, se proyecta que estos eventos extremos se exacerben durante el siglo XXI. Se espera que las olas de calor sean más frecuentes, intensas y duraderas (Almazroui et al. 2021b; Feron et al. 2019). También se proyecta un aumento en la precipitación intensa y en la ocurrencia de sequías repentinas en el SESA (Avila-Diaz et al. 2023; Christian et al. 2023). En consecuencia, es probable que las amenazas de corto plazo ya existentes se intensifiquen en las próximas décadas.

Las amenazas múltiples por EHEs de largo y corto plazo exhiben patrones contrastantes en el dominio de estudio: las amenazas múltiples de largo plazo prevalecen en la porción suroeste y centro-oeste de la región de estudio, mientras que las amenazas múltiples de corto plazo son más comunes en las áreas noreste y centro-este. La región núcleo de cultivos de Argentina está particularmente expuesta tanto a sequías como a excesos hídricos desde escalas estacionales hasta hidrológicas. Estos eventos generalmente se alternan en el tiempo, coincidiendo con los períodos húmedos y secos de la región antes y después de los años 60 (Barreiro et al. 2014; Lovino et al. 2018b; Lovino et al. 2022). Antes de 1966, la amenaza de sequías era más frecuente, mientras que la amenaza por excesos hídricos dominó entre 1966 y 2004. Desde 2005, las amenazas tanto por excesos como por déficits extremos de precipitación en escalas de 3 meses han permanecido altas, indicando que ambos tipos de amenazas estacionales han ocurrido simultáneamente durante las últimas dos décadas. Los resultados muestran que la amenaza múltiple total—que combina los índices de amenazas múltiples de largo y corto plazo—es generalizada y considerablemente alta en casi toda la región de estudio. En su evolución temporal, las

amenazas múltiples de corto plazo alcanzan valores más altos (máximos de 0.6) que las de largo plazo (máximos de 0.4), sugiriendo que las amenazas de corto plazo son más propensas a ocurrir simultáneamente, mientras que las de largo plazo tienden a alternarse en su ocurrencia.

4.3. Vulnerabilidad y riesgo a amenazas hidrometeorológicas múltiples

Los resultados de la tesis muestran que la región presenta un nivel de vulnerabilidad mayoritariamente medio. No obstante, se identificó un patrón espacial que destaca tres áreas específicas con niveles de vulnerabilidad diferenciados, las cuales demandan estrategias de gestión de riesgos adaptadas a sus características particulares. En primer lugar, la región central—que incluye el sur de Santa Fe, el este de Córdoba, y el norte de Buenos Aires—presenta los niveles más bajos de vulnerabilidad (de media-baja a media). Esta zona combina una elevada exposición, resultado de la convergencia de una alta densidad poblacional, infraestructura crítica y rendimientos agrícolas significativos, con una baja sensibilidad y una alta capacidad adaptativa, atribuible a los avances agroindustriales y tecnológicos. En segundo lugar, las regiones del noroeste y centro-oeste—incluyendo Formosa, Chaco, el este de Salta y el este de Santiago del Estero—presentan los niveles más altos de vulnerabilidad (de media-alta a alta). Esto se debe principalmente a su elevada sensibilidad y a una capacidad adaptativa muy limitada, pese a que presentan niveles de exposición más bajos. El limitado desarrollo agroindustrial y tecnológico de estas regiones contrasta marcadamente con las áreas centrales. En tercer lugar, las áreas restantes presentan una vulnerabilidad media, mostrando una situación intermedia definida por niveles de exposición que oscilan entre bajos y moderados, una sensibilidad media-alta y una capacidad adaptativa clasificada como media-baja.

El PCA, utilizado para asignar pesos relativos a las variables que componen el índice de vulnerabilidad, destaca eficazmente las diferencias geográficas. Además, ofrece una representación más precisa de los factores determinantes de la vulnerabilidad al dar prioridad a las variables con mayor varianza (Abson et al. 2012). Los pesos derivados del PCA proporcionan una comprensión más profunda de los factores que impulsan la vulnerabilidad y ayudan a identificar regiones con mayores necesidades de intervención. En este estudio, la capacidad adaptativa, caracterizada por una marcada variabilidad norte-sur, obtuvo el mayor peso ($w_{ac}=0.485$), mientras que la exposición tuvo una contribución menor debido a su limitada variabilidad ($w_e=0.208$). Aunque el método otorga prioridad a las variables con mayor varianza, aquellas con menor varianza pero

que siguen siendo relevantes para la vulnerabilidad pueden estar subrepresentadas. Este aspecto es importante para tener en cuenta al interpretar los resultados y al diseñar estrategias de intervención.

Entre los riesgos individuales, los hallazgos de esta tesis sugieren que las olas de calor representan el riesgo más elevado a nivel local y también el más extendido en el centro-noreste de Argentina. Este riesgo alcanza niveles medios en el sur y de medio-alto a altos en el norte, reflejando el incremento global en la frecuencia y severidad de las olas de calor (Perkins-Kirkpatrick y Lewis 2020), especialmente pronunciado en el norte de Argentina (Cimolai y Aguilar 2024; Lovino et al. 2018a). A las olas de calor, le siguen los eventos extremos de déficit y excesos de precipitación de largo plazo que exhiben niveles de riesgo medio con distribuciones espaciales diferenciadas en la región. En el noroeste, el riesgo atribuido a eventos extremos de déficit de precipitación es alto y el riesgo asociado a eventos extremos de exceso de precipitación es bajo. Por el contrario, en el sureste, el riesgo debido a déficit de precipitación es bajo a medio-bajo, mientras que el riesgo asociado a exceso de precipitación es de medio a medio-alto. Así, el mayor riesgo atribuido a déficit de precipitación se concentra en la región árida del Chaco Seco, mientras que el mayor riesgo atribuido a exceso de precipitación ocurre en las llanuras húmedas del oeste de la región de estudio.

El riesgo asociado a eventos de precipitación intensa es alto en las provincias del noreste, donde ocurren frecuentemente precipitaciones convectivas severas (Rasmussen et al. 2016; Zhang et al. 2021). El riesgo vinculado a sequías repentinas es notoriamente menor en toda la región de estudio debido a su baja frecuencia relativa en comparación con otras amenazas (Pierrestegui et al. 2024). Cabe destacar que las olas de calor y los eventos extremos de déficit de precipitación de largo plazo representan los riesgos más altos tanto a nivel local como regional, coincidiendo con niveles elevados de amenaza en el norte y noroeste, zonas donde la vulnerabilidad también es mayor. En contraste, a pesar de que el noreste presenta los niveles de amenaza más elevados por precipitaciones intensas, el riesgo asociado se ve moderado por una vulnerabilidad media, lo que posiciona este riesgo en el tercer lugar entre los riesgos individuales.

Los resultados sugieren que los riesgos de corto plazo pueden exacerbar los impactos de los eventos extremos de precipitación de largo plazo. En el norte y noroeste, las sequías agrícolas e hidrológicas pueden verse agravadas por las olas de calor. Esta combinación intensifica las condiciones de sequía (Miralles et al. 2019; Naumann et al. 2019; Lovino et al. 2025), agravando los impactos, especialmente dado que los niveles de

vulnerabilidad en la región son más altos. Mientras tanto, en el noreste, los excesos de precipitación de largo plazo pueden exacerbar los impactos por eventos de precipitación intensa concurrentes, amplificando así el riesgo de excesos hídricos.

4.4. Conclusiones y recomendaciones finales

Las amenazas asociadas a eventos hidrometeorológicos extremos en el centro-noreste de Argentina han aumentado al comparar los períodos 1960-1990 y 1991-2020, aunque exhiben patrones espaciales de cambio heterogéneos. En el período reciente, la amenaza múltiple regional por EHEs no solo es más elevada, sino también más generalizada que en el período 1960-1990, lo que indica una amenaza múltiple más extendida en toda la región. Las amenazas múltiples de corto plazo han experimentado el mayor incremento, creciendo 1.7 veces más que las de largo plazo, principalmente debido al marcado aumento en la amenaza por olas de calor. Como consecuencia, los impactos sectoriales se verían exacerbados al conjugarse la intensificación de estos eventos extremos de corto plazo con la coexistencia de eventos extremos de largo plazo. Dado que el centro-noreste de Argentina es una de las regiones más productivas en términos agrícolas a nivel continental, las amenazas por eventos hidrometeorológicos extremos pueden afectar los rendimientos de los cultivos, amenazar la seguridad alimentaria y repercutir en el crecimiento socioeconómico de la región. Por este motivo, resulta fundamental avanzar en la investigación orientada a estudiar de manera específica las amenazas hidrometeorológicas y el riesgo resultante en la región.

A pesar de las incertidumbres inherentes asociadas con el conjunto de datos ERA5 (Hersbach et al. 2020), así como las limitaciones existentes en la disponibilidad de información socioeconómica, los hallazgos de esta tesis proporcionan información valiosa para mejorar la gestión de riesgos hidrometeorológicos en el centro-noreste de Argentina. Los resultados indican que el riesgo más extenso y severo en la región está constituido por amenazas hidrometeorológicas múltiples de largo plazo, determinando la importancia que los períodos de excesos y déficits extremos de precipitación tienen para la región, con el potencial de impactar grandes extensiones. Este riesgo es particularmente alto en el oeste de la región, donde las sequías agrícolas e hidrológicas y los períodos prolongados de excesos hídricos son frecuentes e intensos, los cuales son potenciados por una alta vulnerabilidad (Cerón et al. 2021; Lovino et al. 2022). Por otro lado, el riesgo por amenazas hidrometeorológicas múltiples de corto plazo se encuentra menos extendido, concentrándose principalmente en el centro y norte de la región. A pesar de la

extensión espacial y la severidad de la amenaza por olas de calor en toda la región, el riesgo de corto plazo está moldeado por una concentración de amenazas por precipitaciones intensas en el noreste, y una baja amenaza por sequías repentinas en toda la región, así como una menor vulnerabilidad que actúa como atenuante de la amenaza en el centro-sur y este de la región.

Una mejor comprensión de las diversas amenazas y vulnerabilidades regionales ante eventos hidroclimáticos extremos permitirá a los responsables de la formulación de políticas desarrollar estrategias más específicas y efectivas para mitigar los impactos negativos de los EHEs en el centro-noreste de Argentina. Comprender cómo los diferentes contextos socioeconómicos modelan los riesgos por EHEs es esencial para integrar las estrategias de adaptación climática con los esfuerzos de reducción del riesgo de desastres.

Los resultados muestran cómo las condiciones socioambientales que determinan la vulnerabilidad actúan como atenuantes o amplificadores de la amenaza por EHEs, configurando el riesgo resultante en la región. De este modo, para reducir el riesgo en el sur y centro-este, donde se concentran las actividades económicas y la infraestructura crítica, resulta más eficiente la mejora de los sistemas expuestos a las amenazas por EHEs—principalmente eventos extremos de exceso de precipitación, olas de calor, y precipitación intensa—mediante la adaptación de la infraestructura y el desarrollo de prácticas agrícolas resilientes al clima. Mientras que en el noroeste, resulta de vital importancia promover un desarrollo resiliente al clima con el fin de reducir la sensibilidad y fortalecer la capacidad adaptativa, para disminuir el riesgo ante una amenaza por eventos extremos que resultan frecuentes y severos—principalmente eventos extremos de déficit de precipitación y olas de calor—.

Los hallazgos proporcionan información crítica para mejorar la planificación, gestión del riesgo y adaptación al cambio climático, con importantes implicancias para el desarrollo de políticas públicas orientadas. Los estudios futuros podrían enriquecerse con la incorporación de conjuntos de datos climáticos observacionales para abordar mejor las incertidumbres derivadas de los datos, especialmente para el caso de los extremos hidrometeorológicos. Para el caso de las amenazas, el desarrollo de un análisis de sensibilidad para definir la composición de la amenaza a partir de sus componentes de frecuencia, duración e intensidad sería beneficioso, así como la incorporación de datos de impactos observados para medir el nivel de amenaza. A su vez, las investigaciones futuras deberían refinar la evaluación de vulnerabilidad incorporando datos socioeconómicos y ambientales de alta resolución, e integrando otras técnicas de análisis multivariado para

Capítulo 4: Discusión y conclusiones

complementar el análisis derivado del PCA. El desarrollo de marcos que aborden riesgos compuestos y en cascada, incorporando amenazas compuestas con eventos de ocurrencia simultánea o consecutiva y sus impactos, mejorará aún más la comprensión del riesgo y por lo tanto la formulación de políticas más eficientes. Estos avances son fundamentales para mejorar la gestión del riesgo hidrometeorológico y promover estrategias de adaptación eficientes y sostenibles en regiones vulnerables como lo es el centro-noreste de Argentina.

Listado de siglas y abreviaturas

CCR: Región núcleo de cultivos de Argentina / Argentina's core crop region

DEP: Eventos extremos de déficit de precipitación / Dry extreme precipitation events

DEP3: Eventos extremos de déficit de precipitación a escala estacional (calculados a partir del SPI3)

DEP18: Eventos extremos de déficit de precipitación a escala hidrológica (calculados a partir del SPI18)

EHEs: Eventos hidrometeorológicos extremos / Extreme hydrometeorological events

ENSO: El Niño-Oscilación del Sur / El Niño- Southern Oscillation

EPE: Eventos extremos de precipitación / Extreme precipitation events

ERA5: Quinta versión del reanálisis del European Centre for Medium-Range Weather Forecasts

FD: Sequías repentinhas / Flash droughts

HP: Precipitación intensa / Heavy precipitation events

HW: Olas de calor / Heatwaves

LT-mH : Amenaza múltiple de largo plazo / Long-term multi-hazard

MS: Material suplementario

PCA: Análisis por Componentes Principales / Principal component analysis

SARs: Sequías agrícolas repentinhas

SESA: Sudeste de Sudamérica

SPI: Índice estandarizado de precipitación / Standardized Precipitation Index

SPI3: SPI en escala temporal de 3 meses

SPI18: SPI en escala temporal de 18 meses

ST-mH: Amenaza múltiple de corto plazo / Short-term multi-hazard

SWDI: Índice de Déficit de Humedad del Suelo / Soil Water Deficit Index

T-mH: Amenaza múltiple total / Total multi-hazard

WEP: Eventos extremos de exceso de precipitación / Wet extreme precipitation events

WEP3: Eventos extremos de exceso de precipitación a escala estacional (calculados a partir del SPI3)

WEP18: Eventos extremos de exceso de precipitación a escala hidrológica (calculados a partir del SPI18)

Referencias

- Abdi H, Williams LJ (2010) Principal component analysis. Wiley Interdiscip Rev Comput Stat 2:433–459. <https://doi.org/10.1002/wics.10>
- Abson DJ, Dougill AJ, Stringer LC (2012) Using Principal Component Analysis for information-rich socio-ecological vulnerability mapping in Southern Africa. Applied Geography 35(1-2):515–524. <https://doi.org/10.1016/j.apgeog.2012.08.004>
- AghaKouchak A, Chiang F, Huning LS et al (2020) Climate extremes and compound hazards in a warming world. Annual Review of Earth and Planetary Sciences 519:548–48. <https://doi.org/10.1146/annurev-earth-071719-055228>
- Agosta EA, Rabassa MJ, Florio L, Torrero MP (2021) Floods in Eastern Subtropical Argentina: The Contributing Roles of Climate Change and Socioeconomics. In: Belfiori ME, Rabassa MJ (eds) The Economics of Climate Change in Argentina. The Latin American Studies Book Series. Springer, Cham, pp 45–67. https://doi.org/10.1007/978-3-030-62252-7_3
- Almazroui M, Ashfaq M, Islam MN et al (2021a) Assessment of CMIP6 performance and projected temperature and precipitation changes over South America. Earth Systems and Environment 5:155–183. <https://doi.org/10.1007/s41748-021-00233-6>
- Almazroui M, Saeed F, Saeed S et al (2021b) Projected changes in climate extremes using CMIP6 simulations over SREX regions. Earth Systems and Environment 5:481–497. <https://doi.org/10.1007/s41748-021-00250-5>
- Alvala R, Ribeiro DF, Marengo JA, Seluchi ME, Gonçalves DA, Antunes da Silva L, Cuartas Pineda LA, Saito SM (2024) Analysis of the hydrological disaster that occurred in the state of Rio Grande do Sul in September 2023: Vulnerabilities and risk management capabilities. Int J Disaster Risk Reduct 110:104645. <https://doi.org/10.1016/j.ijdrr.2024.104645>
- Ara Begum R, Lempert R, Ali E et al (2022) Point of Departure and Key Concepts. In: Pörtner H-O, Roberts DC, Tignor M et al (eds.) Climate Change 2022: Impacts, Adaptation and Vulnerability. Contribution of Working Group II to the Sixth Assessment Report of the Intergovernmental Panel on Climate Change. Cambridge University Press, Cambridge, UK and New York, NY, USA, pp. 121–196. <https://doi.org/10.1017/9781009325844.003>
- Avila-Diaz A, Benezoli V, Justino F, Torres R, Wilson A (2020) Assessing current and future trends of climate extremes across Brazil based on reanalyses and earth system model projections. Climate Dynamics 55(5–6):1403–1426. <https://doi.org/10.1007/s00382-020-05333-z>
- Avila-Diaz A, Torres RR, Zuluaga CF et al (2023) Current and Future Climate Extremes Over Latin America and Caribbean: Assessing Earth System Models from High Resolution Model Intercomparison Project (HighResMIP). Earth Syst Environ 7:99–130. <https://doi.org/10.1007/s41748-022-00337-7>
- Balmaceda-Huarte R, Olmo ME, Bettolli ML, Poggi MM (2021) Evaluation of multiple reanalyses in reproducing the spatio-temporal variability of temperature and precipitation

Referencias

- indices over southern South America. *Int J Climatol* 41: 5572–5595. <https://doi.org/10.1002/joc.7142>
- Barreiro M, Diaz N, Renom M (2014) Role of the global oceans and land–atmosphere interaction on summertime interdecadal variability over northern Argentina. *Clim. Dynam.* 42:1733–1753. <https://doi.org/10.1007/s00382-014-2088-6>
- Barros VR, Boninsegna JA, Camilloni IA, Chidiak M, Magrín GO, Rusticucci M (2015) Climate change in Argentina: trends, projections, impacts and adaptation. *WIREs Clim. Change* 6:151–169. <http://dx.doi.org/10.1002/wcc.316>
- Bathrellos GD, Skilodimou HD, Chousianitis K, Youssef AM, Pradhan B (2017) Suitability estimation for urban development using multi-hazard assessment map. *Science of The Total Environment* 575:119–134. <https://doi.org/10.1016/j.scitotenv.2016.10.025>
- Beck H, Zimmermann N, McVicar T et al (2018) Present and future Köppen-Geiger climate classification maps at 1-km resolution. *Sci Data* 5:180214. <https://doi.org/10.1038/sdata.2018.214>
- Berbery EH, Barros V (2002) The hydrologic cycle of the La Plata basin in South America. *J. Hydrometeorol.* 3:630–645. [https://doi.org/10.1175/1525-7541\(2002\)003<0630:THCOTL>2.0.CO;2](https://doi.org/10.1175/1525-7541(2002)003<0630:THCOTL>2.0.CO;2)
- Bernal-Mujica A, Lovino MA, Müller GV, Pierrestegui MJ (2023) Spatiotemporal variability of extreme precipitation events and their impacts on soil moisture and water table depth in Argentina's core crop region. *Hydrological Sciences Journal* 68(6):794–809. <https://doi.org/10.1080/02626667.2023.2192874>
- Bert F, de Estrada M, Naumann G, Negri R, Podestá G, de los Milagros Skansi M, Spennemann P, Quesada M (2021) The 2017-18 drought in the Argentine Pampas—Impacts on agriculture. In: GAR Special Report on Drought. United Nations Office for Disaster Risk Reduction. Available via UNDRR. <https://www.undrr.org/publication/2017-18-drought-argentine-pampas-impacts-agriculture-0>. Accessed 6 Jan 2025
- Binita KC, Shepherd JM, King AW et al (2021) Multi-hazard climate risk projections for the United States. *Nat Hazards* 105:1963–1976. <https://doi.org/10.1007/s11069-020-04385-y>
- Birkmann J, Cardona OD, Carreño ML et al (2013) Framing vulnerability, risk and societal responses: the MOVE framework. *Nat Hazards* 67:193–211. <https://doi.org/10.1007/s11069-013-0558-5>
- Birkmann J, Jamshed A, McMillan JM et al (2022) Understanding human vulnerability to climate change: a global perspective on index validation for adaptation planning. *Sci. Total Environ* 803, 150065. <https://doi.org/10.1016/j.scitotenv.2021.150065>
- Blaikie P, Cannon T, Davis I, Wisner B (2014) At Risk: Natural Hazards, People's Vulnerability and Disasters (2nd ed.). Routledge. <https://doi.org/10.4324/9780203714775>
- Bohn VY, Piccolo MC (2019) Estimation of hydrological vulnerability in river basins of Argentinean plains. *Int J River Basin Manag* 19(4):445–457. <https://doi.org/10.1080/15715124.2019.1683855>

Referencias

- Bortz PG, Toftum N (2023) Changes in rainfall, agricultural exports and reserves: macroeconomic impacts of climate change in Argentina. *J Environ Econ Policy* 13:243–258. <https://doi.org/10.1080/21606544.2023.2236987>
- Borzi G, Roig A, Tanjal C et al (2021) Flood hazard assessment in large plain basins with a scarce slope in the Pampean Plain, Argentina. *Environ Monit Assess* 193:177. <https://doi.org/10.1007/s10661-021-08988-1>
- Bracalenti MA, Müller OV, Lovino MA, Berberry EH (2024) The agricultural expansion in South America's Dry Chaco: regional hydroclimate effects. *Hydrol. Earth Syst. Sci.* <https://doi.org/10.5194/hess-28-3281-2024>
- Caffera RM, Berberry EH (2006) La Plata basin climatology. In: Barros V, Clarke R, Diaz P (eds.) *Climatic Change in the La Plata Basin*. National Scientific and Technical Research Council (CONICET), Argentina, pp. 16–32.
- Camilloni I, Barros V, Moreiras S, Poveda G, Tomasella J (2020) Floods and Droughts. In: Moreno JM, Laguna-Defi C, Barros V, Calvo Buendia E, Marengo JA, Oswald Spring U (eds.) *Adaptation to climate change risks in Ibero-American countries—RIOCCADAPT report*. McGraw Hill, Madrid, Spain (ISBN 9788448621667).
- Castellanos E, Lemos MF, Astigarraga L et al (2022) Central and South America. In: Pörtner H-O, Roberts DC, Tignor M et al (eds.) *Climate Change 2022: Impacts, Adaptation and Vulnerability. Contribution of Working Group II to the Sixth Assessment Report of the Intergovernmental Panel on Climate Change*. Cambridge University Press, Cambridge, UK and New York, NY, USA, pp. 1689–1816. <https://doi.org/10.1017/9781009325844.014>
- Cerón WL, Kayano MT, Andreoli RV et al (2021) Recent intensification of extreme precipitation events in the La Plata Basin in southern South America (1981–2018). *Atmospheric Research* 249:105299. <https://doi.org/10.1016/j.atmosres.2020.105299>
- Christian JI, Martin ER, Basara JB et al (2023) Global projections of flash drought show increased risk in a warming climate. *Commun. Earth. Environ.* 4, 165. <https://doi.org/10.1038/s43247-023-00826-1>
- Cimolai C, Aguilar E (2024) Assessing Argentina's heatwave dynamics (1950–2022): a comprehensive analysis of temporal and spatial variability using ERA5-LAND. *Theor Appl Climatol* 155:4925–4940. <https://doi.org/10.1007/s00704-024-04915-9>
- Clarke B, Otto F, Stuart-Smith R, Harrington L (2022) Extreme weather impacts of climate change: an attribution perspective. *Environ. Res.: Climate* 1:012001. <https://doi.org/10.1088/2752-5295/ac6e7d>
- Coppola E, Raffaele F, Giorgi F. et al (2021) Climate hazard indices projections based on CORDEX-CORE, CMIP5 and CMIP6 ensemble. *Clim Dyn* 57:1293–1383. <https://doi.org/10.1007/s00382-021-05640-z>
- Cramer F (2018) Scientific colour maps. Zenodo. doi:10.5281/ zenodo.1243862. <https://zenodo.org/records/4491293>
- Cramer F, Shephard GE, Heron PJ (2020) The misuse of colour in science communication. *Nature Communications* 11, 5444. <https://doi.org/10.1038/s41467-020-19160-7>

Referencias

- Dai A, Zhao T (2017) Uncertainties in historical changes and future projections of drought. Part I: estimates of historical drought changes. *Climatic Change* 144(3):519–533. <https://doi.org/10.1007/s10584-016-1705-2>
- Dasgupta S, Robinson EJZ (2022) Attributing changes in food insecurity to a changing climate. *Sci Rep* 12, 4709. <https://doi.org/10.1038/s41598-022-08696-x>
- De Angeli S, Malamud BD, Rossi L, Taylor FE, Trasforini E, Rudari R (2022) A multi-hazard framework for spatial-temporal impact analysis. *International Journal of Disaster Risk Reduction* 73,102829. <https://doi.org/10.1016/j.ijdrr.2022.102829>
- De Luca P, Donat MG (2023) Projected changes in hot, dry, and compound hot-dry extremes over global land regions. *Geophysical Research Letters* 50, e2022GL102493. <https://doi.org/10.1029/2022GL102493>
- Dereczynski C, Chou SC, Lyra A et al (2020) Downscaling of climate extremes over South America – Part I: Model evaluation in the reference climate. *Weather and Climate Extremes* 29, 100273. <https://doi.org/10.1016/j.wace.2020.100273>
- Dunn RJH, Alexander LV, Donat MG et al (2020) Development of an Updated Global Land In SituBased Data Set of Temperature and Precipitation Extremes: HadEX3. *Journal of Geophysical Research: Atmospheres* 125(16), e2019JD032263. <https://doi.org/10.1029/2019JD032263>
- Farahmand A, AghaKouchak A (2015) A generalized framework for deriving nonparametric standardized drought indicators. *Advances in Water Resources* 76:140–145. <https://doi.org/10.1016/j.advwatres.2014.11.012>
- Feron S, Cordero RR, Damiani A et al (2019) Observations and Projections of Heat Waves in South America. *Sci Rep* 9, 8173. <https://doi.org/10.1038/s41598-019-44614-4>
- Fischer EM, Sippel S, Knutti R (2021) Increasing probability of record-shattering climate extremes. *Nat. Clim. Chang.* 11:689–695. <https://doi.org/10.1038/s41558-021-01092-9>
- Ford JD, Pearce T, McDowell G et al (2018) Vulnerability and its discontents: the past, present, and future of climate change vulnerability research. *Climatic Change* 151:189–203. <https://doi.org/10.1007/s10584-018-2304-1>
- Forzieri G, Feyen L, Russo S et al (2016) Multi-hazard assessment in Europe under climate change. *Climatic Change* 137:105–119. <https://doi.org/10.1007/s10584-016-1661-x>
- Füssel H-M (2007) Vulnerability: a generally applicable conceptual framework for climate change research. *Glob. Environ. Change* 17:155–167. <https://doi.org/10.1016/j.gloenvcha.2006.05.002>
- Garreaud RD, Vuille M, Compagnucci R, Marengo J (2009) Present-day South American climate, Paleogeogr. Paleocl. 281:180–195. <https://doi.org/10.1016/j.palaeo.2007.10.032>
- Garschagen M, Doshi D, Reith J, Hagenlocher M (2021) Global patterns of disaster and climate risk—an analysis of the consistency of leading index-based assessments and their results. *Climatic Change* 169, 11. <https://doi.org/10.1007/s10584-021-03209-7>
- Gill JC, Malamud BD (2014) Reviewing and visualizing the interactions of natural hazards. *Reviews of Geophysics* 52(4):680–722. <https://doi.org/10.1002/2013RG000445>

Referencias

- González FA I, Santos ME, London S (2021) Multidimensional Poverty and Natural Disasters in Argentina (1970–2010). *J Hum Dev Capabilities* 23:206–227. <https://doi.org/10.1080/19452829.2021.1910220>
- Gringorten II (1963) A plotting rule for extreme probability paper. *J. Geophys. Res.* 68:813–814. <https://doi.org/10.1029/JZ068i003p00813>
- Gulizia CN, Raggio GA, Camilloni IA et al (2022) Changes in mean and extreme climate in southern South America under global warming of 1.5 °C, 2 °C, and 3 °C. *Theor Appl Climatol* 150:787–803. <https://doi.org/10.1007/s00704-022-04199-x>
- Hagen I, Huggel C, Ramajo L, Chacón N, Ometto P, Postigo JC, Castellanos EJ (2022) Climate change-related risks and adaptation potential in Central and South America during the 21st century. *Environmental Research Letters* 17(3):033002. <https://doi.org/10.1088/1748-9326/ac5271>
- Hao Z, AghaKouchak A (2014) A nonparametric multivariate multiindex drought monitoring framework. *Journal of Hydrometeorology* 15(1):89–101. <https://doi.org/10.1175/JHM-D-12-0160.1>
- Hersbach H, Bell B, Berrisford P et al (2020) The ERA5 global reanalysis. *Q. J. R. Meteorol. Soc.* 146:1999–2049. <https://doi.org/10.1002/qj.3803>
- Hersbach H, Bell B, Berrisford P et al (2023a) ERA5 hourly data on single levels from 1940 to present. Copernicus Climate Change Service (C3S) Climate Data Store (CDS). <http://doi.org/10.24381/cds.adbb2d47> (Accessed on March 2023)
- Hersbach H, Bell B, Berrisford P et al (2023b) ERA5 monthly averaged data on single levels from 1940 to present. Copernicus Climate Change Service (C3S) Climate Data Store (CDS). <http://doi.org/10.24381/cds.fl7050d7> (Accessed on May 2023)
- Houspanossian J, Giménez R, Whitworth-Hulse JI et al (2023) Agricultural expansion raises groundwater and increases flooding in the South American plains. *Science* 380:1344–1348. <https://www.science.org/doi/10.1126/science.add5462>
- IGN (Instituto Geográfico Nacional) (2021) Capas de información geoespacial (capas GIS). En: Portal de Información Geoespacial del IGN. Disponible via: <https://www.ign.gob.ar/NuestrasActividades/InformacionGeoespacial/CapasSIG> (Accessed September 2024)
- INDEC (Instituto Nacional de Estadística y Censos) (2022) Resultados finales del Censo Nacional de Población, Hogares y Viviendas 2022. Capas geográficas de información estadística. En: <https://portalgeoestadistico.indec.gob.ar/> (Accessed June 2024)
- IPCC (2022a) Summary for Policymakers [Pörtner H-O, Roberts DC, Poloczanska ES et al (eds.)]. In: Pörtner H-O, Roberts DC, Tignor M et al (eds.) *Climate Change 2022: Impacts, Adaptation and Vulnerability. Contribution of Working Group II to the Sixth Assessment Report of the Intergovernmental Panel on Climate Change*. Cambridge University Press, Cambridge, UK and New York, NY, USA, pp. 3–33. <https://doi.org/10.1017/9781009325844.001>
- IPCC (2022b) Annex II: Glossary [Möller V, van Diemen R, Matthews JBR et al (eds.)]. In: Pörtner H-O, Roberts DC, Tignor M et al (eds.) *Climate Change 2022: Impacts, Adaptation and Vulnerability. Contribution of Working Group II to the Sixth Assessment*

Referencias

- Report of the Intergovernmental Panel on Climate Change. Cambridge University Press, Cambridge, UK and New York, NY, USA, pp. 2897–2930. <https://doi.org/10.1017/9781009325844.029>
- Jolliffe IT, Cadima J (2016) Principal component analysis: a review and recent developments. *Philos Trans R Soc A Math Phys Eng Sci* 374:20150202. <https://doi.org/10.1098/rsta.2015.0202>
- Jurgilevich A, Räsänen A, Groundstroem F, Juhola S (2017) A systematic review of dynamics in climate risk and vulnerability assessments. *Environ. Res. Lett.* 12(1), 13002. <https://doi.org/10.1088/1748-9326/aa5508>
- Kreibich H, Van Loon AF, Schröter K et al (2022) The challenge of unprecedented floods and droughts in risk management. *Nature* 608:80–86. <https://doi.org/10.1038/s41586-022-04917-5>
- Lavers DA, Simmons A, Vamborg F, Rodwell MJ (2022) An evaluation of ERA5 precipitation for climate monitoring. *Q. J.R. Meteorol. Soc.* 148(748):3124–3137. <https://doi.org/10.1002/qj.4351>
- Lesk C, Anderson W, Rigden A et al (2022) Compound heat and moisture extreme impacts on global crop yields under climate change. *Nat Rev Earth Environ* 3:872–889. <https://doi.org/10.1038/s43017-022-00368-8>
- Li C, Zwiers F, Zhang X, Li G, Sun Y, Wehner M (2021) Changes in Annual Extremes of Daily Temperature and Precipitation in CMIP6 Models. *J. Climate* 34:3441–3460. <https://doi.org/10.1175/JCLI-D-19-1013.1>
- Li M, Wu P, Ma Z (2020) A comprehensive evaluation of soil moisture and soil temperature from third-generation atmospheric and land reanalysis data sets. *Int J Climatol* 40:5744–5766. <https://doi.org/10.1002/joc.6549>
- Liu Z, Lv A, Li T (2025) Intensified Drought Threatens Future Food Security in Major Food-Producing Countries. *Atmosphere* 16:34. <https://doi.org/10.3390/atmos16010034>
- Lloyd-Hughes B, Saunders MA (2002) A drought climatology for Europe. *International Journal of Climatology* 22(13):1571–1592. <https://doi.org/10.1002/joc.846>
- Lovino MA, García N, Baethgen W (2014) Spatiotemporal analysis of extreme precipitation events in the Northeast region of Argentina (NEA). *J. Hydrol.: Reg. Stud.* 2:140-158. <http://dx.doi.org/10.1016/j.ejrh.2014.09.001>
- Lovino MA, Müller OV, Berbery EH, Müller GV (2018a) How have daily climate extremes changed in the recent past over northeastern Argentina?. *Global and Planetary Change* 168:78-97. <https://doi.org/10.1016/j.gloplacha.2018.06.008>
- Lovino MA, Müller OV, Müller GV, Sgroi LC, Baethgen WE (2018b) Interannual-to-multidecadal Hydroclimate Variability and its Sectoral Impacts in northeastern Argentina. *Hydrol. Earth Syst. Sci.* 22:3155-3174. <https://doi.org/10.5194/hess-22-3155-2018>
- Lovino MA (2020) Chapter 6: Latin America's vulnerability to climate change and variability. In: Martínez-Austria PF, Coronado-Vásquez B, Patiño-Gómez C (Eds) *Climate change and hydrometeorological risks*. Universidad de las Américas, Puebla, México. Pp. 106-123.

Referencias

- ISBN: 978-607-8674-25-1. Available at: <https://www.udlap.mx/catedraunesco/libro-cambio-climatico-capitulos.aspx#1> (In Spanish).
- Lovino MA, Müller GV, Pierrestegui MJ, Espinosa E, Rodríguez L (2022) Extreme precipitation events in the Austral Chaco region of Argentina. International Journal of Climatology 42(11):5985– 6006. <https://doi.org/10.1002/joc.7572>
- Lovino MA, Pierrestegui MJ, Müller OV, Müller GV, Berbery EH (2024) The prevalent life cycle of agricultural flash droughts. npj ClimAtmos Sci 7, 73. <https://doi.org/10.1038/s41612-024-00618-0>
- Lovino MA, Pierrestegui MJ, Masaro L, Müller OV, Müller GV, Berbery EH (2025) Agricultural flash droughts and their impact on crop yields in southeastern South America. Environ. Res. Lett. 20:054058. <https://doi.org/10.1088/1748-9326/adcd88>
- Lyu H-M, Yin Z-Y (2023) An improved MCDM combined with GIS for risk assessment of multi-hazards in Hong Kong. Sustainable Cities and Society 91, 104427. <https://doi.org/10.1016/j.scs.2023.104427>
- Magrin GO, Marengo JA, Boulanger J-P et al (2014) Central and South America. In: Barros VR, Field CB, Dokken DJ (eds.) Climate Change 2014: Impacts, Adaptation, and Vulnerability. Part B: Regional Aspects. Contribution of Working Group II to the Fifth Assessment Report of the Intergovernmental Panel on Climate Change. Cambridge University Press, Cambridge, United Kingdom and New York, NY, USA, pp. 1499–1566. <https://doi.org/10.1017/CBO9781107415386>
- MAGyP (Ministerio de Agricultura, Ganadería y Pesca de la Nación) (2021a) Series temporales de maíz. En: Datos Argentina. Disponible via: <https://datos.gob.ar/dataset/agroindustria-maiz---siembra-cosecha-produccion-rendimiento> (Accessed April 2024)
- MAGyP (Ministerio de Agricultura, Ganadería y Pesca de la Nación) (2021b) Series temporales de soja. En: Datos Argentina. Disponible via: <https://datos.gob.ar/dataset/agroindustria-soja---siembra-cosecha-produccion-rendimiento> (Accessed April 2024)
- Mallenahalli NK (2020) Comparison of parametric and non-parametric standardized precipitation index for detecting meteorological drought over the Indian region. Theor. Appl. Climatol. 142:219– 236. <https://doi.org/10.1007/s00704-020-03296-z>
- Martínez-Fernández J, González-Zamora A, Sánchez N, Gumuzzio A (2015) A soil water-based index as a suitable agricultural drought indicator. J. Hydrol. 522:265–273. <https://doi.org/10.1016/j.jhydrol.2014.12.051>
- McDowell G, Ford J, Jones J (2016) Community-level climate change vulnerability research: trends, progress, and future directions. Environ. Res. Lett. 11(3), 33001. <https://dx.doi.org/10.1088/1748-9326/11/3/033001>
- Miralles DG, Gentile P, Seneviratne SI, Teuling AJ (2019) Land-atmospheric feedbacks during droughts and heatwaves: state of the science and current challenges. Ann. N. Y. Acad. Sci. 1436:19-35. <https://doi.org/10.1111/nyas.13912>
- Müller OV, McGuire PC, Vidale PL, Hawkins E (2024) River flow in the near future: a global perspective in the context of a high-emission climate change scenario. Hydrol. Earth Syst. Sci. 28:2179–2201. <https://doi.org/10.5194/hess-28-2179-2024>

Referencias

- Naumann G, Barbosa P, Garrote L, Iglesias A, Vogt J (2014) Exploring drought vulnerability in Africa: an indicator based analysis to be used in early warning systems. *Hydrol. Earth Syst. Sci.* 18:1591–1604. <https://doi.org/10.5194/hess-18-1591-2014>
- Naumann G, Vargas WM, Barbosa P, Blauthut V, Spinoni J, Vogt JV (2019) Dynamics of Socioeconomic Exposure, Vulnerability and Impacts of Recent Droughts in Argentina. *Geosciences* 9, 39. <https://doi.org/10.3390/geosciences9010039>
- Naylor A, Ford J, Pearce T, Van Alstine J (2020) Conceptualizing climate vulnerability in complex adaptive systems. *One Earth* 2(5):444–454. <https://doi.org/10.1016/j.oneear.2020.04.011>
- Olmo M, Bettolli ML, Rusticucci M (2020) Atmospheric circulation influence on temperature and precipitation individual and compound daily extreme events: Spatial variability and trends over southern South America. *Weather and Climate Extremes* 29, 100267. <https://doi.org/10.1016/j.wace.2020.100267>
- Olmo ME, Weber T, Teichmann C, Bettolli ML (2022) Compound events in South America using the CORDEX-CORE ensemble: Current climate conditions and future projections in a global warming scenario. *Journal of Geophysical Research: Atmospheres* 127, e2022JD037708. <https://doi.org/10.1029/2022JD037708>
- O'Neill B, van Aalst M, Zaiton Ibrahim Z et al (2022) Key Risks Across Sectors and Regions. In: Pörtner H-O, Roberts DC, Tignor M et al (eds.) *Climate Change 2022: Impacts, Adaptation and Vulnerability. Contribution of Working Group II to the Sixth Assessment Report of the Intergovernmental Panel on Climate Change*. Cambridge University Press, Cambridge, UK and New York, NY, USA, pp. 2411–2538. <https://doi.org/10.1017/9781009325844.025>
- Oppenheimer M, Campos M, Warren R, Birkmann J, Luber G, O'Neill B, Takahashi K (2014) Emergent risks and key vulnerabilities. In: Field CB, Barros VR, Dokken DJ (eds.) *Climate Change 2014: Impacts, Adaptation, and Vulnerability. Part A: Global and Sectoral Aspects. Contribution of Working Group II to the Fifth Assessment Report of the Intergovernmental Panel on Climate Change*. Cambridge University Press, Cambridge, UK and New York, NY, USA, pp. 1039–1099. <https://doi.org/10.1017/CBO9781107415379>
- Ortega G, Arias PA, Villegas JC, Marquet PA, Nobre P (2021) Present-day and future climate over central and South America according to CMIP5/CMIP6 models. *International Journal of Climatology* 41(15):6713–6735. <https://doi.org/10.1002/joc.7221>
- Peduzzi P, Dao H, Herold C, Mouton F (2009) Assessing global exposure and vulnerability towards natural hazards: the Disaster Risk Index. *Nat. Hazards Earth Syst. Sci.* 9:1149–1159. <https://doi.org/10.5194/nhess-9-1149-2009>
- Pendergrass AG, Meehl GA, Pulwarty R et al (2020) Flash droughts present a new challenge for subseasonal-to-seasonal prediction. *Nat. Clim. Chang.* 10:191–199. <https://doi.org/10.1038/s41558-020-0709-0>
- Perkins SE, Alexander LV, Nairn JR (2012) Increasing frequency, intensity and duration of observed global heatwaves and warm spells. *Geophys. Res. Lett.* 39, L20714. <https://doi.org/10.1029/2012GL053361>

Referencias

- Perkins SE, Alexander LV (2013) On the Measurement of Heat Waves. *J. Climate* 26:4500–4517. <https://doi.org/10.1175/JCLI-D-12-00383.1>
- Perkins-Kirkpatrick SE, Lewis SC (2020) Increasing trends in regional heatwaves. *Nat Commun* 11, 3357. <https://doi.org/10.1038/s41467-020-16970-7>
- Pierrestegui MJ, Lovino MA, Müller GV, Müller OV (2024) Multi-hazard Assessment of Extreme Hydrometeorological Events in Southeastern South America. *Earth Syst Environ.* <https://doi.org/10.1007/s41748-024-00450-9>
- Pierrestegui MJ, Lovino MA, Müller GV, Müller OV (2025) Vulnerability and Risk of Hydrometeorological Hazards in Central-Northeastern Argentina. *Earth Syst Environ.* <https://doi.org/10.1007/s41748-025-00587-1>
- Pizzorni M, Innocenti A, Tollin N (2024) Droughts and floods in a changing climate and implications for multi-hazard urban planning: A review. *City and Environment Interactions* 24: 100169. <https://doi.org/10.1016/j.cacint.2024.100169>
- Pörtner H-O, Roberts DC, Adams H et al (2022) Technical Summary. In: Pörtner H-O, Roberts DC, Poloczanska ES et al (eds.) *Climate Change 2022: Impacts, Adaptation and Vulnerability. Contribution of Working Group II to the Sixth Assessment Report of the Intergovernmental Panel on Climate Change*. Cambridge University Press, Cambridge, UK and New York, NY, USA, pp. 37–118. <https://doi.org/10.1017/9781009325844.002>
- Pourghasemi HR, Gayen A, Edalat M, Zarafshar M, Tiefenbacher JP (2020) Is multi-hazard mapping effective in assessing natural hazards and integrated watershed management?. *Geoscience Frontiers* 11(4):1203–1217. <https://doi.org/10.1016/j.gsf.2019.10.008>
- Rahmstorf S, Coumou D (2011) Increase of extreme events in a warming world. *Proceedings of the National Academy of Sciences* 108(44):17905–17909. <https://doi.org/10.1073/pnas.1101766108>
- Rasmussen KL, Chaplin MM, Zuluaga MD, Houze RA (2016) Contribution of Extreme Convective Storms to Rainfall in South America. *J. Hydrometeor.* 17:353–367. <https://doi.org/10.1175/JHM-D-15-0067.1>
- Reboita MS, Kuki CAC, Marrafon VH et al (2022) South America climate change revealed through climate indices projected by GCMs and Eta-RCM ensembles. *Clim Dyn* 58:459–485. <https://doi.org/10.1007/s00382-021-05918-2>
- Regoto P, Dereczynski C, Chou SC, Bazzanella AC (2021) Observed changes in air temperature and precipitation extremes over Brazil. *Int J Climatol.* 41:5125–5142. <https://doi.org/10.1002/joc.7119>
- Ridder NN, Pitman AJ, Westra S et al (2020) Global hotspots for the occurrence of compound events. *Nat Commun* 11, 5956. <https://doi.org/10.1038/s41467-020-19639-3>
- Rising J, Tedesco M, Piontek F, Stainforth DA (2022) The missing risks of climate change. *Nature* 610:643–651. <https://doi.org/10.1038/s41586-022-05243-6>
- Rivera JA, Penalba OC (2018) Spatio-temporal assessment of streamflow droughts over Southern South America: 1961–2006. *Theoretical and Applied Climatology* 133(3):1021–1033. <https://doi.org/10.1007/s00704-017-2243-1>
- Seneviratne SI, Zhang X, Adnan M et al (2021) Weather and Climate Extreme Events in a Changing Climate. In Masson-Delmotte V, Zhai P, Pirani A et al (eds.) *Climate Change*

Referencias

- 2021: The Physical Science Basis. Contribution of Working Group I to the Sixth Assessment Report of the Intergovernmental Panel on Climate Change. Cambridge University Press, Cambridge, United Kingdom and New York, NY, USA, pp. 1513–1766. <https://doi.org/10.1017/9781009157896.013>
- Seong M-G, Min S-K, Kim Y-H, Zhang X, Sun Y (2021) Anthropogenic Greenhouse Gas and Aerosol Contributions to Extreme Temperature Changes during 1951–2015. *Journal of Climate* 34(3):857–870. <https://doi.org/10.1175/JCLI-D-19-1023.1>
- Sfetsos A, Politis N, Vlachogiannis D (2023) Multi-Hazard Extreme Scenario Quantification Using Intensity, Duration, and Return Period Characteristics. *Climate* 11(12):242. <https://doi.org/10.3390/cli1112024>
- Sgroi LC, Lovino MA, Berbery EH, Müller GV et al. (2021) Characteristics of droughts in Argentina's core crop region. *Hydrology and Earth System Sciences* 25(5):2475–2490. <https://doi.org/10.5194/hess-25-2475-2021>
- Sharma J, Ravindranath NH (2019) Applying IPCC 2014 framework for hazard-specific vulnerability assessment under climate change. *Environ. Res. Commun.* 1, 51004. <https://doi.org/10.1088/2515-7620/ab24ed>
- Sirdas S, Sen K (2003) Spatio-temporal drought analysis in the Trankya region, Turkey. *Hydrological Sciences Journal* 48(5):809–820. <https://doi.org/10.1623/hysj.48.5.809.51458>
- Skilodimou HD, Bathrellos GD, Chousianitis K et al (2019) Multi-hazard assessment modeling via multi-criteria analysis and GIS: a case study. *Environ Earth Sci* 78, 47. <https://doi.org/10.1007/s12665-018-8003-4>
- Soci C et al (2024) The ERA5 global reanalysis from 1940 to 2022. *Q. J.R. Meteorol. Soc.* 150(764):4014–4048. <https://doi.org/10.1002/qj.4803>
- Soláková T, De Michele C, Vezzoli R (2014) Comparison between parametric and non-parametric approaches for the calculation of two drought indices: SPI and SSI. *J. Hydrol. Eng.* 19: 04014010. [https://doi.org/10.1061/\(ASCE\)HE.1943-5584.0000942](https://doi.org/10.1061/(ASCE)HE.1943-5584.0000942)
- Stalhandske Z, Steinmann CB, Meiler S et al (2024) Global multi-hazard risk assessment in a changing climate. *Sci Rep* 14, 5875. <https://doi.org/10.1038/s41598-024-55775-2>
- Stanimirova R, Graesser J, Olofsson P, Friedl MA (2022) Widespread changes in 21st century vegetation cover in Argentina, Paraguay, and Uruguay. *Remote Sens. Environ.* 282, 113277. <https://doi.org/10.1016/j.rse.2022.113277>
- Stott P (2016) How climate change affects extreme weather events. *Science* 352:1517-1518. <https://doi.org/10.1126/science.aaf7271>
- Sun Q, Miao C, Hanel M, Borthwick AG, Duan Q, Ji D, Li H (2019) Global heat stress on health, wildfires, and agricultural crops under different levels of climate warming. *Environment international* 128:125-136. <https://doi.org/10.1016/j.envint.2019.04.025>
- Sutanto SJ, Vitolo C, Di Napoli C, D'Andrea M, Van Lanen HA (2020) Heatwaves, droughts, and fires: Exploring compound and cascading dry hazards at the pan-European scale. *Environment international* 134, 105276. <https://doi.org/10.1016/j.envint.2019.105276>

Referencias

- Tabari H, Hosseinzadehtalaei P, Thiery W, Willems P (2021) Amplified drought and flood risk under future socioeconomic and climatic change. *Earth's Future* 9, e2021EF002295. <https://doi.org/10.1029/2021EF002295>
- Tabari H, Willems P (2023) Global risk assessment of compound hot-dry events in the context of future climate change and socioeconomic factors. *npj Clim Atmos Sci* 6, 74. <https://doi.org/10.1038/s41612-023-00401-7>
- Thackeray CW, Hall A, Norris J et al (2022) Constraining the increased frequency of global precipitation extremes under warming. *Nat. Clim. Chang.* 12:441–448. <https://doi.org/10.1038/s41558-022-01329-1>
- Tomasz EO, Vilker AS, Pérez-Franco I, García-García A (2024) Impact valuation of droughts in soybean and maize production: the case of Argentina. *Int J Clim Change Strategies Manage* 16:63–90. <https://doi.org/10.1108/IJCCSM-11-2022-0139>
- UNDRR (UN Office for Disaster Risk Reduction) (2019) Global Assessment Report on Disaster Risk Reduction. United Nations, Geneva, Switzerland
- UNDRR (UN Office for Disaster Risk Reduction) (2020) Hazard Definition and Classification Review: Technical Report. United Nations. In: Documents and Publications. UNDRR. Available via <https://www.undrr.org/publication/hazard-definition-and-classification-review-technical-report>. Accessed 4 Apr 2024
- USAID (United States Agency for International Development) (2016) Climate Vulnerability Assessment: An Annex to the USAID Climate-Resilient Development Framework. Technical report No. AID-OAA-TO-11-00040. Available via: <https://www.climatelinks.org/sites/default/files/asset/document/USAID%20Vulnerability%20Assessment%20Annex.pdf> (Accessed October 2024).
- Viner D, Ekstrom M, Hulbert M, Warner NK, Wreford A, Zommers Z (2020) Understanding the dynamic nature of risk in climate change assessments—A new starting point for discussion. *Atmos Sci Lett.* 21:e958. <https://doi.org/10.1002/asl.958>
- Vogel E, Donat MG, Alexander LV et al (2019) The effects of climate extremes on global agricultural yields. *Environ. Res. Lett.* 14, 054010. <https://doi.org/10.1088/1748-9326/ab154b>
- Volante JN, Mosciaro MJ, Gavier-Pizarro GI, Paruelo JM (2016) Agricultural expansion in the Semiarid Chaco: Poorly selective contagious advance. *Land Use Policy* 55:154–165. <https://doi.org/10.1016/j.landusepol.2016.03.025>
- Wamsler C, Brink E, Rivera C (2013) Planning for climate change in urban areas: from theory to practice. *Journal of Cleaner Production* 50:68–81. <https://doi.org/10.1016/j.jclepro.2012.12.008>
- Wang Z, Jiang Y, Wan H, Yan J, Zhang X (2017) Detection and Attribution of Changes in Extreme Temperatures at Regional Scale. *Journal of Climate* 30(17):7035–7047. <https://doi.org/10.1175/JCLI-D-15-0835.1>
- Ward PJ, Blauthut V, Bloemendaal N et al (2020) Review article: Natural hazard risk assessments at the global scale. *Nat. Hazards Earth Syst. Sci.* 20:1069–1096. <https://doi.org/10.5194/nhess-20-1069-2020>

Referencias

- Weber T, Bowyer P, Rechid D et al (2020) Analysis of compound climate extremes and exposed population in Africa under two different emission scenarios. *Earth's Future* 8, e2019EF001473. <https://doi.org/10.1029/2019EF001473>
- Weis SWM, Agostini VN, Roth LM et al (2016) Assessing vulnerability: an integrated approach for mapping adaptive capacity, sensitivity, and exposure. *Climatic Change* 136:615–629. <https://doi.org/10.1007/s10584-016-1642-0>
- World Meteorological Organization (WMO) (2017) WMO guidelines on the calculation of climate normals. WMO-No. 1203. World Meteorological Organization. Available via WMO Library. <https://library.wmo.int/idurl/4/55797>. Accessed 3 Jan 2025.
- Xu L et al (2021) In-situ and triple-collocation based evaluations of eight global root zone soil moisture products. *Remote Sens. Environ.* 254:112248. <https://doi.org/10.1016/j.rse.2020.112248>
- Yang S, Zeng J, Fan W, Cui Y (2022) Evaluating Root-Zone Soil Moisture Products from GLEAM, GLDAS, and ERA5 Based on In Situ Observations and Triple Collocation Method over the Tibetan Plateau. *J. Hydrometeor* 23:1861–1878. <https://doi.org/10.1175/JHM-D-22-0016.1>
- Yu J, Castellani K, Forsinski K et al (2021) Geospatial indicators of exposure, sensitivity, and adaptive capacity to assess neighbourhood variation in vulnerability to climate change-related health hazards. *Environ Health* 20, 31. <https://doi.org/10.1186/s12940-021-00708-z>
- Zhang H, Delworth TL, Zeng F, Vecchi G, Paffendorf K, Jia L (2016) Detection, attribution, and projection of regional rainfall changes on (multi-) decadal time scales: a focus on southeastern South America. *Journal of Climate* 29:8515–8534. <https://doi.org/10.1175/JCLI-D-16-0287.1>
- Zhang Z, Varble A, Feng Z, Hardin J, Zipser E (2021) Growth of Mesoscale Convective Systems in Observations and a Seasonal Convection-Permitting Simulation over Argentina. *Mon. Wea. Rev.* 149:3469–3490. <https://doi.org/10.1175/MWR-D-20-0411.1>
- Zhou Y, Liu Y, Wu W et al (2015) Integrated risk assessment of multi-hazards in China. *Nat Hazards* 78:257–280. <https://doi.org/10.1007/s11069-015-1713-y>

Anexo I: Material Suplementario

Este anexo reúne información adicional que complementa los análisis presentados en el estudio. Cada apartado incluye detalles metodológicos, validaciones y análisis específicos que enriquecen los resultados:

- **Material Suplementario 1 (MS1):** Respuesta de la humedad del suelo y la profundidad del nivel freático ante eventos extremos de precipitación en la región núcleo de cultivos de Argentina. Contiene información adicional derivada del trabajo de Bernal-Mujica et al. (2023).
- **Material Suplementario 2 (MS2):** Describe la metodología y analiza el ciclo de vida de las sequías agrícolas repentinas, a partir de los trabajos de Lovino et al. (2024; 2025).
- **Material Suplementario 3 (MS3):** Eventos extremos de precipitación en la región del Chaco Austral. Contiene información adicional derivada del trabajo de Lovino et al. (2022).
- **Material Suplementario 4 (MS4):** Incluye un análisis adicional de los componentes de la vulnerabilidad, aportando mayor contexto al estudio de riesgos.

Material Suplementario 1 (MS1): Respuesta de la humedad del suelo y la profundidad del nivel freático ante eventos extremos de precipitación en la región núcleo de cultivos de Argentina (Bernal-Mujica et al. 2023)

Resumen

El estudio de Bernal et al. (2023) analiza la variabilidad espacio-temporal y los cambios en los eventos extremos de precipitación (EPEs), y examina la respuesta de la humedad del suelo y la profundidad de la capa freática ante los EPEs en la región núcleo de cultivos de Argentina. Se aplican índices no paramétricos estandarizados de precipitación, humedad del suelo y aguas subterráneas. La variabilidad temporal de los EPEs muestra un ciclo decadal y modos interanuales con frecuencias dominantes entre 2.5 y 4 años, relacionadas con las periodicidades del fenómeno El Niño-Oscilación del Sur. La humedad del suelo y la profundidad de la capa freática responden a la variabilidad de las precipitaciones, replicando tanto las variaciones decadales como interanuales de los EPEs. La respuesta de la humedad del suelo a los EPEs se atenúa con el tiempo a medida que aumenta la profundidad del suelo. La profundidad de la capa freática responde a los EPEs con un retraso promedio de 10 meses. En las últimas décadas, se observó que la humedad del suelo aumenta rápidamente (la capa freática se vuelve más superficial) ante precipitaciones excesivas, mientras que disminuye (la capa freática se profundiza) lentamente durante y después de los períodos de sequía.

Contribución

Este estudio, al igual que Lovino et al. (2022) en el MS3, brindaron las bases físicas de conocimiento para detectar las amenazas de los eventos extremos de precipitación de largo plazo. En particular, en este trabajo se analizó la variabilidad espacio-temporal y los cambios de los EPEs, junto con la respuesta de la humedad del suelo y el nivel freático a los EPEs en la región núcleo de cultivos de Argentina, lo que otorga información de mucha relevancia para la correcta interpretación de los resultados de la tesis. Este estudio provee el primer análisis de detección de los eventos extremos y su dinámica con la interfaz del suelo. Una breve discusión de esa identificación y las respuestas de la humedad del suelo se presenta a continuación.

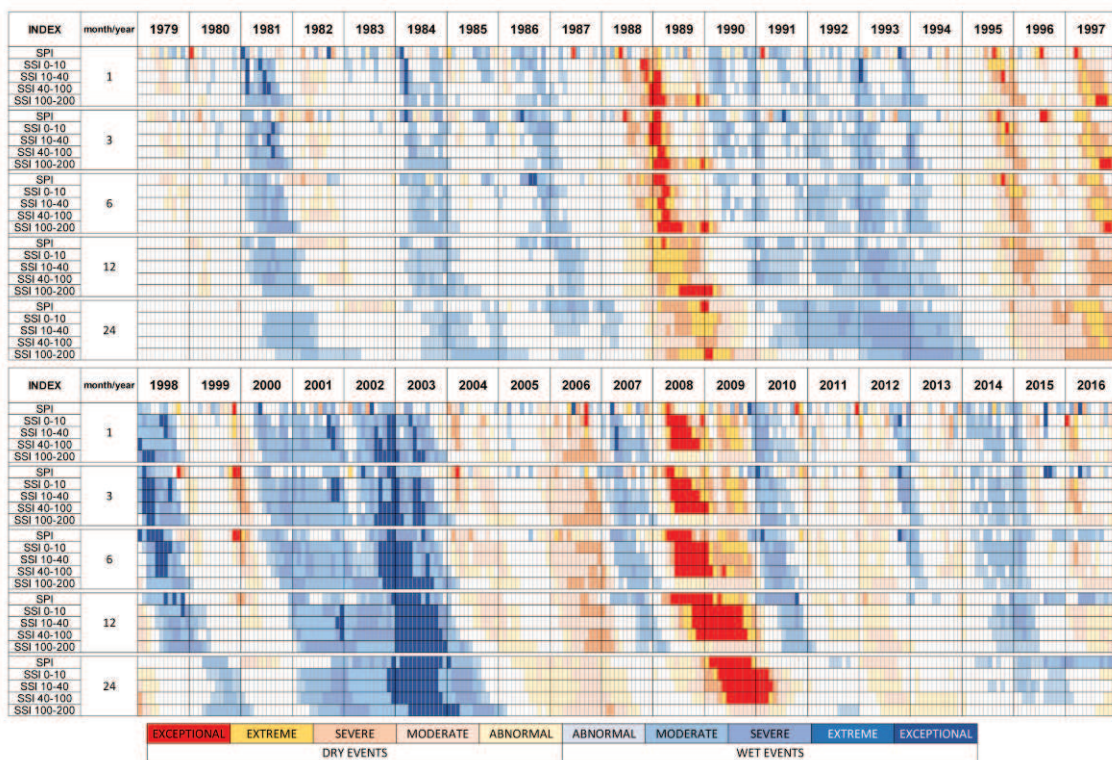


Figura MS1.1. Clasificación de los eventos extremos según los valores promedio areal del SPI y SSI en el período 1979-2016 para la región núcleo agrícola de Argentina. Las escalas temporales de los índices son de 1, 3, 6, 12 y 24 meses. Los valores de SSI se calculan para cada capa del suelo (0-10 cm, 10-40 cm, 40-100 cm, 100-200 cm). Los tonos en rojo (azul) representan la intensidad de los eventos secos (húmedos).

Relación entre la precipitación y la humedad del suelo e identificación de eventos extremos

La Figura MS1.1 presenta los valores promedio areales del SPI y SSI en escalas temporales de 1, 3, 6, 12 y 24 meses para la región núcleo de cultivos de Argentina (CCR). Esta figura muestra gráficamente tanto el efecto de los EPEs como la respuesta de la humedad del suelo en distintas escalas temporales. A medida que la escala de tiempo aumenta, se observa un desfase en el inicio y el final de los eventos extremos, lo que se traduce en un desplazamiento hacia la derecha de cada evento en función de la profundidad del suelo. Es decir, a mayor profundidad del suelo, la respuesta de la humedad del suelo (representada por el SSI) frente a la precipitación (representada por el SPI) es más atenuada. Cuando la precipitación ingresa al sistema, su señal se propaga en el tiempo. Parte del agua precipitada se evapora directamente desde la superficie, otra fracción genera escorrentía superficial y el resto se infiltra en el suelo. Una porción del agua infiltrada regresa a la atmósfera a través de la transpiración de la vegetación, mientras que otra percola hacia las aguas subterráneas o se almacena como humedad del suelo. La humedad del suelo presenta una menor variabilidad en frecuencia que la

precipitación. El tiempo que tarda la precipitación en infiltrarse y desplazarse hacia capas más profundas del suelo genera un efecto de suavizado comparable a un filtro pasa-bajos. La Figura MS1.1 identifica diez eventos húmedos (rangos azules) y cinco eventos secos (rangos rojos) en el período 1979-2016. Se observa un evento excepcionalmente húmedo entre 2000 y 2003 en todas las escalas temporales analizadas. La Figura MS1.1 indica que este evento tuvo una duración promedio de 40 meses en escalas de 12 y 24 meses, pero presenta discontinuidades en escalas estacionales de 1 a 6 meses, lo que sugiere que la variabilidad interanual de la precipitación a corto plazo favoreció condiciones normales durante 2001-2002. Otro evento húmedo excepcional ocurrió en 1998, aunque con una duración más corta (3-5 meses) en escalas de 1 a 6 meses. Se registraron eventos húmedos severos en 1981, 1984 y 1996 en escalas de 1 a 12 meses. Un evento moderado se detectó en 1990 en escalas de corto plazo, evolucionando a un evento severo en escalas de baja frecuencia entre 1991 y principios de 1994. Eventos húmedos extremos de menor duración y con intensidades extremas a excepcionales ocurrieron en 2007, 2010, 2012 y 2014, aunque sin impacto en la escala de 24 meses.

La Figura MS1.1 muestra dos eventos secos excepcionales. El primero tuvo una duración de 10 meses entre 1988 y 1989, persistiendo posteriormente como un evento seco extremo en escalas de baja frecuencia. El segundo evento seco excepcional tuvo una duración promedio de 12 meses en escalas de 12 y 24 meses entre 2008 y 2009. Además, se identificaron dos eventos secos extremos consecutivos en 1995 y 1997, con una duración promedio de 9 meses cada uno. Estos eventos aparecen como un único evento extremo con 30 meses de duración en la escala de 24 meses. Finalmente, se registró una sequía severa en 2006, con una duración promedio de 12 meses en escalas de 1 a 12 meses.

Referencias

- Bernal-Mujica A, Lovino MA, Müller GV, Pierrestegui MJ (2023) Spatiotemporal variability of extreme precipitation events and their impacts on soil moisture and water table depth in Argentina's core crop region. *Hydrological Sciences Journal*, 68:6, 794-809. <https://doi.org/10.1080/02626667.2023.2192874>
- Lovino MA, Müller GV, Pierrestegui MJ, Espinosa E, Rodríguez L (2022) Extreme precipitation events in the Austral Chaco region of Argentina. *International Journal of Climatology*, 1–22. <https://doi.org/10.1002/joc.7572>

Material Suplementario 2 (MS2): Metodología y análisis del ciclo de vida de sequías agrícolas repentinas (Lovino et al. 2024; 2025)

Resúmenes

El estudio publicado por Lovino et al. 2024 examina las características y el ciclo de vida predominante de las sequías agrícolas repentinas (SAR) a nivel global. Utilizando datos de ERA5, el estudio introduce un indicador de sequías repentinas basado en la disponibilidad de agua en el suelo. Este enfoque integra la humedad del suelo en la zona radicular y propiedades hidráulicas del suelo, como la capacidad de campo y el punto de marchitez, para vincular el rápido agotamiento de la humedad del suelo con el estrés hídrico de las plantas. Los hallazgos revelan que las sequías agrícolas repentinas presentan su mayor frecuencia predominantemente durante los períodos críticos de crecimiento de los cultivos. Es de destacar que estas sequías exhiben un ciclo de vida similar independientemente de la ubicación geográfica o el régimen climático. La principal causa del rápido agotamiento de la humedad del suelo es el déficit de precipitación, aunque la evapotranspiración también desempeña un papel significativo. En un entorno limitado por la energía, la evapotranspiración aumenta rápidamente antes del inicio de la sequía y disminuye abruptamente durante el período de intensificación, ya que el sistema se convierte en uno limitado por el agua. Al concluir el período de intensificación, la mayoría de los cultivos experimentan estrés hídrico, lo que reduce sus rendimientos.

El estudio publicado por Lovino et al. (2025) investiga las características de las sequías agrícolas repentinas y su impacto en los períodos críticos de crecimiento de la soja y el maíz en el sureste de América del Sur (SESA). Utilizando datos de ERA5 para el período 1960-2022, se analiza la frecuencia, duración, intensidad, tendencias, estacionalidad y ciclo de vida de las SARs, así como la influencia de las interacciones suelo-atmósfera. Además, se examinan datos históricos de rendimiento de cultivos, correspondientes a distintos períodos en los países de SESA, para evaluar cómo la evolución espacio-temporal y los distintos ciclos de vida de las SARs afectan la producción agrícola. Las mayores frecuencias de SARs (3 a 8 eventos por década) se registran en la región central de SESA. Estos eventos, caracterizados por una intensificación rápida, suelen evolucionar hacia sequías estacionales con una duración de 1.5 a 3 meses. Aunque la frecuencia promedio de SARs no muestra cambios significativos en el centro de SESA, se identifican

tendencias positivas en el sur de Brasil y Uruguay. Hacia el norte de SESA, las SARs son menos frecuentes (1 a 3 episodios por década), aunque su incidencia ha aumentado significativamente desde 1970. En esta región, las SARs tienden a prolongarse más de 3 meses y alcanzar mayor intensidad. Los mecanismos de retroalimentación suelo-atmósfera se reflejan en anomalías positivas del déficit de presión de vapor y la temperatura, lo que agrava los déficits de humedad del suelo a pesar de un déficit de precipitación relativamente estable, acelerando los períodos de intensificación de las SARs. Mientras que las SARs suelen afectar áreas más pequeñas, las sequías de evolución lenta abarcan regiones más extensas. Sin embargo, el momento en que ocurren las SARs dentro de los períodos críticos de crecimiento de los cultivos puede generar importantes pérdidas de rendimiento. En el centro de SESA, las SARs se presentan principalmente entre noviembre y enero, afectando ambos cultivos durante su floración y llenado de grano en diciembre y enero. En el norte, las SARs ocurren más tarde, entre febrero y abril, impactando principalmente al maíz de segunda siembra. El impacto final en los rendimientos depende de la duración, extensión espacial e intensidad de la sequía tras su fase de intensificación.

Contribución

El artículo de Lovino et al (2024) aporta la metodología utilizada para el estudio de las amenazas por sequías repentinas en la presente tesis, presentando un indicador de sequías repentinas basado en la humedad del suelo en la zona radicular y las propiedades hidráulicas del suelo, que permite captar el rápido agotamiento de la humedad junto con el estrés de la vegetación. El artículo de Lovino et al. (2025) aporta las características físicas propias de las sequías repentinas en SESA. En particular, en este anexo se muestra el ciclo de vida y la relevancia de los mecanismos de retroalimentación suelo-atmósfera. A continuación, se presenta un resumen de la metodología mencionada y el ciclo de vida de las SARs en SESA.

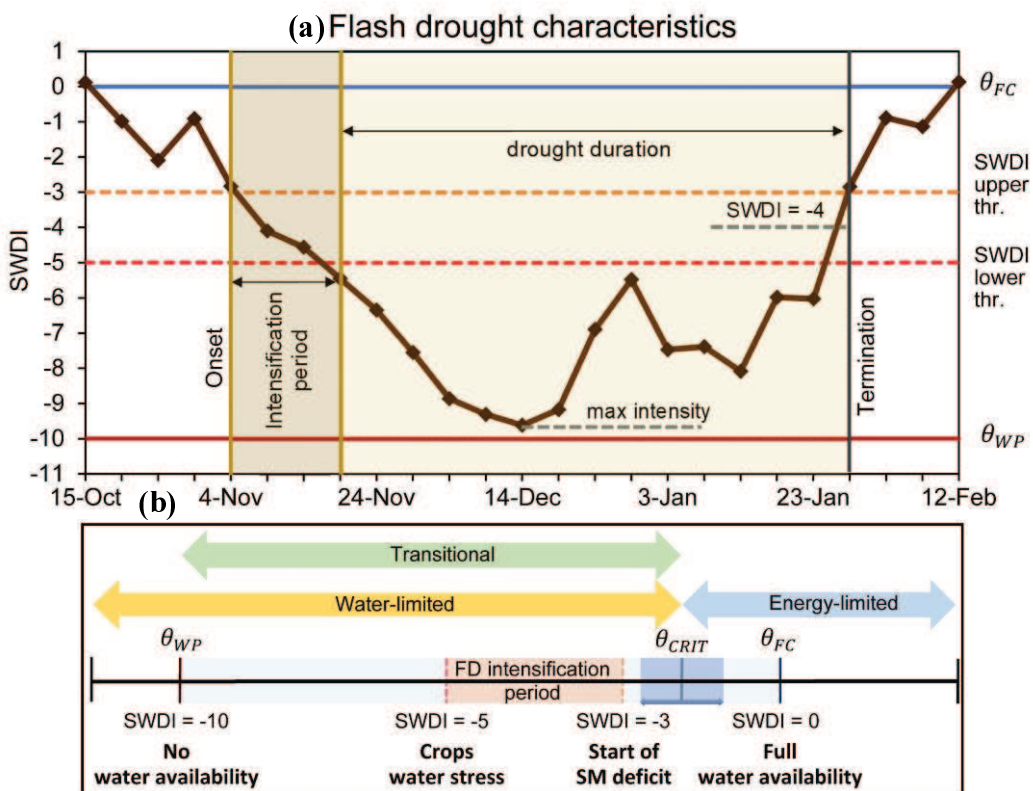


Figura MS2.1. (a) Características de un evento de sequía agrícola repentina (SAR) representado por la variación del SWDI a lo largo del tiempo desde octubre hasta febrero. El periodo de intensificación comienza en el inicio del evento de SAR, donde el SWDI cae desde valores mayores a -3 (umbral representado por la línea discontinua naranja) hasta valores inferiores a -5 (umbral representado por la línea discontinua roja) en 4 pentadas como máximo. Después del periodo de intensificación, la duración de la sequía se extiende hasta que el SWDI alcanza un valor superior a -4. La intensidad máxima es el valor mínimo del SWDI registrado durante la duración de la sequía. La capacidad de campo y el punto de marchitez permanente están indicados por las líneas horizontales azul y roja, respectivamente. (b) Representación esquemática que ilustra la metodología propuesta para la identificación de SARs (adaptado de Lovino et al. 2024).

La disponibilidad de agua en el suelo, entre θ_{FC} y θ_{WP} , se representa con sombreado celeste. θ_{CRIT} divide los regímenes de evapotranspiración limitados por energía y agua.

El rango de variabilidad de θ_{CRIT} se representa mediante un sombreado azul. El rango del periodo de intensificación del evento de SAR, sombreado en marrón, se extiende de SWDI = -3 a SWDI = -5.

La Figura MS2.1a presenta la evolución de un caso de SAR en SESA para representar las principales características de las SARs. Las SARs se caracterizan por un agotamiento rápido de la humedad del suelo en la zona radicular, representado por una disminución del SWDI desde más de -3 a menos de -5 en 20 días (o 4 pentadas) como máximo. La Figura MS2.1b resume el enfoque de identificación. El umbral superior (SWDI = -3) se establece al comienzo del régimen de evapotranspiración de transición (donde la humedad del suelo restringe fuertemente la variabilidad de la evapotranspiración y, en

consecuencia, las retroalimentaciones hacia la atmósfera), asegurando así una disminución en la evapotranspiración y, por lo tanto, capturando un nivel de déficit de humedad en el suelo. El umbral inferior ($SWDI = -5$) marca el límite de disponibilidad de agua del suelo para el crecimiento vegetal. Por debajo de este punto, la vegetación comienza a experimentar estrés hídrico. Además, siguiendo a Yuan et al. (2019; 2023), el método asegura un periodo de intensificación lo suficientemente largo como para evitar eventos sinópticos de corto plazo que agoten la humedad del suelo rápidamente pero se recuperen repentinamente. Esto se logra requiriendo que el periodo de agotamiento de la humedad del suelo dure al menos 15 días (o tres pentadas). El enfoque también propone (adaptado de Koster et al. 2019) condiciones de humedad del suelo razonablemente sin estrés antes del inicio de la sequía, requiriendo que las tres pentadas previas a un evento muestren valores de $SWDI$ superiores a -4 en magnitud. Adicionalmente, el enfoque aborda la superposición temporal de sequías repentinas. Se proporcionan más detalles del método de identificación de SARs en Lovino et al. (2024).

La distribución espacio-temporal de las anomalías estandarizadas en la Figura MS2.2 resalta las regiones de SESA donde este ciclo de vida de las SARs es más fuerte o más débil. Para simplificar la discusión, se refiere a los desfases y variables sin mencionar directamente la Figura MS2.2, ya que son fácilmente identificables. Antes del inicio de la sequía (desfases -2 a -1), predominan condiciones no secas, con anomalías positivas de humedad del suelo en la mayor parte de SESA. Entre el desfase -1 y el inicio del evento, se desarrollan anomalías negativas moderadas de precipitación en el centro y norte de SESA. En el momento del inicio de la sequía repentina, el déficit de precipitación se expande, mientras que la evapotranspiración aumenta significativamente en toda la región. En esta etapa, las anomalías positivas del déficit de presión de vapor (VPD) reflejan un aumento en la demanda evaporativa, lo que intensifica aún más la disminución de la humedad del suelo, principalmente en el norte de SESA.

Después del inicio del evento (desfases +1 y +2), el alto déficit de precipitación se extiende por toda la región, resaltando su papel crítico en el desarrollo de las SARs. El ciclo de vida de la sequía se intensifica rápidamente en el norte de SESA, donde las altas anomalías de VPD y los aumentos significativos de temperatura conducen a una marcada reducción de la humedad del suelo. Esta región experimenta condiciones de sequía severa de manera abrupta, caracterizadas por los déficits más pronunciados de humedad del suelo, un mayor calentamiento y una reducción en la evapotranspiración.

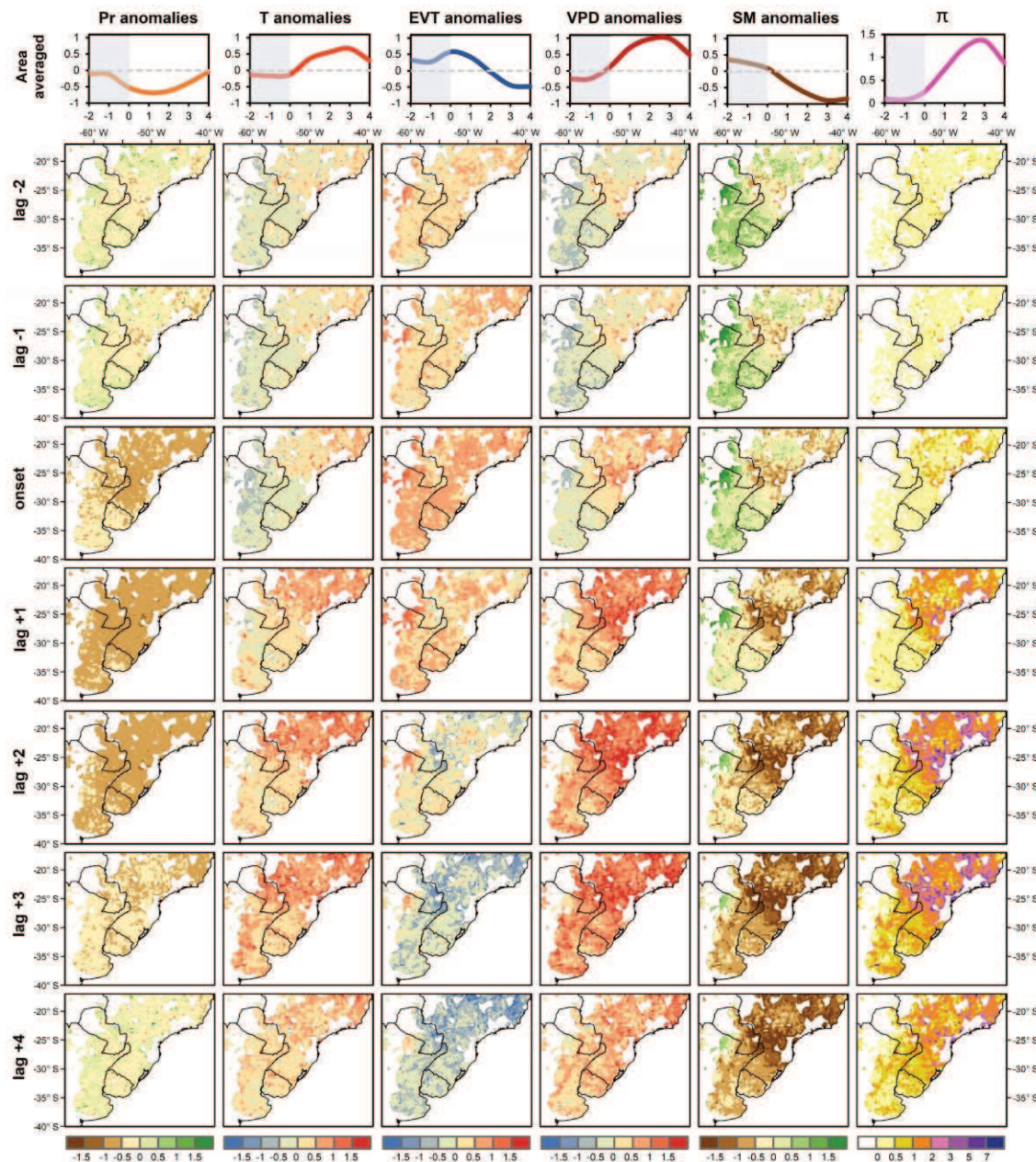


Figura MS2.2. Evolución de las anomalías estandarizadas de variables atmosféricas y de superficie durante eventos de sequía agrícola repentina en el período 1961-2022, considerando únicamente las regiones con una frecuencia de eventos superior a uno por década. Los desfases temporales varían de -2 a +4 en relación con el inicio del evento (desfase 0). De izquierda a derecha, las variables representadas incluyen anomalías estandarizadas de precipitación, temperatura, evapotranspiración (EVT), déficit de presión de vapor (VPD) y humedad del suelo. La columna más a la derecha muestra la evolución del índice de acoplamiento tierra-atmósfera, π (π). La fila superior ilustra las series temporales de las anomalías estandarizadas promediadas espacialmente y del índice π a lo largo de los eventos de AFD. Para mayor detalle, ver Lovino et al. (2025).

En contraste, el proceso es menos abrupto en la región central, donde los déficits de humedad del suelo comienzan a aumentar en los desfases +1 y +2, a medida que se intensifican las anomalías positivas de VPD y temperatura, mientras que la

evapotranspiración disminuye. En el centro de SESA, donde la frecuencia de SARs es mayor, las condiciones de sequía severa se desarrollan después del desfase +3, cuando las anomalías de humedad del suelo caen por debajo de -1, tras períodos de intensificación de al menos 15 días.

La intensificación de las SARs está impulsada en gran medida por las interacciones tierra-atmósfera, específicamente el acoplamiento humedad del suelo-temperatura (SM-T). Las altas anomalías positivas de VPD entre los desfases +1 y +3 agravan aún más los déficits de humedad del suelo en ambas regiones, particularmente en el noreste de SESA. Aunque las anomalías estandarizadas de precipitación en torno a -1 contribuyen a la rápida disminución de la humedad del suelo, las anomalías elevadas de VPD provocan que la humedad del suelo caiga por debajo de -1.5 en el desfase +3. Como resultado, π alcanza sus valores máximos en el norte de SESA en el desfase +3, mientras que en el centro de SESA es más débil, lo que indica que los mecanismos de retroalimentación tierra-atmósfera intensifican las SARs.

La temperatura también desempeña un papel clave en la intensificación de las SARs en SESA. Las anomalías positivas de temperatura persisten más tiempo que los déficits de precipitación, influyendo significativamente en la intensidad y duración de los déficits de humedad del suelo. A medida que la evapotranspiración disminuye en un régimen de disponibilidad hídrica limitada (después del desfase +1), una mayor cantidad de energía se transfiere al flujo de calor sensible, lo que incrementa la temperatura y el VPD. Dependiendo de su duración e intensidad, estas anomalías de temperatura positiva pueden contribuir al desarrollo de olas de calor, exacerbando aún más las condiciones de sequía.

Referencias

- Koster RD, Schubert SD, Wang H, Mahanama SP, DeAngelis, AM (2019) Flash drought as captured by reanalysis data: Disentangling the contributions of precipitation deficit and excess evapotranspiration. *J. Hydrometeor.* 20, 1241–1258.
<https://doi.org/10.1175/JHM-D-18-0242.1>
- Lovino MA, Pierrestegui MJ, Müller OV et al (2024) The prevalent life cycle of agricultural flash droughts. *npj Clim Atmos Sci* 7, 73.
<https://doi.org/10.1038/s41612-024-00618-0>
- Lovino MA, Pierrestegui MJ, Masaro L, Müller OV, Müller GV, Berbery EH (2025) Agricultural flash droughts and their impact on crop yields in southeastern South

Anexo I: Material Suplementario

America. Environ. Res. Lett. 20:054058. <https://doi.org/10.1088/1748-9326/adcd88>

Yuan X et al (2019) Anthropogenic shift towards higher risk of flash drought over China. Nat. Commun. 10, 1–8. <https://doi.org/10.1038/s41467-019-12692-7>

Yuan X et al (2023) A global transition to flash droughts under climate change. Science 380, 187–191. <https://doi.org/10.1126/science.abn6301>

Material Suplementario 3 (MS3): Eventos extremos de precipitación en la región del Chaco Austral (Lovino et al. 2022)

Resumen

Este estudio publicado por Lovino et al. (2022) evalúa la intensidad, distribución espacial y variabilidad temporal de los eventos extremos de precipitación (EPEs) en diferentes escalas temporales relevantes para la agricultura y los recursos hídricos durante el período 1901-2016 en la región del Austral Chaco (ACh) de Argentina. Los EPEs se identificaron utilizando un enfoque no paramétrico para el Índice Estandarizado de Precipitación (SPI). Los principales modos de variabilidad del SPI se detectaron mediante el Análisis Espectral Singular (SSA, por sus siglas en inglés). También se recopilaron y controlaron la calidad de las observaciones de precipitación en una región con escasa red de monitoreo. El número limitado de estaciones condiciona la interpolación de la base de datos GPCC v2018 utilizada en el estudio, principalmente durante las primeras décadas del siglo XX. Los EPEs caracterizados mediante el SPI en una escala temporal de 24 meses, que favorecen excesos o déficits de agua prolongados con impactos hidrológicos, mostraron dos períodos diferenciados de largo plazo: uno seco antes de 1960 y otro húmedo desde 1960 hasta 2005. De manera consistente, los EPEs estacionales por excesos de precipitación fueron más frecuentes durante el período húmedo, mientras que las sequías estacionales fueron más frecuentes y con mayor extensión espacial durante el período seco. Los EPEs estacionales, representados por el SPI en una escala temporal de 3 meses, pueden impactar la agricultura durante el período crítico de crecimiento de los cultivos. Desde 2006, se observa una inversión en la tendencia húmeda de largo plazo. Si este comportamiento continúa en las próximas décadas, se podrían esperar más sequías y menos eventos húmedos. Los EPEs presentan una gran variabilidad interanual con ciclos significativos de 6.3 años y 9 años que, combinados con tendencias a largo plazo, favorecieron EPEs extremadamente húmedos/secos. La mayoría de los EPEs húmedos/secos ocurrieron durante eventos El Niño/La Niña. Aunque esta relación no es directa, se encontró una señal vinculante del ENSO entre octubre del año en que comienza un evento ENSO y febrero del año siguiente. Finalmente, los EPEs severamente secos/húmedos tienden a tener una gran extensión espacial en la región ACh. La región centro-oriental del ACh experimenta las condiciones húmedas y secas más extremas, lo que hace que esta área sea más propensa a EPEs extremos.

Contribución

En este estudio se bridan las bases físicas del análisis de eventos extremos de precipitación que se utilizan en la tesis. A continuación, se presentan los resultados relevantes para esta tesis, que permiten analizar la variabilidad temporal de los eventos extremos de precipitación en una subregión del área de estudio de la tesis. Los principales hallazgos aportan conocimientos sobre los períodos húmedos y secos de largo plazo por los que atraviesa la región y, en particular, los dos períodos diferenciados a largo plazo: uno seco antes de 1960 y otro húmedo desde 1960 hasta 2005.

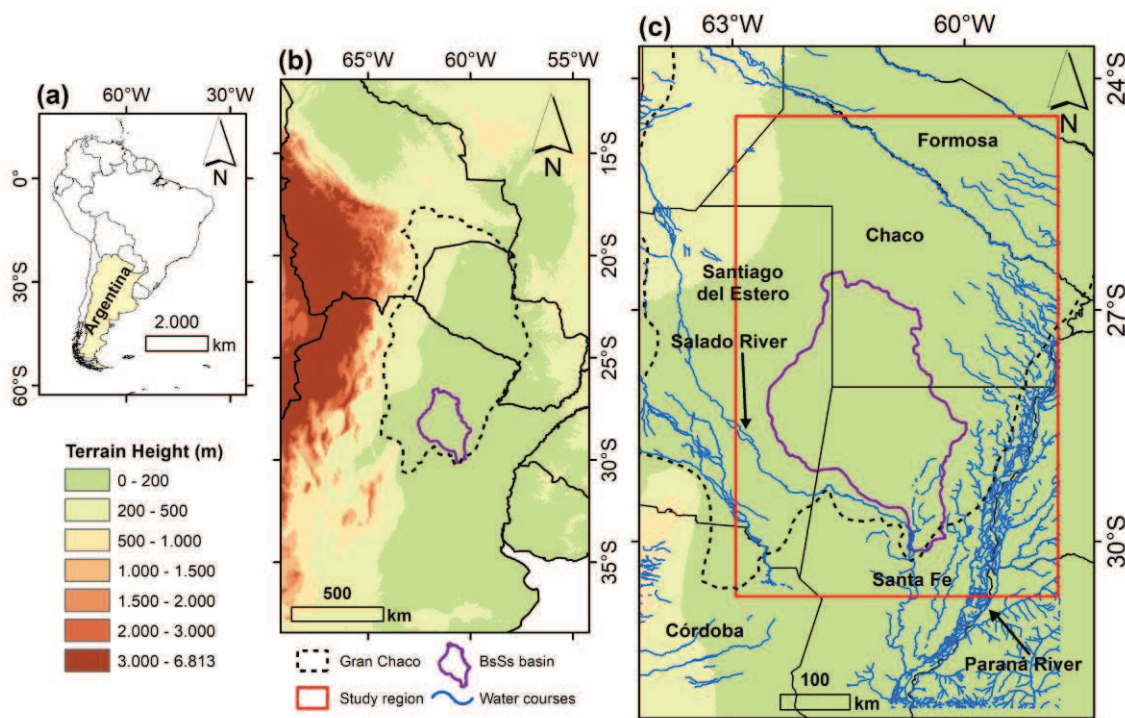


Figura MS3.1. (a) Mapa de América del Sur y la ubicación de Argentina. (b) Mapa topográfico de América del Sur, incluyendo la región del Gran Chaco (línea punteada).

(c) Región de estudio (rectángulo rojo) denominada región del Chaco Austral que incluye la cuenca de los Bajos Submeridionales (línea violeta), los ríos Paraná y Salado, y las provincias de Argentina.

El Gran Chaco es una extensa región (aproximadamente 790 000 km²) que se extiende desde los 16° 55' hasta los 33° 52' S, y desde los 67° 50' hasta los 57° 52' W, abarcando partes de Bolivia, Paraguay, Brasil y Argentina (ver Figuras MS3.1a y MS3.1b). El estudio se centra en la parte argentina del Gran Chaco, ubicada entre las latitudes 24.5 °S-31 °S y las longitudes 63.5 °W-58.5 °W (Figura MS3.1c), región conocida como el Chaco Austral (ACh). La región ACh abarca 284 000 km², está escasamente poblada, y se emplaza en territorio ubicado entre las provincias de Chaco, Santiago del Estero y Santa Fe.

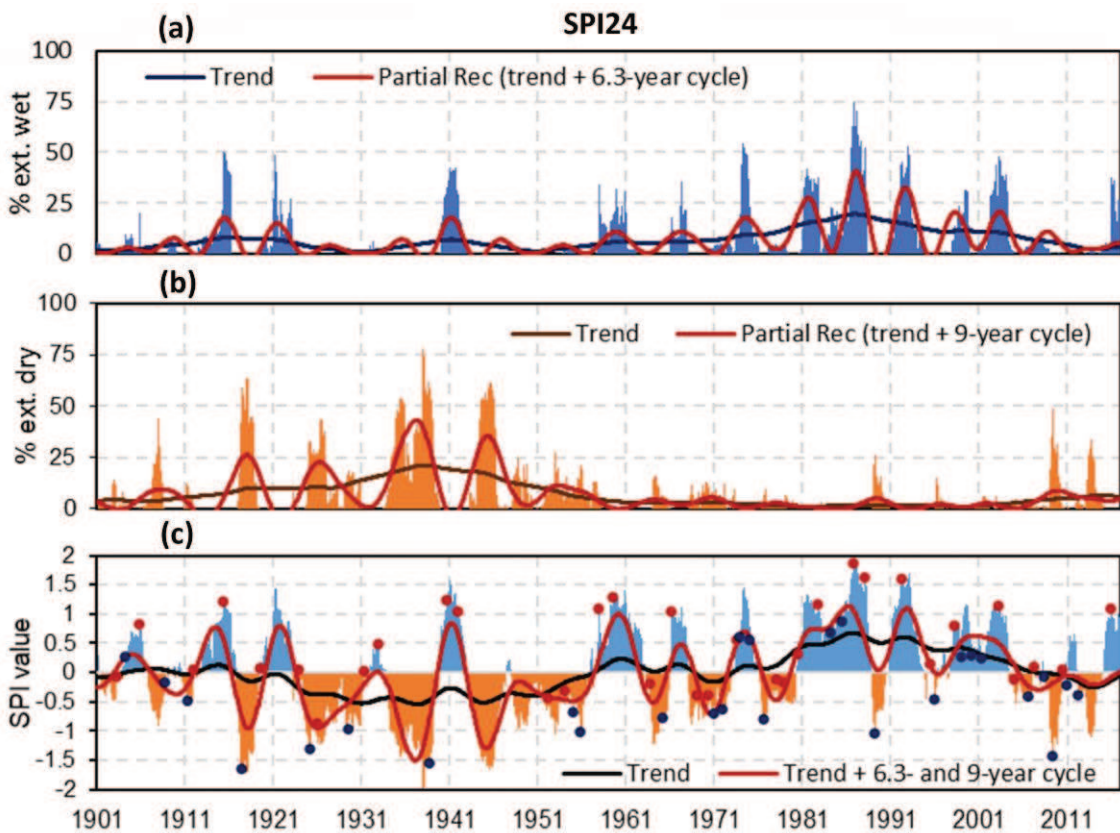


Figura MS3.2. Porcentaje de la región bajo condiciones al menos severamente (a) húmedas ($SPI24 > 1.5$) y (b) secas ($SPI24 < -1.5$). (c) Serie temporal de SPI24 para el período 1901–2016. Los puntos rojos (azules) representan el valor máximo (mínimo) de SPI3 entre octubre (o) y abril (++) durante eventos El Niño (La Niña).

La Figura MS3.2c muestra la serie temporal del SPI24 promedio para toda el área de estudio, que representa la evolución temporal de los EPEs de baja frecuencia en la región ACh. Las Figuras MS3.2a y MS3.2b presentan las series temporales del porcentaje de la región ACh bajo condiciones al menos severamente húmedas y secas, respectivamente. La Tabla MS3.1 muestra que las tendencias no lineales explican altos porcentajes de la varianza total de cada serie temporal: 26% para la serie SPI24 y 18% y 22% para la extensión espacial de las series de EPEs severamente húmedos y secos, respectivamente. Las tendencias no lineales en todas las series temporales (Figura MS3.2a–c) sugieren que la ocurrencia de EPEs de baja frecuencia puede dividirse en dos períodos: uno seco antes de 1960 y otro húmedo desde 1960 hasta 2005. La Figura MS3.2c también muestra que la tendencia no lineal se invirtió después del período húmedo, entrando en una fase dominada por EPEs secos, que incluye las sequías severas de 2008–2009 y 2012–2013. Esta reversión en el período húmedo desde mediados de la década de 2000 podría explicarse por una transición hacia una fase fría del océano Pacífico y un período cálido del océano Atlántico (Barreiro et al. 2014; Lovino et al. 2018). Si estas condiciones

persisten en las próximas décadas, podrían esperarse sequías más severas y menos EPEs de tipo húmedos. Sin embargo, Zhang et al. (2016) reportaron que el reciente descenso de la precipitación en el SESA es temporal y que la tendencia positiva se reanudará en respuesta al aumento de emisiones de gases de efecto invernadero durante el siglo XXI y al retorno de la variabilidad multidecadal a las condiciones previas a la década de 2000.

Tabla MS3.1. Modos dominantes (cuasi-ciclos y tendencias) encontrados en la serie temporal del SPI24 y la extensión espacial de eventos extremadamente húmedos SEEW₂₄ y secos SEEDj₂₄.

| Series temporales | T-PCs | Periodo dominante | Varianza explicada (%) |
|------------------------|---------------|-------------------|------------------------|
| SEEW ₂₄ (t) | T-PC1 | Tendencia | 17.7 |
| | T-PC2 y T-PC3 | 6.3 | 31.3 |
| SEED ₂₄ (t) | T-PC1 | Tendencia | 21.7 |
| | T-PC2 y T-PC3 | 9 | 33.6 |
| SPI ₂₄ (t) | T-PC1 | Tendencia | 26.3 |
| | T-PC2 y T-PC3 | 9 y 6.3 | 40.2 |

La Figura MS3.2a muestra que la extensión espacial de los EPEs severamente húmedos en la escala de 24 meses aumentó marcadamente durante el período húmedo. Los eventos con una gran extensión espacial ocurrieron entre 1970 y 2005, siendo el evento más extenso en 1987, que cubrió el 75% de la región de estudio. Por otro lado, la Figura MS3.2b muestra que las sequías hidrológicas—representadas por el SPI24—with mayor extensión espacial ocurrieron en la primera mitad del siglo XX. Por ejemplo, la sequía hidrológica con mayor extensión espacial se registró en 1938 (cubriendo más del 75% de la región de estudio bajo condiciones extremadamente secas). Por lo tanto, los resultados muestran que las mayores extensiones espaciales coinciden con las intensidades más altas tanto de EPEs secos como húmedos (ver Figuras MS3.2a–c). Esto significa que los EPEs de baja frecuencia con mayor extensión espacial y máxima intensidad fueron principalmente secos durante la primera mitad del siglo XX y húmedos en la segunda mitad del siglo XX y comienzos del siglo XXI.

Los resultados del Análisis de Espectro Singular (SSA) muestran que la extensión espacial de los eventos severamente húmedos presenta un ciclo dominante de 6.3 años (ver Tabla MS3.1). La reconstrucción parcial de la serie temporal (Figura MS3.2a) indica que el ciclo de 6.3 años fue más significativo durante el período húmedo de 1970-2005. La extensión espacial de los eventos severamente secos (Figura MS3.2b) tiene un ciclo

de 9 años (Tabla MS3.1), que adquiere mayor relevancia en el período seco de 1915-1955. Estos ciclos, combinados con la tendencia no lineal, se reflejan en la reconstrucción parcial de la serie temporal SPI24 (Figura MS3.2c). La reconstrucción parcial de la serie temporal SPI24 explica el 66.5% de su varianza (Tabla MS3.1). Por lo tanto, los resultados reportan un cambio significativo a largo plazo en los EPEs de baja frecuencia en la región ACh, representado por la importante tendencia no lineal y la relevancia de los ciclos de variabilidad interanual de 6.3 años para EPEs húmedos y de 9 años para EPEs secos. La tendencia no lineal de baja frecuencia y los modos de variabilidad interanual combinados han favorecido los EPEs que resultaron en sequías e inundaciones en la región de estudio.

Referencias

- Barreiro M, Diaz N, Renom M (2014) Role of the global oceans and land-atmosphere interaction on summertime interdecadal variability over northern Argentina. *Climate Dynamics*, 42(7–8):1733–1753. <https://doi.org/10.1007/s00382-014-2088-6>
- Lovino MA, Müller O, Berbery EH, Müller G (2018) How have daily climate extremes changed in the recent past over northeastern Argentina? *Global and Planetary Change*, 168:78–97. <https://doi.org/10.1016/j.gloplacha.2018.06.008>
- Lovino MA, Müller GV, Pierrestegui MJ, Espinosa E, Rodríguez L (2022) Extreme precipitation events in the Austral Chaco region of Argentina. *International Journal of Climatology*, 1–22. <https://doi.org/10.1002/joc.7572>
- Zhang H, Delworth TL, Zeng F, Vecchi G, Paffendorf K, Jia L (2016) Detection, attribution, and projection of regional rainfall changes on (multi-) decadal time scales: a focus on southeastern South America. *Journal of Climate*, 29:8515–8534. <https://doi.org/10.1175/JCLI-D-16-0287.1>

Material Suplementario 4 (MS4): Análisis adicional de los componentes de la vulnerabilidad

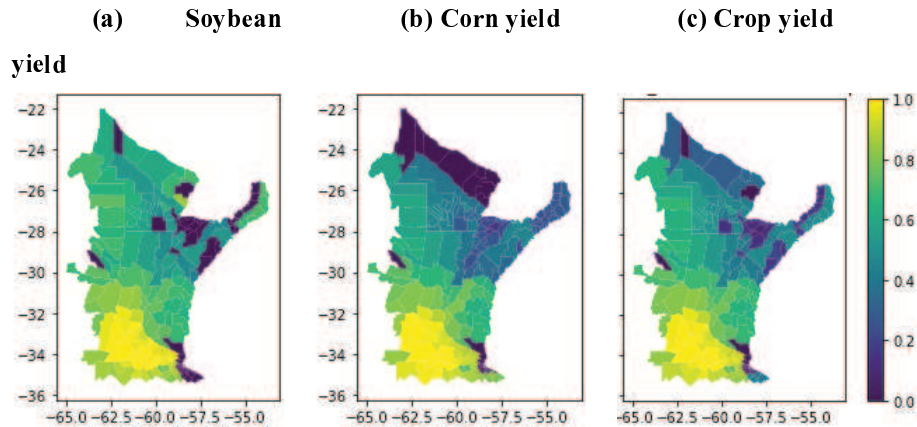


Figura MS4.1. Composición del rendimiento de cultivos. El panel c) presenta el índice de rendimiento de cultivos, obtenido a partir de la agregación de dos variables normalizadas: a) rendimiento de soja, y b) rendimiento de maíz.

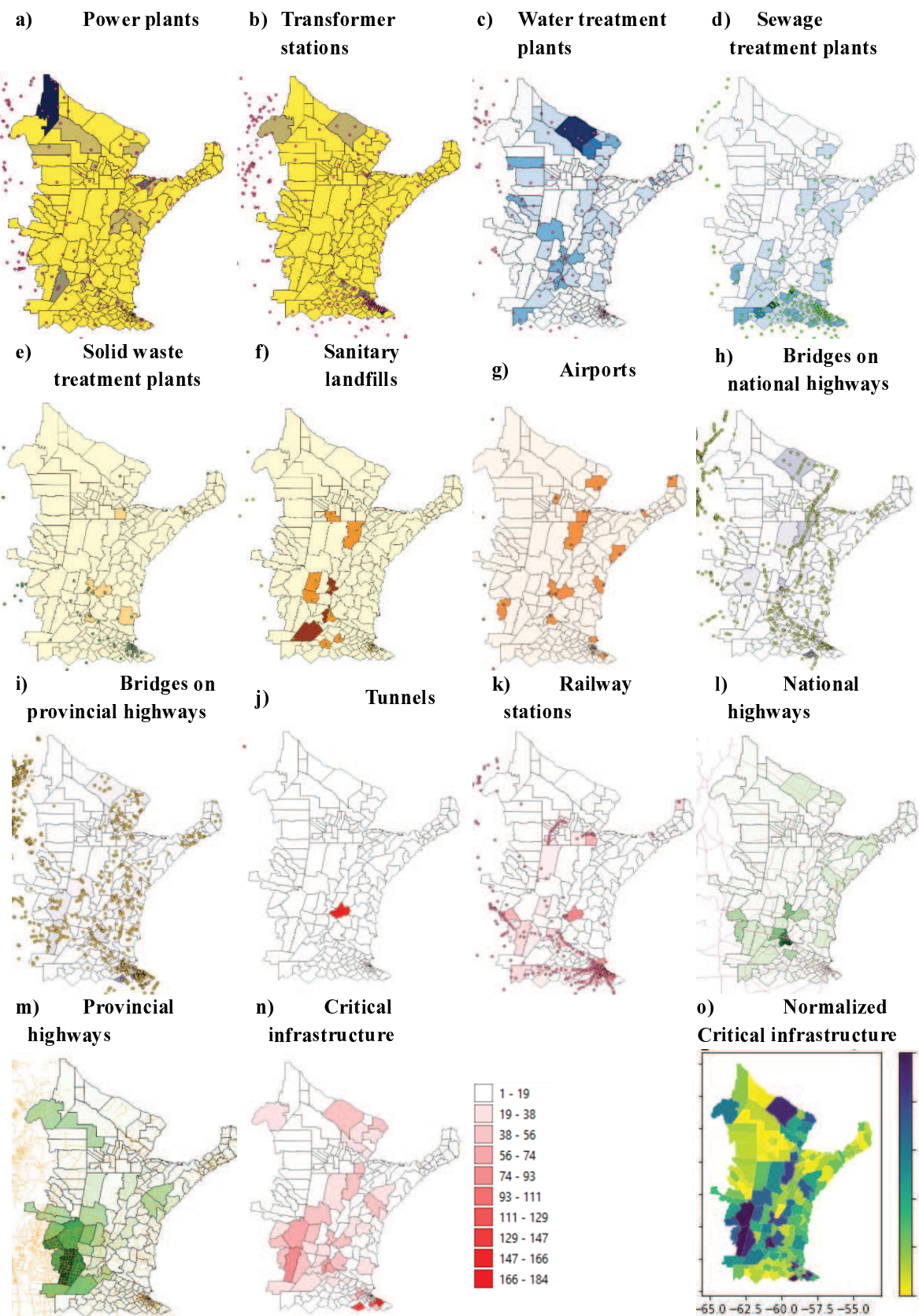


Figura MS4.2. Número total de infraestructura crítica (panel n) e índice de infraestructura crítica (panel o), obtenido a partir de la normalización del número total de infraestructuras. El índice incluye sistemas de energía: a) plantas de energía y b) estaciones transformadoras; sistemas de agua, aguas residuales y residuos sólidos: c)

plantas de tratamiento de agua, d) plantas de tratamiento de aguas residuales, e) plantas de tratamiento de residuos sólidos, f) rellenos sanitarios; y sistemas de transporte: g) aeropuertos, h) puentes en rutas nacionales, i) puentes en rutas provinciales, j) túneles, k) estaciones ferroviarias, l) rutas nacionales, m) rutas provinciales.

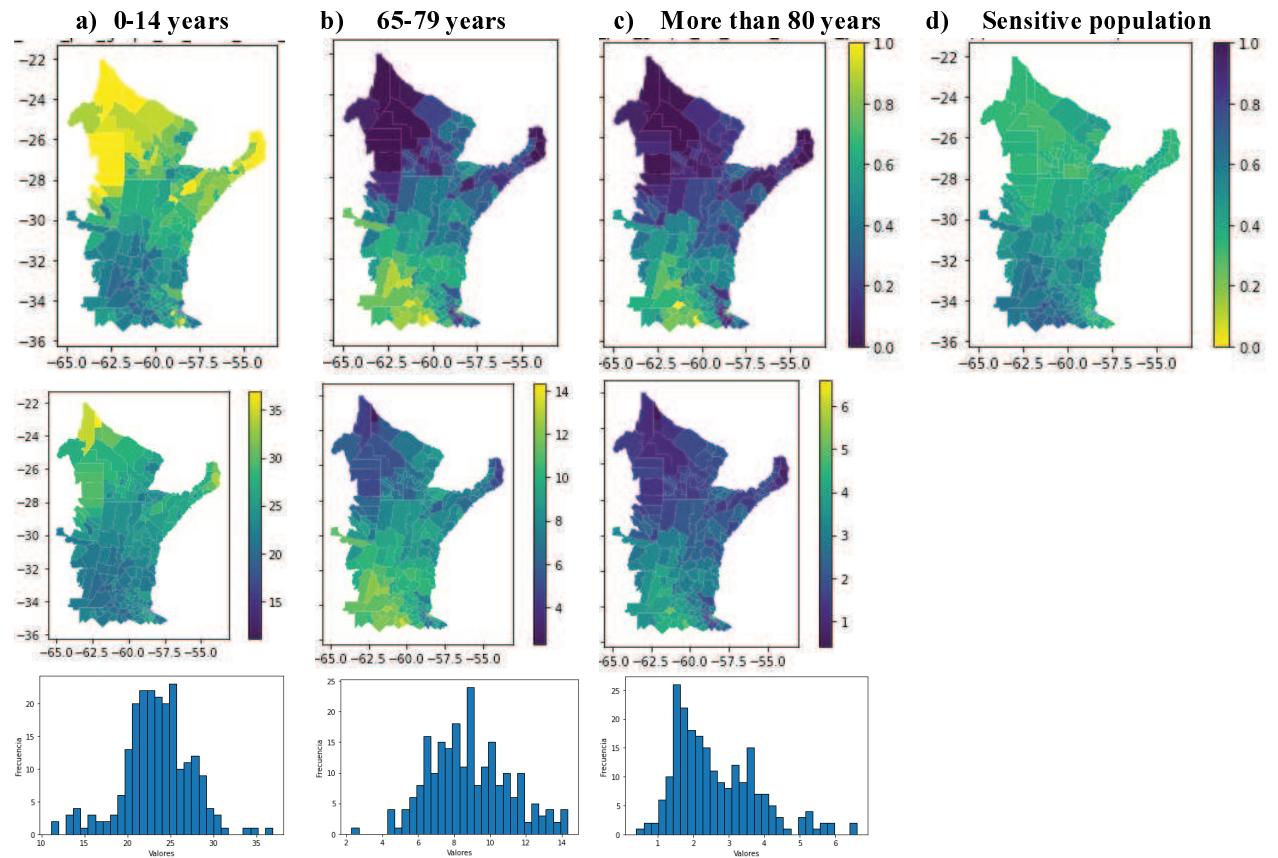


Figura MS4.3. Población sensible. Porcentaje de personas a) menores de 14 años, b) entre 65 y 79 años, y c) mayores de 80 años en relación con la población total. La primera fila muestra los valores normalizados, mientras que la segunda fila muestra los valores totales. La tercera fila muestra los histogramas para los valores totales.

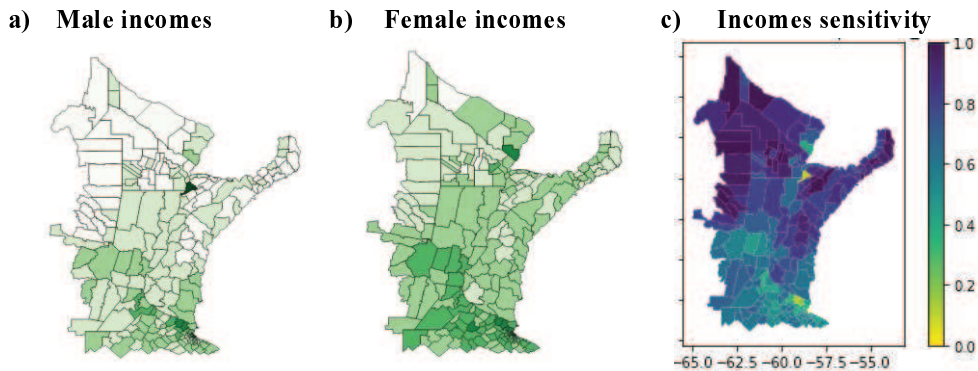


Figura MS4.4. Sensibilidad asociada a los ingresos. Ingreso laboral promedio para a) hombres y b) mujeres que trabajan en el sector privado registrado, en relación con el ingreso total de cada grupo. El panel (c) muestra la sensibilidad compuesta de los ingresos de hombres y mujeres. La sensibilidad asociada a los ingresos se define como la sensibilidad relacionada con la falta de ingresos, y se calcula como el inverso del ingreso.

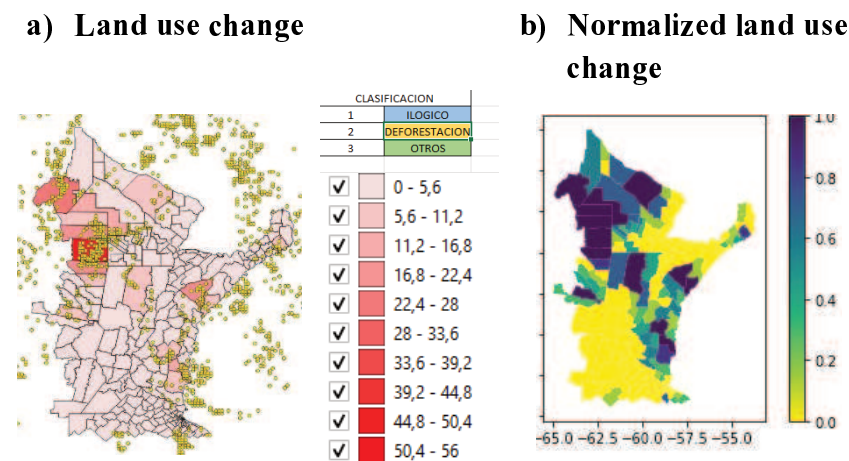


Figura MS4.5. Cambio en el uso del suelo. Se refiere a la deforestación que implica la transición de categorías de vegetación con mayor cobertura arbórea a otras con menor cobertura entre 2001 y 2015, según lo obtenido por Bracalenti et al. (2024).

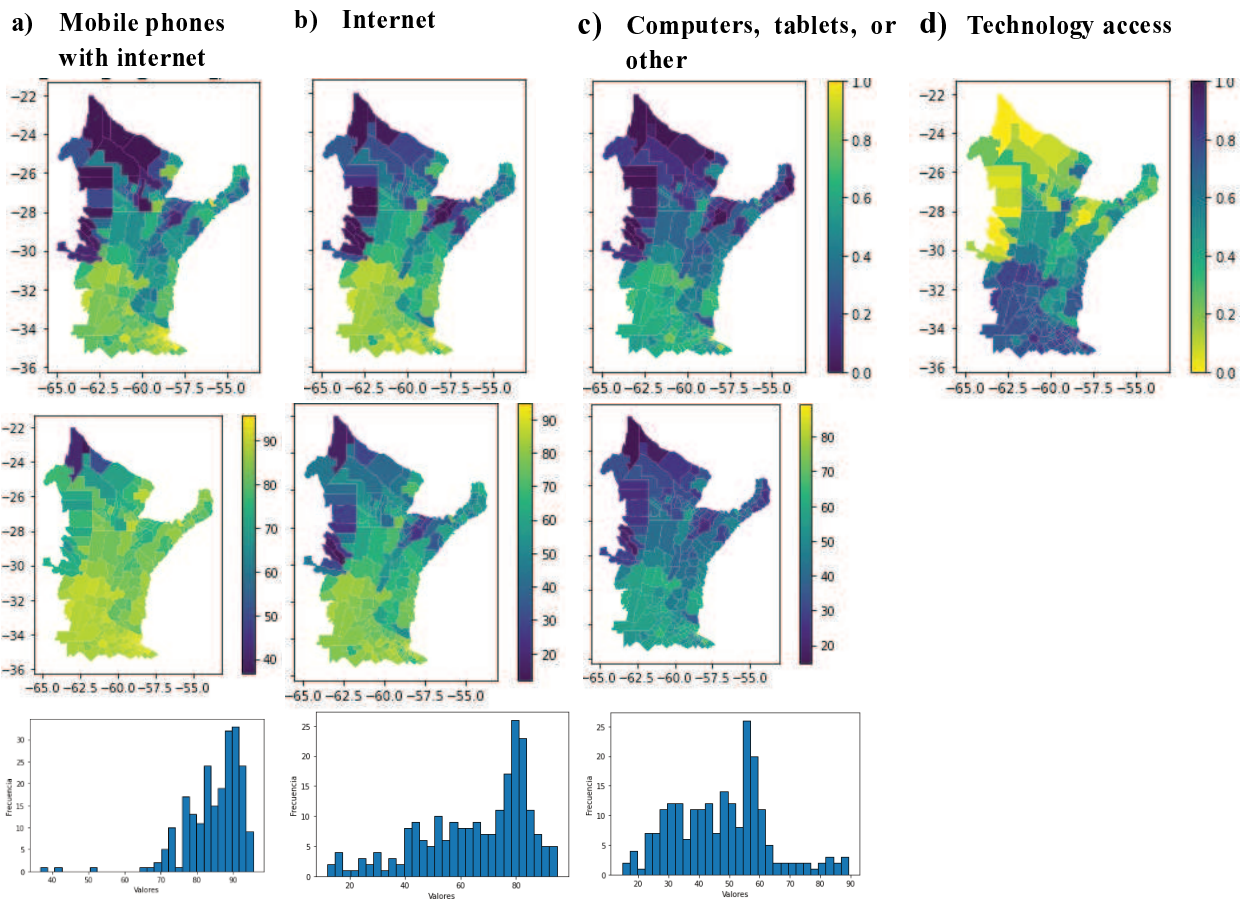


Figura MS4.6. Acceso a la tecnología. Porcentaje de hogares con acceso a: (a) teléfonos móviles con internet, (b) internet, y (c) computadoras, tablets u otros dispositivos de almacenamiento y procesamiento de información. La fila superior de mapas muestra los indicadores normalizados, mientras que la fila inferior presenta los indicadores totales (no normalizados). Los histogramas muestran los intervalos de distribución de frecuencia para cada indicador no normalizado. El panel (d) ilustra el índice compuesto de acceso a tecnología, derivado de los indicadores normalizados.

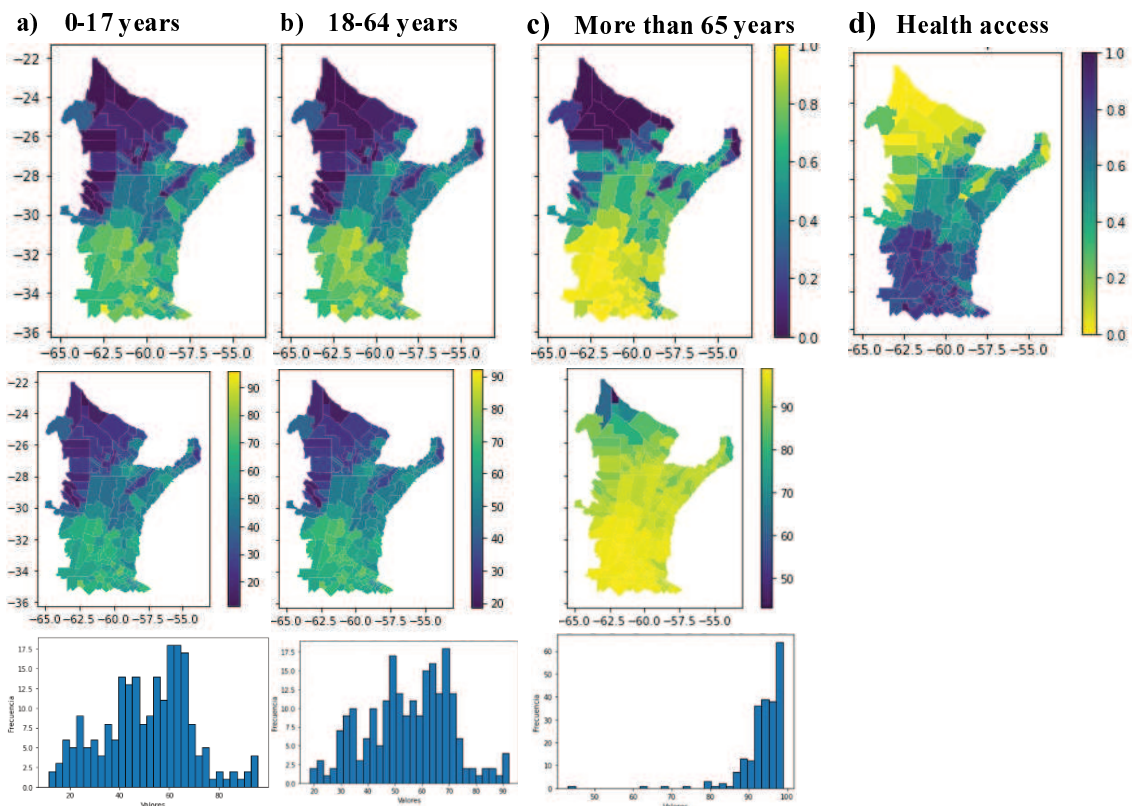


Figura MS4.7. Cobertura de salud. Porcentaje de la población con acceso a servicios de salud sociales o prepagos, o a programas de salud financiados por el estado: (a) de 0 a 17 años, (b) de 18 a 64 años, y (c) mayores de 65 años. La fila superior de mapas muestra los indicadores normalizados, mientras que la fila inferior presenta los indicadores totales (no normalizados). Los histogramas muestran los intervalos de distribución de frecuencia para cada indicador no normalizado. El panel (d) ilustra el índice compuesto de acceso a la salud, derivado de los indicadores normalizados.

Referencias

Bracalenti MA, Müller OV, Lovino MA, Berbery EH (2024) The agricultural expansion in South America's Dry Chaco: regional hydroclimate effects. Hydrol. Earth Syst. Sci. <https://doi.org/10.5194/hess-28-3281-2024>

Anexo II: Artículos científicos compilados en la tesis

Este Anexo reúne los artículos científicos que componen esta tesis, detallando sus contribuciones al avance del conocimiento y su relación con los objetivos generales de la tesis. También se destacan las contribuciones específicas de la autora en cada trabajo.

Contribuciones de la autora y relevancia de los artículos científicos en el marco de la tesis

La presente tesis, estructurada en formato de compilación, incluye una serie de artículos científicos que forman el núcleo de esta investigación. Este anexo tiene como objetivo detallar las contribuciones específicas realizadas por la autora en cada uno de los trabajos incluidos, destacando su rol en el desarrollo conceptual, la recopilación y análisis de datos, la redacción y revisión de los manuscritos, entre otros aspectos relevantes. Además, se proporciona una descripción de cómo cada artículo se vincula con los objetivos generales de la tesis y contribuye al avance del conocimiento en el campo de estudio. Este apartado busca no solo evidenciar la participación de la autora, sino también contextualizar el impacto de cada artículo en el marco global de la investigación.

Artículos principales incluidos en la tesis

Artículo 1: Evaluación de amenazas múltiples por eventos hidrometeorológicos extremos en el sudeste de Sudamérica

- Publicación: Pierrestegui, M.J., Lovino, M.A., Müller, G.V., Müller, O.V. (2024). Multi-hazard Assessment of Extreme Hydrometeorological Events in Southeastern South America. *Earth Syst Environ.* <https://doi.org/10.1007/s41748-024-00450-9>. Reproduced with permission from Springer Nature.
- Contribuciones: M. Josefina Pierrestegui y Miguel A. Lovino diseñaron el estudio. M. Josefina Pierrestegui llevó a cabo la investigación. M. Josefina Pierrestegui, Miguel A. Lovino, Omar V. Müller y Gabriela V. Müller analizaron y discutieron los resultados. Miguel A. Lovino y Gabriela V. Müller obtuvieron los fondos y los recursos necesarios. M. Josefina Pierrestegui elaboró el primer borrador del manuscrito, y todos los autores contribuyeron a sus versiones previas. Todos los autores leyeron y aprobaron la versión final del manuscrito.

- Relevancia: El artículo aborda los objetivos específicos 1 y 2 de la tesis, desarrollando un análisis multi-amenaza de eventos hidrometeorológicos extremos y sus variaciones temporales en el sureste de América del Sur, identificándose áreas críticas de amenazas por EHE y su evolución temporal en el centro-noreste de Argentina.

Artículo 2: Vulnerabilidad y riesgo de amenazas hidrometeorológicas en el centro-noreste de Argentina

- Publicación: Pierrestegui, M.J., Lovino, M.A., Müller, G.V., Müller, O.V. (2025). Vulnerability and Risk of Hydrometeorological Hazards in Central-Northeastern Argentina. *Earth Syst Environ.* <https://doi.org/10.1007/s41748-025-00587-1>. Reproduced with permission from Springer Nature.
- Contribuciones: M. Josefina Pierrestegui y Miguel A. Lovino diseñaron el estudio. M. Josefina Pierrestegui llevó a cabo la investigación. M. Josefina Pierrestegui, Miguel A. Lovino, Omar V. Müller y Gabriela V. Müller analizaron y discutieron los resultados. Miguel A. Lovino y Gabriela V. Müller obtuvieron los fondos y recursos necesarios. M. Josefina Pierrestegui elaboró el primer borrador del manuscrito, y todos los autores contribuyeron a sus versiones previas. Todos los autores leyeron y aprobaron la versión final del manuscrito.
- Relevancia: El artículo abordara los objetivos específicos 3 y 4 de la tesis, desarrollando un estudio de la vulnerabilidad y el riesgo del centro-noreste de Argentina frente a eventos hidrometeorológicos extremos tanto para amenazas individuales como para amenazas múltiples, elaborándose métricas de las componentes de la vulnerabilidad.

Ing. M. Josefina Pierrestegui

Dra. Gabriela V. Müller
Directora

Dr. Miguel A. Lovino
Codirector

Artículos complementarios incluidos en la tesis

Artículo 3: El ciclo de vida predominante de las sequías repentinas agrícolas

- Publicación: Lovino, M.A., Pierrestegui, M.J., Müller, O.V. et al. (2024). The prevalent life cycle of agricultural flash droughts. *npj Clim Atmos Sci* 7, 73. <https://doi.org/10.1038/s41612-024-00618-0>
- Contribuciones: Omar V. Müller, Miguel A. Lovino y Ernesto H. Berbery diseñaron el estudio. Miguel A. Lovino y M. Josefina Pierrestegui llevaron a cabo la investigación. Miguel A. Lovino, M. Josefina Pierrestegui, Omar V. Müller, Gabriela V. Müller y Ernesto H. Berbery analizaron y discutieron los resultados. Miguel A. Lovino, Gabriela V. Müller y Ernesto H. Berbery obtuvieron los fondos y recursos necesarios. Miguel A. Lovino elaboró el manuscrito original, y todos los autores contribuyeron a sus versiones posteriores.
- Relevancia: El artículo aporta la metodología utilizada para el estudio de las amenazas por sequías repentinas en la presente tesis, presentando un indicador de sequías repentinas basado en la humedad del suelo en la zona radicular y las propiedades hidráulicas del suelo, que permite captar el rápido agotamiento de la humedad junto con el estrés de la vegetación.

Artículo 4: Sequías agrícolas repentinas y su impacto en el rendimiento de los cultivos en el sudeste de Sudamérica.

Publicación: Lovino, M.A., Pierrestegui, M.J., Masaro, L., et al. (2025). Agricultural Flash Droughts and Their Influence on Crop Yields in Southeastern South America. *Environ. Res. Lett.* 20:054058. <https://doi.org/10.1088/1748-9326/adcd88>

- Contribuciones: Miguel A. Lovino, M. Josefina Pierrestegui y Ernesto H. Berbery diseñaron el estudio. Miguel A. Lovino, M. Josefina Pierrestegui y Lumila Masaro llevaron a cabo la investigación. Todos los autores analizaron y discutieron los resultados. Miguel A. Lovino, Gabriela V. Müller y Ernesto H. Berbery obtuvieron los fondos y recursos necesarios. Miguel A. Lovino elaboró el manuscrito original, y todos los autores contribuyeron a sus versiones posteriores.
- Relevancia: El artículo aporta las bases físicas de las sequías agrícolas repentinas en la región de estudio. Particularmente, el artículo investiga las características de

las sequías agrícolas repentinas y sus impactos en los períodos críticos de soja y maíz. En esta tesis, se discuten hallazgos propios del ciclo de vida de estas sequías.

Artículo 5: Eventos extremos de precipitación en la región del Chaco Austral de Argentina

- Publicación: Lovino, M.A., Müller, G.V., Pierrestegui, M.J., Espinosa, E., Rodríguez, L. (2022). Extreme precipitation events in the Austral Chaco region of Argentina. International Journal of Climatology, 1–22.
<https://doi.org/10.1002/joc.7572>
- Contribuciones: Miguel A. Lovino: Conceptualización; análisis formal; investigación; metodología; administración del proyecto; visualización; redacción – borrador original; redacción – revisión y edición. Gabriela V. Müller: Conceptualización; análisis formal; investigación; supervisión; redacción – borrador original; redacción – revisión y edición. María Josefina Pierrestegui: Depuración de datos; análisis formal; investigación; software; validación; visualización; redacción – borrador original; redacción – revisión y edición. Edna Espinosa: Depuración de datos; análisis formal; investigación; metodología; visualización; redacción – borrador original; redacción – revisión y edición. Leticia Rodríguez: Análisis formal; investigación; administración del proyecto; supervisión; redacción – borrador original; redacción – revisión y edición.
- Relevancia: Los resultados permiten analizar la variabilidad temporal de los eventos extremos de precipitación en una subregión del área de estudio de la tesis, que aportan entendimiento sobre los períodos húmedos y secos de largo plazo por los que atraviesa la región, y en los que se desarrollan las amenazas hidrometeorológicas.

Artículo 6: Variabilidad espaciotemporal de los eventos extremos de precipitación y sus impactos en la humedad del suelo y la profundidad del nivel freático en la región núcleo de cultivos de Argentina

- Publicación: Bernal-Mujica, A., Lovino, M.A., Müller, G.V., Pierrestegui, M.J. (2023). Spatiotemporal variability of extreme precipitation events and their impacts on soil moisture and water table depth in Argentina's core crop region. Hydrological Sciences Journal, 68:6, 794-809.
<https://doi.org/10.1080/02626667.2023.2192874>

Anexo II: Artículos científicos compilados en la tesis

- Contribuciones: Anelim Bernal y Miguel A. Lovino diseñaron el estudio. Anelim Bernal y M. Josefina Pierrestegui llevaron a cabo la investigación. Todos los autores analizaron y discutieron los resultados. Miguel A. Lovino y Gabriela V. Müller obtuvieron los fondos y recursos necesarios. Anelim Bernal y Miguel A. Lovino elaboraron el manuscrito original, y todos los autores contribuyeron a sus versiones posteriores.
- Relevancia: Este estudio brinda las bases físicas de conocimiento para detectar las amenazas de los eventos extremos de precipitación de largo plazo. En particular, en este trabajo se analizó la variabilidad espacio-temporal y los cambios de los EPEs, junto con la respuesta de la humedad del suelo y el nivel freático a los EPEs en la región núcleo de cultivos de Argentina, lo que otorga información de mucha relevancia para la correcta interpretación de los resultados de la tesis.

Ing. M. Josefina Pierrestegui

Dra. Gabriela V. Müller
Directora

Dr. Miguel A. Lovino
Codirector

Publicaciones de los artículos científicos

Se adjuntan las publicaciones de los artículos científicos compilados en la tesis y mencionados en la sección anterior. Se incluyen en el orden en que fueron mencionados previamente, facilitando la continuidad y organización del material compilado.

ÍNDICE DE ARTÍCULOS

| | |
|--|-----|
| Artículo 1: Evaluación de amenazas múltiples por eventos hidrometeorológicos extremos en el sudeste de Sudamérica..... | 105 |
| Artículo 2: Vulnerabilidad y riesgo de amenazas hidrometeorológicas en el centro-noreste de Argentina..... | 123 |
| Artículo 3: El ciclo de vida predominante de las sequías repentina agrícolas..... | 143 |
| Artículo 4: Sequías agrícolas repentina y su impacto en el rendimiento de los cultivos en el sudeste de Sudamérica..... | 155 |
| Artículo 5: Eventos extremos de precipitación en la región del Chaco Austral de Argentina..... | 171 |
| Artículo 6: Variabilidad espaciotemporal de los eventos extremos de precipitación y sus impactos en la humedad del suelo y la profundidad del nivel freático en la región núcleo de cultivos de Argentina..... | 194 |

Artículo 1

Evaluación de amenazas múltiples por eventos hidrometeorológicos extremos en el sudeste de Sudamérica



Multi-hazard Assessment of Extreme Hydrometeorological Events in Southeastern South America

M. Josefina Pierrestegui^{1,2} · Miguel A. Lovino^{1,2} · Gabriela V. Müller^{1,2} · Omar V. Müller^{1,2}

Received: 10 June 2024 / Revised: 15 August 2024 / Accepted: 19 August 2024
© King Abdulaziz University and Springer Nature Switzerland AG 2024

Abstract

Southeastern South America is particularly vulnerable to extreme hydrometeorological events (EHEs). This study presents a multi-hazard analysis of long-term and short-term EHEs and their changes across southeastern South America for the 1961–1990 and 1991–2020 periods, using daily to monthly ERA5 data. Long-term EHEs are studied using the standardized precipitation index at 3- and 18-month timescales. Short-term EHEs are characterized by heatwaves, heavy precipitation, and flash droughts. Individual hazard components are derived by multiplying the frequency, duration, and intensity of the identified EHEs. The long-term and short-term EHE multi-hazard indices are formulated by aggregating these individual hazard components. Long-term multi-hazards prevail in the southwest and central west of the study region, including Argentina's core crop region. A substantial water excess hazard hotspot is found in the southern areas, while the hotspot of seasonal to hydrological drought hazard is in northern and western areas. Short-term multi-hazards are more common in the north and central east, primarily impacting northeastern Argentina, southern Brazil, and southeastern Paraguay. In this hotspot region, heatwave hazard has increased by 30% in the last decades and flash drought and heavy precipitation frequencies are the highest. The current total multi-hazard, combining long-term and short-term multi-hazard indices, is higher and more widespread than between 1960 and 1990. Short-term hazards are more likely to co-occur, while long-term hazards tend to alternate. The study region is one of the most productive agricultural areas worldwide, so high EHE hazards can impact crop yields, threaten food security, and affect human well-being.

Keywords Extreme hydrometeorological events · Multi-hazards · Standardized precipitation index · Heatwaves · Heavy precipitation · Flash droughts

1 Introduction

Extreme hydrometeorological events (EHEs) negatively impact ecosystems, human settlements, food production, water resources, and public health worldwide (Aghakouchak et al. 2020; Pörtner et al. 2022). Droughts and heatwaves can threaten farmer's livelihoods and community food security (Dasgupta and Robinson 2022; Lesk et al. 2022).

Simultaneously, they can lead to forest fires that devastate natural habitats and biodiversity (Sutanto et al. 2020; Vogel et al. 2019). Floods and storms also affect agriculture, damage urban infrastructure, disrupt communities, and contaminate water sources (Kreibich et al. 2022; Müller et al. 2024; Rahmstorf and Coumou 2011). Moreover, the magnitude and frequency of extreme hot events have increased globally due to climate change, while extreme precipitation events have intensified in specific regions (Perkins et al. 2012; Seneviratne et al. 2021; Thackeray et al. 2022). As global temperatures continue to rise, unprecedented extremes will increase, compounded by the simultaneous occurrence of multiple extreme events, leading to unprecedented impacts (Fischer et al. 2021; Seneviratne et al. 2021; Sun et al. 2019).

In southeastern South America (SESA), consistent with global patterns, hot temperature extremes have significantly increased since 1960 (Almazroui et al. 2021a; Dereczynski et al. 2020; Reboita et al. 2022), with robust evidence of a

✉ M. Josefina Pierrestegui
mj pierrestegui@unl.edu.ar

¹ Consejo Nacional de Investigaciones Científicas y Técnicas (CONICET), Santa Fe, Argentina

² Centro de Estudios de Variabilidad y Cambio Climático (CEVARCAM), Facultad de Ingeniería y Ciencias Hídricas (FICH), Universidad Nacional del Litoral (UNL), Ruta Nacional N° 168 Km 472.4, CC 217, Ciudad Universitaria, 3000 Santa Fe, Argentina

human contribution (Seong et al. 2021; Wang et al. 2017). Furthermore, the intensity and frequency of hot events are projected to increase at 1.5 °C, 2 °C, and 4 °C of global warming (Gulizia et al. 2022; Li et al. 2021). Precipitation extremes—including events such as heavy rainfall, precipitation excesses, and droughts—do not show significant trends, and there is low confidence about the human contribution to observed trends (Avila-Diaz et al. 2023; Lovino et al. 2018a; Regoto et al. 2021). However, heavy precipitation events—defined as short-duration, intense rainfall episodes—have significantly increased (Avila-Diaz et al. 2020; Dunn et al. 2020; Olmo et al. 2020), and they are projected to rise throughout the twenty-first century (Almazroui et al. 2021b; Li et al. 2021). Meteorological, agricultural, and ecological droughts exhibit mixed observed and projected trend signals (Seneviratne et al. 2021). Hydrological droughts are the only category showing a medium-confidence reduction in occurrence (Dai and Zhao 2017; Rivera and Penalba 2018).

Climate risk management strategies and adaptation plans typically focus on single hazards impacting exposed systems, but multiple hazards can occur and have a substantial effect on these systems (AghaKouchak et al. 2020; Stalhandske et al. 2024). The risk increases when hazards co-occur in time or space, so adopting a multi-hazard framework provides a more comprehensive analysis for understanding climate risk (Binita et al. 2021). A multi-hazard approach considers multiple major hazards that a region faces, which may occur concurrently or independently (UNDRR 2020). Combining multiple single hazards by assuming them to be independent, called multi-layer single hazard analysis, is a first step towards a more comprehensive risk assessment (Stalhandske et al. 2024). The multi-layer single hazard analysis, as used in this study, helps identify spatially relevant hazards or key ‘hotspots’ where exposure to hazards is particularly high (De Angeli et al. 2022; Gill and Malamud 2014).

Multi-hazard studies have been conducted in various regions around the world (AghaKouchak et al. 2020; Bathrellos et al. 2017; Pourghasemi et al. 2020; Ridder et al. 2020; Sfetsos et al. 2023; Skilodimou et al. 2019). In Europe, extreme events multi-hazard is expected to increase in the south and southwest due to more frequent heatwaves, droughts, and wildfires, with critical multi-hazard hotspots projected along coastlines and floodplains where floods and windstorms are prevalent (Forzieri et al. 2016). In the United States, extreme events multi-hazard is projected to increase, particularly in hotspots like Florida and Gulf Coast counties due to frequent heatwaves and extreme precipitation, in Central-western USA due to intensified heatwaves and droughts, and in the Pacific Northwest due to increased cold spells and extreme precipitation (Binita et al. 2021). On a local scale, a high multi-hazard risk of flood, muddy water flow, and landslide is found in over 15% of the areas in Hong

Kong (Lyu and Yin 2023). However, multi-hazards studies are still lacking in SESA, a region frequently impacted by extreme hydrometeorological events.

The SESA region faces heightened vulnerability to hydrometeorological hazards due to its dense population and heavy reliance on agriculture (Castellanos et al. 2022; Lovino et al. 2018b). Population growth, urban expansion, and agricultural activities in hazard-prone areas, compounded by shifting climate patterns, contribute to worsening hazardous conditions (Blaikie et al. 2014; Ward et al. 2020). Therefore, advancing toward climate-resilient development is a key objective for the SESA region. Thus, it is crucial to assess hydrometeorological multi-hazards across diverse spatial and temporal scales to develop effective climate risk management strategies and adaptation plans.

This study introduces a multi-hazard analysis of extreme hydrometeorological events and their temporal variations across southeastern South America. We estimate the frequency, duration, and intensity of both short-term and long-term EHEs for the periods 1961–1990 and 1991–2020. By employing a multi-layer single hazard analysis, we identify critical EHE hazard hotspots and analyze their temporal evolution. Section 2 introduces the study region and details the data and methods used for detecting short-term and long-term EHEs as well as quantifying hazards. Section 3 presents the results on short-term and long-term extreme hydrometeorological hazards and the multi-hazard composite. Section 4 discusses the findings and provides concluding remarks.

2 Data and Methods

2.1 Study Region

The study region is located in SESA, covering an extended flat region delimited by 63W–53W and 35S–22S (Fig. 1). This region has a relatively uniform climate, classified as temperate without a drying season and with a hot summer, according to the Köppen-Geiger classification (Beck et al. 2018). SESA experiences maximum annual precipitation in northeastern Argentina, Uruguay, and southeastern Brazil, while the minimum annual precipitation occurs in western Argentina and western Paraguay (Berbery and Barros 2002). Temperature follows a latitudinal gradient, decreasing from north to south (Caffera and Berbery 2006). SESA is key for the socioeconomic development of the continent, has a complex system of water resources, and generates a high percentage of the continent's agricultural production (Houspanossian et al. 2023; Lovino et al. 2018b). The study region experiences hydroclimate variability on interannual to decadal time scales and is prone to extreme events, which may increase in frequency and severity in the coming years

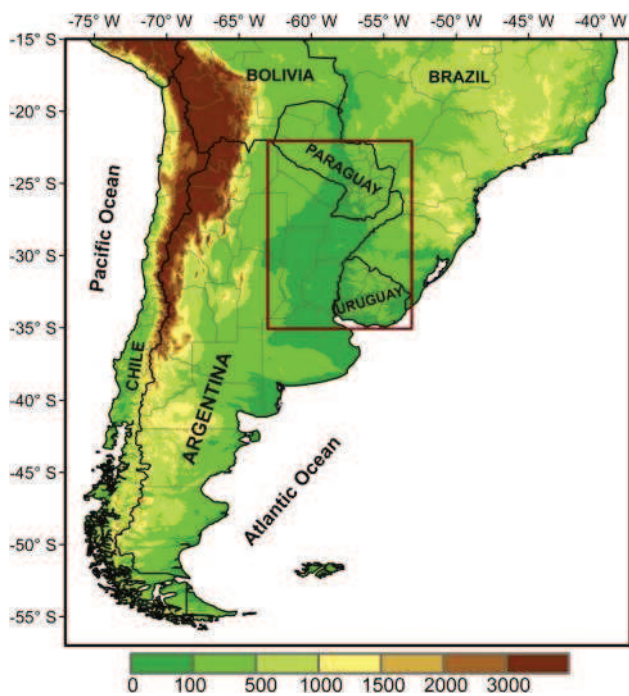


Fig. 1 Topographic map of southern South America. The study region in southeastern South America is highlighted with a dark red rectangle

(Garreaud et al. 2009; Hagen et al. 2022; Olmo et al. 2020; Zhang et al. 2016). These climate factors, combined with the high concentration of economic activities, make the region particularly vulnerable to hydroclimate variability and extremes.

2.2 Data

Regional hydrometeorological extreme events are studied using precipitation, soil moisture, and temperature data from the European Centre for Medium-Range Weather Forecasts (ECMWF) reanalysis version 5 (ERA5, Hersbach et al. 2020, 2023a, b). ERA5 data are used at a $0.25^\circ \times 0.25^\circ$ latitude–longitude grid spacing within the 1961–2020 period. ERA5 precipitation and temperature data have demonstrated good performance when compared with observed data in SESA, particularly in representing extreme events (Balmaceda-Huarte et al. 2021; Olmo et al. 2022). Furthermore, ERA5 soil moisture data have demonstrated superior accuracy compared to other reanalysis products when validated against in-situ observations at various locations worldwide (e.g., Li et al. 2020; Yang et al. 2022).

In this study, monthly ERA5 precipitation data are used to study long-term hydrometeorological events. Daily maximum temperature and daily precipitation, computed from hourly ERA5 data, are used to study short-term hydroclimatic events. Following Lovino et al. (2024),

non-overlapped pentads (five-day means) of root-zone soil moisture in the top meter of the soil are calculated to assess the spatiotemporal evolution of flash droughts.

2.3 Detection of Long-Term Extreme Hydrometeorological Events

Long-term extreme hydrometeorological events are analyzed using the nonparametric Standardized Precipitation Index (SPI; Farahmand and AghaKouchak 2015; Hao and Agha-Kouchak 2014). The SPI serves as a standardized metric for assessing precipitation anomalies, specifically designed to quantify both deficits and excesses of rainfall across diverse temporal scales. In this study, the SPI is estimated from monthly precipitation data. Further details of the nonparametric standardized SPI and its computation can be found in Sgroi et al. (2021) and Bernal-Mujica et al. (2023).

We identify wet and dry extreme precipitation events, referred to as WEP and DEP, respectively. A WEP is identified when $\text{SPI} > 1$ for a sequence of months, with at least one month with $\text{SPI} > 1.5$. Conversely, a DEP is identified when $\text{SPI} < -1$, with at least one month with $\text{SPI} < -1.5$. Note that the ± 1.5 threshold indicates the occurrence of an extreme event by reaching this intensity in at least one month, while the ± 1 threshold is used to determine the event's duration. Therefore, following the classification proposed by Lloyd-Hughes and Saunders (2002), we distinguish periods—without imposing a minimum or maximum duration—characterized by moderately wet or dry conditions ($\text{SPI} > 1$ or $\text{SPI} < -1$), provided that at least one month experiences severely wet or dry conditions ($\text{SPI} > 1.5$ or $\text{SPI} < -1.5$).

We compute WEP and DEP based on SPI at 3-month and 18-month time scales. Thus, extreme events at a 3-month time scale are called WEP3 and DEP3, while those at an 18-month time scale are called WEP18 and DEP18. WEP3 and DEP3 (shorter time scale) indicate short to intermediate periods of wet or dry conditions that affect soil moisture, providing climate insights for critical crop growth stages, and making them valuable for agricultural applications (Sgroi et al. 2021). WEP18 and DEP18 (longer time scale) identify extended rainfall anomalies reflected in streamflow, reservoir storage, and water table levels, allowing for the examination of long-term hydrological droughts and wet events (Lovino et al. 2014; Sirdas and Sen 2003).

2.4 Detection of Short-Term Extreme Hydrometeorological Events

Short-term EHEs are characterized by heatwaves (HW), heavy precipitation events (HP), and flash droughts (FD). Short-term EHEs can immediately impact agriculture and urban areas, negatively affecting food production, public

health, and infrastructure (Hagen et al. 2022). An HW is identified as a period of at least 3 consecutive days with a daily maximum temperature exceeding the 90th percentile of the reference period (De Luca and Donat 2023; Perkins and Alexander 2013). An HP is identified as a sequence of consecutive days when daily precipitation exceeds the 95th percentile of precipitation on wet days (≥ 1 mm) during the reference period (Weber et al. 2020). Note that the 90th percentile of daily maximum temperature and the 95th percentile of daily precipitation on wet days are calculated for the reference period spanning 1991–2020.

Agricultural FDs are identified following the methodology outlined by Lovino et al. (2024), which integrates root-zone soil moisture and soil hydraulic properties to capture the rapid depletion of soil moisture along with vegetation stress. This approach relies on the Soil Water Deficit Index (SWDI, Martínez-Fernández et al. 2015) to assess soil water availability. A FD is detected as the rapid decline in soil moisture quantified by a SWDI decay from above – 3 to below – 5 in 20 days (or 4 pentads). The upper SWDI threshold marks the initiation of the soil moisture deficit, while the lower SWDI threshold signifies water stress conditions for crops. The method also incorporates an intensification period of sufficient duration to filter out short-term synoptic events that might rapidly deplete soil moisture but then recover abruptly. It also requires reasonably unstressed soil moisture conditions prior to the FD onset. More details regarding the FD identification method can be found in Lovino et al. (2024).

2.5 Hazard Quantification

First, we estimate the decadal frequency, average duration, and mean maximum intensity of each EHE during two distinct periods: 1961–1990 (past) and 1991–2020 (present). The decadal frequency is computed as the total number of events divided by the number of decades in each period. Duration refers to the length of each event, expressed in days or months. Average duration is calculated by dividing the sum of all event durations by the total number of events in the study period. Mean maximum intensity is computed by averaging the highest intensities of all the events within the specified period, where the maximum intensity is the peak value reached by the variable during the event.

Second, following Tabari et al. (2021), we calculate the individual hazard component (h) for each EHE by multiplying the decadal frequency (DF), average duration (AD), and mean maximum intensity (MMI) of identified events (Eq. 1):

$$h = DF * AD * MMI \quad (1)$$

Equal weight is assigned to the three hazard components, considering their equal importance in generating hazardous impacts, as suggested by Tabari et al. (2021) for drought hazard assessment. Negative intensities (MMI values) for dry conditions, characterized by SPI or SWDI, are converted into positive values, to prevent negative hazard values. Note that the magnitude of the MMI is maintained during this conversion, ensuring that the final value of the individual hazard component remains unaffected. Then, following Binita et al. (2021), the resulting hazard components are rescaled to a range of 0–1 (Eq. 2):

$$H(0,1) = (h - \min(h)) / (\max(h) - \min(h)) \quad (2)$$

where $H(0,1)$ is the normalized individual hazard for each EHE, $\min(h)$ and $\max(h)$ are the minimum and maximum values of the individual hazard component, respectively. Rescaling is performed using global minimum and maximum values for the entire study period -including both 1961–1990 and 1991–2020 periods-, thus allowing the comparison of normalized individual hazards between periods.

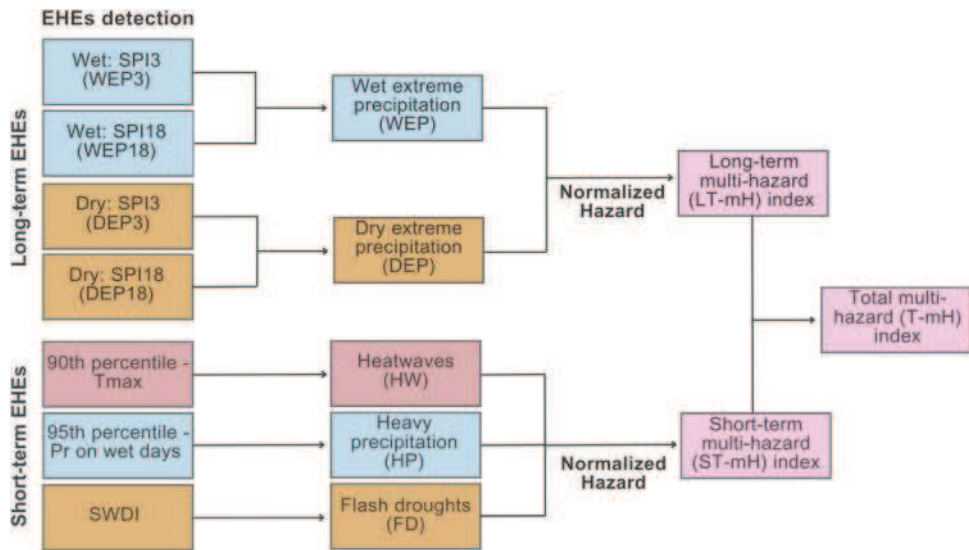
Finally, also following Binita et al. (2021), the rescaled individual hazard components are summed and divided by the total number of components to obtain the multi-hazard index (Eq. 3):

$$mH(0,1) = \sum H_i(0,1) / n \quad (3)$$

where $mH(0,1)$ is the multi-hazard index ranging between 0 and 1, $H_i(0,1)$ is the normalized individual hazard with $i = 1, \dots, n$, being n the number of hazard components. We calculate long-term (LT-mH), short-term (ST-mH), and total (T-mH) multi-hazard indices. EHE individual hazard components and multi-hazard indices are compared between the 1961–1990 and 1991–2020 periods to determine observed changes.

Figure 2 presents a schematic overview of the process used to estimate multi-hazard indices. First, long-term normalized hazard components include wet (WEP) and dry (DEP) extreme precipitation events, derived from a combination of their 3- and 18-month time scale variables (WEP3, WEP18, DEP3, and DEP18, as detailed in Sect. 2.3). Then, the long-term multi-hazard (LT-mH) index integrates both WEP and DEP normalized hazard components. Similarly, the short-term multi-hazard (ST-mH) index combines heatwaves (HW), extreme precipitation events (HP) and flash droughts (FD) normalized hazard components. Finally, long-term and short-term multi-hazard indices are combined to estimate the total multi-hazard (T-mH) index.

Fig. 2 Schematic diagram summarizing the methodology employed for assessing multi-hazard indices. SPI denotes the standardized precipitation index, while SWDI represents the soil water deficit index (see further details in the text). T_{max} maximum temperature, P_r precipitation



3 Results

3.1 Long-Term Extreme Hydrometeorological Hazards

3.1.1 Wet Extreme Precipitation Events

Figure 3 shows the decadal frequency, average duration, mean maximum intensity, and normalized hazard of wet extreme precipitation events (WEP3, WEP18) for the periods 1991–2020 and 1961–1990, along with the hazard changes between the present and past periods. The decadal frequency of current WEP3 presents a southwest-to-northeast gradient, decreasing from 5–6 events per decade in the south to 1–2 events per decade in the north (Fig. 3a). The average duration ranges between 2.5 and 4.4 months (Fig. 3b). The highest frequencies towards the center and the south correspond to lower durations (1.5–2.5 months) while the lowest frequencies towards the north and east correspond to higher durations (4.4–5.7 months). The mean maximum intensity shows a heterogeneous spatial pattern, with an area-averaged SPI3 reaching 1.9 (Fig. 3c). The normalized WEP3 hazard presents the maximum values towards the center, south, and northeast, covering most of the core crop region of Argentina and Uruguay (Fig. 3d). The maximum WEP3 hazard is located towards the southeastern corner of the study region, largely influenced by the higher frequency of WEP3 events in that area. These results suggest that the southern domain is exposed to frequent and intense extreme precipitation events at 3-month time scales, which pose a substantial risk of waterlogging and floods. Such occurrences could adversely affect agriculture, particularly in the highly productive lands of the Argentinian and Uruguayan Pampas.

The current WEP3 hazard has changed compared with the results from the 1961–1990 period (Fig. 3e–h). Figure 3i shows that the WEP3 hazard has notably increased in the southern and northeastern parts of the region, while it has decreased in a strip extending over the center and east. These changes are primarily driven by shifts in the frequency and duration of WEP3. Figure 3a, b and e, f show that the decadal frequency of WEP3 has increased towards the south and decreased in the center of the study region, while the duration of WEP3 has increased in the center-east and decreased mainly in the northeast. Although the spatial pattern of hazard change is not homogeneous, the area-averaged WEP3 hazard has increased by 9% in the study region.

The WEP18 events are less frequent but last longer than WEP3 events in the present period (Fig. 3j and k). The decadal frequency of WEP18 ranges from 0 events per decade in the north to more than 2 events per decade in the south (Fig. 3j). The mean duration spans from 0 to 23 months, with the highest durations occurring towards the northeast, reaching 23–34 months (Fig. 3k). The mean maximum intensity reaches 2.4 (Fig. 3l). The areas with the lowest WEP18 frequencies in the northeast exhibit the highest durations and intensities. Similar to WEP3, the highest WEP18 hazards occur in the center and south of the study region (Fig. 3m), although WEP18 hazards are slightly lower than WEP3 hazards. Our results suggest that the southern portion of the study region is more exposed to water excess affecting hydrological variables than the northern areas. Thus, hydrological floods are expected to be more frequent in the productive lands of the southern domain, but severe events (with long duration and high intensity, although less frequent) can also occur primarily in southeastern Paraguay.

The WEP18 hazard has changed when comparing the 1991–2020 and 1961–1990 periods (Fig. 3m and q). The WEP18 hazard has notably increased towards the south

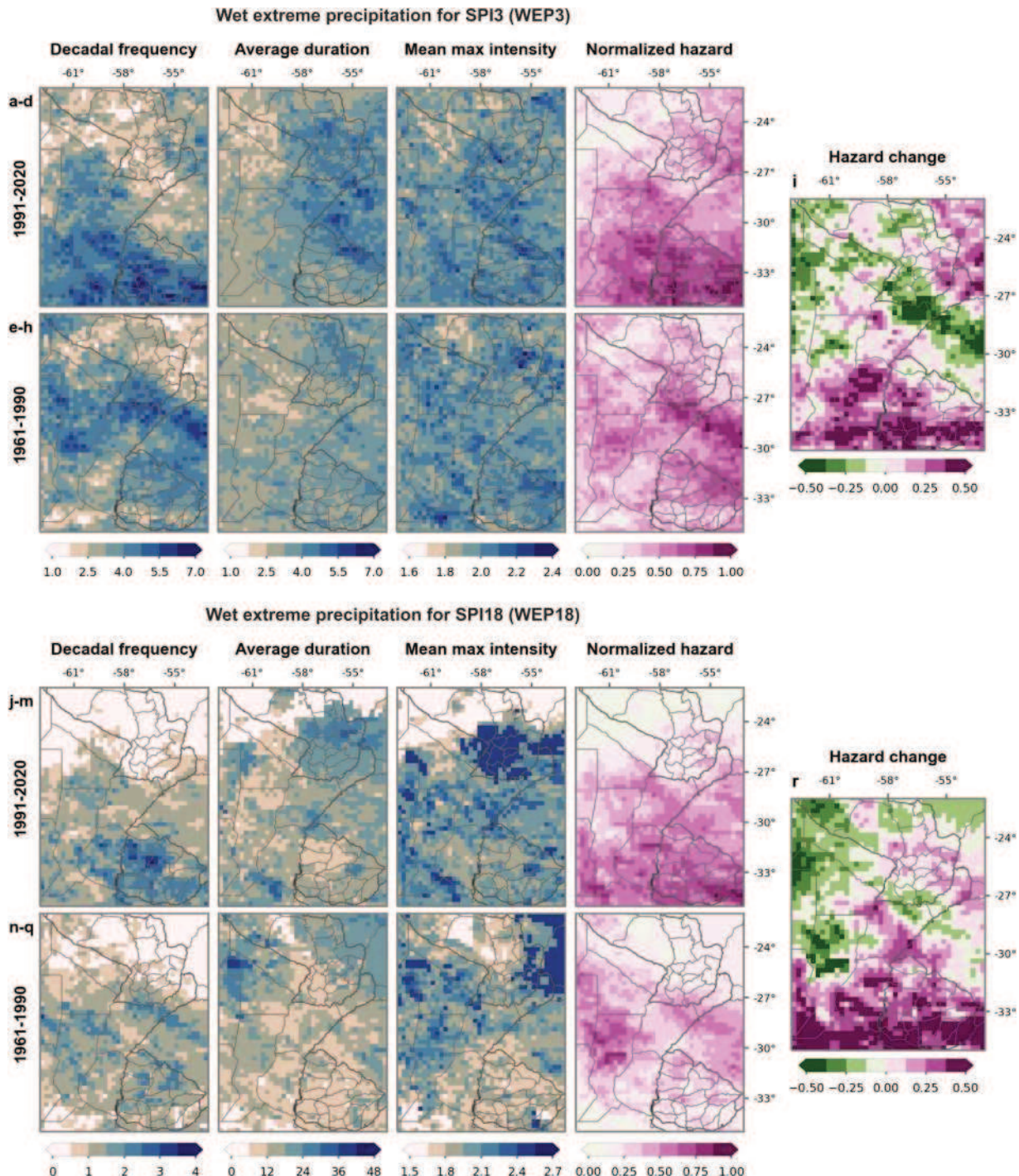


Fig. 3 Hazard analysis of wet extreme precipitation events computed using SPI3 (WEP3, panels **a–i**) and SPI18 (WEP18, panels **j–r**). The analysis covers two time periods: 1991–2020 (panels **a–d** and **j–m**) and 1961–1990 (panels **e–h** and **n–q**). Each row of panels presents the decadal frequency (number of events per decade, first column),

average duration (months, second column), mean maximum intensity (SPI value, third column), and normalized hazard (dimensionless, fourth column). Panels (**i**) and (**r**) illustrate the changes in hazard between the two periods

and decreased towards the central and northwest regions (Fig. 3r). The normalized hazard spatial patterns for both WEP3 and WEP18 have shifted from north to south at both

time scales, indicating increasing long-term wet extreme precipitation hazards in the south and decreasing hazards in the north. The area-averaged WEP18 hazard has risen

by 21%, more than double the increase observed for WEP3. This increase is primarily due to a rise in the duration of the WEP18 events, while the frequency and intensity have remained stable on average.

3.1.2 Dry Extreme Precipitation Events

Figure 4 presents the decadal frequency, average duration, mean maximum intensity, and normalized hazard of dry extreme precipitation events (DEP3, DEP18) for the periods 1991–2020 and 1961–1990, along with the hazard changes between the present and past periods. In the present period, the higher frequency and duration of DEP3 occur in the northern and western areas of the study region (Fig. 4a, b). The decadal frequency of DEP3 ranges between 2 and 4.3 events per decade (Fig. 4a), while the average duration spans from 2.3 and 3.7 months (Fig. 4b). The mean maximum intensity has an average value of 1.9, with a relatively uniform distribution across the region (Fig. 4c). Particularly noteworthy are the northern and western regions, where frequencies exceed 4.3 events per decade and durations extend beyond 4 months. In contrast, Uruguay and southern Brazil experience DEP3 events of lower frequency and shorter duration. Thus, the spatial pattern of DEP3 hazard exhibits a gradient decreasing from northwest to southeast (Fig. 4d), with higher hazards in the northern and western areas due to higher frequencies and longer durations. Our results suggest that the western and northern portions of the study region are more exposed to DEP3, potentially leading to seasonal droughts that can impact agriculture in the western portion of the core crop region, northern Argentina, and Paraguay.

The DEP3 hazard has changed when comparing the 1991–2020 and 1961–1990 periods (Fig. 4i). In the 1961–1990 period, the spatial pattern of DEP3 hazard exhibits higher values in the east, gradually decreasing toward the west (Fig. 4h). However, in the 1991–2020 period, the DEP3 hazard considerably increases in the west and decreases in the east of the study region (Fig. 4i). These results indicate a notable increase in seasonal drought hazard towards the western and northern areas, while a decrease is observed in southern Brazil and Uruguay over the past decades.

The current frequency of DEP18 is lower than that of DEP3, while their duration is higher (Fig. 4j and k), which is consistent with their longer time scales. The decadal frequency distribution of DEP18 is relatively uniform, ranging from 0.3 to 1 event per decade, with higher values observed in the northern and western regions (1–1.5 event per decade). The average durations span from 7 to 27 months across the region, with the longest durations (exceeding 27 months) concentrated in the central-northern area, including northern Argentina, eastern Paraguay, and southern Brazil. In contrast, the shortest DEP18 durations (less than 7 months) occur in southern areas, mainly towards eastern Uruguay.

Notably, the maximum duration of dry extreme events (27 to 48 months, located in eastern Paraguay) surpasses that of wet extreme events (up to 34 months). The mean maximum intensity maintains an average value of 2, with the most intense events (exceeding SPI18 = −2.4) occurring in central-eastern Argentina and northern Uruguay (Fig. 4l). The DEP18 hazard is higher in the western and northern areas (Fig. 4m), exhibiting a gradient similar to that of DEP3 hazard. Thus, the hydrological drought hazard is high in these regions, although intense and less frequent DEP18 events also occur in the productive lands of the core crop region in Argentina and Uruguay.

The change in the DEP18 hazard (Fig. 4r) presents a spatial pattern similar to that of the DEP3 hazard (Fig. 4i), with a negative change observed in the east and a positive change in the west. The area-averaged change in DEP18 hazard has increased by 22.5%. This notable increase, particularly evident in western areas, primarily results from a rise in duration and intensity, while frequency has remained stable on average. Consequently, similar to the seasonal drought hazard, the hydrological drought hazard has considerably increased towards the western portion of the study region.

3.2 Short-Term Extreme Hydrometeorological Hazards

3.2.1 Heatwaves

Figure 5 illustrates the decadal frequency, average duration, mean maximum intensity, and normalized hazard of heatwaves (HW) for the periods 1991–2020 and 1961–1990, along with the hazard changes between these periods. The current decadal frequency of HW events ranges between 35 and 42 occurrences per decade, occasionally reaching 51 occurrences (Fig. 5a). Average durations span from 3.8 to 4.3 days, with maximum values of 4.8 days observed in the north and northeast, while minimum durations of 3.4 days occur in Uruguay, towards the southwest (Fig. 5b). The mean maximum intensity exhibits a marked northwest-to-southeast gradient (Fig. 5c), with values decreasing from 39 to 29 °C, aligning with the climatological gradient of maximum temperature. The heatwave hazard is high across the entire region (Fig. 5d), showing a decreasing spatial gradient from north to south. Higher intensities and durations contribute to the heightened HW hazard in the north.

Compared with the past period (1961–1990), the HW hazard has expanded from the northwest to encompass all the northern and central areas (see Fig. 5d and h). Figure 5i shows a notable increase in HW hazard in the northwest (particularly in Paraguay). Additionally, HW hazard has increased over northeastern Argentina and southern Brazil, attributed to a marked rise in the HW frequency, which has increased from 15–25 events per decade to 40–45 events (see

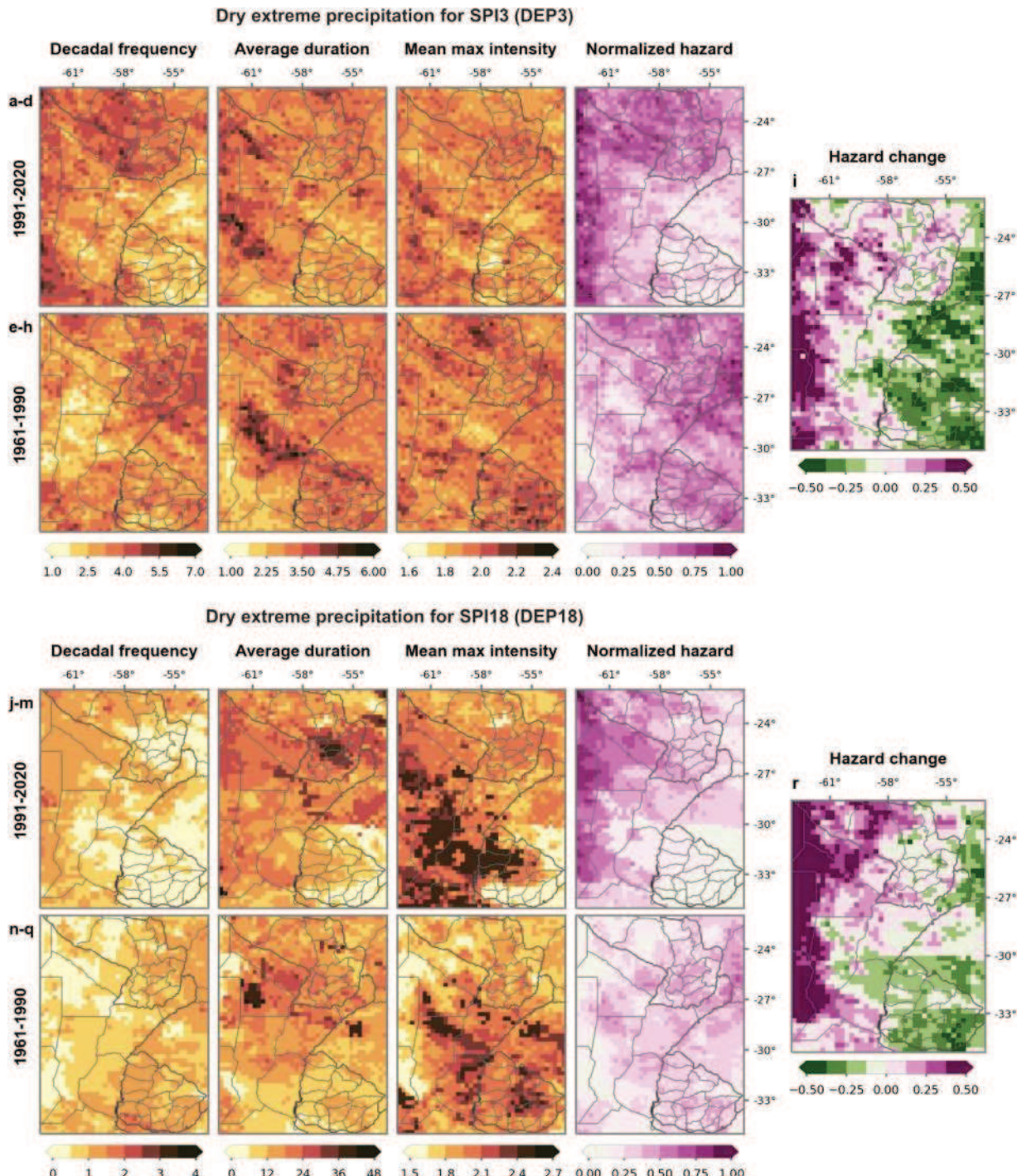


Fig. 4 Hazard analysis of dry extreme precipitation events computed using SPI3 (DEP3, panels **a–i**) and SPI18 (DEP18, panels **j–r**). The analysis covers two time periods: 1991–2020 (panels **a–d** and **j–m**) and 1961–1990 (panels **e–h** and **n–q**). Each row of panels presents the decadal frequency (number of events per decade, first column),

average duration (months, second column), mean maximum intensity (SPI value converted to its positive equivalent, third column), and normalized hazard (dimensionless, fourth column). Panels (**i**) and (**r**) illustrate the changes in hazard between the two periods

Fig. 4a and Fig. 4e). In contrast, HW hazard has decreased in western areas, mainly related to a decrease in HW frequency, which has shifted from 45–50 events per decade

to 35–40 events. Overall, the area-averaged change of the HW hazard in the region is positive, increasing by 31.5%. The area-averaged frequency component shows the major

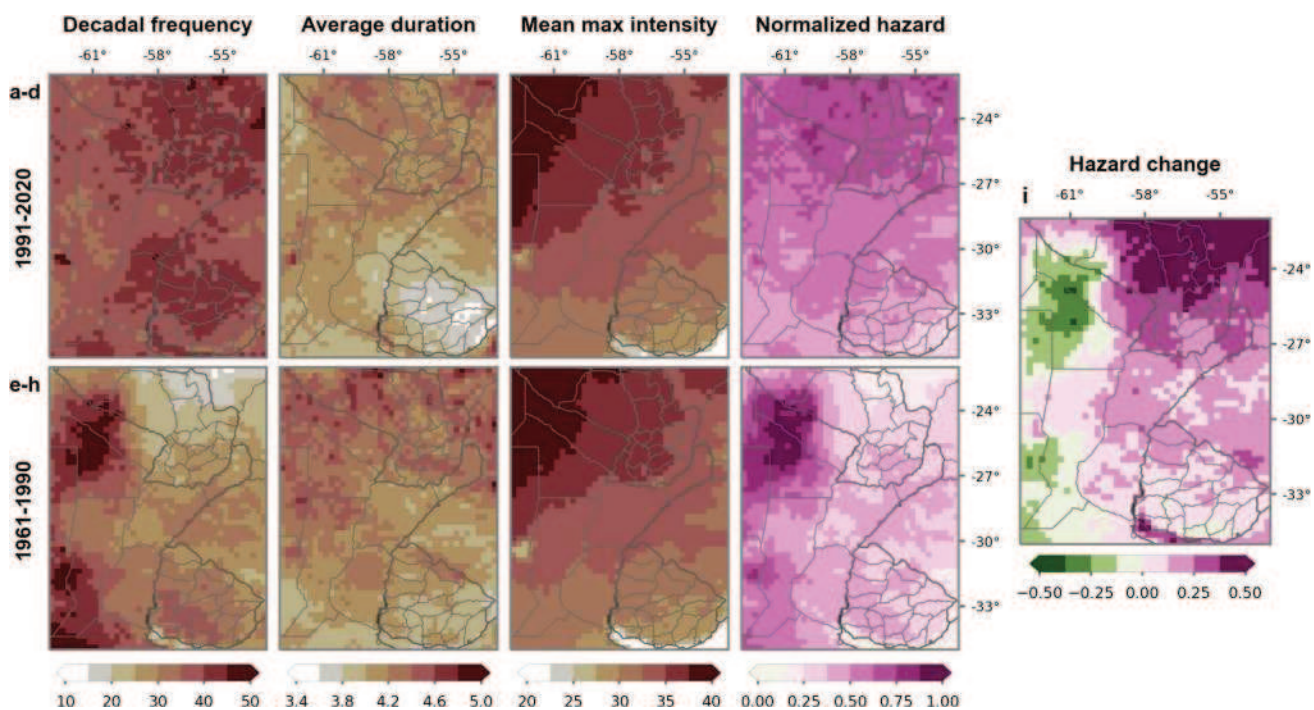


Fig. 5 Hazard analysis of heatwave events (HW). The analysis covers two time periods: 1991–2020 (panels **a–d**) and 1961–1990 (panels **e–h**). Each row of panels presents the decadal frequency (number of events per decade, first column), average duration (days, second col-

umn), mean maximum intensity (temperature in °C, third column), and normalized hazard (dimensionless, fourth column). Panel (**i**) illustrates the change in HW hazard between the two periods

rise—from 31.3 events per decade to 38.8 events per decade on average -, followed by the intensity in a lesser proportion, while the duration remains stable on average.

3.2.2 Heavy Precipitation Events

Figure 6 presents the decadal frequency, average duration, mean maximum intensity, and normalized hazard of heavy precipitation events (HP) for the periods 1991–2020 and 1961–1990, along with the hazard changes between these periods. HP events are frequent in the study region in the present, with decadal frequencies ranging from 43 to 67 events per decade, reaching maximum frequencies close to 80 events per decade (Fig. 6a). The frequency distribution exhibits a northeast-to-southwest gradient, with the highest frequencies in the northeast (around 67–77 events per decade) and the lowest in the southwest (around 39–43 events per decade), reflecting the region's precipitation climatology. However, the intensity and duration of HP events do not follow the same gradient. The maximum HP intensity is concentrated in the center of the study region (Fig. 6c), encompassing northeastern Argentina (with mean maximum intensities exceeding 61 mm/day), northern Uruguay, southern Brazil, and eastern Paraguay. While the average duration does not exhibit a defined pattern, the longest durations are observed in the northeast (Fig. 6b). On average, HP events

last 1 day, but can extend up to 5 days. The highest HP hazard is observed in southern Brazil, southeastern Paraguay, and northeastern Argentina (Fig. 6d), with a decreasing gradient from the northeast to the southwest. Thus, the HP hazard is highest in the wettest regions and lowest in the driest regions of the study domain.

Comparing the current period with the past, the HP hazard presents small and heterogeneous changes across the study region (Fig. 6i). The HP hazard has increased towards the southern and northeastern areas but decreased in a strip that extends over the center and east of the region, mirroring the change pattern for WEP3 and WEP18 (see Fig. 3i and r). Although the components of HP hazard show no notable changes compared to the 1961–1990 period (Figs. 6e–g), there is a slight increase in frequency and intensity, coupled with a decrease in duration. Despite these minor shifts, the area-averaged HP hazard has increased by 6% across the study region.

3.2.3 Flash Droughts

Figure 7 shows the decadal frequency, average duration, mean maximum intensity, and normalized hazard of flash droughts (FD) for the periods 1991–2020 and 1961–1990, along with the hazard changes between these periods. The current FD frequencies range from 0.3 to 6.3 events per

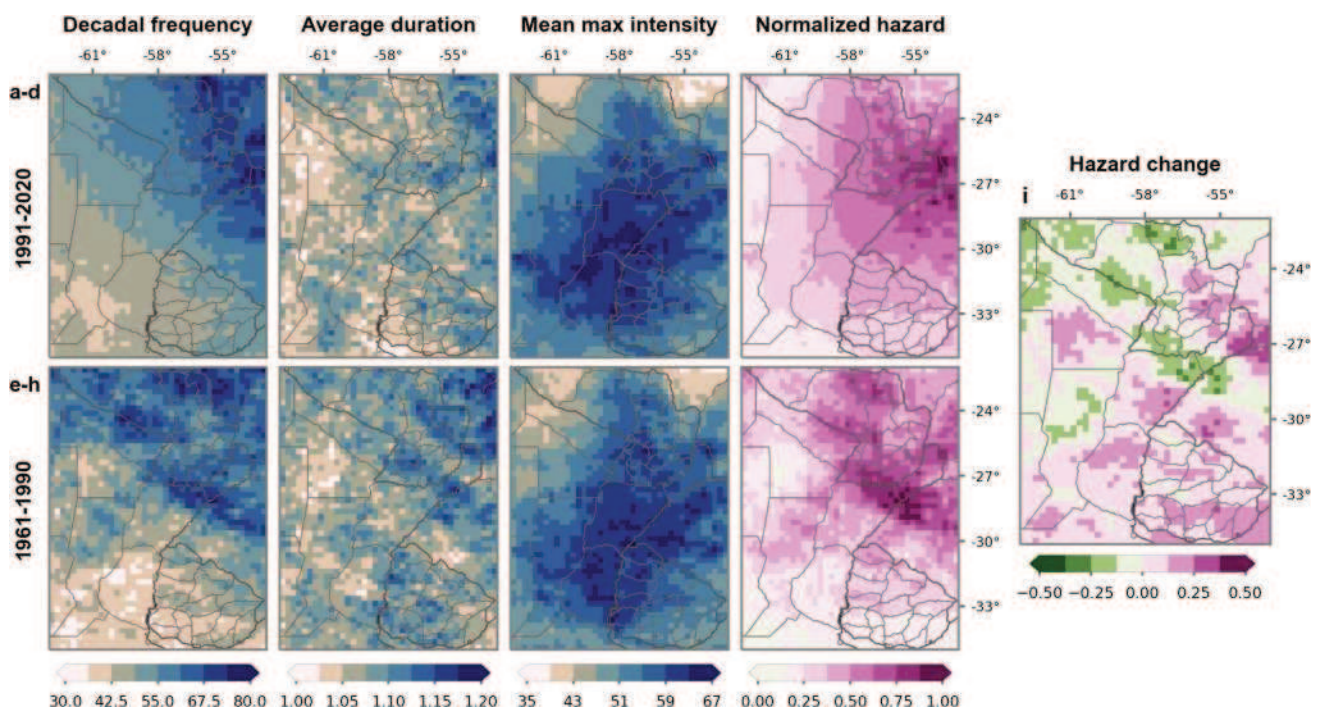


Fig. 6 Hazard analysis of heavy precipitation events (HP). The analysis covers two time periods: 1991–2020 (panels **a–d**) and 1961–1990 (panels **e–h**). Each row of panels presents the decadal frequency (number of events per decade, first column), average duration (days,

second column), mean maximum intensity (precipitation in mm/day, third column), and normalized hazard (dimensionless, fourth column). Panel (i) illustrates the change in HP hazard between the two periods

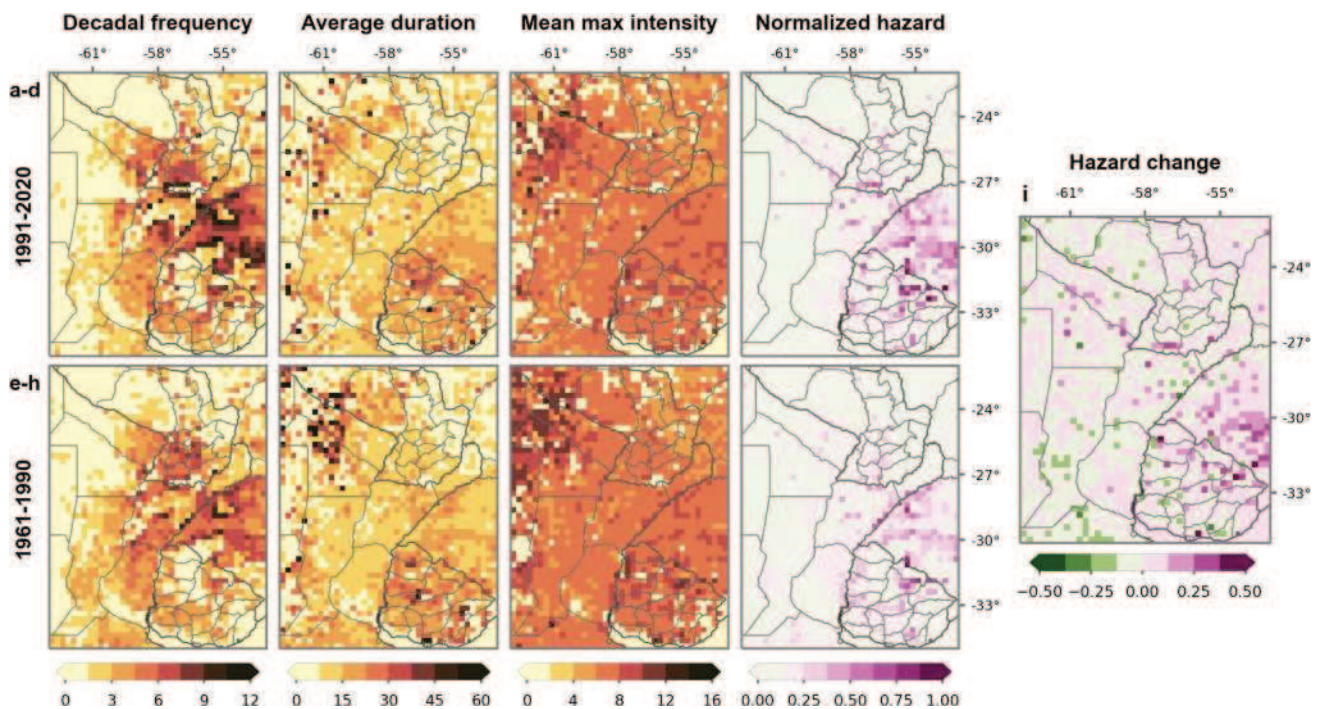


Fig. 7 Hazard analysis of flash drought events (FD). The analysis covers two time periods: 1991–2020 (panels **a–d**) and 1961–1990 (panels **e–h**). Each row of panels presents the decadal frequency (number of events per decade, first column), average duration (pen-

tads, second column), mean maximum intensity (SWDI value converted to its positive equivalent, third column), and normalized hazard (dimensionless, fourth column). Panel (i) illustrates the change in FD hazard between the two periods

decade (Fig. 7a), with the highest decadal frequencies (6.3 to 11 events per decade) located in southern Brazil, northeastern Argentina, and Uruguay. Following the FD intensification period, the duration of drought conditions, referred to here as FD duration, spans from 5 to 22 pentads on average (Fig. 7b). The highest FD durations (exceeding 22 pentads) are observed in Uruguay, southern Brazil, and the western corner of the region. The mean maximum intensity presents typical SWDI values from -5.6 to -8.1 (Fig. 7c). The highest FD hazard is observed in Uruguay, southern Brazil, and central-east Argentina (Fig. 7d). In Uruguay and southern Brazil, FDs combine high frequencies with long duration and high intensity, resulting in the highest hazard values. Despite the high durations and intensities observed in the western corner of the region, possibly due to the low FD frequencies, the FD hazard remains low.

The spatial pattern of FD hazard change shows minimal variations (Fig. 7i). On average, FD hazard has experienced a slight positive change, with the area-averaged hazard increasing by 1.9%. However, a notable increase in FD hazard is observed in northern Uruguay and southern Brazil.

This change is attributed to an increase in FD frequency in these areas (Fig. 7a and 7e).

3.3 Long-Term and Short-Term Extreme Hydrometeorological Multi-Hazards

3.3.1 Long-Term Multi-Hazard

Figure 8 shows the long-term extreme hydrometeorological multi-hazard (LT-mH) for the periods 1991–2020 (Fig. 8a) and 1961–1990 (Fig. 8b), along with the hazard changes between these periods (Fig. 8c). As discussed in Sect. 2.5, the LT-mH index integrates the hazard components of WEP3, WEP18, DEP3, and DEP18. The LT-mH spatial distribution presents a southwest-to-northeast gradient, with higher values in the southwestern domain (highlighted with a rectangle in Fig. 8a). This hotspot area exhibits a high hazard of both WEP and DEP events, with a higher WEP hazard towards the southern portion of the study region (see Fig. 3d and m) and a higher DEP hazard in the western areas (see Fig. 4d and m). These composite results underscore the importance of LT-mHs for the core crop region

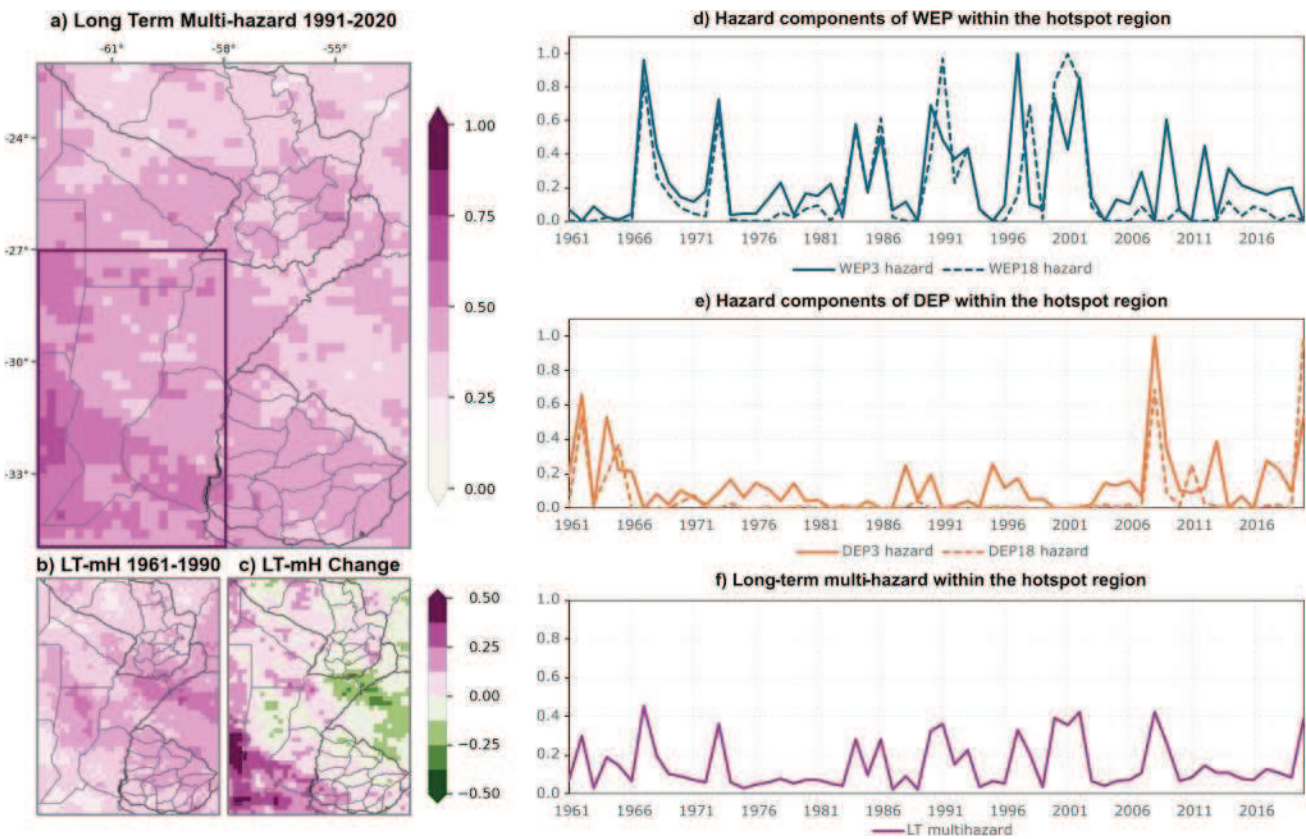


Fig. 8 Long-term extreme hydrometeorological multi-hazard (LT-mH) analysis. The left column shows the LT-mH (dimensionless) spatial distribution for the periods 1991–2020 (panel a) and 1961–1990 (panel b), and panel (c) illustrates the changes between these

periods. The current LT-mH hotspot is highlighted with a purple rectangle. The right column shows the time series of the WEP (panel d) and DEP (panel e) hazard components and the LT-mH (panel f), all computed as areal averages of the hotspot area

of central-eastern Argentina, where the co-occurrence of both wet and dry extremes can have substantial impacts on agriculture.

The extreme hydrometeorological LT-mH has considerably increased toward the southwest, driven by the simultaneous rise in both WEP and DEP hazard components in this area (Fig. 3i, r, i, and r). On the other hand, the LT-mH has decreased in a strip that extends over the center and east of the region, primarily due to a reduction in the WEP hazard component. In addition, DEP hazard has also decreased in the eastern part of the study region. The area-averaged LT-mH has increased by 10.4% across the study region.

Figure 8d and e show the time series of the area-averaged WEP and DEP hazard components within the hotspot region. Between 1966 and 2004, WEP hazards dominated, with several peaks in WEP3 and WEP18 hazards exceeding 0.6, and some reaching 1.0 in the years 1967, 1991, 1997, and 2001 (Fig. 8d). In contrast, before 1966, DEP hazards were more prevalent, with both DEP3 and DEP18 values closer to 0.6 (Fig. 8e). Our results indicate that since 2005, WEP3 and DEP3 hazards have remained high, suggesting that both wet and dry seasonal extreme precipitation event hazards have

been occurring concurrently over the last two decades. Notably, the DEP18 hazard also shows high values (0.7 in 2008 and 1.0 in 2020), suggesting that both agricultural drought and hydrological drought hazards have intensified in the last two decades. Figure 8f indicates that LT-mH exhibits peak values coinciding with peak wet and dry events. The temporal variability of the LT-mH is influenced by the co-occurrence of both wet and dry events at 3-month and 18-month time scales. Therefore, despite the high DEP3 and WEP3 hazards since 2005, the LT-mH index shows lower values due to the lower DEP18 and WEP18 hazards.

3.3.2 Short-Term Multi-Hazard

Figure 9 shows the short-term extreme hydrometeorological multi-hazard (ST-mH) for the present (1991–2020, Fig. 9a) and past (1961–1990, Fig. 9b) periods, along with the changes in hazard between those periods (Fig. 9c). As noted in Sect. 2.5, the ST-mH index combines HW, HP, and FD hazard components. The short-term multi-hazard displays an inverse pattern compared to the long-term multi-hazard, with northeast to southwest gradient showing higher values

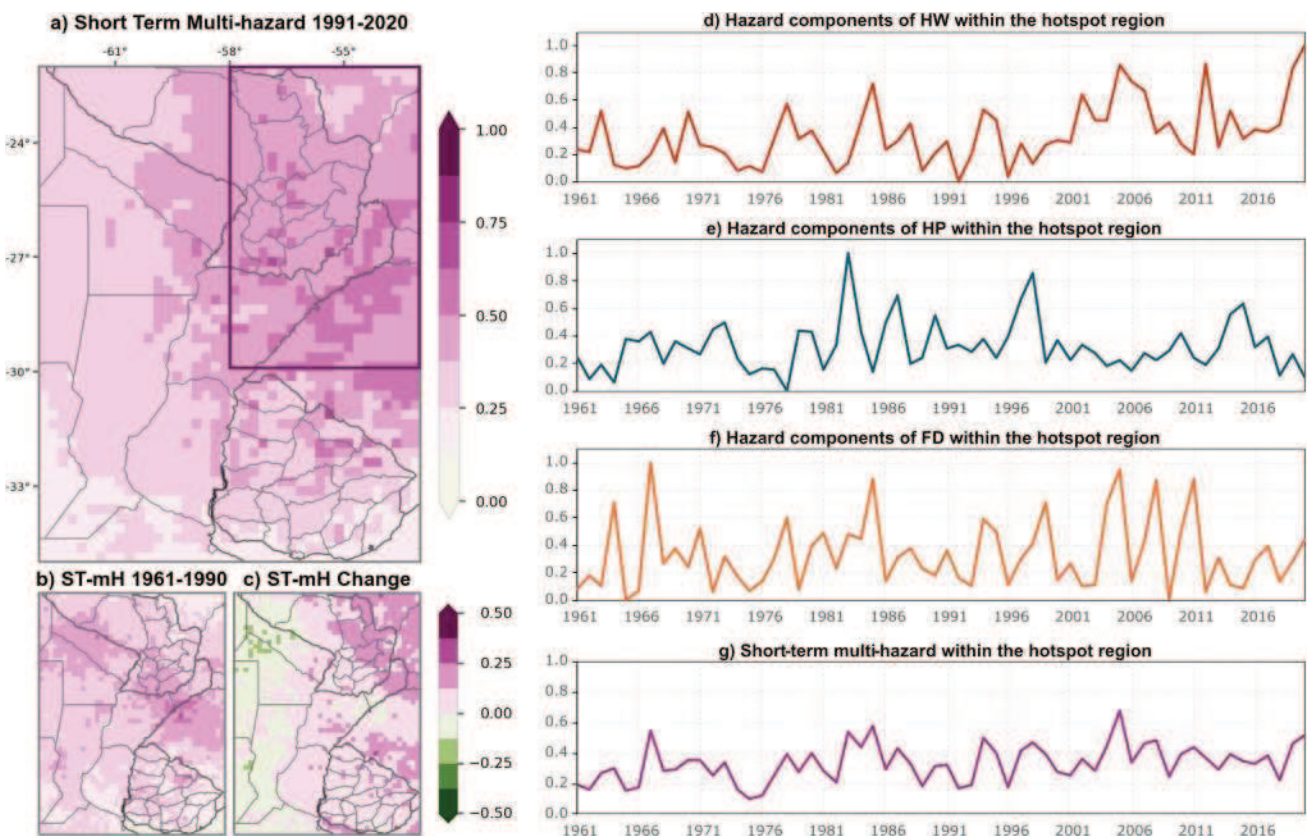


Fig. 9 Short-term extreme hydrometeorological multi-hazard (ST-mH) analysis. The left column shows the ST-mH (dimensionless) spatial distribution for the periods 1991–2020 (panel a) and 1961–1990 (panel b), and panel (c) illustrates the changes between these

periods. The current ST-mH hotspot is highlighted with a purple rectangle. The right column shows the time series of the HW (panel d), HP (panel e), and FD (panel f) hazard components and the ST-mH (panel g), all computed as areal averages of the hotspot area

in northeastern and central eastern portions of the study region (highlighted with a rectangle in Fig. 9a). This hotspot area is characterized by a high hazard of HW, HP, and FD events, with the highest HW hazard towards the north (see Fig. 5d), the highest HP hazard towards the east (see Fig. 6d), and the highest FD hazard in the central-eastern areas (see Fig. 7d).

The extreme hydrometeorological ST-mH has increased towards the northeast (Fig. 9c), primarily due to the simultaneous rise in HW and HP hazard components in this area (see Figs. 5i and 6i). The FD hazard component mainly contributes to the increase in ST-mH in southern Brazil. Conversely, ST-mH has slightly decreased in western areas, attributed to a combined decrease in the HW, HP, and FD hazard components. Overall, ST-mH has increased by an average of 17.3% over the study region. This area-averaged increase in ST-mH hazard is higher than the 10.7% increase in LT-mH, although the spatial pattern of change is more contrasting for LT-mH.

Figure 9d to f present the time series of the area-averaged HW, HP, and FD hazard components within the hotspot region (highlighted with a purple rectangle in Fig. 9a). The HW hazard has notably increased from the 1990s to the present, exhibiting the highest values after 2004, exceeding 0.8 and reaching 1.0 (Fig. 9d). Similar to the WEP hazards, the HP hazard shows higher magnitudes between 1966 and 2004, with peaks ranging from 0.6 to 1.0 (Fig. 9e). Conversely, before 1966, the FD hazard exhibits high magnitudes (Fig. 9f), similar to the DEP hazards. Notably, the highest FD hazard occurs after 2004, coinciding with high HW hazard. Substantial FD hazard persisted from 1966 to 2004. This result aligns with the inherent characteristics of the FD phenomenon, which involves a rapid depletion of soil moisture that can occur alongside high-temperature anomalies and increased evapotranspiration when soil moisture levels are initially high (see Lovino et al. 2024; Pendergrass et al. 2020). Lastly, the ST-mH reached its highest magnitude between 1966 and 2006, with hazard peaks up to 0.6 (Fig. 9g). This period coincides with the greatest overlap in the occurrence of the three hazard components (HW, HP, and FD).

3.3.3 Total Multi-Hazard Composition

Figure 10 presents the total extreme hydrometeorological multi-hazard (T-mH) composition, combining the long-term and short-term multi-hazard indices. The current T-mH in the region (Fig. 10a) exhibits a more uniform spatial distribution compared to the historical period (Fig. 10b). Currently, the extreme hydrometeorological hazard is high across almost the entire region. The higher T-mH values predominate in southeastern Paraguay, southern Brazil, central and northern Uruguay, as well as

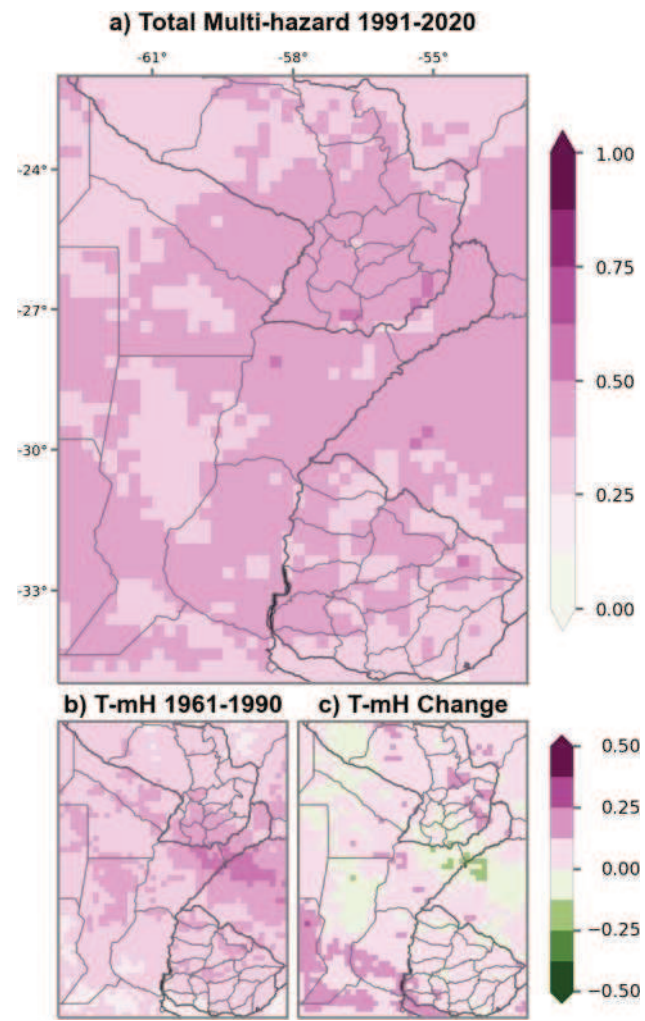


Fig. 10 Total extreme hydrometeorological multi-hazard (T-mH) analysis. The analysis covers two time periods: 1991–2020 (panel a) and 1961–1990 (panel b). Panel (c) illustrates the change in T-mH between the two periods

central and northeastern Argentina. This region is one of the most productive agricultural regions in the continent and the world, so the high extreme hydrometeorological hazards can impact crop yields and affect the region's food security.

The extreme hydrometeorological T-mH has increased over most of the study region in the last decades (Fig. 10c). During the 1961–1990 period, the higher hazard values were concentrated in a band spanning the central and eastern parts of the region, particularly in southern Brazil, northeastern Argentina, and southern Paraguay. Comparing the two periods (Fig. 10c), T-mH has reduced within this band. Despite this localized decrease, the regional mean of the T-mH index has increased by 13.6%, indicating a generalized increase in both long-term and short-term hazards.

4 Discussion and Concluding Remarks

This study provides a multi-hazard analysis of extreme hydrometeorological events and their temporal variations across southeastern South America, using ERA5 reanalysis data. We conduct a multi-layer single hazard analysis to identify critical hotspots for both short-term and long-term EHE hazards and examine their changes between the periods 1961–1990 and 1991–2020. By constructing multi-hazard indices based on the frequency, duration, and intensity of individual EHEs, we enhance our understanding of each hazard type and the region's exposure to multiple hazards. Furthermore, the time series analysis of individual EHE hazards and composite multi-hazard indices reveals the temporal dynamics and co-occurrence of these hazards over time. Despite the inherent uncertainties associated with the ERA5 dataset (Hersbach et al. 2020), our findings provide valuable insights for improving hydrometeorological risk management in the region. Future analyses would benefit from incorporating observational datasets to better address uncertainties, especially for hydrometeorological extremes.

Our findings reveal a significant hazard of long-term water excess at both seasonal (3-month) and hydrological (18-month) time scales in the southern portion of the region. This hazard has increased in the 1991–2020 period compared to the 1961–1990 period. Consequently, recurrent seasonal to hydrological floods pose a frequent threat to the most agriculturally productive regions, including central-eastern Argentina, Uruguay, and southern Brazil. These long-term water excesses lead to high river discharges, affecting agricultural lands and densely populated areas (Camilioni et al. 2020; Ridder et al. 2020). Moreover, precipitation during the wet season and intense precipitation events are projected to increase in this region during the twenty-first century (Almazroui et al. 2021a, b; Olmo et al. 2022; Ortega et al. 2021). The Uruguay river discharge is also expected to rise by 15% by 2050 (Müller et al. 2024). Thus, the water excess hazard could be exacerbated in the coming decades.

In contrast, the northern and western areas of the study region face the highest hazard of long-term precipitation deficits. Seasonal droughts can impact agriculture in the western portion of the core crop region, northern Argentina and Paraguay, while hydrological droughts can lead to urban water scarcity, reduced hydropower potential, and challenges in water supply management (Lovino et al. 2018b; Naumann et al. 2019). Drought occurrences in SESA often coincide with other short-term hazards like heatwaves and heightened wildfire risk (Ridder et al. 2020). This combination of hazards, along with local socioeconomic vulnerabilities such as inadequate

infrastructure and poverty, can exacerbate drought impacts, affecting not only agricultural productivity but also ecosystem integrity and urban environments (Castellanos et al. 2022; Coppola et al. 2021).

Short-term extreme hydrometeorological events present the highest hazard levels in the northeastern portion of the study region, including northeastern Argentina, southern Brazil, and southeastern Paraguay. This high hazard is mainly attributed to frequent heatwaves, flash droughts, and heavy precipitation events. Heatwave hazard has increased by 30% between 1961–1990 and 1991–2020, consistent with global trends (Perkins-Kirkpatrick and Lewis 2020). The increased heatwave hazard poses severe impacts on human health, urban environments, ecosystems, agriculture, and energy production (Coppola et al. 2021). Heavy precipitation hazard, highest in the northeastern portion of the study region—the wettest areas—, leads to extensive waterlogging and floods that can affect urban infrastructure and agricultural activities (Cerón et al. 2021). Flash drought hazard, mainly attributed to increased frequencies, threatens agriculture in southern Brazil, northeastern Argentina, and Uruguay. Flash droughts can diminish crop yields as they often occur during critical crop periods (Lovino et al. 2024). Moreover, these extreme events are projected to exacerbate in the twenty-first century. Heatwaves are expected to become more frequent, intense, and longer-lasting (Almazroui et al. 2021b; Feron et al. 2019). Intense precipitation and flash drought occurrence are also projected to increase over SESA (Avila-Diaz et al. 2023; Christian et al. 2023). Consequently, the current high short-term hazards are likely to magnify in the coming decades.

Long-term and short-term multi-hazards exhibit contrasting patterns across the study domain: long-term multi-hazard prevails in the southwestern and central-western portion of the study region, while short-term multi-hazard is more common in the northeastern and central-eastern areas. The core crop region of Argentina is particularly exposed to both droughts and water excess from seasonal to hydrological time scales. These events generally alternate over time, coinciding with the region's wet and dry periods before and after the 1960s (Barreiro et al. 2014; Lovino et al. 2018b). Before 1966, drought hazard was more prevalent, whereas water excess hazard dominated between 1966 and 2004. Since 2005, wet and dry extreme precipitation hazards at 3-month time scales have remained high, indicating that both types of seasonal extreme precipitation hazards have occurred concurrently over the last two decades. Our results show that the total multi-hazard, combining long-term and short-term multi-hazard indices, is widespread and fairly high across almost the entire study region. In their temporal evolution, short-term multi-hazard achieves higher values than long-term multi-hazard (0.6 maximums for short-term versus 0.4 for long-term), suggesting that short-term hazards are more

likely to occur simultaneously, while long-term hazards tend to alternate their occurrence.

Extreme hydrometeorological event hazards in the study region have increased when comparing the 1960–1990 and 1991–2020 periods, although they exhibit heterogeneous spatial patterns of change. The current total multi-hazard is not only higher but also more widespread than in the 1960–1990 period, indicating a more generalized multi-hazard across the region. Short-term multi-hazard has undergone the highest increase, growing 1.7 times more than long-term multi-hazard, primarily due to the marked rise in heatwave hazard. Thus, when these increased short-term extreme events overlap with long-term extreme events, sectoral impacts are exacerbated. Given that the study region is one of the most productive agricultural regions worldwide, the high extreme hydrometeorological hazards can impact crop yields, threaten food security, and affect human well-being.

Acknowledgements The Scientific color maps lapaz, lajolla, bilbao, and bam (Cramer 2018) are used in this study to prevent visual distortion of the data and exclusion of readers with color-vision deficiencies (Cramer et al. 2020).

Author Contributions M. Josefina Pierrestegui and Miguel A. Lovino designed the study. M. Josefina Pierrestegui carried out the research. M. Josefina Pierrestegui, Miguel A. Lovino, Omar V. Müller, and Gabriela. V. Müller analyzed and discussed the results. Miguel A. Lovino and Gabriela V. Müller acquired funding and resources. M. Josefina Pierrestegui prepared the first draft of the manuscript, and all authors contributed to its previous versions. All authors read and approved the final manuscript.

Funding This research was funded by the National Agency for Scientific and Technological Promotion of Argentina (Projects PICT-2019-03982 and PICT- 2019-2019-00481), the Argentine National Council for Scientific and Technical Research (Grant PIP-CONICET-11220200102257CO), and the Universidad Nacional del Litoral, Argentina (Grant CAI +D-2020-50620190100082LI).

Data availability The ERA5 hourly data are available at <https://doi.org/10.24381/cds.adbb2d47> and the monthly averaged data at <https://doi.org/10.24381/cds.f17050d7>

Declarations

Conflict of interest The authors have no relevant financial or non-financial interests to disclose.

References

- AghaKouchak A, Chiang F, Huning LS et al (2020) Climate extremes and compound hazards in a warming world. *Annu Rev Earth Planet Sci* 51:548–648. <https://doi.org/10.1146/annurev-earth-071719-055228>
- Almazroui M, Ashfaq M, Islam MN et al (2021a) Assessment of CMIP6 performance and projected temperature and precipitation changes over South America. *Earth Syst Environ* 5:155–183. <https://doi.org/10.1007/s41748-021-00233-6>
- Almazroui M, Saeed F, Saeed S et al (2021b) Projected changes in climate extremes using CMIP6 simulations over SREX regions. *Earth Syst Environ* 5:481–497. <https://doi.org/10.1007/s41748-021-00250-5>
- Avila-Diaz A, Benzoli V, Justino F, Torres R, Wilson A (2020) Assessing current and future trends of climate extremes across Brazil based on reanalyses and earth system model projections. *Clim Dyn* 55(5–6):1403–1426. <https://doi.org/10.1007/s00382-020-05333-z>
- Avila-Diaz A, Torres RR, Zuluaga CF et al (2023) Current and future climate extremes over latin america and caribbean: assessing earth system models from high resolution model intercomparison project (HighResMIP). *Earth Syst Environ* 7:99–130. <https://doi.org/10.1007/s41748-022-00337-7>
- Balmaceda-Huarte R, Olmo ME, Bettolli ML, Poggi MM (2021) Evaluation of multiple reanalyses in reproducing the spatio-temporal variability of temperature and precipitation indices over southern South America. *Int J Climatol* 41:5572–5595. <https://doi.org/10.1002/joc.7142>
- Barreiro M, Diaz N, Renom M (2014) Role of the global oceans and land-atmosphere interaction on summertime interdecadal variability over northern Argentina. *Clim Dynam* 42:1733–1753. <https://doi.org/10.1007/s00382-014-2088-6>
- Bathrellos GD, Skilodimou HD, Chousianitis K, Youssef AM, Pradhan B (2017) Suitability estimation for urban development using multi-hazard assessment map. *Sci Total Environ* 575:119–134. <https://doi.org/10.1016/j.scitotenv.2016.10.025>
- Beck H, Zimmermann N, McVicar T et al (2018) Present and future Köppen-Geiger climate classification maps at 1-km resolution. *Sci Data* 5:180214. <https://doi.org/10.1038/sdata.2018.214>
- Berbery EH, Barros V (2002) The hydrologic cycle of the La Plata basin in South America. *J Hydrometeorol* 3:630–645. [https://doi.org/10.1175/1525-7541\(2002\)003%3c0630:THCOTL%3e2.0.CO;2](https://doi.org/10.1175/1525-7541(2002)003%3c0630:THCOTL%3e2.0.CO;2)
- Bernal-Mujica A, Lovino MA, Müller GV, Pierrestegui MJ (2023) Spatiotemporal variability of extreme precipitation events and their impacts on soil moisture and water table depth in Argentina's core crop region. *Hydrol Sci J* 68(6):794–809. <https://doi.org/10.1080/02626667.2023.2192874>
- Binita KC, Shepherd JM, King AW et al (2021) Multi-hazard climate risk projections for the United States. *Nat Hazards* 105:1963–1976. <https://doi.org/10.1007/s11069-020-04385-y>
- Blaikie P, Cannon T, Davis I, Wisner B (2014) At risk: natural hazards, people's vulnerability and disasters, 2nd edn. Routledge, New York. <https://doi.org/10.4324/9780203714775>
- Caffera RM, Berbery EH (2006) La Plata basin climatology. In: Barros V, Clarke R, Diaz P (eds.) Climatic Change in the La Plata Basin. National Scientific and Technical Research Council (CONICET), Argentina. pp. 16–32.
- Camilloni I, Barros V, Moreiras S, Poveda G, Tomasella J (2020) Floods and Droughts. In: Moreno JM, Laguna-Defi C, Barros V, Calvo Buendia E, Marengo JA, Oswald Spring U (eds.) Adaptation to climate change risks in Ibero-American countries —RIOCCADAPT report. McGraw Hill, Madrid, Spain (ISBN 9788448621667).
- Castellanos E, Lemos MF, Astigarraga L et al (2022) Central and South America. In: Pörtner H-O, Roberts DC, Tignor M et al (eds.) Climate Change 2022: Impacts, Adaptation and Vulnerability. Contribution of Working Group II to the Sixth Assessment Report of the Intergovernmental Panel on Climate Change. Cambridge University Press, Cambridge, UK and New York. pp. 1689–1816. <https://doi.org/10.1017/9781009325844.014>
- Cerón WL, Kayano MT, Andreoli RV et al (2021) Recent intensification of extreme precipitation events in the La Plata Basin in southern South America (1981–2018). *Atmos Res* 249:105299. <https://doi.org/10.1016/j.atmosres.2020.105299>

- Christian JI, Martin ER, Basara JB et al (2023) Global projections of flash drought show increased risk in a warming climate. *Commun Earth Environ* 4:165. <https://doi.org/10.1038/s43247-023-00826-1>
- Coppola E, Raffaele F, Giorgi F et al (2021) Climate hazard indices projections based on CORDEX-CORE, CMIP5 and CMIP6 ensemble. *Clim Dyn* 57:1293–1383. <https://doi.org/10.1007/s00382-021-05640-z>
- Cramer F (2018) Scientific colour maps. Zenodo. <https://doi.org/10.5281/zenodo.1243862>
- Cramer F, Shephard GE, Heron PJ (2020) The misuse of colour in science communication. *Nat Commun* 11:5444. <https://doi.org/10.1038/s41467-020-19160-7>
- Dai A, Zhao T (2017) Uncertainties in historical changes and future projections of drought. Part I: estimates of historical drought changes. *Climatic Change* 144(3):519–533. <https://doi.org/10.1007/s10584-016-1705-2>
- Dasgupta S, Robinson EJZ (2022) Attributing changes in food insecurity to a changing climate. *Sci Rep* 12:4709. <https://doi.org/10.1038/s41598-022-08696-x>
- De Luca P, Donat MG (2023) Projected changes in hot, dry, and compound hot-dry extremes over global land regions. *Geophys Res Lett* 50:e2022GL102493. <https://doi.org/10.1029/2022GL102493>
- De Angeli S, Malamud BD, Rossi L, Taylor FE, Trasforini E, Rudari R (2022) A multi-hazard framework for spatial-temporal impact analysis. *Int J Disaster Risk Reduct* 73:102829. <https://doi.org/10.1016/j.ijdr.2022.102829>
- Dereczynski C, Chou SC, Lyra A et al (2020) Downscaling of climate extremes over South America—part I: model evaluation in the reference climate. *Weather Clim Extremes* 29:100273. <https://doi.org/10.1016/j.wace.2020.100273>
- Dunn RJH, Alexander LV, Donat MG et al (2020) Development of an updated global land in situ-based data set of temperature and precipitation extremes: HadEX3. *J Geophys Res Atmos* 125(16):e2019JD032263. <https://doi.org/10.1029/2019JD032263>
- Farahmand A, AghaKouchak A (2015) A generalized framework for deriving nonparametric standardized drought indicators. *Adv Water Resour* 76:140–145. <https://doi.org/10.1016/j.advwatres.2014.11.012>
- Feron S, Cordero RR, Damiani A et al (2019) Observations and projections of heat waves in South America. *Sci Rep* 9:8173. <https://doi.org/10.1038/s41598-019-44614-4>
- Fischer EM, Sippel S, Knutti R (2021) Increasing probability of record-shattering climate extremes. *Nat Clim Chang* 11:689–695. <https://doi.org/10.1038/s41558-021-01092-9>
- Forzieri G, Feyen L, Russo S et al (2016) Multi-hazard assessment in Europe under climate change. *Clim Change* 137:105–119. <https://doi.org/10.1007/s10584-016-1661-x>
- Garreaud RD, Vuille M, Compagnucci R, Marengo J (2009) Present-day South American climate. *Paleogeogr Paleocl* 281:180–195. <https://doi.org/10.1016/j.palaeo.2007.10.032>
- Gill JC, Malamud BD (2014) Reviewing and visualizing the interactions of natural hazards. *Rev Geophys* 52(4):680–722. <https://doi.org/10.1002/2013RG000445>
- Gulizia CN, Raggio GA, Camilloni IA et al (2022) Changes in mean and extreme climate in southern South America under global warming of 1.5 °C, 2 °C, and 3 °C. *Theor Appl Climatol* 150:787–803. <https://doi.org/10.1007/s00704-022-04199-x>
- Hagen I, Huggel C, Ramajo L, Chacón N, Ometto P, Postigo JC, Castellanos EJ (2022) Climate change-related risks and adaptation potential in Central and South America during the 21st century. *Environ Res Lett* 17(3):033002. <https://doi.org/10.1088/1748-9326/ac5271>
- Hao Z, AghaKouchak A (2014) A nonparametric multivariate multi-index drought monitoring framework. *J Hydrometeorol* 15(1):89–101. <https://doi.org/10.1175/JHM-D-12-0160.1>
- Hersbach H, Bell B, Berrisford P et al (2020) The ERA5 global reanalysis. *Q J R Meteorol Soc* 146:1999–2049. <https://doi.org/10.1002/qj.3803>
- Hersbach H, Bell B, Berrisford P et al (2023a) ERA5 hourly data on single levels from 1940 to present. Copernicus Climate Change Service (C3S) Climate Data Store (CDS). <https://doi.org/10.24381/cds.adbb2d47> (Accessed on March 2023)
- Hersbach H, Bell B, Berrisford P et al (2023b) ERA5 monthly averaged data on single levels from 1940 to present. Copernicus Climate Change Service (C3S) Climate Data Store (CDS). <https://doi.org/10.24381/cds.f17050d7> (Accessed on May 2023)
- Houspanossian J, Giménez R, Whitworth-Hulse JI et al (2023) Agricultural expansion raises groundwater and increases flooding in the South American plains. *Science* 380:1344–1348. <https://doi.org/10.1126/science.add5462>
- Kreibich H, Van Loon AF, Schröter K et al (2022) The challenge of unprecedented floods and droughts in risk management. *Nature* 608:80–86. <https://doi.org/10.1038/s41586-022-04917-5>
- Lesk C, Anderson W, Rigden A et al (2022) Compound heat and moisture extreme impacts on global crop yields under climate change. *Nat Rev Earth Environ* 3:872–889. <https://doi.org/10.1038/s43017-022-00368-8>
- Li M, Wu P, Ma Z (2020) A comprehensive evaluation of soil moisture and soil temperature from third-generation atmospheric and land reanalysis data sets. *Int J Climatol* 40:5744–5766. <https://doi.org/10.1002/joc.6549>
- Li C, Zwiers F, Zhang X, Li G, Sun Y, Wehner M (2021) Changes in annual extremes of daily temperature and precipitation in CMIP6 models. *J Climate* 34:3441–3460. <https://doi.org/10.1175/JCLI-D-19-1013.1>
- Lloyd-Hughes B, Saunders MA (2002) A drought climatology for Europe. *Int J Climatol* 22(13):1571–1592. <https://doi.org/10.1002/joc.846>
- Lovino MA, García N, Baethgen W (2014) Spatiotemporal analysis of extreme precipitation events in the Northeast region of Argentina (NEA). *J. Hydrol. Reg Stud* 2:140–158. <https://doi.org/10.1016/j.ejrh.2014.09.001>
- Lovino MA, Müller OV, Berbery EH, Müller GV (2018a) How have daily climate extremes changed in the recent past over northeastern Argentina? *Global Planet Change* 168:78–97. <https://doi.org/10.1016/j.gloplacha.2018.06.008>
- Lovino MA, Müller OV, Müller GV, Sgroi LC, Baethgen WE (2018b) Interannual-to-multidecadal hydroclimate variability and its sectoral impacts in Northeastern Argentina. *Hydrol Earth Syst Sci* 22:3155–3174. <https://doi.org/10.5194/hess-22-3155-2018>
- Lovino MA, Müller GV, Pierrestegui MJ, Espinosa E, Rodríguez L (2022) Extreme precipitation events in the Austral Chaco region of Argentina. *Int J Climatol* 42(11):5985–6006. <https://doi.org/10.1002/joc.7572>
- Lovino MA, Pierrestegui MJ, Müller OV, Müller GV, Berbery EH (2024) The prevalent life cycle of agricultural flash droughts. *npj Clim Atmos Sci* 7:73. <https://doi.org/10.1038/s41612-024-00618-0>
- Lyu H-M, Yin Z-Y (2023) An improved MCDM combined with GIS for risk assessment of multi-hazards in Hong Kong. *Sustain Cities Soc* 91:104427. <https://doi.org/10.1016/j.scs.2023.104427>
- Martínez-Fernández J, González-Zamora A, Sánchez N, Gumuzzio A (2015) A soil water-based index as a suitable agricultural drought indicator. *J Hydrol* 522:265–273. <https://doi.org/10.1016/j.jhydr.2014.12.051>
- Müller OV, McGuire PC, Vidale PL, Hawkins E (2024) River flow in the near future: a global perspective in the context of a high-emission climate change scenario. *Hydrol Earth Syst Sci* 28:2179–2201. <https://doi.org/10.5194/hess-28-2179-2024>
- Naumann G, Vargas WM, Barbosa P, Blauthut V, Spinoni J, Vogt JV (2019) Dynamics of socioeconomic exposure, vulnerability

- and impacts of recent droughts in Argentina. *Geosciences* 9:39. <https://doi.org/10.3390/geosciences9010039>
- Olmo M, Bettolli ML, Rusticucci M (2020) Atmospheric circulation influence on temperature and precipitation individual and compound daily extreme events: Spatial variability and trends over southern South America. *Weather Clim Extremes* 29:100267. <https://doi.org/10.1016/j.wace.2020.100267>
- Olmo ME, Weber T, Teichmann C, Bettolli ML (2022) Compound events in South America using the CORDEX-CORE ensemble: Current climate conditions and future projections in a global warming scenario. *J Geophys Res Atmos* 127:e2022JD037708. <https://doi.org/10.1029/2022JD037708>
- Ortega G, Arias PA, Villegas JC, Marquet PA, Nobre P (2021) Present-day and future climate over central and South America according to CMIP5/CMIP6 models. *Int J Climatol* 41(15):6713–6735. <https://doi.org/10.1002/joc.7221>
- Pendergrass AG, Meehl GA, Pulwarty R et al (2020) Flash droughts present a new challenge for subseasonal-to-seasonal prediction. *Nat Clim Chang* 10:191–199. <https://doi.org/10.1038/s41558-020-0709-0>
- Perkins SE, Alexander LV (2013) On the Measurement of Heat Waves. *J Climate* 26:4500–4517. <https://doi.org/10.1175/JCLI-D-12-00383.1>
- Perkins SE, Alexander LV, Nairn JR (2012) Increasing frequency, intensity and duration of observed global heatwaves and warm spells. *Geophys Res Lett* 39:L20714. <https://doi.org/10.1029/2012GL053361>
- Perkins-Kirkpatrick SE, Lewis SC (2020) Increasing trends in regional heatwaves. *Nat Commun* 11:3357. <https://doi.org/10.1038/s41467-020-16970-7>
- Pörtner H-O, Roberts DC, Adams H et al (2022) Technical Summary. In: Pörtner H-O, Roberts DC, Poloczanska ES et al (eds.) *Climate Change 2022: Impacts, Adaptation and Vulnerability. Contribution of Working Group II to the Sixth Assessment Report of the Intergovernmental Panel on Climate Change*. Cambridge University Press, Cambridge, UK and New York. pp. 37–118. <https://doi.org/10.1017/9781009325844.002>
- Pourghasemi HR, Gayen A, Edalat M, Zarafshar M, Tiefenbacher JP (2020) Is multi-hazard mapping effective in assessing natural hazards and integrated watershed management? *Geosci Front* 11(4):1203–1217. <https://doi.org/10.1016/j.gsf.2019.10.008>
- Rahmstorf S, Coumou D (2011) Increase of extreme events in a warming world. *Proc Natl Acad Sci* 108(44):17905–17909. <https://doi.org/10.1073/pnas.1101766108>
- Reboita MS, Kuki CAC, Marrafon VH et al (2022) South America climate change revealed through climate indices projected by GCMs and Eta-RCM ensembles. *Clim Dyn* 58:459–485. <https://doi.org/10.1007/s00382-021-05918-2>
- Regoto P, Dereczynski C, Chou SC, Bazzanella AC (2021) Observed changes in air temperature and precipitation extremes over Brazil. *Int J Climatol* 41:5125–5142. <https://doi.org/10.1002/joc.7119>
- Ridder NN, Pitman AJ, Westra S et al (2020) Global hotspots for the occurrence of compound events. *Nat Commun* 11:5956. <https://doi.org/10.1038/s41467-020-19639-3>
- Rivera JA, Penalba OC (2018) Spatio-temporal assessment of streamflow droughts over Southern South America: 1961–2006. *Theoret Appl Climatol* 133(3):1021–1033. <https://doi.org/10.1007/s00704-017-2243-1>
- Seneviratne SI, Zhang X, Adnan M et al (2021) Weather and Climate Extreme Events in a Changing Climate. In Masson-Delmotte V, Zhai P, Pirani A et al (eds.) *Climate Change 2021: The Physical Science Basis. Contribution of Working Group I to the Sixth Assessment Report of the Intergovernmental Panel on Climate Change*. Cambridge University Press, Cambridge, United Kingdom and New York. pp. 1513–1766. <https://doi.org/10.1017/9781009157896.013>
- Seong M-G, Min S-K, Kim Y-H, Zhang X, Sun Y (2021) Anthropogenic greenhouse gas and aerosol contributions to extreme temperature changes during 1951–2015. *J Clim* 34(3):857–870. <https://doi.org/10.1175/JCLI-D-19-1023.1>
- Sfetsos A, Politis N, Vlachogiannis D (2023) Multi-hazard extreme scenario quantification using intensity, duration, and return period characteristics. *Climate* 11(12):242. <https://doi.org/10.3390/cli11120242>
- Sgroi LC, Lovino MA, Berbery EH, Müller GV et al (2021) Characteristics of droughts in Argentina's core crop region. *Hydrol Earth Syst Sci* 25(5):2475–2490. <https://doi.org/10.5194/hess-25-2475-2021>
- Sirdas S, Sen K (2003) Spatio-temporal drought analysis in the Trakya region, Turkey. *Hydrol Sci J* 48(5):809–820. <https://doi.org/10.1623/hysj.48.5.809.51458>
- Skilodimou HD, Bathrellos GD, Chousianitis K et al (2019) Multi-hazard assessment modeling via multi-criteria analysis and GIS: a case study. *Environ Earth Sci* 78:47. <https://doi.org/10.1007/s12665-018-8003-4>
- Stalhandske Z, Steinmann CB, Meiler S et al (2024) Global multi-hazard risk assessment in a changing climate. *Sci Rep* 14:5875. <https://doi.org/10.1038/s41598-024-55775-2>
- Sun Q, Miao C, Hanel M, Borthwick AG, Duan Q, Ji D, Li H (2019) Global heat stress on health, wildfires, and agricultural crops under different levels of climate warming. *Environ Int* 128:125–136. <https://doi.org/10.1016/j.envint.2019.04.025>
- Sutanto SJ, Vitolo C, Di Napoli C, D'Andrea M, Van Lanen HA (2020) Heatwaves, droughts, and fires: exploring compound and cascading dry hazards at the pan-European scale. *Environ Int* 134:105276. <https://doi.org/10.1016/j.envint.2019.105276>
- Tabari H, Hosseinzadehtalaei P, Thiery W, Willems P (2021) Amplified drought and flood risk under future socioeconomic and climatic change. *Earth's Future* 9:e2021EF002295. <https://doi.org/10.1029/2021EF002295>
- Thackeray CW, Hall A, Norris J et al (2022) Constraining the increased frequency of global precipitation extremes under warming. *Nat Clim Chang* 12:441–448. <https://doi.org/10.1038/s41558-022-01329-1>
- UN Office for Disaster Risk Reduction (UNDRR) (2020) Hazard Definition and Classification Review: Technical Report. United Nations. In: Documents and Publications. UNDRR. Available via <https://www.unrr.org/publication/hazard-definition-and-classification-review-technical-report>. Accessed 4 Apr 2024
- Vogel E, Donat MG, Alexander LV et al (2019) The effects of climate extremes on global agricultural yields. *Environ Res Lett* 14:054010. <https://doi.org/10.1088/1748-9326/ab154b>
- Wang Z, Jiang Y, Wan H, Yan J, Zhang X (2017) Detection and attribution of changes in extreme temperatures at regional scale. *J Clim* 30(17):7035–7047. <https://doi.org/10.1175/JCLI-D-15-0835.1>
- Ward PJ, Blauthut V, Bloemendaal N et al (2020) Review article: natural hazard risk assessments at the global scale. *Nat Hazards Earth Syst Sci* 20:1069–1096. <https://doi.org/10.5194/nhess-20-1069-2020>
- Weber T, Bowyer P, Rechid D et al (2020) Analysis of compound climate extremes and exposed population in Africa under two different emission scenarios. *Earth's Future* 8:e2019EF001473. <https://doi.org/10.1029/2019EF001473>
- Yang S, Zeng J, Fan W, Cui Y (2022) Evaluating root-zone soil moisture products from GLEAM, GLDAS, and ERA5 based on in situ observations and triple collocation method over the tibetan plateau. *J Hydrometeorol* 23:1861–1878. <https://doi.org/10.1175/JHM-D-22-0016.1>
- Zhang H, Delworth TL, Zeng F, Vecchi G, Paffendorf K, Jia L (2016) Detection, attribution, and projection of regional rainfall changes on (multi-) decadal time scales: a focus on southeastern South America. *J Clim* 29:8515–8534. <https://doi.org/10.1175/JCLI-D-16-0287.1>

Springer Nature or its licensor (e.g. a society or other partner) holds exclusive rights to this article under a publishing agreement with the author(s) or other rightsholder(s); author self-archiving of the accepted manuscript version of this article is solely governed by the terms of such publishing agreement and applicable law.

Artículo 2

Vulnerabilidad y riesgo de amenazas hidrometeorológicas en el centro-noreste de Argentina



Vulnerability and Risk of Hydrometeorological Hazards in Central-Northeastern Argentina

M. Josefina Pierrestegui^{1,2} · Miguel A. Lovino^{1,2} · Gabriela V. Müller^{1,2} · Omar V. Müller^{1,2}

Received: 18 October 2024 / Revised: 15 January 2025 / Accepted: 1 February 2025
© King Abdulaziz University and Springer Nature Switzerland AG 2025

Abstract

Extreme hydrometeorological events (EHEs) pose significant risks to central-northeastern Argentina, requiring a nuanced understanding of subnational-level vulnerability and risk. This study integrates physical and socio-economic data to evaluate individual and multi-hazard risks across long-term and short-term time scales. Vulnerability is analyzed through exposure, sensitivity, and adaptive capacity. Risk is assessed as the interaction between EHE hazards and vulnerability. The analysis reveals a medium average vulnerability across the region, with marked spatial differences. Central Argentina—encompassing southern Santa Fe, eastern Córdoba, and northern Buenos Aires—shows medium vulnerability due to high exposure, counterbalanced by low sensitivity and high adaptive capacity. In contrast, northwest and central-western regions—including Formosa, eastern Salta, and eastern Santiago del Estero—exhibit high vulnerability driven by high sensitivity and low adaptive capacity despite low exposure. Heatwave risk is the highest and most widespread, particularly in northern Argentina. Risks from long-term dry and wet extreme precipitation display distinct regional patterns. Heavy precipitation risks are locally high in the northeast. Flash drought risk remains comparatively low across the region. The findings highlight that long-term multi-hazard risk is the most extensive and severe, while short-term multi-hazard risk is less widespread but dominated by heatwaves. Despite limitations, including uncertainties in input data and a constrained set of indicators, these results underscore the need for tailored adaptation strategies. Efforts should focus on reducing exposure in the south through improved infrastructure and agricultural practices and enhancing adaptive capacity in the north. Future research should explore compound risks and identify practical adaptation measures.

Keywords Risk · Vulnerability · Hydrometeorological multi-hazards

1 Introduction

Climate change affects natural and socio-economic systems, with climate hazards posing substantial risks to people and assets globally (Hagen et al. 2022; Stalhandske et al. 2024). The risks and vulnerabilities associated with climate change and extreme events are shaped not only by the occurrence of climate hazards—such as heatwaves, storms, floods, or

droughts—but also by socio-economic factors that influence a community's preparedness and ability to respond (Birkmann et al. 2013, 2022; IPCC et al. 2022a; UNDRR 2019). Understanding the interaction between climate hazards and populations or infrastructure in specific areas is crucial for planning effective mitigation and adaptation strategies (Jurgilevich et al. 2017; O'Neill et al. 2022). Vulnerability and risk assessments, which combine physical and socio-economic data, have emerged as essential tools to identify and address these risks within a given region or sector (Birkmann et al. 2022; Füssel 2007; Stalhandske et al. 2024).

The scientific consensus is that risks, in the context of climate change, result from the dynamic interaction of climate hazards, and the exposure and vulnerability of affected human and ecological systems (Ara Begum et al. 2022 and references therein; Oppenheimer et al. 2014). While climate hazard describes the physical characteristics of events, vulnerability refers to the predisposition of a system to be

✉ M. Josefina Pierrestegui
mjpierrestegui@unl.edu.ar

¹ Consejo Nacional de Investigaciones Científicas y Técnicas (CONICET), Santa Fe, Argentina

² Centro de Estudios de Variabilidad y Cambio Climático (CEVARCAM), Facultad de Ingeniería y Ciencias Hídricas (FICH), Universidad Nacional del Litoral (UNL), Ruta Nacional N° 168 – km 472.4, CC 217, Ciudad Universitaria, 3000 Santa Fe, Argentina

adversely affected, shaped by the social and ecological characteristics that determine its ability to anticipate and respond to risks (Ara Begum et al. 2022; Sharma and Ravindranath 2019). Vulnerability is dynamic and influenced by sensitivity and adaptive capacity factors, which determine how severely climate impacts will be felt (Ford et al. 2018; McDowell et al. 2016; Naylor et al. 2020; Viner et al. 2020). Consequently, climate-related risk—the potential for adverse consequences for human or ecological systems—varies across communities, influenced by inequalities and context-specific conditions (IPCC et al. 2022a; Rising et al. 2022).

Single weather and climate events pose significant risks, but many locations are exposed to multiple extreme events (Garschagen et al. 2021; Tabari and Willems 2023). At the same time, different sectors of society face heightened climate risks. Urban areas are especially vulnerable due to dense populations and infrastructure (Wamsler et al. 2013). Specific socio-demographic groups, including the youngest and oldest age groups, natural resource-dependent communities, and lower-income populations, are disproportionately affected by climate hazards (Binita et al. 2021). In southeastern South America, the frequency and severity of extreme events—such as droughts, floods, heatwaves, and heavy rainfall—have significantly increased in recent decades (Almazroui et al. 2021a; Avila-Diaz et al. 2020; Lovino et al. 2018a; Olmo et al. 2022). Central and northeastern Argentina are particularly vulnerable to these recurring extreme hydrometeorological events due to the region's large population, its role as a major agricultural producer, and its high poverty rates (Lovino et al. 2018b; Lovino 2020; Naumann et al. 2019). The lack of comprehensive research and targeted risk assessments addressing the region's vulnerabilities further exacerbates this situation. Therefore, there is an urgent need for a thorough understanding of the risks posed by extreme events in this area to inform the development of effective mitigation and adaptation strategies.

Despite their importance, limited attention has been given to expanding our understanding of the risks and vulnerabilities related to extreme events in southeastern South America. The key climate risks identified for the region include (1) food insecurity from recurrent and severe droughts, (2) threats to life and infrastructure from floods and landslides, (3) water scarcity, and (4) public health risks from increasing epidemics of vector-borne diseases (Castellanos et al. 2022 and references therein; Hagen et al. 2022; Magrin et al. 2014). Vulnerability to droughts and floods tends to be inversely related to the level of economic and social development. Socioeconomic factors like population growth, rapid urbanization of informal settlements, inadequate infrastructure, high levels of social inequality and poverty, agriculture-dependent economies, and unsustainable environmental

practices exacerbate vulnerability, intensifying the impacts of water deficits and excesses (Alvala et al. 2024; Barros et al. 2015; Camillon et al. 2020; Liu et al. 2025; Pizzorni et al. 2024). In Argentina, droughts and floods, compounded by local vulnerabilities such as low-income conditions and lack of infrastructure, can trigger widespread disasters that affect the entire national economy (Agosta et al. 2021; Bert et al. 2021; Bohn and Piccolo 2019; Bortz and Toftum 2023; Borzi et al. 2021; González et al. 2021; Houspanossian et al. 2023; Naumann et al. 2019; Tomasz et al. 2024). Given the critical role these vulnerabilities play in amplifying the impacts of extreme events, addressing the persistent gaps in our understanding of regional risks and vulnerabilities is essential for informing climate-resilient public policies and developing effective prevention and adaptation strategies to manage climate-related disasters.

This study assesses the vulnerability and risk of central-eastern Argentina to extreme hydrometeorological events. We develop and analyze metrics for vulnerability components, including exposure, sensitivity, and adaptative capacity. Risk levels are explored for both individual and multi-hazards associated with EHE. Individual hazards include long-term dry and wet extreme precipitation events and short-term extreme events such as heatwaves, heavy precipitation events, and flash droughts. Multi-hazards integrate long-term, short-term, and total (short- and long-term) EHEs.

2 Data and Methods

2.1 Study Region

The study area covers central and northeastern Argentina, extending from 65 W to 53 W and 36 S–22 S (Fig. 1). This vast flat region encompasses the fertile soils of the Pampas and Chaco plains. Its topography supports a distinct latitudinal thermal gradient, with average temperatures of 24 °C in the north, gradually decreasing to 15 °C in the south. According to the Köppen-Geiger classification (Beck et al. 2018), the region predominantly experiences a temperate climate without a drying season and with a hot summer. Precipitation patterns vary substantially, with northeastern Argentina receiving the highest annual rainfall (1800 mm/year), while central Argentina experiences the lowest (close to 700 mm/year) (Benítez et al. 2024; Berbery and Barros 2002).

This region plays a critical role in the continent's socio-economic development and is particularly vulnerable to EHE due to three key factors. First, it produces over 80% of the nation's crops and livestock (Lovino et al. 2018a). Second, it experiences hydroclimate variability on interannual

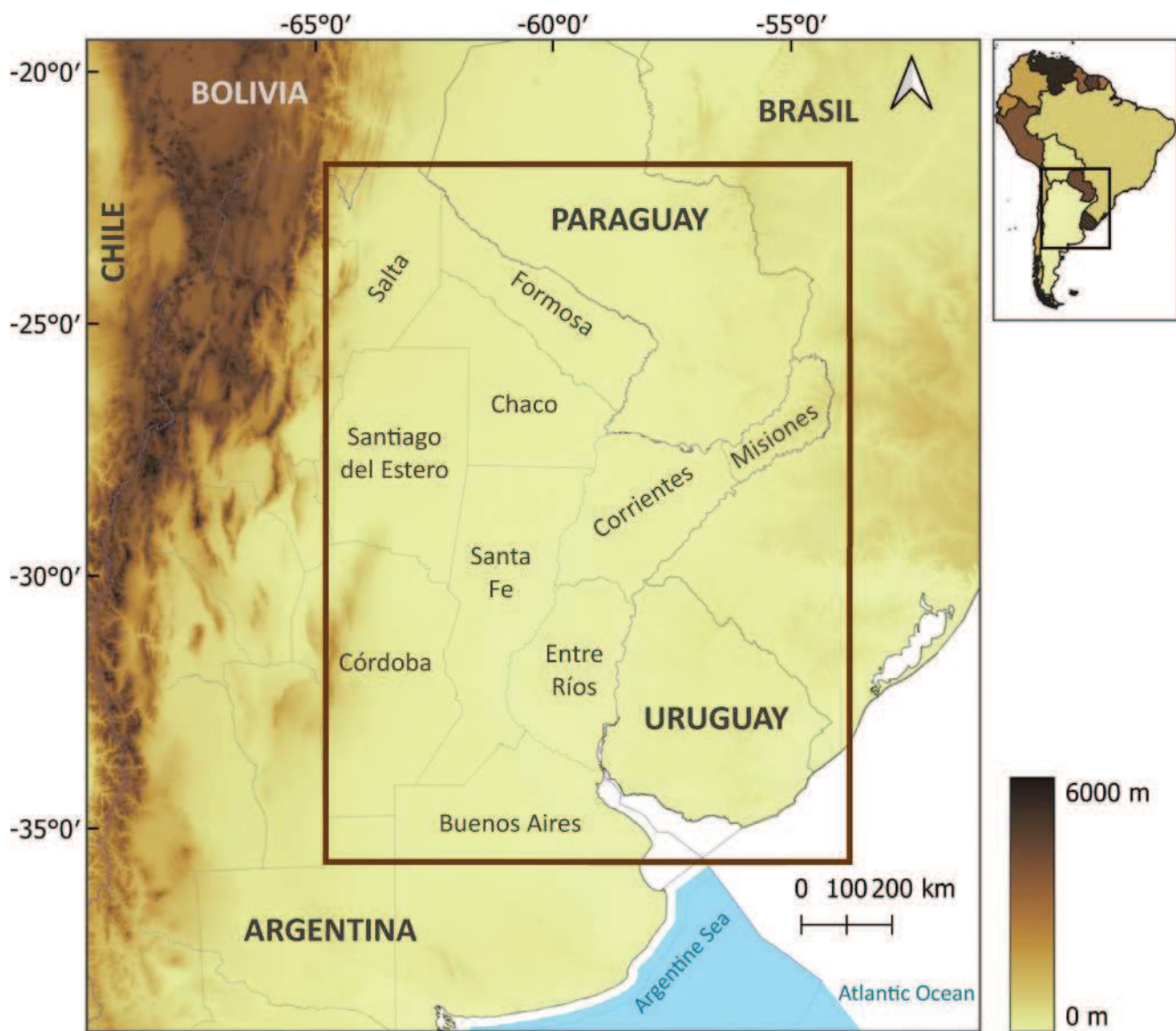


Fig. 1 Topographic map of southeastern South America, highlighting the study area in central-northeastern Argentina with a dark brown rectangle. The map also names the Argentinian provinces included in the study region

to decadal time scales and faces frequent and severe EHE, which may exacerbate in the coming years (Almazroui et al. 2021b; Hagen et al. 2022; Lovino et al. 2018a, b; Olmo et al. 2020). Finally, it is home to most of Argentina's population and serves as the hub for key economic activities.

2.2 Data

Individual EHE hazards and multi-hazards are derived from our previous study, Pierrestegui et al. (2024) (hereafter called P2024). P2024 used precipitation, soil moisture, and temperature data from the European Centre for Medium-Range Weather Forecasts (ECMWF) reanalysis version 5 (ERA5, Hersbach et al. 2020, 2023a, b) with a spatial

resolution of $0.25^\circ \times 0.25^\circ$, covering the period from 1991 to 2020. This period was chosen as it represents the most recent 30-year decadal climate normal, as defined by the World Meteorological Organization (WMO, 2017). EHE risks are analyzed using various datasets, as outlined in Table 1. Vulnerability components are quantified using data from Argentine national institutions, at the departmental geographic units, which are administrative divisions below provinces. Social indicators—including total population, vulnerable populations, potential dependency, technological access, educational access, and healthcare access—are derived from the latest National Census of Population, Households, and Housing conducted in 2022 by the National Institute of Statistics and Censuses (INDEC 2022). Crop

Table 1 Hazard and vulnerability components. Summary table of variables used, along with their data sources

| Component | Variable | Description | Relevance | Data source |
|----------------------|-------------------------|--|---|----------------------------|
| <i>Hazards</i> | | | | |
| Individual hazards | WEP | Wet extreme precipitation events based on SPI3 and SPI18. | Agricultural and hydrological extreme wet conditions. | Pierrestegui et al. (2024) |
| | DEP | Dry extreme precipitation events based on SPI3 and SPI18. | Agricultural and hydrological droughts. | |
| | HW | Heatwaves based on De Luca and Donat (2023). | Immediate impact in food production, public health, and infrastructure. | |
| | HP | Heavy precipitation events based on Weber et al. (2020). | | |
| | FD | Flash droughts based on Lovino et al. (2024). | | |
| Multi-hazards | LT-mH | Long-term multi-hazards compounded by WEP and DEP. | Wet and dry extreme events at seasonal and hydrological scales. | Pierrestegui et al. (2024) |
| | ST-mH | Short-term multi-hazards compounded by HW, HP and FD. | Wet, dry and hot extreme events with impacts at daily scale. | |
| | T-mH | Total multi-hazard compounded by long-term and short-term multi-hazards. | Wet, hot and dry extreme events with impacts at daily, seasonal and hydrological scales. | |
| <i>Vulnerability</i> | | | | |
| Exposure | Total population | Absolute number of people. | Direct impacts on the population: health, security, housing, livelihoods. | INDEC (2022) |
| | Crop yield | Mean value of corn and soybean yields from 2000 to 2020. | Impacts on livelihoods, food production, food security. | MAGyP (2021a, 2021b) |
| | Critical Infrastructure | Total number of systems and facilities essential for societal functioning. | Disruption in essential services and systems. | IGN (2021) |
| Sensitivity | Sensitive population | Percentage of population under 14 years and over 65 years, over total population. | Health and socioeconomic sensitivity. | INDEC (2022) |
| | Potential dependency | Population of potentially inactive ages in relation to the population of potentially active ages. | Material conditions that predispose to be negatively affected. | |
| | Income sensitivity | Inverse of the ratio of average labor income in the registered private sector to the total income. | Material conditions that predispose to be negatively affected. | IGN (2021) |
| | Land use change | Land use changes that include deforestation between 2001 and 2015. | State of the environment that predispose or magnify negative effects. | Bra-calenti et al. (2024) |
| Adaptive capacity | Technological access | Percentage of households with technological access. | Capacity to prepare for hazards, take advantage of opportunities, and respond to consequences | INDEC (2022) |
| | Educational attainment | Percentage of the population over 25 years with completed secondary education. | Capacity to prepare for hazards and take advantage of opportunities. | |
| | Healthcare availability | Percentage of the population with private or public health services or programs. | Capacity to respond to and recover from consequences. | |

yield data for corn and soybean, covering the period 2000–2020, are obtained from historical records provided by the National Ministry of Agriculture, Livestock, and Fisheries (MAGyP 2021a, b). Critical infrastructure and income data are derived from data provided by the National Geographic Institute (IGN 2021), with geospatial information updated to 2021. Finally, land use change data is obtained from Bracalenti et al. (2024), who estimated the dominant land cover and its evolution from 2001 to 2015 using land use maps derived from the MODIS Land Cover Climate Modeling Grid product (MCD12C1) at 0.05° grid spacing, following the classification of the International Geosphere-Biosphere Programme. Note that the socioeconomic indicators represent the most up-to-date data available, crop yields are estimated over a 20-year period to ensure robust data quality, and land use data are sourced from a previous study. These datasets are all considered representative of the period used to estimate hazards (1991–2020).

2.3 Risk and Vulnerability Framework

Figure 2a presents a schematic diagram summarizing the approach used to assess the vulnerability and risk indices. Climate risk is a consequence of the interaction between climate hazards and the vulnerability of a specific society with distinct characteristics, resulting in potential economic, social, and environmental impacts (Birkmann et al. 2013; O'Neill et al. 2022; Stalhandske et al. 2024). Hazards refer to climate-related physical events, whether natural or human-induced, that have the potential to cause loss of life, injury, or other health impacts, as well as damage or loss to property, infrastructure, livelihoods, service provision, ecosystems, and environmental resources (IPCC et al. 2022b). In this study, climate hazards encompass extreme hydrometeorological hazards and multi-hazards. Vulnerability indicates the predisposition or propensity of a system to be adversely affected by a hazardous climatic event (IPCC et al. 2022b). Therefore, vulnerability shapes how the interaction between hazards and societies defines risk and is analyzed through its three components: exposure, sensitivity, and adaptive capacity (e.g., Weis et al. 2016; Yu et al. 2021). Although vulnerability is a component of risk, it is also a crucial independent factor that enhances the understanding of the differential impacts of climate hazards across various socioeconomic contexts. The following sections will explain the methodology and criteria used to assess vulnerability and risk of EHE.

2.3.1 Extreme Hydrometeorological Hazards and Multi-hazards

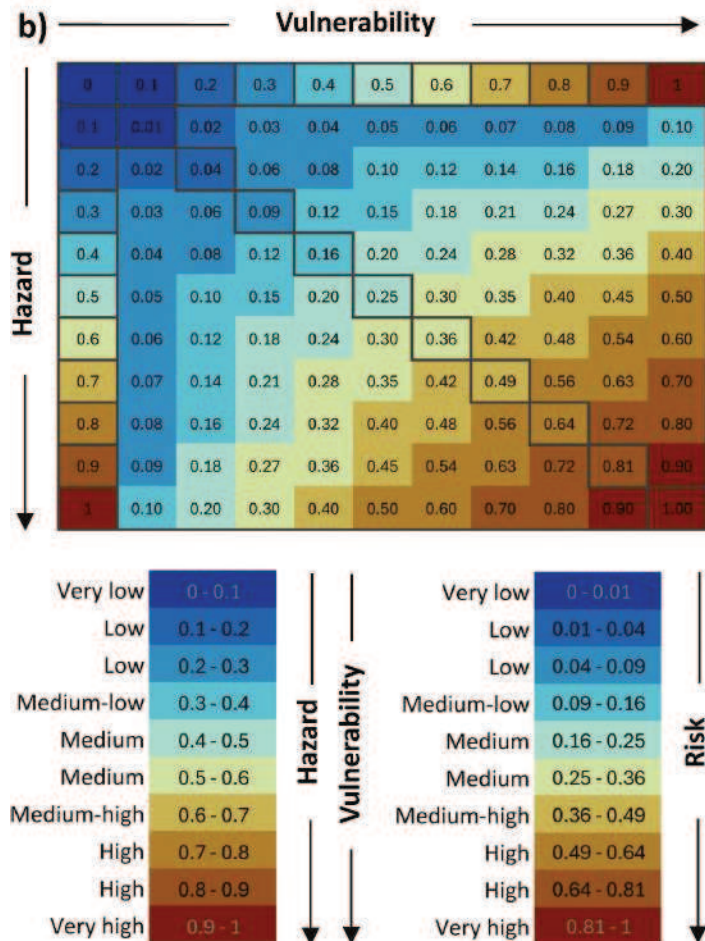
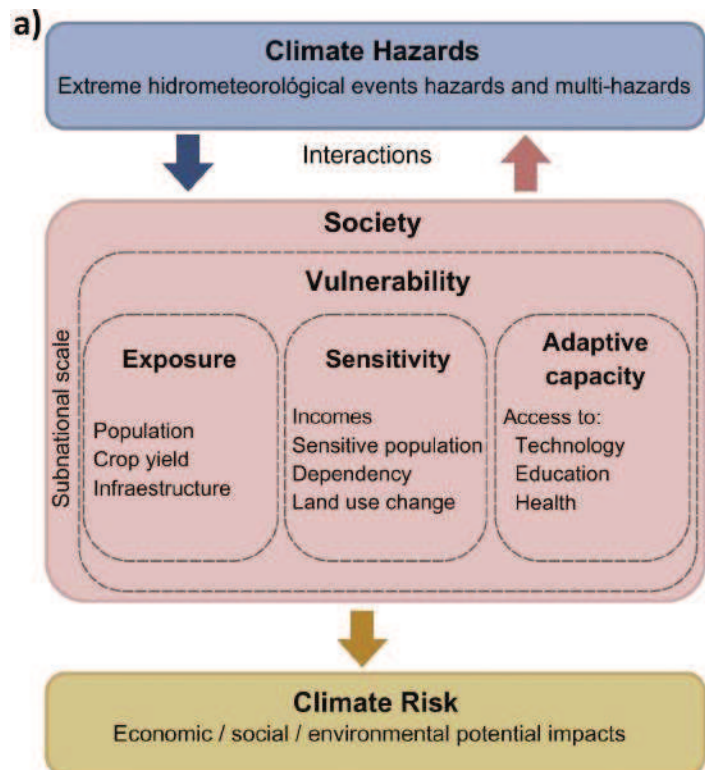
This study evaluates climate risks associated with various EHEs derived from P2024. Key definitions are provided below (see P2024 for further details). The analysis incorporates individual hazards, characterized by their frequency, duration, and intensity, and multi-hazards, assessed through a multi-layer single hazard framework. Individual and multi-hazards are analyzed over long- and short-term time scales (Table 1).

Individual hazards include wet (WEP) and dry (DEP) extreme precipitation events, heatwaves (HW), heavy precipitation events (HP), and flash droughts (FD) (see Table 1). WEP and DEP represent long-term EHEs calculated using the nonparametric Standardized Precipitation Index (SPI; Farahmand and AghaKouchak 2015; Hao and AghaKouchak 2014) at 3-month (SPI3) and 18-month (SPI18) time scales. SPI3 provides insights into wet or dry conditions relevant to agriculture, while SPI18 reflects extended rainfall anomalies, impacting streamflow, reservoir storage, and groundwater levels. HW, HP, and FD represent short-term EHEs. HWs are defined as periods of at least 3 consecutive days with a daily maximum temperature exceeding the 90th percentile of the reference period (De Luca and Donat 2023; Perkins and Alexander 2013). HPs are identified as sequences of consecutive days when daily precipitation exceeds the 95th percentile on wet days (≥ 1 mm) (Weber et al. 2020). Agricultural FDs are identified following Lovino et al. (2024), which integrates root-zone soil moisture and soil hydraulic properties to capture the rapid depletion of soil moisture and vegetation stress. These short-term EHEs can rapidly impact agriculture, urban areas, food production, public health, and infrastructure (Hagen et al. 2022).

Time series of individual hazard components for each EHE are constructed by multiplying the decadal frequency, average duration, and mean maximum intensity of events in the 1991–2020 period. Each time series is then normalized on a 0–1 scale (see P2024 for methodological details). Spatially, the variables are re-gridded from a resolution of $0.25^\circ \times 0.25^\circ$ to $0.125^\circ \times 0.125^\circ$. Hazard values are averaged for grid points within departmental boundaries in Argentina—the smallest administrative unit—providing a single value per department for risk analysis.

The rescaled individual hazard components are subsequently composited to generate three multi-hazard indices: the long-term multi-hazard (LT-mH) index, combining WEP and DEP; the short-term multi-hazard (ST-mH) index, integrating HW, HP, and FD; and the total multi-hazard (T-mH) index, aggregating LT-mH and ST-mH (see Table 1). The LT-mH index characterizes hazards for wet and dry extreme events at seasonal and hydrological scales. The ST-mH

Fig. 2 Schematic diagram detailing the methodology for assessing vulnerability and risk. (a) Overview of the methodological framework, adapted from Birkmann et al. (2013). (b) Risk matrix depicting the relationship between hazard and vulnerability levels. The scales highlight the categories or levels of hazard, vulnerability, and risk, ranging from very low (blue) to very high (dark brown)



index represents hazards for wet, dry, and hot extreme events on daily to weekly time scales. T-mH combines hazards for EHEs at all time scales.

2.3.2 Vulnerability Components

Vulnerability is analyzed through its three components—exposure, sensitivity, and adaptive capacity—following the definitions provided by IPCC et al. (2022b). Exposure refers to the presence of people, livelihoods, and infrastructure in areas prone to potential hazards. Sensitivity reflects the degree to which a system or society may be affected by such exposure, either positively or negatively. Adaptive capacity represents the ability of a system to adjust its characteristics or behavior to adapt and cope with changes, involving the capacity to prepare for hazards, take advantage of opportunities, and respond to consequences. To evaluate these components within the study region, representative variables are carefully selected based on their relevance and reliability.

Exposure is quantified through three variables: total population, crop yield, and critical infrastructure (Table 1). Total population, defined as the absolute number of inhabitants per department, represents direct social exposure to hazards. Crop yield, calculated as the average yield of corn and soybean between 2000 and 2020 (the region's predominant crops; Sgroi et al. 2021), captures agricultural exposure to climate variability. Critical infrastructure refers to the number of systems, facilities, and assets essential for societal functioning. Critical infrastructure, encompassing energy systems (power plants and transformer stations), water and waste management facilities (water treatment plants, sewage treatment plants, solid waste treatment plants, sanitary landfills), and transportation networks (airports, bridges, tunnels, railway stations, highways), highlights the potential for cascading impacts when vital systems are disrupted.

Sensitivity is assessed using four variables: sensitive population, potential dependency, income sensitivity, and land use change (Table 1). Sensitive population refers to the percentage of individuals under 14 years and over 65 years relative to the total population, groups with limited physical resilience. Potential dependency quantifies the ratio of the population of potentially inactive ages to that of potentially active ages, expressed as the number of inactive individuals per 100 active individuals. Income sensitivity, defined as the inverse of average labor income for males and females in the registered private sector relative to their group's total income, highlights vulnerability stemming from low financial resources. Land use change, derived from deforestation data reflecting transitions from vegetation categories of higher tree coverage to others with lower coverage between 2001 and 2015 (Bracalenti et al. 2024), indicates

environmental sensitivity, highlighting ecosystem degradation that exacerbates hazard impacts.

Adaptive capacity encompasses reducing negative impacts, mitigating harm, or seizing beneficial opportunities arising from climate extremes and long-term climate change. This study considers three key indicators of adaptive capacity (following USAID 2016): technological access, educational attainment, and healthcare availability (Table 1). Technological access, measured as the percentage of households with internet, mobile phones, and computing devices, reflects the capacity to prepare for and respond to hazards. Educational attainment, defined as the proportion of individuals aged 25 and older who have completed secondary education or higher, indicates the readiness to adapt to evolving challenges and seize opportunities. Healthcare availability, expressed as the percentage of the population with access to social, prepaid, or state-sponsored health programs, represents the capacity to respond to and recover from the adverse effects of EHEs.

2.3.3 Vulnerability Quantification

First, the selected variables (see Table 1) are normalized to create indices that can be compared and aggregated. Following Tabari and Willems (2023), we conduct the normalization using linear min-max rescaling between 0.05 (lowest) and 0.95 (highest) percentiles (Eq. 1):

$$Nv(0,1) = (vc - \min(vc)) / (\max(vc) - \min(vc)) \quad (1)$$

where $Nv(0,1)$ are the normalized indices of the vulnerability components, vc are the individual variables of vulnerability components, and $\min(vc)$ and $\max(vc)$ are the minimum (0.05 percentile) and maximum (0.95 percentile) values of the corresponding variables. Values exceeding $\max(vc)$ are capped at 1, while values below $\min(vc)$ are set to 0.

Second, following Naumann et al. (2014), the normalized indices are aggregated to derive each of the three vulnerability components: exposure (C_e), sensitivity (C_s) and adaptive capacity (C_{ac}). All normalized indices $Nv_i(0,1)$ have values between 0 and 1. Then, for each geographical unit, the vulnerability component $C_k(0,1)$ is calculated as the weighted mean of the n normalized variables $Nv_i(0,1)$ that define each component (Eq. 2):

$$C_k(0,1) = \sum_{i=1}^n w_i Nv_i(0,1) \quad (2)$$

where $C_k(0,1)$ is each vulnerability component (C_e , C_s , C_{ac}) ranging between 0 and 1. w_i are the weights of the normalized indices $Nv_i(0,1)$ of each component, with n

being the total number of normalized indices. The weights are determined through Principal Component Analysis (PCA) (Abdi and Williams 2010; Jolliffe and Cadima 2016). PCA is a robust dimensionality reduction method that identifies patterns in multivariate data by capturing maximum variance along orthogonal axes. In this study, the weights are based on the loadings of the first principal component (PC1), which explains the largest proportion of variance in each component's variables. The loadings associated with PC1, reflecting the contribution of each variable to the component, are taken in their absolute values and normalized so that their sum equaled one. This normalization process ensures that the weights accurately represent the relative contribution of each variable to the overall dataset variability. This data-driven approach avoids subjective biases, effectively accounts for correlations among variables, and ensures objective weighting within each component.

Third, the three vulnerability components are aggregated into an overall vulnerability index as the weighted mean of the components (Eq. 3):

$$V(0,1) = (w_e C_e + w_s C_s + w_{ac} (1 - C_{ac})) \quad (3)$$

where $V(0,1)$ represents the vulnerability index, C_e the exposure component, C_s the sensitivity component and C_{ac} the adaptative capacity component. To determine the weights of the components (w_e, w_s, w_{ac}), an additional PCA is conducted on the three aggregated components ($C_e, C_s, 1 - C_{ac}$). This approach ensures that the maximum variability across the components is captured, while maintaining consistency between the contributions of variables within each component and their impact on the overall index (Abdi and Williams 2010). Since there is an inverse relationship between adaptive capacity and vulnerability (i.e., lower adaptive capacity corresponds to higher vulnerability), we use $1 - C_{ac}$ for vulnerability quantification

(Tabari and Willems 2023). This approach ensures that all vulnerability components range from the least vulnerable (0) to the most vulnerable (1).

2.3.4 Risk Quantification

Risk is quantified as the product of normalized hazard and vulnerability (Peduzzi et al. 2009; Ward et al. 2020; Zhou et al. 2015), with equal weights assigned to each component (Binita et al. 2021) (Eq. 4).

$$R(0,1) = H(0,1) \times V(0,1) \quad (4)$$

where $R(0,1)$ is the risk index, $H(0,1)$ is the hazard index, and $V(0,1)$ is the vulnerability index. Both $H(0,1)$ and $V(0,1)$ are normalized on a linear scale from 0 to 1. As either component approaches zero, the risk value similarly approaches zero. Conversely, when both hazard and vulnerability reach their maximum values, the risk approaches its maximum value of 1. Consequently, $R(0,1)$ ranges between 0 and 1, though it does not follow a linear scale. Figure 2b illustrates the risk categories corresponding to various ranges of $R(0,1)$, derived from the combination of hazard and vulnerability values.

3 Vulnerability Assessment

3.1 Vulnerability Components

3.1.1 Exposure

Figure 3 presents the exposure index derived from aggregating three normalized indices: total population, crop yield, and critical infrastructure (Fig. 3a-d). The total population index (Fig. 3a) indicates that the population is generally low

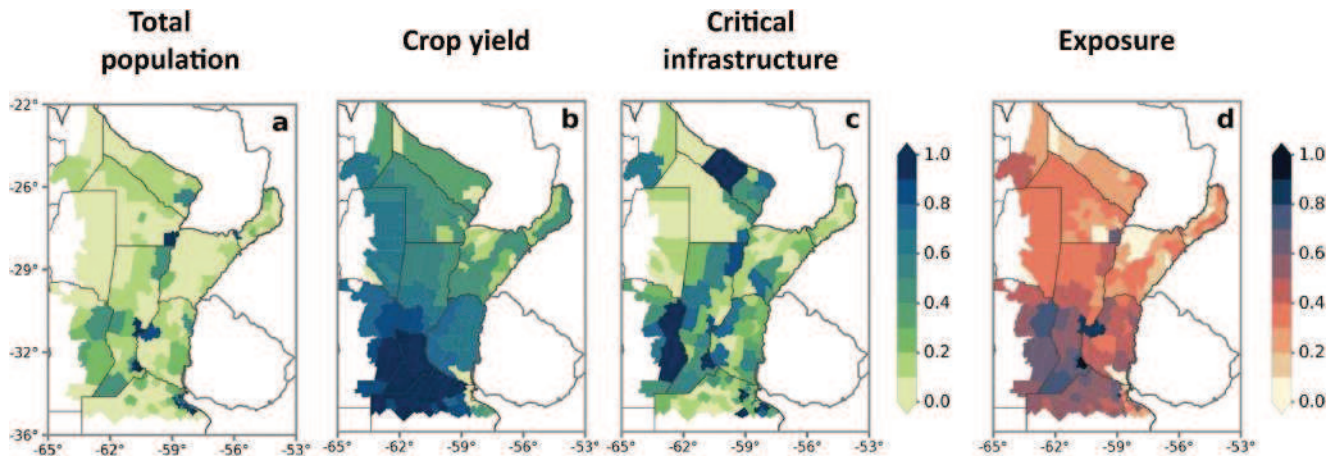


Fig. 3 Spatial distribution of the exposure index (panel d), derived from the aggregation of three normalized indices: (a) total population, (b) crop yield, and (c) critical infrastructure. The maps are presented at the departmental geographic units (administrative divisions within provinces)

Table 2 Weights of normalized variables and vulnerability components derived from principal component analysis (PCA)

| | PCA realization | Variables and components | Weights |
|--------------------------|-----------------|--------------------------|---------|
| Normalized variables | 1 | Total population | 0.392 |
| | | Crop yield | 0.534 |
| | | Critical infrastructure | 0.074 |
| | 2 | Sensitive population | 0.043 |
| | | Potential dependency | 0.272 |
| | | Income sensitivity | 0.306 |
| Vulnerability components | 3 | Land use change | 0.379 |
| | | Technological access | 0.361 |
| | | Educational attainment | 0.289 |
| | 4 | Healthcare availability | 0.351 |
| | | Exposure | 0.208 |
| | | Sensitivity | 0.306 |
| | | Adaptive capacity | 0.485 |

across the region, with an average index of 0.23. The highest population concentrations are located in departments housing major metropolitan areas, including Corrientes, Santa Fe, Paraná, Rosario, and Buenos Aires. Notably, La Matanza (Buenos Aires) and Rosario (Santa Fe) have populations 2.4 and 1.8 times greater than the third most populous department, La Plata (Buenos Aires).

The crop yield index averages 0.49 for the entire region and follows a distinct south-to-north gradient. The highest values are concentrated in Argentina's core crop region (CCR, as defined by Sgroi et al. 2021), encompassing southern Córdoba, southern Santa Fe, and northern Buenos Aires (Fig. 3b), where the highest corn and soybean yields are found (see Fig. S1). In contrast, the lowest values are observed in the northern provinces of Formosa, Corrientes, and Misiones. Nevertheless, the crop yield index remains high across most of the study area, with more than half of the region scoring above 0.6.

The critical infrastructure index (Fig. 3c) exhibits elevated values in the central and southern provinces of Santa

Fe, Buenos Aires, and Córdoba, where economic activity, population, and infrastructure are heavily concentrated. The index also highlights key transportation corridors connecting Argentina with Paraguay, Uruguay, and Brazil (see Fig. S2 for index composition). Fig. S2 shows that the most prevalent infrastructure includes land transportation networks (national and provincial highways, bridges, and railways), energy facilities (power plants and transformer stations), and water and sewage treatment plants.

The variables contribute to the exposure index with weights of 0.534 for crop yield, 0.392 for total population, and 0.074 for critical infrastructure (Table 2). Crop yield has the greatest influence, driven by its substantial spatial variability and dominance in the region, particularly in the southern areas with high agricultural productivity. Total population also plays an important role, reflecting the urban concentrations. Despite its spatial variability, the lower weight of critical infrastructure may be attributed to its correlation with population patterns, as infrastructure is often concentrated in areas with higher population densities. Consequently, its unique contribution to the variance captured by PCA is reduced.

The overall exposure index varies widely, ranging from 0 to 0.96, with a regional mean of 0.37. The highest exposure levels are concentrated in central and southern Santa Fe, eastern Córdoba, and northern Buenos Aires. This is attributed to the convergence of high crop yields in the CCR, dense population, and critical infrastructure. Conversely, the lowest exposure values occur in the northeastern provinces of Corrientes, Chaco, Formosa, and Misiones.

3.1.2 Sensitivity

Figure 4 presents the sensitivity component (Fig. 4a-e), derived from aggregating four normalized indices: sensitive population, potential dependency, income sensitivity, and land use change. The sensitive population index (Fig. 4a)

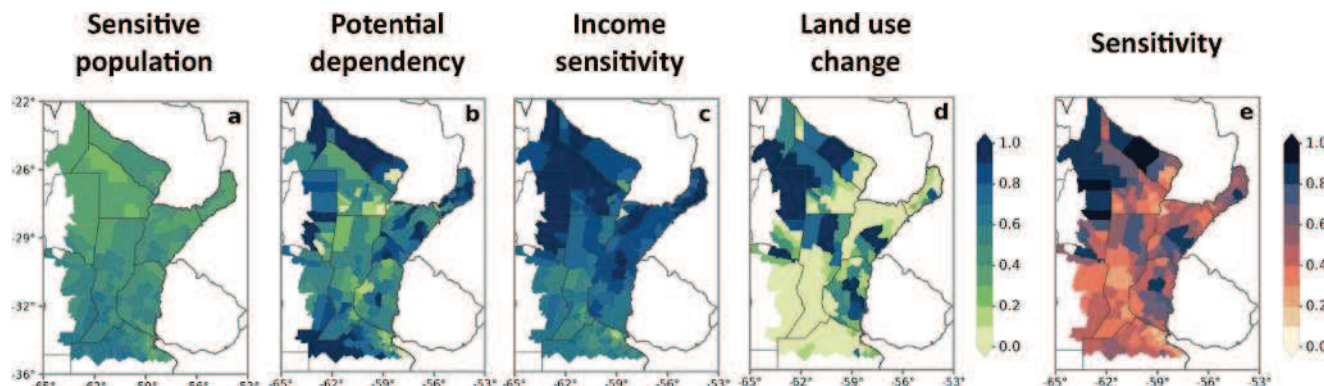


Fig. 4 Spatial distribution of the sensitivity index (panel e), derived from the aggregation of four normalized indices: (a) sensitive population, (b) potential dependency, (c) income sensitivity, and (d) land use

change. The maps are presented at the departmental geographic units (administrative divisions within provinces)

averages 0.46 across the region, with higher values concentrated in the south (up to 0.7), where a larger proportion of the population is over 65 years old (see Fig. S3). In contrast, the potential dependency index (Fig. 4b) has a regional average of 0.54, with notably higher values in the northern and southern parts of the region. This pattern reflects the age distribution, with a higher proportion of individuals under 14 years old in the north and over 65 years old in the south (see Fig. S3).

The income sensitivity index (Fig. 4c, see also Fig. S4) shows a distinct north-south gradient, with a relatively high area-averaged value of 0.67. Lower values are concentrated in the central and southern parts of the region, specifically in central and southern Santa Fe, northeastern Buenos Aires, and central-western Córdoba. This lower income sensitivity can be attributed to the dominance of agricultural activities in the CCR and the higher levels of industrial and service sector activities, as indicated in the critical infrastructure index (Fig. 3c). In contrast, the northern part of the region exhibits higher income sensitivity, primarily due to its lower agro-industrial and technological development.

The land use change index (Fig. 4d) presents high spatial variability. High values are observed in the northwest and central-east, while very low values are found in the southwest and northeast. When compared to the crop yield index (Fig. 3b), regions with very high yields, such as the CCR in the southwest, and areas with very low yields in the northeast, dominated by savannas and forests (see Bracalenti et al. 2024), align with the lowest land use change index values. In high-yield areas like the CCR, this is likely due to extensive land use for cultivation. In contrast, regions with intermediate crop yields display the highest land use change index values, likely attributable to the agricultural frontier's expansion in recent decades (Stanimirova et al. 2022; Volante et al. 2016).

The variables contribute to the sensitivity index with weights of 0.379 for land use change, 0.306 for income sensitivity, 0.272 for potential dependency, and 0.043 for sensitive population (Table 2). Land use change has the highest weight due to its significant spatial variability and impact on sensitivity, especially in regions undergoing rapid agricultural expansion in the northwest. Income sensitivity follows closely, reflecting the economic vulnerability to extreme events. Potential dependency also plays a notable role, while sensitive population has the lowest weight. This is likely due to its lower relative variability and more limited range of data, which reduces its contribution to the overall variance captured by PCA.

Sensitivity values range from 0.02 to 0.97 across the study region, with a regional mean of 0.44—higher than the average exposure value. The highest sensitivity values are linked to high income sensitivity, land use change, and potential dependency, mainly in the northwest (western Formosa, western Chaco, northern Santiago del Estero, and eastern Salta). In contrast, lower sensitivity values are found in central and southern areas (central and southern Santa Fe, northeastern Buenos Aires, and central-western Córdoba), where reduced income sensitivity reflects the concentration of the country's main economic activities.

3.1.3 Adaptive Capacity

Figure 5 illustrates the adaptive capacity component (Fig. 5a-d), derived from the aggregation of three normalized indices: access to technology, health, and education services. The technological and healthcare access indices (Fig. 5a-b) exhibit a clear south-to-north gradient, with area-averaged values of 0.57 and 0.56, respectively. When compared with the income sensitivity index (Fig. 4c), regions with higher access to technology and health services show lower

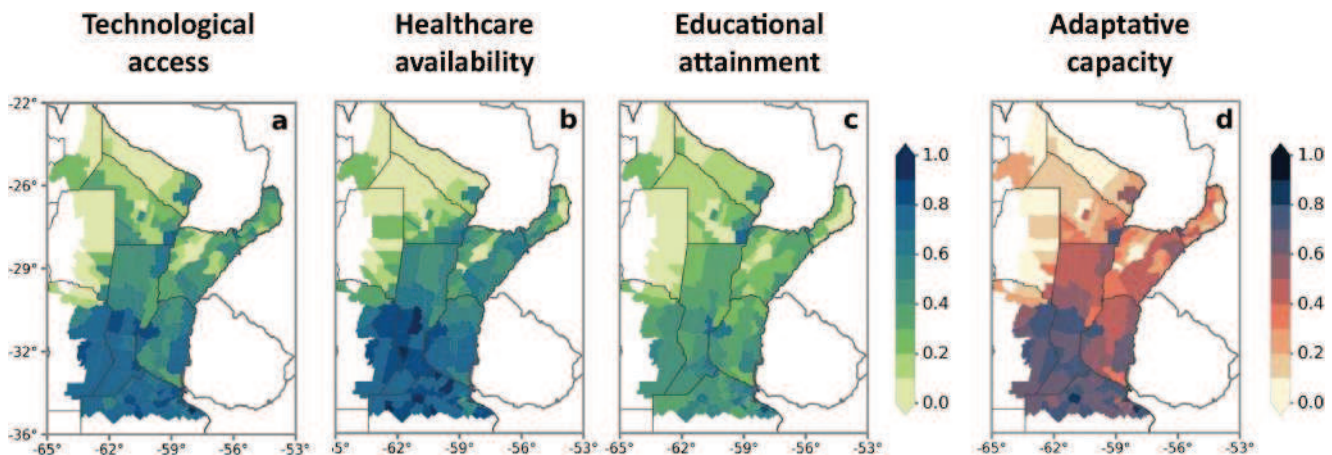


Fig. 5 Spatial distribution of the adaptive capacity index (panel d), derived from the aggregation of three normalized indices: (a) technological access, (b) healthcare availability, and (c) educational attain-

ment. The maps are presented at the departmental geographic units (administrative divisions within provinces)

income sensitivity, suggesting a potential link to greater resource availability. These regions also correspond to areas of higher productive activity, associated with higher crop yields and more critical infrastructure. Technological access is primarily achieved through mobile phones with internet connectivity, with over 70% of the population across the region having access, and more than 90% in the southern areas (see Fig. S6). Regarding healthcare access, all age groups have better access in the southern part of the region, especially adults over 65, of whom more than 95% benefit from social coverage (see Fig. S7). The educational access index (Fig. 5c) follows a similar south-to-north gradient but with a smoother transition and a lower regional average of 0.40.

The variables contribute to the adaptive capacity index with weights of 0.361 for technological access, 0.351 for healthcare availability, and 0.289 for educational attainment (Table 2). Technological access and healthcare availability have the highest weights due to their greater spatial variability and significant role in improving adaptive capacity, especially in the southern regions. Educational attainment, although important, has a slightly lower weight due to its more limited range and lower relative variability across the region. Despite exhibiting similar spatial patterns—higher values in the south and lower values in the north—these variables have similar contributions, as their variability and impact on adaptive capacity are closely linked.

The adaptive capacity index shows high spatial variability, following a clear south-to-north gradient. Since adaptive capacity is inversely related to vulnerability, higher values indicate higher ability to adapt to or cope with impacts. The highest adaptive capacity values, ranging from 0.6 to 1, are concentrated in the central and southern areas, where access to technology, health, and education is more widespread. In contrast, adaptive capacity decreases noticeably in the northern areas, with values ranging between 0 and 0.4. This disparity highlights the region's uneven ability to cope with extreme events: access to education and technology in the south enhances preventive measures, while healthcare access supports recovery and response efforts after disasters.

3.2 Vulnerability Index

Figure 6 illustrates the vulnerability index along with its contributing components. The vulnerability index is constructed using weights of 0.208 for exposure, 0.306 for sensitivity, and 0.485 for adaptive capacity (Table 2). Adaptive capacity has the highest weight, reflecting its significant role in reducing vulnerability, especially in areas with better access to resources and infrastructure. Sensitivity follows with a moderate weight, highlighting the importance of socio-economic and environmental factors in determining

vulnerability in this region. Exposure has the lowest weight, likely due to its relatively lower variability than the other components and its more uniform regional distribution.

Vulnerability within the study region varies from low to high, with values ranging from 0.1 to 0.84 and an area-averaged value of 0.45. Most of the region exhibits medium vulnerability to extreme hydrometeorological events (ranging from 0.3 to 0.7). The highest vulnerability (0.7–0.84) is concentrated in the northwest and central west areas, where high sensitivity is coupled with low adaptive capacity, despite lower exposure. In contrast, the lowest vulnerability values (from 0.1 to 0.4) are found in the central and southern regions, where lower sensitivity and higher adaptive capacity counterbalance higher exposure levels. In the central and central-west areas (central and south of Santa Fe, central-west of Córdoba), medium-low to medium vulnerability (0.3 to 0.5) results from the highest exposure but low sensitivity and high adaptive capacity. The northeastern part of Buenos Aires province shows low vulnerability (values between 0.2 and 0.3) due to medium sensitivity and exposure combined with high adaptive capacity. In the northeastern region, medium to medium-high vulnerability values (from 0.5 to 0.7) arise from low exposure, medium sensitivity, and low adaptive capacity.

4 Risk Assessment

4.1 Individual Hazard Risk

Figure 7 illustrates the risk assessment for individual hazards, derived from the product of each hazard and the vulnerability index. For long-term EHE hazards, we examine WEP and DEP events. The WEP hazard shows a regional mean of 0.51, with values ranging from very low in the northwest to high in the southeast (Fig. 7b). The resulting risk map (Fig. 7c) is similar to the hazard map but smoother due to the inverse relationship between hazard and vulnerability (Fig. 7b and a). In the southeast, high WEP hazard is moderated by lower vulnerability, leading to medium risk. In the northwest, despite low WEP hazard, high vulnerability raises the risk to medium-low. Overall, WEP risk spans from low in the northwest to medium-high in the southeast, with a regional mean of 0.21 and high frequencies within the medium range [0.17–0.21] (see histogram). The highest WEP risks, at medium levels, are concentrated in Entre Ríos, Corrientes, and Misiones.

The DEP hazard map (Fig. 7d) reveals a distinct spatial pattern, with DEP hazards ranging from low in the east to high in the west and north. In northern and western provinces (Formosa, Chaco, Salta, and Santiago del Estero), high DEP hazards combine with high vulnerabilities (Fig.

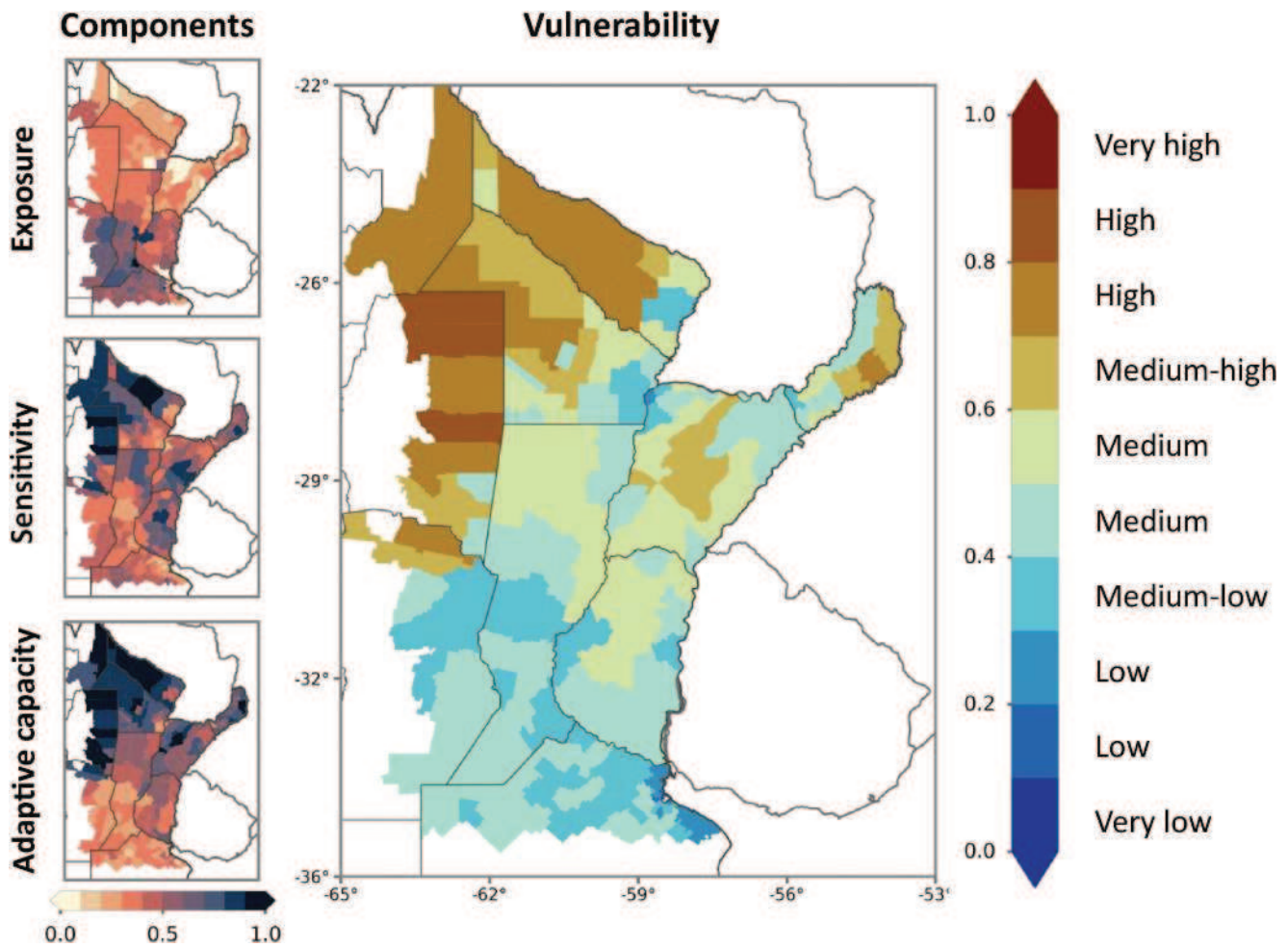


Fig. 6 Spatial distribution of the vulnerability index (main panel) derived from the aggregation of the three vulnerability components shown in the left panels: exposure, sensitivity, and adaptive capacity. The vulnerability components are disaggregated in Figs. 3 and 4, and Fig. 5, respectively. The adaptive capacity is shown on an inverted

scale compared to Fig. 5: lower capacity (increasing vulnerability) is closer to one, while higher capacity (reducing vulnerability) is closer to zero. Vulnerability levels are highlighted in the color reference, ranging from blue (very low) to dark brown (very high)

7a), resulting in medium to medium-high risk levels (Fig. 7e). These risk levels are driven by high sensitivity and low adaptive capacity (see Fig. 6). In the eastern region, where DEP hazard is low, medium vulnerability leads to medium-low and medium risk levels. The regional mean DEP risk is 0.2, representing a medium value, with the most frequent risk values falling within the medium-low range [0.10–0.16].

For short-term EHE hazards, we examine HWs, HPs, and FDs. The HW hazard (Fig. 7f) exhibits a clear north-south pattern, characterized by high hazard levels in the northern regions transitioning to medium levels in the south. In the northern provinces (Formosa, Chaco, Salta, Santiago del Estero), high HW hazards combine with high vulnerability (Fig. 7a) resulting in medium-high and high HW risks (Fig. 7g). These provinces, which commonly face extreme heat, present high sensitivity and low adaptive capacity

(Fig. 6), explaining a high level of HW risk. In the southern provinces, medium HW hazard combined with medium to medium-low vulnerability results in medium to medium-low HW risk. Overall, HW risk decreases from high in the north to medium in the south, with a regional mean risk of 0.25 and the highest frequencies observed in the medium-risk range [0.16–0.20].

The HP hazard map (Fig. 7h) shows a noticeable maximum in northeastern areas, gradually decreasing towards the south and west. In Misiones, high HP hazard combined with medium-high vulnerability (Fig. 7a) leads to high HP risk (Fig. 7i). In Corrientes and eastern Formosa, lower vulnerability helps reduce the overall risk. The rest of the domain presents medium to low risk, mostly driven by low HP hazard. The most frequent risk values are observed in the low range [0.05–0.08].

The FD hazard (Fig. 7j) is predominantly very low across the region. Since vulnerability acquires medium and high levels in certain areas, the resulting FD risk is generally low across the study region (Fig. 7k). The FD risk exhibits a smooth east-to-west gradient, ranging from medium-low to low in the east to very low to low in the west.

4.2 Multi-hazard Risk

Figure 8 presents the risk assessment for multi-hazards, derived from the product of each multi-hazard and the vulnerability index. We assess the long-term multi-hazard (LT-mH), short-term multi-hazard (ST-mH), and total multi-hazard (T-mH) that combines LT-mH and ST-mH indices. The LT-mH (Fig. 8b) shows an area-averaged value of 0.46, with medium to medium-high levels in the west and southwest, and medium-low in the north and northeast. In the southwestern region, encompassing southwestern Córdoba, southern Santa Fe, and northern Buenos Aires, medium to medium-high LT-mH are associated with the concurrence of high WEP and DEP hazards. Across the region, LT-mH risk (Fig. 8c) is predominantly medium, with the highest frequencies within the range of [0.17–0.21]. Notably, LT-mH risk has the highest regional mean among all the multi-hazard risks evaluated (Fig. 8c, e, g). The LT-mH risk remains medium across most of the region, although the underlying factors vary: in the northern provinces, medium-low LT-mH combined with medium-high to high vulnerabilities elevates the risk to medium levels, while in the south, medium to medium-high LT-mH values coupled with medium to medium-low vulnerabilities, keep the risk at medium levels.

The ST-mH (Fig. 8d) predominantly shows low to medium-low values, with a regional mean of 0.31, following a northeast-to-southwest gradient. Maximum values (~0.5) occur in the northeast due to the combination of high HW and HP hazards (see Fig. 7f and h). ST-mH risk ranges from low to medium, being the lowest regional risk among the assessed multi-hazards. In many areas, risk levels exceed the hazard levels due to the combination of low to medium-low hazard values with medium-high to high vulnerability.

The T-mH (Fig. 8f) exhibits predominantly medium-low to medium values, heterogeneously distributed across the domain. In the west, medium values are associated with higher long-term multi-hazards, while in the northeast, they are driven by higher short-term multi-hazards. When combined with vulnerability, the T-mH results in a higher overall risk, with many areas experiencing an increase from medium-low hazard to medium risk (Fig. 8g). The regional mean for T-mH risk is 0.18, indicating a medium level of risk.

5 Discussion

This study assesses vulnerability and risk to extreme hydrometeorological events at a subnational scale in central-northeastern Argentina. Our approach combines physical and socio-economic data from multiple sources to evaluate vulnerability and considers individual EHE hazards and multi-hazards across long- and short-term scales. By examining individual and multi-hazard risks separately, the study provides a deeper understanding of how the region's overall risk to EHEs is composed. EHE risk emerges from the interaction between EHE hazard and vulnerability. Vulnerability is analyzed through its three components: exposure, sensitivity, and adaptive capacity. Vulnerability is studied as a risk component and an independent factor to enhance our understanding of how different socio-economic contexts can shape EHE risks. This understanding is critical in linking climate adaptation strategies with disaster risk reduction efforts (IPCC et al. 2022a).

We apply PCA to assign weights to the variables in the vulnerability index, effectively highlighting geographic differences. PCA provides a more accurate representation of the factors driving vulnerability by emphasizing variables with higher variance (Abson et al. 2012). The PCA-derived weights enhance the overall variance of the index, providing a clearer understanding of vulnerability drivers and helping to identify regions with greater intervention needs. In this study, adaptive capacity, which shows substantial north-south variability, received the highest weight ($w_{ac} = 0.485$), while exposure contributed less due to its limited variability ($w_e = 0.208$). Although the method prioritizes variables with higher variance, those with lower variance but still relevant for vulnerability may be underrepresented, a factor to consider when interpreting the results and designing strategies.

Our vulnerability assessment reveals a dominant medium average vulnerability level across the region. However, distinct patterns highlight three specific areas with varying vulnerability levels that require tailored risk management strategies. First, the central region—particularly southern Santa Fe, eastern Córdoba, and northern Buenos Aires—presents medium-low to medium vulnerability. This region combines the highest exposure due to the convergence of high population, critical infrastructure, and significant crop yields, with low sensitivity and high adaptive capacity due to agro-industrial and technological advancements. Second, the northwest and central-west regions—specifically Formosa, eastern Salta, and eastern Santiago del Estero—present the highest vulnerability (medium-high to high levels), mainly due to high sensitivity and very low adaptive capacity, despite lower exposure levels. These regions' limited agro-industrial and technological development contrasts

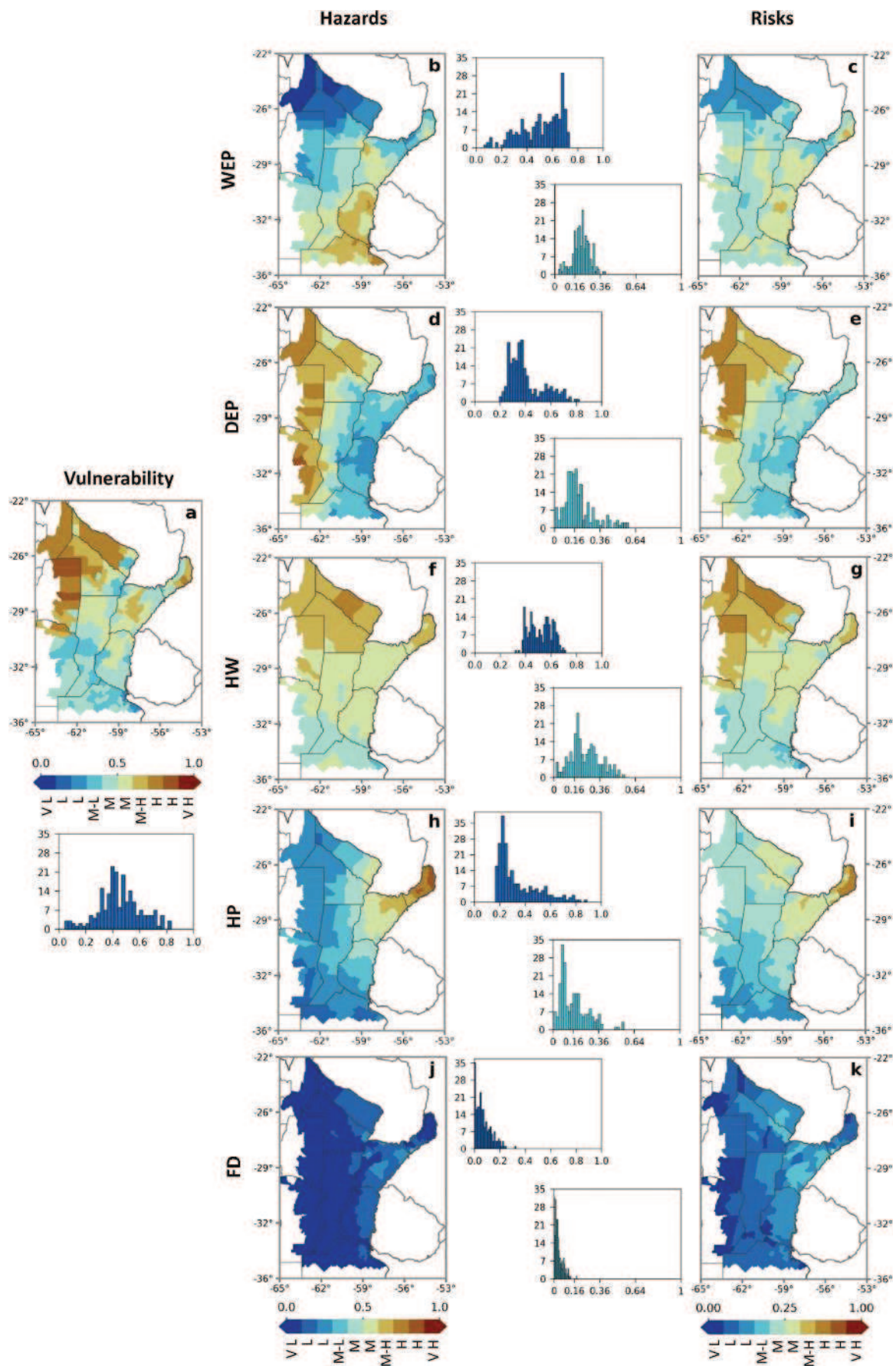


Fig. 7 Spatial analysis of individual hazard risks. Panel (a) presents the vulnerability index (detailed in Fig. 6) to support the assessment of the risk components. The figure displays the hazard levels (left column) and their corresponding risks (right column) for five types of extreme hydrometeorological events: wet extreme precipitation events (WEP, panels b and c), dry extreme precipitation events (DEP, panels d and e), heatwaves (HW, panels f and g), heavy precipitation events (HP, panels h and i), and flash droughts (FD, panels j and k). Each map is accompanied by a histogram showing the frequency distribution of values

sharply with the central areas. Third, the remaining areas experience medium vulnerability, characterized by low to moderate exposure, medium-high sensitivity, and medium-low adaptive capacity.

Among individual risks, our findings suggest that heatwave risk is the highest and most widespread across central-northeastern Argentina. It reaches medium-high to high levels in the north and low to medium levels in the south. This high risk aligns with the global increase in heatwave frequency and severity (Perkins-Kirkpatrick and Lewis 2020), particularly notable in northern Argentina (Cimolai and Aguilar 2024; Lovino et al. 2018a). Following heatwaves, long-term dry and wet extreme precipitation events exhibit medium risk levels, with distinct spatial distributions. In the northwest, DEP risk is high and WEP risk is low. Conversely, in the southeast, DEP risk is low to medium-low while WEP risk is medium to medium-high. Thus, the highest DEP risk (and lowest WEP risk) is concentrated in the arid Chaco Seco region, while the highest WEP risk (and lowest DEP risk) occurs in the humid plains of the western study area.

Our results report that heavy precipitation risk is high in the northeastern provinces, where frequent and severe convective precipitation occurs (Rasmussen et al. 2016; Zhang et al. 2021). Flash drought risk is notably lower in the study region due to the relatively low frequency of these events compared to other hazards (Pierrestegui et al. 2024). Importantly, heatwaves and long-term dry extreme precipitation events, which exhibit the highest local and regional risk, coincide with high hazard levels in the north and northwest, where vulnerability is also highest. In contrast, despite presenting the highest local hazard levels, heavy precipitation risk is mitigated by medium vulnerability, placing it third among individual risks.

Our findings suggest that short-term risk may exacerbate the impacts of long-term extreme precipitation events. In the north and northwest, agricultural and hydrological droughts may be compounded by heatwaves. This combination intensifies drought conditions (Miralles et al. 2019; Naumann et al. 2019), exacerbating the impacts, especially given the region's higher vulnerability levels. Meanwhile, in the northeast, long-term wet extreme events may be

favored and exacerbated by heavy precipitation events, thus amplifying the risk of water excesses.

6 Conclusions

Despite uncertainties in the datasets, this study offers valuable insights for improving hydrometeorological risk management in central-northeastern Argentina. Long-term multi-hazard risk is the most extensive and severe across the region, indicating the potential for both wet and dry extreme precipitation events to impact large areas. This risk is particularly medium-high in the west, where agricultural and hydrological droughts and extended periods of water excess are frequent and intense (Cerón et al. 2021; Lovino et al. 2022). Short-term multi-hazard risk is less widespread, primarily due to concentrated heavy precipitation hazards in the northeast and a low flash drought hazard across the region, despite extensive and severe heatwave hazards.

Our findings provide critical insights for improving risk planning, management, and climate change adaptation, with important implications for public policy. A better understanding of the diverse hazards and regional vulnerabilities to extreme hydroclimatic events will enable policymakers to develop more targeted and effective strategies to mitigate impacts in central-northeastern Argentina. Tailored risk management strategies should reflect the varying levels of vulnerability and risk. In the south, where economic activities and critical infrastructure are concentrated, reducing exposure through infrastructure adaptation and climate-smart agricultural practices is crucial. In the north, promoting climate-resilient development can reduce sensitivity and enhance adaptive capacity, addressing frequent and severe extreme events.

Future research should refine vulnerability assessments by incorporating high-resolution socio-economic and environmental data, integrating other multivariate analysis techniques to complement the insights derived from PCA. Developing frameworks to address cascading and compounding risks will further enhance understanding and inform policy. These advancements are crucial for improving hydrometeorological risk management and promoting sustainable adaptation strategies in vulnerable regions like central-northeastern Argentina.

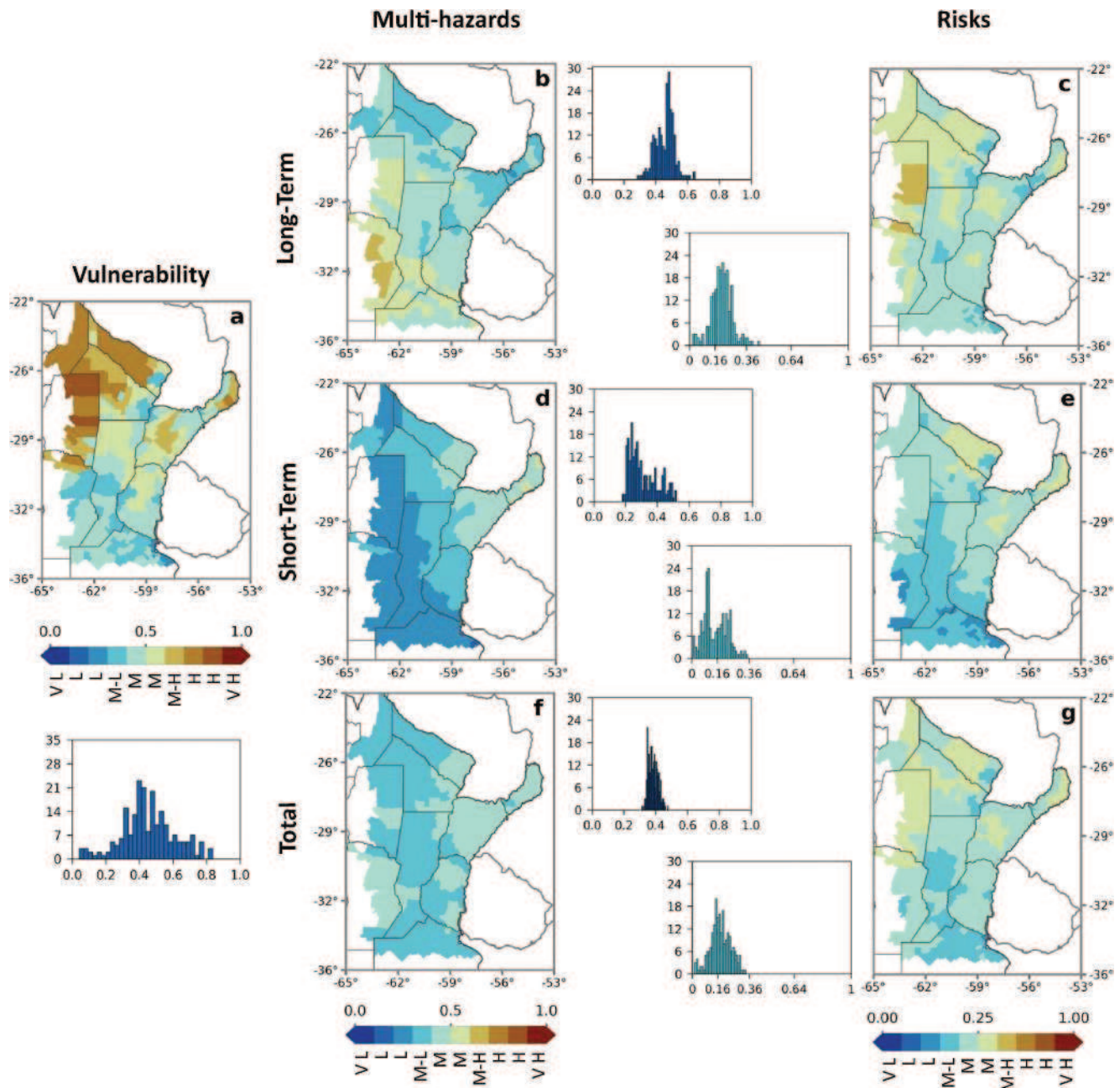


Fig. 8 Spatial analysis of multi-hazard risks. Panel (a) shows the vulnerability index (details in Fig. 6) to support the assessment of risk components. The figure displays the hazard levels (left column) and their corresponding risks (right column) for long-term multi-hazard

(panels b and c), short-term multi-hazard (panels d and e), and total multi-hazard (panels f and g). Each map is accompanied by a histogram showing the frequency distribution of values

Supplementary Information The online version contains supplementary material available at <https://doi.org/10.1007/s41748-025-00587-1>.

Acknowledgements The Scientific color maps Navia, Lipari, and Roma (Cramer 2018) are used in this study (Figs. 2, 3, 4, 5, 6, 7 and 8) to prevent visual distortion of the data and exclusion of readers with color-vision deficiencies (Cramer et al. 2020).

Author Contributions M. Josefina Pierrestegui and Miguel A. Lovino designed the study. M. Josefina Pierrestegui carried out the research.

M. Josefina Pierrestegui, Miguel A. Lovino, Omar V. Müller, and Gabriela V. Müller analyzed and discussed the results. Miguel A. Lovino and Gabriela V. Müller acquired funding and resources. M. Josefina Pierrestegui prepared the first draft of the manuscript, and all authors contributed to its previous versions. All authors read and approved the final manuscript.

Funding This research was funded by Argentina's National Agency for Scientific and Technological Promotion (Projects PICT-2019-2019-03982 and PICT-2019-2019-00481), and the Argentine National Council for Scientific and Technical Research (Grant PIP-CONICET-

11220200102257CO).

Declarations

Competing Interests The authors declare that they have no competing financial or non-financial interests to disclose.

References

- Abdi H, Williams LJ (2010) Principal component analysis. Wiley Interdiscip Rev Comput Stat 2:433–459. <https://doi.org/10.1002/wics.10>
- Abson DJ, Dougill AJ, Stringer LC (2012) Using principal component analysis for information-rich socio-ecological vulnerability mapping in Southern Africa. Appl Geogr 35(1–2):515–524. <https://doi.org/10.1016/j.apgeog.2012.08.004>
- Agosta EA, Rabassa MJ, Florio L, Torrero MP (2021) Floods in Eastern Subtropical Argentina: the contributing roles of Climate Change and Socioeconomics. In: Belfiori ME, Rabassa MJ (eds) The Economics of Climate Change in Argentina. The Latin American Studies Book Series. Springer, Cham, pp 45–67. https://doi.org/10.1007/978-3-030-62252-7_3
- Almazroui M, Ashfaq M, Islam MN et al (2021a) Assessment of CMIP6 performance and projected temperature and precipitation changes over South America. Earth Syst Environ 5:155–183. <https://doi.org/10.1007/s41748-021-00233-6>
- Almazroui M, Saeed F, Saeed S et al (2021b) Projected changes in climate extremes using CMIP6 simulations over SREX regions. Earth Syst Environ 5:481–497. <https://doi.org/10.1007/s41748-021-00250-5>
- Alvala R, Ribeiro DF, Marengo JA, Seluchi ME, Gonçalves DA, Antunes da Silva L, Cuartas Pineda LA, Saito SM (2024) Analysis of the hydrological disaster that occurred in the state of Rio Grande do Sul in September 2023: vulnerabilities and risk management capabilities. Int J Disaster Risk Reduct 110:104645. <https://doi.org/10.1016/j.ijdr.2024.104645>
- Ara Begum R, Lempert R, Ali E et al (2022) Point of departure and key concepts. In: Pörtner H-O, Roberts DC, Tignor M et al (eds) Climate Change 2022: impacts, adaptation and vulnerability. Contribution of Working Group II to the Sixth Assessment Report of the Intergovernmental Panel on Climate Change. Cambridge University Press, Cambridge, UK and New York, NY, USA, pp 121–196. <https://doi.org/10.1017/9781009325844.003>
- Avila-Díaz A, Benezoli V, Justino F, Torres R, Wilson A (2020) Assessing current and future trends of climate extremes across Brazil based on reanalyses and earth system model projections. Clim Dyn 55(5–6):1403–1426. <https://doi.org/10.1007/s00382-020-05333-z>
- Barros VR, Boninsegna JA, Camilloni IA, Chidiak M, Magrin GO, Rusticucci M (2015) Climate change in Argentina: trends, projections, impacts and adaptation. WIREs Clim Change 6:151–169. <https://doi.org/10.1002/wcc.316>
- Beck H, Zimmermann N, McVicar T et al (2018) Present and future Köppen-Geiger climate classification maps at 1-km resolution. Sci Data 5:180214. <https://doi.org/10.1038/sdata.2018.214>
- Benítez V, Forgione F, Lovino MA, Sgroi L, Doyle M, Müller GV (2024) Capability of satellite data to estimate observed precipitation in southeastern South America. Int J Climatol 44(3):792–811. <https://doi.org/10.1002/joc.8356>
- Berbery EH, Barros V (2002) The hydrologic cycle of the La Plata basin in South America. J Hydrometeor 3:630–645. https://journals.ametsoc.org/view/journals/hydr/3/6/1525-7541_2002_003_0630_thcotl_2_0_co_2.xml
- Bert F, de Estrada M, Naumann G, Negri R, Podestá G, de los Milagros Skansi M, Spennemann P, Quesada M (2021) The 2017–18 drought in the Argentine Pampas—Impacts on agriculture. In: GAR Special Report on Drought. United Nations Office for Disaster Risk Reduction. Available via UNDRR. <https://www.unndrr.org/publication/2017-18-drought-argentine-pampas-impacts-agriculture-0>. Accessed 6 Jan 2025
- Binita KC, Shepherd JM, King AW et al (2021) Multi-hazard climate risk projections for the United States. Nat Hazards 105:1963–1976. <https://doi.org/10.1007/s11069-020-04385-y>
- Birkmann J, Cardona OD, Carreño ML et al (2013) Framing vulnerability, risk and societal responses: the MOVE framework. Nat Hazards 67:193–211. <https://doi.org/10.1007/s11069-013-0558-5>
- Birkmann J, Jamshed A, McMillan JM et al (2022) Understanding human vulnerability to climate change: a global perspective on index validation for adaptation planning. Sci Total Environ 803:150065. <https://doi.org/10.1016/j.scitotenv.2021.150065>
- Bohn VY, Piccolo MC (2019) Estimation of hydrological vulnerability in river basins of Argentinean plains. Int J River Basin Manag 19(4):445–457. <https://doi.org/10.1080/15715124.2019.1683855>
- Bortz PG, Toftum N (2023) Changes in rainfall, agricultural exports and reserves: macroeconomic impacts of climate change in Argentina. J Environ Econ Policy 13:243–258. <https://doi.org/10.1080/21606544.2023.2236987>
- Borzi G, Roig A, Tanjal C et al (2021) Flood hazard assessment in large plain basins with a scarce slope in the Pampean Plain, Argentina. Environ Monit Assess 193:177. <https://doi.org/10.1007/s10661-021-08988-1>
- Bracalenti MA, Müller OV, Lovino MA, Berbery EH (2024) The agricultural expansion in South America's dry Chaco: regional hydro-climate effects. Hydrol Earth Syst Sci. <https://doi.org/10.5194/hess-28-3281-2024>
- Camilloni I, Barros V, Moreiras S, Poveda G, Tomasella J (2020) Floods and droughts. In: Moreno JM, Laguna-Defi C, Barros V, Calvo Buendia E, Marengo JA, Oswald Spring U (eds) Adaptation to climate change risks in Ibero-American countries—RIOC-CADAPT report. McGraw Hill, Madrid, Spain, pp 391–417. ISBN 9788448621667
- Castellanos E, Lemos MF, Astigarraga L et al (2022) Central and South America. In: Pörtner H-O, Roberts DC, Tignor M et al (eds) Climate Change 2022: impacts, adaptation and vulnerability. Contribution of Working Group II to the Sixth Assessment Report of the Intergovernmental Panel on Climate Change. Cambridge University Press, Cambridge, UK and New York, NY, USA, pp 1689–1816. <https://doi.org/10.1017/9781009325844.014>
- Cerón WL, Kayano MT, Andreoli RV et al (2021) Recent intensification of extreme precipitation events in the La Plata Basin in southern South America (1981–2018). Atmos Res 249:105299. <https://doi.org/10.1016/j.atmosres.2020.105299>
- Cimolai C, Aguilar E (2024) Assessing Argentina's heatwave dynamics (1950–2022): a comprehensive analysis of temporal and spatial variability using ERA5-LAND. Theor Appl Climatol 155:4925–4940. <https://doi.org/10.1007/s00704-024-04915-9>
- Crameri F (2018) Scientific colour maps. <https://doi.org/10.5281/zenodo.1243862>. Zenodohttps://zenodo.org/records/4491293
- Crameri F, Shephard GE, Heron PJ (2020) The misuse of colour in science communication. Nat Commun 11:5444. <https://doi.org/10.1038/s41467-020-19160-7>
- De Luca P, Donat MG (2023) Projected changes in hot, dry, and compound hot-dry extremes over global land regions. Geophys Res Lett 50. <https://doi.org/10.1029/2022GL102493.e2022GL102493>
- Farahmand A, AghaKouchak A (2015) A generalized framework for deriving nonparametric standardized drought indicators. Adv Water Resour 76:140–145. <https://doi.org/10.1016/j.advwatres.2014.11.012>

- Ford JD, Pearce T, McDowell G et al (2018) Vulnerability and its discontents: the past, present, and future of climate change vulnerability research. *Clim Change* 151:189–203. <https://doi.org/10.1007/s10584-018-2304-1>
- Füssel H-M (2007) Vulnerability: a generally applicable conceptual framework for climate change research. *Glob Environ Change* 17:155–167. <https://doi.org/10.1016/j.gloenvcha.2006.05.002>
- Garschagen M, Doshi D, Reith J, Hagenlocher M (2021) Global patterns of disaster and climate risk—an analysis of the consistency of leading index-based assessments and their results. *Clim Change* 169:11. <https://doi.org/10.1007/s10584-021-03209-7>
- González FAI, Santos ME, London S (2021) Multidimensional Poverty and Natural disasters in Argentina (1970–2010). *J Hum Dev Capabilities* 23:206–227. <https://doi.org/10.1080/19452829.2021.1910220>
- Hagen I, Huggel C, Ramajo L, Chacón N, Ometto P, Postigo JC, Castellanos EJ (2022) Climate change-related risks and adaptation potential in Central and South America during the 21st century. *Environ Res Lett* 17(3):033002. <https://doi.org/10.1088/1748-9326/ac5271>
- Hao Z, AghaKouchak A (2014) A nonparametric multivariate multiindex drought monitoring framework. *J Hydrometeorol* 15(1):89–101. <https://doi.org/10.1175/JHM-D-12-0160.1>
- Hersbach H, Bell B, Berrisford P et al (2020) The ERA5 global reanalysis. *Q J R Meteorol Soc* 146:1999–2049. <https://doi.org/10.1002/qj.3803>
- Hersbach H, Bell B, Berrisford P et al (2023a) ERA5 hourly data on single levels from 1940 to present. Copernicus Climate Change Service (C3S) Climate Data Store (CDS). <https://doi.org/10.24381/cds.adbb2d47> (Accessed September 2023)
- Hersbach H, Bell B, Berrisford P et al (2023b) ERA5 monthly averaged data on single levels from 1940 to present. Copernicus Climate Change Service (C3S) Climate Data Store (CDS). <https://doi.org/10.24381/cds.f17050d7> (Accessed May 2023)
- Houspanossian J, Giménez R, Whitworth-Hulse JI et al (2023) Agricultural expansion raises groundwater and increases flooding in the South American Plains. *Science* 380:1344–1348. <https://doi.org/10.1126/science.add5462>
- IGN (Instituto Geográfico Nacional) (2021) GIS layers. In: IGN Geospatial Information Portal. Available via: <https://www.ign.gob.ar/NuestrasActividades/InformacionGeoespacial/CapasSIG> (Accessed September 2024)
- INDEC (Instituto Nacional de Estadística y Censos) (2022) Final results of the 2022 National Population, Household and Housing Census. Geographic layers of statistical information. In: Statistical geoportal. Available in: <https://portalgeoestadistico.indec.gob.ar/> (Accessed June 2024)
- IPCC (2022a) Summary for policymakers [Pörtner]. In: Roberts H-O, Poloczanska DC, Pörtner ES, Roberts H-O, Tignor DC M et al (eds) Climate Change 2022: impacts, adaptation and vulnerability. Contribution of Working Group II to the Sixth Assessment Report of the Intergovernmental Panel on Climate Change. Cambridge University Press, Cambridge, UK and New York, NY, USA, pp 3–33. <https://doi.org/10.1017/9781009325844.001>
- IPCC, Annex II (2022b) Glossary [Möller V. In: van Diemen R, Matthews JBR J. In:, Pörtner H-O, Roberts DC, Tignor M et al (eds) Climate Change 2022: impacts, adaptation and vulnerability. Contribution of Working Group II to the Sixth Assessment Report of the Intergovernmental Panel on Climate Change. Cambridge University Press, Cambridge, UK and New York, NY, USA, pp 2897–2930. <https://doi.org/10.1017/9781009325844.029>
- Jolliffe IT, Cadima J (2016) Principal component analysis: a review and recent developments. *Philos Trans R Soc Math Phys Eng Sci* 374:20150202. <https://doi.org/10.1098/rsta.2015.0202>
- Jurgilevich A, Räsänen A, Groundstroem F, Juhola S (2017) A systematic review of dynamics in climate risk and vulnerability assessments. *Environ Res Lett* 12(1):13002. <https://doi.org/10.1088/1748-9326/aa5508>
- Liu Z, Lv A, Li T (2025) Intensified Drought Threatens Future Food Security in Major Food-Producing Countries. *Atmosphere* 16:34. <https://doi.org/10.3390/atmos16010034>
- Lovino MA (2020) Chap. 6: Latin America's vulnerability to climate change and variability. In: Martínez-Austria PF, Coron-Vásquez B, Patiño-Gómez C (Eds) Climate change and hydrometeorological risks. Universidad de las Américas, Puebla, México. Pp. 106–123. ISBN: 978-607-8674-25-1. Available at: <https://www.udlap.mx/catedraunesco/libro-cambio-climatico-capitulos.aspx#1> (In Spanish)
- Lovino MA, Müller OV, Berbery EH, Müller GV (2018a) How have daily climate extremes changed in the recent past over northeastern Argentina? *Glob Planet Change* 168:78–97. <https://doi.org/10.1016/j.gloplacha.2018.06.008>
- Lovino MA, Müller OV, Müller GV, Sgroi LC, Baethgen WE (2018b) Interannual-to-multidecadal hydroclimate variability and its sectoral impacts in northeastern Argentina. *Hydrol Earth Syst Sci* 22:3155–3174. <https://doi.org/10.5194/hess-22-3155-2018>
- Lovino MA, Müller GV, Pierrestegui MJ, Espinosa E, Rodríguez L (2022) Extreme precipitation events in the Austral Chaco region of Argentina. *Int J Climatol* 42(11):5985–6006. <https://doi.org/10.1002/joc.7572>
- Lovino MA, Pierrestegui MJ, Müller OV, Müller GV, Berbery EH (2024) The prevalent life cycle of agricultural flash droughts. *Npj ClimAtmos Sci* 7:73. <https://doi.org/10.1038/s41612-024-00618-0>
- Magrin GO, Marengo JA, Boulanger J-P et al (2014) Central and South America. In: Barros VR, Field CB, Dokken DJ (eds) Climate Change 2014: impacts, adaptation, and vulnerability. Part B: Regional aspects. Contribution of Working Group II to the Fifth Assessment Report of the Intergovernmental Panel on Climate Change. Cambridge University Press, Cambridge, United Kingdom and New York, NY, USA, pp 1499–1566. <https://doi.org/10.1017/CBO9781107415386>
- MAGyP (Ministerio de Agricultura, Ganadería y Pesca de la Nación) (2021a) Corn time series. In: Datos Argentina. Available via: <https://datos.gob.ar/dataset/agroindustria-maiz---siembra-cosecha-produccion-rendimiento> (Accessed April 2024)
- MAGyP (Ministerio de Agricultura, Ganadería y Pesca de la Nación) (2021b) Soybean time series. In: Datos Argentina. Available via: <https://datos.gob.ar/dataset/agroindustria-soja---siembra-cosecha-produccion-rendimiento> (Accessed April 2024)
- McDowell G, Ford J, Jones J (2016) Community-level climate change vulnerability research: trends, progress, and future directions. *Environ Res Lett* 11(3):33001. <https://doi.org/10.1088/1748-9326/11/3/033001>
- Miralles DG, Gentile P, Seneviratne SI, Teuling AJ (2019) Land-atmospheric feedbacks during droughts and heatwaves: state of the science and current challenges. *Ann N Y Acad Sci* 1436:19–35. <https://doi.org/10.1111/nyas.13912>
- Naumann G, Barbosa P, Garrote L, Iglesias A, Vogt J (2014) Exploring drought vulnerability in Africa: an indicator based analysis to be used in early warning systems. *Hydrol Earth Syst Sci* 18:1591–1604. <https://doi.org/10.5194/hess-18-1591-2014>
- Naumann G, Vargas WM, Barbosa P, Blauth V, Spinoni J, Vogt JV (2019) Dynamics of Socioeconomic exposure, vulnerability and impacts of recent droughts in Argentina. *Geosciences* 9:39. <https://doi.org/10.3390/geosciences9010039>
- Naylor A, Ford J, Pearce T, Van Alstine J (2020) Conceptualizing climate vulnerability in complex adaptive systems. *One Earth* 2(5):444–454. <https://doi.org/10.1016/j.oneear.2020.04.011>
- O'Neill B, van Aalst M, Zaiton Ibrahim Z et al (2022) Key risks across sectors and regions. In: Pörtner H-O, Roberts DC, Tignor M et al (eds) Climate Change 2022: impacts, adaptation and vulnerability.

- Contribution of Working Group II to the Sixth Assessment Report of the Intergovernmental Panel on Climate Change. Cambridge University Press, Cambridge, UK and New York, NY, USA, pp 2411–2538. <https://doi.org/10.1017/9781009325844.025>
- Olmo M, Bettolli ML, Rusticucci M (2020) Atmospheric circulation influence on temperature and precipitation individual and compound daily extreme events: spatial variability and trends over southern South America. *Weather Clim Extremes* 29:100267. <https://doi.org/10.1016/j.wace.2020.100267>
- Olmo ME, Weber T, Teichmann C, Bettolli ML (2022) Compound events in South America using the CORDEX-CORE ensemble: Current climate conditions and future projections in a global warming scenario. *Journal of Geophysical Research: Atmospheres* 127, e2022JD037708. <https://doi.org/10.1029/2022JD037708>
- Oppenheimer M, Campos M, Warren R, Birkmann J, Luber G, O'Neill B, Takahashi K (2014) Emergent risks and key vulnerabilities. In: Field CB, Barros VR, Dokken DJ (eds) Climate Change 2014: impacts, adaptation, and vulnerability. Part A: global and sectoral aspects. Contribution of Working Group II to the Fifth Assessment Report of the Intergovernmental Panel of Climate Change. Cambridge University Press, Cambridge, UK and New York, NY, USA, pp 1039–1099. <https://doi.org/10.1017/CBO9781107415379>
- Peduzzi P, Dao H, Herold C, Mouton F (2009) Assessing global exposure and vulnerability towards natural hazards: the Disaster Risk Index. *Nat Hazards Earth Syst Sci* 9:1149–1159. <https://doi.org/10.5194/nhess-9-1149-2009>
- Perkins SE, Alexander LV (2013) On the measurement of heat waves. *J Clim* 26:4500–4517. <https://doi.org/10.1175/JCLI-D-12-00383.1>
- Perkins-Kirkpatrick SE, Lewis SC (2020) Increasing trends in regional heatwaves. *Nat Commun* 11:3357. <https://doi.org/10.1038/s41467-020-16970-7>
- Pierrestegui MJ, Lovino MA, Müller GV, Müller OV (2024) Multi-hazard Assessment of Extreme Hydrometeorological events in Southeastern South America. *Earth Syst Environ.* <https://doi.org/10.1007/s41748-024-00450-9>
- Pizzorni M, Innocenti A, Tollin N (2024) Droughts and floods in a changing climate and implications for multi-hazard urban planning: a review. *City Environ Interact* 24:100169. <https://doi.org/10.1016/j.cacint.2024.100169>
- Rasmussen KL, Chaplin MM, Zuluaga MD, Houze RA (2016) Contribution of Extreme Convective storms to Rainfall in South America. *J Hydrometeorol* 17:353–367. <https://doi.org/10.1175/JHM-D-15-0067.1>
- Rising J, Tedesco M, Piontek F, Stainforth DA (2022) The missing risks of climate change. *Nature* 610:643–651. <https://doi.org/10.1038/s41586-022-05243-6>
- Sgroi LC, Lovino MA, Berbery EH, Müller GV et al (2021) Characteristics of droughts in Argentina's core crop region. *Hydroclim Earth Syst Sci* 25(5):2475–2490. <https://doi.org/10.5194/hess-25-2475-2021>
- Sharma J, Ravindranath NH (2019) Applying IPCC 2014 framework for hazard-specific vulnerability assessment under climate change. *Environ Res Commun* 1:51004. <https://doi.org/10.1088/2515-7620/ab24ed>
- Stalhandske Z, Steinmann CB, Meiler S et al (2024) Global multi-hazard risk assessment in a changing climate. *Sci Rep* 14:5875. <https://doi.org/10.1038/s41598-024-55775-2>
- Stanimirova R, Graesser J, Olofsson P, Friedl MA (2022) Widespread changes in 21st century vegetation cover in Argentina, Paraguay, and Uruguay. *Remote Sens Environ* 282:113277. <https://doi.org/10.1016/j.rse.2022.113277>
- Tabari H, Willems P (2023) Global risk assessment of compound hot-dry events in the context of future climate change and socioeconomic factors. *npj Clim Atmos Sci* 6:74. <https://doi.org/10.1038/s41612-023-00401-7>
- Tomasz EO, Vilker AS, Pérez-Franco I, García-García A (2024) Impact valuation of droughts in soybean and maize production: the case of Argentina. *Int J Clim Change Strategies Manage* 16:63–90. <https://doi.org/10.1108/IJCCSM-11-2022-0139>
- UNDRR (UN Office for Disaster Risk Reduction) (2019) Global Assessment Report on Disaster Risk reduction. United Nations, Geneva, Switzerland
- USAID (United States Agency for International Development) (2016) Climate Vulnerability Assessment: An Annex to the USAID Climate-Resilient Development Framework. Technical report No. AID-OAA-TO-11-00040. Available via: <https://www.climateinknowledge.org/sites/default/files/asset/document/USAID%20Vulnerability%20Assessment%20Annex.pdf> (Accessed October 2024)
- Viner D, Ekstrom M, Hulbert M, Warner NK, Wreford A, Zommers Z (2020) Understanding the dynamic nature of risk in climate change assessments—A new starting point for discussion. *Atmos Sci Lett* 21:e958. <https://doi.org/10.1002/asl.958>
- Volante JN, Mosciaro MJ, Gavier-Pizarro GI, Paruelo JM (2016) Agricultural expansion in the Semiarid Chaco: poorly selective contagious advance. *Land Use Policy* 55:154–165. <https://doi.org/10.1016/j.landusepol.2016.03.025>
- Wamsler C, Brink E, Rivera C (2013) Planning for climate change in urban areas: from theory to practice. *J Clean Prod* 50:68–81. <https://doi.org/10.1016/j.jclepro.2012.12.008>
- Ward PJ, Blauthut V, Bloemendaal N et al (2020) Review article: natural hazard risk assessments at the global scale. *Nat Hazards Earth Syst Sci* 20:1069–1096. <https://doi.org/10.5194/nhess-20-1069-2020>
- Weber T, Bowyer P, Rechid D et al (2020) Analysis of compound climate extremes and exposed population in Africa under two different emission scenarios. *Earths Future* 8. <https://doi.org/10.1029/2019EF001473>
- Weis SWM, Agostini VN, Roth LM et al (2016) Assessing vulnerability: an integrated approach for mapping adaptive capacity, sensitivity, and exposure. *Clim Change* 136:615–629. <https://doi.org/10.1007/s10584-016-1642-0>
- World Meteorological Organization (WMO) (2017) WMO guidelines on the calculation of climate normals. WMO-No. 1203. World Meteorological Organization. Available via WMO Library. <https://library.wmo.int/idurl/4/55797>. Accessed 3 Jan 2025
- Yu J, Castellani K, Forsyinski K et al (2021) Geospatial indicators of exposure, sensitivity, and adaptive capacity to assess neighbourhood variation in vulnerability to climate change-related health hazards. *Environ Health* 20:31. <https://doi.org/10.1186/s12940-021-00708-z>
- Zhang Z, Varble A, Feng Z, Hardin J, Zipser E (2021) Growth of Mesoscale Convective Systems in observations and a Seasonal Convection-Permitting Simulation over Argentina. *Mon Wea Rev* 149:3469–3490. <https://doi.org/10.1175/MWR-D-20-0411.1>
- Zhou Y, Liu Y, Wu W et al (2015) Integrated risk assessment of multi-hazards in China. *Nat Hazards* 78:257–280. <https://doi.org/10.1007/s11069-015-1713-y>

Publisher's Note Springer Nature remains neutral with regard to jurisdictional claims in published maps and institutional affiliations.

Springer Nature or its licensor (e.g. a society or other partner) holds exclusive rights to this article under a publishing agreement with the author(s) or other rightsholder(s); author self-archiving of the accepted manuscript version of this article is solely governed by the terms of such publishing agreement and applicable law.

Artículo 3

El ciclo de vida predominante de las sequías repentinas agrícolas

<https://doi.org/10.1038/s41612-024-00618-0>

The prevalent life cycle of agricultural flash droughts



Miguel A. Lovino ^{1,2}, M. Josefina Pierrestegui ^{1,2}, Omar V. Müller ^{1,2}, Gabriela V. Müller^{1,2} & Ernesto H. Berbery³

This work examines the characteristics and prevalent life cycle of agricultural flash droughts globally. Using ERA5 data, the study introduces a flash drought indicator based on soil water availability. This approach integrates root-zone soil moisture and hydraulic soil properties, such as field capacity and wilting point, to couple the rapid soil moisture depletion and plant water stress. Our findings reveal that agricultural flash droughts present their higher frequency predominantly during the critical growth periods of crops. Notably, these droughts exhibit a similar life cycle regardless of the location or climatic regime. The primary cause of the rapid soil moisture depletion is the precipitation deficit, but evapotranspiration also plays a significant role. In an energy-limited environment, evapotranspiration rapidly increases before the onset and decreases rapidly during the intensification period as the system becomes water-limited. Upon concluding the intensification period, most crops experience water stress, diminishing their yields.

Flash droughts, characterized by the rapid drying of soils over durations lasting weeks to a couple of months^{1,2}, have become more common than slow droughts over much of the world since the 1950s³. The frequency and severity of flash droughts are projected to increase worldwide during the 21st century, especially over croplands under high global warming scenarios^{4,5}. Given their rapid onset and intensification, flash droughts are often unexpected and challenging to predict⁶. They can negatively impact crop yields in agricultural regions and damage natural ecosystems worldwide^{7–9}.

Agricultural flash droughts affect vegetation when there is a soil moisture deficit and plant water requirements are not met, especially during the critical growth period of crops. The primary forcings are precipitation deficits and positive temperature anomalies that favor rapid soil moisture depletion rates^{2,10,11}. Soil moisture can be considered a proxy representing the moisture state of the land-atmosphere system as it dominates dryness stress on vegetation productivity across most of the world's vegetated land areas¹². Thus, plants with shallow roots, such as crops and pastures, are sensitive to soil moisture deficits in the upper soil layer and can become moisture-stressed faster than plants with deep roots¹¹. Hence, rapid soil moisture depletion is expected to impact crops and grasslands more severely than forests¹³.

Any attempt at predicting flash droughts requires a better understanding of their evolution and life cycle. During the evolution of flash droughts, precipitation rapidly decreases, playing a key role in the rapid soil

moisture depletion^{10,14}. Case studies show that the coevolution of anomalous meteorological conditions, such as high evaporative demand and temperatures, favor the development and propagation of flash droughts^{11,15–17}. Land-atmospheric coupling also accelerates flash drought onsets^{18,19}.

The main flash drought drivers have been studied at the regional and global scales^{14,20–22} employing different indicators²³ primarily based on soil moisture variability^{24–26}, the evaporative stress ratio²⁷, evaporative demand²⁸, or multivariate approaches^{14,15,29}. The variety of definitions responds to specific needs, as flash drought physical processes are complex and difficult to represent using a single definition. However, different classifications may produce diverse results regarding flash drought characteristics and key drivers^{30,31}.

As highlighted by ref. 31, a crucial aspect of flash drought development involves coupling rapid depletion rates of soil moisture in the root zone with impacts on vegetation health. To this end, we propose a flash drought indicator that relies on soil water availability and can integrate the dominant physical processes with the corresponding effects on vegetation health, mainly for agricultural regions. Using this method, this study assesses the prevalent life cycle of agricultural flash droughts, highlighting global similarities. We analyze atmospheric and surface drivers throughout this cycle and discuss the impact of these droughts during the critical growth period of crops.

¹Consejo Nacional de Investigaciones Científicas y Técnicas (CONICET), Santa Fe, Argentina. ²Centro de Estudios de Variabilidad y Cambio Climático (CEVARCAM), Facultad de Ingeniería y Ciencias Hídricas (FICH), Universidad Nacional del Litoral (UNL), Ciudad Universitaria, Ruta Nacional N° 168 - km 472,4. (3000), Santa Fe, Argentina. ³Earth System Science Interdisciplinary Center/Cooperative Institute for Satellite Earth System Studies, University of Maryland, College Park, College Park, MD 20740, USA. e-mail: mlovino@unl.edu.ar

Results

Overview of the proposed method to detect agricultural flash droughts

Soil moisture (θ) is a crucial variable for monitoring the stress of the land system^{10,32}. Its conditions reflect the actual water availability for plants while considering the time-integrated impact of preceding meteorological states that affect the soil wetness (e.g., precipitation, solar radiation, and wind speed). A soil moisture deficit limits direct soil evaporation, water uptake by roots for plant transpiration, and groundwater recharge³³. The decreased soil moisture and the corresponding increase in evaporative demand induce plant water stress². The soil moisture deficit and plant water stress can be explained through the hydraulic properties of the soil, specifically the field capacity (θ_{FC}) and the permanent wilting point (θ_{WP}). Soil cannot retain water above the field capacity because gravitational drainage predominates in the soil matrix. Plants cannot use soil moisture below the wilting point because the soil matrix holds water too tightly around the soil particles^{32,34}. Consequently, the maximum amount of water that soil can store and provide for plant growth and transpiration is the available water capacity ($\theta_{AWC} = \theta_{FC} - \theta_{WP}$) (see, e.g., ref. 35 for further details).

Building from these principles, ref. 36 defined the Soil Water Deficit Index (SWDI) as an agricultural drought index formulated as:

$$\text{SWDI} = \left(\frac{\theta - \theta_{FC}}{\theta_{FC} - \theta_{WP}} \right) \times 10 \quad (1)$$

The SWDI equals zero when the soil moisture is at the field capacity, i.e., when plants have full water availability and no soil moisture deficit. Negative SWDI values indicate a soil moisture deficit, which becomes absolute when $\theta < \theta_{WP}$ (SWDI ≤ -10). Below this point, there is no available water for plants, i.e., roots cannot absorb soil water, and plants wilt³⁷.

The critical soil moisture value^{32,38} (θ_{CRIT}), an essential threshold lying between θ_{WP} and θ_{FC} , differentiates evapotranspiration regimes (see Fig. 1a adapted from refs. 10,32; and Supplementary Fig. 1): When $\theta > \theta_{CRIT}$, evapotranspiration is independent of soil moisture (energy-limited regime). When $\theta < \theta_{CRIT}$, evapotranspiration is constrained by soil moisture (water-limited regime). Thus, θ_{CRIT} occurs at the point when evapotranspiration becomes water-limited and is identified when a slight decrease in soil moisture leads to diminished evaporative fraction (the ratio of latent heat to the combined latent and sensible heat fluxes)^{32,38}. A transitional regime corresponds to the range $\theta_{WP} \leq \theta \leq \theta_{CRIT}$, where soil moisture limits evapotranspiration and, thus, land-atmosphere feedback. The system is in a dry regime when no evapotranspiration can occur, that is, when $\theta < \theta_{WP}$ (or SWDI < -10 , Fig. 1a).

The proposed approach considers fundamental characteristics of a flash drought (e.g., refs. 2,3,10,24): (1) a rapid depletion of the root-zone soil moisture, (2) an intensification period sufficiently long to avoid short synoptic scale events that deplete soil moisture rapidly but recover suddenly, (3) reasonably unstressed soil moisture conditions prior to drought onset, and (4) plant water stress. First, the rapid decay of the soil moisture is represented by an SWDI decay from more than -3 to less than -5 in 20 days (or 4 pentads) (see Fig. 1b). The SWDI thresholds are based on the following refs. 10,32,39,40 that have addressed the relationship between soil moisture and evapotranspiration. The upper threshold (SWDI = -3), at the beginning of the transitional regime, guarantees a discernible decrease in evapotranspiration and thus effectively identifies a level of moisture deficit within the land system. The lower threshold (SWDI = -5) ensures that plants begin to experience water stress (see further details on Methods). Second, the minimum duration of the intensification period is met (following ref. 25) by requiring the soil moisture depletion period to last at least 15 days (or three pentads). Third, the non-drought condition prior to the drought onset is fulfilled (adapted from ref. 10) by requiring the three pentads preceding an event to exhibit SWDI values higher than -4 in magnitude. It also prevents flash droughts to overlap in time when, following the conclusion of a flash drought due to partial soil moisture recovery from a precipitation event, rapid soil moisture depletion takes place due to

preceding conditions. Fourth, the plant water stress is intrinsically integrated into the proposed indicator, as it directly addresses the water availability loss for plants by defining the SWDI thresholds.

With a primary focus on crops, the proposed definition couples the rapid intensification of soil moisture drying and vegetation stress as crucial factors. Therefore, the method targets agricultural flash droughts—that is, specifically those occurring in areas prone to agriculture—rather than all instances of flash droughts. Notably, agricultural flash droughts are rare in regions with extreme climates (see Methods for details). Furthermore, the proposed approach does not remove the annual soil moisture cycle. Then, it is expected that the higher soil moisture decreases will occur during the growing season (mainly in spring and extending into summer) when soil moisture is largely influenced by increases in evapotranspiration rates that exacerbate precipitation deficits. Thus, aligning with their definition, agricultural flash droughts are susceptible to occur during the growing season regardless of the climatic regime.

Representation of well-known historical flash droughts

The proposed method is implemented using the European Centre for Medium-Range Weather Forecasts reanalysis version 5 (ERA5) data. This method, focused on characterizing agricultural flash drought by tracking the spatiotemporal evolution of the SWDI (as illustrated in Fig. 2), effectively identifies the prevalent pattern of the well-documented 2012 flash drought in the central-eastern United States^{11,30,41,42} that severely impacted agriculture³³. The agricultural flash drought began to develop rapidly in late April towards the north of the southeastern region (Fig. 2f, b, g). Throughout late May and June, the agricultural flash drought expanded in a radial pattern with varying rates of intensification (Fig. 2f, c, h, d, i). By July it reaches its maximum spatial extent, spreading further into the northern States of the Midwestern region (Fig. 2e, j). Agricultural flash drought conditions do not develop towards the semi-arid regions west of 100°W and the desert areas of the Southwest USA (Fig. 2f), as they show low SWDI values (SWDI < -7 , and SWDI < -10 , respectively) but constant over time (Fig. 2a–e).

We also assess the robustness of the proposed method by testing its ability to detect several well-documented flash droughts in different regions of the world. The approach successfully identifies (a) a severe flash drought in southwestern Russia and eastern Ukraine that rapidly intensified during late April and early May 2010 (see Supplementary Fig. 2, consistent with findings by refs. 44,45), (b) one of the most severe flash droughts experienced in India occurred at the end of the 2001 monsoon season (see Supplementary Fig. 3, in agreement with ref. 46), and (c) the extremely rapid intensification and spatiotemporal evolution of the once-a-century 2013 flash drought in southern China (see Supplementary Fig. 4, in line with the studies by refs. 47,48).

Annual and seasonal frequencies of agricultural flash drought

Our approach is employed to estimate the global spatial distribution of agricultural flash drought frequencies over the 1960–2020 period. Regions with the highest annual frequency of agricultural flash drought events are identified as hotspots, that is, regions where agricultural flash droughts have an area-averaged frequency higher than two events per decade and in which half of the area experiences at least three events per decade. Eight world regions prone to high agricultural flash drought occurrence are identified with the proposed method. These regions, highlighted in Fig. 3a, are presented in Table 1 along with the corresponding flash drought frequencies. Southern China (SCh), central-eastern Europe (CEEu), India (In), south-eastern South America (SESA), and southern Russia (SRus) present the highest frequencies per decade (with area-averaged frequencies between 3.3 and 2.8 events per decade). Central-eastern USA (CEUSA) shows a lower area-averaged frequency (2.3 events per decade) but an extended area that experiences more than three events per decade (see Fig. 3a). Lastly, the transition belt between the Sahel and the tropical forests in central-western Africa (CWAF), northern South America (NSA), and southeastern Asia (SEAs) are also identified as agricultural flash drought hotspots with area-

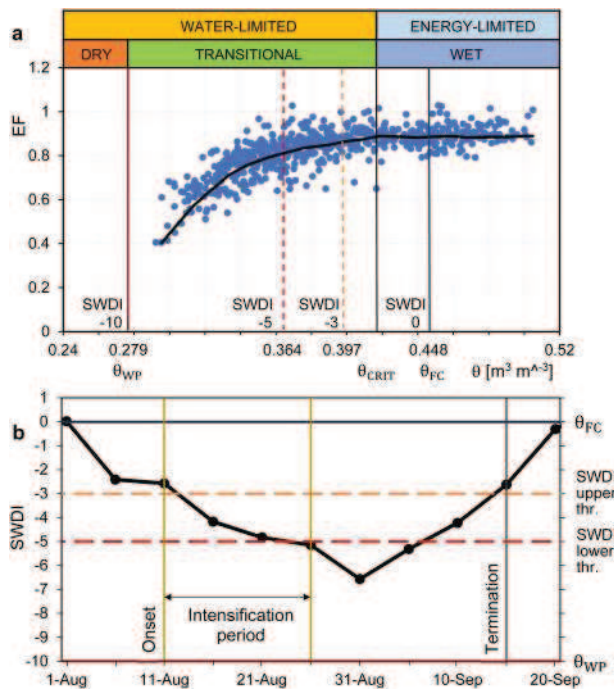


Fig. 1 | Illustration of the proposed agricultural flash drought definition.

a Scatterplot of evaporative fraction (EF) vs. volumetric soil moisture (θ) at the grid point corresponding to the agricultural flash drought case presented in b (adapted from refs. 10,32). The blue dots represent the pentad values from 1 Aug–20 Sep during the 1960–2020 period. The black line represents the average EF- θ relationship computed by binning the data within θ ranges close to $0.01 \text{ m}^3 \text{ m}^{-3}$. Soil moisture (dry, transitional, and wet) and evapotranspiration (water- and energy-limited) regimes are highlighted with colors. The solid vertical lines indicate the soil property values, namely permanent wilting point (θ_{WP}), soil moisture critical value (θ_{CRIT}), and field capacity (θ_{FC}) with their corresponding soil water deficit index (SWDI) values. The dashed vertical lines highlight the SWDI thresholds. The upper SWDI threshold (SWDI = -3) is at the beginning of the transitional regime and the lower SWDI threshold (SWDI = -5) ensures that several crops begin to experience water stress. b Representative example of an agricultural flash drought case experienced in southern China (112°E, 28°N) during the summer of 2020. The solid black line shows the pentads (5-day means) for the SWDI (left axis) and θ (right axis) during the flash drought event. The upper and lower SWDI thresholds are shown as dashed lines, while θ_{FC} and θ_{WP} are presented as solid lines.

averaged frequencies between 2.3 to 2 events per decade. Notably, the most prominent event frequencies occur in croplands (Supplementary Figs. 5 and 6) of SCh, CEEu and SRus, central In, SESA, and the northern and southeastern portions of the CEUSA (Fig. 3a).

While the number of area-averaged cases is seemingly low, they encompass smaller regions with frequent agricultural flash droughts (Fig. 3a). SCh, In, SESA, and SEAs present small regions with frequencies of more than eight events per decade, where also a few grid points show maximum frequencies approaching or exceeding one flash drought event per year (Table 1). Large regions of SRus and the eastern CEEu and isolated areas of CEUSA and NSA experience between 5 and 8 events per decade.

Agricultural flash droughts tend to occur during the critical growth period of crops according to the analysis of their seasonal frequency (Fig. 3b,c). In extratropical areas, agricultural flash droughts are most frequent in springtime (Fig. 3b). Central-eastern Europe and southern Russia have the most prominent flash drought event frequencies during boreal spring (March–April–May; MAM), thus impacting the planting and pollination periods of diverse rainfed crops, including wheat, barley, corn, soybeans, and rice (see Supplementary Fig. 6b). The main crops grown in the southern USA eastern seaboard and the midwestern USA corn belt (e.g., ref. 49) are impacted during the same season (MAM), with effects extending into June for the latter region. Last, in southeastern South America,

agricultural flash droughts are most frequent in austral spring (November and December), thus impacting the planting and pollination periods of corn, soybean, and sunflower (see, e.g., ref. 50).

In subtropical and tropical regions, the highest agricultural flash drought frequency may occur during the spring and summer seasons (Fig. 3b). In southern China, the maximum flash drought frequency occurs during boreal summer (July and August, Fig. 3c), thus reducing the water availability for rice cultivation in an area that concentrates most of the country's rice production⁵¹. Agricultural flash droughts in India, south-eastern Asia, and central-western Africa are most frequent during September–October–November (SON), affecting the main crop yields (e.g., refs. 46,52,53). In the croplands of northern South America (Colombia and Venezuela), frequent flash drought events in December–January–February (DJF) affect the critical growth periods of mixed crops, cotton, and coffee (Supplementary Fig. 6b, ref. 54).

Physical evolution of agricultural flash droughts

Analyzing the temporal progression of agricultural flash droughts helps understand the physical processes involved in their life cycle and the associated land-atmosphere feedbacks. All hotspot regions under agricultural flash drought conditions exhibit a similar temporal evolution of the area-averaged standardized anomalies of relevant variables (Fig. 4), suggesting worldwide analogous agricultural flash drought life cycle. The generic spatial structure of agricultural flash droughts (Fig. 5) reveals a consistent spatiotemporal flash drought development. Before the agricultural flash drought onset (lags -4 to -1), temperature has almost constant values and precipitation slightly decreases (Fig. 4a, b). As non-drought conditions persist within the energy-limited regime (refer to Fig. 1b) during this phase, sufficient soil moisture (Fig. 4d) allows a slight increase in evapotranspiration (Fig. 4c). Between the lag -1 and the onset, precipitation quickly decays while the temperature rises (Fig. 4a,b; 5, first and second columns). At this point, an enhanced evaporative demand favored by the warming rapidly increases evapotranspiration (Figs. 4c and 5, third column). Together with the precipitation decay, this increased evapotranspiration produces a soil moisture dry-down that accelerates over the following pentads.

At the flash drought onset (lag = 0), when the SWDI is above the upper threshold (SWDI = -3; Figs. 4e and 5, fifth column), the precipitation deficit deepens, and the soil moisture starts depleting (Figs. 4a, d; 5, first and fourth columns). At this time, temperature and evapotranspiration play a crucial role in flash drought development. After the flash drought onset (lag +1), the precipitation deficit reaches its maximum intensity and extent (Fig. 5, first column) and soil moisture becomes insufficient to supply further water for evapotranspiration, signaling the start of the water-limited conditions (see Fig. 1b). From lag +1, evapotranspiration starts to decrease, despite the increased temperature, due to water stress (Figs. 4c and 5, third column). As the flash drought progresses (lags +1 to +3), the mechanism intensifies, that is, the temperature continues to rise, evapotranspiration drops, and soil moisture diminishes. By lag +2 the precipitation deficit begins stabilizing and reverses slightly by lag +3, although negative precipitation anomalies persist (Figs. 4a and 5, first column). At this time (lag +3), the temperature starts to drop (while positive anomalies continue), and the negative anomalies of both evapotranspiration and soil moisture stabilize, indicating the approaching end of the flash drought intensification period.

The characteristics just described are notably seen in all regions with agricultural flash droughts, regardless of the location or climatic regime. The features are more marked in the main hotspots (SCh, CEEu and SRus, In, SESA, and CEUSA), where the largest negative precipitation anomalies and the highest positive evapotranspiration anomalies occur (see Supplementary Fig. 7).

Discussion

Flash droughts are challenging to predict, but we can better understand their development by identifying common features across all regions. We have introduced an approach to recognize agricultural flash droughts based on

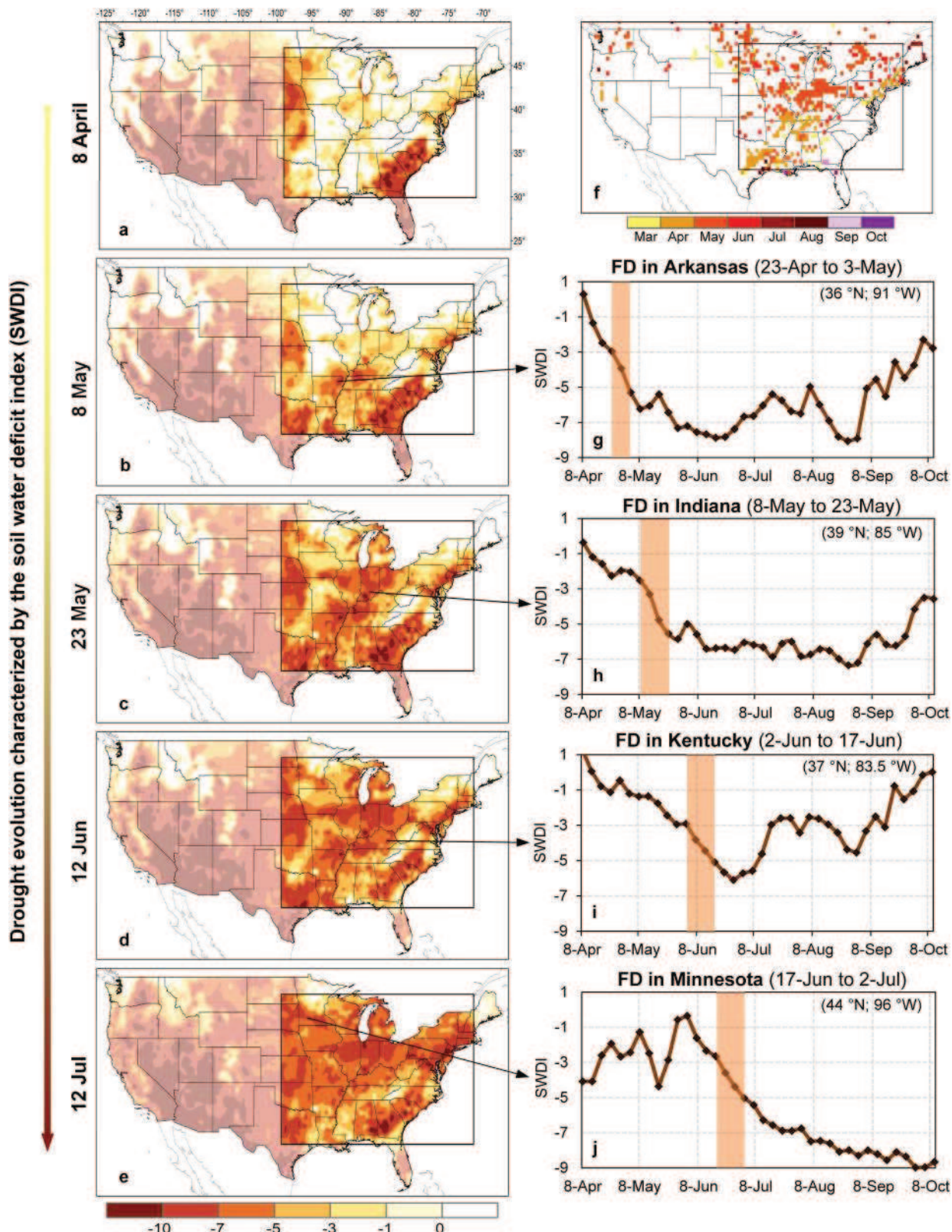


Fig. 2 | Evolution of the 2012 flash drought in the central-eastern United States characterized by the proposed SWDI-based indicator. **a–e** Spatial distribution of the SWDI on key dates during the flash drought evolution. The impacted area in the central-eastern United States stands out. The rest of the country is shown opaqued.

f Onset months of grid points under agricultural flash droughts in 2012.
g–j Temporal evolution of the SWDI at selected grid points (referenced in the upper right corner of each panel). The flash drought's intensification period is emphasized in brown shading.

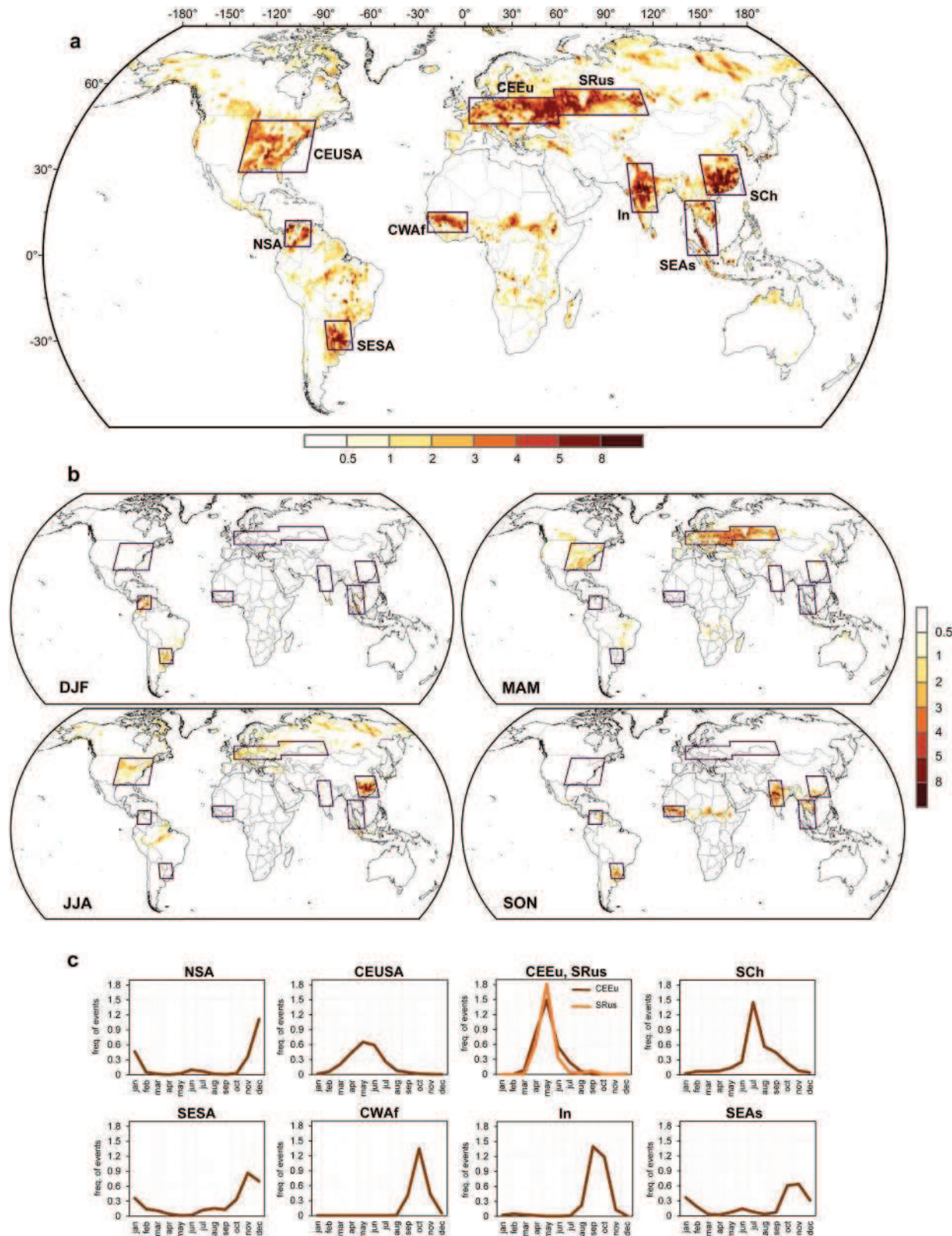


Fig. 3 | Annual and seasonal agricultural flash drought frequencies. **a** Annual and **b** seasonal frequency of agricultural flash drought events (number of events per decade) from 1960–2020. Meteorological seasons are December–January–February (DJF), March–April–May (MAM), June–July–August (JJA), and September–October–November (SON). Hotspots are highlighted with boxes, including northern South

America (NSA), central-eastern United States of America (CEUSA), central-eastern Europe (CEEu) and southern Russia (SRus), southern China (SCh), southeastern South America (SESA), central-western Africa (CWAf), India (In), and southeastern Asia (SEAs). **c** Annual cycles of the area-averaged agricultural flash drought frequency in each hotspot.

Table 1 | Regions identified as agricultural flash drought occurrence hotspots

| Hotspot | Acronym | Area-averaged FD frequency | Maximum FD frequency |
|--|---------|----------------------------|----------------------|
| Southern China | SCh | 3.3 | 12.5 |
| Central-eastern Europe | CEEu | 3.2 | 8.2 |
| India | In | 3 | 9.7 |
| Southeastern South America | SESA | 2.9 | 10.1 |
| Southern Russia | SRus | 2.8 | 8.3 |
| Central-eastern United States of America | CEUSA | 2.3 | 7.7 |
| Southeastern Asia | SEAs | 2.3 | 10.6 |
| Northern South America | NSA | 2.1 | 8.5 |
| Central-western Africa | CWAf | 2 | 8.5 |

The columns show the acronyms used to identify the agricultural flash drought hotspots and the area-averaged and maximum decadal frequencies of flash droughts (FD) in each hotspot. Even though CEUSA and SRus frequencies are displayed separately, both regions represent a unified hotspot region (see Fig. 3a).

soil water availability. The method utilizes the root-zone soil moisture and two soil hydraulic properties, namely field capacity and wilting point, to capture the rapid depletion of soil moisture, along with vegetation stress that severely impacts agriculture and ecosystems. To detect such occurrences, we suggest using the well-known SWDI along with a threshold range within the transitional regime. The upper SWDI threshold marks the initiation of the soil moisture deficit, while the lower SWDI threshold indicates water stress conditions on crops (see Supplementary Fig. 8).

We utilized the ERA5 dataset for our study, but it should be noted that this dataset has some known uncertainties⁵⁵. While we acknowledge that there are also inaccuracies in estimating soil hydraulic properties and that these estimates may not be representative in certain regions^{56,57}, our approach correctly identifies several well-known flash drought events across the globe. It's important to note that different definitions of flash droughts and the use of varying input data can lead to differences in the occurrence, intensity, onset, intensification period, and drivers of these events^{30,31}. Our method relies on soil moisture and soil-specific water availability, aligning our findings more closely with studies that use soil moisture indicators at either global scales^{9,14} or regional scales (such as in China²⁵ and India⁵⁸), rather than evapotranspiration indicators^{5,11,2,12,17}. Additionally, it's worth noting that our method is specifically designed to identify agricultural flash droughts, and therefore excludes flash droughts that occur in soils and climates that are less suitable for agriculture.

Agricultural flash droughts are most frequent in croplands of southern China, central-eastern Europe, southern Russia, India, southeastern South America, and the central-eastern USA. These types of droughts are more common during the critical growth periods of crops. This finding aligns with the underlying mechanisms, as the transition from an energy-limited regime to a water-limited regime is more likely to occur during the growing season when evaporative demand is at its highest climatological levels^{2,42}. When this transition takes place, the vegetation becomes stressed quickly, and the impact of agricultural flash droughts is magnified^{2,11}.

Our study finds that agricultural flash droughts exhibit similar evolution of relevant atmospheric and surface variables regardless of the geographical location or climatic regime. As expected, a precipitation deficit is the main driver for rapid soil moisture depletion. Before the flash drought onset, there is sufficient soil moisture (energy-limited regime). The favorable conditions of abundant soil moisture, combined with a decrease in precipitation, allow evapotranspiration to increase considerably, intensifying and accelerating soil moisture depletion. During the flash drought's intensification period, soil moisture becomes insufficient to supply more water

for evapotranspiration, which in turn decreases. In this water-limited regime with decreased evapotranspiration, energy is transferred to sensible heat flux^{11,59}, i.e., to an increase in temperature that is crucial in the persistence of flash drought events and which may conduct to subsequent heat waves⁴⁴.

Methods

Data

The primary variable used in this study was the root-zone volumetric soil moisture in the soil's top meter. Soil moisture data representing the 1960–2020 period at a $0.5^\circ \times 0.5^\circ$ latitude-longitude grid spacing was obtained from the ERA5 product^{55,60}. ERA5 soil moisture data has shown better accuracy than data from other reanalyses compared to in-situ observations at various locations around the world^{61,62}. The evaporative fraction, $EF = LH/(LH + SH)$, was estimated from ERA5's latent heat (LH) and sensible heat (SH). Total precipitation, evapotranspiration, and 2-m air temperature were also used. Non-overlapped pentads (5-day means) of these variables were computed from the original hourly data. The pentad values were then used to assess the spatiotemporal evolution of flash droughts' main variables. Such a method avoids higher-frequency variabilities while capturing short-duration flash droughts^{15,24}. The pentad anomalies at each grid point were computed as departures from the 1960–2020 mean annual cycle and normalized with their corresponding standard deviations. Such standardized anomalies facilitate worldwide comparisons.

The proposed flash drought definition also employed ERA5 parameters representing soil hydraulic properties. These parameters included the field capacity (θ_{FC}) and the wilting point (θ_{WP}). Both parameters depend on the soil class at each grid point and do not vary temporally. The global soil datasets needed by Earth System Models are often based on limited and heterogeneously distributed soil profiles (e.g., refs. 63,64). The soil properties also present uncertainty due to the pedotransfer functions used in their estimation⁶⁵. However, significant efforts have been made in recent decades to mitigate these limitations. Information on the uncertainty is commonly provided along with the soil datasets (e.g., refs. 66,67), thereby enhancing the accuracy of Earth System Models' land component.

Vegetation types were employed to identify the dominant land cover in agricultural flash drought-prone regions. These vegetation types were defined in ERA5 as a percentage of high and low vegetation coverage for each grid point following the Global Land Cover Characteristics data⁶⁸ of the Biosphere-Atmosphere Transfer Scheme biome classification⁶⁹. Our interest focused on discussing the impacts of agricultural flash droughts on croplands. For this reason, the ERA5 data were complemented with products representing the cropland extent, irrigated vs. rainfed crops, and crop dominance. These products were taken from the Global Food Security-Support Analysis Data (GFSAD) Project: The Global Cropland-extent product at a 30-m resolution⁷⁰ and the Global Cropland-extent 1-km Cropland Dominance product⁷¹.

Proposed agricultural flash drought definition

The main features of the proposed method for identifying agricultural flash droughts are discussed in the Results section (see "Overview of the proposed method to detect agricultural flash droughts"). Complementary, this section discusses the selection of thresholds and the pros and cons of the proposed method.

Selection of SWDI thresholds. The choice of $SWDI = -3$ as the upper threshold reflects the fact that this value is less than the θ_{CRIT} value, which determines the beginning of the transitional regime (see Fig. 1a and Supplementary Fig. 1). By setting the upper threshold within the transitional regime, it ensures a discernible reduction in evapotranspiration, effectively capturing the moisture deficit in the land system. The θ_{CRIT} value may be difficult to establish because of the vast influence of varying soil textures, climate conditions, and vegetation characteristics. Reference 72 reported that it is typically 50–80% of θ_{FC} .

The fraction of available water content a plant can extract from the root zone without suffering water stress is known as the readily available soil

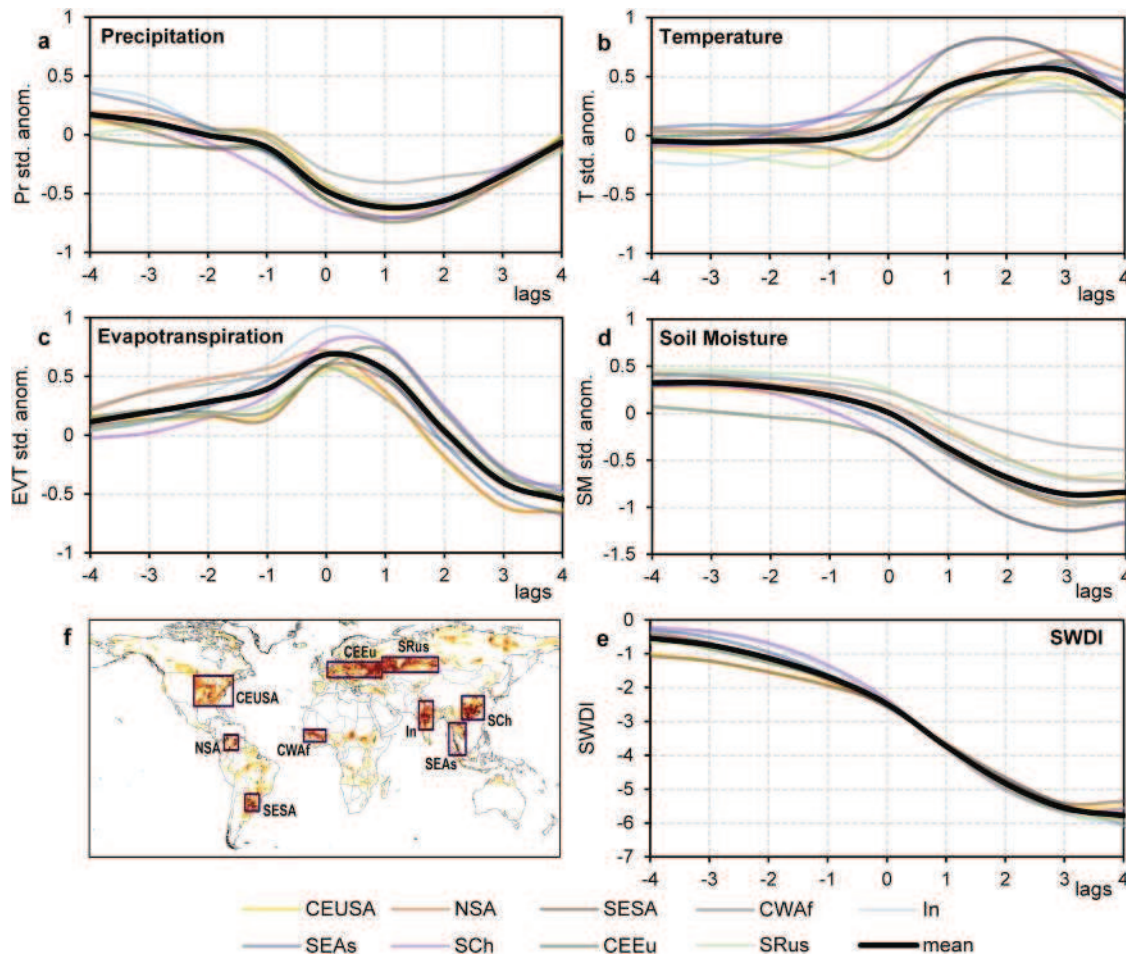


Fig. 4 | Temporal evolution of area-averaged standardized anomalies during agricultural flash drought events. The temporal evolution is shown for the nine-pentad period centered at FD onset (lag = 0) for: **a** precipitation (Pr), **b** temperature (T), **c** evapotranspiration (EVT), and **d** soil moisture (SM). **e** Shows the temporal

evolution of the soil water deficit index (SWDI). **f** Map that highlights the agricultural flash drought hotspots. The colored lines represent the individual hotspots. The average value over all hotspots is shown as a thick black line. The full names of the agricultural flash drought hotspots are presented in Table 1.

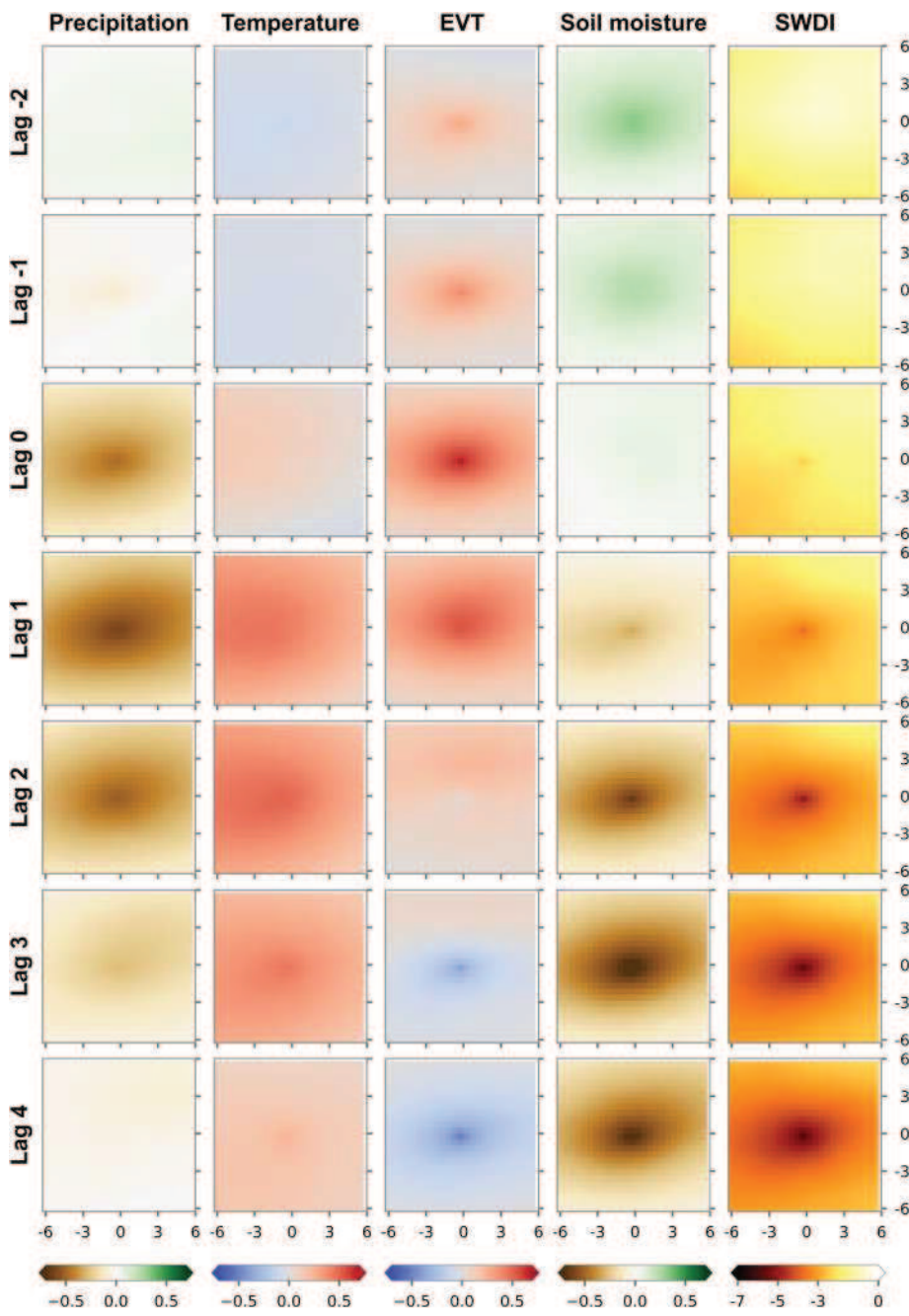
water⁷³. An average fraction of available water content close to 0.5, corresponding to SWDI = -5, is a common feature of several crops^{73,74}. Thus, below the SWDI = -5 threshold, plant roots can no longer extract soil water rapidly enough to respond to the transpiration demand, and plants begin to experience water stress. Although soil water is theoretically available for plants before reaching θ_{WP} , the plant water uptake is reduced well before that value (see Supplementary Fig. 8). In addition, ref. 36 classify soil moisture droughts below the SWDI = -5 threshold as severe.

Although the thresholds have been defined based on physical constraints, the precise values have some arbitrariness. Thus, we tested the sensitivity of the threshold range by modifying threshold values and examining their influence on drought frequency results (see Supplementary Fig. 9). The flash drought occurrence patterns remain unaffected across varied threshold ranges, although the frequency of events fluctuates, suggesting that the proposed method is robust. Specifically, flash drought frequencies increase for less stringent ranges (e.g., exceeding five events per decade in larger regions when $-4 < \text{SWDI} < -2$) and significantly decrease for more stringent ranges (e.g., fluctuating between 2 and 4 events per decade for $-6 < \text{SWDI} < -3$). The chosen range ($-5 < \text{SWDI} < -3$), positioned at an intermediate level, was selected based on physical criteria (as discussed above), thereby mitigating the arbitrariness associated with range selection. In addition, the selected thresholds allow proper recognition of the spatiotemporal evolution of several well-documented flash drought events that are distinguished using other definitions in different world regions (e.g., refs. 16,41,44,46; see also Results).

Comparison of the SWDI-based method with an θ percentile-based method. We compared the characteristics of agricultural flash droughts identified in this article with flash droughts obtained with a widely used indicator based on root-zone soil moisture percentiles (e.g., refs. 24,25) (see Supplementary Fig. 10). Note that the soil moisture percentile method has also been used with additional constraints to ensure soil moisture stress on the land system, account for prior non-drought conditions, or address cases in extreme climates (see, e.g., ref. 10). However, the comparison conducted here was restricted to the original soil moisture percentile method.

Flash drought identification under extreme climates presents interesting differences between the two approaches. To illustrate this, we examined a grid point in a hot desert climate (Case 1, Sahara Desert; Supplementary Fig. 10a, b) where agricultural flash droughts would not be feasible under these circumstances. Still, the time series of θ percentiles from 2015 to 2020 (Supplementary Fig. 10a) suggests repeated flash drought conditions, as θ frequently decreases from at least 40th to the 20th percentile within four pentads or less. In contrast, the SWDI time series (Supplementary Fig. 10b) indicates that soil moisture fluctuates within a narrow range consistently well below the wilting point throughout the five years. This means that the soil remains under conditions of permanent dryness. An equivalent situation is observed in a very wet climate (Case 2, Indonesia, Supplementary Fig. 10c, d). The θ percentiles time series (Supplementary Fig. 10c) suggests the existence of flash drought conditions. However, the SWDI time series (Supplementary Fig. 10d) reveals that soil moisture varies in a small range always around the field capacity, never reaching the drought

Fig. 5 | Key atmospheric and surface variables that influence agricultural flash drought events before, during, and after their onset. For each variable and each lag, each box represents the composite of all flash drought events for a $12^\circ \times 12^\circ$ window with the event occurring in the center. The lags vary between -2 and $+4$ around the onset (lag 0). From left to right, the variables are standardized anomalies of precipitation, temperature, evapotranspiration (EVT), and soil moisture. The rightmost column shows the evolution of the soil water deficit index (SWDI).



onset threshold ($\text{SWDI} < -3$), recognizing that there is no plant water stress, and therefore, no drought periods. These results suggest that identifying soil moisture flash droughts based on physical thresholds helps avoid misrepresentation in extreme climates.

We also studied flash drought cases in agricultural-suitable non-extreme climates, aligning with the indicator's focus on agricultural droughts (Supplementary Fig. 10e–h). Case 3 shows a flash drought event in southern China during Aug-Sep 2020 (as in Fig. 1), characterized by the evolution of the θ percentiles (Supplementary Fig. 10e) and by the SWDI and θ time series (Supplementary Fig. 10f). The SWDI-based approach identifies a flash drought of shorter duration and lower intensity than the one estimated from the θ percentile thresholds. Case 4 presents a flash drought event in southeastern South America during Nov-Dec 1970. Both definitions (Supplementary Fig. 10g, h) identify a flash drought of similar duration, but the proposed method in this study indicates a higher intensity. These examples demonstrate that both the SWDI-based and θ percentile-based methods identify similar

characteristics of soil moisture flash droughts with slight differences. The θ percentile-based indicators' thresholds may be sensitive to soil moisture variabilities in non-extreme climate regimes. The thresholds of the SWDI-based method are based on the physical conditions of each type of soil.

Evolution of crucial atmospheric and surface variables

Composites of precipitation, temperature, evapotranspiration, and soil moisture standardized anomalies were constructed to examine agricultural flash droughts' characteristic temporal and spatial evolution. First, flash drought events were detected at each grid point within the hotspots. Then, area averages for all hotspots were computed for their onset (lag 0), the four preceding pentads (lags -4 to -1), and the four subsequent pentads (lags $+1$ to $+4$). Next, the spatial structure of standardized anomalies across all identified events worldwide was examined by generating a flash drought composite over a $12^\circ \times 12^\circ$ window centered on each event location.

Data availability

The ERA5 data are available at <https://doi.org/10.24381/cds.adbb2d47>. The Global Cropland-extent product at a 30-m resolution and the Global Cropland-extent 1-km Cropland Dominance product can be obtained from <https://doi.org/10.3133/pp1868> and <https://doi.org/10.5067/MEaSUREs/GFSAD/GFSAD1KCD.001>, respectively.

Code availability

Python scripts for running the proposed method and performing calculations are available at <https://github.com/mjpierretegui/flash-droughts.git>.

Received: 14 September 2023; Accepted: 7 March 2024;

Published online: 19 March 2024

References

1. Svoboda, M. et al. The drought monitor. *Bull. Am. Meteor. Soc.* **83**, 1181–1190 (2002).
2. Otkin, J. et al. Flash droughts: a review and assessment of the challenges imposed by rapid onset droughts in the United States. *Bull. Am. Meteor. Soc.* **99**, 911–919 (2018).
3. Yuan, X. et al. A global transition to flash droughts under climate change. *Science* **380**, 187–191 (2023).
4. Sreeparvathy, V. & Srinivas, V. V. Meteorological flash droughts risk projections based on CMIP6 climate change scenarios. *npj Clim. Atmos. Sci.* **5**, 77, <https://doi.org/10.1038/s41612-022-00302-1> (2022).
5. Christian, J. I. et al. Global projections of flash drought show increased risk in a warming climate. *Commun. Earth. Environ.* **4**, 165, <https://doi.org/10.1038/s43247-023-00826-1> (2023).
6. Otkin, J. A. et al. Getting ahead of flash drought: from early warning to early action. *Bull. Am. Meteor. Soc.* **103**, E2188–E2202, <https://doi.org/10.1175/BAMS-D-21-0288.1> (2022).
7. He, M. et al. Impacts of the 2017 flash drought in the US Northern plains informed by satellite-based evapotranspiration and solar-induced fluorescence. *Environ. Res. Lett.* **14**, 074019 (2019).
8. Yao, T., Liu, S., Hu, S. & Mo, X. Response of vegetation ecosystems to flash drought with solar-induced chlorophyll fluorescence over the Hai River Basin, China during 2001–2019. *J. Environ. Manag.* **313**, 114947 (2022).
9. Mahto, S. S. & Mishra, V. Increasing risk of simultaneous occurrence of flash drought in major global croplands. *Environ. Res. Lett.* **18**, 044044 (2023).
10. Koster, R. D., Schubert, S. D., Wang, H., Mahanama, S. P. & DeAngelis, A. M. Flash drought as captured by reanalysis data: Disentangling the contributions of precipitation deficit and excess evapotranspiration. *J. Hydrometeorol.* **20**, 1241–1258 (2019).
11. Pendergrass, A. G. et al. Flash droughts present a new challenge for subseasonal-to-seasonal prediction. *Nat. Clim. Chang.* **10**, 191–199 (2020).
12. Liu, L. et al. Soil moisture dominates dryness stress on ecosystem production globally. *Nat. Commun.* **11**, 4892 (2020).
13. Zhang, M. & Yuan, X. Rapid reduction in ecosystem productivity caused by flash droughts based on decade-long FLUXNET observations. *Hydroclim. Earth Syst. Sci.* **24**, 5579–5593 (2020).
14. Mukherjee, S. & Mishra, A. K. A multivariate flash drought indicator for identifying global hotspots and associated climate controls. *Geophys. Res. Lett.* **49**, e2021GL096804 (2022).
15. Mo, K. C. & Lettenmaier, D. P. Heat wave flash droughts in decline. *Geophys. Res. Lett.* **42**, 2823–2829 (2015).
16. Basara, J. B. et al. The evolution, propagation, and spread of flash drought in the Central United States during 2012. *Environ. Res. Lett.* **14**, 084025 (2019).
17. Nguyen, H., Wheeler, M. C., Otkin, J. A., Nguyen-Huy, T. & Cowan, T. Climatology and composite evolution of flash drought over Australia and its vegetation impacts. *J. Hydrometeorol.* **24**, 1087–1101 (2023).
18. Wang, Y. & Yuan, X. Land-atmosphere coupling speeds up flash drought onset. *Sci. Total Environ.* **851**, 158109 (2022).
19. Mahto, S. S., & Mishra, V. Flash drought intensification due to enhanced land-atmospheric coupling in India. *J. Clim.* 1–31, <https://doi.org/10.1175/JCLI-D-22-0477.1> (2023).
20. Osman, M. et al. Diagnostic classification of flash drought events reveals distinct classes of forcings and impacts. *J. Hydrometeorol.* **23**, 275–289 (2022).
21. Christian, J. I. et al. Global distribution, trends, and drivers of flash drought occurrence. *Nat. Commun.* **12**, 6330 (2021).
22. Lowman, L. E. L., Christian, J. I. & Hunt, E. D. How land surface characteristics influence the development of flash drought through the drivers of soil moisture and vapor pressure deficit. *J. Hydrometeorol.* **24**, 1395–1415 (2023).
23. Lisonbee, J., Woloszyn, M. & Skumanich, M. Making sense of flash drought: definitions, indicators, and where we go from here. *J. Appl. Serv. Climatol.* **2021**, 1–19 (2021).
24. Ford, T. W. & Labosier, C. F. Meteorological conditions associated with the onset of flash drought in the eastern United States. *Agric. Meteorol.* **247**, 414–423 (2017).
25. Yuan, X. et al. Anthropogenic shift towards higher risk of flash drought over China. *Nat. Commun.* **10**, 1–8 (2019).
26. Liu, Y. et al. Two different methods for flash drought identification: comparison of their strengths and limitations. *J. Hydrometeorol.* **21**, 691–704 (2020).
27. Christian, J. I. et al. A methodology for flash drought identification: application of flash drought frequency across the United States. *J. Hydrometeorol.* **20**, 833–846 (2019).
28. Hobbins, M. T. et al. The evaporative demand drought index. Part I: Linking drought evolution to variations in evaporative demand. *J. Hydrometeorol.* **17**, 1745–1761 (2016).
29. Li, J. et al. A voxel-based three-dimensional framework for flash drought identification in space and time. *J. Hydrol.* **608**, 127568 (2022).
30. Osman, M. et al. Flash drought onset over the contiguous United States: sensitivity of inventories and trends to quantitative definitions. *Hydroclim. Earth Syst. Sci.* **25**, 565–581 (2021).
31. Mukherjee, S. & Mishra, A. K. Global flash drought analysis: uncertainties from indicators and datasets. *Earth's Future* **10**, e2022EF002660 (2022).
32. Seneviratne, S. I. et al. Investigating soil moisture–climate interactions in a changing climate: a review. *Earth. Sci. Rev.* **99**, 125–161 (2010).
33. Van Loon, A. F. Hydrological drought explained. *Wiley Interdiscip. Rev. Water* **2**, 359–392 (2015).
34. Hillel, D. *Environmental Soil Physics*. (Academic Press, San Diego, 1998).
35. Kirkham, M. B Field capacity, wilting point, available water, and the non-limiting water range. In *Principles of Soil and Plant Water Relations* 101–115 (Academic Press, Burlington, 2005).
36. Martínez-Fernández, J., González-Zamora, A., Sánchez, N. & Gumuzzio, A. A soil water-based index as a suitable agricultural drought indicator. *J. Hydrol.* **522**, 265–273 (2015).
37. Savage, M. J., Ritchie, J. T., Bland, W. L. & Dugas, W. A. Lower limit of soil water availability. *Agron. J.* **88**, 644–651 (1996).
38. Fu, Z. et al. Critical soil moisture thresholds of plant water stress in terrestrial ecosystems. *Sci. Adv.* **8**, eabq7827 (2022).
39. Koster, R. D. et al. Regions of strong coupling between soil moisture and precipitation. *Science* **305**, 1138–1140 (2004).
40. Seneviratne, S. I., Lüthi, D., Litschi, M. & Schär, C. Land–atmosphere coupling and climate change in Europe. *Nature* **443**, 205–209 (2006).
41. Otkin, J. A. et al. Assessing the evolution of soil moisture and vegetation conditions during the 2012 United States flash drought. *Agric. Meteorol.* **218–219**, 230–242 (2016).
42. Otkin, J. A. et al. Development of a Flash Drought Intensity Index. *Atmosphere* **12**, 741 (2021).

43. Jin, C., Luo, X. & Xiao, X. et al. The 2012 flash drought threatened US Midwest Agroecosystems. *Chin. Geogr. Sci.* **29**, 768–783 (2019).
44. Christian, J. I., Basara, J. B., Hunt, E. D., Otkin, J. A. & Xiao, X. Flash drought development and cascading impacts associated with the 2010 Russian heatwave. *Environ. Res. Lett.* **15**, 094078 (2020).
45. Hunt, E. D. et al. Agricultural and food security impacts from the 2010 Russia flash drought. *Weather Clim. Extrem.* **34**, 100383 (2021).
46. Mahto, S. S. & Mishra, V. Dominance of summer monsoon flash droughts in India. *Environ. Res. Lett.* **15**, 104061 (2020).
47. Yuan, X., Ma, Z., Pan, M. & Shi, C. Microwave remote sensing of short-term droughts during crop growing seasons. *Geophys. Res. Lett.* **42**, 4394–4401 (2015).
48. Zhang, L. et al. Analysis of flash droughts in China using machine learning. *Hydrol. Earth Syst. Sci.* **26**, 3241–3261 (2022).
49. Mishra, V. & Cherkauer, K. A. Retrospective droughts in the crop growing season: implications to corn and soybean yield in the Midwestern United States. *Agric. Meteorol.* **150**, 1030–1045 (2010).
50. Sgroi, L. C., Lovino, M. A., Berberry, E. H. & Müller, G. V. Characteristics of droughts in Argentina's Core Crop Region. *Hydrol. Earth Syst. Sci.* **25**, 2475–2490 (2021).
51. Deng, N. et al. Closing yield gaps for rice self-sufficiency in China. *Nat. Commun.* **10**, 1725 (2019).
52. Sultan, B., Defrance, D. & Izumi, T. Evidence of crop production losses in West Africa due to historical global warming in two crop models. *Sci. Rep.* **9**, 12834 (2019).
53. Venkatappa, M., Sasaki, N., Han, P. & Abe, I. Impacts of droughts and floods on croplands and crop production in southeast Asia: an application of Google Earth engine. *Sci. Total Environ.* **795**, 148829 (2021).
54. Geng, G. et al. Agricultural drought hazard analysis during 1980–2008: a global perspective. *Int. J. Climatol.* **36**, 389–399 (2016).
55. Hersbach, H. et al. The ERA5 global reanalysis. *Q. J. R. Meteorol. Soc.* **146**, 1999–2049 (2020).
56. Hengl, T. et al. SoilGrids1km—Global soil information based on automated mapping. *PLOS One* **9**(8), e105992, <https://doi.org/10.1371/journal.pone.0105992> (2014).
57. Folberth, C. et al. Uncertainty in soil data can outweigh climate impact signals in global crop yield simulations. *Nat. Commun.* **7**, 11872 (2016).
58. Mishra, V., Aadhar, S. & Mahto, S. S. Anthropogenic warming and intraseasonal summer monsoon variability amplify the risk of future flash droughts in India. *NPJ Clim. Atmos. Sci.* **4**, 1–10 (2021).
59. Fischer, E. M., Seneviratne, S. I., Lüthi, D. & Schär, C. Contribution of land–atmosphere coupling to recent European summer heat waves. *Geophys. Res. Lett.* **34**, L06707 (2007).
60. Bell, B. et al. The ERA5 global reanalysis: preliminary extension to 1950. *Q. J. R. Meteorol. Soc.* **147**, 4186–4227 (2021).
61. Li, M., Wu, P. & Ma, Z. A comprehensive evaluation of soil moisture and soil temperature from third-generation atmospheric and land reanalysis data sets. *Int. J. Climatol.* **40**, 5744–5766 (2020).
62. Yang, S., Zeng, J., Fan, W. & Cui, Y. Evaluating root-zone soil moisture products from GLEAM, GLDAS, and ERA5 based on in situ observations and triple collocation method over the Tibetan Plateau. *J. Hydrometeorol.* **23**, 1861–1878 (2022).
63. Dai, Y. et al. A review of the global soil property maps for Earth system models. *Soil* **5**, 137–158 (2019).
64. Fatichi, S., Or, D. & Walko, R. et al. Soil structure is an important omission in Earth System Models. *Nat. Commun.* **11**, 522 (2020).
65. Szabó, B., Weynants, M. & Weber, T. K. D. Updated European hydraulic pedotransfer functions with communicated uncertainties in the predicted variables (euptfv2). *Geosci. Model Dev.* **14**, 151–175 (2021).
66. Poggio, L. et al. SoilGrids 2.0: producing soil information for the globe with quantified spatial uncertainty. *Soil* **7**, 217–240 (2021).
67. Chen, S. et al. Digital mapping of GlobalSoilMap soil properties at a broad scale: a review. *Geoderma* **409**, 115567 (2022).
68. Loveland, T. R. et al. Development of a global land cover characteristics database and IGBP DISCover from the 1km AVHRR data. *Int. J. Remote Sens.* **21**, 1303–1330 (2000).
69. Dickinson, R., Henderson-Sellers, A. & Kennedy, P. Biosphere–Atmosphere Transfer Scheme (BATS) Version 1e as Coupled to the NCAR Community Climate model. *Technical Report NCAR/TN-387 + STR* (NCAR Boulder, Colorado, 1993).
70. Thenkabail, P. S. et al. Global cropland-extent product at 30-m resolution (GCEP30) derived from Landsat satellite time-series data for the year 2015 using multiple machine-learning algorithms on Google Earth Engine cloud. *U. S. Geol. Surv. Prof. Pap.* **1868**, 1–63 (2021).
71. Thenkabail, P. S. et al. Assessing future risks to agricultural productivity, water resources and food security: how can remote sensing help? *Photogram. Eng. Remote Sens.* **78**, 773–782 (2012).
72. Shuttleworth, W. J. Evaporation. In *Handbook of Hydrology* 4.1–4.53 (McGraw-Hill Inc, New York, 1993).
73. Allen R.G., Pereira L.S., Raes, D., & Smith M. Crop Evapotranspiration: Guidelines for Computing Crop Water Requirements: Irrigation and Drainage Paper **56** (Food and Agriculture Organization of the United Nations, Rome, 1998).
74. Ceppi, A. et al. Realtime drought forecasting system for irrigation management. *Hydrol. Earth Syst. Sci.* **18**, 3353–3366 (2014).

Acknowledgements

This research was supported by Argentina's National Agency for Scientific and Technological Promotion (Projects PICT-2019-2019-03982 and PICT-2019-2019-00481), the Argentine National Council for Scientific and Technical Research (Grant PIP-CONICET-11220200102257CO), and the Universidad Nacional del Litoral (Grant CAI + D-2020-50620190100082LI). E.H.B. was supported by NOAA grant NA19NES4320002 (Cooperative Institute for Satellite Earth System Studies (CISESS)) at the University of Maryland/ESSIC. E.H.B. thanks the Fulbright Commission for facilitating the last stages of this research.

Author contributions

O.V.M., M.A.L., and E.H.B. designed the study. M.A.L. and M.J.P. carried out the research. M.A.L., M.J.P., O.V.M., G.V.M., and E.H.B. analyzed and discussed the results. M.A.L., G.V.M., and E.H.B. acquired funding and resources. M.A.L. prepared the original manuscript, and all authors contributed to its subsequent versions.

Competing interests

The authors declare no competing interests.

Additional information

Supplementary information The online version contains supplementary material available at <https://doi.org/10.1038/s41612-024-00618-0>.

Correspondence and requests for materials should be addressed to Miguel A. Lovino.

Reprints and permissions information is available at <http://www.nature.com/reprints>

Publisher's note Springer Nature remains neutral with regard to jurisdictional claims in published maps and institutional affiliations.

Open Access This article is licensed under a Creative Commons Attribution 4.0 International License, which permits use, sharing, adaptation, distribution and reproduction in any medium or format, as long as you give appropriate credit to the original author(s) and the source, provide a link to the Creative Commons licence, and indicate if changes were made. The images or other third party material in this article are included in the article's Creative Commons licence, unless indicated otherwise in a credit line to the material. If material is not included in the article's Creative Commons licence and your intended use is not permitted by statutory regulation or exceeds the permitted use, you will need to obtain permission directly from the copyright holder. To view a copy of this licence, visit <http://creativecommons.org/licenses/by/4.0/>.

© The Author(s) 2024

Artículo 4

Sequías agrícolas repentina y su impacto en el rendimiento de los cultivos en el sudeste de Sudamérica.

Agricultural flash droughts and their impact on crop yields in southeastern South America

Miguel A. Lovino^{1,2*}, M. Josefina Pierrestegui^{1,2}, Lumila Masaro^{1,2}, Omar V. Müller^{1,2}, Gabriela V. Müller^{1,2} and Ernesto H. Berbery³

¹ Consejo Nacional de Investigaciones Científicas y Técnicas (CONICET), Argentina

² Centro de Estudios de Variabilidad y Cambio Climático (CEVARCAM), Facultad de Ingeniería y Ciencias Hídricas (FICH), Universidad Nacional del Litoral (UNL), Ciudad Universitaria, Ruta Nacional N° 168 - km 472,4. (3000) Santa Fe, Argentina.

³ Earth System Science Interdisciplinary Center/Cooperative Institute for Satellite Earth System Studies, University of Maryland, College Park, College Park, MD 20740, USA.

E-mail: mlovino@unl.edu.ar

Received xxxxxx

Accepted for publication xxxxxx

Published xxxxxx

Abstract

This study investigates the characteristics of agricultural flash droughts (AFDs) and their impacts on critical growth periods of soybean and corn in southeastern South America (SESA). Using ERA5 data from 1960 to 2022, we examine AFD frequency, duration, intensity, trends, seasonality, life cycle, and the influence of land-atmosphere interactions. Historical crop data, spanning different time periods across SESA countries, are analyzed to assess how the spatiotemporal evolution and varying life cycles of AFDs affect crop yields. The highest AFD frequencies (3 to 8 events per decade) occur in the central portion of SESA. These rapidly intensifying events often evolve into seasonal droughts lasting 1.5 to 3 months. Although area-averaged AFD frequency shows no significant change in central SESA, positive trends are noticeable in southern Brazil and Uruguay. Towards the north of SESA, AFDs are less frequent, with 1 to 3 episodes per decade, although the frequency has significantly increased since 1970. AFDs tend to last over 3 months and reach higher intensity. Land-atmosphere feedback mechanisms are reflected in high positive vapor pressure deficit and temperature anomalies that exacerbate soil moisture deficits despite a relatively stable precipitation deficit, accelerating AFD intensification periods. AFDs typically impact smaller areas, while slow-evolving droughts affect larger regions. However, AFDs' timing during the critical growth periods of the crops can lead to substantial yield losses. In central SESA, AFDs mainly occur between November and January, affecting both crops during their flowering and grain filling in December and January. In northern SESA, AFDs occur later, from February to April, primarily impacting second-season corn. The overall impact on crop yields depends on the duration, spatial extent, and intensity of the drought after its intensification.

Keywords: agricultural flash droughts, crops, soil moisture, land-atmosphere interactions

* corresponding author

1. Introduction

The economies of southeastern South America (SESA) heavily rely on rainfed agriculture, making them vulnerable to severe droughts that can significantly impact Gross National Products [1, 2]. In Argentina, severe droughts in 2009, 2012, and 2018 caused combined losses of about US\$ 20,000 million in soybean and corn production, equivalent to approximately 50% of the Argentinean Central Bank's international reserves in 2021 [3]. These severe droughts particularly led to crop yield losses when occurring during corn and soybean sensitive growth periods [4]. In Brazil, droughts have significantly affected water, food, and energy security [5]. For instance, severe flash droughts in 2005 and 2012, peaking in January and February during the grain-filling stage, significantly impacted first-season corn yields in southern Brazil [6].

Droughts are generally considered slow-evolving climatic phenomena. However, droughts of rapid intensification on sub-seasonal time scales—called flash droughts—have been identified in recent decades. These flash droughts thwart drought monitoring and forecasting [7-9]. Flash droughts are forced by extreme precipitation deficits, high temperatures, and abnormally high evapotranspiration that favor rapid soil moisture depletion rates [10-12]. Flash droughts have become more frequent, widespread, faster-developing, and longer-lasting due to global warming [13-16]. Flash droughts are projected to increase significantly in the 21st century, particularly in global croplands [17-19].

SESA has been identified as a hotspot for agricultural flash droughts (AFDs), which occur when plant water requirements are unmet, particularly during critical growth periods of crops [20]. These AFDs occur more frequently in spring and summer [20], coinciding with critical growth periods of major crops like corn and soybean [4]. Despite their socio-economic impacts, flash droughts have been scarcely studied in South America (e.g., [21]), particularly in SESA (e.g., [22]).

Land-atmosphere interactions have been suggested to intensify and propagate droughts and heatwaves, increasing the risk of crop failures [23-29]. SESA is a recognized land-atmospheric coupling hotspot, characterized by high soil moisture–temperature coupling during dry summers [30, 31]. This coupling intensifies temperature extremes, increasing the persistence of hot days [32,33]. Land-atmosphere interactions are thus particularly relevant in studies of AFDs in SESA.

This study documents the main characteristics of agricultural flash droughts and their impacts on critical crop periods in SESA. We assess their main features, i.e., frequency of occurrence, duration, intensity, seasonality, and trends of agricultural flash droughts. We also discuss their onset and evolution, including the land-atmosphere coupling processes that favor these events.

2. Data and methods

2.1 Datasets

In the absence of spatially distributed soil moisture observations, root-zone volumetric soil moisture estimates in the soil's top meter (SM) were obtained from the European Center for Medium-Range Weather Forecasts Reanalysis version 5 (ERA5; [34-36]) for the 1960-2022 period, with a spatial resolution of $0.25^\circ \times 0.25^\circ$ latitude-longitude. ERA5 was selected due to its full representation of the coupled land-atmosphere system, ensuring a physically consistent simulation of the processes driving AFDs. Moreover, ERA5 soil moisture simulations have demonstrated temporal stability since 1960 in South America [35]. Although ERA5 soil moisture data have some known uncertainties [34, 35], it outperforms other reanalyses in several world regions [37]. In southeastern South America, root zone soil moisture and its primary driver, precipitation, show reliable accuracy [38-40].

Soil field capacity and wilting point are represented by ERA5 parameters that depend on the soil class at each grid point and remain constant over time. Additional ERA5 variables include total precipitation (pr), evapotranspiration (EVT), 2-m air temperature (T), and 2-m dew-point temperature (Tdew). These data were used to assess land-atmosphere interactions and investigate the dominant processes before and during AFD events. Non-overlapping pentads (five-day means) of the studied variables were calculated from ERA5 hourly data to minimize daily variability and capture the rapid flash drought onset [41]. Pentad standardized anomalies were calculated as deviations from the 1960-2022 climatological mean for each corresponding pentad, normalized by their respective standard deviations.

Historical data on corn and soybean production, yield, and harvested area were collected at the smallest geographic units (departments or municipalities) across SESA countries. Following [42], critical quality requirements for crop data were considered, including the number of available data years, spatial resolution, and data quality. Crop data were provided by national agencies (see Data availability statement), with records from 1970 in Argentina, 1974 in Brazil, 1990 in Paraguay, 1985 in Bolivia, and 2000 in Uruguay (where data are sparse and contain gaps). Data quality was assessed by identifying and removing erroneous values and outliers. To maximize crop data utilization, the entire available time series were used, excluding geographic units with over 50% missing data between 2000 and 2020. A common 2000–2020 period was adopted to estimate mean crop yields, production, and harvested areas. Yearly standardized anomalies were calculated for each country's crop yield data by applying a least-squares linear detrending over the entire available period. While the drought study covers 1960 to 2022, crop

impact analysis is constrained by data availability in each country.

To complement the assessment of AFD impacts on crop yields, we analyzed the MODIS MOD17A2H v006 Gross Primary Productivity (GPP, gC m^{-2}) 8-day composite at 500 m resolution for the 2000–2020 period [43]. GPP quantifies photosynthetic activity and directly estimates plant carbon assimilation, making it a proxy for biomass generation and crop productivity [44]. As GPP estimations integrate climatic and biome-specific radiation efficiency parameters, it serves as a reliable indicator of drought-induced yield reductions [45]. GPP standardized anomalies were computed as

deviations from the 2000–2020 climatological mean for 10-day intervals, normalized by their respective standard deviations.

2.2 Study region and characteristics of major crops

SESA, defined as the continental region east of the Andes between 17–40 °S and 38–65 °W (red box in figure 1a), includes southern Brazil, southern Bolivia, Paraguay, Uruguay, and central-northeastern Argentina. It encompasses large fertile plains and is a key global food-producing region [46]. The main crops in SESA are soybean and corn. Soybean

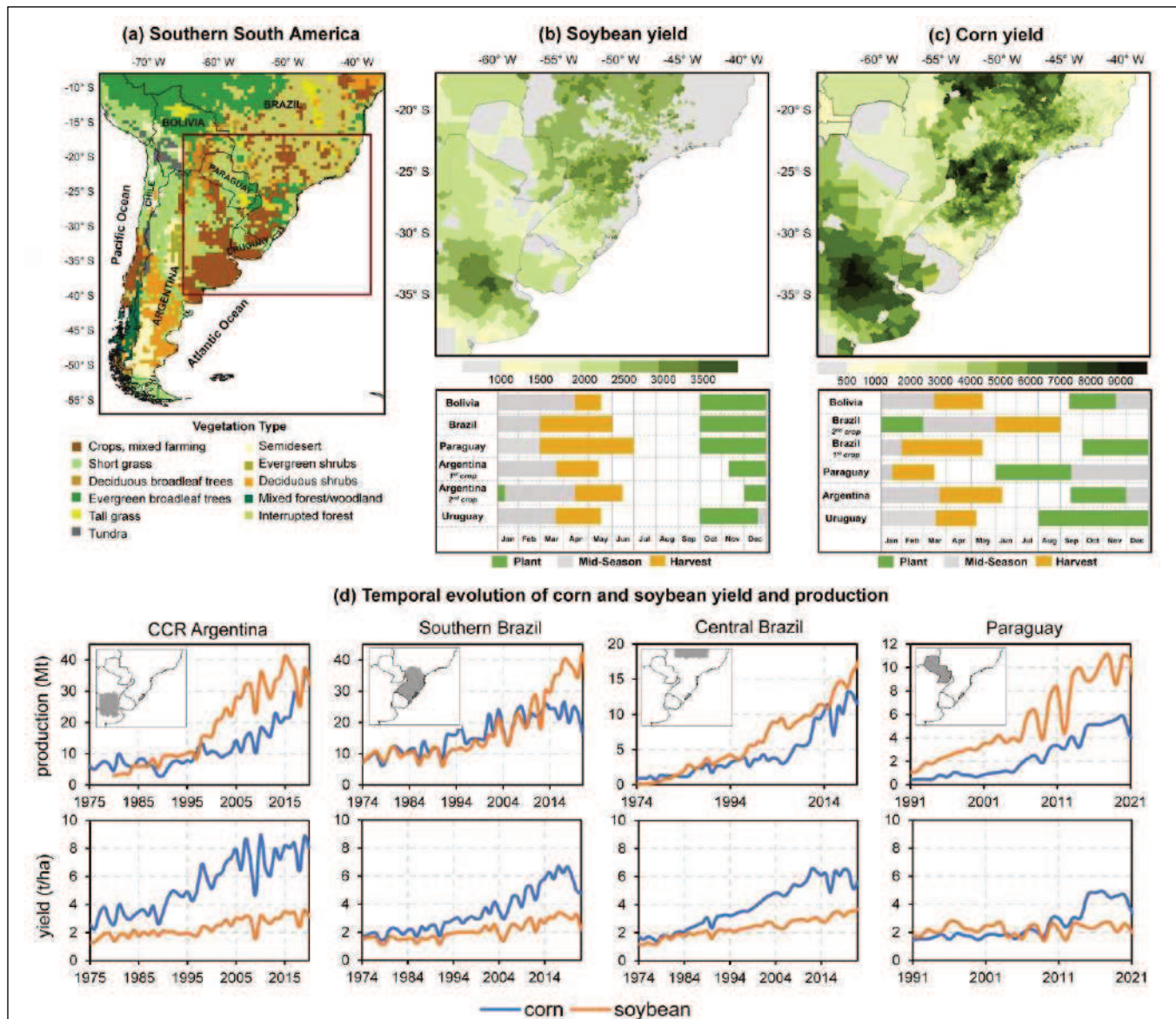


Figure 1. (a) Southern South America countries with the dominant vegetation types in the ERA5 dataset according to each pixel's high or low vegetation coverage. The study region in southeastern South America (SESA) is highlighted with a red rectangle. Average (b) soybean yields and (c) corn yields during the 2000–2020 period, with crop life cycles displayed for each country. (d) Temporal evolution of corn and soybean yields and production across key agricultural regions: Argentina's core crop region (CCR, 1975–2020), southern Brazil (1974–2022), central Brazil (1974–2014), and Paraguay (1991–2021).

yields exceed 2500 t/ha in the plains of Argentina, eastern Paraguay, and southern and central Brazil (figure 1b, see also figure S1a). Soybean follows a similar 8-month-long life cycle across all SESA countries, being planted from October to December and harvested from March to June (figure 1b). Soybean critical period of high sensitivity to water availability is January–February, during flowering and grain filling. Corn production is also widespread, achieving the highest yields in regions like those for soybean cultivation (figure 1c, see also figure S1b). Corn yields range from 6000 to 10000 t/ha in the core crop region of Argentina (CCR), as well as in southern and central Brazil. Corn's critical period generally occurs in summer, except in Paraguay, where it takes place in spring due to earlier planting (figure 1c). Second-season corn in central Brazil experiences its critical period between March and May (figure 1c and figure S1c).

Corn and soybean production and yields have significantly increased in key SESA regions since 1990 (figure 1d, see also [4]). Soybean production has quadrupled in the CCR, southern Brazil, and central Brazil, while in Paraguay, it has quintupled. In Argentina and Brazil, soybean yields have risen by 50%, from 2 t/ha to 3 t/ha. Corn production has tripled in the CCR and central Brazil, doubled in southern Brazil, and quintupled in Paraguay. Corn yields have increased from 4 t/ha to 8 t/ha in the CCR and from 2 t/ha to 6 t/ha in southern and central Brazil. These increases are attributed to advances in agricultural technology, genetic improvements, enhanced agronomic practices (particularly corn double cropping), and cropland expansion [47, 48].

2.3 Agricultural flash drought characteristics and trends

Agricultural flash droughts were identified using an approach proposed by ref. [20] (see supplementary material for details) based on the soil water deficit index (SWDI, [49]), reflecting both soil moisture deficit and plant water stress. The upper SWDI threshold (SWDI = -3) marks the initiation of the soil moisture deficit, while the lower SWDI threshold (SWDI = -5) signals crop water stress. Note that different flash drought indicators and input datasets can result in differences in flash drought climatological characteristics [50–52] (see [20] for further details). This study adopted a soil-specific water availability indicator, ensuring our findings are consistent with prior research that relies on soil moisture-based indices [20].

The flash characteristic of these droughts stems from their rapid intensification, during which soil moisture depletes rapidly (see figure S2a). After the intensification, drought duration and intensity vary. In this study, maximum intensity is the lowest SWDI value while mean intensity is the average SWDI value over the drought period, excluding the intensification period. Drought duration continues until SWDI acquires values greater than -4 (see figure S2a). This threshold

is chosen to include events that slightly exceed SWDI = -5 (the drought threshold) but quickly transition to lower SWDI values.

Linear and nonlinear trends were estimated for the 1960 to 2022 period. A linear trend analysis of AFDs per year was performed to approximate the overall spatial patterns of changes in AFD occurrence. Linear trends were estimated using the least squares method, which is well-suited for time series with a high frequency of zero values, as in the case of yearly AFD occurrences. The statistical significance of linear trends at the 5% significance level was evaluated using the Mann–Kendall test [53, 54]. Given the region's known nonlinear climatic changes [55–57], nonlinear trends were computed using Singular Spectrum Analysis (SSA; [58, 59]) to detect complex temporal variations in area-averaged AFDs per year. Area-averaged AFD frequency was calculated as the spatial mean of the annual AFD frequency over land-only grid points. SSA detects nonlinear trends via eigenvalue decomposition, resulting in temporal-empirical orthogonal functions (T-EOFs) and temporal-principal components (T-PCs). Each T-PC represents a filtered version of the original time series, capturing variance associated with its eigenvalue. Nonlinear trend significance at the 95% level was tested using the Monte Carlo method [60]. A total of 1,000 red noise series preserving the data's autocorrelation were generated, and their trends were computed. The observed trend was considered significant if it exceeded the 95th percentile of the synthetic trends. By integrating linear and nonlinear methods, this approach allows a more comprehensive analysis of changes in AFDs over time.

2.4 Land-atmosphere interactions

Land-atmosphere interactions are crucial in drought development [61–63]. These interactions may respond to many possible processes, especially through soil moisture-temperature (SM-T) and soil moisture-precipitation (SM-P) couplings [61]. Such interactions are particularly strong in transition zones between wet and dry climates [61, 64].

According to ref. [65], SESA lies in a transition zone identified as an austral summer hotspot, where SM-T coupling can intensify drought conditions [63, 66]. In SM-T coupling, drying/warming processes are driven by: (1) reduced soil moisture leading to decreased evapotranspiration, (2) decreased evapotranspiration increasing sensible heat flux, which raises air temperature, and (3) rising temperature further increasing vapor pressure deficit (VPD) and evaporative demand, possibly leading to a further decrease in soil moisture [61]. Therefore, SM-T coupling may contribute to more severe droughts and heatwaves, mainly during spring and summer [30, 32]. The SM-P coupling signal is less certain. Single model experiments have suggested a coupling signal in northern SESA, within the South American Monsoon region, where precipitation responds to soil moisture changes [67].

However, most SESA exhibits a weak coupling, with precipitation showing no significant response to soil moisture variations [e.g., 65, 68].

Given the dominance of SM-T feedback in SESA, and the availability of various land-atmosphere coupling metrics [69], we used an indicator that combines soil moisture with VPD [29]. VPD reflects atmospheric water demand, representing the difference between how much moisture the air can hold versus how much is present. While evapotranspiration represents the actual water flux into the atmosphere, VPD better captures plant physiological responses, such as stomatal regulation, making it a more robust indicator of atmospheric drying potential and vegetation stress [63,70,71]. During droughts, VPD typically increases, even in water-limited systems where evaporation decreases, thereby raising evaporative demand [49]. This SM-VPD feedback is particularly relevant during flash drought intensifications, characterized by a rapid rise in the evaporative demand and a simultaneous decrease in soil moisture [11].

Following refs. [72, 73], VPD is derived from T and Tdew as the difference between saturated vapor pressure (SVP, equation 1) and actual vapor pressure (AVP, equation 2).

$$SVP = 6.1084 \cdot e^{\frac{17.625 T_{dew}}{T_{dew} + 243.04}} \quad (1)$$

$$AVP = 6.1084 \cdot e^{\frac{17.625 T}{T + 243.04}} \quad (2)$$

$$VPD = SVP - AVP \quad (3)$$

The strength of SM-VPD coupling is quantified using the π diagnostic [63, 74], adapted by ref. [29] to study flash droughts on pentad timesteps. The long-term SM-VPD coupling metric (π) is defined in terms of the covariance (cov) and the standard deviation (σ):

$$\pi = -\frac{cov(SM, VPD)}{\sigma_{SM} \cdot \sigma_{VPD}} \quad (4)$$

The metric π captures land-atmospheric coupling strength during flash droughts by examining how the atmospheric moisture demand (through VPD) and soil moisture supply (through SM) regulate EVT. For each i^{th} pentad, π_i is defined as:

$$\pi_i = -\frac{SM_i - \overline{SM}}{\sigma_{SM}} \cdot \frac{VPD_i - \overline{VPD}}{\sigma_{VPD}} = -SM'_i \cdot VPD'_i \quad (5)$$

where \overline{SM} and \overline{VPD} are climatological means over the study period, and SM' and VPD' are standardized anomalies. To specifically address dry spells within flash droughts, following [29], VPD' is set to zero when SM' is positive, (soil moisture meets atmospheric demand and EVT is energy-limited), making π_i zero. Positive π_i values occur under

negative SM' (soil moisture deficit conditions, water-limited EVT) and positive VPD' (high atmospheric demand). Higher positive π_i values reflect stronger coupling. Negative π_i values, corresponding to negative SM' and VPD' , are not considered as coupling, indicating no influence on drought development.

Following [75], the statistical significance of the metric π was estimated with a Monte Carlo bootstrap method. We generated 500 π values from shuffled time series and estimated significance as the fraction of these values with a magnitude smaller than the observed feedback parameter.

3. Results

3.1 Climatological characteristics and changes of agricultural flash droughts

Agricultural flash droughts are more frequent in SESA's central region (figure 2a, center box). AFDs occur 3 to 8 times per decade, with the highest frequencies (5 to 8 AFDs per decade) in southern Brazil and Paraguay, covering nearly 10% of SESA's total area (inset histogram, figure 2a). In central SESA, drought conditions typically last 10 to 20 pentads (1.5 to 3 months, figure 2b), or even longer in Uruguay, indicating that these rapidly-intensifying events can evolve into seasonal droughts. Following the AFD intensification phase, agricultural drought conditions reach high intensity (up to SWDI = -7) across central SESA, with even greater intensity (-7 > SWDI > -8) in Uruguay and southern Brazil, where AFDs are most frequent (figure 2c). According to the spatial distribution of linear trends (figure 2d), AFDs show positive changes in southern Brazil and Uruguay and negative changes in central-northeastern Argentina and southern Paraguay. Consequently, the area-averaged AFD frequency across central SESA shows no significant change, as revealed by the nonlinear trend analysis (figure 2e).

The northern part of SESA (figure 2a, northern box) is the second most frequent region for AFDs, with 1–2 events per decade, rising to 2–3 events in the western portion of this region. Although less frequent than in central SESA, AFDs tend to be longer and more intense. Drought conditions in northern SESA can last more than 20 pentads and reach high intensity (-7 > SWDI > -9). Notably, AFDs show increasing trends throughout the region, with a maximum rate of change of 0.05 events per decade (figure 2d). The average number of AFD events doubled from the 1970s to the 2010s (see the nonlinear trend in figure 2e). However, this increasing trend appears to have stabilized since 2010 (figure 2e).

Agricultural flash droughts are sparse in western SESA's arid Chaco Seco region, with less than one event per decade. However, these occasional droughts tend to have the longest duration and highest intensities, as soil moisture often approaches the wilting point. AFDs in this zone have declined

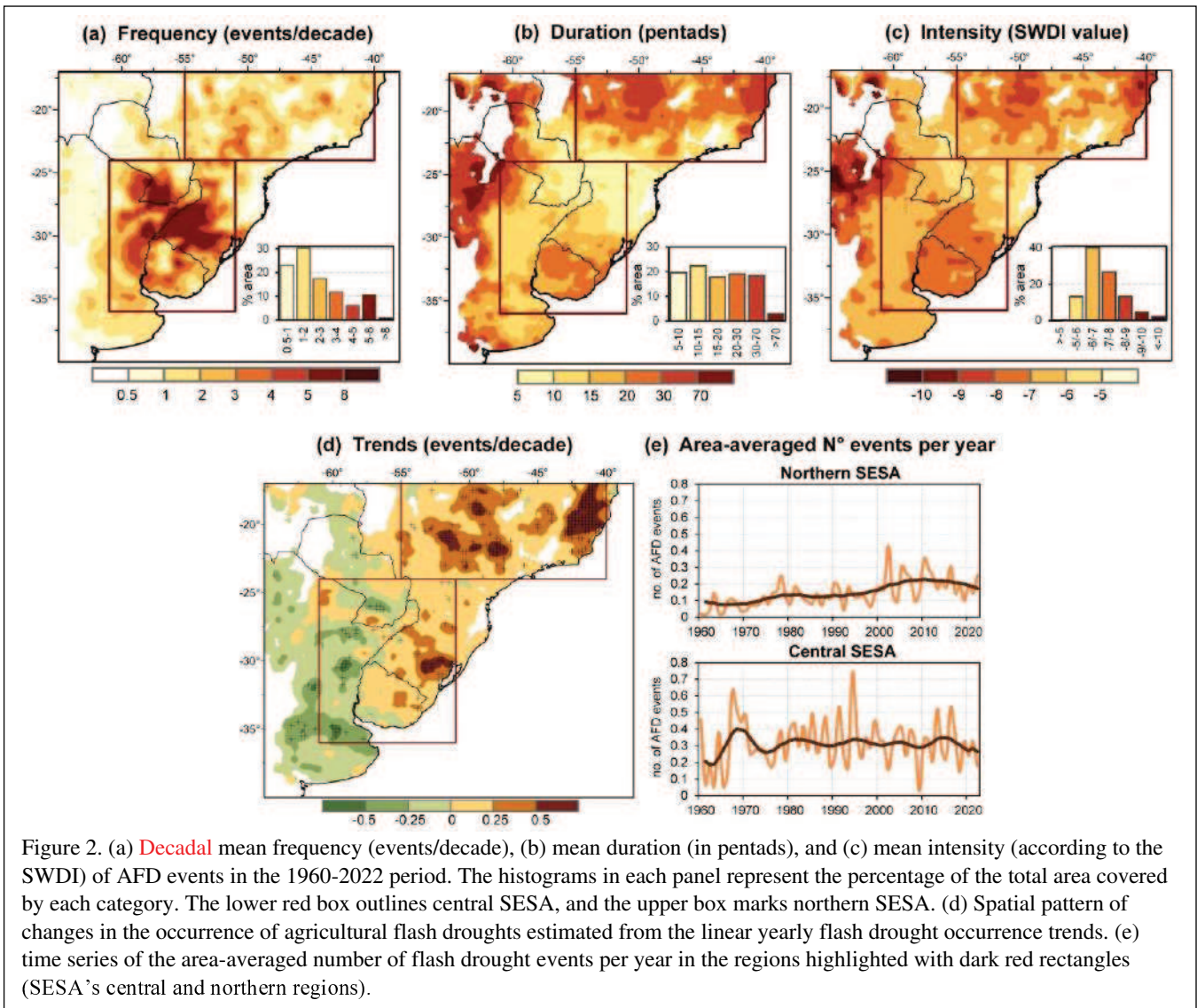


Figure 2. (a) Decadal mean frequency (events/decade), (b) mean duration (in pentads), and (c) mean intensity (according to the SWDI) of AFD events in the 1960–2022 period. The histograms in each panel represent the percentage of the total area covered by each category. The lower red box outlines central SESA, and the upper box marks northern SESA. (d) Spatial pattern of changes in the occurrence of agricultural flash droughts estimated from the linear yearly flash drought occurrence trends. (e) time series of the area-averaged number of flash drought events per year in the regions highlighted with dark red rectangles (SESA's central and northern regions).

over recent decades, reducing their already infrequent occurrence (figure 2d).

The droughts' timing of occurrence is critical for crops. In SESA's central region, AFDs are more frequent during austral spring (SON) and peak in austral summer (DJF) (figure 3a). During these seasons, 1 to 2 events per decade are common throughout the area, with higher frequencies at specific places. In summer, AFDs can reach up to 3 events per decade in northeastern Argentina and southern Paraguay, and up to 4 events in southern Brazil. The highest probabilities of AFD occurrence are observed in December, November, and January (figure 3b). When drought intensification reaches its maximum in December and January, AFDs can coincide with critical growth periods of corn and soybean. Depending on the drought's duration, typically lasting between 5 to 20 pentads (1 to 3 months), these crops can face substantial yield losses.

SESA's northern region, and more specifically central Brazil, has a high corn production (figure S1b). Due to the

infrequent frosts, this region supports two corn-growing cycles each year. The second cycle spans from January to August, with its critical growth period occurring in MAM (figure 1c). AFDs are frequent during MAM in this region (figure 3a), particularly in April (figure 3b), and are often long-lasting and intense (see figure 2b–c). Consequently, AFDs can coincide with the critical growth period of second-season corn, leaving it under vulnerable conditions.

3.2 Development, evolution, and the impact of land-atmospheric coupling on AFDs

According to the top row in figure 4, a composite of AFDs shows that they rapidly intensify in SESA following a common life cycle pattern identified globally by ref. [20]. Before the AFD onset (lags –2 to –1), anomalies of all variables (pr, T, EVT, VPD, SM) remain relatively stable. As the onset approaches (from lag –1 to the onset), precipitation

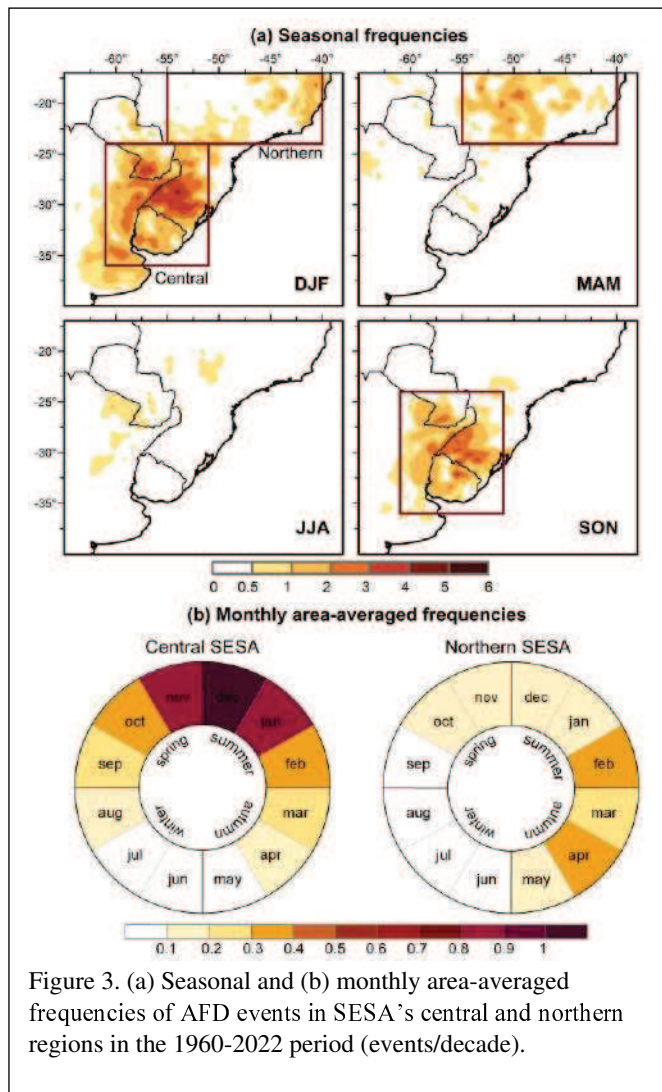


Figure 3. (a) Seasonal and (b) monthly area-averaged frequencies of AFD events in SESA's central and northern regions in the 1960-2022 period (events/decade).

decays while evapotranspiration begins to rise, driven by elevated VPD and sufficient soil moisture within the energy-limited regime. At the onset, the precipitation deficit deepens, evapotranspiration reaches its highest positive anomalies, and soil moisture starts to deplete. After the onset (lag +1), the precipitation deficit reaches its maximum severity, the temperature rapidly rises, and evapotranspiration starts to decrease due to water stress. As the flash drought progresses (lags +1 to +3), this process intensifies: temperature keeps rising, evapotranspiration continues to decline, and soil moisture further diminishes.

The spatiotemporal distribution of standardized anomalies in figure 4 highlights regions in SESA where this life cycle is strong or weak. For simplicity, we will discuss lags and variables without referencing figure 4, as they are easily identified. Before the onset (lags -2 to -1), non-drought conditions prevail, with positive soil moisture anomalies across most of SESA. Between lag -1 and the onset, mild negative precipitation anomalies develop in central and northern SESA, where AFDs frequently develop (see section

3.1). At the flash drought onset, the precipitation deficit expands while evapotranspiration increases markedly throughout SESA. At this stage, positive VPD anomalies indicate increasing evaporative demand that further deepens the soil moisture depletion, mainly in the northern region. After the onset (lags +1 and +2), the high precipitation deficit extends across the entire SESA, highlighting its critical role in AFD development.

The drought's life cycle intensifies sharply in SESA's northern region, where high VPD and significant temperature increases lead to a pronounced soil moisture decline. This region experiences severe drought conditions rapidly, marked by the most significant soil moisture deficits, warming, and reductions in evapotranspiration. Notably, this is also where flash drought intensity peaks (figure 2c). In contrast, the process is less abrupt in the central region, where soil moisture deficits rise from lags +1 and +2 as positive VPD and temperature anomalies intensify, while evapotranspiration decreases. Central SESA, which has the highest frequency of AFDs, undergoes severe drought conditions after lag +3 when SM anomalies fall below -1, following intensification periods of at least 15 days.

The AFD intensification is largely driven by land-atmosphere interactions, specifically the SM-T coupling, which is significant at the 90% confidence level across more than 90% of the study region, as determined by the Monte Carlo bootstrap method (figure S3). However, AFD mechanisms are multiple and complex and may also be influenced by non-local effects and atmospheric intraseasonal variability, which are not considered in this analysis. First, the SM-VPD coupling metric π presents large values during the AFD intensification period compared to non-drought periods (figure S4). Second, high positive VPD anomalies between lags +1 and +3 further exacerbate soil moisture deficits in the two regions, particularly toward northeastern SESA. Although standardized precipitation anomalies of about -1 contribute to rapid soil moisture depletion, high VPD anomalies result in soil moisture anomalies falling below -1.5 at lag +3. Consequently, π reaches its highest values in northern SESA at lag +3 (weaker in central SESA), indicating that land-atmosphere feedback mechanisms intensify AFDs. Consistently, northern SESA shows the strongest coupling during MAM, when most AFDs develop (figure S5).

Temperature also plays a crucial role in the intensification of AFDs in SESA. Positive temperature anomalies persist longer than precipitation deficits, significantly influencing the intensity and duration of soil moisture deficits. As evapotranspiration diminishes in a water-limited regime (after lag +1, figure 4), more energy is transferred to sensible heat flux, elevating temperature and VPD. Depending on their duration and intensity, these positive temperature anomalies may contribute to heatwaves, further exacerbating drought conditions.

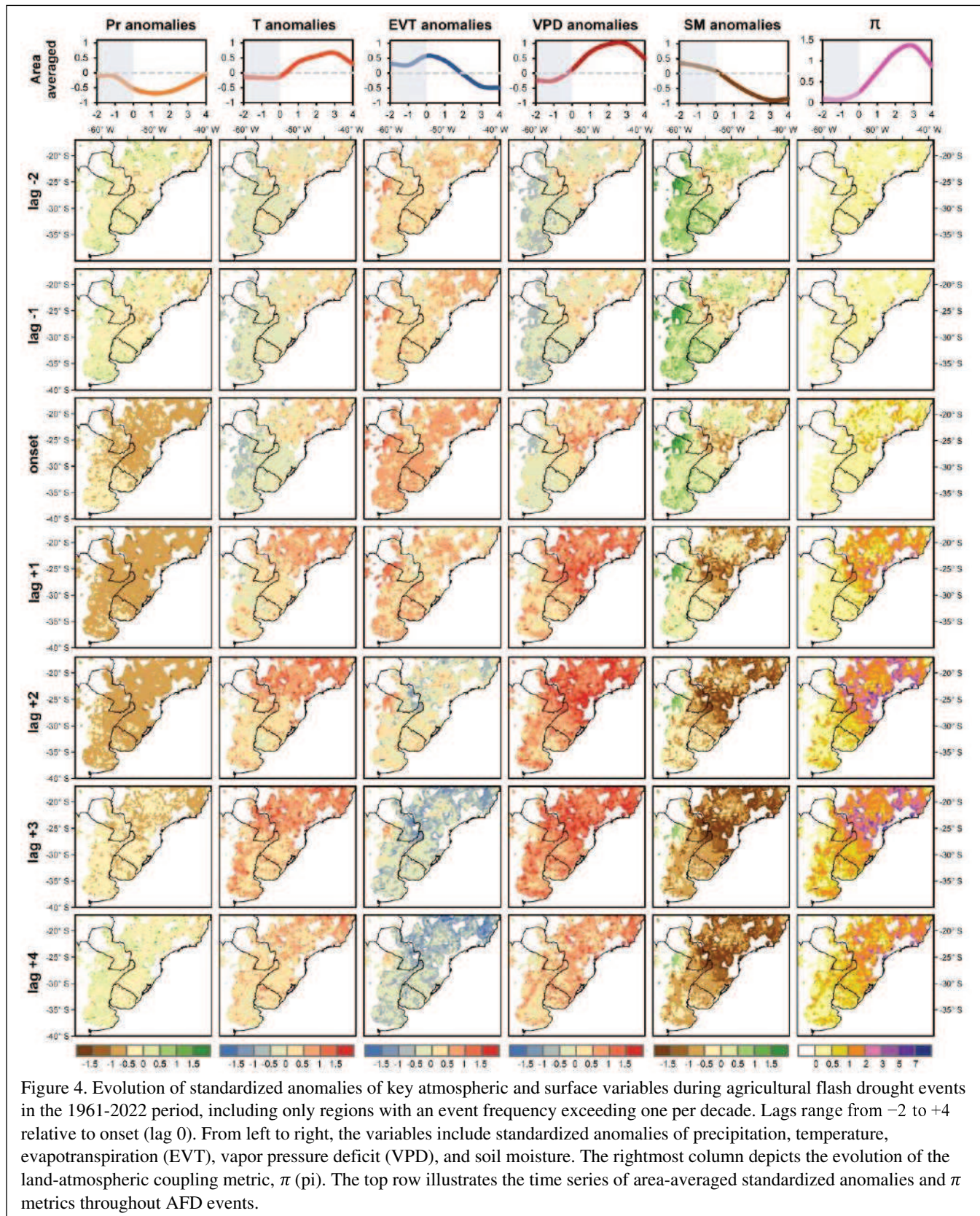


Figure 4. Evolution of standardized anomalies of key atmospheric and surface variables during agricultural flash drought events in the 1961–2022 period, including only regions with an event frequency exceeding one per decade. Lags range from -2 to $+4$ relative to onset (lag 0). From left to right, the variables include standardized anomalies of precipitation, temperature, evapotranspiration (EVT), vapor pressure deficit (VPD), and soil moisture. The rightmost column depicts the evolution of the land-atmospheric coupling metric, π (pi). The top row illustrates the time series of area-averaged standardized anomalies and π metrics throughout AFD events.

3.3 Impacts on crops

The impact of AFDs on crops is first analyzed by contrasting AFD cases in areas within central and northern SESA and crop yield anomalies during these events. One of the most intense AFDs in central SESA developed in November 2005 and persisted as a severe drought until May 2006 (figure 5a). This event led to substantial yield reductions in corn and soybean across much of the area (figure 5b and 5c; see a similar case in figure S6). The severity—defined as the

combined effect of duration and intensity—of this austral summer event was exacerbated as the negative precipitation anomalies favored the development of hot spells and prevented soil recovery in between rainfall events (figure 5a). While not all regions affected by this AFD show negative standardized yield anomalies for corn and soybean, the largest declines were concentrated in southern Brazil (figure 5b-c), where the event reached its greatest duration and intensity (figure S7). In regions where AFDs occurred but did not cause

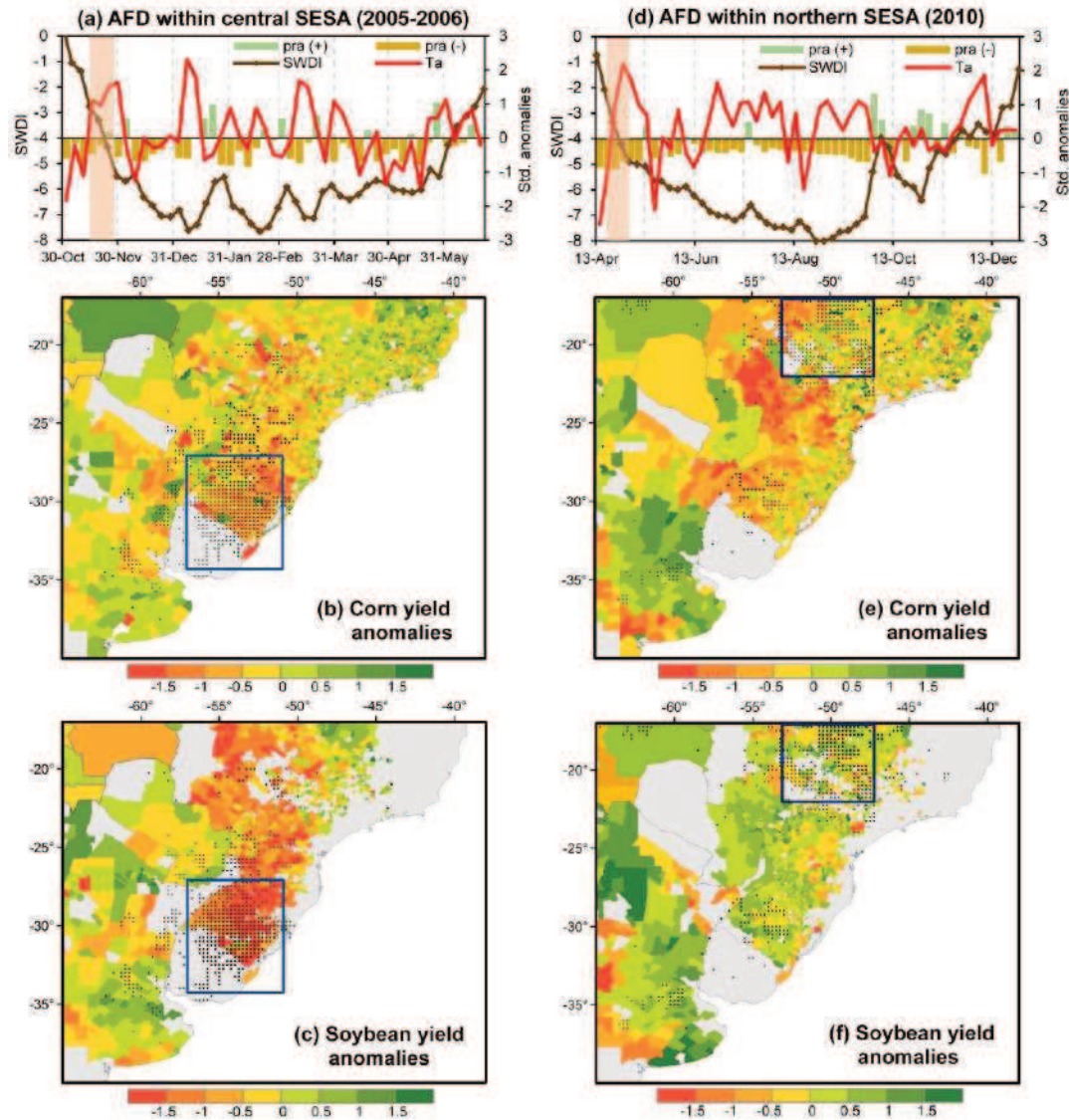


Figure 5. (a) Temporal evolution of an agricultural flash drought event that developed between November 2005 and May 2006 in the central region of SESA, as characterized by the Soil Water Deficit Index (SWDI). The panel also shows standardized anomalies of temperature (Ta) and precipitation (Pra(+)) and Pra(-)). Panels (b) and (c) present the standardized yield anomalies for corn and soybean, respectively, during the 2005-2006 crop season. The blue box delineates the sub-region within central SESA where the highest density of grid points experienced AFD, which was used to compute the area-averaged variables shown in (a). Black points mark the grid points where AFDs occurred. (d-f) Similar to (a-c), but for an AFD event in northern SESA between April and November 2010. Maps (e) and (f) show the standardized crop anomalies for the 2009-2010 crop season. The blue box delineates the sub-region within northern SESA where the highest density of grid points experienced AFD, which was used to compute the area-averaged variables shown in (d).

significant yield losses (e.g., Buenos Aires, in southern SESA), two key factors likely played a role: (i) short-lived or moderate AFDs may not impose prolonged stress, allowing crop recovery (see figure S8 for the case in Buenos Aires); and (ii) agronomic management, including soil water-holding capacity and adaptive management practices, could have helped mitigate impacts [76,77]. Conversely, in regions where yield declined despite the absence of detected AFDs, non-climatic factors such as pest outbreaks, plant diseases, soil degradation, and market-driven agronomic decisions likely contributed to the observed losses. A note of caution is that potential inaccuracies in ERA5 would reflect in the quality of the AFD detection.

In northern SESA, a severe AFD intensified in April 2010 and persisted until November, reaching its peak intensity ($\text{SWDI} = -8$) in August (figure 5d, see a similar case in figure S6). This event was characterized by a significant precipitation deficit extending into August and above-normal temperatures. This severe event led to a marked decrease in crop productivity over time, as illustrated by the evolution of GPP (see figure S8). It predominantly impacted corn yields in areas where drought intensified during the critical growth phase for second-season corn (figure 5e, see also figure S1c). In contrast, soybean yields were not adversely impacted (figure 5d), as soybeans are harvested between April and May in that region of Brazil (see figure 1b).

To further assess the impacts of AFDs on crops, we analyze the annual time series of standardized crop yield anomalies and GPP, the percentage of area affected by AFDs, and the average duration and intensity of these events in SESA's agricultural hotspots (figure 6). In Rio Grande do Sul, where AFDs occur most frequently, corn and soybean yield anomalies exhibit similar temporal evolution (figure 6a), likely due to their overlapping life cycles (figure 1b, c). The largest negative anomalies in soybean and corn yields correspond to peaks in high areal extent, duration, and intensity of AFDs (figure 6a). AFD characteristics show an inverse relationship with crop yields and GPP, where more extensive, longer-lasting, and more intense events lead to higher crop yield reductions and lower crop productivity (figure 6b). These variables show correlations between -0.5 and -0.6, with duration having a slightly stronger influence on corn yield losses ($r = -0.6$).

In Paraná, Brazil—one of the highest-yielding regions in SESA—the impact of AFDs is similar to that in Rio Grande do Sul (figure 6c-d). The correlations in Paraná are lower, likely due to the lower frequency of AFDs and the additional harvest of second-season corn (figure S1c). As a result, yield anomalies for soybean and corn differ slightly, with soybean yield reductions more closely aligned with AFD characteristics (figure 6c). Furthermore, AFDs can affect up to 40% of the area in Paraná, whereas in Rio Grande do Sul,

this can extend to 60%, suggesting that events with reduced areal extension may have a weaker impact.

In the CCR and central Brazil (other agricultural hotspots), no consistent correlation patterns between crop yields and AFD characteristics emerged (not shown). Notably, in central Brazil, GPP exhibits moderate correlations with AFD characteristics (r up to -0.4). While not as pronounced as in other regions, these correlations reinforce the reliability of GPP in capturing the effects of AFDs in crops. Conversely, in the CCR of Argentina, no significant relationship between GPP and AFD events was identified, likely because this region covers a large area where AFDs are spatially localized and infrequent. As a result, when averaging over the entire region, correlations between GPP and AFD characteristics may be diluted. These findings suggest that, unlike long-term droughts, which can span large areas and persist for years [4, 78], AFDs produce more localized impacts confined to smaller areas.

4. Summary

Southeastern South America is one of the world's most productive agricultural regions. In SESA, rainfed agriculture dominates, while irrigation remains scarce [79]. At the same time, SESA is also a hotspot for agricultural flash droughts [20]. These rapidly intensifying droughts can trigger severe water deficits within weeks, significantly reducing crop yields and threatening food security. This study explores key AFD characteristics in the 1960-2022 period to enhance our understanding of their historical behavior. We assess the impacts on two major crops, soybean and corn, by analyzing yield data across SESA and investigating how the spatiotemporal evolution and varying life cycles of AFDs can affect critical growth periods. Our findings lay the groundwork for developing AFD monitoring and forecasting systems, an essential step toward improving early warning capabilities, particularly in core crop-producing areas where AFDs are frequent and can have significant impacts. This study provides new insights into the specific characteristics of AFDs in SESA, underscoring their relevance for agricultural risk assessments to strengthen adaptation strategies.

Central SESA, covering northeastern Argentina, Uruguay, southern Brazil, and southeastern Paraguay, has the highest AFD frequency (3 to 8 events per decade), mostly in austral spring and summer. The highest frequency of AFDs occurs in November through January, interfering with the critical growth periods for soybean and corn in December and January. These rapidly intensifying events often evolve into seasonal droughts, with high-intensity conditions lasting 1.5 to 3 months. The intensification period typically takes more than 15 days to reach severe drought conditions, which are mainly driven by mild SM-VPD coupling, and moderate warming that increases VPD. While no significant mean

change in AFD frequency is observed across central SESA, positive trends are evident in southern Brazil and Uruguay.

In Northern SESA, which encompasses central-eastern Brazil, AFDs are less frequent (1 to 3 events per decade). AFDs typically intensify later (from March to May), reach higher intensity, and last longer (more than 3 months) than in

central SESA. They primarily impact the critical growth periods of second-season corn around March and April. High AFD intensity is favored by high positive VPD and temperature anomalies that exacerbate soil moisture deficits during the first 15 days of the intensification period. This rapid intensification is primarily driven by strong SM-VPD

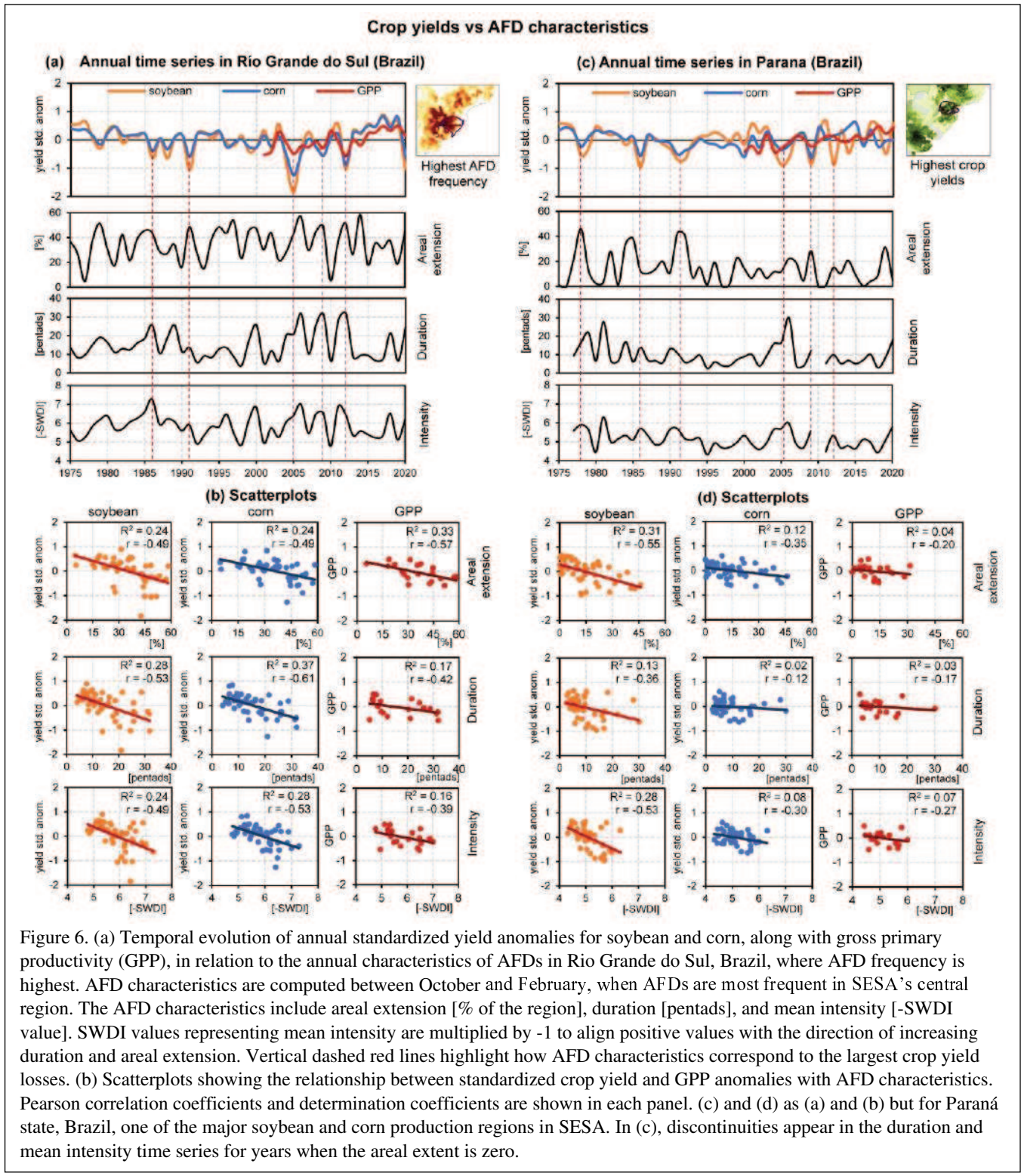


Figure 6. (a) Temporal evolution of annual standardized yield anomalies for soybean and corn, along with gross primary productivity (GPP), in relation to the annual characteristics of AFDs in Rio Grande do Sul, Brazil, where AFD frequency is highest. AFD characteristics are computed between October and February, when AFDs are most frequent in SESA's central region. The AFD characteristics include areal extension [% of the region], duration [pentads], and mean intensity [-SWDI value]. SWDI values representing mean intensity are multiplied by -1 to align positive values with the direction of increasing duration and areal extension. Vertical dashed red lines highlight how AFD characteristics correspond to the largest crop yield losses. (b) Scatterplots showing the relationship between standardized crop yield and GPP anomalies with AFD characteristics. Pearson correlation coefficients and determination coefficients are shown in each panel. (c) and (d) as (a) and (b) but for Paraná state, Brazil, one of the major soybean and corn production regions in SESA. In (c), discontinuities appear in the duration and mean intensity time series for years when the areal extent is zero.

coupling, despite relatively stable precipitation deficits, leading to an intensified drought life cycle with severe drought conditions developing in less than 15 days. These findings suggest that land-atmosphere feedback mechanisms favor rapid AFD intensification in northern SESA, consistent with results found in other countries [25-29]. AFD frequency in northern SESA increased significantly between 1970 and 2010. This upward trend may be partially linked to increasing concurrent hot and dry climatic conditions [15] and growing heatwave hazards [80].

The impact of AFDs on soybean and corn yields tends to be more localized than the widespread effects of slow-developing droughts, which can cause prolonged crop yield losses throughout SESA [2, 78, 81]. As expected, more extensive, longer-lasting, and more intense AFD events lead to higher crop yield reductions. Among these characteristics, drought duration strongly correlates with crop yield losses. Therefore, the overall impact of AFDs on crop yields primarily depends on the duration of the drought after the intensification period, while areal extension and intensity can further amplify crop losses. These findings underscore the importance of early warning systems that integrate flash drought prediction with conventional drought monitoring for detecting flash droughts' onset and tracking drought evolution. Such systems should ultimately provide valuable information to help mitigate agricultural impacts.

Data availability statement

The ERA5 dataset is available at <https://doi.org/10.24381/cds.adbb2d47>. Crop time series data are available from the National Ministry of Agriculture, Livestock and Fisheries in Argentina (www.datos.gob.ar), the Brazilian Institute of Geography and Statistics in Brazil (sidra.ibge.gov.br/pesquisa/pam/tabelas), the National Ministry of Agriculture and Livestock in Paraguay, the National Institute of Statistics in Bolivia (www.ine.gob.bo/index.php/estadisticas-economicas/agropecuaria/), and the Ministry of Agriculture, Livestock, and Fisheries in Uruguay ([https://www.gub.uy/ministerio-ganaderia-agricultura-pesca/datos-y-estadisticas/datos](http://www.gub.uy/ministerio-ganaderia-agricultura-pesca/datos-y-estadisticas/datos)).

Acknowledgments

We sincerely appreciate the constructive feedback from the anonymous reviewers, which enhanced the quality and clarity of this manuscript. This work was funded by Argentina's National Agency for Scientific and Technological Promotion (Projects PICT-2019-2019-03982 and PICT-2019-2019-00481), the Argentine National Council for Scientific and Technical Research (Grant PIP-CONICET-11220200102257CO). Ernesto H. Berberry was supported by NOAA grant NA19NES4320002 (Cooperative Institute for

Satellite Earth System Studies (CISESS)) at the University of Maryland/ESSIC.

References

- [1] Lovino M A, Müller O V, Müller G V, Sgroi L C and Baethgen W E 2018 Interannual-to-multidecadal hydroclimate variability and its sectoral impacts in Northeastern Argentina *Hydrol. Earth Syst. Sci.* **22** 3155-3174 <https://doi.org/10.5194/hess-22-3155-2018>
- [2] Naumann G, Vargas W M, Barbosa P, Blauhut V, Spinoni J and Vogt J V 2019 Dynamics of socioeconomic exposure, vulnerability and impacts of recent droughts in Argentina *Geosci. J.* **9**(1) 39 <https://doi.org/10.3390/geosciences9010039>
- [3] Thomasz E O, Vilker A S, Pérez-Franco I and García-García A 2024 Impact valuation of droughts in soybean and maize production: the case of Argentina *Int. J. Clim. Change Strategies Manage.* **16**(1) 63-90 <https://doi.org/10.1108/IJCCSM-11-2022-0139>
- [4] Sgroi L C, Lovino M A, Berberry E H and Müller G V 2021 Characteristics of droughts in Argentina's core crop region *Hydrol. Earth Syst. Sci.* **25** 2475–2490 <https://doi.org/10.5194/hess-25-2475-2021>
- [5] Cunha A P M A et al. 2019 Extreme drought events over Brazil from 2011 to 2019 *Atmos.* **10**(11) 642 <https://doi.org/10.3390/atmos10110642>
- [6] Anderson M C et al. 2016 The Evaporative Stress Index as an indicator of agricultural drought in Brazil: An assessment based on crop yield impacts *Remote Sens. Environ.* **174** 82–99 <https://doi.org/10.1016/j.rse.2015.11.034>
- [7] Svoboda M et al. 2002 The drought monitor *Bull. Am. Meteorol. Soc.* **83** 1181–1190 <https://doi.org/10.1175/1520-0477-83.8.1181>
- [8] Otkin J A, Svoboda M, Hunt E D, Ford T W, Anderson M C, Hain C and Basara J B 2018 Flash droughts: a review and assessment of the challenges imposed by rapid onset droughts in the United States *Bull. Am. Meteorol. Soc.* **99** 911–919 <https://doi.org/10.1175/BAMS-D-17-0149.1>
- [9] Otkin J A et al. 2022 Getting ahead of flash drought: from early warning to early action *Bull. Am. Meteorol. Soc.* **103** E2188–E2202 <https://doi.org/10.1175/BAMS-D-21-0288.1>
- [10] Koster R D, Schubert S D, Wang H, Mahanama S P and DeAngelis A M 2019 Flash drought as captured by reanalysis data: disentangling the contributions of precipitation deficit and excess evapotranspiration *J. Hydrometeorol.* **20** 1241–1258 <https://doi.org/10.1175/JHM-D-18-0242.1>
- [11] Pendergrass A G et al. 2020 Flash droughts present a new challenge for subseasonal-to-seasonal prediction *Nat. Clim. Change* **10** 191–199 <https://doi.org/10.1038/s41558-020-0709-0>
- [12] Christian J I, Hobbins M, Hoell A, Otkin J A, Ford T W, Cravens A E, Powlen K A, Wang H, and Mishra V 2024 Flash drought: a state of the science review *WIREs Water* **11**(3) e1714 <https://doi.org/10.1002/wat2.1714>

- [13] Yuan X, Wang Y, Ji P, Wu P, Sheffield J and Otkin J A 2023 A global transition to flash droughts under climate change *Sci.* **380** 187–191 <https://doi.org/10.1126/science.abn6301>
- [14] Christian J I, Basara J B, Hunt E D, Otkin J A, Furtado J C, Mishra V, Xiao X and Randall R M 2021 Global distribution, trends, and drivers of flash drought occurrence *Nat. Commun.* **12** 6330 <https://doi.org/10.1038/s41467-021-26692-z>
- [15] Zeng Z, Wu W, Peñuelas J, Li Y, Jiao W, Li Z, Ren X, Wang K and Ge Q 2023 Increased risk of flash droughts with raised concurrent hot and dry extremes under global warming *npj Clim. Atmos. Sci.* **6** 134 <https://doi.org/10.1038/s41612-023-00468-2>
- [16] Neelam M and Hain C 2024 Global flash droughts characteristics: onset, duration, and extent at watershed scales *Geophys. Res. Lett.* **51(10)** e2024GL109657 <https://doi.org/10.1029/2024GL109657>
- [17] Christian J I, Martin E R, Basara J B, Furtado J C, Otkin J A, Lowman L E L, Hunt E D, Mishra V and Xiao X 2023 Global projections of flash drought show increased risk in a warming climate *Commun. Earth Environ.* **4** 165 <https://doi.org/10.1038/s43247-023-00826-1>
- [18] Black E 2024 Global change in agricultural flash drought over the 21st Century *Adv. Atmos. Sci.* **41** 209–220 <https://doi.org/10.1007/s00376-023-2366-5>
- [19] Mahto S S and Mishra V 2023 Increasing risk of simultaneous occurrence of flash drought in major global croplands *Environ. Res. Lett.* **18(4)** 044044 <https://iopscience.iop.org/article/10.1088/1748-9326/acc8ed>
- [20] Lovino M A, Pierrestegui M J, Müller O V, Müller G V and Berbery E H 2024 The prevalent life cycle of agricultural flash droughts *npj Clim. Atmos. Sci.* **7** 73 <https://doi.org/10.1038/s41612-024-00618-0>
- [21] Barbosa H A 2023 Flash drought and its characteristics in Northeastern South America during 2004–2022 using satellite-based products *Atmosphere* **14** 1629 <https://doi.org/10.3390/atmos14111629>
- [22] Kucheruk L L, Spennemann P C, Naumann G and Rivera J C 2024 Climatología de sequías de rápido desarrollo en la Pampa húmeda Argentina *Meteorológica* **49** 025–025 <https://doi.org/10.24215/1850468Xe025>
- [23] Miralles D G, Gentile P, Seneviratne S I and Teuling A J 2019 Land-atmospheric feedbacks during droughts and heatwaves: state of the science and current challenges *Ann. N. Y. Acad. Sci.* **1436** 19–35 <https://doi.org/10.1111/nyas.13912>
- [24] Li H, Keune J, Smessaert F, Nieto R, Gimeno L and Miralles D 2023 Land-atmosphere feedbacks contribute to crop failure in global rainfed breadbaskets *npj Clim. Atmos. Sci.* **6** 51 <https://doi.org/10.1038/s41612-023-00375-6>
- [25] Wang Y and Yuan X 2022 Land-atmosphere coupling speeds up flash drought onset *Sci. Total Environ.* **851** 158109 <https://doi.org/10.1016/j.scitotenv.2022.158109>
- [26] Fu K and Wang K 2023 Contributions of local land–Atmosphere coupling and mesoscale atmospheric circulation to the 2013 extreme flash drought and heatwave compound event over Southwest China *J. Geophys. Res.: Atmos.* **128** e2023JD039406 <https://doi.org/10.1029/2023JD039406>
- [27] Gerken T, Bromley G T, Ruddell B L, Williams S and Stoy P C 2018 Convective suppression before and during the United States Northern Great Plains flash drought of 2017 *Hydrol. Earth Syst. Sci.* **22** 4155–4163 <https://doi.org/10.5194/hess-22-4155-2018>
- [28] Basara J B, Christian J I, Wakefield R A, Otkin J A, Hunt E H and Brown D P 2012 The evolution, propagation, and spread of flash drought in the Central United States during 2012 *Environ. Res. Lett.* **14** 084025 <https://doi.org/10.1088/1748-9326/ab2cc0>
- [29] Mahto S S and Mishra V 2024 Flash drought intensification due to enhanced land-atmospheric coupling in India *J. Clim.* **37** 5291–5307 <https://doi.org/10.1175/JCLI-D-22-0477.1>
- [30] Ruscica R C, Sörensson A A and Menéndez C G 2015 Pathways between soil moisture and precipitation in southeastern South America *Atmos. Sci. Lett.* **16** 267–272 <https://doi.org/10.1002/asl2.552>
- [31] Spennemann P C, Salvia M, Ruscica R C, Sörensson A A, Grings F and Karszenbaum H 2018 Land-atmosphere interaction patterns in southeastern South America using satellite products and climate models *Int. J. Appl. Earth Obs. Geoinf.* **64** 96–103 <https://doi.org/10.1016/j.jag.2017.08.016>
- [32] Menéndez C G, Giles J, Ruscica R, Zaninelli P, Coronato T, Flaco M, Sörensson A A, Fita L, Carril A and Li L 2019 Temperature variability and soil–atmosphere interaction in South America simulated by two regional climate models *Clim. Dyn.* **53** 2919–2930 <https://doi.org/10.1007/s00382-019-04668-6>
- [33] Coronato T, Carril A F, Zaninelli P, Giles J, Ruscica R, Flaco M, Sörensson A A, Fita L, Li L and Menéndez C G 2020 The impact of soil moisture–atmosphere coupling on daily maximum surface temperatures in Southeastern South America *Clim. Dyn.* **55** 2543–2556 <https://doi.org/10.1007/s00382-020-05399-9>
- [34] Hersbach H *et al.* 2020 The ERA5 global reanalysis *Q. J. R. Meteorol. Soc.* **146(730)** 1999–2049 <https://doi.org/10.1002/qj.3803>
- [35] Soci C *et al.* 2024 The ERA5 global reanalysis from 1940 to 2022. *Q. J.R. Meteorol. Soc.* **150(764)** 4014–4048 <https://doi.org/10.1002/qj.4803>
- [36] Hersbach H *et al.* (2023a) ERA5 hourly data on single levels from 1940 to present. *Copernicus Climate Change Service (C3S) Climate Data Store (CDS)* (Accessed on March 2024) <http://doi.org/10.24381/cds.adbb2d47>
- [37] Li M, Wu P and Ma Z 2020 A comprehensive evaluation of soil moisture and soil temperature from third-generation atmospheric and land reanalysis data sets *Int. J. Climatol.* **40** 5744–5766 <https://doi.org/10.1002/joc.6549>
- [38] Xu L *et al.* 2021 In-situ and triple-collocation based evaluations of eight global root zone soil moisture products *Remote Sens. Environ.* **254** 112248 <https://doi.org/10.1016/j.rse.2020.112248>
- [39] Lavers D A, Simmons A, Vamborg F and Rodwell M J 2022 An evaluation of ERA5 precipitation for climate

- monitoring. *Q. J.R. Meteorol. Soc.* **148**(748) 3124–3137 <https://doi.org/10.1002/qj.4351>
- [40] Balmaceda-Huarte R, Olmo M E, Bettolli M L and Poggi M M 2021 Evaluation of multiple reanalyses in reproducing the spatiotemporal variability of temperature and precipitation indices over southern South America *Int. J. Climatol.* **41** 5572–5595 <https://doi.org/10.1002/joc.7142>
- [41] Ford T W and Labosier C F 2017 Meteorological conditions associated with the onset of flash drought in the eastern United States *Agric. For. Meteorol.* **247** 414–423 <https://doi.org/10.1016/j.agrformet.2017.08.031>
- [42] Grassini P *et al.* 2015 How good is good enough? Data requirements for reliable crop yield simulations and yield-gap analysis. *Field Crops Res.* **177** 49–63 <https://doi.org/10.1016/j.fcr.2015.03.004>
- [43] Running S, Mu Q, Zhao M 2015 MOD17A2H MODIS/Terra Gross Primary Productivity 8-Day L4 Global 500m SIN Grid V006 NASA EOSDIS Land Processes Distributed Active Archive Center <https://doi.org/10.5067/MODIS/MOD17A2H.006>
- [44] Geng G, Yang R, Chen Q, Deng T, Yue M, Zhang B and Gu Q 2023 Tracking the influence of drought events on winter wheat using long-term gross primary production and yield in the Wei River Basin, China *Agric. Water Manag.* **275** 108019 <https://doi.org/10.1016/j.agwat.2022.108019>
- [45] Wu X, Zhang R, Bento V A, Leng S, Qi J, Zeng J and Wang Q 2022 The effect of drought on vegetation gross primary productivity under different vegetation types across China from 2001 to 2020 *Remote Sens.* **14**(18) 4658 <https://doi.org/10.3390/rs14184658>
- [46] Fischer R A, Byerlee D and Edmeades G 2014 Crop yields and global food security: will yield increase continue to feed the world? *Australian Centre for International Agricultural Research: Canberra, Australia ACIAR Monograph No. 158*
- [47] Xu, J *et al.* 2021 Double cropping and cropland expansion boost grain production in Brazil *Nat. Food* **2** 264–273 <https://doi.org/10.1038/s43016-021-00255-3>
- [48] Zalles V *et al.* 2019 Near doubling of Brazil's intensive row crop area since 2000 *PNAS* **116**(2) 428–435 <https://doi.org/10.1073/pnas.1810301115>
- [49] Martínez-Fernández J, González-Zamora A, Sánchez N and Gumuzzio A 2015 A soil water-based index as a suitable agricultural drought indicator *J. Hydrol.* **522** 265–273 <https://doi.org/10.1016/j.jhydrol.2014.12.051>
- [50] Osman M *et al.* 2021 Flash drought onset over the contiguous United States: Sensitivity of inventories and trends to quantitative definitions *Hydrol. Earth Syst. Sci.* **25** 565–581 <https://doi.org/10.5194/hess-25-565-2021>
- [51] Mukherjee S and Mishra A K 2022 Global flash drought analysis: uncertainties from indicators and datasets. *Earth's Future* **10**(6) e2022EF002660 <https://doi.org/10.1029/2022EF002660>
- [52] Otkin J *et al.* 2024 Multivariate Evaluation of Flash Drought Across the United States. *Water Resour. Res.* **60**(11) e2024WR037333 <https://doi.org/10.1029/2024WR037333>
- [53] Mann H B 1945 Non-parametric tests against trend *Econometrica* **13**(3) 245–259 <http://dx.doi.org/10.2307/1907187>
- [54] Kendall M G 1975 *Rank Correlation Methods 4th edition* (London: Charles Griffin)
- [55] Rivera J A and Penalba O C 2014 Trends and spatial patterns of drought affected area in Southern South America. *Climate* **2**(4):264–278 <https://doi.org/10.3390/cli2040264>
- [56] Lovino M A, Müller O V, Müller G V, Sgroi L C and Baethgen W E 2018 Interannual-to-multidecadal Hydroclimate Variability and its Sectoral Impacts in northeastern Argentina *Hydrol. Earth Syst. Sci.* **22** 3155–3174 <https://doi.org/10.5194/hess-22-3155-2018>.
- [57] Lovino M A, Müller O, Berbery E H, Müller G 2018 How have daily climate extremes changed in the recent past over northeastern Argentina? *Glob. Planet. Change* **168** 78–97. <https://doi.org/10.1016/j.gloplacha.2018.06.008>
- [58] Ghil M *et al.* 2002 Advanced spectral method for climatic time series *Rev. Geophys.* **40**(1) 1–41 <https://doi.org/10.1029/2000RG000092>
- [59] Wilks D S 2006 *Statistical Methods in the Atmospheric Sciences 2nd edn* London, UK: Elsevier Inc.
- [60] Allen M R and Smith L A 1996 Monte Carlo SSA: detecting irregular oscillations in the presence of colored noise *J. Clim.* **9** 3373–3404 [http://dx.doi.org/10.1175/1520-0442\(1996\)009<3373:MCSDIO>2.0.CO;2](http://dx.doi.org/10.1175/1520-0442(1996)009<3373:MCSDIO>2.0.CO;2)
- [61] Seneviratne S I, Corti T, Davin E L, Hirschi M, Jaeger E B, Lehner I, Orlowsky B and Teuling A J 2010 Investigating soil moisture–climate interactions in a changing climate: a review *Earth Sci. Rev.* **99** 125–161 <https://doi.org/10.1016/j.earscirev.2010.02.004>
- [62] Koster R D *et al.* 2004 Regions of strong coupling between soil moisture and precipitation *Sci.* **305** 1138–1140 <https://www.science.org/doi/10.1126/science.1100217>
- [63] Miralles D G, van den Berg M J, Teuling A J and de Jeu R A M 2012 Soil moisture–temperature coupling: a multiscale observational analysis *Geophys. Res. Lett.* **39**(21) <https://doi.org/10.1029/2012GL053703>
- [64] Koster R D *et al.* 2006 GLACE: The Global Land–Atmosphere Coupling Experiment. Part I: overview *J. Hydrometeorol.* **7** 590–610 <https://doi.org/10.1175/JHM510.1>
- [65] Baker J C A *et al.* 2021 An assessment of land–atmosphere interactions over South America using satellites, reanalysis, and two Global Climate Models *J. Hydrometeorol.* **22** 905–922 <https://doi.org/10.1175/JHM-D-20-0132.1>
- [66] Giles J A, Menéndez C G and Ruscica R C 2022 Nonlocal impacts of soil moisture variability in South America: linking two land–atmosphere coupling hot spots *J. Clim.* **36** 227–242 <https://doi.org/10.1175/JCLI-D-21-0510.1>
- [67] Collini E A, Berbery E B, Barros V R and Pyle M E 2008 How does soil moisture influence the early stages of the South American Monsoon? *J. Clim.* **21** 195–213 <https://doi.org/10.1175/2007JCLI1846.1>
- [68] Sörensson A A and Menéndez C G 2011 Summer soil–precipitation coupling in South America *Tellus Ser. A* **63** 56–68 <https://doi.org/10.1111/j.1600-0870.2010.00468.x>
- [69] Santanello J A *et al.* 2018 Land–atmosphere interactions: the LoCo perspective *Bull. Am. Meteorol. Soc.* **99** 1253–1272 <https://doi.org/10.1175/BAMS-D-17-0001.1>
- [70] Vicente-Serrano S M, McVicar T R, Miralles D G, Yang Y, Tomas-Burguera M 2020 Unraveling the influence of

- atmospheric evaporative demand on drought and its response to climate change *WIREs Clim. Change* **11** e632
<https://doi.org/10.1002/wcc.632>
- [71] Kimm H *et al.* 2020 Redefining droughts for the U.S. Corn Belt: The dominant role of atmospheric vapor pressure deficit over soil moisture in regulating stomatal behavior of Maize and Soybean *Agric. For. Meteorol.* **287** 107930<https://doi.org/10.1016/j.agrformet.2020.107930>
- [72] Alduchov O A and Eskridge R E 1996 Improved Magnus form approximation of saturation vapor pressure *J. Appl. Meteorol. Climatol.* **35**(4) 601-609
[https://doi.org/10.1175/1520-0450\(1996\)035<0601:IMFAOS>2.0.CO;2](https://doi.org/10.1175/1520-0450(1996)035<0601:IMFAOS>2.0.CO;2)
- [73] Yuan W *et al.* 2019 Increased atmospheric vapor pressure deficit reduces global vegetation growth *Sci. Adv.* **5**(8) eaax1396 <https://doi.org/10.1126/sciadv.aax1396>
- [74] Gevaert A I, Miralles D G, de Jeu R A M, Schellekens J and Dolman A J 2018 Soil moisture-temperature coupling in a set of land surface models *J. Geophys. Res.: Atmos.* **123**(3) 1481–1498 <https://doi.org/10.1002/2017JD027346>
- [75] Notaro M. 2008, Statistical identification of global hot spots in soil moisture feedbacks among IPCC AR4 models *J. Geophys. Res.* **113**, D09101
<https://doi:10.1029/2007JD009199>.
- [76] Mahaut L *et al.* 2022 Matches and mismatches between the global distribution of major food crops and climate suitability *Proc. R. Soc. B* **289** 20221542
<https://doi.org/10.1098/rspb.2022.1542>
- [77] Seleiman M F, Al-Suhaimi, N, Ali N, Akmal M, Alotaibi M, Refay Y, Dindaroglu T, Abdul-Wajid H H and Battaglia M L 2021 Drought stress impacts on plants and different approaches to alleviate its adverse effects *Plants* **10** 259 <https://doi.org/10.3390/plants10020259>
- [78] Bert F, de Estrada M, Naumann G, Negri R, Podestá G, de los Milagros Skansi M, Spennemann P and Quesada M 2021 The 2017-18 drought in the Argentine Pampas—Impacts on agriculture *United Nations Office for Disaster Risk Reduction. GAR Special Report on Drought* <https://www.undrr.org/publication/2017-18-drought-argentine-pampas-impacts-agriculture-0>
- [79] Nagaraj D, Proust E, Todeschini A, Rulli M C and D'Odorico P 2021 A new dataset of global irrigation areas from 2001 to 2015 *Adv. Water Resour.* **152** 103910
<https://doi.org/10.1016/j.advwatres.2021.103910>
- [80] Pierrestegui M J, Lovino M A, Müller O V and Müller G V 2024 Multi-hazard assessment of extreme hydrometeorological events in southeastern South America *Earth Syst. Environ.* <https://doi.org/10.1007/s41748-024-00450-9>
- [81] Naumann G *et al.* 2023 Extreme and long-term drought in the La Plata Basin: event evolution and impact assessment until September 2022 *A joint report from EC-JRC, CEMADEN, SISSA and WMO, Publications Office of the European Union* <https://data.europa.eu/doi/10.2760/62557>

Artículo 5

Eventos extremos de precipitación en la región del Chaco Austral de Argentina

Extreme precipitation events in the Austral Chaco region of Argentina

Miguel A. Lovino¹  | Gabriela V. Müller¹  | María Josefina Pierrestegui¹ | Edna Espinosa² | Leticia Rodríguez²

¹Consejo Nacional de Investigaciones Científicas y Técnicas (CONICET), Centro de Estudios de Variabilidad y Cambio Climático (CEVARCAM), Universidad Nacional del Litoral, Santa Fe, Argentina

²Centro de Estudios Hidro-ambientales (CENEHA), Universidad Nacional del Litoral, Santa Fe, Argentina

Correspondence

Gabriela V. Müller, CONICET,
CEVARCAM (FICH-UNL) Ciudad
Universitaria, Santa Fe, 3000, Argentina.
Email: gvmuller@fich.unl.edu.ar

Funding information

National Agency for Scientific and
Technological Promotion of Argentina,
Grant/Award Numbers: PICT-2016-1334,
PICT-2019-2019-00481, PICT-
2019-2019-03982; Universidad Nacional
del Litoral, Grant/Award Number:
CAI+D-2020-50620190100082LI

Abstract

This study assesses the intensity, spatial distribution and temporal variability of extreme precipitation events (EPEs) on different time scales relevant to agriculture and water resources during the 1901–2016 period over Argentina's Austral Chaco (ACh). EPEs were identified using a nonparametric approach for the Standardized Precipitation Index (SPI). The leading modes of SPI's variability were detected using the Singular Spectrum Analysis. We also compile and control the quality of precipitation observations in a scarcely monitored region. The limited number of stations conditions the interpolation of the GPCC v2018 database here used, mainly during the early twentieth century. The EPEs characterized by SPI at a 24-month time scale, which favour long-lasting water excesses or deficits with hydrological impacts, underwent two differentiated long-term periods: a dry one before 1960 and a wet one from 1960 to 2005. Consistently, seasonal wet EPEs were more frequent during the wet period while seasonal droughts were more frequent and with larger spatial extent during the dry period. Seasonal EPEs, represented by the SPI at 3-month time scale, can impact agriculture during the crops' critical growth period. Since 2006, the long-term wetting trend has been reversed. If this behaviour continues into the coming decades, more droughts and less wetness might be expected. The EPEs present a large interannual variability with 6.3- and 9-year significant cycles that, combined with long-term trends, favoured extremely wet/dry EPEs. Most of the wet/dry EPEs occurred during El Niño/La Niña events. Although this relationship is not straightforward, we found a discriminant ENSO signal between October of the year when an ENSO event starts and February of the next year. Finally, severely dry/wet EPEs tend to have large spatial extent in the ACh region. The central-eastern ACh region experiences the most extreme wet and dry conditions, which makes this area more prone to extreme EPEs.

KEY WORDS

Austral Chaco, Bajos Submeridionales, extreme precipitation events, standardized precipitation index

1 | INTRODUCTION

Extreme weather and climate events have major impacts on natural and socioeconomic systems worldwide. Impacts of hydroclimate variability, including the occurrence of extreme events, are more relevant in regions where population and the productive sectors depend on climate or are vulnerable to climate hazards. One of such regions is southeastern South America (SESA)—which includes northern Argentina, Uruguay, southern Brazil, and Paraguay (Magrin et al., 2014). In SESA, droughts and floods caused by extreme precipitation events produce large economic losses; two iconic examples have been the extraordinary flood of the Paraná River in 1983 (Camilloni and Barros, 2000, 2003) and the extended and persistent drought of 2008–2009 (Müller et al., 2014; Sgroi et al., 2021). Furthermore, extreme climate events have increased in frequency and intensity in SESA during the past decades (Cavalcanti et al., 2015; Carril et al., 2016; Avila-Diaz et al., 2020). The number of intense precipitation events has been growing steadily since 1970 in most of SESA (Skansi et al., 2013; Lovino et al., 2018a, Cerón et al., 2021). More frequent heavy precipitation events constitute a magnifying risk for urban settlements and agriculture, and cause significant infrastructure losses and decreased livestock productivity (Barros et al., 2015; Lovino et al., 2018a, b). On the other hand, longer dry events in recent decades suggest that more persistent short-term droughts affect agricultural activities (Llano and Penalba, 2010; Sgroi et al., 2021).

Within SESA, the Gran Chaco region is particularly vulnerable to climate hazards for being one of the most threatened ecoregions worldwide: its biome corresponds to tropical and subtropical dry broadleaf forests that are at risk due to their high rates of ecosystem loss and their sensitivity to climate variability and climate change (Hansen et al., 2013; Kuemmerle et al., 2017; Ortega et al., 2021). The Gran Chaco region underwent an accelerated expansion of cattle ranching and soybean cultivation (Vallejos et al., 2015; Baumann et al., 2016) which, in turn, generated high deforestation rates (Fehlenberg et al., 2017). Thus, the fragile ecosystem of the Gran Chaco region is vulnerable to current precipitation variability (including extreme events) and to the expected exacerbation of extreme precipitation events for the 21st century (Ortega et al., 2021; Almazroui et al., 2021a). The Argentinean part of the Gran Chaco region is called Austral Chaco (ACh). Favoured by the large climate variability of SESA (e.g., Garreaud et al., 2009; Grimm, 2011), the ACh is subject to alternating periods of water excess and deficit (Penalba and Rivera, 2016), which cause large floods and severe droughts that negatively impact agriculture and cattle ranching in the region (Sosa, 2012).

Most of the studies on hydroclimate variability, extreme events, and precipitation changes that include the ACh region focus on SESA (e.g., Re and Barros, 2009; Seager et al., 2010; Krepper and Zucarelli, 2010; Zhang et al., 2016) or southern South America (e.g., Rivera, 2014; Rivera and Penalba, 2014; Penalba and Rivera, 2016). Another group of studies performed regional analyses over some areas of the ACh (e.g., González et al. 2012; Hurtado et al., 2020a, b). Gonzalez et al. (2012) reported the circulation patterns that influence seasonal precipitation in the Chaco region of Argentina. Hurtado et al. (2020a) found a breakpoint around 1976 towards wetter conditions in the wet season in observed precipitation time series scattered in ACh. They suggested the link between this precipitation change with the well-documented 1976/1977 climate transition (Huang et al., 2005; Agosta and Compagnucci, 2008). Hurtado et al. (2020b) studied the precipitation variability in the Argentinian Chaco Province. They reported that seasonal precipitation is strongly associated to ENSO and regional anomalous circulations that increase anomalous northerly warm and wet air mass transport.

The current research assesses the intensity, spatial distribution and dominant temporal variability modes of extreme precipitation events on different time scales in the Austral Chaco region of Argentina. In order to fulfil the objective, we study century-long SPI time series (1901–2016) to describe and characterize extreme precipitation events. We also explored the leading modes of SPI's variability on time scales relevant to agriculture and water resources applications. This article reports novel findings regarding variability modes and their influence in the occurrence of extreme events. In addition, we compile and carry out a quality control of precipitation observations in a scarcely monitored region. The complexity involved in managing water resources in the ACh and its high vulnerability to climate extremes provides greater relevance to the results presented here. The structure of the article follows: Section 2 presents the study region, datasets used, and the methodological approach. Section 3 covers the analysis of precipitation climatology and variability. Section 4 assesses extreme precipitation events at different time scales in the ACh region. Lastly, Section 5 conveys the concluding remarks.

2 | DATA AND METHODOLOGY

2.1 | Study region

The Gran Chaco is an extensive region (about 790,000 km²) that stretches from 16° 55' to 33° 52' S, and from 67° 50' to 57° 52' W over parts of Bolivia, Paraguay,

Brazil, and Argentina (see Figure 1a,b). The Gran Chaco is the second largest natural biome—after Amazonia—in South America (Bucher and Huszar, 1999). Our study focuses on the Argentinean part of the Gran Chaco located between latitudes 24.5–31°S and longitudes 63.5–58.5 °W (Figure 1c), known as ACh. The ACh region covers 284,000 km² and is sparsely populated. It has a flat topography with elevation varying between 100 and 500 m.

The Bajos Submeridionales (BsSs) basin (see Figure 1b,c) is a sensible ecosystem hotspot in the ACh. The BsSs basin has 53,824 km² and stretches over parts of three Argentine provinces: Santa Fe, Chaco, and Santiago del Estero (Thalmeier et al., 2017). It belongs to the middle and lower Salado River basin, a tributary to the Paraná River (Matteucci et al., 2007). In the BsSs, both the large climatic variability and a long-term precipitation change have favoured EPEs, which, in turn, negatively impact the human water access and the growing agriculture and livestock activity (Sosa, 2012; Lovino et al., 2018a).

2.2 | Data

Data used in this study include precipitation records from 101 precipitation stations of the National Weather Service

(SMN), the National Institute of Agricultural Technology (INTA), the former National Under-secretariat for Water Resources (RHN), the Provincial Water Administration of Chaco (APA), cooperatives, and citizens (Figure 2a). Although previous studies used observational data from some of the institutions we use here (e.g., González et al., 2012; Hurtado et al., 2020a), the data compilation of this work provides an observational basis to a region characterized by a low density of weather stations (Hurtado et al., 2021) and where information is inhomogeneous, scarce and difficult to access (Espinosa, 2021).

Precipitation stations data were selected considering temporal resolution, spatial distribution, period of information and record consistency. In particular, consistency was assessed using the double mass method (Gupta, 2016). After applying the double mass method, the SMN and INTA stations (which are the national official agencies) were considered more reliable and were used as reference stations to contrast the rest of the stations. Following Orsolini et al. (2009), we considered that the stations present nonconsistent records when there is a change in the slope formed by more than five consecutive points in the double mass analysis; in that case, the observation station was discarded. As a result, 49 stations were selected. Figure 2b shows the station locations and Table 1 lists the observation periods. The longest observation period was

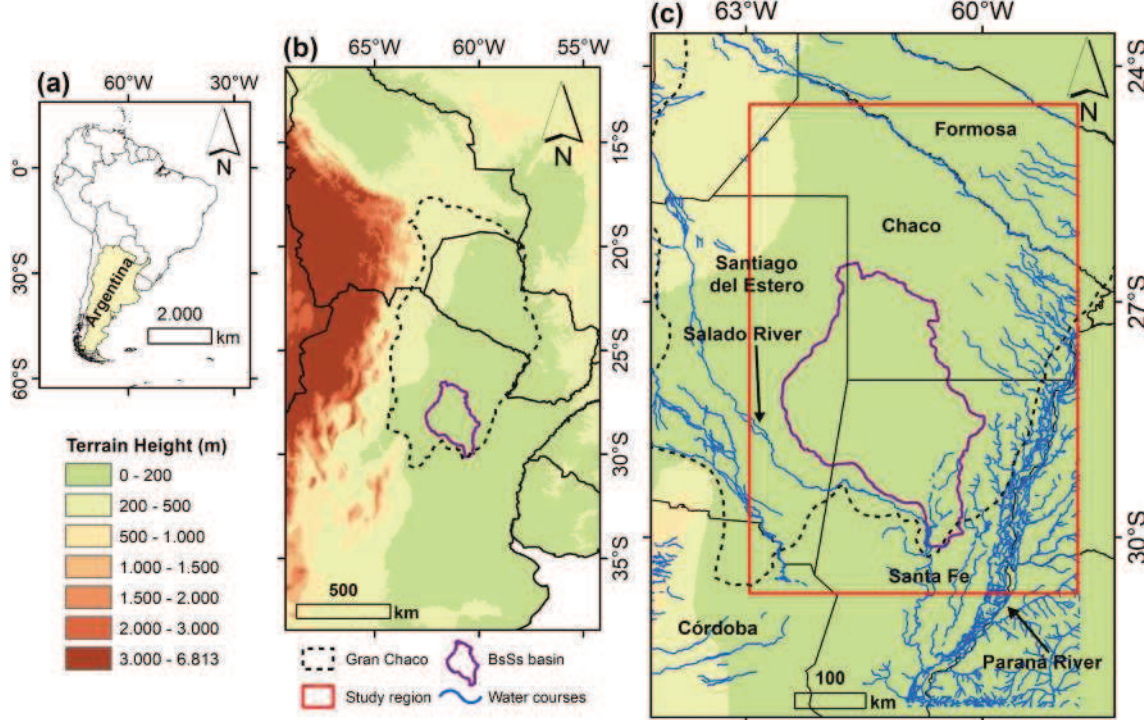


FIGURE 1 (a) South America and the location of Argentina. (b) Topography map of the South America, including the Gran Chaco region. (c) Study region (red rectangle) including the Bajos Submeridionales basin, the Paraná and Salado Rivers and the provinces of Argentina [Colour figure can be viewed at wileyonlinelibrary.com]

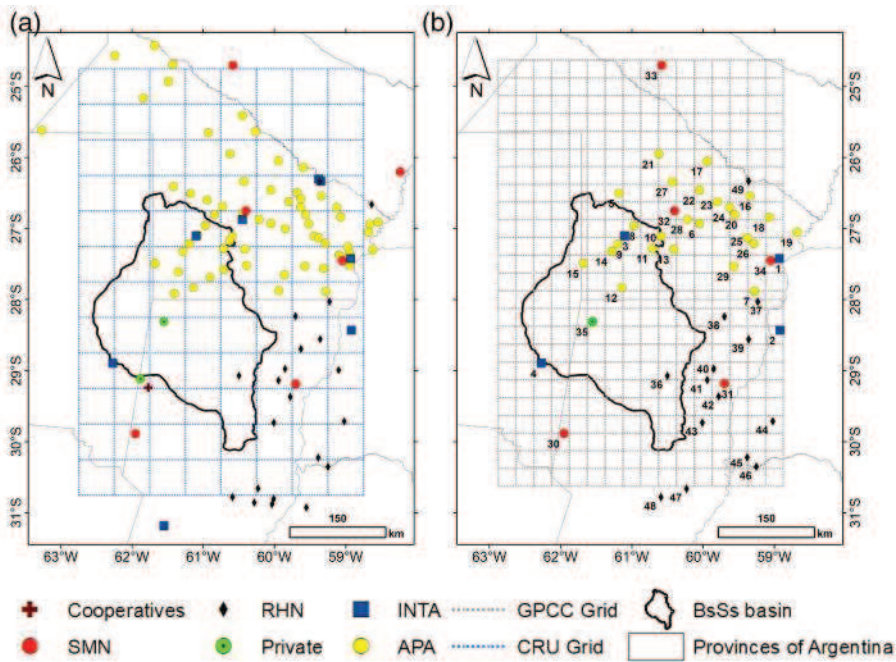


FIGURE 2 (a) Precipitation stations in the study area and CRU TS 4.03 grid resolution. Stations belong to different government agencies (RHN, INTA, SMN, and APA), cooperatives, and private owners; (b) stations selected according to the verified quality of the data (see Table 1 for further information) and GPCC v 2018 grid resolution [Colour figure can be viewed at wileyonlinelibrary.com]

registered in Los Guasunchos station since January 1944. A number of APA stations have records starting between 1954 and 1956. Figure 2b shows that the distribution of the selected stations is irregular, with some areas lacking observations, mainly within the BsSs basin.

Observations were complemented with two global gridded databases: CRU TS 4.03 (University of East Anglia Climatic Research Unit, 2020; Harris et al., 2020) and GPCC Version 2018 (Global Precipitation Climatology Centre, Schneider et al., 2018). CRU TS 4.03 consists of monthly $0.5^\circ \times 0.5^\circ$ gridded data from January 1901 to December 2016. The GPCC Version 2018 includes monthly $0.25^\circ \times 0.25^\circ$ gridded data from January 1901 to December 2016. These grids are shown in Figure 2a and b, respectively.

We assessed the ability of the gridded databases CRU TS 4.03 and GPCC v2018 to represent observed precipitation at the selected stations. Each of the databases was subjected to a linear regression analysis between observed monthly precipitation and the gridded series at the grid-point closest to each station. Figure 3 presents the scatter plots between precipitation data from different stations with the longest available record periods and the closest CRU TS 4.03 and GPCC v2018 grid-points. The deviation from the 1:1 line of the linear adjustments by least squares indicates that both global databases tend to underestimate precipitation amounts during the rainy months and overestimate them during dry months in most stations. The exceptions are Reconquista Aero and Ceres Aero stations, where GPCC v2018 perfectly fits the precipitation observations, achieving a correlation

coefficient of 1 (Figure 3d, e). This result suggests that these stations were used to interpolate the GPCC v2018 database over the entire time period. However, GPCC v2018 achieves a better fit to the observations and higher correlation coefficients than those of CRU TS 4.03 in all analysed stations. In particular, the shape of the scattering clouds shows that GPCC v2018 can reproduce dry and rainy months more efficiently than CRU TS 4.03. Similar results were obtained for the remaining stations and the corresponding closest grid-points (not shown). These results suggest that GPCC v2018 data have a greater ability than CRU TS 4.03 data to represent precipitation in the study region.

We also used the Root Mean Square Error (RMSE) and the Pearson correlation coefficient (r) (see Déqué, 2012 for definitions) as statistical evaluation metrics to quantify how well gridded data represent observed data at each station. Figure 4 shows that values of r and RMSE are clearly better for GPCC v2018 than for CRU TS 4.03 at all the analysed stations. The Pearson correlation coefficient ranges between 0.63 and 1 for GPCC v2018, and between 0.55 and 0.80 for CRU TS 4.03. The ranges of RMSE are 5.14–67.67 mm for GPCC v2018 and 46.25–90.98 mm for CRU TS 4.03. These results are common to each of the information sources. The metrics for the SMN and INTA stations stand out significantly for GPCC v2018 dataset. In summary, our results show that the performance of GPCC v2018 is better than the performance of CRU TS 4.03 at each station. Based on these analyses, we selected the GPCC v2018 database to carry out our study.

TABLE 1 Precipitation stations used in this study with information in different time periods

| Nº | Name | Lat | Lon | Institution | Temporal resolution | Missing data [%] | Start of series | End of series |
|----|------------------------|--------|--------|-------------|---------------------|------------------|-----------------|---------------|
| 1 | Colonia Benítez | -27.42 | -58.93 | INTA | Daily | 0 | Jan-68 | Jul-19 |
| 2 | Bellavista | -28.43 | -58.92 | INTA | Daily | 6.46 | Jan-59 | Jul-19 |
| 3 | Las Breñas | -27.1 | -61.1 | INTA | Daily | 0.32 | Jan-67 | Jul-19 |
| 4 | Bandera | -28.89 | -62.27 | INTA | Monthly | 0 | Jan-80 | Jul-18 |
| 5 | Pampa del Infierno | -26.5 | -61.18 | APA | Monthly | 0.82 | Sep-56 | Aug-17 |
| 6 | Machagai | -26.93 | -60.05 | APA | Monthly | 0 | Sep-54 | Aug-17 |
| 7 | Basail | -27.88 | -59.28 | APA | Monthly | 0 | Sep-55 | Aug-17 |
| 8 | Corzuela | -26.96 | -60.97 | APA | Monthly | 0 | Sep-54 | Aug-17 |
| 9 | Charata | -27.22 | -61.2 | APA | Monthly | 0 | Sep-54 | Aug-17 |
| 10 | La Tigra | -27.11 | -60.59 | APA | Monthly | 0 | Sep-78 | Aug-17 |
| 11 | San Bernardo | -27.28 | -60.71 | APA | Monthly | 0 | Sep-59 | Aug-17 |
| 12 | Santa Sylvina | -27.83 | -61.14 | APA | Monthly | 0.66 | Sep-54 | Aug-17 |
| 13 | Villa Berthet | -27.29 | -60.41 | APA | Monthly | 0 | Sep-52 | Aug-17 |
| 14 | Gral. Pinedo | -27.32 | -61.28 | APA | Monthly | 0 | Sep-54 | Aug-17 |
| 15 | Gancedo | -27.49 | -61.68 | APA | Monthly | 0 | Sep-54 | Aug-17 |
| 16 | Gral. San Martín | -26.54 | -59.34 | APA | Monthly | 0 | Sep-55 | Aug-17 |
| 17 | Pampa del Indio | -26.05 | -59.94 | APA | Monthly | 0 | Sep-56 | Aug-17 |
| 18 | La Eduvigis | -26.84 | -59.07 | APA | Monthly | 2.78 | Sep-81 | Aug-17 |
| 19 | Las Palmas | -27.05 | -58.68 | APA | Monthly | 0 | Sep-56 | Aug-17 |
| 20 | Capitán Solari | -26.8 | -59.56 | APA | Monthly | 0 | Sep-56 | Aug-17 |
| 21 | Juan José Castelli | -25.95 | -60.62 | APA | Monthly | 0.13 | Sep-54 | Aug-17 |
| 22 | El Tacuruzal-El palmar | -26.46 | -60.05 | APA | Monthly | 0.64 | Sep-78 | Aug-17 |
| 23 | Las Garcitas | -26.62 | -59.8 | APA | Monthly | 0 | Sep-56 | Aug-17 |
| 24 | Colonia Unidas | -26.7 | -59.63 | APA | Monthly | 0.13 | Sep-54 | Aug-17 |
| 25 | La Verde | -27.13 | -59.38 | APA | Monthly | 0 | Sep-56 | Aug-17 |
| 26 | Makalle | -27.21 | -59.29 | APA | Monthly | 0 | Sep-55 | Aug-17 |
| 27 | Tres Isletas | -26.34 | -60.43 | APA | Monthly | 0 | Sep-54 | Aug-17 |
| 28 | Quitilipi | -26.87 | -60.22 | APA | Monthly | 0 | Sep-54 | Aug-17 |
| 29 | Cote Lai | -27.53 | -59.57 | APA | Monthly | 0 | Sep-54 | Aug-17 |
| 30 | Ceres | -29.88 | -61.95 | SMN | Daily | 0.27 | Jan-56 | Abr-17 |
| 31 | Reconquista | -29.18 | -59.7 | SMN | Daily | 2.04 | Feb-56 | Abr-17 |
| 32 | Roque Saenz Peña | -26.75 | -60.4 | SMN | Daily | 0.27 | Jan-56 | Abr-17 |
| 33 | Las Lomitas | -24.7 | -60.58 | SMN | Daily | 0 | Jan-59 | Abr-17 |
| 34 | Resistencia aero | -27.45 | -59.05 | SMN | Daily | 0 | Jan-63 | Abr-17 |
| 35 | Los Guasunchos | -28.31 | -61.55 | Private | Monthly | 0 | Jan-44 | Dic-18 |
| 36 | Fortín Olmos | -29.07 | -60.5 | RHN | Daily | 4.48 | Jan-73 | Jun-19 |
| 37 | Florencia | -28.03 | -59.23 | RHN | Daily | 0.23 | Aug-83 | May-19 |
| 38 | Escuela 1256 | -28.24 | -59.7 | RHN | Daily | 6.02 | Nov-84 | May-19 |
| 39 | Ruta Nacional N° 011 | -28.56 | -59.36 | RHN | Daily | 5.44 | Jan-75 | May-19 |
| 40 | La Sarita | -28.97 | -59.85 | RHN | Daily | 6.33 | Jan-76 | May-19 |

(Continues)

TABLE 1 (Continued)

| Nº | Name | Lat | Lon | Institution | Temporal resolution | Missing data [%] | Start of series | End of series |
|----|--------------------------|--------|--------|-------------|---------------------|------------------|-----------------|---------------|
| 41 | Ruta provincial N° 042 S | -29.13 | -59.94 | RHN | Daily | 0.24 | Nov-84 | May-19 |
| 42 | Ruta provincial N° 088 S | -29.36 | -59.78 | RHN | Daily | 1.83 | Nov-82 | May-19 |
| 43 | Margarita | -29.73 | -60.01 | RHN | Daily | 11.22 | May-76 | May-19 |
| 44 | Malvinas Sur | -29.71 | -59.02 | RHN | Daily | 1.35 | May-76 | May-19 |
| 45 | Pueblo Libertador | -30.22 | -59.38 | RHN | Daily | 3.45 | Mar-83 | May-19 |
| 46 | Paso Junce | -30.35 | -59.25 | RHN | Daily | 5.03 | May-76 | May-19 |
| 47 | Cacique Ariacaiquín | -30.66 | -60.23 | RHN | Daily | 1.3 | Jan-81 | May-19 |
| 48 | San Justo | -30.78 | -60.59 | RHN | Daily | 0.9 | Jul-81 | May-18 |
| 49 | El Colorado | -26.33 | -59.36 | RHN | Daily | 3.27 | Jan-66 | Jun-19 |

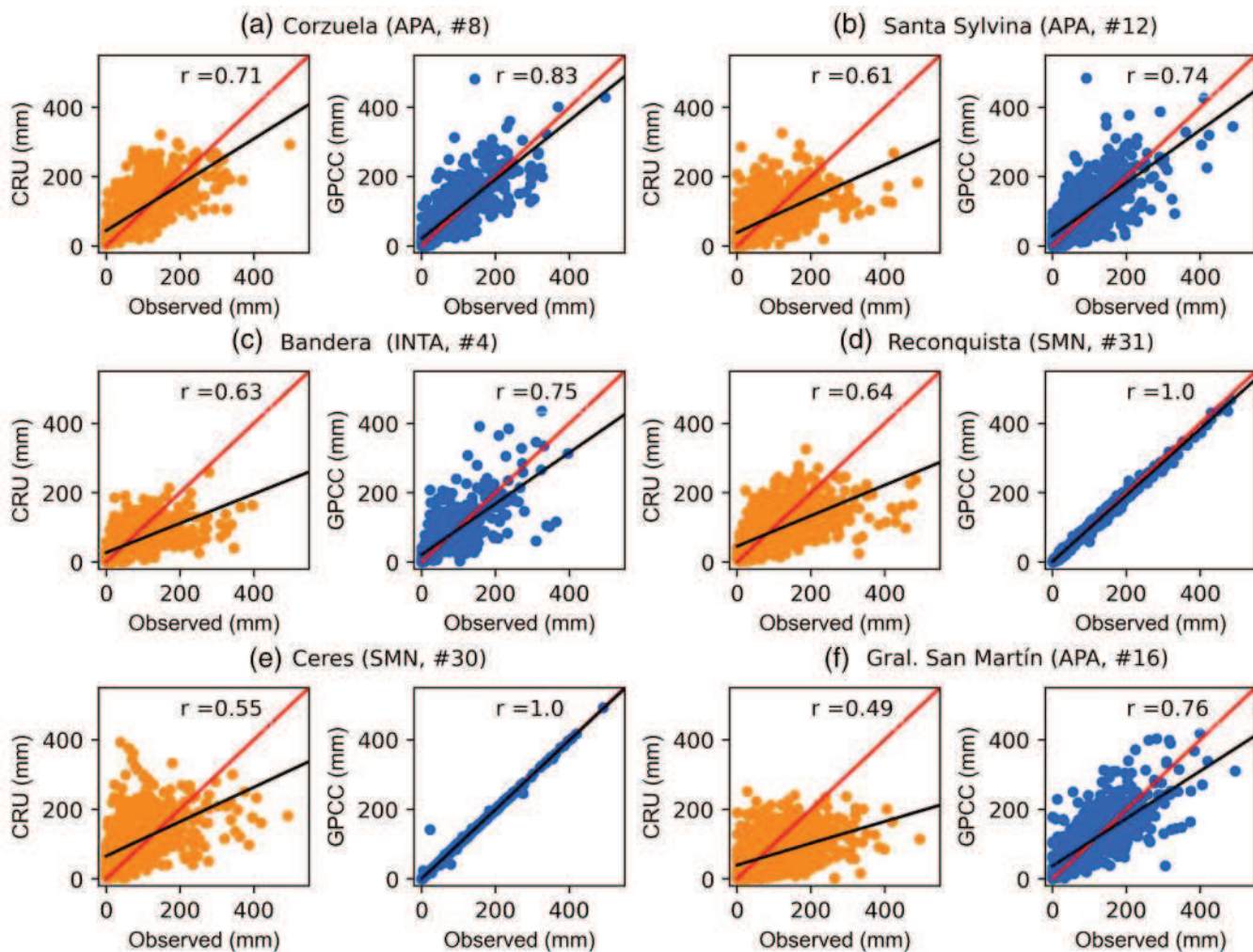


FIGURE 3 Scatterplots of CRU TS 4.03 (orange dots) and GPCC v2018 (light blue dots) precipitation versus observed precipitation at different stations with the longest time periods over the study area (for reference see Table 1 and Figure 2) [Colour figure can be viewed at wileyonlinelibrary.com]

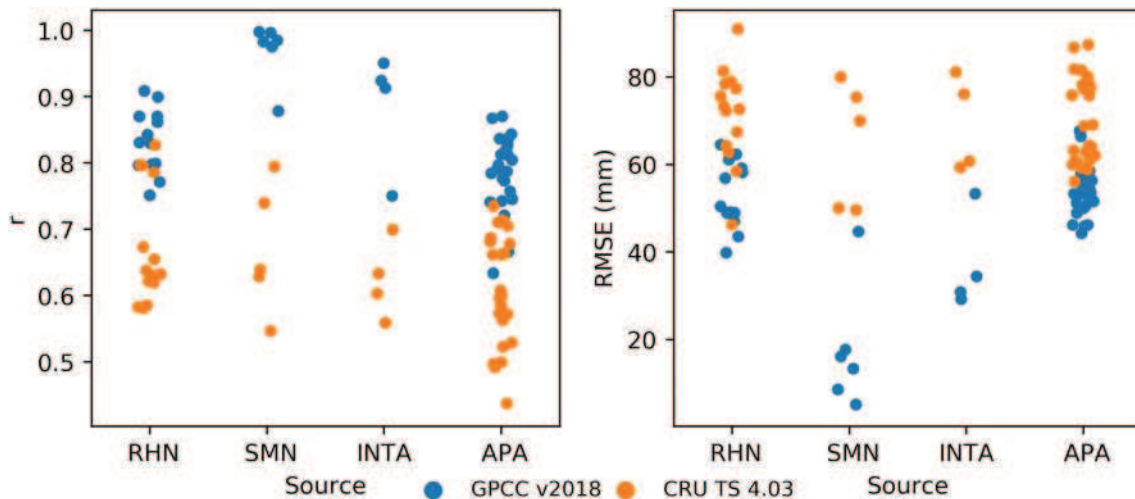


FIGURE 4 Summary of statistical metrics (r and RMSE) between GPCC v2018 and CRU TS 4.03 versus observations by data source [Colour figure can be viewed at wileyonlinelibrary.com]

After selecting the database, we analysed its uncertainty based on the number of precipitation stations included in the GPCC v2018 interpolation during the 1901–2016 period. Figure 5 indicates that there is a very low density of historical data in the ACh region, in agreement with Hurtado et al. (2021). Figure 5a shows that the historical data coverage in the ACh region has varied during the study period. There were about five stations between 1901 and 1930, almost eight stations until 1950, 12 stations in the 1951–1970 period, and a peak of 14 stations between 1970 and 2000. During the 2000s, the number of stations declined to 10 stations and during the 2010s there were about as many stations as there were in the 1930s. Figure 5b exhibits the spatial distribution of the average number of reporting station per grid cell during different periods. The coverage is better towards the east and sparse towards the west of the ACh region. There was a very low density of stations during the 1901–1920 period, which confers high uncertainty to the analysis of extremes carried out in that period. The spatial coverage increased until 1940, although mainly towards the east of the ACh region. The western ACh and the BsSs have very low coverage throughout the study period. Therefore, the results discussed in this article are conditioned by the low density of stations used for the interpolation of the GPCC v2018 database, mainly during the first decades of the twentieth century.

2.3 | Standardized precipitation index

The standardized precipitation index (SPI, McKee et al., 1993, 1995) represents a standardized precipitation anomaly and was developed to quantify rainfall deficit

and excess at different time-scales (Keyantash and Dracup, 2002; Krepper and Zucarelli, 2010). SPI stands among the most used indices to assess EPEs (Mishra et al., 2009; Hao et al., 2014; Chiang et al., 2021), and it is the reference index of the World Meteorological Organization for effective monitoring of droughts and climate risk management (Hayes et al., 2011).

In this study, SPI was computed following a nonparametric approach (Hao and AghaKouchak, 2014; Farahmand and AghaKouchak, 2015). Unlike parametric approaches, nonparametric methods are not based on any theoretical distribution. The parametric (empirical) probability density functions may not be a good fit in the tails (Farahmand and AghaKouchak, 2015). The nonparametric approach can better categorize the drought/wetness classes, representing dryness/wetness and normality conditions better than parametric approaches (Soláková et al., 2014; Mallenahalli, 2020). Thus, the differences in the SPI calculation can be significant in terms of the extreme event intensity (Soláková et al., 2014).

In this study, the marginal probability of precipitation was derived using the Gringorten plotting position formula for extreme events (Gringorten, 1963):

$$p(x_i) = \frac{i - 0.44}{n + 0.12} \quad (1)$$

where n is the sample size, i indicates the rank of non-zero precipitation values, and $p(x_i)$ is the corresponding empirical probability. The outputs of Equation (1) are then transformed into SPI applying the inverse of the standard normal distribution function (ϕ):

$$\text{SPI} = \phi^{-1}(p(x_i)) \quad (2)$$

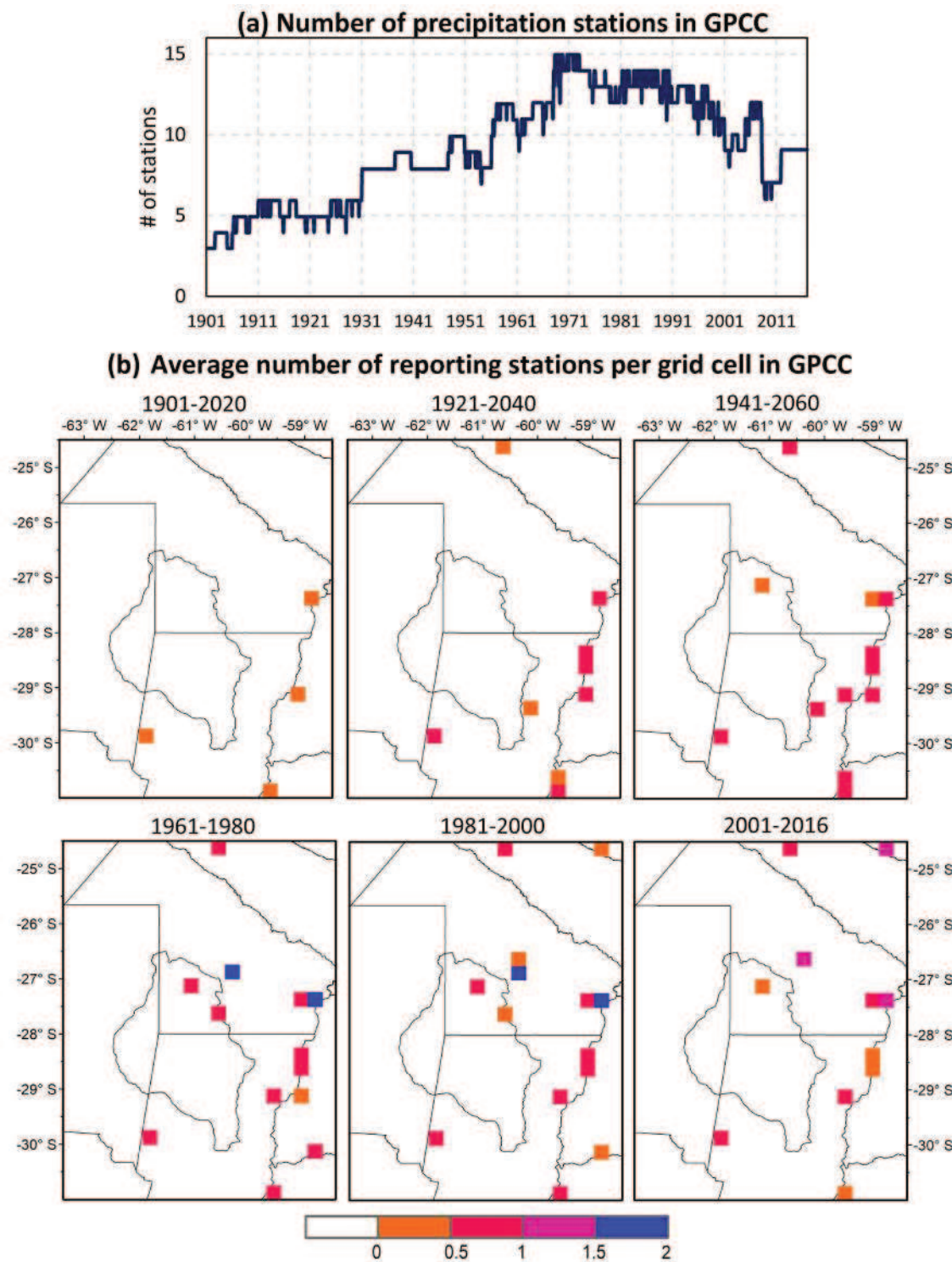


FIGURE 5 (a) Total number of precipitation stations in the Austral Chaco from 1901 to 2016 considered in the GPCC v2018 data set. (b) Average number of reporting stations per grid cell in GPCC v2018 data set through different time periods between 1901 and 2016 [Colour figure can be viewed at wileyonlinelibrary.com]

First, GPCC v2018 monthly precipitation time series were transformed into SPI_j (t) series at different time scales, that is, $j = 3, 9, 12, 18$, and 24 months. The information and use of the SPI depend on its time scale. The shorter

time scales (weeks to months) have application in agriculture while the longer time scales (seasons to years) would identify long-term rainfall anomalies reflected in underground water and reservoir levels (Sirdas and

Sen, 2003). SPI values on a 3-month time scale (SPI3) reflect wet or dry conditions for short to intermediate periods and provide climate estimates for critical growth stages of crops (Sgroi et al., 2021). SPI9 provides inter-seasonal information; it is useful to represent hydrological drought/wetness (Lloyd-Hughes and Saunders, 2002). SPI12, SPI18, and SPI24 are used to study long-term hydrological droughts and wet events.

Second, wet and dry events were classified using the SPI ranges associated to each category and occurrence probability as in Table 2 (Lloyd-Hughes and Saunders, 2002). We computed the area-averaged SPI_j (t) time series at 3- and 24-month time scales, in order to assess the seasonal (SPI3) and low frequency behaviour (SPI24) of EPEs. Note that although the ACh may be divided in dry and humid regions (see Section 3.1), we tested that annual cycles and precipitation time series during the rainy season (including their interannual variability and trends) do not show significant variations in shape between regions (not shown). Therefore, the variability modes of the EPEs here reported represent the whole ACh region.

In this study, we focused on severely wet/dry extreme precipitation events; that is, those events when SPI > 1.5 or SPI < -1.5. We calculated the time series of spatial extension of severely wet/dry events at each time scale by computing the percentage of grid points under at least severe conditions for each month. Then, critical months were identified as those months when the area affected with at least severe wet/dry condition was larger than 50% of the region. Finally, in order to detect the areas with most extreme conditions, we calculated the spatial fields of average SPI_j intensity for those critical months at each grid point and for each time scale ($j = 3, 9, 12, 18$, and 24 months).

2.4 | Singular Spectrum analysis

The Singular Spectrum Analysis (SSA, Ghil et al., 2001; Wilks, 2006) describes the variability of discrete and

TABLE 2 Classification scales for SPI used in this study and the associated event probabilities (adapted from Lloyd-Hughes and Saunders, 2002)

| SPI | Category | Probability (%) |
|---------------|----------------|-----------------|
| 2.00 or more | Extremely wet | 2.3 |
| 1.50 a 1.99 | Severely wet | 4.4 |
| 1.00 a 1.49 | Moderately wet | 9.2 |
| -0.99 a 0.99 | Near normal | 68.2 |
| -1.00 a -1.49 | Moderately dry | 9.2 |
| -1.50 a -1.99 | Severely dry | 4.4 |
| -2.00 or less | Extremely dry | 2.3 |

finite time series by its eigenvalue decomposition into eigenvectors (known as temporal-empirical orthogonal functions or T-EOFs) and temporal-principal components (T-PCs). Each T-PC filters a deterministic signal of the original time series explaining a portion of its variance associated with the corresponding eigenvalue. The structures of deterministic signals are determined as nonlinear trends and quasi-oscillatory modes. To distinguish significant T-PCs at the 95% confidence level, we applied a Monte Carlo test (Allen and Smith, 1996) with an ensemble of 1000 independent realizations.

In this study, SSA was applied to study the temporal variability of (1) the area-averaged time series of SPI_j (t) at different time scales, and (2) the time series of spatial extension of severely wet/dry events. In the SSA method, the window length M should not exceed one third of the time series length to adequately represent quasi-cycles between M/5 and M (Von Storch and Navarra, 1995). Considering the length of the GPCC v2018 dataset, a window length of $M = 360$ months (30 years) was used to represent the frequency spectrum between 6 and 30 years (following Krepper and Zucarelli, 2010).

2.5 | ENSO events

The main characteristic of El Niño—Southern Oscillation (ENSO) events is a slow change with time of the sea surface temperature (SST) anomalies over the equatorial and tropical Pacific Ocean. ENSO events usually begin during the first part of a year, reach a maximum at the end of that year and begin to disappear during the following year (Trenberth, 1997). Therefore, ENSO events involve two consecutive years. Berri et al. (2019) discussed the importance of considering the 2-year period for determining ENSO related climate anomalies, since the equatorial Pacific Ocean SST anomalies peak at the end of the year when the ENSO event starts.

The identification of ENSO events follows Berri et al. (2019), which is based on the most accepted classifications. From 1950, the ENSO event classification is based on the analysis of the Oceanic Niño Index (ONI, NOAA/NWS/CPC 2020). ENSO events are classified as warm or El Niño (cold or La Niña) when the ONI exceeds the +0.5°C (-0.5°C) threshold for a minimum of five consecutive overlapping seasons (Trenberth, 1997). Prior to 1950, when the ONI is not available, El Niño events (EN) follow the classification of Rasmusson and Carpenter (1983), which is based on SST anomalies in the equatorial and tropical Pacific Ocean. La Niña events (LN) are taken from the ENSO classification of Ropelewski and Jones (1987), in terms of the Southern Oscillation Index (SOI). Figure 6

presents the timeline of the 2-year periods of EN and LN used in the present study for the 1901–2016 period.

This study adopts the methodology used by Berri et al. (2019), in line with Ropelewski and Halpert (1987). Two data subsets were created from the original time series of precipitation, SPI3 and SPI24: one with the years of EN events and the other one with the years of LN events. The elements of the subsets are composites of 24 consecutive months starting in January of the year when an ENSO event starts (0) and ending in December of the following year (+). Biannual EN and LN composites of monthly precipitation, SPI3 and SPI24 were computed and compared with the climatological mean annual cycle of each variable. The analysis of this comparison identifies a discriminant ENSO signal for precipitation, SPI3 and SPI24.

We also used the identified EN and LN events to assess the intensity and sign of EPEs during the highest signal phases of each ENSO event. To do this, we recognized the maximum (minimum) values of SPI3 and SPI24 for EN (LN) events from October (0) to February (+) and from October (0) to April (++) respectively. Further discussion is provided in Section 3.2.

3 | PRECIPITATION CLIMATOLOGY AND VARIABILITY

3.1 | Spatial pattern and temporal evolution of precipitation

Figure 7a shows the spatial distribution of annual precipitation in the 1981–2010 period. Annual precipitation presents an east–west gradient, with rainfall amounts ranging from 1500 mm/year towards the east to 700 mm/year towards the west over ACh region. According to the precipitation spatial gradient, the Gran Chaco region

is usually divided into two regions (Bucher, 1982; Fehlenberg et al., 2017): Dry Chaco (450–900 mm) and Humid Chaco (900–1,500 mm). Following Bucher (1982) and Fehlenberg et al. (2017), the ACh region here studied includes most of the humid Chaco and a small portion of the Dry Chaco towards the west of the study region.

Figure 7c presents the annual precipitation cycle (see black line). It exhibits two distinct periods: a rainy season between October and April and a dry season between May and September. During the rainy season, precipitation varies from 80 to 135 mm/month, reaching the maximum monthly value in March. It is forced by unstable tropical air masses that create the perfect conditions for intense convective activity (Berberry and Barros, 2002; Rasmussen et al., 2016). During the dry season, precipitation registers the minimum monthly values in July and August (23 mm on average).

Figure 7b exhibits the temporal evolution of the rainy season precipitation (Oct–Apr), along with the long-term nonlinear trend computed with the SSA method. Total precipitation during the rainy season shows a marked nonlinear trend. Precipitation increased from mid to late twentieth century, when the trend reverts its slope to negative in the two first decades of the 21st century. Consistently, there is evidence of a long-term increase in SESA precipitation since the 1960s (Haylock et al., 2006, Lovino et al., 2018a). The long-term trend might be influenced by inter-decadal variability in tropical Pacific SSTs (Huang et al., 2005, Jacques-Coper and Garreaud, 2015) and by a multi-decadal cooling in the tropical Atlantic Ocean (Seager et al., 2010; Barreiro et al., 2014). Other decadal-to-multidecadal forcing factors that may have influenced SESA precipitation include the Pacific decadal variability, and the South Atlantic Convergence Zone (Kayano and Andreoli, 2007; Mo and Berberry, 2011; Grimm et al., 2016). Figure 7b also shows that the precipitation during the rainy season presents a

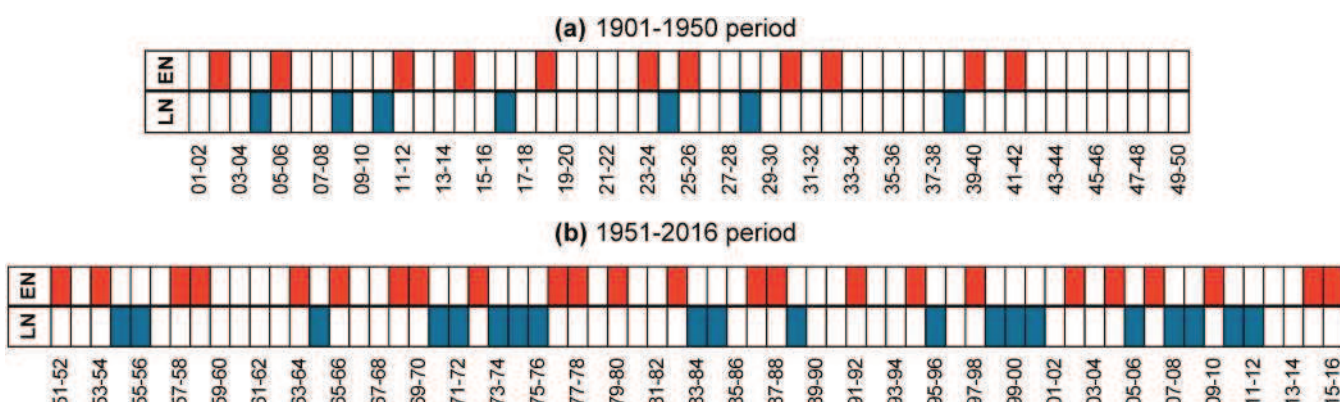


FIGURE 6 Timeline of El Niño (EN) and La Niña (LN) events considered in the study for the (a) 1901–1950 period and (b) the 1951–2016 period [Colour figure can be viewed at wileyonlinelibrary.com]

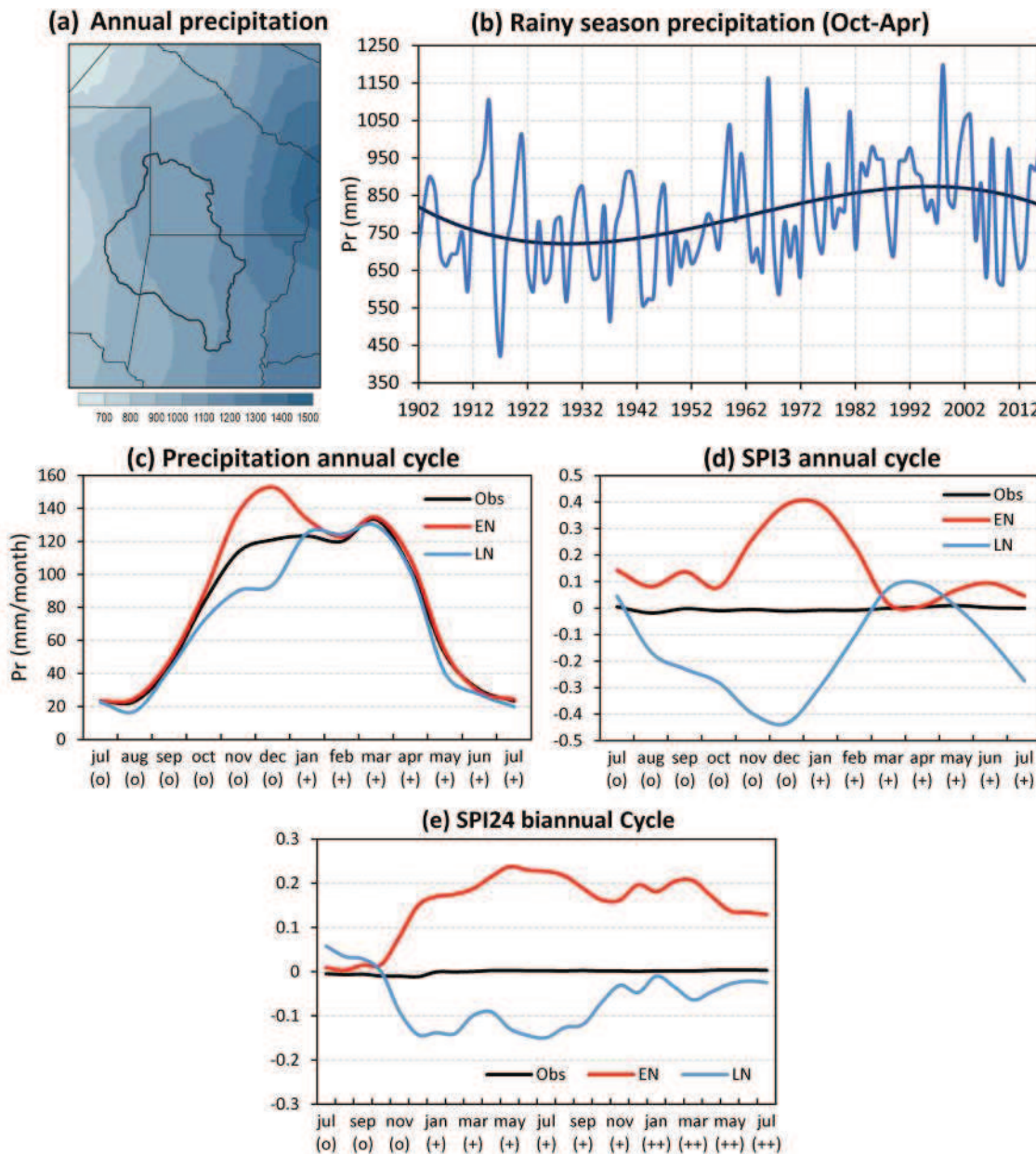


FIGURE 7 Climatological features of the study region. (a) Spatial distribution of annual precipitation in the 1981–2010 period. (b) Time series of precipitation in the rainy season (Oct–Apr) in the 1901–2016 period and nonlinear trend. (c) Precipitation annual cycle for the 1901–2016 period (black line) compared with the biannual EN and LN composites Jul (0) to Jul (+). (d) As in (c) but for SPI3. (e) As in (c) but for SPI24. A two-year period is shown given the low frequency of the SPI24. EN and LN periods are extended for 3 years: The starting year (0), the second (+), and the third (++) year [Colour figure can be viewed at wileyonlinelibrary.com]

large interannual variability, with a minimum value close to 400 mm in 1917 and a maximum value of 1200 mm in 1998. The variability of SESA precipitation at interannual time scales is mostly related to the ENSO with periodicities between 3 and 6 years (Krepper and García, 2004; Lovino et al., 2018a) and slightly related to the North Atlantic Oscillation with a near-decadal frequency (Robertson and Mechoso, 1998; Robertson et al., 2001).

3.2 | ENSO influence on precipitation and its extreme events

Precipitation and its extreme events are mostly associated with the ENSO over SESA: EN conditions would cause increased precipitation while LN conditions might favour dry anomalies (Berri et al., 2002; Grimm and Tedeschi, 2009; Penalba and Rivera, 2016; Cai et al., 2020).

In order to assess this association in the ACh region, Figure 7c presents the mean annual precipitation cycle from 1901 to 2016 compared with the biannual EN and LN composites (only the period from July (0) to July (+) is shown). The EN precipitation composite (Figure 7c, red line) shows a positive departure from the mean value (black line) between October (0) and February (+), that peaks in December (0). The LN precipitation composite (Figure 7c, blue line) shows a departure from the mean value between October (0) and January (+). Thus, there is a clear discriminant ENSO signal in precipitation towards the end of the year (0).

Figure 7d,e present the biannual EN and LN composites of SPI3 and SPI24, respectively, and their 1901–2016 means. As in precipitation, only the July (0) to July (+) period is shown in Figure 7d for the SPI3 composites. Figure 7d shows that both the LN composite (blue line) and EN composite (red line) present a main minimum and maximum, respectively, in December (0). Thus, the discriminant ENSO signal in SPI3 is clearly present towards the end of the year (0). Our results show how EN (LN) events influence precipitation and its seasonal extreme events in the ACh region, favouring conditions above (below) climatological values mainly in austral spring and summer of the year when the ENSO event starts.

Figure 7e shows that the SPI24 EN and LN composites do not change sign throughout the 2-year period; therefore, the discriminant ENSO signal in SPI24 is more sustained over time than in the SPI3. This finding reveals that, although EN and LN events tend to be shorter-lived

than 24 months, the effects of extreme EN and LN can persist even on low-frequency time scales such as that represented by the SPI24.

4 | WET AND DRY EXTREME PRECIPITATION EVENTS

4.1 | Seasonal time scale characterized by SPI3

Figure 8c shows the area-averaged SPI3 time series that characterizes the temporal evolution of seasonal EPEs over the ACh region. Figure 8a,b present the percentage of the ACh region under at least severely wet conditions ($SPI3 > 1.5$) and at least severely dry conditions ($SPI3 < -1.5$), respectively. The temporal evolution of the time series that represent the spatial extension of severely wet and dry extremes coincides greatly with the temporal evolution of the area-averaged SPI3 time series. All severely wet and dry EPEs at a seasonal time scale (those events whose SPI3 exceeded 1.5 or -1.5) affected 50% or more of the ACh region.

Seasonal droughts characterized by SPI3 were more frequent and with larger spatial extension from 1915 to 1955 (see Figure 8b,c). The most severe seasonal drought occurred in 1916 and 1933, with peak intensities of $SPI3 = -2.3$ and $SPI3 = -2$, and spatial extents of 92% and 77%, respectively. Other severe events stand out between September and December 1937, May and July 1976, and April and June 1978 (peak intensities between

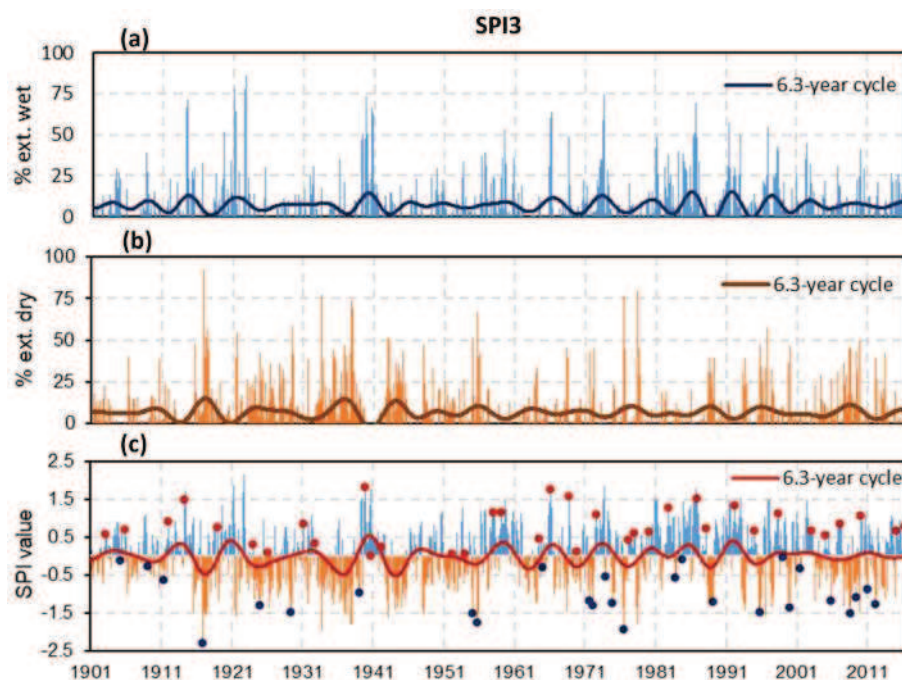


FIGURE 8 Percentage of the region under at least severely (a) wet ($SPI3 > 1.5$) and (b) dry ($SPI3 < -1.5$) conditions. (c) SPI3 time series of the 1901–2016 period. The red (blue) dots represent the maximum (minimum) value of SPI3 between October (0) and February (+) during EN (LN) events [Colour figure can be viewed at wileyonlinelibrary.com]

$-1.9 < \text{SPI}3 < -1.5$, spatial extents between 75% and 78%). There were less severe events as from 1978. The most remarkable droughts occurred in 1996 and 2008, both with $\text{SPI} = -1.5$ and a 50% affected area.

Seasonal wet EPEs were more frequent from 1960 to 2005, although less intense and with lesser spatial extension than those of the first half of the twentieth century (see Figure 8a,c). The most severe wet EPE in the time series occurred from August to September 1922 ($\text{SPI}3 = 2.2$) and affected 86% of the ACh region. Other major severity peaks were observed in February 1921, October 1939, August 1973, and September 1940 (all with $\text{SPI}3 = 1.8$ and spatial extents between 77% and 66% of the study area). To sum up, our results exhibit the large temporal variability of seasonal EPEs in the ACh region. At the 3-month scale, the severest droughts and wet EPEs were registered during the early twentieth century. The wet EPEs were more frequent and less intense since 1960 than those recorded during the early twentieth century.

The temporal variability of the seasonal EPE in the ACh region was assessed applying the SSA method to the area-averaged time series of the SPI3 and to the time series of spatial extension of severely dry/wet extreme events. Regarding the low-frequency variability, nonlinear trends were identified in each of the time series (see Table 3). Consistent with what was discussed above, nonlinear trends indicate an increase in the frequency of wet EPEs as from 1970 and higher preponderance of seasonal droughts in the first half of the 20th century (not shown). Our results highlight the relevance of the interannual variability with a 6.3-year cycle (see Table 3 and Figure 8). The 6.3-year cycle explains more than 9% of the variance of each time series (Table 3). As noted above, the interannual variability of extreme precipitation events in the ACh region is strongly influenced by the extreme phases of the ENSO. Consistently, Figure 8c shows that most of the seasonal extreme wet EPE

occurred during EN events while most of the seasonal droughts occurred during LN events, mainly since 1950, when the recorded ENSO events have been more frequent. However, not all EN or LN events caused seasonal EPEs in the ACh region. Consequently, in the ACh region, not all precipitation deficits and excesses are exclusively associated with the occurrence of an ENSO event, in agreement with Grimm and Tedeschi (2009), Penalba and Rivera (2016), Lovino et al. (2018a), among others.

4.2 | Low-frequency time scale characterized by SPI24

Figure 9c shows the area-averaged SPI24 time series that represents the temporal evolution of low-frequency EPEs over the ACh region. Figure 9a,b present the time series of the percentage of the ACh region under at least severely wet/dry conditions. Table 3 shows that nonlinear trends explain high percentages of the total variance of each time series: 26% for the SPI24 time series and 18% and 22% for the spatial extension of severely wet and dry EPE time series, respectively. The nonlinear trends in all the time series (Figure 9a–c) suggest that the occurrence of low-frequency EPEs can be divided into two periods: a dry one before 1960 and a wet one from 1960 to 2005. Figure 9c also shows that the nonlinear trend has inverted after the wet period, entering a phase of dominating dry EPEs that includes the severe droughts of 2008–2009 and 2012–2013. The reversal in the wet period since the mid-2000s could be explained by a transition to a cold phase of the Pacific Ocean and a warm period of the Atlantic Ocean (Barreiro et al., 2014; Lovino et al., 2018a). If these conditions continue into the coming decades, more severe droughts and less wet EPEs might be expected. However, Zhang et al. (2016) reported

TABLE 3 Dominant modes (quasi-cycles and trends) found in the SPI time series $\text{SPI}_j(t)$ and spatial extent of extremely wet $\text{SEEW}_j(t)$ and dry $\text{SEED}_j(t)$ events for $j = 3$ and 24 months

| Time series | T-PCs | Dominant period | Explained variance (%) |
|-----------------------|-----------------|-----------------|------------------------|
| $\text{SEEW}_3(t)$ | T-PC1 and T-PC2 | 6.3 | 10.1 |
| | T-PC3 | Trend | 3.8 |
| $\text{SEED}_3(t)$ | T-PC1 and T-PC2 | 6.3 | 8.9 |
| | T-PC3 | Trend | 4 |
| $\text{SPI}_3(t)$ | T-PC1 and T-PC2 | 6.3 | 13.2 |
| | T-PC3 | Trend | 5.5 |
| $\text{SEEW}_{24}(t)$ | T-PC1 | Trend | 17.7 |
| | T-PC2 and T-PC3 | 6.3 | 31.3 |
| $\text{SEED}_{24}(t)$ | T-PC1 | Trend | 21.7 |
| | T-PC2 and T-PC3 | 9 | 33.6 |
| $\text{SPI}_{24}(t)$ | T-PC1 | Trend | 26.3 |
| | T-PC2 and T-PC3 | 9 and 6.3 | 40.2 |

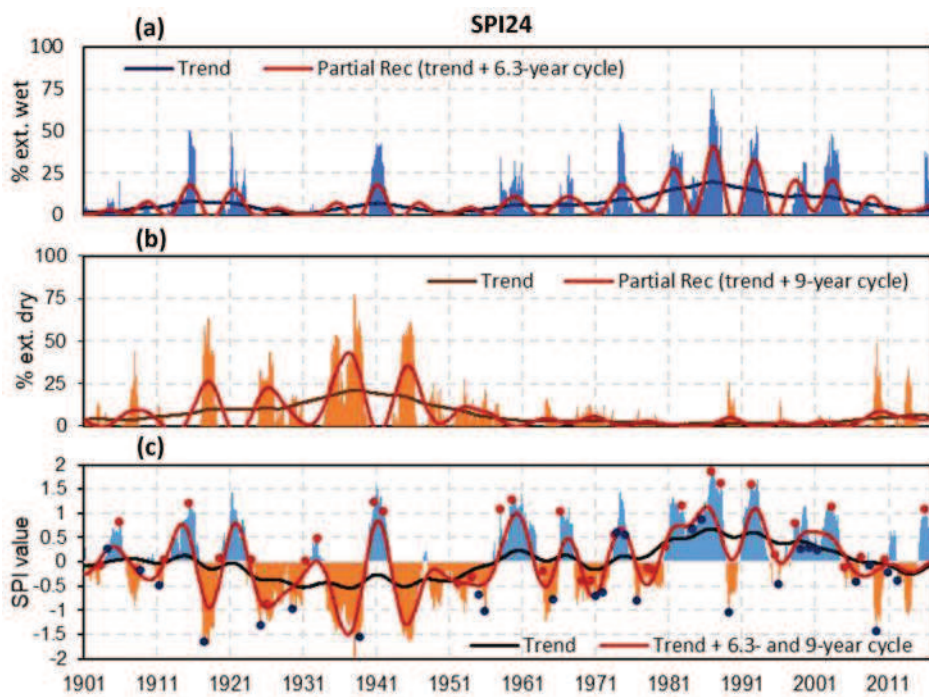


FIGURE 9 Percentage of the region under at least severely (a) wet ($SPI_{24} > 1.5$) and (b) dry ($SPI_{24} < -1.5$) conditions. (c) SPI_{24} time series of the 1901–2016 period. The red (blue) dots represent the maximum (minimum) value of SPI_3 between October (o) and April (++) during EN (LN) events [Colour figure can be viewed at wileyonlinelibrary.com]

that the recent precipitation decline in SESA is temporary and that the positive trend will resume in response to both increasing greenhouse gas emissions during the 21st century and a return of multidecadal variability to the conditions before the 2000s.

Figure 9a shows that the spatial extent of severely wet EPEs at 24-month time scale has increased markedly in the wet period. The events with large spatial extent occurred from 1970 to 2005, with the most extensive event in 1987 that covered 75% of the study region. On the other hand, Figure 9b shows that the hydrological droughts—represented by SPI_{24} —with the largest spatial extent occurred in the first half of the 20th century. For instance, the hydrological drought with the largest spatial extent was registered in 1938 (above 75% of the study region under extremely dry conditions). Thus, our results show that the larger spatial extents coincide with the higher intensities of both dry and wet EPEs (see Figure 9a–c). This means that those low-frequency EPEs with the largest spatial extent and the highest intensity were mainly dry during the first half of the 20th century and wet in the second half of the 20th century and beginning of the 21st century.

Figure 9b,c show that an extended period with severe hydrological droughts was registered from 1922 to 1940. The extended drought period, only interrupted by values of SPI slightly above zero in 1932, coincides with the so-called “Pampas Dust Bowl” (Viglizzo and Frank, 2006). The “Pampas Dust Bowl” was caused by a symmetric hemispherical pattern of precipitation deficit with drought in both North and South America (Seager

et al., 2010). In agreement with those findings, a multi-year period of droughts in northeastern Argentina between 1920s and 1940s was reported by Lovino et al. (2018a). They argued that this drought period was coincident with a negative phase of a long-term precipitation trend and a dry episode of the Multidecadal Atlantic Oscillation and the Interdecadal Pacific Oscillation. Our results suggest that the “Pampas Dust Bowl” also affected the ACh region.

The results from SSA show that the spatial extension of severely wet events presents a dominant cycle of 6.3 years (see Table 3). The partial reconstruction of the time series (Figure 9a) shows that the 6.3-year cycle was more significant during the 1970–2005 wet period. The spatial extension of severely dry events (Figure 9b) has a cycle of 9 years (Table 3), which becomes more relevant in the 1915–1955 dry period. These cycles combined, together with the nonlinear trend, appear in the partial reconstruction of the SPI_{24} time series (Figure 9c). The partial reconstruction of the SPI_{24} time series account for 66.5% of its variance (Table 3). Thus, our results report the significant long-term change in low-frequency EPEs over the ACh region represented by the significant nonlinear trend and the relevance of the interannual variability cycles of 6.3 years for wet EPEs and of 9 years for dry EPEs. The low-frequency nonlinear trend and the interannual variability modes combined have favoured the EPEs that led to droughts and floods in the study region.

Figure 9c shows in red (blue) dots the maximum (minimum) values of SPI_{24} during EN (LN) events between October (0) and April (++). Note that the

duration of the EPEs here analysed was counted from moderately dry/wet conditions ($SPI24 > 1$ or $SPI24 < -1$) onwards. The most intense wet EPE persisted 31 months (September 1986–January 1988) under moderate and severe conditions (maximum SPI24 of 1.9, affected area of 75%). It occurred during two consecutive EN events (1986–1987, 1987–1988). The following wet EPE in terms of intensity lasted 24 months (May 1991–April 1993) with moderate and severe conditions (maximum SPI24 of 1.7, affected area of 52%). This event was registered during an EN event (1991–1992). Finally, less intense peaks occurred in August 1940 to September 1941 ($SPI24 = 1.6$, affected area of 42%), March 1959 to December 1960 ($SPI24 = 1.4$; affected area <30%), and February 1974 to October 1974 ($SPI24 = 1.4$; affected area of 55%). The first two events occurred during neutral ENSO conditions, although EN events had developed in previous years. Instead, the 1974 event occurred during a LN event.

Figure 9c shows that the most intense hydrological drought identified by SPI24 occurred between November 1936 and January 1939 (27 months), reached extreme conditions ($SPI24 = -2$) and affected 78% of the region. A LN event took place during the 1938–1939 period. Two events followed in intensity. One, a hydrological drought with 20 months of duration registered from March 1917 to October 1918 that reached severe conditions ($SPI24 = -1.7$) and affected 63% of the study region. It also took place during a LN event. The second dry event lasted 26 months (from February 1944 to March 1946), was classified as severe ($SPI24 = -1.7$), and affected 58% of the study region. It occurred during neutral ENSO conditions. In recent years, the drought of March–October 2009 stands out ($SPI24 = -1.4$ and affected area of 50%). This drought was recorded during the 2008–2009 LN event.

Our results highlight that most of the dry/wet low-frequency EPEs as characterized by area-averaged SPI24 over the ACh region occurred during EN or LN events (see Figure 9c). However, certain ENSO events have not caused EPEs and some of the most intense EPEs in the ACh region did not occur under ENSO conditions. For instance, we have detected moderately (e.g., in 1999, 1984, and 1985) or severely (e.g., in 1974) wet conditions during LN events. On the other hand, dry conditions occurred during EN events (e.g., in 1926 and 1968). Therefore, possible normal conditions or dry (wet) EPEs can occur in the ACh region even during EN (LN) events.

4.3 | Spatial distribution of EPEs during critical months

We detected the areas of the ACh region where the most intense EPEs were recorded during the composite of the

critical months. Thus, we identified the regions of the ACh prone to severely or extremely dry/wet EPEs. Figures 10 and 11 present the average spatial distribution of SPIj (t) series for critical months with at least severely dry/wet conditions, respectively.

Figure 10a shows that severely dry conditions occurred during critical months in most of the ACh region at a 3-month time scale, except for the south-west corner where moderate dry conditions were recorded. There were no extremely dry conditions ($SPI3 < -2$) during the composite of critical month at the 3-month time scale. At the 9-month time scale (Figure 10b), severely dry conditions were registered in most of the study region while extremely dry conditions occurred towards the northwestern corner. At low-frequency time scales of 12, 18, and 24 months (Figure 10c–e), severely dry conditions occur further east of the ACh as the timescale grows. Extremely dry conditions may occur towards the centre-east, including northern Santa Fe and southern Chaco. Therefore, our results suggest that both severe seasonal and hydrological droughts may affect almost the entire ACh during critical months. The longest-lasting severe droughts, represented by SPI on 12, 18, and 24-month time scales, are concentrated towards the east of the ACh region. Finally, the largest extreme droughts are more likely to develop in the central-eastern ACh region.

As in seasonal droughts, wet EPEs at 3-month time scale registered severe conditions in most of the study region on critical months (Figure 11a). At time scales between 9 and 24 months (Figure 11b–e), the area affected by severe conditions is concentrated towards the north. Extremely wet EPEs can occur in a smaller portion than the area covered by severe wet EPEs, mainly in the centre of the province of Chaco and varying with time scales from 9 to 24 months. Our results suggest that although most of the region is prone to severely wet EPEs on a seasonal time scale, the longest-lasting severely wet EPEs are concentrated in the northern portion of the ACh region, even achieving extremely wet conditions. At a 24-month time scale, extremely wet EPEs can be registered in much of the northern ACh region, causing significant impacts on water resources management.

It is of particular interest to assess the behaviour of EPEs in the BsSs basin. The entire BsSs basin is prone to severe droughts at time scales of 3 and 9 months (see Figure 10a,b), except for a small portion towards the west where moderate drought conditions prevail. At low-frequency time scales of 18 and 24 months (Figures 10d, e), the intensity of droughts grows from west to east, with moderate conditions in the dry western region and extremely dry conditions in the humid eastern region. Figure 11b–e shows that the intensity of wet EPEs grows

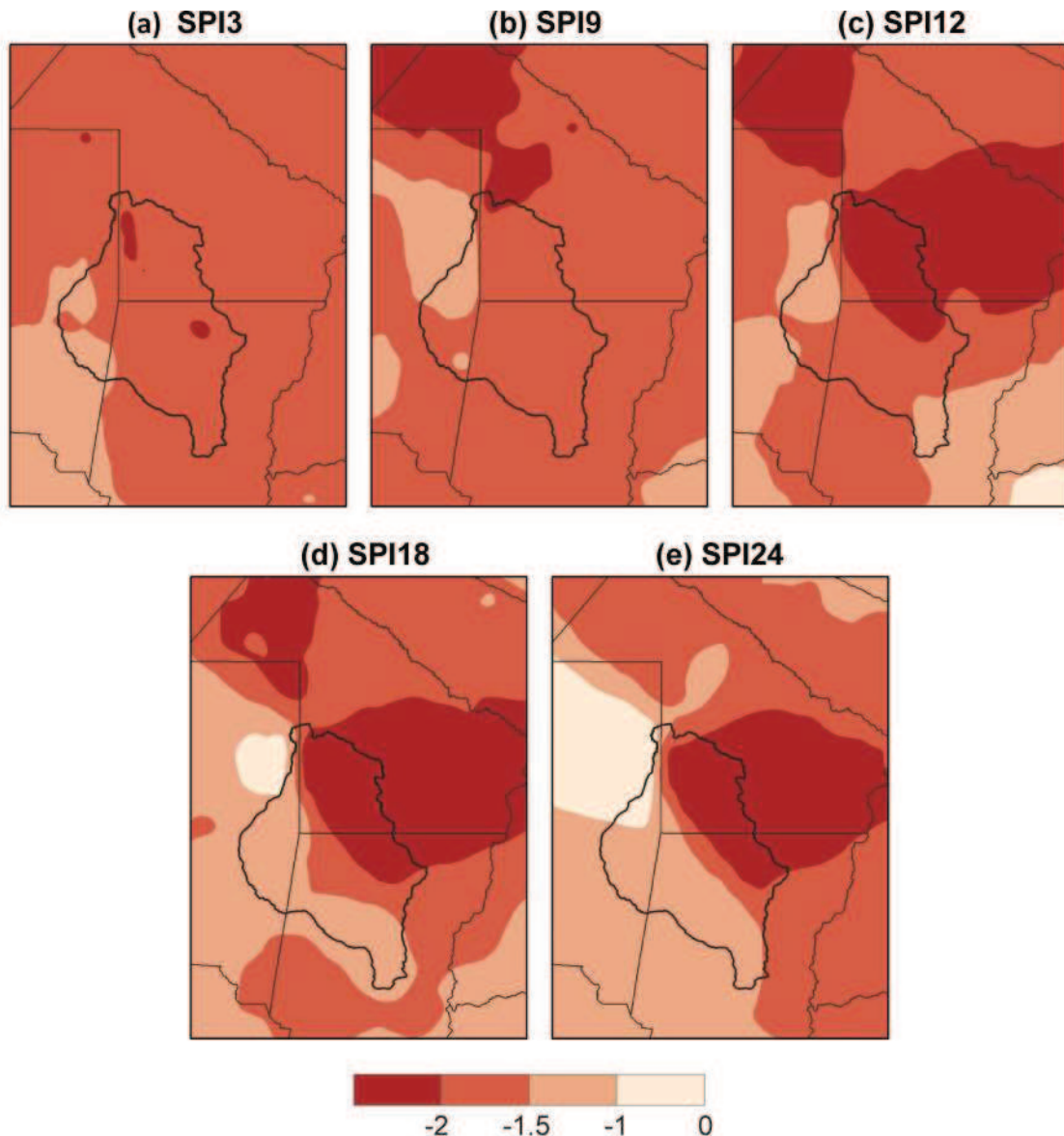


FIGURE 10 Spatial fields of average SPI_j intensity in the critical months (more than 50% of the region exceeds the threshold) with at least severely dry conditions ($\text{SPI}_j < -1.5$) for (a) $j = 3$ months, (b) $j = 9$ months, (c) $j = 12$ months, (d) $j = 18$ months, and (e) $j = 24$ months [Colour figure can be viewed at [wileyonlinelibrary.com](#)]

from south to north on time scales from 9 to 24 months. The northern region of the BsSs basin can be affected by extremely wet EPEs on 9- and 12-month time scales.

5 | DISCUSSION AND CONCLUDING REMARKS

The Austral Chaco region is particularly vulnerable to extreme precipitation events for being a fragile ecosystem due to its high deforestation rates and its sensitivity to climate variability and climate change. Therefore, studies that assess the historical behaviour of the EPEs can

provide valuable information to support water resources management as well as land use and agricultural planning. In this study, EPEs were assessed in their intensity, spatial distribution and temporal variability at different time scales in the Austral Chaco for the 1901–2016 period using the GPCC v2018 dataset. EPEs on time scales relevant to agriculture and water resources applications were studied using a nonparametric approach for the SPI that can properly represent the drought/wetness intensity. The leading modes of SPI's variability were detected using the SSA method. We also conducted a thorough compilation and quality control of precipitation observations in a scarcely monitored region. Note also that the

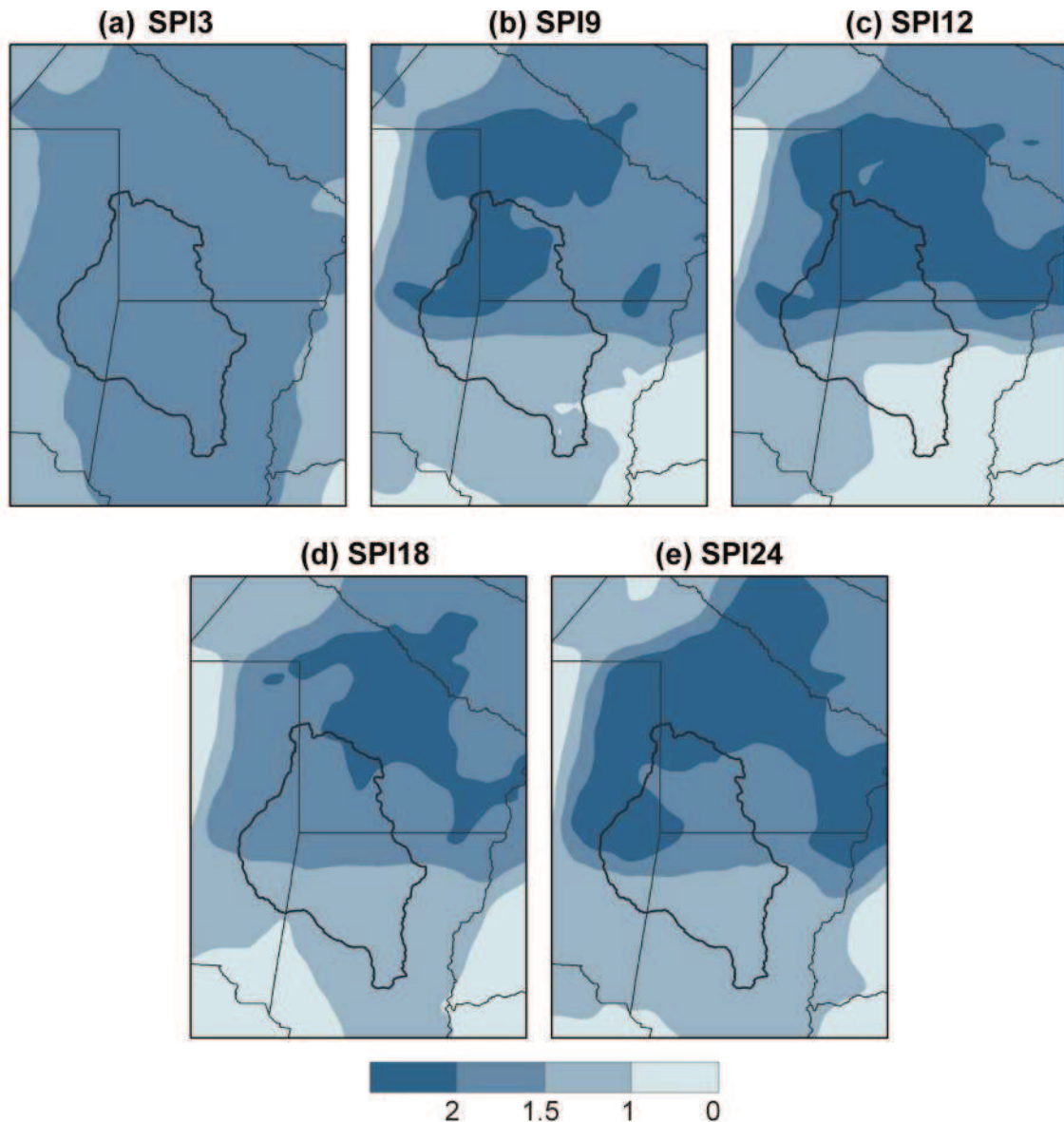


FIGURE 11 Spatial fields of average SPI_j intensity in the critical months (more than 50% of the region exceeds the threshold) with at least severely wet conditions ($\text{SPI}_{\text{j}} > 1.5$) for (a) $j = 3$ months, (b) $j = 9$ months, (c) $j = 12$ months, (d) $j = 18$ months, and (e) $j = 24$ months [Colour figure can be viewed at wileyonlinelibrary.com]

low density of stations used for the interpolation of the GPCC v2018 database conditions our findings, mainly during the first decades of the twentieth century.

The SPI at a 24-month time scale characterizes EPEs which represent long-lasting water excess or deficit that produce hydrological impacts. The EPEs characterized by SPI24 underwent two differentiated long-term periods: a dry one before 1960 and a wet one from 1960 to 2005. Within the dry period, severe hydrological droughts took place from 1922 to 1940. This extended drought period coincided with the so-called “Pampas Dust Bowl” (Viglizzo and Frank, 2006). Therefore, our results suggest that the “Pampas Dust Bowl” has also affected the ACh

region severely. On the other hand, the most severe hydrological wet EPEs (both in intensity and spatial extent) occurred in the 1960–2005 period. Since 2006, a reversal of the long-term trend towards drier conditions has been observed, favouring droughts in the last years of the study period. If the long-term trend behaviour continues into the coming decades, more severe droughts and less wetness might be expected.

Interannual variability also plays a role in low-frequency EPEs with two main dominant frequencies: a 6.3-year cycle in the spatial extension of severely wet EPEs, more significant during the wet period, and a 9-year cycle in the spatial extension of extremely dry

events, more significant during the dry period. These results suggest that interannual variability combined with long-term trends intensified hydrological wet and dry EPEs during the wet and dry periods, respectively. Furthermore, these results are robust because the nonlinear trends along with the combined 6.3-year and 9-year cycles explained 66.5% of the variance in the partial reconstruction of the SPI24 time series.

Consistently with the long-term periods identified, our results report that seasonal wet EPEs represented by the SPI3 were more frequent—although with less intensity and spatial extent—in the wet period than in the dry period. On the other hand, seasonal droughts were more frequent and with larger spatial extent during the dry period. Seasonal EPEs also present a large interannual variability. A 6.3-year cycle was found in both intensity and wet/dry spatial extension time series. These seasonal EPEs can severely affect crop yields if seasonal water deficits or excesses occur during critical growing periods.

We found a clear discriminant ENSO signal in precipitation and in seasonal EPEs that stands out between October (0) and February (+), with a peak in December (0). Our results also report that most of the dry/wet seasonal and low-frequency EPEs occurred during EN and LN events. However, this relationship is not straightforward: certain ENSO events have not caused EPEs and, conversely, some EPEs have not occur under ENSO conditions. For instance, wet EPEs can be associated to forcing factors on other time scales such as Mesoscale Convective Systems (Salio et al., 2007; Zhang et al., 2021), the Madden Julian oscillation (MJO; Alvarez et al., 2017; Grimm, 2019) or the seasonal-intraseasonal (SIS) pattern (Vera et al., 2017). Those forcing factors may favour intense precipitation events during non-EN years. Furthermore, even during non-LN years, droughts may be intensified by persistent atmospheric circulations like blocking episodes (Rodrigues and Woollings, 2017), or by regional and local factors such as the moisture transports and soil moisture conditions (Müller et al., 2014; Drumond et al., 2019).

Our results suggest that severely dry/wet EPEs tend to have large spatial extent in the ACh region. Thus, we identified the areas of the ACh region that underwent the most intense EPEs during the critical months (those months when the area affected with at least severely wet/dry conditions was larger than 50% of the region). Both seasonal droughts and wet EPEs registered severe conditions in most of the study region on critical months at a 3-month time scale. The longest-lasting severe droughts and wet EPEs, represented by SPI on 12, 18, and 24-month time scales, are concentrated towards the central-east and north-east of the ACh region, while

extremely wet/dry EPEs are more likely to develop in the central-eastern ACh region. Therefore, central-eastern ACh region—including the northeast portion of the BsSs basin—experiences the most extreme wet and dry EPEs, which makes this area more prone to extreme EPEs.

In the ACh region, the Coupled Model Intercomparison Project phase 6 (CMIP6) projections show little change of 21 century annual mean precipitation, with a slight precipitation increase during summer (DJF) and fall (MAM) and a slight precipitation decrease during winter (JJA) and spring (SON) (Ortega et al., 2021; Almazroui et al., 2021b). These seasonal changes increase from a sustainable development and low emissions scenario (SSP1-2.6) to a fossil-fuelled development and high emissions scenario (SSP5-8.5), and from the mid-term (2040–2059) to the long-term (2080–2099) period (Almazroui et al., 2021b). The CMIP6 models also project more frequent and more intense precipitation extremes as characterized by the annual maximum 5-day precipitation under continued global warming (Li et al., 2021; Almazroui et al., 2021a). Global warming would also cause extreme El Niño events to double their occurrence towards the end of the 21st century; therefore, intense precipitation extremes would increase their frequency (Gulizia and Pirotte, 2021). The consecutive dry days are also projected to increase, with the magnitude of the changes increasing from the weakest (SSP1-2.6) to the strongest (SSP5-8.5) forcing scenario and from mid- to end-century. These scenarios assume an intensification of extreme precipitation events in the ACh region during the 21 century, which may exacerbate both droughts and flood impacts.

Understanding and monitoring the regional climate features will facilitate to study the vulnerability of the ACh region to EPEs. Such information can contribute to the design of measures for a more sustainable land use and for adaptation for climate risk management. The contribution from our results is expected to be incorporated into regional decision systems to improve planning by water resources managers and agricultural stakeholders.

ACKNOWLEDGEMENTS

The authors are grateful to the anonymous reviewers for their constructive comments and recommendations that improved the article. This research was supported by the National Agency for Scientific and Technological Promotion of Argentina (Projects Nos. PICT-2016-1334, PICT-2019-2019-03982, and PICT-2019-2019-00481), the Universidad Nacional del Litoral (Grant no. CAI+D-2020-50620190100082LI), and the Argentine National Council for Scientific and Technical Research. The authors thank Hugo Terré and Mario Basán for kindly providing precipitation data.

AUTHOR CONTRIBUTIONS

Miguel A. Lovino: Conceptualization; formal analysis; investigation; methodology; project administration; visualization; writing – original draft; writing – review and editing. **Gabriela V. Müller:** Conceptualization; formal analysis; investigation; supervision; writing – original draft; writing – review and editing. **María Josefina Pierrestegui:** Data curation; formal analysis; investigation; software; validation; visualization; writing – original draft; writing – review and editing. **Edna Espinosa:** Data curation; formal analysis; investigation; methodology; visualization; writing – original draft; writing – review and editing. **Leticia Rodríguez:** Formal analysis; investigation; project administration; supervision; writing – original draft; writing – review and editing.

ORCID

Miguel A. Lovino  <https://orcid.org/0000-0002-8558-6324>

Gabriela V. Müller  <https://orcid.org/0000-0003-3843-9089>

REFERENCES

- Agosta, E.A. and Compagnucci, R.H. (2008) The 1976/77 Austral summer climate transition effects on the atmospheric circulation and climate in southern South America. *Journal of Climate*, 21(17), 4365–4383. <https://doi.org/10.1175/2008JCLI2137.1>.
- Allen, M.R. and Smith, L.A. (1996) Monte Carlo SSA: detecting irregular oscillations in the presence of colored noise. *Journal of Climate*, 9, 3373–3404. [https://doi.org/10.1175/1520-0442\(1996\)009<3373:MCSSA>2.0.CO;2](https://doi.org/10.1175/1520-0442(1996)009<3373:MCSSA>2.0.CO;2).
- Almazroui, M., Saeed, F., Saeed, S., et al. (2021a) Projected changes in climate extremes using CMIP6 simulations over SREX regions. *Earth Systems and Environment*, 5, 481–497. <https://doi.org/10.1007/s41748-021-00250-5>.
- Almazroui, M., Ashfaq, M., Islam, M.N., et al. (2021b) Assessment of CMIP6 performance and projected temperature and precipitation changes over South America. *Earth Systems and Environment*, 5, 155–183. <https://doi.org/10.1007/s41748-021-00233-6>.
- Alvarez, M.S., Vera, C.S. and Kiladis, G.N. (2017) MJO modulating the activity of the leading mode of intraseasonal variability in South America. *Atmosphere*, 8(12), 232. <https://doi.org/10.3390/atmos8120232>.
- Avila-Diaz, A., Benezoli, V., Justino, F., Torres, R. and Wilson, A. (2020) Assessing current and future trends of climate extremes across Brazil based on reanalyses and earth system model projections. *Climate Dynamics*, 55, 1403–1426. <https://doi.org/10.1007/s00382-020-05333-z>.
- Barreiro, M., Diaz, N. and Renom, M. (2014) Role of the global oceans and land-atmosphere interaction on summertime interdecadal variability over northern Argentina. *Climate Dynamics*, 42(7–8), 1733–1753. <https://doi.org/10.1007/s00382-014-2088-6>.
- Barros, V.R., Boninsegna, J.A., Camilloni, I.A., Chidiak, M., Magrín, G.O. and Rusticucci, M. (2015) Climate change in Argentina: trends, projections, impacts and adaptation. *Wiley Interdisciplinary Reviews: Climate Change*, 6(2), 151–169. <https://doi.org/10.1002/wcc.316>.
- Baumann, M., Gasparri, I., Piquer-Rodríguez, M., Gavier Pizarro, G., Griffiths, P., Hostert, P. and Kuemmerle, T. (2016) Carbon emissions from agricultural expansion and intensification in the Chaco. *Global Change Biology*, 23(5), 1902–1916. <https://doi.org/10.1111/gcb.13521>.
- Berbery, E.H. and Barros, V.R. (2002) The hydrologic cycle of the La Plata basin in South America. *Journal of Hydrometeorology*, 3(6), 630–645. [https://doi.org/10.1175/1525-7541\(2002\)003<0630:THCOTL>2.0.CO;2](https://doi.org/10.1175/1525-7541(2002)003<0630:THCOTL>2.0.CO;2).
- Berri, G.J., Flamenco, E.A., Spescha, L., Tanco, R.A. and Hurtado, R. (2002) Some effects of La Niña on summer rainfall, water resources and crops in Argentina. In: Glantz, M. H. (Ed.) *La Niña and its Impacts: Facts and Speculation*. Tokio, New York and Paris: United Nations University Press, pp. 124–133.
- Berri, G.J., Bianchi, E. and Müller, G.V. (2019) El Niño and La Niña influence on mean river flows of southern South America along the twentieth century. *Hydrological Sciences Journal*, 64(8), 900–909. <https://doi.org/10.1080/02626667.2019.1609681>.
- Bucher, E.H. (1982) Chaco and Caatinga: South American arid savannas, woodlands and thickets. In: *Ecology of Tropical Savannas*. Berlin, Heidelberg: Springer, pp. 48–79.
- Bucher, E.H. and Huszar, P.C. (1999) Sustainable management of the Gran Chaco of South America: ecological promise and economic constraints. *Journal of Environmental Management*, 57(2), 99–108. <https://doi.org/10.1006/jema.1999.0290>.
- Cai, W., McPhaden, M.J., Grimm, A.M., Rodrigues, R.R., Taschetto, A.S., Garreaud, R.D., Dewitte, B., Poveda, G., Ham, Y.-G., Santoso, A., Ng, B., Anderson, W., Wang, G., Geng, T., Jo, H.-S., Marengo, J.A., Alves, L.M., Osman, M., Li, S., Wu, L., Karamperidou, C., Takahashi, K. and Vera, C. (2020) Climate impacts of the El Niño–southern oscillation on South America. *Nature Reviews Earth & Environment*, 1(4), 215–231. <https://doi.org/10.1038/s43017-020-0040-3>.
- Camilloni, I. and Barros, V. (2000) The Paraná River response to El Niño 1982–83 and 1997–98 events. *Journal of Hydrometeorology*, 1(5), 412–430.
- Camilloni, I. and Barros, V. (2003) Extreme discharge events in Paraná River and their climate forcing. *Journal of Hydrology*, 278, 94–106. [https://doi.org/10.1016/S0022-1694\(03\)00133-1](https://doi.org/10.1016/S0022-1694(03)00133-1).
- Carril, A.F., Cavalcanti, I.F.A., Menéndez, C.G., Sörensson, A., López-Franca, N., Rivera, J., Robledo, F., Zaninelli, P., Ambrizzi, T., Penalba, O., da Rocha, R., Sánchez, E., Bettolli, M., Pessacq, N., Renom, M., Ruscica, R., Solman, S., Tencer, B., Grimm, A., Rusticucci, M., Cherchi, A., Tedeschi, R. and Zamboni, L. (2016) Extreme events in the La Plata basin: a retrospective analysis of what we have learned during CLARIS-LPB project. *Climate Research*, 68, 95–116. <https://doi.org/10.3354/cr01374>.
- Cavalcanti, I.F.A., Carril, A.F., Penalba, O.C., Grimm, A.M., Menéndez, C.G., Sanchez, E., Chechi, A., Sörensson, A., Robledo, F., Rivera, J., Pántano, V., Bettolli, L.M., Zaninelli, P., Zamboni, L., Tedeschi, R.G., Dominguez, M., Ruscica, R. and Flach, R. (2015) Precipitation extremes over La Plata Basin: review and new results from observations and climate simulations. *Journal of Hydrology*, 523, 211–230. <https://doi.org/10.1016/j.jhydrol.2015.01.028>.

- Cerón, W.L., Kayano, M.T., Andreoli, R.V., Avila-Diaz, A., Rivera, I.A., Freitas, E.D., Martins, J.A. and Souza, R.A.F. (2021) Recent intensification of extreme precipitation events in the La Plata Basin in southern South America (1981–2018). *Atmospheric Research*, 249, 105299. <https://doi.org/10.1016/j.atmosres.2020.105299>.
- Chiang, F., Mazdiyasi, O. and AghaKouchak, A. (2021) Evidence of anthropogenic impacts on global drought frequency, duration, and intensity. *Nature Communication*, 12, 2754. <https://doi.org/10.1038/s41467-021-22314-w>.
- Déqué, M. (2012) Continuous variables. In: Jolliffe, I.T. and Stephenson, D.B. (Eds.) *Forecast Verification: A Practitioner's Guide in Atmospheric Science*, 2nd edition. Chichester: John Wiley & Sons, pp. 97–120.
- Drumond, A., Stojanovic, M., Nieto, R., Vicente-Serrano, S.M. and Gimeno, L. (2019) Linking anomalous moisture transport and drought episodes in the IPCC reference regions. *Bulletin of the American Meteorological Society*, 100(8), 1481–1498. <https://doi.org/10.1175/BAMS-D-18-0111.1>.
- Espinosa E.L. (2021). Analysis of the hydrological behavior of the "Bajos Submeridionales" plain system, Argentina. Master Thesis, Universidad Nacional del Litoral, Argentina. <https://hdl.handle.net/11185/6238>
- Farahmand, A. and AghaKouchak, A. (2015) A generalized framework for deriving non-parametric standardized drought indicators. *Advances in Water Resources*, 76, 140–145. <https://doi.org/10.1016/j.advwatres.2014.11.012>.
- Fehlenberg, V., Baumann, M., Gasparri, N.I., Piquer-Rodriguez, M., Gavier-Pizarro, G. and Kuemmerle, T. (2017) The role of soybean production as an underlying driver of deforestation in the South American Chaco. *Global Environmental Change*, 45, 24–34. <https://doi.org/10.1016/j.gloenvcha.2017.05.001>.
- Garreaud, R.D., Vuille, M., Compagnucci, R. and Marengo, J. (2009) Present-day south American climate. *Palaeogeography Palaeoclimatology, Palaeoecology*, 281(3–4), 180–195. <https://doi.org/10.1016/j.palaeo.2007.10.032>.
- Ghil, M., Allen, M.R., Dettinger, M.D., Ide, K., Kondrashov, D., Mann, M.E., Robertson, A.W., Saunders, A., Tian, Y., Varadi, F. and Yiou, P. (2001) Advanced spectral method for climatic time series. *Reviews of Geophysics*, 40(1), 1003. <https://doi.org/10.1029/2000RG000092>.
- González, M.H., Cariaga, M.L. and Skansi, M.D.L.M. (2012) Some factors that influence seasonal precipitation in Argentinean Chaco. *Advances in Meteorology*, 359164. 2012, 1–13. <https://doi.org/10.1155/2012/359164>.
- Grimm, A.M. and Tedeschi, R.G. (2009) ENSO and extreme rainfall events in South America. *Journal of Climate*, 22(7), 1589–1609. <https://doi.org/10.1175/2008JCLI2429.1>.
- Grimm, A.M. (2011) Interannual climate variability in South America: impacts on seasonal precipitation, extreme events, and possible effects of climate change. *Stochastic Environmental Research and Risk Assessment*, 25, 537–554. <https://doi.org/10.1007/s00477-010-0420-1>.
- Grimm, A.M., Laureanti, N.C., Rodakoviski, R.B. and Gama, C.B. (2016) Interdecadal variability and extreme precipitation events in South America during the monsoon season. *Climate Research*, 68, 277–294. <https://doi.org/10.3354/cr01375>.
- Grimm, A.M. (2019) Madden-Julian oscillation impacts on south American summer monsoon season: precipitation anomalies, extreme events, teleconnections, and role in the MJO cycle. *Climate Dynamics*, 53, 907–932. <https://doi.org/10.1007/s00382-019-04622-6>.
- Gringorten, I.I. (1963) A plotting rule for extreme probability paper. *Journal of Geophysical Research*, 68, 813–814. <https://doi.org/10.1029/JZ068i003p00813>.
- Gulizia, C. and Pirotte, M. N. (2021). Characterization of simulated extreme El Niño events and projected impacts on south American climate extremes by a set of coupled model Intercomparison project phase 5 global climate models. *International Journal of Climatology*, 1–15. 42(1), 48–62. <https://doi.org/10.1002/joc.7231>
- Gupta, R.S. (2016) *Hydrology and Hydraulic Systems*, 4th edition. Long Grove: Waveland Press Inc., p. 820.
- Hansen, M.C., Potapov, P.V., Moore, R., et al. (2013) High-resolution global maps of 21st-century forest cover change. *Science*, 342(6160), 850–853. <https://doi.org/10.1126/science.1244693>.
- Hao, Z. and AghaKouchak, A. (2014) A non-parametric multivariate multi-index drought monitoring framework. *Journal of Hydrometeorology*, 15, 89–101. <https://doi.org/10.1175/JHM-D-12-0160.1>.
- Hao, Z., AghaKouchak, A., Nakhjiri, N. and Farahmand, A. (2014) Global integrated drought monitoring and prediction system. *Scientific Data*, 1, 140001. <https://doi.org/10.1038/sdata.2014.1>.
- Harris, I., Osborn, T.J., Jones, P. and Lister, D. (2020) Version 4 of the CRU TS monthly high-resolution gridded multivariate climate dataset. *Scientific Data*, 7(109), 1–18. <https://doi.org/10.1038/s41597-020-0453-3>.
- Hayes, M., Svoboda, M., Wall, N. and Widhalm, M. (2011) The Lincoln declaration on drought indices: universal meteorological drought index recommended. *Bulletin of the American Meteorological Society*, 92(4), 485–488. <https://doi.org/10.1175/2010BAMS3103.1>.
- Haylock, M.R., Peterson, T.C., Alves, L.M., Ambrizzi, T., Anunciação, Y.M.T., Baez, J., Barros, V.R., Berlato, M.A., Bidegain, M., Coronel, G., Corradi, V., Garcia, V.J., Grimm, A. M., Karoly, D., Marengo, J.A., Marino, M.B., Moncunill, D.F., Nechet, D., Quintana, J., Rebello, E., Rusticucci, M., Santos, J. L., Trebejo, I. and Vincent, L.A. (2006) Trends in total and extreme South American rainfall in 1960–2000 and links with sea surface temperature. *Journal of Climate*, 19(8), 1490–1512. <https://doi.org/10.1175/JCLI3695.1>.
- Huang, H.-P., Seager, R. and Kushnir, Y. (2005) The 1976/77 transition in precipitation over the Americas and the influence of tropical SST. *Climate Dynamics*, 24(7–8), 721–740. <https://doi.org/10.1007/s00382-005-0015-6>.
- Hurtado, S.I., Agosta, E.A. and Godoy, A. (2020a) Estudio exploratorio de forzantes de la variabilidad en baja frecuencia de la precipitación en el chaco, Argentina. *Meteorologica*, 45, 71–92.
- Hurtado, S.I., Zaninelli, P.G. and Agosta, E.A. (2020b) A multi-breakpoint methodology to detect changes in climatic time series. An application to wet season precipitation in subtropical Argentina. *Atmospheric Research*, 241, 104955. <https://doi.org/10.1016/j.atmosres.2020.104955>.
- Hurtado, S.I., Zaninelli, P.G., Agosta, E.A. and Ricetti, L. (2021) Infilling methods for monthly precipitation records with poor station network density in subtropical Argentina. *Atmospheric Research*, 254, 105482. <https://doi.org/10.1016/j.atmosres.2021.105482>.
- Jacques-Coper, M. and Garreaud, R.D. (2015) Characterization of the 1970s climate shift in South America. *International Journal of Climatology*, 35(8), 2164–2179. <https://doi.org/10.1002/joc.4120>.

- Kayano, M.T. and Andreoli, R.V. (2007) Relation of south American summer rainfall interannual variations with the Pacific decadal oscillation. *International Journal of Climatology*, 27, 531–540. <https://doi.org/10.1002/joc.1417>.
- Keyantash, J. and Dracup, J.A. (2002) The quantification of drought: an evaluation of drought indices. *Bulletin of the American Meteorological Society*, 83, 1167–1180. <https://doi.org/10.1175/1520-0477-83.8.1167>.
- Krepper, C.M. and García, N.O. (2004) Spatial and temporal structure of trends and interannual variability of precipitation over La Plata Basin. *Quaternary International*, 114, 11–21. [https://doi.org/10.1016/S1040-6182\(03\)00038-7](https://doi.org/10.1016/S1040-6182(03)00038-7).
- Krepper, C.M. and Zucarelli, G.V. (2010) Climatology of water excesses and shortages in the La Plata Basin. *Theoretical and Applied Climatology*, 102(1–2), 13–27. <https://doi.org/10.1007/s00704-009-0234-6>.
- Kuemmerle, T., Altrichter, M., Baldi, G., Cabido, M., Camino, M., Cuellar, E., Cuellar, R.L., Decarre, J., Díaz, S., Gasparri, I., Gavier-Pizarro, G., Ginzburg, R., Giordano, A.J., Grau, H.R., Jobbág, E., Leynaud, G., Macchi, L., Mastrangelo, M., Matteucci, S.D., Noss, A., Paruelo, J., Piquer-Rodríguez, M., Romero-Muñoz, A., Semper-Pascual, A., Thompson, J., Torrella, S., Torres, R., Volante, J.N., Yanosky, A. and Zak, M. (2017) Forest conservation: remember Gran Chaco. *Science*, 355(6324), 465. <https://doi.org/10.1126/science.aal3200>.
- Li, C., Zwiers, F., Zhang, X., Li, G., Sun, Y. and Wehner, M. (2021) Changes in annual extremes of daily temperature and precipitation in CMIP6 models. *Journal of Climate*, 34(9), 3441–3460. <https://doi.org/10.1175/JCLI-D-19-1013.1>.
- Llano, M.P. and Penalba, O.C. (2010) A climatic analysis of dry sequences in Argentina. *International Journal of Climatology*, 31(4), 504–513. <https://doi.org/10.1002/joc.2092>.
- Lloyd-Hughes, B. and Saunders, M.A. (2002) A drought climatology for Europe. *International Journal of Climatology*, 22(13), 1571–1592. <https://doi.org/10.1002/joc.846>.
- Lovino, M.A., Müller, O., Berbery, E.H. and Müller, G. (2018a) How have daily climate extremes changed in the recent past over northeastern Argentina? *Global and Planetary Change*, 168, 78–97. <https://doi.org/10.1016/j.gloplacha.2018.06.008>.
- Lovino, M.A., Müller, O.V., Müller, G.V., Sgroi, L.C. and Baethgen, W.E. (2018b) Interannual-to-multidecadal hydroclimate variability and its sectoral impacts in northeastern Argentina. *Hydrology and Earth System Sciences*, 22(6), 3155–3174. <https://doi.org/10.5194/hess-22-3155-2018>.
- Magrin, G.O., Marengo, J.A., Boulanger, J.-P., Buckeridge, M.S., Castellanos, E., Poveda, G., Scarano, F.R. and Vicuña, S. (2014) Central and South America. In: Barros, V.R., Field, C.B., Dokken, D.J., Mastrandrea, M.D., Mach, K.J., Bilir, T.E., Chatterjee, M., Ebi, K.L., Estrada, Y.O., Genova, R.C., Girma, B., Kissel, E.S., Levy, A.N., MacCracken, S., Mastrandrea, P.R. and White, L.L. (Eds.) *Climate Change 2014: Impacts, Adaptation, and Vulnerability. Part B: Regional Aspects. Contribution of Working Group II to the Fifth Assessment Report of the Intergovernmental Panel on Climate Change*. Cambridge and New York, NY: Cambridge University Press, pp. 1499–1566.
- Mallenahalli, N.K. (2020) Comparison of parametric and non-parametric standardized precipitation index for detecting meteorological drought over the Indian region. *Theoretical and Applied Climatology*, 142, 219–236. <https://doi.org/10.1007/s00704-020-03296-z>.
- Matteucci, S.D., Herrera, P., Miñarro, F., Adámoli, J., Torrela, S., Ginzburg, R. and Naturales, U.B.A. (2007) Decision-making tools in zoning for sustainable use of the southeastern wetlands of the Chaco region (in Spanish). In: *Proceeding Ibero-American Conference on Geographic Information Systems*. Luján: Sociedad Iberoamericana de Sistemas de Información Geográfica (SIBSIG)-Universidad Nacional de Luján, pp. 1–25.
- McKee, T.B., Doesken, N.J. and Kleist, J. (1993) The relationship of drought frequency and duration to time scales. In: *Proceedings of the 8th Conference on Applied Climatology*. American Meteorological Society, Boston, MA, pp. 179–183.
- McKee, T. B., Doesken, N. J., Kleist, J. (1995). Drought monitoring with multiple time scales. In: *Proceedings of the 9th Conference on Applied Climatology*. 15–20 January 1995, Dallas, TX, pp. 233–236.
- Mishra, A.K., Singh, V.P. and Desai, V.R. (2009) Drought characterization: a probabilistic approach. *Stochastic Environmental Research and Risk Assessment*, 23, 41–55. <https://doi.org/10.1007/s00477-007-0194-2>.
- Mo, K.C. and Berbery, E.H. (2011) Drought and persistent wet spells over South America based on observations and the U.S. CLIVAR drought experiments. *Journal of Climate*, 24(6), 1801–1820. <https://doi.org/10.1175/2010JCLI3874.1>.
- Müller, O.V., Berbery, E.H., Alcaraz-Segura, D. and Ek, M.B. (2014) Regional model simulations of the 2008 drought in southern South America using a consistent set of land surface properties. *Journal of Climate*, 27(17), 6754–6778.
- NOAA/NWS/CPC. Cold & Warm Episodes by Season. https://origin.cpc.ncep.noaa.gov/products/analysis_monitoring/ensostuff/ONI_v5.php 2020
- Orsolini, H., Zimmermann, E. and Basile, P. (2009) *HIDROLOGÍA: PROCESOS Y MÉTODOS - Tercera Edición*. Rosario, Argentina: UNR Editora, p. 245.
- Ortega, G., Arias, P.A., Villegas, J.C., Marquet, P.A. and Nobre, P. (2021) Present-day and future climate over central and South America according to CMIP5/CMIP6 models. *International Journal of Climatology*, 41(15), 6713–6735. <https://doi.org/10.1002/joc.7221>.
- Penalba, O.C. and Rivera, J.A. (2016) Regional aspects of future precipitation and meteorological drought characteristics over southern South America projected by a CMIP5 multi-model ensemble. *International Journal of Climatology*, 36, 974–986. <https://doi.org/10.1002/joc.4398>.
- Rasmussen, K.L., Chaplin, M.M., Zuluaga, M.D. and Houze, R.A. (2016) Contribution of extreme convective storms to rainfall in South America. *Journal of Hydrometeorology*, 17(1), 353–367. <https://doi.org/10.1175/JHM-D-15-0067.1>.
- Rasmusson, E.M. and Carpenter, T.H. (1983) The relationship between eastern equatorial Pacific Sea surface temperatures and rainfall over India and Sri Lanka. *Monthly Weather Review*, 111, 517–528. [https://doi.org/10.1175/1520-0493\(1983\)111<0517:TRBEEP>2.0.CO;2](https://doi.org/10.1175/1520-0493(1983)111<0517:TRBEEP>2.0.CO;2).
- Re, M. and Barros, V.R. (2009) Extreme rainfalls in SE South America. *Climatic Change*, 96, 119–136. <https://doi.org/10.1007/s10584-009-9619-x>.
- Rivera, J. A. (2014). Climatological aspects of meteorological droughts in southern South America. Regional analysis and future projections, PhD thesis, Universidad de Buenos Aires, Argentina. http://hdl.handle.net/20.500.12110/tesis_n5504_Rivera, 351 pp. (in Spanish).

- Rivera, J.A. and Penalba, O.C. (2014) Trends and spatial patterns of drought affected area in southern South America. *Climate*, 2(4), 264–278. <https://doi.org/10.3390/cli2040264>.
- Robertson, A.W. and Mechoso, C.R. (1998) Interannual and decadal cycles in river flows of southeastern South America. *J. Climate*, 11, 2570–2581. [https://doi.org/10.1175/1520-0442\(1998\)011<2570:IADCIR>2.0.CO;2](https://doi.org/10.1175/1520-0442(1998)011<2570:IADCIR>2.0.CO;2).
- Robertson, A.W., Mechoso, C.R. and García, N.O. (2001) Interannual prediction of the Paraná River. *Geophysical Research Letters*, 22, 4235–4238. <https://doi.org/10.1029/2000GL012197>.
- Rodrigues, R.R. and Woollings, T. (2017) Impact of atmospheric blocking on South America in austral summer. *Journal of Climate*, 30(5), 1821–1837. <https://doi.org/10.1175/JCLI-D-16-0493.1>.
- Ropelewski, C.F. and Jones, P.D. (1987) An extension of the Tahiti-Darwin southern oscillation index. *Monthly Weather Review*, 115, 2161–2165. [https://doi.org/10.1175/1520-0493\(1987\)115<2161:AEOTTS>2.0.CO;2](https://doi.org/10.1175/1520-0493(1987)115<2161:AEOTTS>2.0.CO;2).
- Ropelewski, C.F. and Halpert, M.S. (1987) Global and regional scale precipitation patterns associated with the El Niño/southern oscillation. *Monthly Weather Review*, 115, 1606–1626.
- Salio, P., Nicolini, M. and Zipser, E.J. (2007) Mesoscale convective systems over southeastern South America and their relationship with the South American low-level jet. *Monthly Weather Review*, 135(4), 1290–1309. <https://doi.org/10.1175/MWR3305.1>.
- Schneider, U., Becker, A., Finger, P., Meyer-Christoffer, A. and Ziese, M. (2018). GPCC full data monthly product version 2018 at 0.25°: monthly land-surface precipitation from rain-gauges built on GTS-based and historical data. https://doi.org/10.5676/DWD_GPCC/FD_M_V2018_025.
- Seager, R., Naik, N., Baethgen, W., Robertson, A., Kushnir, Y., Nakamura, J. and Jurburg, S. (2010) Tropical oceanic causes of interannual to multidecadal precipitation variability in Southeast South America over the past century. *Journal of Climate*, 23(20), 5517–5539. <https://doi.org/10.1175/2010JCLI3578.1>.
- Sgroi, L.C., Lovino, M.A., Berbery, E.H. and Müller, G.V. (2021) Characteristics of droughts in Argentina's core crop region. *Hydrology and Earth System Sciences*, 25, 2475–2490. <https://doi.org/10.5194/hess-25-2475-2021>.
- Skansi, M.M., Brunet, M., Sigró, J., Aguilar, E., Arevalo Groening, J.A., Betancour, O.J., Castellón Geier, Y.R., Correa Amaya, R.L., Jácome, H., Malherios Ramos, A., Oria Rojas, C., Pasten, A., Sallons Mitro, S., Villaroel, C., Martínez, R., Alexander, L.V. and Jones, P.D. (2013) Warming and wetting signals emerging from analysis of changes in climate extreme indices over South America. *Global and Planetary Change*, 100, 295–307. <https://doi.org/10.1016/j.gloplacha.2012.11.004>.
- Sirdas, S. and Sen, K. (2003) Spatio-temporal drought analysis in the Trankya region, Turkey. *Hydrological Sciences Journal*, 48(5), 809–820. <https://doi.org/10.1623/hysj.48.5.809.51458>.
- Soláková, T., de Michele, C. and Vezzoli, R. (2014) Comparison between parametric and non-parametric approaches for the calculation of two drought indices: SPI and SSI. *Journal of Hydrologic Engineering*, 19, 4014010. [https://doi.org/10.1061/\(ASCE\)HE.1943-5584.0000942](https://doi.org/10.1061/(ASCE)HE.1943-5584.0000942).
- Sosa D., 2012. Water, excesses and deficits in rainfed agricultural and livestock production in the Salado River basin (In Spanish). [Tesis Doctoral]. Universidad de La Coruña, España. <http://hdl.handle.net/2183/10158>
- Thalmeier, B., Veizaga, E., Rodríguez, L., Heredia, J., Sosa, D. and Díaz, E. (2017) Structural geology and regional geomorphology as determinants of the hydrogeological functioning of the Bajos Submeridionales in the Austral Chaco. In: *XXVI National Water Congress*. Argentina: Córdoba, pp. 254–255.
- Trenberth, K.E. (1997) The definition of El Niño. *Bulletin of the American Meteorological Society*, 78, 2771–2777. [https://doi.org/10.1175/1520-0477\(1997\)078<2771:TDOENO>2.0.CO;2](https://doi.org/10.1175/1520-0477(1997)078<2771:TDOENO>2.0.CO;2).
- Harris, I.C., Jones, P.D. & University of East Anglia Climatic Research Unit (2020). CRU TS4.03: climatic research unit (CRU) time-series (TS) version 4.03 of high-resolution gridded data of month-by-month variation in climate (Jan. 1901–Dec. 2018). Centre for Environmental Data Analysis, 22 January 2020. <https://doi.org/10.5285/10d3e3640f004c578403419aac167d82>.
- Vallejos, M., Volante, J.N., Mosciaro, M.J., Vale, L.M., Bustamante, M.L. and Paruelo, J.M. (2015) Transformation dynamics of the natural cover in the dry Chaco ecoregion: a plot level geo-database from 1976 to 2012. *Journal of Arid Environments*, 123, 3–11. <https://doi.org/10.1016/j.jaridenv.2014.11.009>.
- Vera, C.S., Alvarez, M.S., Gonzalez, P.L.M., Liebmann, B. and Kiladis, G.N. (2017) Seasonal cycle of precipitation variability in South America on intraseasonal timescales. *Climate Dynamics*, 51(5–6), 1991–2001. <https://doi.org/10.1007/s00382-017-3994-1>.
- Viglizzo, E. and Frank, F.C. (2006) Ecological interactions, feedbacks, thresholds and collapses in the argentine pampas in response to climate and farming during the last century. *Quaternary International*, 158(1), 122–126. <https://doi.org/10.1016/j.quaint.2006.05.022>.
- Von Storch, H. and Navarra, A. (1995) *Analysis of Climate Variability*. New York: Springer, p. 334. <https://doi.org/10.1007/978-3-662-03167-4>.
- Wilks, D.S. (2006) *Statistical methods in the atmospheric sciences*, 2nd edition. London: Academic Press, p. 627.
- Zhang, H., Delworth, T.L., Zeng, F., Vecchi, G., Paffendorf, K. and Jia, L. (2016) Detection, attribution, and projection of regional rainfall changes on (multi-) decadal time scales: a focus on southeastern South America. *Journal of Climate*, 29, 8515–8534. <https://doi.org/10.1175/JCLI-D-16-0287.1>.
- Zhang, Z., Varble, A., Feng, Z., Hardin, J. and Zipser, E. (2021) Growth of Mesoscale convective Systems in Observations and a seasonal convection-permitting simulation over Argentina. *Monthly Weather Review*, 149(10), 3469–3490. <https://doi.org/10.1175/MWR-D-20-0411.1>.

How to cite this article: Lovino, M. A., Müller, G. V., Pierrestegui, M. J., Espinosa, E., & Rodríguez, L. (2022). Extreme precipitation events in the Austral Chaco region of Argentina. *International Journal of Climatology*, 1–22. <https://doi.org/10.1002/joc.7572>

Artículo 6

Variabilidad espaciotemporal de los eventos extremos de precipitación y sus impactos en la humedad del suelo y la profundidad del nivel freático en la región núcleo de cultivos de Argentina



Spatiotemporal variability of extreme precipitation events and their impacts on soil moisture and water table depth in Argentina's core crop region

Anelim Bernal-Mujica, Miguel A. Lovino, Gabriela V. Müller & M. Josefina Pierrestegui

To cite this article: Anelim Bernal-Mujica, Miguel A. Lovino, Gabriela V. Müller & M. Josefina Pierrestegui (2023): Spatiotemporal variability of extreme precipitation events and their impacts on soil moisture and water table depth in Argentina's core crop region, *Hydrological Sciences Journal*, DOI: [10.1080/02626667.2023.2192874](https://doi.org/10.1080/02626667.2023.2192874)

To link to this article: <https://doi.org/10.1080/02626667.2023.2192874>

 View supplementary material 

 Published online: 18 Apr 2023.

 Submit your article to this journal 

 Article views: 26

 View related articles 

 View Crossmark data 



Spatiotemporal variability of extreme precipitation events and their impacts on soil moisture and water table depth in Argentina's core crop region

Anelim Bernal-Mujica ^a, Miguel A. Lovino ^{a,b}, Gabriela V. Müller ^{a,b} and M. Josefina Pierrestegui ^{a,b}

^aFacultad de Ingeniería y Ciencias Hídricas, Centro de Estudios de Variabilidad y Cambio Climático (CEVARCAM), Universidad Nacional del Litoral, Santa Fe, Argentina; ^bConsejo Nacional de Investigaciones Científicas y Técnicas (CONICET), Santa Fe, Argentina

ABSTRACT

This study reassesses the spatiotemporal variability of and changes in extreme precipitation events (EPEs) and examines the response of soil moisture and water table depth to EPEs in Argentina's core crop region. Standardized nonparametric indices are applied to precipitation, soil moisture, and groundwater. The temporal variability of EPEs exhibits a decadal cycle and inter-annual modes with dominant frequencies between 2.5 and 4 years related to El Niño Southern Oscillation periodicities. The soil moisture and water table depth respond to precipitation variability replicating both decadal and inter-annual EPE variability. The response of soil moisture to EPEs attenuates in time as soil depth increases. Water table depth responds to EPEs with an average delay of 10 months. In recent decades, soil moisture increases (water table depth becomes shallower) rapidly when reacting to excess precipitation, while soil moisture decreases (water table depth deepens) slowly during and after drought events.

ARTICLE HISTORY

Received 27 June 2022
Accepted 10 February 2023

EDITOR

A. Fiori

ASSOCIATE EDITOR

B. Bonaccorso

KEY WORDS

extreme precipitation events; soil moisture; water table depth; Argentina's core crop region

1 Introduction

Extreme events are part of the natural variability of the earth-atmosphere system. "Extreme events" refers to the occurrence of values related to a weather or climate variable which is above (or below) a threshold value near the upper (or lower) ends in the range of observed values of the variable (Seneviratne *et al.* 2012). Several studies have suggested that the characteristics of extreme events, such as their onset, persistence, and termination, cannot be identified precisely by analysing a single hydro-meteorological variable (Dracup *et al.* 1980, Hao and AghaKouchak 2014, AghaKouchak 2015). Each component of the hydrological cycle has a different response to precipitation anomalies. Soil moisture content responds in relatively short time scales, whereas groundwater, runoff, and reservoir storage reflect long-term precipitation anomalies (Lloyd-Hughes and Saunders 2002). Short-term durations of extreme events (from weeks to months) affect agricultural activities, while long-term durations of extreme events (from seasons to years) impact the management hydrological water resources. Thus, multivariate assessments seem to be effective for the study of extreme events (Hao and AghaKouchak 2014, Zhang *et al.* 2017, Chen *et al.* 2020).

To study extreme events, several indices applied to hydro-climatic variables on multiple time scales have been developed. Hao and AghaKouchak (2013, 2014) and Farahmand and AghaKouchak (2015) developed a nonparametric method to calculate standardized indices on different variables: the Standardized Precipitation Index (SPI), originally defined by McKee *et al.* (1993); the Standardized Soil Moisture Index

(SSI); and the Standardized Groundwater Level Index (SGI). The SPI, SSI and SGI were successfully used in previous studies for different regions of the world. Folland *et al.* (2015) used SPI and SGI to demonstrate a strong link between La Niña events and precipitation and groundwater deficits in the English Lowlands. Bloomfield and Marchant (2013) and Bloomfield *et al.* (2015) found that the relationship between SPI and SGI is robust and meaningful when analysing the local effects of droughts on the United Kingdom's groundwaters. Kumar *et al.* (2016) reported similar results in southern Germany and central Netherlands. Chen *et al.* (2020) successfully combined SPI and SSI to assess drought features and drought propagation over the soil in the North China Plain, while Muthuvel and Mahesha (2021) used the same indices to assess the propagation of meteorological drought to agricultural drought in India. Finally, Sgroi *et al.* (2021) used SPI and SSI to conclude that relatively short-term droughts have been more frequent than long-term droughts in South America.

Extreme events have undergone a statistically significant increase on a global scale and for large regions of the world. They are projected to grow even in the face of relatively small increases in global warming (Hoegh-Guldberg *et al.* 2018, Seneviratne *et al.* 2021). In South America, consistent with global changes, extreme events tend towards warmer and wetter conditions (Penalba and Robledo 2009, de LosMilagros Skansi *et al.* 2013, Cavalcanti *et al.* 2015, Carril *et al.* 2016, Saurral *et al.* 2017, Avila-Diaz *et al.* 2020). In fact, the intensity and frequency of heavy rainfall have increased since the second half of the 20th century (Rivera *et al.* 2013,

Lovino *et al.* 2018a, Cerón *et al.* 2021). In northeastern Argentina, where most of the country's rainfed agro-industrial production is concentrated (Siebert *et al.* 2013), periods of excesses and deficits of precipitation have caused extended flooding and severe droughts, generating large losses in agro-industrial production (Barros *et al.* 2015, Lovino *et al.* 2018b, Naumann *et al.* 2021, Sgroi *et al.* 2021).

Argentina's core crop region (CCR) is highly vulnerable to extreme precipitation events (EPEs) on time scales relevant to agriculture (Krepper and Zucarelli 2010, Lovino *et al.* 2014, Müller *et al.* 2021). In particular, there is a large climatic variability which is mainly forced by El Niño Southern Oscillation (ENSO) on inter-annual time scales (Berri *et al.* 2002, Boulanger *et al.* 2005, Cai *et al.* 2020, Robledo *et al.* 2020). This variability favours increased severe precipitation (Krepper and García 2004, Lovino *et al.* 2018a), alternating with periods of precipitation deficit (Penalba and Vargas 2004, Llano and Penalba 2011, Rivera *et al.* 2013, Sgroi *et al.* 2021). The ENSO-related variability that forces precipitation also influences the response of soil moisture and evapotranspiration; however, such response is also conditioned by edaphic factors and even by the sub-monthly distribution of precipitation (Pántano *et al.* 2022, Ruscica *et al.* 2022). Moreover, the balance between precipitation and evapotranspiration variability influences water table depth fluctuations at inter-annual time scales, whereas the land cover (mainly with annual crops) can be a relevant control of water table depths at intra-annual or seasonal time scales (Mercau *et al.* 2016, Zellner *et al.* 2020). In particular, during El Niño years, when higher than normal precipitation may occur, water table depth becomes shallower, favouring waterlogging or flooding in urban and rural areas (Pal *et al.* 2021).

The literature on the subject includes several studies that assess precipitation variability and EPEs in southeastern South America (e.g. Grimm 2011, Carril *et al.* 2016, Lovino *et al.* 2018b, Cerón *et al.* 2021). Yet there is a knowledge gap about the integrated response of soil moisture and groundwater to EPEs. Therefore, it is necessary to perform a joint study of the main hydroclimatic variables at different time scales to provide accurate and integrated information that will facilitate decision making processes.

This study has two main objectives: firstly, to reassess the spatiotemporal variability of and changes in EPEs; and, secondly, to investigate the response of soil moisture and water table depth to these EPEs in Argentina's CCR. To achieve these goals, we provide an integrated and comprehensive discussion based on a multivariable study of extreme hydroclimatic events at different time scales, their spatial distributions, the directions of their trends, and the oscillatory cycles that characterize their temporal variability. Section 2 presents the region under study, and describes the data and methods used. Section 3 describes the extreme events, characterized by nonparametric standardized indices. Section 4 discusses the spatiotemporal variability of extreme events characterized by precipitation and soil moisture. Section 5 assesses the interaction of EPEs with the soil moisture and the water table depth at the Rafaela Station in the centre of Argentina's CCR. Finally, Section 6 provides the discussion and conclusions of this study.

2 Data and methodology

2.1 Study region

The study region (27.5° – 34.5° S, 58.5° – 63.5° W; see Fig. 1(a) and (b)) is known as Argentina's CCR because it concentrates around 80% of this country's production of wheat, corn, sunflower, and soybean (Sgroi *et al.* 2021). The CCR has highly fertile and productive soils and is recognized as one of the world's breadbaskets, playing a strategic role in global food security (Fischer *et al.* 2014). These fertile soils present a variety of textures but are dominated by clay and loam (see Fig. 1(d)). The CCR is mostly flat, except for the low mountains that lie towards the west (see Fig. 1(b)); therefore, drainage systems are poorly developed, and vertical water transfers predominate (Jobbagy *et al.* 2008).

The CCR is relatively homogeneous from a climatic perspective, identified as a zone which is temperate with hot summers and no dry season, according to the Köppen-Geiger climate classification (Beck *et al.* 2018). Figure 1(c) shows the spatial pattern of annual precipitation in the CCR. Precipitation presents an east–west gradient, ranging from 1500 mm/year towards the northeast to 600 mm/year towards the west. The most important contributions of precipitation throughout the year occur in the warm season, which is between October and April (see Fig. 2(b)). Warm season precipitation is mainly caused by mesoscale convective systems (Laing and Fritsch 2000). Precipitation is around 40 mm/month during the austral cold season, between May and September (see Fig. 2(b)). Cold season precipitation is mainly driven by mid-latitude synoptic-scale activity (Vera *et al.* 2002). The spatiotemporal variability of precipitation strongly influences both the soil water retention and the soil water availability for rainfed crops. Note that different soil types (Fig. 1(d)) may respond differently to precipitation variability.

Extreme climate events have a significant impact on rainfed agricultural productivity in the CCR. For example, the floods in January 2017 and in 2018–2019 caused economic losses to the agricultural-livestock sector, reaching US\$1.75 billion and US\$230 million, respectively (La Nación 2017, El Informe 2019). The severe droughts of 2008–2009 and 2011–2012 caused losses of about 40% of grain production in the CCR (Lovino *et al.* 2018b), and economic losses of US\$727 million and US\$484 million, respectively (Thomasz *et al.* 2019). Hence, the yields of the main crops, including wheat, corn and soybean, are sensitively conditioned by the response of soil moisture to water excesses or deficits (Holzman and Rivas 2016).

2.2 Data

Monthly gridded precipitation data from the Global Precipitation Climatology Centre Version 2018 dataset (GPCC v. 2018; Schneider *et al.* 2018) and the Climatic Research Unit (CRU TS 4.01, Harris *et al.* 2020) are used. GPCC v. 2018 covers the 1891–2016 time period with a spatial resolution of $0.25^{\circ} \times 0.25^{\circ}$. CRU TS 4.01 covers the 1901–2016 time period with a resolution of $0.5^{\circ} \times 0.5^{\circ}$. The performances of the GPCC v. 2018 and CRU TS 4.01 datasets over the CCR are assessed in the 1901–2016 time period by contrasting the

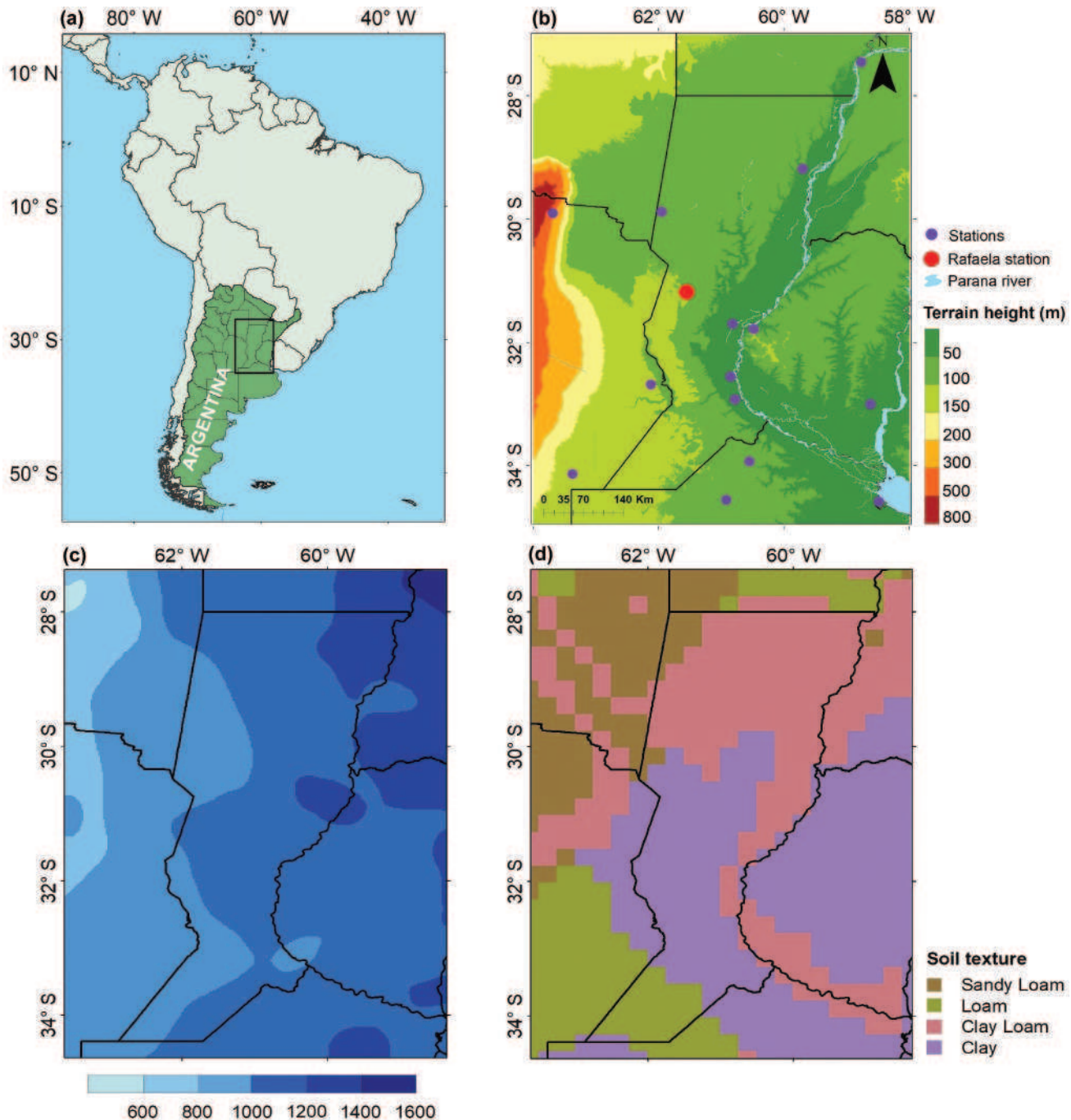


Figure 1. (a) South America and the location of Argentina. (b) Topographical map of the study region in Argentina. Purple dots represent the precipitation stations with available long-period data. The larger red point indicates Rafaela station, the only one in the study region that has good-quality and long-period water table depth data. (c) The spatial distribution of annual precipitation during the 1986–2015 period calculated with GPCC v. 2018 data. (d) The spatial distribution of the FAO soil texture classes (IUSS Working Group WRB 2015) used in GLDAS.

gridded data with the observed data in 15 weather stations (see their locations in Fig. 1(b)). Figure 2(a) shows that both GPCC v. 2018 and CRU TS 4.01 correctly identify the area-averaged annual precipitation variability, achieving a very good performance according to the Pearson correlation coefficient (r), the mean bias error (MBE), and the root mean square error (RMSE) (see Déqué 2012 for definitions). Although the statistical evaluation metrics are slightly better for CRU TS 4.01 than for GPCC v. 2018, Fig. 2(a) indicates that GPCC v. 2018 fits the observed EPEs better than CRU TS 4.01 does. Figure 2(b) shows that GPCC v. 2018 validates the annual precipitation

cycle better than CRU TS 4.01 does. Finally, Fig. S1 (see the Supplementary material) presents scatter plots of observed precipitation data from different stations, and the closest CRU TS 4.01 and GPCC v. 2018 grid points. All the scatter plots show less dispersion for the GPCC v. 2018 precipitation than for the CRU TS 4.01 precipitation, especially for dry and wet months. In addition, most of the GPCC v. 2018 statistical metrics achieve better values than those of CRU TS 4.01.

To evaluate the GPCC v. 2018 performance in representing EPEs, we computed statistical evaluation metrics between SPI3 time series at each station and the time series of GPCC v. 2018

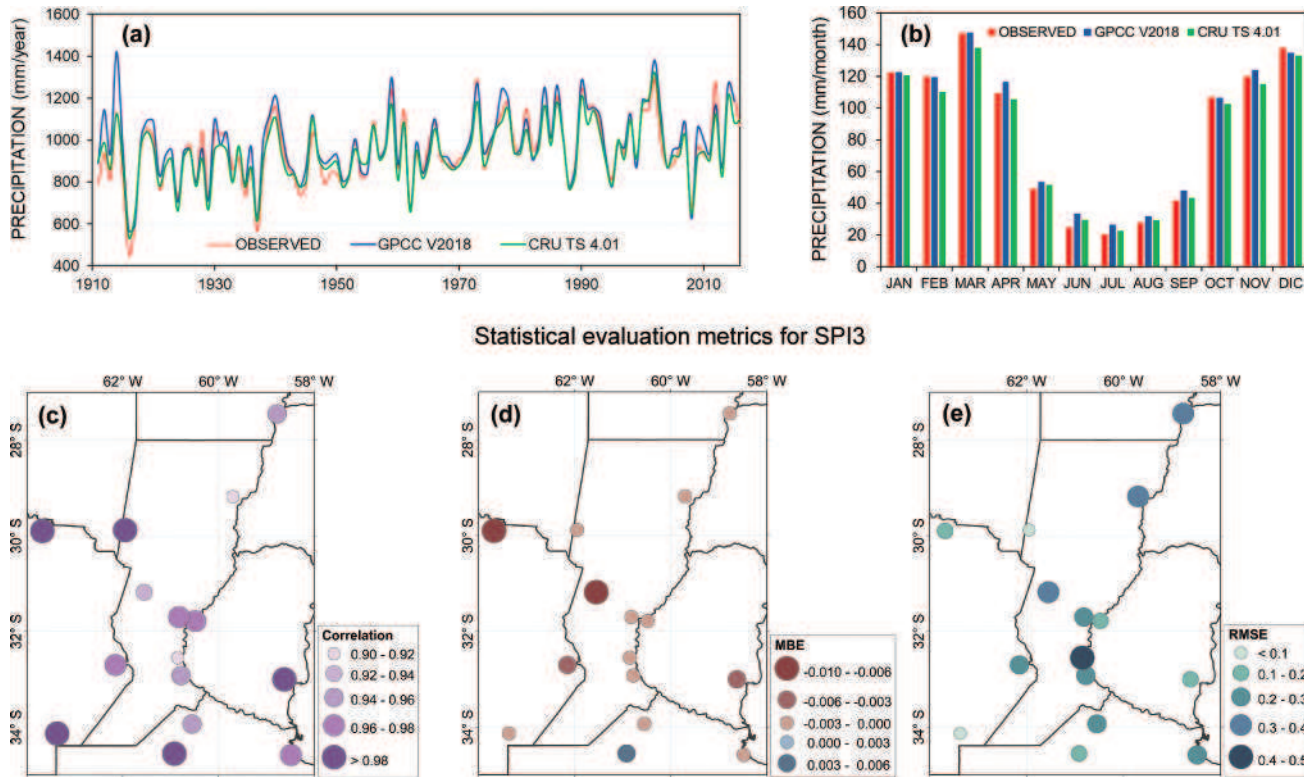


Figure 2. (a) Area-averaged time series of annual precipitation over Argentina's core crop region computed with station observations, GPCC v. 2018, and CRU TS 4.01 datasets in the 1911–2016 period. (b) As in (a) but for the precipitation annual cycle (1986–2015 period). Panels (c–e) present the statistical evaluation metrics for the Standardized Precipitation Index at 3-month time scale (SPI3) when comparing GPCC v. 2018 data with station observations: (c) Pearson correlation coefficient (r), (d) mean bias error (MBE), (e) root mean square error (RMSE).

at the closest grid point. Figure 2(c–e) show that correlations are higher than 0.9, MBE values are negative but higher than -0.01 (i.e. closer to zero), and RMSE values are lower than 0.5. These results suggest that GPCC v. 2018 correctly recognizes observed EPEs. Therefore, we use the GPCC v. 2018 dataset here. A local analysis is also carried out with observed precipitation data from the National Institute of Agricultural Technology (INTA) at the station located in the town of Rafaela (see the red point in Fig. 1(b)).

Soil moisture data of the Global Land Data Assimilation System (GLDAS; Rodell *et al.* 2004, Meng *et al.* 2012) is used. GLDAS monthly data used here have a spatial resolution of $0.25^\circ \times 0.25^\circ$, and cover the period 1979–2016. Soil moisture is not directly measured; it is calculated with the Noah land surface process model. The Noah model considers four soil layers (0–10, 10–40, 40–100, and 100–200 cm) totaling 2 m in depth (Rodell *et al.* 2004). The soil moisture generated by GLDAS products has been evaluated in the study area by Grings *et al.* (2015) and Spennemann *et al.* (2015, 2020), who found that GLDAS correctly reproduce observed soil moisture patterns. Grings *et al.* (2015) reported that GLDAS achieved a high correlation ($r > 0.80$) with in situ soil moisture measurements.

Monthly mean water table depth data measured at the Rafaela Station of INTA in the 1970–2017 time period is used. The Rafaela Station was selected considering its record history and the quality of its data. Note that this study does not consider anthropogenic processes that could affect water table depth variations, such as the local management of aquifer pumping, or the progressive deforestation of regional vegetation with high

water demand (forests and scrublands), which alter surface runoff and groundwater dynamics (Viglizzo *et al.* 2011). The analysis of the water table depth data will be carried out only at the Rafaela Station, as a study case. Note that this station is not representative of the entire study area.

2.3 Nonparametric standardized indices

Extreme events are characterized by three nonparametric standardized indices: SPI, SSI and SGI (Hao and AghaKouchak 2014, Farahmand and AghaKouchak 2015). The SGI is estimated using the water table depth. A nonparametric method outperforms a parametric approach for studies of extreme events. This method is not based on any theoretical distribution that may underrepresent extreme events, because the parametric (empirical) probability density functions may not be a good fit in the tails (Farahmand and AghaKouchak 2015). Soláková *et al.* (2014) and Mallenahalli (2020) reported that nonparametric SPI can represent dryness/wetness and normality conditions better than a parametric approach can.

In this study, SPI, SSI, and SGI are calculated following a non-exceedance probability function for extreme events. The marginal probability is derived using the Gringorten plotting position equation (Gringorten 1963):

$$p(x_i) = \frac{i - 0.44}{n + 0.12} \quad (1)$$

Table 1. Classification of the intensity of events based on non-parametric standardized index values (range column) according to Hao *et al.* (2014).

| INTENSITY | RANGE |
|------------|-------------------------|
| WET | Exceptional >2.0 |
| | Extreme 1.60–1.99 |
| | Severe 1.30–1.59 |
| | Moderate 0.80–1.29 |
| | Abnormal 0.50–0.79 |
| NORMAL DRY | 0.50 to –0.50 |
| | Abnormal –0.50 to –0.79 |
| | Moderate –0.80 to –1.29 |
| | Severe –1.30 to –1.59 |
| | Extreme –1.60 to –1.99 |
| | <–2.0 |

where n is the sample size, i indicates the rank of non-zero precipitation values, and $p(x_i)$ is the corresponding empirical probability. This probability is then transformed into standardized indices (SIs), applying the inverse of the standard normal distribution function (ϕ):

$$SI = \phi^{-1}(p(x_i)) \quad (2)$$

Nonparametric indices allow us to quantify precipitation deficits/excesses and their incidence in the unsaturated and saturated soil zones, as well as their interrelationships. When the SI exceeds a certain threshold, it is classified as an extreme event. In this study, we classify extreme events following the classification scale proposed by Hao *et al.* (2014) (see Table 1). This scale categorizes the severity of extreme events from abnormal dry/wet conditions (SI values lower than –0.5/greater than 0.5) to exceptional dry/wet conditions (SI values lower than –2/greater than 2). Normal conditions occur between SI values of –0.5 and 0.5. In this study, the duration of extreme events is defined as the number of months above or below the normality thresholds (0.5 and –0.5, respectively).

All indices are computed on time scales of 1, 3, 6, 12, and 24 months. Area-averaged time series of SPI and SSI in the 1979–2016 time period are constructed. The responses of soil moisture and water table depth to EPEs are assessed through a comparison of the spatial patterns and the temporal evolution of SPI, SSI and SGI, as well as by analysing the number of events represented by those three variables together, including their duration. To identify the time scales of the indices that best characterize the relationship between precipitation and soil moisture, we calculated Pearson correlation coefficients (r) between the SPI and SSI for different time scales and soil moisture levels.

2.4 Spatiotemporal variability approach

A principal component analysis (PCA; Von Storch and Zwiers 1999, Wilks 2006) is applied to the precipitation and soil moisture standardized indices to study the spatial and temporal variability of extreme events. The PCA is performed using the correlation matrix and the S method, i.e. considering the SIs in each grid point as variables, and the time periods as individuals. In this study, the PCA is applied to the SPI on time scales of 3, 12, and 24 months, and to the SSI on a time scale of 6 months for 10, 40, 100, and 200 cm. The time scales for SPI are selected

according to practical reasons. The 3-month time scales represent the short period or seasonal scales, which allow us to identify how extreme events affect crop yields. The low-frequency time scales (12 and 24 months) allow us to identify the deficit or excess and their effects on the hydrological cycle. Since soil moisture is studied here at different depths, the PCA is applied to a single SSI time scale. This time scale is selected according to the correlations of SSI and SPI on different time scales (see the Supplementary material, Table S1). Table S1 shows that SSI6 at different depths achieves the highest Pearson correlation values with SPI12 ($r \sim 0.82$ at 0–100 cm depths, and $r = 0.72$ for the 100–200 cm layer).

A singular spectral analysis (SSA; Ghil *et al.* 2002, Wilks 2006) is used to determine the spatiotemporal structures of nonlinear trends and oscillatory modes of the SI time series. SSA is applied here to the principal component (PC) time series of SPI and SSI, and to the SPI, SSI and SGI time series at the Rafaela Station. The SSA method performs an eigenvalue decomposition of a time series into eigenvectors or temporal empirical orthogonal functions (T-EOFs) and temporal principal components (T-PCs). Each T-PC explains a portion of the time series variance associated with its corresponding eigenvalue, and represents a filtered version of the original time series. In this study, significant T-PCs at a 95% confidence level are found by applying a significance test against a red noise null hypothesis, using a Monte Carlo method (Allen and Robertson 1996) with an ensemble of 1000 independent realizations.

In the SSA method, the choice of the window length (M) limits the longer periods that the method can resolve. In practice, the window length should not exceed one third of the time series length to adequately represent cycles between $M/5$ and M (Vautard 1999). Considering that the common data period available for precipitation, soil moisture, and water table depth is 37 years (1979–2016), a window length of $M = 10$ years is selected. Therefore, inter-annual variability is represented by the spectrum between 2 and 10 years (following Krepper and García 2004, Krepper *et al.* 2006).

3 Relationship between precipitation and soil moisture and identification of extreme events

Figure 3 presents the area-averaged SPI and SSI values on the time scales of 1, 3, 6, 12, and 24 months for the CCR. Figure 3 graphically shows both the compound effect of EPEs and the soil moisture response on different time scales. There is a lag at the start and end of extreme events as the time scale increases. This lag is shown like a shift to the right in each event as the time scale and the depth of the soil increase. This result reveals the physical consistency of the surface modelling, since, when the soil depth increases, the soil moisture (represented by the SSI) has an attenuated response to precipitation (represented by the SPI). When precipitation enters the system, its signal will propagate in time. Part of the precipitation that reaches the ground will evaporate from the surface, another part will turn into surface runoff, and the rest will infiltrate into the ground. Some of the infiltrated water may go back to the atmosphere through vegetation transpiration or water extracted by roots. Another portion may percolate to groundwater, and the rest will be stored as soil moisture (Van Loon 2015). Soil moisture has a lower frequency of variability than

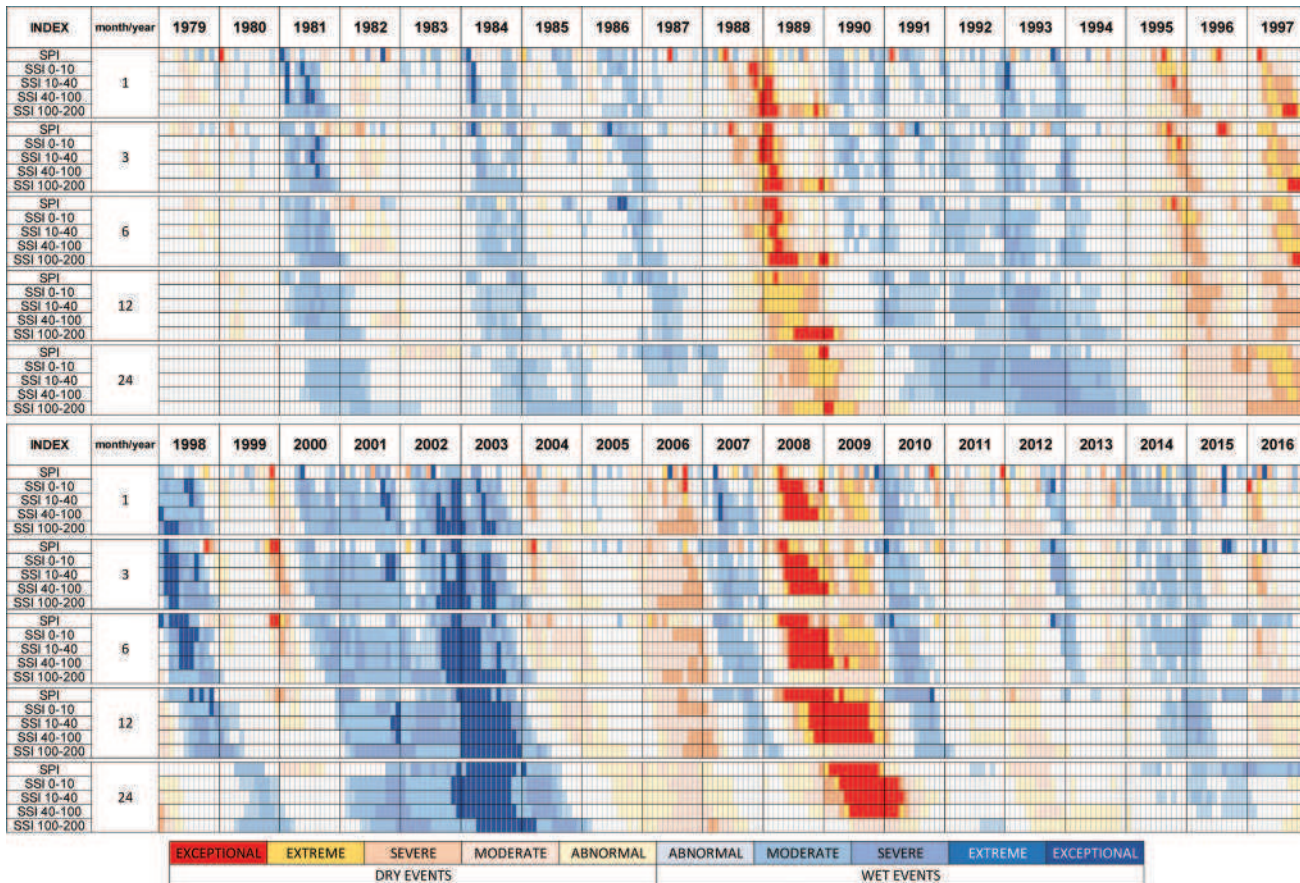


Figure 3. Categorization of extreme events according to the area-averaged Standardized Precipitation Index (SPI) and Standardized Soil Moisture Index (SSI) values in the 1979–2016 period for Argentina's core crop region. Index time scales are 1, 3, 6, 12 and 24 months. SSI values are computed in each soil layer (0–10, 10–40, 40–100, 100–200 cm). Shades in red (blue) represent the intensity of dry (wet) events according to Table 1.

precipitation. The time it takes for precipitation to infiltrate the soil and move through deeper soil layers has a smoothing impact that can be compared to a low-pass filter (Entekhabi *et al.* 1996).

Table S1 (see the Supplementary material) shows that coefficients of correlation between SPI and SSI for different time scales and soil moisture levels range between 0.47 and 0.82. The highest correlations occur between SPIs with a larger time scale than that of the SSIs, due to the filter-type impact of the soil in the response of the soil moisture to precipitation. The lowest correlation ($r = 0.47$) is found for the combination SPI3–SSI1 at 100–200 cm soil depth, while the maximum correlation ($r \sim 0.82$) is found between SPI12 and SSI6 at 0–100 cm soil depth, as pointed out above. These results match those of Spennemann *et al.* (2015) who reported that longer SPI time scales correlate better with deeper layer soil moisture anomalies in South America.

Fig. 3 reveals 10 wet events (blue ranges) and five dry events (red ranges) during the 1979–2016 period. Table 2 summarizes the extreme events categorized according to their intensity (see Table 1 for definitions of the categories). An exceptionally wet extreme event is identified between the years 2000 and 2003 on all analysed time scales. Figure 3 shows that the 2000–2003 event had an average duration of 40 months at 12-month and 24-month time scales. This event presents discontinuities on seasonal time scales from 1 to 6 months, suggesting that short-term inter-annual precipitation variability favoured normal conditions in the 2001–2002 period. Another exceptionally wet extreme event occurred in 1998, although with a shorter duration (3–5 months) on seasonal time scales of 1–6 months. Severe wet events occurred in 1981, 1984, and 1996 on time scales from 1 to 12 months. A moderate event was recorded in 1990 on short-term time scales, changing to a severe event on low-frequency time scales between 1991 and early 1994.

Table 2. Summary of extreme events detected in the 1979–2016 period. In this study, an extreme event is categorized following Table 1 if it exceeds the threshold in at least 6 consecutive months.

| DRY EVENTS | | | WET EVENTS | | | |
|-------------|---------|--------|------------|--------|---------|-------------|
| EXCEPTIONAL | EXTREME | SEVERE | MODERATE | SEVERE | EXTREME | EXCEPTIONAL |
| 1988–1989 | 1995 | 2006 | 1990 | 1981 | 2007 | 2000–2003 |
| 2008–2009 | 1997 | | | 1984 | 2010 | 1998 |

Extreme wet events of shorter duration and with extreme to exceptional intensities were registered in 2007, 2010, 2012, and 2014, although they had no impact on the 24-month time scale.

Figure 3 shows two exceptional dry events. The first one lasted 10 months spanning 1988 and 1989, later persisting as an extreme dry event on low-frequency time scales. The second one had an average duration of 12 months, on 12-month and 24-month time scales, in 2008 and 2009. Two consecutive extreme dry events occurred in 1995 and in 1997, with an average duration of 9 months each. These events are seen as

a single extreme event with a duration of 30 months on the 24-month time scale. Finally, a severe drought event was recorded in 2006, with an average duration of 12 months on time scales ranging from 1 to 12 months.

4 Spatiotemporal variability of extreme events characterized by precipitation and soil moisture

We studied the spatiotemporal variability of extreme events in the CCR by applying a PCA to SPI3, SPI12, SPI24, and SSI6. Figure 4 presents the correlation patterns (left column)

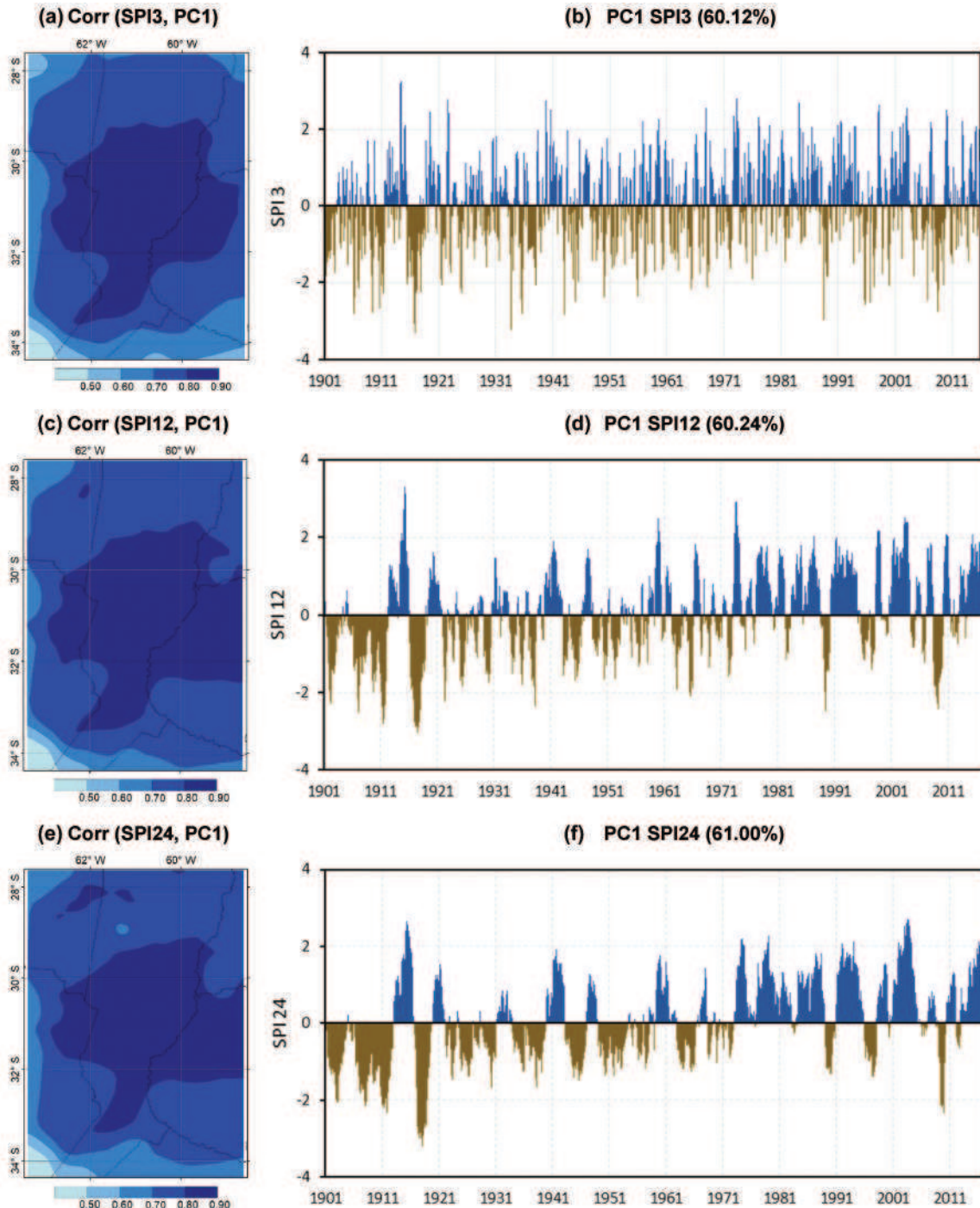


Figure 4. Panels (a), (c) and (e) show the spatial distribution of the correlation between the first principal component time series (PC1) in (b), (d), and (f) and each SPI3, SPI12 and SPI24 time series at a single grid point in the 1901–2016 period. The percentage of explained variance of each PC1 is given in brackets. SPI3, SPI12 and SPI24 refer to the Standardized Precipitation Index on time scales of 3, 12, and 24 months.

between the first PCs (right column) and the SPI3, SPI12 and SPI24 time series. The PC1s represent more than 60% of the total variance, and show similar spatial patterns for the three studied time scales. Positive correlations higher than 0.70 are seen in most of the CCR, except towards the southwest, where correlations range between 0.60 and 0.50. The maximum correlation ($r = 0.90$) is found in the centre of the CCR, and it extends towards the east as the SPI time scale increases.

The temporal evolution of EPEs defined by the PC1 of SPI3, SPI12 and SPI24 (right column, Fig. 4) shows two periods: one between 1901 and 1975, with frequent and intense dry EPEs; and another between 1976 and 2016, with higher frequency and intensity of wet EPEs. These periods are more noticeable on the time scales of 12 and 24 months. During the dry period, two low-frequency dry EPEs with exceptional intensity and long duration stand out at the beginning of the 20th century (see Fig. 4(d) and (f)): in the 1906–1911 period (average SPI24 = -2.40, duration of 79 months), and in the 1916–1919 period (average SPI24 = -3.10, with a duration of 32 months). Other severe dry EPEs were recorded during 1933–1939, 1943–1946, and 1949–1954. During the wet period, the most intense and longest low-frequency wet EPEs were recorded between 1976 and 1982 (average SPI = 2.10, with a duration of 75 months), at the end of the 20th century, as well as in the 2001–2003 period.

Figure 5 shows the patterns of correlation (left column) between the first PCs (right column) and the SSI6 time series at different depths. PC1 explains high percentages of the SSI6 variance at different depths. High correlations ($0.65 < r < 0.95$) can be seen in the layers between 0 and 100 cm (Fig. 5(a),(c), and (e)). The maximum correlation value ($r = 0.95$) occurs in the centre of the CCR, which is consistent with the spatial patterns of SPI. The spatial pattern of the 100–200 cm layer differs from the spatial pattern of the upper layers. The maximum correlation ($r = 0.95$) can be seen next to the Paraná River and towards the northwest of the CCR, mostly related to clay loam soils (see Fig. 1(d)). Much of the northwestern portion of the CCR overlaps with Argentina's Bajos Submeridionales basin (see Lovino *et al.* 2022). This basin presents numerous bodies of surface water. The lowest correlation values (r lower than 0.5) are found in the central zone of the CCR, collocated with clay soils (see Fig. 1(d)).

The PC1s at different soil depths show a high degree of similarity, mainly in the first metre of the soil. The PC1 of the SSI6 in the 100–200 cm layer (Fig. 5(h)) shows an attenuation of the intensity of extreme events, which is consistent with the low-frequency effect that follows soil moisture with increasing depth (discussed in Section 3). This attenuation effect is most noticeable in dry events, suggesting that drying is slower than wetting in the 100–200 cm layer of soil – that is, the recharge of the deepest layer of the soil is much faster than its desiccation.

Figure 6 reveals that the intensity, duration, and frequency of the extreme events shown by the time series of the PC1 of SSI6 in the first three soil layers (1 m of soil) coincide with the events found with the time series of SPI12. These results suggest how the soil moisture in the first metre of the soil consistently responds to precipitation variability. The scatter plots shown in Fig. 6(b–e) reveal a direct relationship, achieving good coefficients of determination in the first three soil

layers ($0.65 < R^2 < 0.73$). The time series of Fig. 6(a) show that the response of soil moisture to precipitation is delayed as the depth of the soil layer increases. The SSI response to the SPI is not the same throughout the study period, possibly conditioned by the soil moisture content prior to the EPEs. In addition to the expected delay according to the increase in depth, a common behaviour is observed in the soil response. The scatter plots show that the values of SSI6 are greater than those of SPI12 as SPI12 approaches -3 (see Fig. 6(b–d)). On the other hand, for high values of SPI6 (related to wet events), the fit improves. This result suggests that the soil moisture response to water deficits is less intense than the response to water excesses.

Table 3 summarizes the oscillatory modes detected by applying the SSA to the PC1 of the SPI and SSI time series in the 1979–2016 period. Consistent with the periodicities found by Lovino *et al.* (2018b) for precipitation, Table 3 shows that there are two bands of variability for SPI and SSI: one with dominant periods of $T \approx 10$ years, and another with dominant periods of high frequency of $T \approx 2.5\text{--}4$ years. These bands appear in all SPI time scales, although only the near-decadal band is detected in SSI24 in all soil layers and in SSI12, in the layer which is 1–2 m deep. This may be due to two factors: (1) the "filtering" effect of the deep layer of the soil discussed above; and (2) the smoothing effect of low-frequency time scales.

The near-decadal variability explains the increasing percentages of variance in the SSI time series in all soil layers (from near 25–30% to almost 60%) as the index time scale increases, suggesting the relevance of the decadal variability in the soil response to precipitation. Moreover, the 10-year mode shows the highest percentages of explained variance in the 1–2 m soil layer, suggesting that the near-decadal signal is exacerbated in the deeper soil layer.

5 Study case: relationship of extreme events and the water table depth at Rafaela

5.1 Response of groundwater to EPEs

We studied the response of groundwater to EPEs at the Rafaela Station (see the red point in Fig. 1). The Rafaela Station was selected because it is the only station that has a long and significant record and high-quality water table depth data in the study region. Figure 7 presents the time series of the water table depth and precipitation anomalies at the Rafaela Station. The water table depth decreased markedly in the 1970s, moving 10 m towards the surface (from 12 m in 1972 to approximately 2 m in 1980, not shown). This considerable decrease in water table depth was influenced by the combined effect of the significant increase in precipitation (see e.g. Barreiro *et al.* 2014, Lovino *et al.* 2018b; see also Fig. 4(f)) and the changes in land use (Zak *et al.* 2008, Viglizzo *et al.* 2011). The land use changes – mainly the replacement of perennial crops by annual ones – affected moisture and energy fluxes, favouring shallower water table depths and increased baseflow (Pal *et al.* 2021). From the 1980s to 2016, the mean water table depth remained almost constant, although it was influenced by significant inter-annual variability.

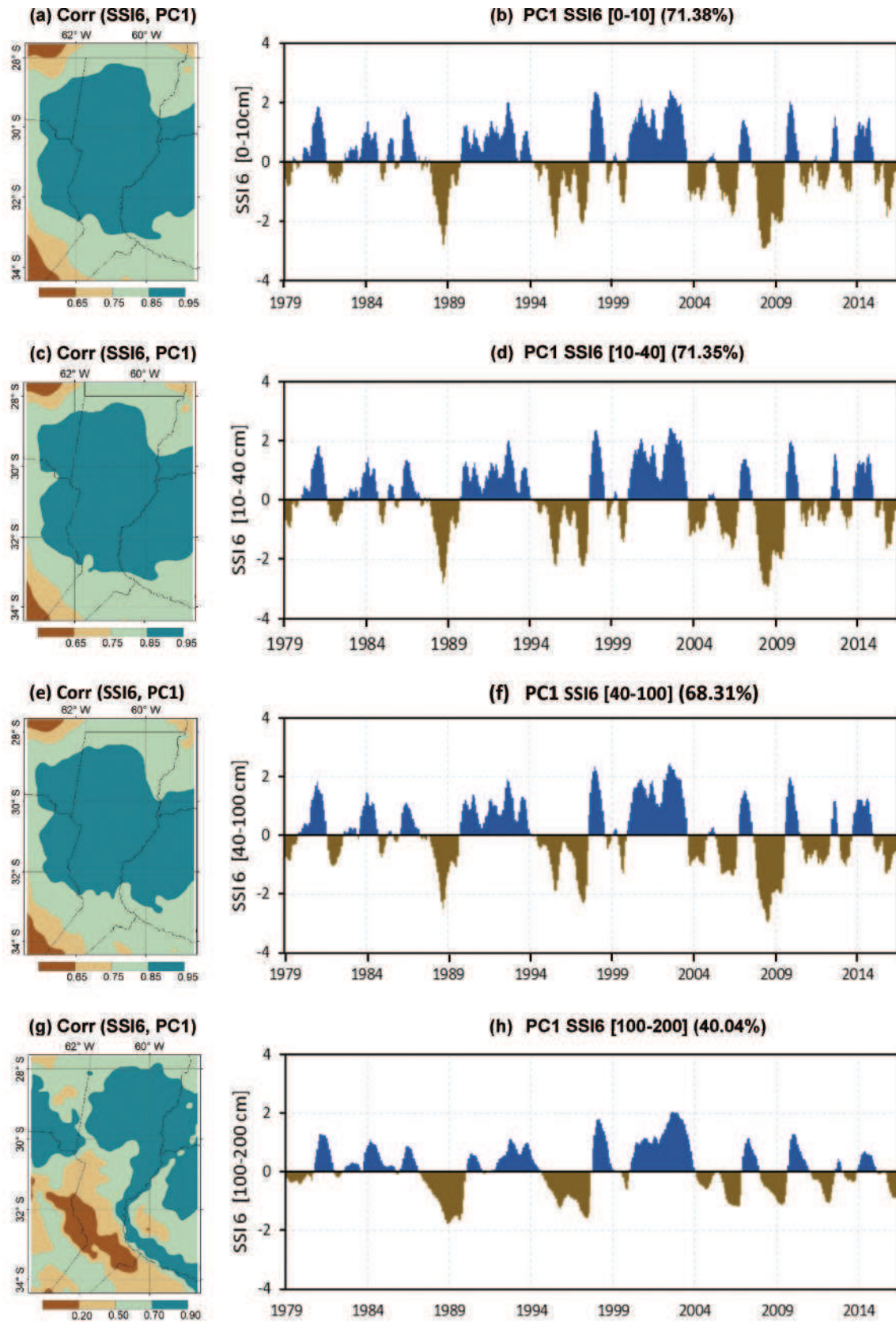


Figure 5. Panels (a), (c), (e), and (g) show the spatial distribution of the correlation between the first principal component time series (PC1) in (b), (d), (f), and (h) and each time series of SSI6 at soil depths of 0–10, 10–40, 40–100, and 100–200 cm at a single grid point in the 1901–2016 period. The percentage of explained variance is given in brackets. SSI6 refers to the Standardized Soil Moisture Index at 6-month time scale.

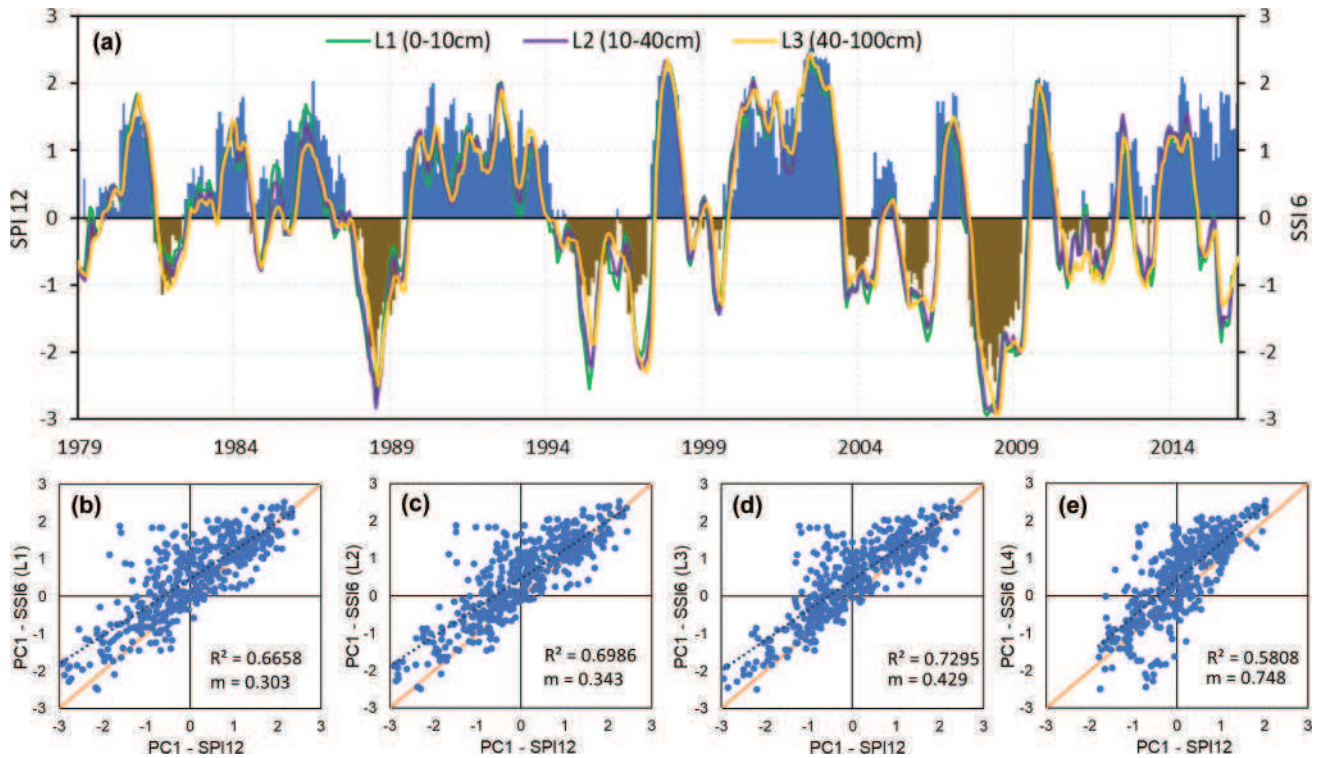


Figure 6. (a) Time series of SS16 (lines) at different soil depths ($L1 = 0\text{--}10\text{ cm}$, $L2 = 10\text{--}40\text{ cm}$, $L3 = 40\text{--}100\text{ cm}$) and SPI12 (bars) in the 1979–2016 period. Panels (b–e) show the scatter plot of SPI12 and SS16 at different depths. SPI12 refers to the Standardized Precipitation Index at 12-month time scale and SS16 refers to the Standardized Soil Moisture Index at 6-month time scale. The linear regression line (dashed lines) is plotted, and its slope m is presented together with the coefficient of determination (R^2) in the bottom right corner of each scatter plot.

Table 3. Significant variability modes and their corresponding percentage of explained variance obtained by applying SSA to the first principal component (PC1) time series of the standardized soil moisture index (SSI) and to the standardized precipitation index (SPI) at different time scales.

| Time scale (months) | 3 | | 6 | | 12 | | 24 | | |
|------------------------|------------|---------------------------------------|------------------------|-------|---------------------------------------|------------------------|-------|---------------------------------------|------------------------|
| | Index | Trend or dominant period (year/cycle) | Explained variance (%) | Index | Trend or dominant period (year/cycle) | Explained variance (%) | Index | Trend or dominant period (year/cycle) | Explained variance (%) |
| SPI | | 9.3 | 12.1 | | 9.2 | 16.3 | | 9.1 | 20.7 |
| | | 4.0 | 9.0 | | 4.0 | 14.2 | | 3.9 | 24.8 |
| | | 2.3 | 9.9 | | 2.3 | 16.9 | | 2.3 | 18.4 |
| SSI | 0–10 cm | 9.9 | 23.0 | 9.9 | 28.4 | 9.7 | 39.6 | 9.4 | 59.1 |
| | | 4.3 | 6.4 | | 4.2 | 14.4 | | 4.2 | 17.4 |
| | | 2.3 | 16.4 | | 2.3 | 19.4 | | 2.3 | 15.2 |
| SSI | 10–40 cm | 9.9 | 24.2 | 9.9 | 30.2 | 9.7 | 30.2 | 9.4 | 61.8 |
| | | 4.3 | 11.8 | | 4.2 | 13.3 | | 4.2 | 19.5 |
| | | 2.3 | 17.6 | | 2.3 | 19.5 | | 2.3 | 13.3 |
| SSI | 40–100 cm | 9.9 | 25.2 | 9.9 | 28.7 | 9.7 | 38.8 | 9.4 | 57.9 |
| | | 4.3 | 12.6 | | 4.2 | 14.2 | | 4.2 | 18.0 |
| | | 2.3 | 18.1 | | 2.3 | 19.5 | | 2.3 | 14.7 |
| SSI | 100–200 cm | 9.9 | 35.9 | 9.7 | 37.7 | 9.7 | 43.7 | 9.4 | 58.8 |
| | | 5.0 | 15.6 | | 4.2 | 17.8 | | | |
| | | 2.3 | 12.7 | | 2.3 | 12.6 | | | |

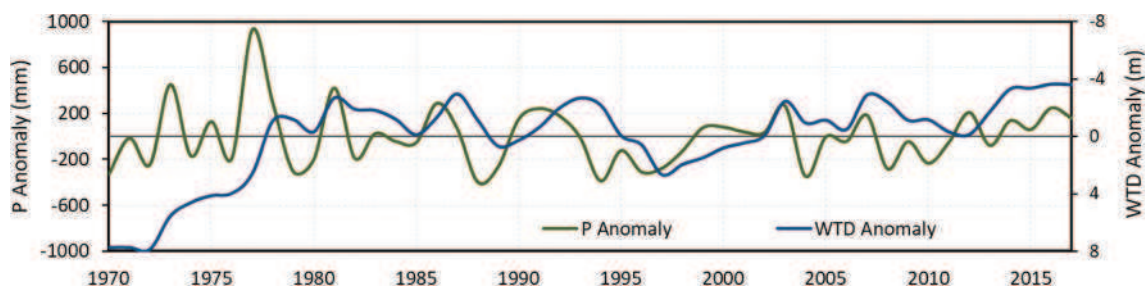


Figure 7. Time series of precipitation (P) and water table depth (WTD) anomalies in the Rafaela station for the 1970–2017 time period.

Figure 7 shows how the water table depth responds to precipitation variability, i.e. dry/wet anomalies of precipitation cause increases/decreases in the water table depth. Figure 7 also indicates that the response of the water table depth to precipitation has not been the same for different EPEs. In recent decades, the water table depth rapidly became shallower in response to excess precipitation and took longer to deepen during and after drought events. Pal *et al.* (2021) found that the inter-annual variability of water table depth is partially linked to inter-annual climate variability, and it is partially related to the vegetation type. Thus, land cover changes not only may have partially induced the decrease in the water table depth, as discussed above, but also may have affected its response capacity for precipitation deficits or excesses.

Fig. 8 presents the SPI and SSI categories on the time scales of 1, 3, 6, 12, and 24 months, together with the SGI on a 3-month time scale, at the Rafaela Station. Figure 8 highlights the behaviour of the saturated zone (through the SGI) in response to precipitation extremes (SPI) and their passage through the unsaturated zone (SSI). The results are similar to those shown in Section 3. The standardized indices identify nine wet events and four dry events of different intensity (see Table 4). The response of soil moisture and the water table depth to EPEs delays as soil depth increases. Figure 8 indicates an average delay of 10 months in the water table depth, as characterized by the SGI3. This result is consistent with what was found by Han *et al.* (2019), who reported that the spread of meteorological drought to groundwater is slow (close to 8 months). Note that



Figure 8. Categorization of extreme events according to the Standardized Precipitation Index (SPI) and Standardized Soil Moisture Index (SSI) and the Standardized Groundwater Level Index (SGI) values in the 1979–2016 period for the Rafaela station. Index time scales are 1, 3, 6, 12 and 24 months. SSI are computed in each soil layer (0–10, 10–40, 40–100, 100–200 cm). Shades in red (blue) represent the intensity of dry (wet) events according to Table 1.

Table 4. Summary of extreme events detected in the 1979–2016 period at the Rafaela station. In this study, an extreme event is categorized following Table 1 if it exceeds the threshold in at least 6 consecutive months.

| DRY EVENTS | | | WET EVENTS | | | |
|-------------|---------|--------|------------|--------|---------|-------------|
| EXCEPTIONAL | EXTREME | SEVERE | MODERATE | SEVERE | EXTREME | EXCEPTIONAL |
| 1988 | 1995 | 2013 | 1991 | 1986 | 1984 | 1981 |
| 2008 | | | | 2010 | 2007 | 1998 |
| | | | | 2014 | | 2002 |

the SGI3 acquires lower intensities than the SSI on different time scales and depths, mainly in drought events (see e.g. the 2008–2009 drought in Fig. 8). This may be due to two conditions: (1) the attenuation effect of droughts as they spread through the underground (e.g. Hisdal and Tallaksen 2000, Van Loon 2015); and (2) the significant decrease in water table depth that occurred in the 1970s (see Fig. 7). The decreased water table depth may condition the calculation of the SGIs, mainly abating the intensity of the SGI dry categories.

5.2 Temporal variability of SPI, SSI, and SGI

We applied the SSA method to study the temporal variability of the combination of indices with the highest correlation – that is, SPI12 (1901–2016 period), SSI6 (at 10–40 cm depth, 1979–2016 period), and SGI3 (1970–2017 period). Figure 9 and Table 5

show that the time series of SPI12 and SSI6 are mostly influenced by inter-annual variability, with dominant cycles of 6.5 and 4.3 years for SPI12 (explaining 37% of the variance of the SPI12 time series), and of 4.3 years for SSI6 (explaining 22% of the variance of the SSI6 time series). The 4.3-year frequency is also replicated in the SGI3 time series, although with less explained variability. The SSI6 and SGI3 time series are mostly influenced by decadal variability (see Table 5). The SGI3 (Fig. 9 (c)) shows a trend modulated by the decadal variability. The trend in SGI3 explains 33% of the time series variability, and it is closely related to the water table depth decrease which took place in the 1970s. The decadal variability – here represented by a 10-year cycle that explains 26% and 31.5% of the SSI6 and SGI3 time series variability, respectively (see Table 5) – influences long-term dry periods as well as wet periods.

Figure 9 indicates that there is a consistent response of soil moisture and water table depth to EPEs. The SSI6 time series

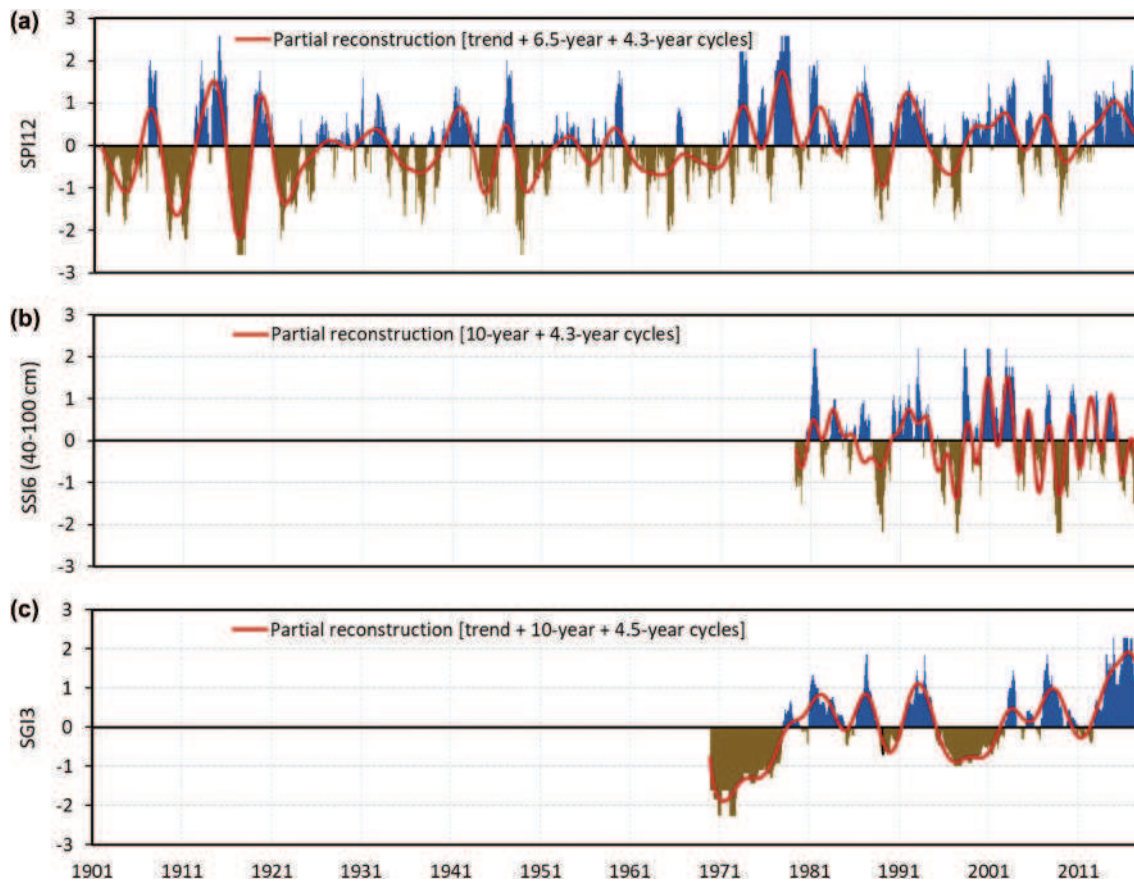


Figure 9. Time series of SPI12, SSI6 and SGI3 at the Rafaela station and their partial reconstructions (red lines) using the significant variability modes summarized in Table 5 (see also the reference in each panel). SPI12: Standardized Precipitation Index at 12-month time scale. SSI6: Standardized Soil Moisture Index at 6-month time scale. SGI3: Standardized Groundwater Level Index at 3-month time scale.

Table 5. Significant variability modes and their corresponding percentage of explained variance obtained by applying SSA to the time series of SPI12, SSI6 and SGI3 in the Rafaela station. SPI12: Standardized Precipitation Index at 12-month time scale. SSI6: Standardized Soil Moisture Index at 6-month time scale. SGI3: Standardized Groundwater Level Index at 3-month time scale.

| Index | Trend or dominant period (year/cycle) | Explained variance (%) |
|-------------------|---------------------------------------|------------------------|
| SPI12 | tr | 15,3 |
| | 6.5 | 27.5 |
| | 4.3 | 9.9 |
| SSI6 40–100 cm | 10.0 | 25.9 |
| | 4.3 | 22.7 |
| SGI3 | tr | 33.4 |
| | 10.0 | 31.5 |
| | 4.5 | 16.6 |

(Fig. 9(b)) correctly reflects the main dry/wet EPEs (Fig. 9(a)) in the 1979–2016 period. The SGI3 time series (Fig. 9(c)) shows a long period of negative values in the 1970s as a result of consecutive dry EPEs represented by SPI12 with consistent responses in SSI6. Later, in the 1980–1987 period, positive values of SGI3 are displayed, responding to dominant wet events in the upper levels of the soil, and in precipitation. These positive SGI3 values are interrupted in response to the mid-1990s droughts, when the SGI3 acquires negative values. Note that positive SGI3 values extend from 2002 to 2016 despite registering important water deficits in 2004, 2008, and in the mid-2010s, as shown by SPI12 and SSI6. These results suggest that the response of the water table depths to droughts has been modified, as discussed above.

6 Discussion and conclusions

The CCR of Argentina is one of the most productive agricultural areas in the world; therefore, it plays a strategic role in global food security. The CCR's agricultural production is almost entirely rainfed, so climate variability and extreme events directly impact crop yields. This study reassessed the spatiotemporal variability and the changes of EPEs since the beginning of the 20th century, and analysed the response of soil moisture and the water table depth to EPEs in Argentina's CCR during the 1979–2016 period. A multivariable study of extreme hydroclimatic events was performed using nonparametric standardized indices on different time scales, including an analysis of their spatial distribution, the direction of their trends, and the oscillatory cycles that characterize their temporal variability. Note that due to a lack of data with long time periods, the results referring to water table depth were conditioned to a study case at the Rafaela Station (towards the centre-west of the CCR).

The analysis of the long-term SPI time series showed a remarkable change in the 1970s: dry EPEs were more frequent and severe between 1901 and the 1970s, while wet EPEs predominated from the 1970s onwards. This change matches the 1970s climate shift in South America (Jacques-Coper and Garreaud 2015). In particular, northeastern Argentina has undergone a transition from dry and cooler decades to wet and warmer decades since the 1970s (Barreiro *et al.* 2014). Our results also indicate that water table depth decreased (i.e. it was closer to the soil surface) in the same decade. Decreased water table depths may have responded to the combined effect of increased precipitation and land use changes. At the same time, land use changes were induced by increased precipitation that favoured agriculture over regions previously relegated (Zak *et al.* 2008, Viglizzo *et al.* 2011). These joint changes reduced the soil infiltration capacity and increased surface runoff, leading to extraordinary floods since the 1970s and 2000s (Lovino *et al.* 2018b).

Our results revealed that the temporal variability of extreme events displayed by SPI, SSI and SGI is modulated by two variability bands: a near-decadal cycle and an inter-annual variability band with dominant periods of 2.5–4 years. The inter-annual variability band corresponds to ENSO-like frequencies. This relationship is well known for precipitation (e.g. Grimm *et al.* 2000, Garreaud *et al.* 2009,

Lovino *et al.* 2018b, Cai *et al.* 2020). The near-decadal cycle seems to be related to the North Atlantic Oscillation (Robertson and Mechoso 1998, Robertson *et al.* 2001). The Pacific Decadal Oscillation (PDO, Mantua and Hare 2002) and the Atlantic Multidecadal Oscillation (AMO, Enfield *et al.* 2001) also play a key role, modulating the ENSO intensity (Reboita *et al.* 2021). Warm (cold) phases of the PDO and cold (warm) phases of the AMO favour wet (dry) anomalies in decadal time scales over northeastern Argentina (Seager *et al.* 2010, Wang *et al.* 2014, Lovino *et al.* 2018b). The combined analysis of SPI, SSI, and SGI revealed that the soil moisture and the water table depth respond to precipitation, replicating the ENSO-like and near-decadal variability frequencies. The near-decadal variability showed the highest relevance in the soil response to precipitation, for it explained increasing percentages of variance in the SSI time series in all soil layers (from near 25–30% to almost 60%) as the index time scale rose.

When soil depth increases, soil moisture has an attenuated response to EPEs. Thus, water table depth, as characterized by SGI3, responds with a 10-month delay to EPEs. The soil moisture and water table depth responses are not the same for each of the EPEs, mainly because they are strongly conditioned by the soil moisture content prior to the EPEs (Pántano *et al.* 2022). However, our results revealed a common behaviour that was exacerbated in recent decades. Soil moisture increases (water table level becomes shallower) fast in response to excess precipitation, and takes longer to decrease (water table level deepens) during and after drought events. This modified response could be partially explained by land cover changes – the replacement of perennial crops by annual crops – that affected groundwater dynamics, favouring higher recharges and shallower water table depths (Pal *et al.* 2021). Due to their influence in the formation or attenuation of droughts or floods, water table depth and soil moisture content proved to be critical information for regional decision systems. We expect that this multivariate approach will help to clarify the development of extreme hydroclimatic events in the CCR, by providing information to improve the planning of water managers and agricultural stakeholders.

Acknowledgements

The authors are grateful to all the anonymous reviewers for their constructive comments and recommendations that improved this article. AB has received funding from the Education and Training Program of the World Meteorological Organization for the completion of a master's degree in water resources engineering at FICH-UNL, Argentina.

Disclosure statement

No potential conflict of interest was reported by the authors.

Funding

This research was supported by the National Agency for Scientific and Technological Promotion of Argentina, under Grants PICT-2019-2019-03982 and PICT-2019-2019-00481; by the Universidad Nacional del Litoral, under Grant CAI+D-2020-50620190100082LI; and by the Argentine National Council for Scientific and Technical Research,

under Grant PIP 11220200102257CO Consejo Nacional de Investigaciones Científicas y Técnicas.

ORCID

Anelim Bernal-Mujica  <http://orcid.org/0000-0003-4834-3208>
 Miguel A. Lovino  <http://orcid.org/0000-0002-8558-6324>
 Gabriela V. Müller  <http://orcid.org/0000-0003-3843-9089>
 M. Josefina Pierrestegui  <http://orcid.org/0000-0001-8312-7426>

References

- AghaKouchak, A., 2015. A multivariate approach for persistence-based drought prediction: application to the 2010–2011 East Africa drought. *Journal of Hydrology*, 526, 127–135. doi:10.1016/j.jhydrol.2014.09.063
- Allen, M.R. and Robertson, A.W., 1996. Distinguishing modulated oscillations from coloured noise in multivariate datasets. *Climate Dynamics*, 12 (11), 775–784. doi:10.1007/s003820050142
- Avila-Diaz, A., et al., 2020. Assessing current and future trends of climate extremes across Brazil based on reanalyses and earth system model projections. *Climate Dynamics*, 55 (5–6), 1403–1426. doi:10.1007/s00382-020-05333-z
- Barreiro, M., Díaz, N., and Renom, M., 2014. Role of the global oceans and land-atmosphere interaction on summertime interdecadal variability over northern Argentina. *Climate Dynamics*, 42 (7–8), 1733–1753. doi:10.1007/s00382-014-2088-6
- Barros, V.R., et al., 2015. Climate change in Argentina: trends, projections, impacts and adaptation. *Wiley Interdisciplinary Reviews. Climate Change*, 6 (2), 151–169.
- Beck, H.E., et al., 2018. Present and future Köppen-Geiger climate classification maps at 1-km resolution. *Scientific Data*, 5 (1), 180214. doi:10.1038/sdata.2018.214
- Berri, G., et al., 2002. Some effects of La Niña on summer rainfall, water resources, and crops in Argentina. In: M.H. Glantz, ed. *La Niña and its impacts: facts and speculation*. New York: United Nations University Press, 124–133.
- Bloomfield, J.P. and Marchant, B.P., 2013. Analysis of groundwater drought building on the standardised precipitation index approach. *Hydrology and Earth System Sciences*, 17 (12), 4769–4787. doi:10.5194/hess-17-4769-2013
- Bloomfield, J.P., et al., 2015. Regional analysis of groundwater droughts using hydrograph classification. *Hydrology and Earth System Sciences*, 19 (10), 4327–4344. doi:10.5194/hess-19-4327-2015
- Boulanger, J.P., et al., 2005. Observed precipitation in the Paraná-Plata hydrological basin: long-term trends, extreme conditions and ENSO teleconnections. *Climate Dynamics*, 24 (4), 393–413. doi:10.1007/s00382-004-0514-x
- Cai, W., et al., 2020. Climate impacts of the El Niño–Southern Oscillation on South America. *Nature Reviews Earth and Environment*, 1 (4), 215–231. doi:10.1038/s43017-020-0040-3
- Carril, A.F., et al., 2016. Extreme events in the La Plata basin: a retrospective analysis of what we have learned during CLARIS-LPB project. *Climate Research*, 68 (2–3), 95–116. doi:10.3354/cr01374
- Cavalcanti, I.F.A., et al., 2015. Precipitation extremes over La Plata Basin – review and new results from observations and climate simulations. *Journal of Hydrology*, 523, 211–230. doi:10.1016/j.jhydrol.2015.01.028
- Cérón, W.L., et al., 2021. Recent intensification of extreme precipitation events in the La Plata Basin in Southern South America (1981–2018). *Atmospheric Research*, 249, 105299. doi:10.1016/j.atmosres.2020.105299
- Chen, N., et al., 2020. Drought propagation in Northern China Plain: a comparative analysis of GLDAS and MERRA-2 datasets. *Journal of Hydrology*, 588 (588), 125026. doi:10.1016/j.jhydrol.2020.125026
- de Los Milagros Skansi, M., et al., 2013. Warming and wetting signals emerging from analysis of changes in climate extreme indices over South America. *Global and Planetary Change*, 100, 295–307. doi:10.1016/j.gloplacha.2012.11.004
- Déqué, M., 2012. Deterministic forecasts of continuous variables. In: I.T. Jolliffe and D.B. Stephenson, eds. *Forecast verification: a practitioner's guide in atmospheric science*. 2nd ed. Chichester, UK: John Wiley & Sons, 77–94.
- Dracup, J.A., Lee, K.S., and Paulson, E.G. 1980. On the definition of droughts. *Water Resources Research*, 16 (2), 297–302. doi:10.1029/WR016i002p00297
- El Informe, 28 Jan 2019. *La Bolsa de Rosario estima en 230 millones de dólares las pérdidas de ingresos por las inundaciones*. El Informe. Available from: <https://www.diarioelinforme.com.ar/2019/01/28/la-bolsa-de-rosario-estima-en-230-millones-de-dolares-las-perdidas-de-ingresos-por-las-inundaciones> [Accessed 22 Jan 2022]. (In Spanish).
- Enfield, D.B., Mestas-Nuñez, A.M., and Trimble, P.J., 2001. The Atlantic multidecadal oscillation and its relation to rainfall and river flows in the continental U.S. *Geophysical Research Letters*, 28 (10), 2077–2080. doi:10.1029/2000GL012745
- Entekhabi, D., Rodriguez-Iturbe, I., and Castelli, F., 1996. Mutual interaction of soil moisture state and atmospheric processes. *Journal of Hydrology*, 184 (1–2), 3–17. doi:10.1016/0022-1694(95)02965-6
- Farahmand, A. and AghaKouchak, A., 2015. A generalized framework for deriving nonparametric standardized drought indicators. *Advances in Water Resources*, 76, 140–145. doi:10.1016/j.advwatres.2014.11.012
- Fischer, T., Byerlee, D., and Edmeades, G., 2014. *Crop yields and global food security: will yield increase continue to feed the world?* Canberra: Australian Centre for International Agricultural Research, xxii + 634.
- Folland, C.K., et al., 2015. Multi-annual droughts in the English Lowlands: a review of their characteristics and climate drivers in the winter half-year. *Hydrology and Earth System Sciences*, 19 (5), 2353–2375. doi:10.5194/hess-19-2353-2015
- Garreaud, R.D., et al., 2009. Present-day South American climate. *Palaeogeography, Palaeoclimatology, Palaeoecology*, 281 (3–4), 180–195. doi:10.1016/j.palaeo.2007.10.032
- Ghil, M., et al., 2002. Advanced spectral methods for climatic time series. *Reviews of Geophysics*, 40 (1), 3–1–3–41. doi:10.1029/2000RG000092
- Grimm, A.M., 2011. Interannual climate variability in South America: impacts on seasonal precipitation, extreme events, and possible effects of climate change. *Stochastic Environmental Research and Risk Assessment*, 25 (4), 537–554. doi:10.1007/s00477-010-0420-1
- Grimm, A.M., Barros, V.R., and Doyle, M.E., 2000. Climate variability in Southern South America associated with El Niño and La Niña events. *Journal of Climate*, 13 (1), 35–58. doi:10.1175/1520-0442(2000)013<0035:CVISSA>2.0.CO;2
- Gringorten, I.I., 1963. A plotting rule for extreme probability paper. *Journal of Geophysical Research*, 68 (3), 813–814. doi:10.1029/JZ068i003p00813
- Grings, F., et al., 2015. Validation strategies for satellite-based soil moisture products over Argentine Pampas. *IEEE Journal of Selected Topics in Applied Earth Observations and Remote Sensing*, 8 (8), 4094–4105. doi:10.1109/JSTARS.2015.2449237
- Han, Z., et al., 2019. Propagation dynamics from meteorological to groundwater drought and their possible influence factors. *Journal of Hydrology*, 578, 124102. doi:10.1016/j.jhydrol.2019.124102
- Hao, Z. and AghaKouchak, A., 2013. Multivariate standardized drought index: a parametric multi-index model. *Advances in Water Resources*, 57, 12–18. doi:10.1016/j.advwatres.2013.03.009
- Hao, Z. and AghaKouchak, A., 2014. A nonparametric multivariate multi-index drought monitoring framework. *Journal of Hydrometeorology*, 15 (1), 89–101. doi:10.1175/JHM-D-12-0160.1
- Hao, Z., et al., 2014. Global integrated drought monitoring and prediction system. *Scientific Data*, 1 (1), 140001. doi:10.1038/sdata.2014.1
- Harris, I., et al., 2020. Version 4 of the CRU TS monthly high-resolution gridded multivariate climate dataset. *Scientific Data*, 7 (1), 109. doi:10.1038/s41597-020-0453-3
- Hisdal, E.H. and Tallaksen, L.M., 2000. *Drought event definition*. Oslo, Norway: Department of Geophysics, University of Oslo.
- Hoegh-Guldberg, O., et al. (2018). *Impacts of 1.5°C global warming on natural and human systems*. *Global Warming of 1.5°C*. An IPCC special report on the impacts of global warming of 1.5°C above pre-industrial levels and related global greenhouse gas emission pathways, in the context of strengthening the global response to the threat of climate change. Edited by T. Waterfield Masson-Delmotte, et al. IPCC, in press.



- Holzman, M.E. and Rivas, R.E., 2016. Early maize yield forecasting from remotely sensed temperature/vegetation index measurements. *IEEE Journal of Selected Topics in Applied Earth Observations and Remote Sensing*, 9 (1), 507–519. doi:10.1109/JSTARS.2015.2504262
- IUSS Working Group WRB, 2015. *World reference base for soil resources 2014, update 2015*. Prepared by Schad P., van Huyssteen C., Micheli E. 192. World Soil Resources Reports No. 106, FAO, Rome. Available from: <http://www.fao.org/soils-portal/soil-survey/soil-classification/world-reference-base/en/> [Accessed 10 May 2022].
- Jacques-Coper, M. and Garreaud, R.D., 2015. Characterization of the 1970s climate shift in South America. *International Journal of Climatology*, 35 (8), 2164–2179. doi:10.1002/joc.4120
- Jobbagy, E., et al., 2008. The ecohydrological challenge of woody-herbaceous transitions in the Chaco-Pampas plains. *Ecología Austral*, 18 (3), 305–322.
- Krepper, C.M. and García, N.O., 2004. Spatial and temporal structures of trends and interannual variability of precipitation over the La Plata Basin. *Quaternary International*, 114 (1), 11–21. doi:10.1016/S1040-6182(03)00038-7
- Krepper, C.M., García, N.O., and Jones, P.D., 2006. Paraguay river basin response to seasonal rainfall. *International Journal of Climatology*, 26 (9), 1267–1278. doi:10.1002/joc.1313
- Krepper, C.M. and Zucarelli, G., 2010. Climatology of water excesses and shortages in the La Plata Basin. *Theoretical and Applied Climatology*, 102 (1), 13–27. doi:10.1007/s00704-009-0234-6
- Kumar, R., et al., 2016. Multiscale evaluation of the standardized precipitation index as a groundwater drought indicator. *Hydrology and Earth System Sciences*, 20 (3), 1117–1131. doi:10.5194/hess-20-1117-2016
- La Nación, 17 Jan 2017. *Inundaciones: pronostican pérdidas para el campo de hasta U\$S 1750 millones*. La Nación. Available from: <http://www.lanacion.com.ar/1976462-inundaciones-pronostican-perdidas-para-el-campo-de-hasta-us-1750-millones> [Accessed 16 Mar 2022]. (In Spanish).
- Laing, A.G. and Fritsch, J.M., 2000. The large-scale environments of the global populations of mesoscale convective complexes. *Monthly Weather Review*, 128 (8), 2756–2776. doi:10.1175/1520-0493(2000)128<2756:TLSEOT>2.0.CO;2
- Llano, M.P. and Penalba, O.C., 2011. A climatic analysis of dry sequences in Argentina. *International Journal of Climatology*, 31 (4), 504–513. doi:10.1002/joc.2092
- Lloyd-Hughes, B. and Saunders, M.A., 2002. A drought climatology for Europe. *International Journal of Climatology*, 22 (13), 1571–1592. doi:10.1002/joc.846
- Lovino, M.A., et al., 2018a. How have daily climate extremes changed in the recent past over northeastern Argentina? *Global and Planetary Change*, 168, 78–97. doi:10.1016/j.gloplacha.2018.06.008
- Lovino, M.A., et al., 2018b. Interannual-to-multidecadal hydroclimate variability and its sectoral impacts in northeastern Argentina. *Hydrology and Earth System Sciences*, 22 (6), 3155–3174. doi:10.5194/hess-22-3155-2018
- Lovino, M.A., et al., 2022. Extreme precipitation events in the Austral Chaco region of Argentina. *International Journal of Climatology*, 42 (11), 5985–6006. doi:10.1002/joc.7572
- Lovino, M.A., García, N.O., and Baethgen, W., 2014. Spatiotemporal analysis of extreme precipitation events in the Northeast region of Argentina (NEA). *Journal of Hydrology: Regional Studies*, 2, 140–158.
- Mallenahalli, N.K., 2020. Comparison of parametric and nonparametric standardized precipitation index for detecting meteorological drought over the Indian region. *Theoretical and Applied Climatology*, 142 (1), 219–236. doi:10.1007/s00704-020-03296-z
- Mantua, N.J. and Hare, S.R., 2002. The Pacific decadal oscillation. *Journal of Oceanography*, 58 (1), 35–44. doi:10.1023/A:1015820616384
- McKee, T.B., Doesken, N.J., and Kleist, J., 1993. The relationship of drought frequency and duration to time scales. In: *Proceedings of the 8th Conference on Applied Climatology*. Boston, MA: American Meteorological Society, 179–183.
- Meng, J., et al., 2012. The land surface analysis in the NCEP climate forecast system reanalysis. *Journal of Hydrometeorology*, 13 (5), 1621–1630. doi:10.1175/JHM-D-11-090.1
- Mercau, J.L., et al., 2016. Shallow groundwater dynamics in the Pampas: climate, landscape and crop choice effects. *Agricultural Water Management*, 163, 159–168. doi:10.1016/j.agwat.2015.09.013
- Müller, G.V., Lovino, M.A., and Sgroi, L.C., 2021. Observed and projected changes in temperature and precipitation in the core crop region of the Humid Pampa, Argentina. *Climate 2021*, Vol. 9, Page 40, 9 (3), 40.
- Muthuvel, D. and Mahesha, A., 2021. Spatiotemporal analysis of compound agrometeorological drought and hot events in India using a standardized index. *Journal of Hydrologic Engineering*, 26 (7), 04021022. doi:10.1061/(ASCE)HE.1943-5584.0002101
- Naumann, G., et al., 2021. *The 2019–2021 extreme drought episode in La Plata Basin*. Luxembourg: Publications Office of the European Union, EUR 30833 EN.
- Pal, S., et al., 2021. Investigating the effects of land use change on subsurface, surface, and atmospheric branches of the hydrologic cycle in central Argentina. *Water Resources Research*, 57 (11), e2021WR029704. doi:10.1029/2021WR029704
- Pántano, V.C., et al., 2022. ENSO signal on subseasonal precipitation distribution and soil moisture response in the Argentine Pampas. *Pure and Applied Geophysics*, 179 (2), 879–896. doi:10.1007/s0024-022-02949-6
- Penalba, O.C. and Robledo, F.A., 2009. Spatial and temporal variability of the frequency of extreme daily rainfall regime in the La Plata Basin during the 20th century. *Climatic Change*, 98 (3), 531–550. doi:10.1007/s10584-009-9744-6
- Penalba, O.C. and Vargas, W.M., 2004. Interdecadal and interannual variations of annual and extreme precipitation over central-northeastern Argentina. *International Journal of Climatology*, 24 (12), 1565–1580. doi:10.1002/joc.1069
- Reboita, M.S., et al., 2021. Impacts of teleconnection patterns on South America climate. *Annals of the New York Academy of Sciences*, 1504 (1), 116–153. doi:10.1111/nyas.14592
- Rivera, J.A., Penalba, O.C., and Bettolli, M.L., 2013. Inter-annual and inter-decadal variability of dry days in Argentina. *International Journal of Climatology*, 33 (4), 834–842. doi:10.1002/joc.3472
- Robertson, A.W. and Mechoso, C.R., 1998. Interannual and decadal cycles in river flows of Southeastern South America. *Journal of Climate*, 11 (10), 2570–2581. doi:10.1175/1520-0442(1998)011<2570:IADCIR>2.0.CO;2
- Robertson, A.W., Mechoso, C.R., and Garcia, N.O., 2001. Interannual prediction of the Paraná River. *Geophysical Research Letters*, 28 (22), 4235–4238. doi:10.1029/2000GL012197
- Robledo, F., Vera, C., and Penalba, O., 2020. Multi-scale features of the co-variability between global sea surface temperature anomalies and daily extreme rainfall in Argentina. *International Journal of Climatology*, 40 (9), 4289–4299. doi:10.1002/joc.6462
- Rodell, M., et al., 2004. The global land data assimilation system. *Bulletin of the American Meteorological Society*, 85 (3), 381–394. doi:10.1175/BAMS-85-3-381
- Ruscica, R.C., et al., 2022. Evapotranspiration trends and variability in southeastern South America: the roles of land-cover change and precipitation variability. *International Journal of Climatology*, 42 (4), 2019–2038. doi:10.1002/joc.7350
- Saurral, R.I., Camilloni, I.A., and Barros, V.R., 2017. Low-frequency variability and trends in Centennial precipitation stations in Southern South America. *International Journal of Climatology*, 37 (4), 1774–1793. doi:10.1002/joc.4810
- Schneider, U., et al., 2018. GPCC full data monthly product version 2018 at 0.25°: monthly Land-Surface precipitation from rain-gauges built on GTS-based and historical data.
- Seager, R., et al., 2010. Tropical oceanic causes of interannual to multidecadal precipitation variability in Southeast South America over the past century. *Journal of Climate*, 23 (20), 5517–5539. doi:10.1175/2010JCLI3578.1
- Seneviratne, S., et al., 2012. Changes in climate extremes and their impacts on the natural physical environment. In: C.B. Field, et al., eds. *Managing the risks of extreme events and disasters to advance climate change adaptation. A Special report of working groups I and II of the Intergovernmental Panel on Climate Change (IPCC)*. Cambridge, UK: Cambridge University Press, 109–230.
- Seneviratne, S.I., et al., 2021. Weather and climate extreme events in a changing climate. In: V. MassonDelmotte, et al., eds. *Climate change 2021: the physical science basis. Contribution of working*

- group I to the sixth assessment report of the intergovernmental panel on climate change. Cambridge, UK: Cambridge University Press, 1513–1766.
- Sgroi, L.C., et al., 2021. Characteristics of droughts in Argentina's core crop region. *Hydrology and Earth System Sciences*, 25 (5), 2475–2490. doi:[10.5194/hess-25-2475-2021](https://doi.org/10.5194/hess-25-2475-2021)
- Siebert, S., et al., 2013. Update of the digital Global Map of Irrigation Areas (GMIA) to version 5. doi: [10.13140/2.1.2660.6728](https://doi.org/10.13140/2.1.2660.6728)
- Soláková, T., de Michele, C., and Vezzoli, R., 2014. Comparison between parametric and nonparametric approaches for the calculation of two drought indices: SPI and SSI. *Journal of Hydrologic Engineering*, 19 (9), 04014010. doi:[10.1061/\(ASCE\)HE.1943-5584.0000942](https://doi.org/10.1061/(ASCE)HE.1943-5584.0000942)
- Spennemann, P.C., et al., 2015. A comparison of GLDAS soil moisture anomalies against standardized precipitation index and multisatellite estimations over South America. *Journal of Hydrometeorology*, 16 (1), 158–171. doi:[10.1175/JHM-D-13-0190.1](https://doi.org/10.1175/JHM-D-13-0190.1)
- Spennemann, P.C., et al., 2020. Soil moisture evaluation over the Argentine Pampas using models, satellite estimations and in-situ measurements. *Journal of Hydrology: Regional Studies*, 31, 100723. doi:[10.1016/j.ejrh.2020.100723](https://doi.org/10.1016/j.ejrh.2020.100723)
- Thomasz, E.O., Vilker, A.S., and Rondinone, G., 2019. The economic cost of extreme and severe droughts in soybean production in Argentina. *Contaduria y Administracion*, 64, 1.
- Van Loon, A.F., 2015. Hydrological drought explained. *WIREs Water*, 2 (4), 359–392. doi:[10.1002/wat2.1085](https://doi.org/10.1002/wat2.1085)
- Vautard, R., 1999. Patterns in Time: SSA and MSSA. In: H. von Storch and A. Navarra, eds. *Analysis of Climate Variability*. Berlin, Heidelberg: Springer. doi:[10.1007/978-3-662-03744-7_14](https://doi.org/10.1007/978-3-662-03744-7_14)
- Vera, C.S., Vigliarolo, P.K., and Berbery, E.H., 2002. Cold season synoptic-scale waves over subtropical South America. *Monthly Weather Review*, 130 (3), 684–699. doi:[10.1175/1520-0493\(2002\)130<0684:CSSSWO>2.0.CO;2](https://doi.org/10.1175/1520-0493(2002)130<0684:CSSSWO>2.0.CO;2)
- Viglizzo, E.F., et al., 2011. Assessing the cross-scale impact of 50 years of agricultural transformation in Argentina. *Field Crops Research*, 124 (2), 186–194. doi:[10.1016/j.fcr.2011.05.014](https://doi.org/10.1016/j.fcr.2011.05.014)
- Von Storch, H. and Zwiers, W., 1999. *Statistical analysis in climate research*. Cambridge, UK: Cambridge University Press.
- Wang, S., et al., 2014. Combined effects of the Pacific decadal oscillation and El Niño-Southern oscillation on global land dry-wet changes. *Scientific Reports*, 4 (1), 1–8.
- Wilks, D., 2006. *Statistical methods in the atmospheric sciences*. UK: Elsevier Inc.
- Zak, M.R., et al., 2008. What drives accelerated land cover change in central Argentina? Synergistic consequences of climatic, socioeconomic, and technological factors. *Environmental Management*, 42 (2), 181–189. doi:[10.1007/s00267-008-9101-y](https://doi.org/10.1007/s00267-008-9101-y)
- Zellner, M., et al., 2020. Exploring reciprocal interactions between groundwater and land cover decisions in flat agricultural areas and variable climate. *Environmental Modelling and Software*, 126, 104641. doi:[10.1016/j.envsoft.2020.104641](https://doi.org/10.1016/j.envsoft.2020.104641)
- Zhang, X., et al., 2017. Droughts in India from 1981 to 2013 and implications to wheat production. *Scientific Reports*, 7 (1), 1–12. doi:[10.1038/s41598-016-0028-x](https://doi.org/10.1038/s41598-016-0028-x)